A seismic study of the Krafla volcanic system, Iceland

Stuart K. Arnott

A Seismic Study of the Krafla Volcanic System, Iceland

by

Stuart K. Arnott

A Thesis submitted in partial fulfilment
of the requirements for the degree of
Doctor of Philosophy

Department of Geological Sciences

The University of Durham
1990

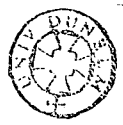

Abstract

Following a major crustal rifting episode centred on the Krafla volcanic system in Northeast Iceland, the local seismicity was monitored for three months using a dense network of single component seismometers.

Initial earthquake locations were computed for 489 local events using a one–dimensional velocity model derived from seismic refraction data. Activity was concentrated in clusters beneath a geothermal area within the Krafla caldera and below the Bjarnarflag geothermal well field to the south, and in a narrow linear zone coincident with a site of recent dyke injection. Events of magnitudes –2.4 to 2.1 were located. The b–value for the entire dataset is 0.77 ± 0.10, and is lower for events at Bjarnarflag than for events in the dyke injection zone. Seismicity was continuous.

A simultaneous inversion of 1771 P–wave arrival times was carried out to calculate the 3–d velocity structure and refine hypocentral locations. The derivative weight sum was used to identify the well–resolved volume. High velocity bodies at depth beneath the rim of the caldera are high density intrusives, probably gabbros. Volumes of low velocity coincide with zones of geothermal exploitation within the caldera and beneath Bjarnarflag, and result from intense fracturing and hydrothermal alteration. After relocation through the three–dimensional velocity structure, the spatial distribution of hypocentres is more focussed and considerably shallower than before. This led to a closer correlation between zones of seismicity and detailed features within the source volumes, such as geothermal reservoirs, fault surfaces and zones of known recent magmatic intrusion.

Focal mechanisms were determined using P–wave polarity data for 153 of the best located earthquakes, of which 139 have double couple solutions. Fourteen events were non–double couple, 4 of which could be solved as either opening or closing tensile cracks assuming small circle nodal lines. The biasing effect of using incorrect hypocentres and an over–simplified velocity structure were investigated by 3–d ray tracing. The effects on ray angles are large and variable. The impact of these effects on double couple solutions is generally small, but can be critical for the confident identification of non–double couple events.

Seismicity in geothermal areas results from cooling and fracturing of hot intrusives at depth, and fault surfaces are marked by enhanced seismicity when they provide efficient migratory paths for geothermal fluids. Seismicity may be induced partially by geothermal mining.

The stress field in the Krafla volcanic system at the time of the survey was variable along its length, as was the mode of fracturing. The stress field at Bjarnarflag was chaotic. In the geothermal area within the caldera σ_3 was perpendicular to the plate boundary, and in the dyke injection zone σ_1 was perpendicular to the plate boundary. Such heterogeneity in the stress field is contrary to what might be expected at a spreading axis, and is attributed to variation in regional extensional stress release during the recent rifting episode.

Acknowledgements

I wish to thank the following individuals and institutions for their support during this research project : –

My supervisors, Drs. Gill Foulger and Roger Long, for their enthusiastic and stimulating scientific guidance throughout my research, and their thorough criticisms of earlier drafts of this thesis.

Dave Stevenson, for solving many of my computing difficulties, enduring my incessant pestering, and getting the 'Versatec man' out on time !

Dave Asbery, for easing innumerable day–to–day problems. Thanks also to Carol Blair, Karen Atkinson, George Ruth, Alan Carr and Paul Laverick for additional logistical support.

Bruce Julian, of U.S.G.S., Menlo Park, for providing software and advice on its application, without which parts of this research would not have been possible. Additional thanks to Andy Michael of the same institute for providing software to plot focal mechanisms, and Doug Toomey of the University of Oregon for general advice on tomography.

Bryndís Brandsdóttir and Páll Einarsson, of the University of Iceland, for information and advice relating to the seismicity of Krafla, and for my inclusion in the Askja project, 1989. Thanks also to those at the Icelandic Meteorological Office, for giving me the opportunity to participate in the Nordic South Iceland seismic project, 1988. I am especially indebted to Bryndís Brandsdóttir and Bardi Thorkelsson for their generous personal help while in Iceland.

The Natural Environmental Research Council, for financial support.

Chris Roberts, for proof reading this thesis and making such a *pure dead brilliant* job of it. Also, thanks to all the postgrads in the department, for keeping me entertained for the last three years.

Finally, and above all, I am deeply grateful to my wife Heather for her constant support and encouragement. I dedicate this thesis to her.

Declaration

I declare that this thesis, which I submit for the degree of Doctor of Philosophy at the University of Durham, is my own work and is not substantially the same as any which has previously been submitted for a degree at this or another university.

Stuart K. Arnott

University of Durham

November 1990

Contents

Abstract ..... (i)
Acknowledgements ..... (ii)
Declaration ..... (iii)
Contents ..... (iv)

1 Iceland : Structure and Tectonic Evolution 1
1.1 Introduction 1
1.2 Geology 3
1.2.1 Introduction 3
1.2.2 Axial Rift Zones 3
1.2.3 Flank Zones 5
1.2.4 The Volcanic Pile of Iceland 5
1.3 Geophysics 7
1.3.1 The Seismicity of Iceland 7
1.3.2 The Seismic Structure of the Icelandic Lithosphere 9
1.3.3 Other Geophysical Research 14
1.4 The Evolution of Iceland 16
1.4.1 The Icelandic Hotspot 16
1.4.2 The Evolution of the Icelandic Platform 16
1.4.3 The Evolution of the Plate Boundary on Iceland 20
1.5 Summary 24

2 The Krafla Volcanic System 27
2.1 The Plate Boundary in Northeast Iceland 27
2.2 The Krafla Area 29
2.2.1 Geology 29
2.2.2 Subsurface Geological Investigations 33
2.2.3 Geophysical Research 39
2.3 The Recent Rifting Episode in the Krafla Area 45
2.3.1 Introduction 45
2.3.2 The First Event 46
2.3.3 Subsequent Activity 47

2.3.4 Dyke Injection 54
2.3.5 Dynamics of Crustal Rifting 58
2.3.6 Comparisons with other Spreading Systems 59
2.3.6.1 Other Systems in the Northern Volcanic Zone 59
2.3.6.2 Afar 60
2.3.6.3 The Sea Floor 61
2.4 Summary 63
2.4.1 Geology and Geophysics 63
2.4.2 Crustal Rifting 64

3 The Seismicity of the Krafla Volcanic System 66
3.1 The NISE Field Program 66
3.1.1 Introduction 66
3.1.2 Design 66
3.1.3 Equipment 70
3.1.4 Logistics 71
3.1.4.1 Out–Stations 71
3.1.4.2 Recording Stations 71
3.1.4.3 Maintenance 72
3.2 Data Playback 73
3.3 Local Earthquake Locations 75
3.3.1 The Earthquake Location Problem 75
3.3.2 Velocity Model 78
3.3.3 Location Procedure and Pitfalls 80
3.3.4 The Hypocentral Locator and Plotting System 84
3.3.5 Seismicity 84
3.3.5.1 Presentation of the Data 84
3.3.5.2 Epicentral Distribution 85
3.3.5.3 Hypocentral Distribution 85
3.3.5.4 Temporal Distribution 91
3.4 Local Earthquake Magnitudes 94
3.4.1 Introduction 94
3.4.2 Application to the NISE Data 95
3.4.3 Temporal Distribution 98
3.4.4 Frequency–Magnitude Relationships and b–Values 98

3.4.4.1 Introduction 98
3.4.4.2 Application to the NISE Data 103
3.4.4.3 Variation in b–Values 106
3.5 Summary 110

4 Simultaneous Tomographic Inversion 111
4.1 Introduction 111
4.2 Simultaneous Inversion 112
4.2.1 Introduction 112
4.2.2 The Simultaneous Inversion Algorithm 112
4.2.3 Software 117
4.3 Model Development 119
4.3.1 Event Selection 119
4.3.2 Velocity Model Parameterization 119
4.3.2.1 Parameter Values 119
4.3.2.2 Parameter Distribution 120
4.3.3 Resolution 128
4.4 Inversion Results 133
4.4.1 The Final Inversion Solution 133
4.4.2 Presentation of Results 133
4.4.3 Krafla P–wave Velocity Anomalies 149
4.5 Earthquake Relocation 152
4.5.1 The Effects 152
4.5.1.1 Introduction 152
4.5.1.2 Relocation Using the 'Evolved 1–d' Model 152
4.5.1.3 Relocation Using the Final 3–d Model 152
4.5.2 Final Epicentral Distribution 159
4.5.3 Final Hypocentral Distribution 161
4.6 Summary 164

5 Focal Mechanisms 165
5.1 Introduction 165
5.2 Representation of a Seismic Source 169
5.2.1 Introduction 169
5.2.2 Moment Tensor Representation 171

5.3 The Data 176
5.3.1 Introduction 176
5.3.2 Removal of Biases 176
5.3.2.1 Introduction 176
5.3.2.2 Software 178
5.3.2.3 Application to the Data 178
5.3.3 Double Couple Events 182
5.3.3.1 Introduction 182
5.3.3.2 Bjarnarflag 182
5.3.3.3 Fissure Zone 185
5.3.3.4 Leirhnjúkur 188
5.3.4 Non–Double Couple Events 191
5.3.4.1 Introduction 191
5.3.4.2 Removal of Bias 192
5.3.4.3 Source Models 196
5.3.4.4 Implications for the Stress Field 204
5.4 Summary 205

6 Synthesis and Conclusions 207
6.1 Seismicity and Structure 207
6.1.1 Krafla Caldera 207
6.1.2 Námafjall–Bjarnarflag 212
6.1.3 Fissure Zone 214
6.2 Conclusions 218
6.2.1 Geology 218
6.2.2 Data Limitations 219
6.3 Suggestions for Further Research 220

References 221

Appendices 232
A Earthquake Locations Using HYPOINVERSE 232
B Tomography Final Run 238
C Program MOD3D 250
D Relocated and Original Hypocentres 253
E Focal Mechanisms 260

Chapter I

Iceland : Structure and Tectonic Evolution

1.1 Introduction

Iceland is a geological curiosity for many reasons. The existence of active volcanic centres, hot springs and conspicuous surface fissures are clear indications that it is geologically dynamic. A striking statement expressing the country's geological youth is that more than one tenth of its area is covered by lava less than ten thousand years old. Indeed the oldest exposed rocks are only about sixteen million years old (and the exposure certainly is good !). However, until recent years the most pressing question regarding the geology of Iceland was its uniqueness. Why is Iceland an isolated land mass in the middle of the Atlantic ?

Wegener (1912) anticipated a fundamental idea of the modern theory of plate tectonics when he wrote that "the Mid-Atlantic Ridge is that zone in which the floor of the Atlantic in its progressive spreading is rifting open and making space for fresh, relatively fluid, high-temperature sima rising from depth". However, he never made the connection between these processes at the Mid-Atlantic Ridge and the anomalous island of Iceland, which he later envisaged as being a relic of continental scum left over from the separation of Greenland from Europe (Steinthorsson and Jacoby, 1985).

Diverse geophysical, geological and geochemical evidence, discussed in this chapter, indicate that Iceland is a result of accretion at an anomalous section of the Mid-Atlantic Ridge. With ever increasing clarity, these observations can be seen as evidence for a single geological process in Iceland : crustal accretion over a ridge-centred hotspot. However, by establishing the influence of the hotspot on the ridge, it may be possible to apply the observations made on Iceland to increasing our understanding of mid-ocean ridge processes in general. Iceland is, after all, a far more convenient place to carry out research than the ocean floor.

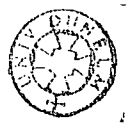

This thesis documents one such study which targeted the structure and seismicity of a single spreading centre. The onset of a spectacular crustal rifting episode in December 1975, centred in the Krafla volcanic system in North Iceland, provided a rare opportunity for geophysicists to study the mechanism of crustal accretion close at hand. The dataset analysed in this study was collected during the latter stages of this episode.

1.2 Geology

1.2.1 Introduction

This section is largely a summary of the comprehensive reviews of Sæmundsson (1978, 1979). Only references for information complementary to these reviews are cited. The main tectonic features and geological units on Iceland are shown in figure 1.1.

1.2.2 Axial Rift Zones

Fracturing in the axial rift zones is concentrated in fissure swarms which are 10–100 km or more in length and up to 20 km wide. The swarms typically form *en échelon* arrays which are sinistral or dextral depending on the trend of the individual rift zone relative to the direction of spreading (about N100°E). The fissure trend is fairly uniform within each branch of the rift zone, but variable between zones. The swarms feature volcanic fissures and vertical faults which tend to be sinuous, branching and often *en échelon*. Normal faults with dips as shallow as 30° also occur. Dyke widths are usually 1–3m, but can be less than 1m or more than 20m. Fissure eruptives are dominantly olivine–poor tholeiitic basalts, which typically form aa lavas if they are erupted subaerially or serrated ridges of pillow lavas and hyaloclastite tuffs (moberg) if erupted subglacially. Voluminous porphyritic flows also occur.

Most of the fissure swarms contain a central volcano, and together they form a 'volcanic system'. The central volcanoes are the foci of the most frequent eruptions, maximum lava production and most intense geothermal activity; acid and intermediate rocks are virtually confined to them. The confinement of acidic and intermediate rocks to the vicinity of central volcanoes and the exclusive eruption of basalts in the fissure swarms are thought to be indicative of shallow magma reservoirs under the central volcanoes (Jakobsson, 1979). About half of the active central volcanoes in the axial rift zones have developed calderas. Caldera collapse has been related to either explosive acidic eruptions producing sheets of ash flow or airfall tuffs (Krafla, Tindfjallajökull, Askja) or to the withdrawl of magma from chambers beneath them (Askja, Grimsvötn). Basaltic flows from central volcanoes

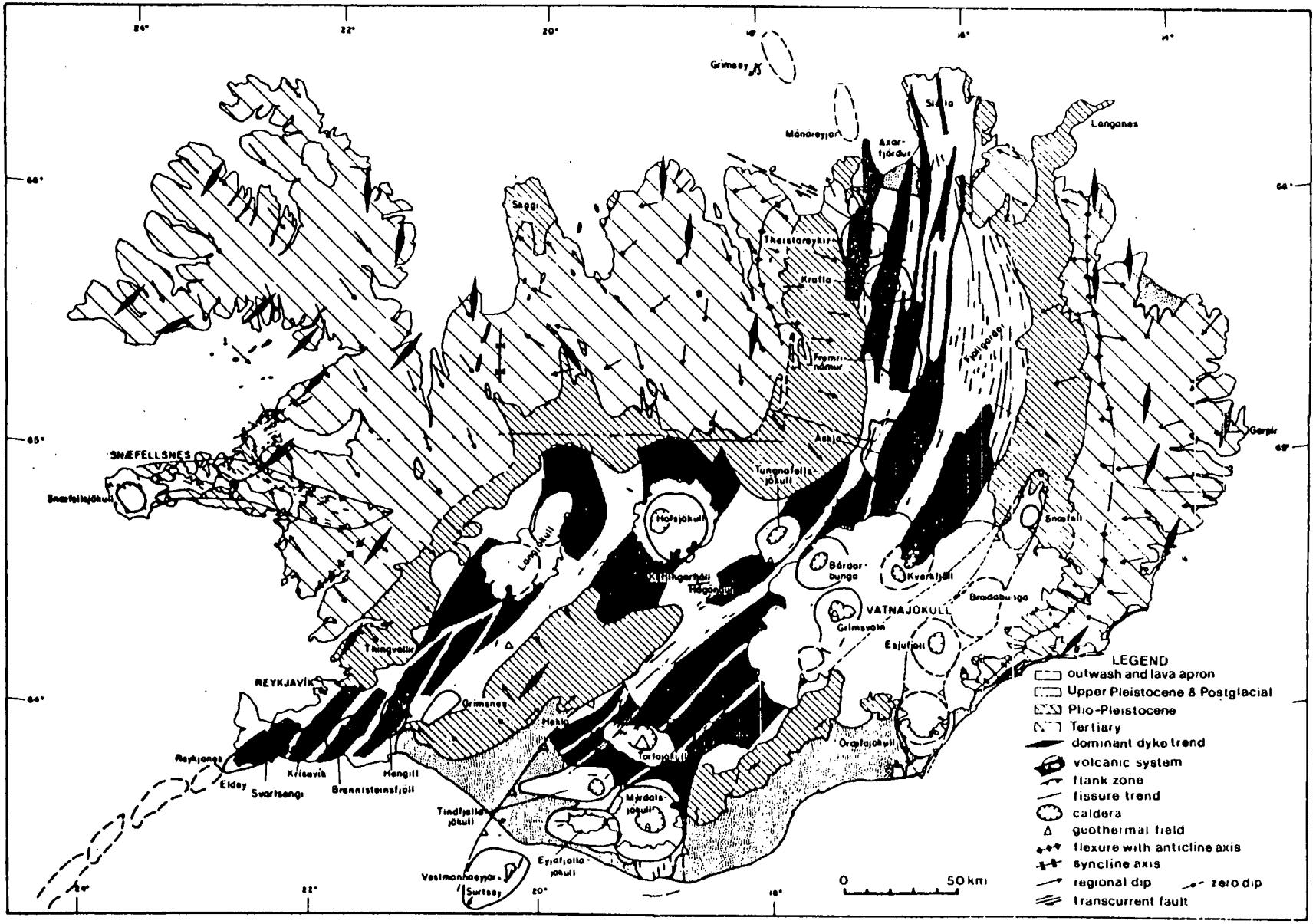

Figure 1.1 : Tectonic map of Iceland (from Sæmundsson, 1979).

are largely composed of either olivine–poor tholeiites, forming aa lavas, or olivine–rich tholeiites which form thick pahoehoe lavas. The lavas are generally highly mobile and therefore form a volcano with gently sloping flanks, unless they are erupted subglacially to form hyaloclastite piles. There are many examples of subglacially erupted intermediate and acid lavas, the more acid members of which form steep rhyolitic domes. The axial rift zone also contains many large monogenetic lava shields which are mainly composed of olivine tholeiites, indicating that they have been fed by subcrustal magma sources.

1.2.3 Flank Zones

The flank zones of Iceland are the Snæfellsnes, Torfajökull–Vestmannaeyjar and Öræfajökull–Snaefell neovolcanic zones (figure 1.1). They are characterized by transitional to alkalic lavas and are dominated by large stratovolcanoes or shield volcanoes and are both petrologically and structurally distinct from the axial rift zones. There are only poorly developed extensional faults and fissures. The Öræfajökull–Snæfell stratovolcanoes overlie an older basement and it is thought, from evidence of large exposed intrusions of gabbro and granophyre, that similar volcanoes probably existed there in the past.

1.2.4 The Volcanic Pile of Iceland

The volcanic pile of Iceland has exposed rock sequences of up to 1500m in thickness, below which (from seismic evidence) lie at least another 2–5 km of extrusives. Mapping of the older parts of the lava pile was carried out largely by G.P.L. Walker in the 1950's and a summary is given by Walker (1974).

The lava pile grew as lenticular units from elongate volcanic systems which included swarms of dykes and fissures usually localized about central volcanoes. On a regional scale, the lavas of the pile dip gently towards Central Iceland (figure 1.1) and individual lava groups thicken down–dip. The extensive subaerial tholeiitic lava flows which formed the classic plateau basalt series typical of the fjord landscapes of eastern Iceland and much of northern and western Iceland were produced during the Tertiary (prior to 3.1 Ma; the oldest measured is 16 Ma). These flood basalts were extruded from the vicinity of central volcanoes. Exposures of

deeply eroded central volcanoes show intrusions of dolerite, gabbro and/or granophyre with cross–sectional areas of up to 10 km^2. Their roots are also invaded by intrusive sheets which dip at 30–40° towards the core of the volcanoes, and which sometimes form discrete cone sheet swarms up to 15 km in diameter. Hydrothermal alteration is also a common feature of these exposed volcanic cores.

The onset of the Plio–Pleistocene (3.1–0.7 Ma) saw the appearance of the first tillites to be inter–stratified with the lavas, although the pattern of volcanism was unchanged. Instead of the primarily subaerial flows of the Tertiary, subglacial volcanic products such as pillow lavas, breccias and hyaloclastites became increasingly inter–stratified with the lavas as the climate underwent alternating stages of warmth and coldness. Subglacial volcanism led to a much more uneven topography and to the formation of the Tertiary fjords by glacial erosion. This continued throughout the Upper Pleistocene (0.7 Ma - 9000a), during which time the glacial periods were of longer duration than during the build–up of the Plio–Pleistocene. Modern subaerial volcanism then ensued, exhibiting the same pattern as the last glacial and interglacial periods.

The present day volcanic zone of Iceland differs markedly in appearance from the Tertiary flood basalt areas in terms of the much greater number of visible volcanic vents, faults and fissures. Pálmason (1980) produced a two–dimensional steady–state plate–tectonic kinematic model of Iceland which quantitatively describes the overall time–averaged trajectories of solid crustal elements, which are produced by both dyke intrusion and lava extrusion, as they drift away from the spreading axis. The model predicts that evidence of volcanic and tectonic processes in the central part of the active zone gradually disappear in the deeper part of the distant crust, where they cannot be observed directly. It was concluded from this that no major change in the behaviour of the volcanic processes in Iceland is required to account for the conspicuous difference in appearance between Tertiary and modern volcanic zones, and that consequently there may have been a degree of uniformity in the volcanic processes during the last 10–15 Ma (Pálmason, 1980).

1.3 Geophysics

1.3.1 The Seismicity of Iceland

Figure 1.2 shows the epicentres and focal mechanisms of large earthquakes in the Iceland area during the period 1963–1987. Most of the seismicity of Iceland is associated with the Mid–Atlantic Ridge which appears onshore on Iceland at the tip of the Reykjanes Peninsula in the south. The Reykjanes Peninsula is an area of high seismicity in which most of the earthquakes are at a depth of 1–5 km and are not located on a single fault (Klein et al., 1977). The stress regime implied from focal mechanism studies is characterized by a northwest trending direction of minimum compressive stress, suggesting that dykes are formed when fissures normal to this direction open up (Einarsson and Björnsson, 1979).

The plate boundary in Iceland is displaced to the east by two major fracture zones, the South Iceland Seismic Zone (SISZ) in the south and the Tjörnes Fracture Zone (TFZ) in the north. The most severe earthquakes in Iceland have occurred within these zones, with magnitudes (M_S) which may have exceeded 7 in historical times compared with a maximum magnitude of about 5 for events occurring within the rift zones (Einarsson and Björnsson, 1979). Concentrations of activity in Iceland are seen in the TFZ near the coast of North Iceland, on the Reykjanes Peninsula, and in the SISZ in Southwest Iceland. Most focal mechanisms for the fracture zones indicate strike–slip motion which is dextral in the TFZ and sinistral in the SISZ, if the east–west trending nodal planes are taken as the fault planes. This interpretation is consistent with a transform fault model for these zones. However, destruction areas of individual earthquakes in the SISZ show that each major historical event has been associated with faulting on north–south trending planes. This is thought to indicate that the gross sinistral transform motion predicted by plate movements along the SISZ is in fact accommodated by block rotation which results in dextral motion on north–south trending faults perpendicular to the main zone (Einarsson, 1990).

If the SISZ is a transform fault zone then a ridge–ridge–transform triple junction is present in the Hengill area. The seismicity of the Hengill area has been found to extend over both the active Hengill volcano and the extinct Grensdalur volcano, with hypocentres in the depth range 1–7 km (Foulger, 1984, 1988a,b). About

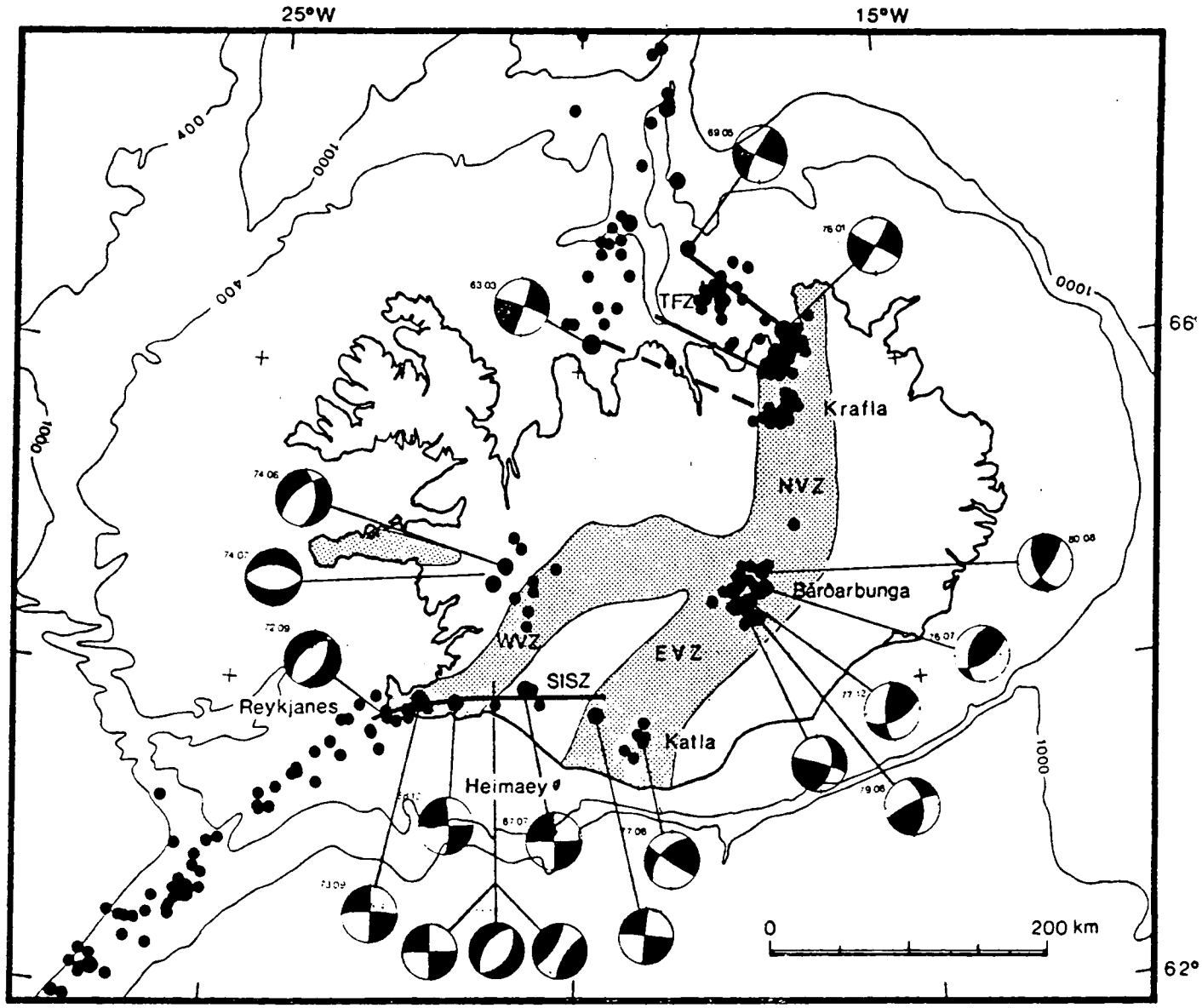

Figure 1.2 : Epicentres and focal mechanisms of earthquakes in the Iceland area. Epicentres are taken from the PDE lists of the U.S. Geological Survey for the period 1963–1987; only epicentres determined with 10 or more stations are included. Large dots are events of $m_b = 5$ and larger. Focal mechanisms are shown schematically on lower hemisphere projection of the focal sphere. compressional quadrants black. The volcanic zones (WVZ. EVZ and NVZ) are stippled. and seismic belts in the South Iceland Seismic Zone (SISZ) and the Tjörnes Fracture Zone (TFZ) are shown with heavy lines (from Einarsson, 1990).

half the events exhibited normal and strike–slip focal mechanisms related to a similar stress field to that found on the Reykjanes Peninsula. The other events had mechanisms which indicated the formation of tensile cracks at depth and were interpreted as resulting from the cooling and contraction of hot rock by circulating geothermal fluids. Fluid circulation is also thought to account for the intense heat release of the Grímsvötn central volcano and at other Icelandic and mid–ocean ridge geothermal areas (Björnsson et al., 1982).

Most clusters of seismic activity in Iceland coincide with the positions of central volcanoes, most of which have associated high temperature geothermal areas. A close correlation between central volcanoes/high temperature geothermal areas, and zones of high microearthquake activity has been established by local earthquake surveys (e.g. Ward et al., 1969; Ward and Björnsson, 1971). It is therefore possible that much of the observed background small magnitude seismicity of the central volcanoes results from geothermal processes such as those operating at Hengill. However, bursts of activity have been observed at the sites of several central volcanoes and have been interpreted as having resulted from magma chamber deflation (Bárdarbunga, Katla), magma chamber inflation (Krafla, Grímsvötn), magma movements at depth (Krafla, Torfajökull, Vestmannaeyjar) and the increase in pore pressure due to glacial melting (Katla), (Einarsson, 1990).

A small number of Icelandic earthquakes are not directly related to the plate boundary or the volcanic zones and have been classed as intraplate events (Einarsson, 1989). One group of these events occur in the lithospheric block between the transform zones and are thought to be associated with crustal extension above the Icelandic hotspot. The other group includes events on the insular shelf off the coast to the east and southeast, which may be a result of a differential cooling rate in the crust across the shelf edge (Einarsson, 1989, 1990).

1.3.2 The Seismic Structure of the Icelandic Lithosphere

Early seismic surveys on Iceland were interpreted in terms of a crustal structure consisting of layers with constant velocities (Båth, 1960; Tryggvason and Båth, 1961; Pálmason, 1963, 1971). The Pálmason interpretation of seismic refraction data consisted of a four layer model overlying an anomalous mantle with a P–wave velocity of 7.2 kms^{-1}, the depth to which was observed to increase from about

8–10 km beneath the neovolcanic zone in the southwest to as much as 15 km beneath the older southeastern portion of Iceland. The lowest crustal layer, which he equated with oceanic layer 3, had a P–velocity of 6.5 kms^{-1} and generally had a thickness of 4–5 km. However, Flovenz (1980) found that this simple layered model could not explain the amplitude variation of Pálmason's data. Instead, it was proposed (Flovenz, 1980) that the Icelandic crust should be divided into an upper crust, in which velocities increase continuously with depth (section 3.3.2), and a lower crust with an almost constant velocity of 6.5 kms^{-1} corresponding to Pálmason's deepest crustal layer. The depth to the Icelandic lower crust based on seismic refraction data is shown in figure 1.3. The lower crust is generally found at a depth of 3–6 km, except under central volcanoes where it is thought to be shallower. It is thought that the boundary between the upper and lower crust is a metamorphic facies because of an observed increase in epidote content in deep boreholes (Pálmason, 1971).

Zverev et al. (1980a,b) carried out combined seismic reflection and refraction experiments in Northeast and Southwest Iceland, each of which was found to have similar characteristics. The section across Northeast Iceland is shown in figure 1.4. In the flood basalts, the near–surface refractors correspond closely to geological layers. Near the neovolcanic zones the whole basalt series is slightly tilted towards their centres and the depressions in the rift zones are filled by low velocity formations. Steeply dipping reflectors are found at depths of up to 15 km or more and also tilt towards the rift zone. In both seismic sections, volumes of limited lateral extent were identified beneath the rift zones where no reflectors occurred. These volumes suggest the presence of seismically homogeneous bodies below about 8 km depth, which have been interpreted as magma chambers or regions of partial melt (Zverev et al., 1980a,b; Björnsson, 1983). One of these bodies of low seismic reflectivity lies beneath the Krafla central volcano (figure 1.4).

A long range seismic refraction experiment (RRISP 77) was carried out in 1977 along a line extending 800 km across Iceland and the southeastern flank of the Reykjanes Ridge (figure 1.5a). The main purpose of the experiment was to resolve the structure of the crust and upper mantle to a greater depth than was previously possible and to study the transition from oceanic to Icelandic structure (Angenheister et al., 1980; Gebrande et al., 1980; Goldflam et al., 1980). A

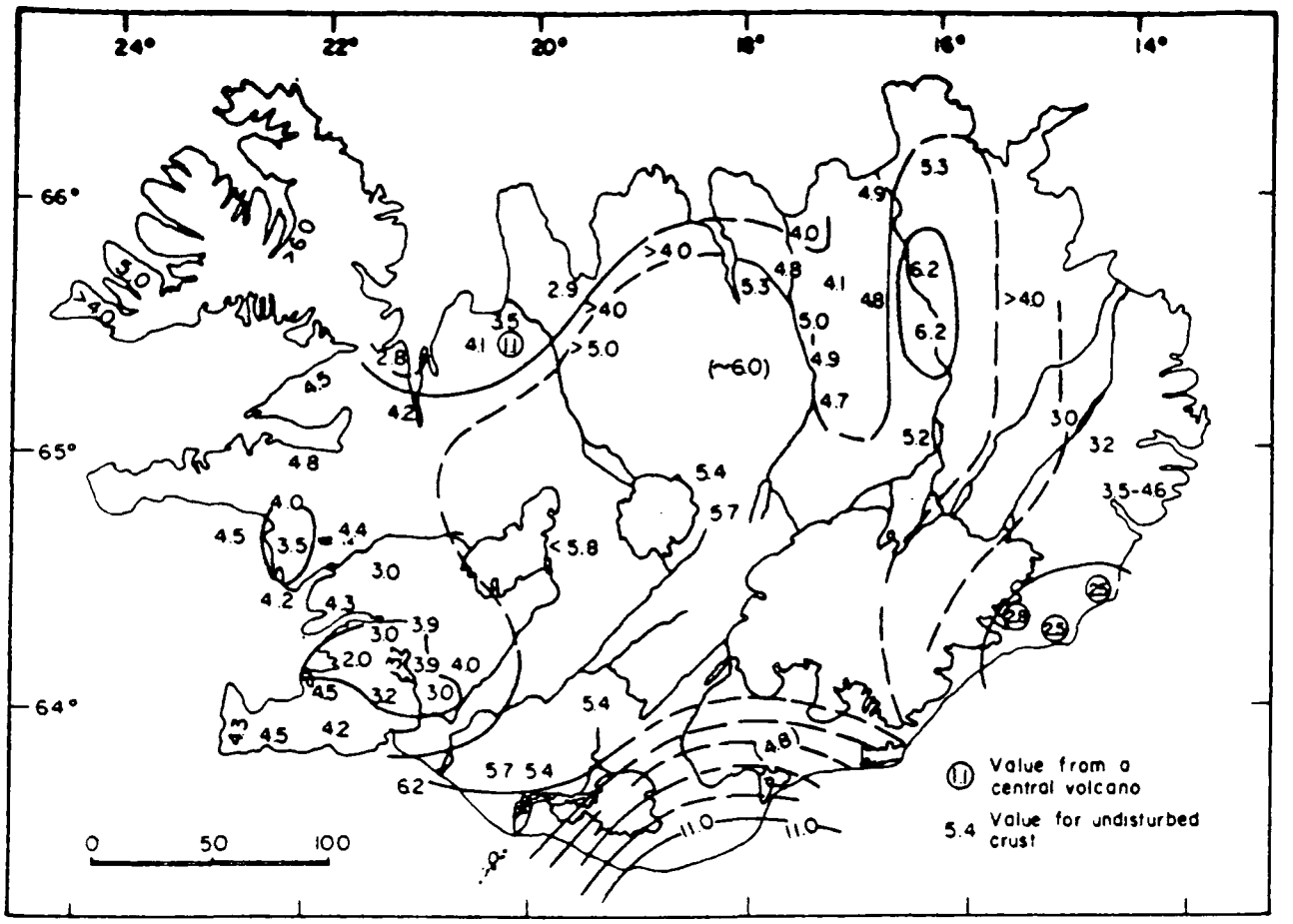

Figure 1.3 : Depth to the lower crust (layer 3) in Iceland. The velocity of the upper crust is assumed to increase continuously with depth (from Flóvenz, 1980).

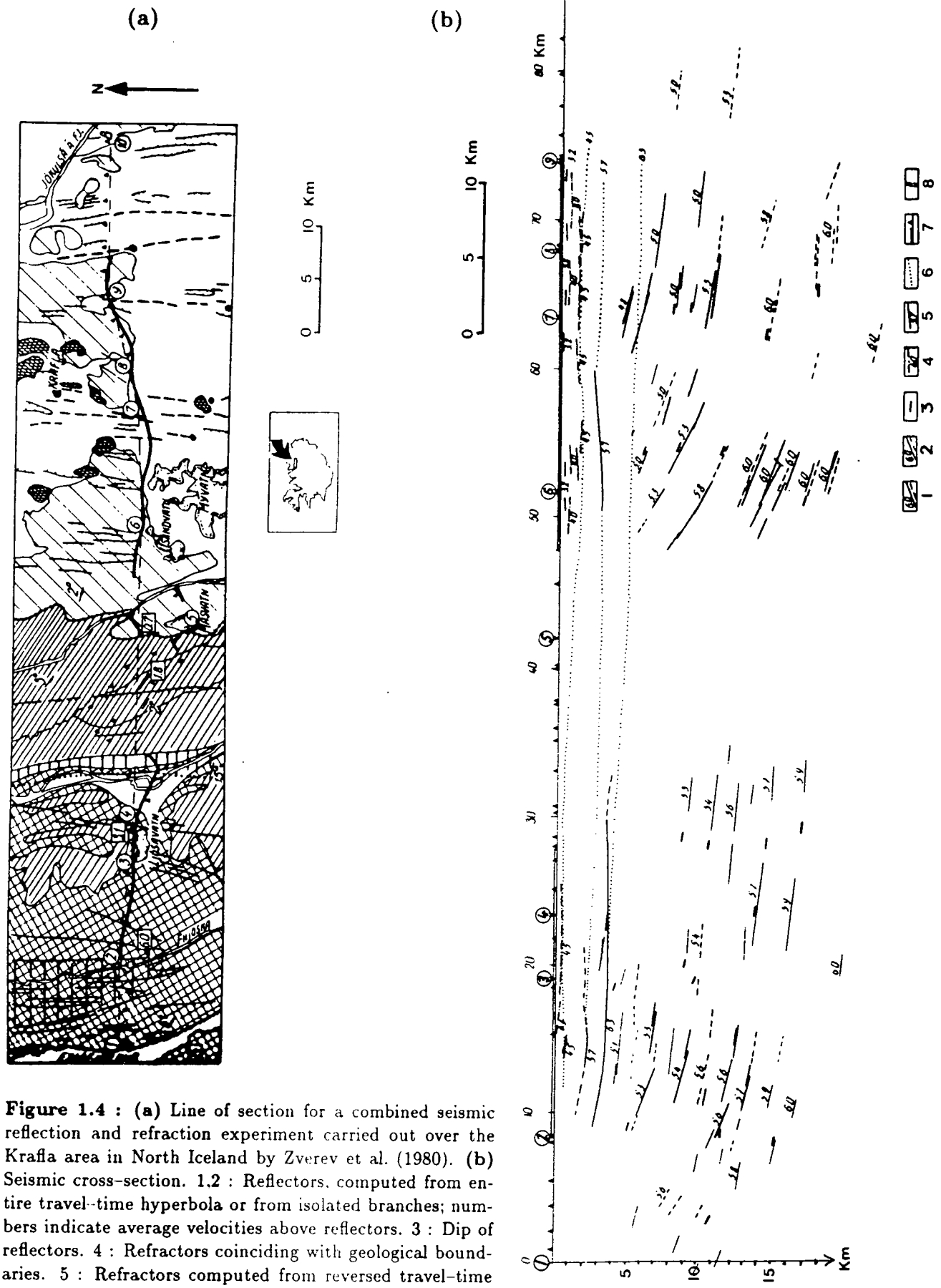

Figure 1.4 : **(a)** Line of section for a combined seismic reflection and refraction experiment carried out over the Krafla area in North Iceland by Zverev et al. (1980). **(b)** Seismic cross-section. 1.2 : Reflectors, computed from entire travel-time hyperbola or from isolated branches; numbers indicate average velocities above reflectors. 3 : Dip of reflectors. 4 : Refractors coinciding with geological boundaries. 5 : Refractors computed from reversed travel-time curves and from unreversed lines; numbers indicate refractor velocities. 6 : Velocity contours : 4.5, 5.7, 6.3 kms^{-1}. 7 : Regions of multi-channel coverage and projected positions of automatic stations. 8 : Shot points (adapted from Zverev et al., 1980).

(a)

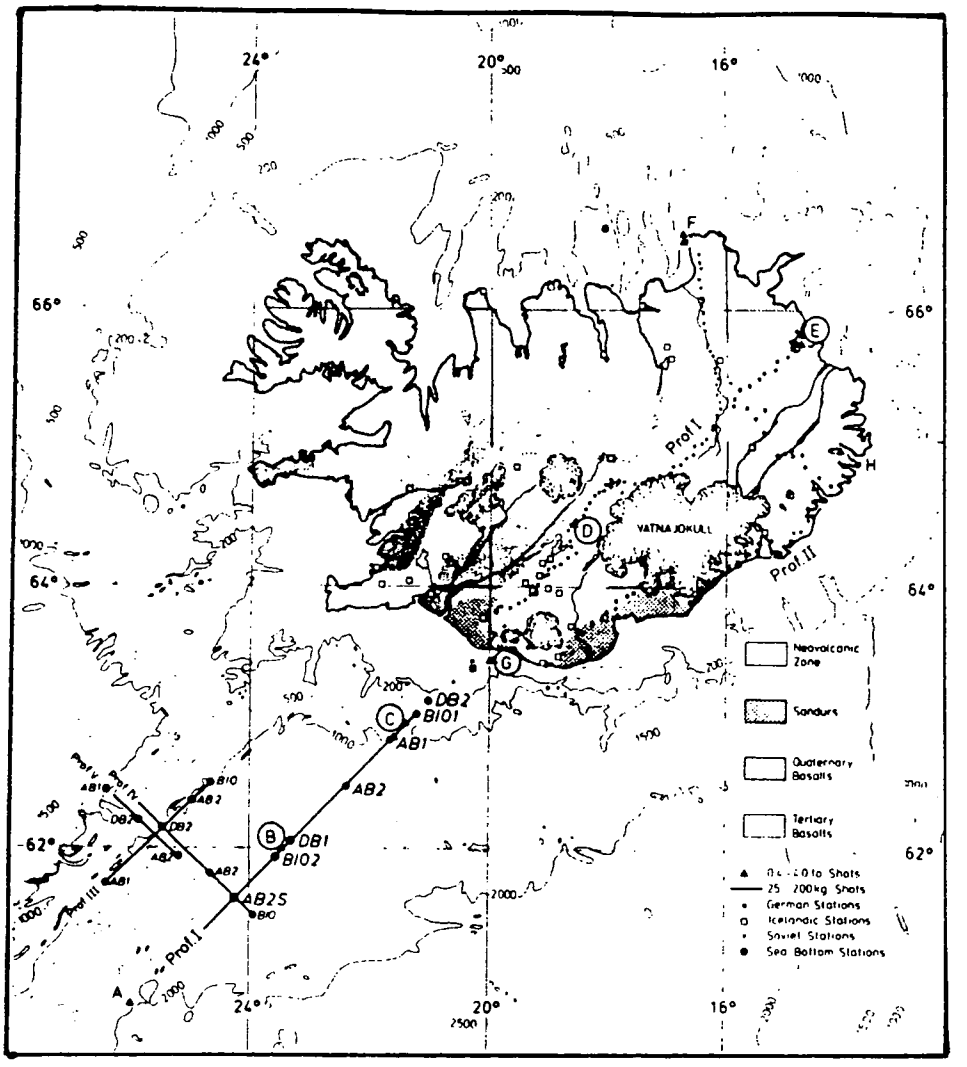

(b)

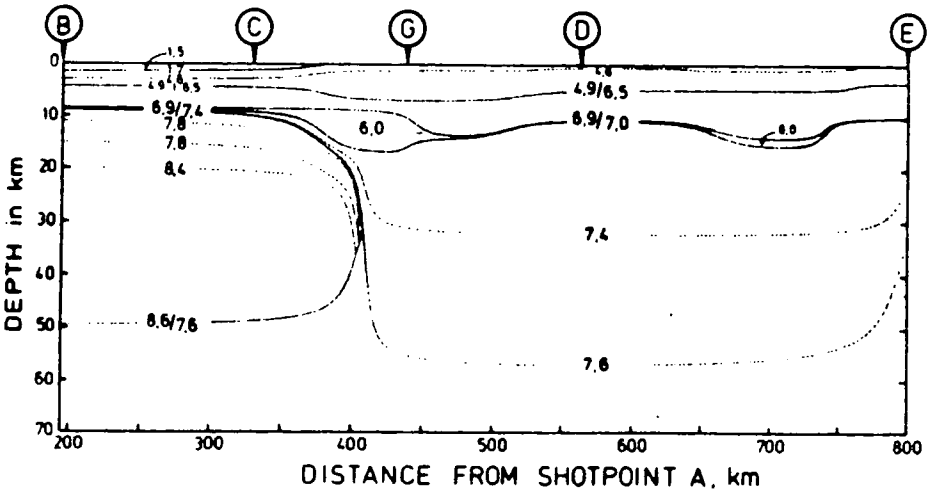

Figure 1.5 : **(a)** Simplified geological map of Iceland and bathymetric chart of the surrounding ocean showing shot points and recording sites of the RRISP 77 project (from Angenheister et al., 1980). **(b)** Crust and upper mantle model beneath Iceland and the eastern flank of the Reykjanes Ridge between shot-points B and E. Distances are given from shotpoint A. Numbers give the velocity at each isoline. The velocity of 6.0 kms^{-1} in the two blisters at the base of the crust must be less than 5 kms^{-1} to explain observed travel-time delays (from Gebrande et al., 1980).

generalized crustal and upper mantle cross-section of the main profile is shown in figure 1.5b. A well developed 10 km thick oceanic crust was observed along the 10 Ma isochron on the eastern flank of the Reykjanes Ridge, beneath which the lower lithosphere was found to be stratified with P-wave velocities as high as 8.6 kms^{-1}. The crustal layers extend on to Iceland with increased thickness but the subcrustal lithosphere is abruptly terminated near the shelf margin. The crustal thickness was found to vary between 10–15 km. No clear relationship was identified with the axial rift zones. The crust is underlain throughout Iceland by a low P-wave velocity (7.0–7.6 kms^{-1}) upper mantle, with no evidence for sharp velocity discontinuities. This has been interpreted as the result of diapiric updoming of the asthenosphere (Angenheister et al., 1980). Two regions of relatively low velocity were identified in the lower crust (figure 1.5b), one beneath the active volcanic Westmann Islands (Vestmannaeyjar) to the South and the other in the vicinity of the Askja central volcano in the Northern Volcanic Zone (figure 1.1), although their depths and horizontal dimensions were not well resolved. It is thought that these may be zones of relatively high partial melt concentration (Gebrande et al., 1980). A normal P–S velocity ratio of 1.76 was found within the crust, but this ratio was found to reach unusually high values of up to 2.2 in the anomalous upper mantle beneath Iceland. Significant S-wave attennuation was also observed in the upper mantle beneath Iceland. About 20% partial melt was estimated to be present at the top of the mantle with melt content decreasing with depth, which indicates that differentiation occurs in the upper mantle (Gebrande et al., 1980). These observations of the presence of relatively low velocities in the upper mantle beneath Iceland are in accordance with observations of large teleseismic delays on Iceland relative to stations in Scotland, Sweden and Greenland (Tryggvason, 1964; Long and Mitchell, 1970), which were interpreted to indicate that low velocities extend to depths greater than 200 km beneath Iceland. The same effect was also demonstrated by a block inversion of teleseismic P-wave arrival times (Tryggvason et al., 1984), in which the low velocity anomaly was resolved to a depth of 275–375 km.

1.3.3 Other Geophysical Research

A major Bouguer gravity low occurs over Iceland and is at its deepest over the topographic high of central Iceland (Einarsson, 1954). Hermance (1981) showed

that isostatic compensation on Iceland may be achieved if the crust thickens with age, as observed by Pálmason (1971), and suggested an underplating mechanism in which low density mantle–derived melt accumulates at the base of the crust beneath the active rift zones and slowly accretes to it as the plates drift apart.

Further evidence for the presence of a layer of partial melt at the crust–mantle interface is provided by magnetotelluric measurements which were carried out in Northeast Iceland (Beblo and Björnsson, 1978, 1980; Beblo et al., 1983). A low resistivity layer (with a resistivity of about 10Ωm) was found at a depth of about 10 km along the active rift zone, the depth of which decreases towards Central Iceland and increases to about 20 km with increasing distance from the rift axis. It was subsequently deduced from comparisons with laboratory–derived temperature–resistivity data that the degree of partial melt at the top of the mantle is about 5–20% (Beblo et al., 1983). Very low resistivity (about 5%) was found at a depth of only 5 km within the region of the Krafla central volcano, approximately coinciding with the location of the zone of low seismic reflectivity below 8 km which was reported by Zverev et al. (1980a), and an S–wave shadow zone at about 3–7 km (Einarsson, 1978).

1.4 The Evolution of Iceland

1.4.1 The Icelandic Hotspot

The geophysical anomalies of the Icelandic crust and upper mantle relative to the surrounding lithosphere are indications that the 'normal' process of crustal accretion which operates on the adjacent sections of Mid–Atlantic Ridge is affected in some way by another dynamic subcrustal mechanism. In addition, the Icelandic crust also features geochemical anomalies in trace elemental and isotopic compositions compared with normal oceanic crust. These variations have been interpreted to show that Icelandic crust is derived from a chemically distinct mantle source (e.g. Schilling, 1973) or, in places, by the assimilation of crust–derived partial melts into mantle–derived olivine tholeiites (Oskarsson et al., 1985).

There is thus evidence that a relatively low density, low seismic velocity partial melt zone underlies the topographic and geochemical anomaly of Iceland, which supports the existence of an Icelandic hotspot (e.g. Vogt, 1971; Schilling, 1973). It then becomes possible to understand the diverse geological, geophysical and geochemical observations in and around Iceland in the context of a single process : crustal accretion over a mantle plume. The thermal anomaly of the hotspot causes the updoming of the asthenophere, resulting in excessive volcanism at the Mid–Atlantic Ridge and the subsequent accretion of the volcanic pile of Iceland. The shallow partial melt zone beneath Iceland, the depth to which generally increases with distance from the ridge axis and the centre of the hotspot, has low seismic velocities and results in the attenuation of S–waves (Gebrande et al, 1980). The relatively low density of the rising plume helps to provide isostatic compensation for the large topographic anomaly of Iceland, and the reworking of old crust of the hotspot trail by plume–enriched magma (Oskarsson et al, 1985) produces complex surface geochemistry.

1.4.2 The Evolution of the Icelandic Platform

Iceland and its insular shelf are part of the Icelandic Transverse Ridge which crosses the North Atlantic from East Greenland to the Faeroe Islands, as shown in figure 1.6. An integrated interpretation of the results of a major seismic refraction experiment (NASP 1972) over the aseismic Iceland–Faeroe Ridge, along with earlier

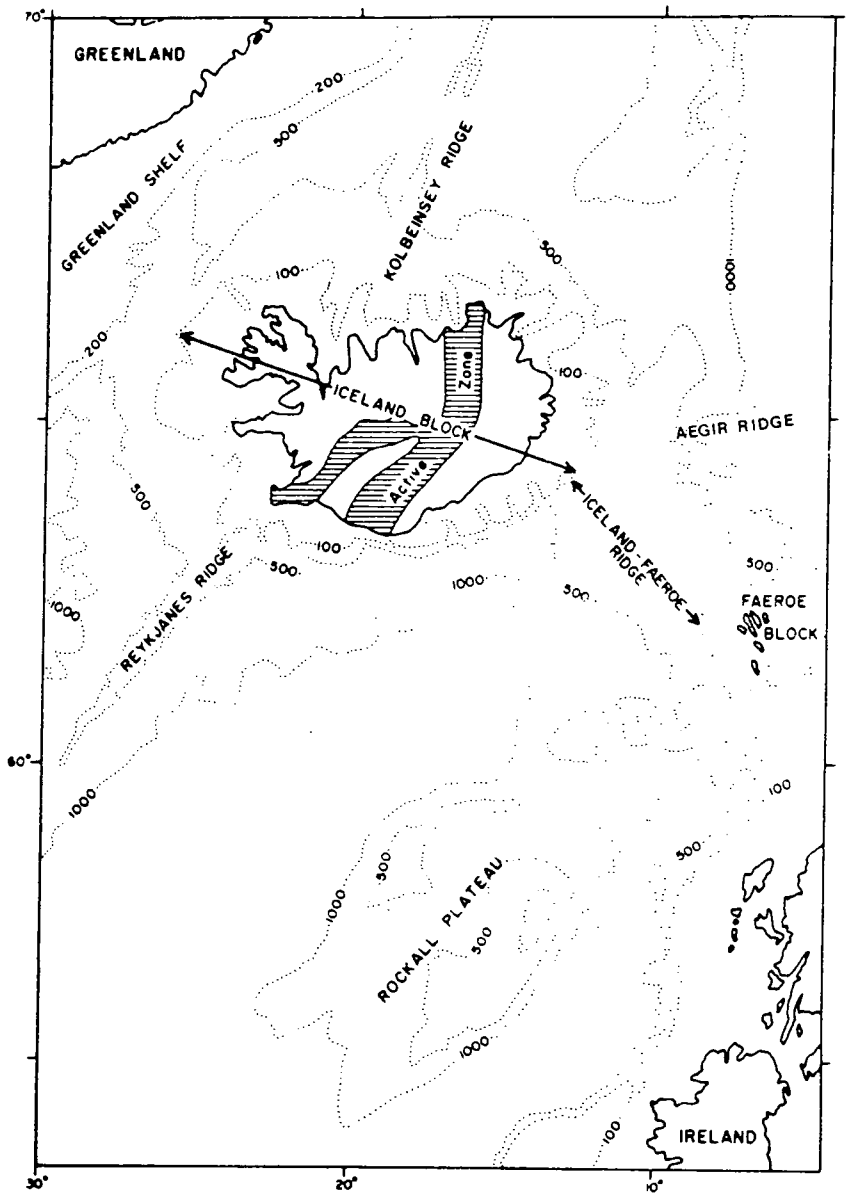

Figure 1.6 : Map of the Icelandic transverse ridge and neighbouring features, showing bathymetric depth contours at 100, 500 and 1000 fathoms, and 200 fathoms at the edge of the Greenland shelf (adapted from Bott, 1974).

refraction, reflection, gravity and magnetic surveys was carried out by Bott and Gunnarsson (1980). They found that the crust beneath the Iceland–Faeroe Ridge has seismic velocities resembling those beneath Iceland, but has a significantly greater thickness. It is 30–35 km thick and therefore one of the thickest sections of oceanic crust in the world, and more than four times thicker than normal oceanic crust (Bott, 1983b). However, the upper mantle beneath the Iceland–Faeroe Ridge does not feature the geophysical anomalies observed beneath Iceland, and it is now widely believed (e.g. Bott, 1983a,b; Vogt, 1983; Vink, 1984) that this ridge formed at the Mid–Atlantic Ridge under the influence of the Icelandic hotspot during the early stages of the evolution of the North Atlantic. The anomalously thick crust may then be attributed to (a) unusually intense differentiation of magma from the mantle during the early stages of the opening of the North Atlantic (Bott, 1983b) or possibly (b) subsequent underplating (Bott, 1983a).

According to the reconstruction of marine magnetic anomalies by Nunns (1983), the Greenland–Faeroe Ridge evolved in three stages. Until about 44 Ma, a major transform fault existed along the northern flank of the Greenland–Faeroe Ridge which offset the mid–ocean ridge dextrally, forming the Aegir spreading axis to the north and the Reykjanes Ridge to the south. A ridge–ridge–transform triple junction then formed between 44 Ma and 26 Ma as the Jan Mayan microcontinent separated from Greenland and to the north sea floor spreading proceeded along both the Aegir axis and the new Kolbeinsey axis to the west. The Aegir axis then became extinct and the Reykjanes and Kolbeinsey ridges joined along an eastward arc in response to the position of the hotspot, and the Iceland platform subsequently built up around this ridge geometry in an asymmetrical manner (Bott, 1985). According to this scheme, the crust underlying the sediment cover between Iceland and Greenland should be identical to that which underlies the Iceland–Faeroe Ridge. However, the Greenland–Iceland Ridge is thought to form a narrower strip because of the westward migration of the spreading axis prior to the time of magnetic anomaly 22 (about 50 Ma), (Bott, 1985).

Vink (1984) reconstructed the plate tectonic evolution of the Greenland–Faeroe plateau using magnetic isochrons and a fixed hotspot reference frame, and by modelling the flow of asthenosphere from the hotspot to the closest section of the Mid–Atlantic Ridge. Figure 1.7 schematically shows this 'hotspot–fed rise

(a)

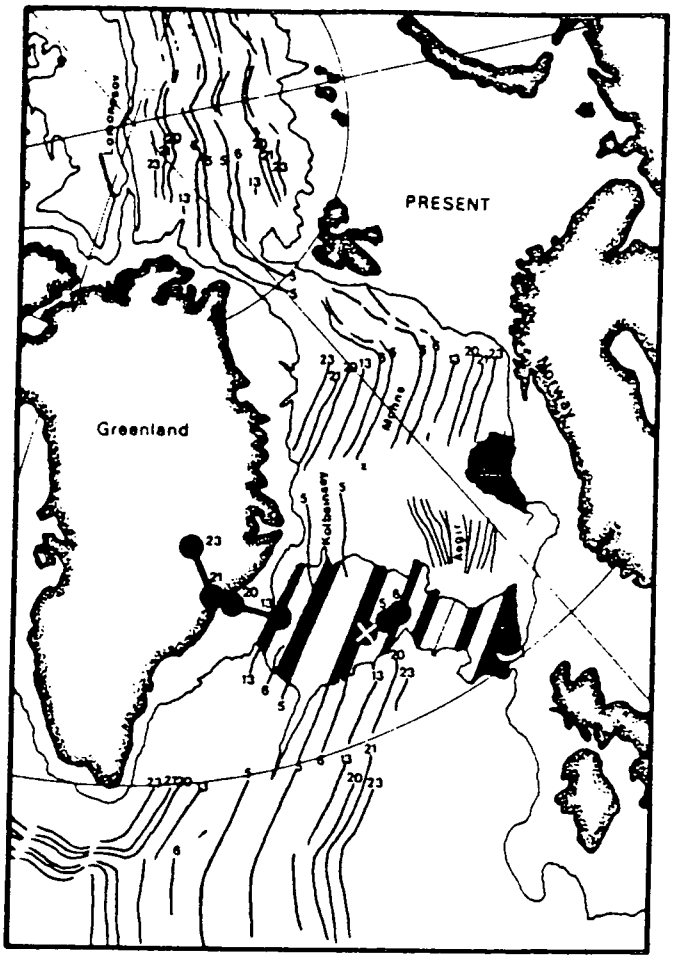

(b)

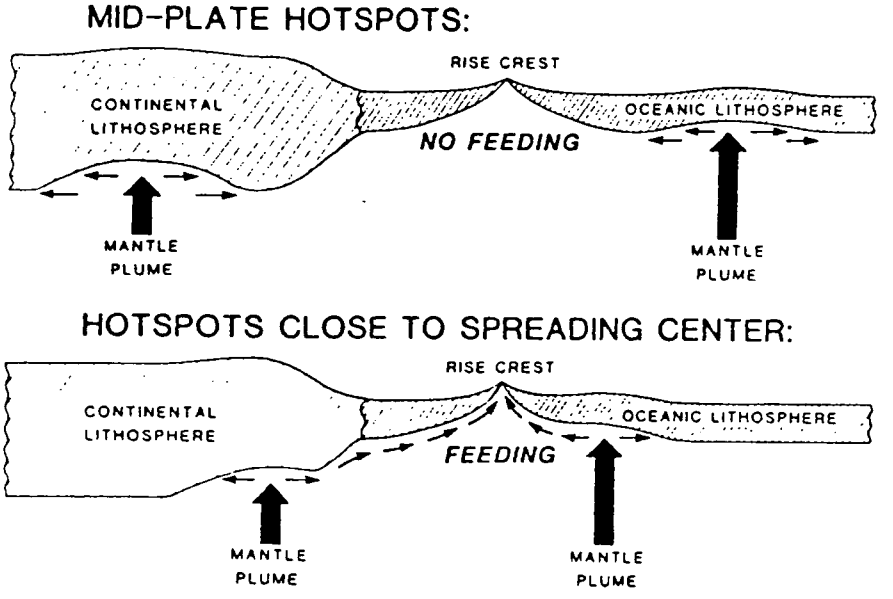

Figure 1.7 : (a) The position of the Icelandic hotspot from magnetic anomaly 23 time (55 Ma) to the present. Dots indicate the hotspot positions through time. The cross marks its present position beneath Iceland. **(b)** Cross–sectional view of a mantle plume located under lithosphere. The heat flux from mid–plate plumes thins the lithosphere. Proximity of plume to spreading centre results in excess asthenosphere rising along base of lithosphere to the closest section of the spreading centre. In a young ocean basin where the spreading centre is near the ocean–continent boundary, material can feed to the spreading centre, although the plume is located under nearby continental lithosphere (from Vink, 1984).

model' and the relative positions of the hotspot and rise crest throughout the evolution of the Greenland–Faeroe Ridge and the Icelandic block. According to this reconstruction the hotspot started feeding the Mid–Atlantic Ridge while situated beneath Greenland, thus initiating the formation of the Iceland–Faeroe Ridge. In contrast to the above scheme by Nunns (1983), the Iceland–Faeroe Ridge is seen to have been completed when the spreading ridge jumped westwards when the hotspot emerged from beneath Greenland at about 36 Ma, although the Aegir axis may have continued to spread until 26 Ma. The ridge had formed the Greenland–Iceland section of the Greenland–Faeroe plateau by about 20 Ma, since which time a series of ridge jumps have periodically repositioned the westward migrating ridge crest over the hotspot throughout the subsequent evolution of Iceland (Vink, 1984).

1.4.3 Evolution of the Plate Boundary on Iceland

The neovolcanic zones of Iceland are the principal areas of active tectonism and are marked by the presence of Upper Pleistocene (0.7 Ma – 9000a) and Postglacial (9000a – present) rocks (figure 1.1). The neovolcanic zones consist of the axial rift zones (Sæmundsson, 1974), which are marked by pronounced extensional features, and the flank zones (Jakobsson, 1972) which display poorly developed extensional features and lie unconformably on older volcanic piles. The axial rift zones are thought to mark the trace of the plate boundary where active plate growth is taking place (Sæmundsson, 1978, 1979).

The western branch of the axial rift zone (the Western Volcanic Zone) extends from the Reykjanes Ridge in the southwest up to Langjökull in western Central Iceland. The neovolcanic zone connects with the eastern branch at Kverkfjöll, via the Hofsjökull zone. The Northern Volcanic Zone extends from here to Axarfjördur in the northeast, and the Eastern Volcanic Zone extends towards the Torfajökull – Vestmannaeyjar flank zone in the south.

The evolution of the plate boundary on Iceland from the Tertiary is not easily determined because identifiable magnetic anomalies are scarce on land. Figure 1.8 shows some offshore magnetic anomalies around Iceland along with the traces of extinct rift zones onshore. Ocean floor anomalies which have been observed to the northwest and southwest of Iceland (Talwani and Eldholm, 1977) cannot be traced onto Iceland, with the exception of anomaly 5 (10 Ma) in the far northwest.

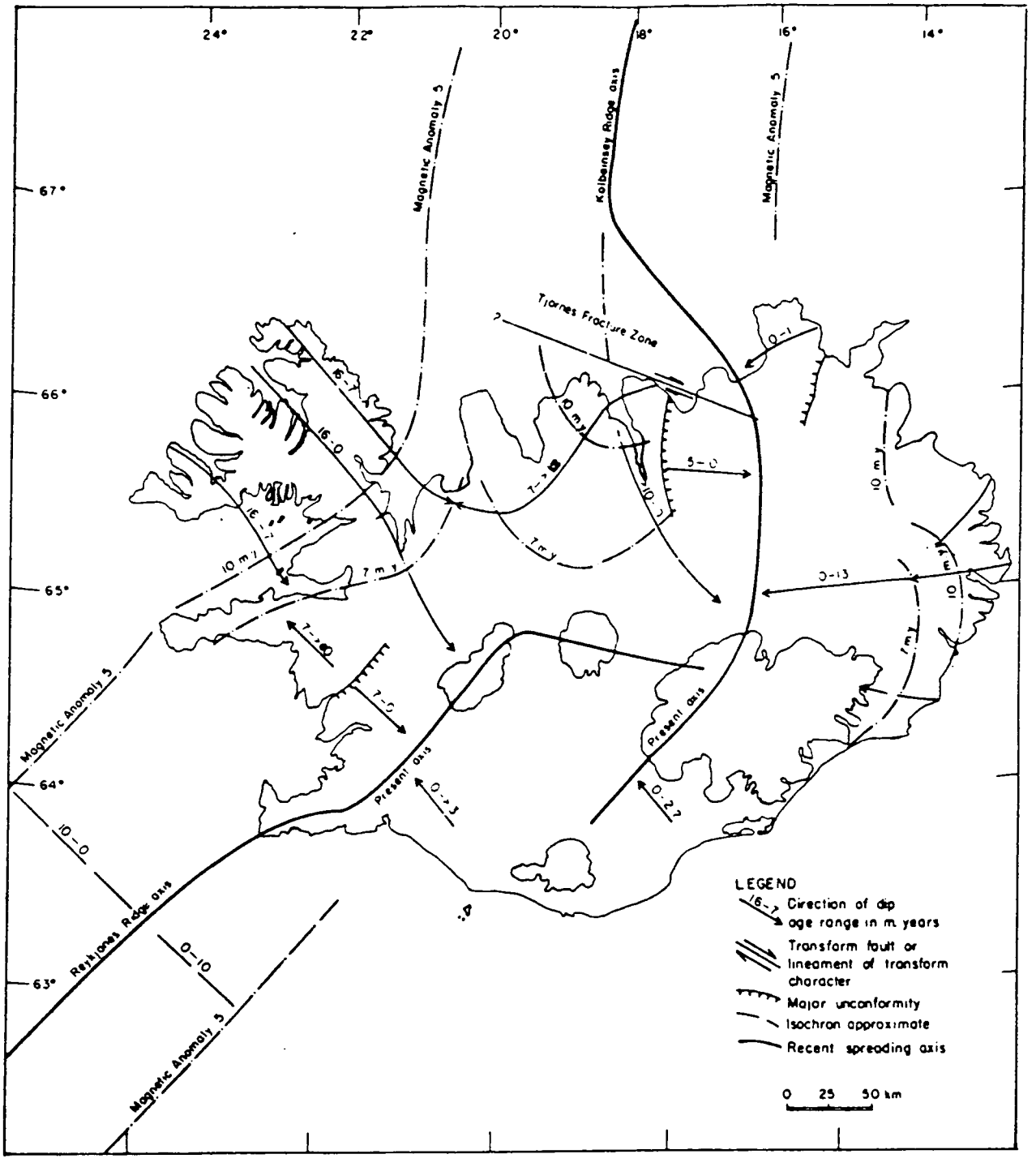

Figure 1.8 : Development of the present geometry of the tectonically active zones in Iceland. Magnetic anomalies and ridge axes at sea are from Talwani and Eldholm, 1977. Traces of extinct rift zones are left as structural synclines in the Tertiary areas. Major unconformities developed between sequences produced within extinct rift zones and those produced from the presently active ones. Note asymmetrical position of Reykjanes Ridge axis relative to Anomaly 5. This is not necessarily due to asymmetric spreading but rather a result of eastward displacement of the ridge axis nearest to Iceland. This scheme should be regarded as preliminary since much more dating studies and stratigraphic mapping have to be done before the trace of isochrons on land can be plotted more accurately (from Sæmundsson, 1979).

Bott (1985) suggested that a double active rift zone on Iceland first developed at 26 Ma, when the Aegir spreading axis became extinct, and has persisted to the present day. According to Sæmundsson (1979), flexures in the Tertiary lava pile of western Iceland (figure 1.1) may indicate the location of an extinct rift zone (the Skagi zone), where crustal extension and downsagging occurred in a manner similar to that occurring today. This suggests, together with K/Ar ages for the lavas, that extinction of volcanism in these syncline areas occurred at about 6–7 Ma, at the same time as new rift zones were initiated to the south and east (Sæmundsson, 1978, 1979). It is thought that this eastward migration may have been in response to the continued relative eastward drift of the hotspot over the last 10 m.y. or so (Sæmundsson, 1974; Helgason, 1985). Figure 1.9 illustrates the development of the present rift zones on Iceland. On the basis of a peak in the K, P and Ti content of the post glacial basalts of central Iceland, Sigvaldason et al. (1974) proposed that the Iceland hotspot is now centred beneath Kverkfjöll, and so the Langjökull–Kverkfjöll transverse zone may represent the trajectory of the hotspot (figure 1.1). As the hotspot continued to drift eastwards, the ridge to the north jumped eastwards first because the plate boundary there was normal to the migratory path of the hotspot, causing longitudinal flow from the hotspot northwards to cease at an early stage (Foulger, 1988a). Ridge response south of the hotspot has therefore lagged behind that to the north of it, and although the Western Volcanic Zone is still active it may be slowly being replaced by the Eastern Volcanic Zone. A result of the eastward jumping of the rift zone is thought to have been the reworking of old crust of the hotspot trail by plume–enriched partial melts, on the basis of geochemical evidence for the assimilation of crustal–derived partial melts into rising mantle material (Oskarsson et al., 1985). It has also been speculated that the South Iceland Seismic Zone (section 1.3.1) is migrating southwards in response to the southward propagation of the Eastern Volcanic Zone (Einarsson and Eiríksson, 1982). Alternatively, Sæmundsson (1979) suggested that this zone may represent the early stage of an oblique rift axis that will eventually connect the Reykjanes Peninsula to the southern part of the Eastern Volcanic Zone.

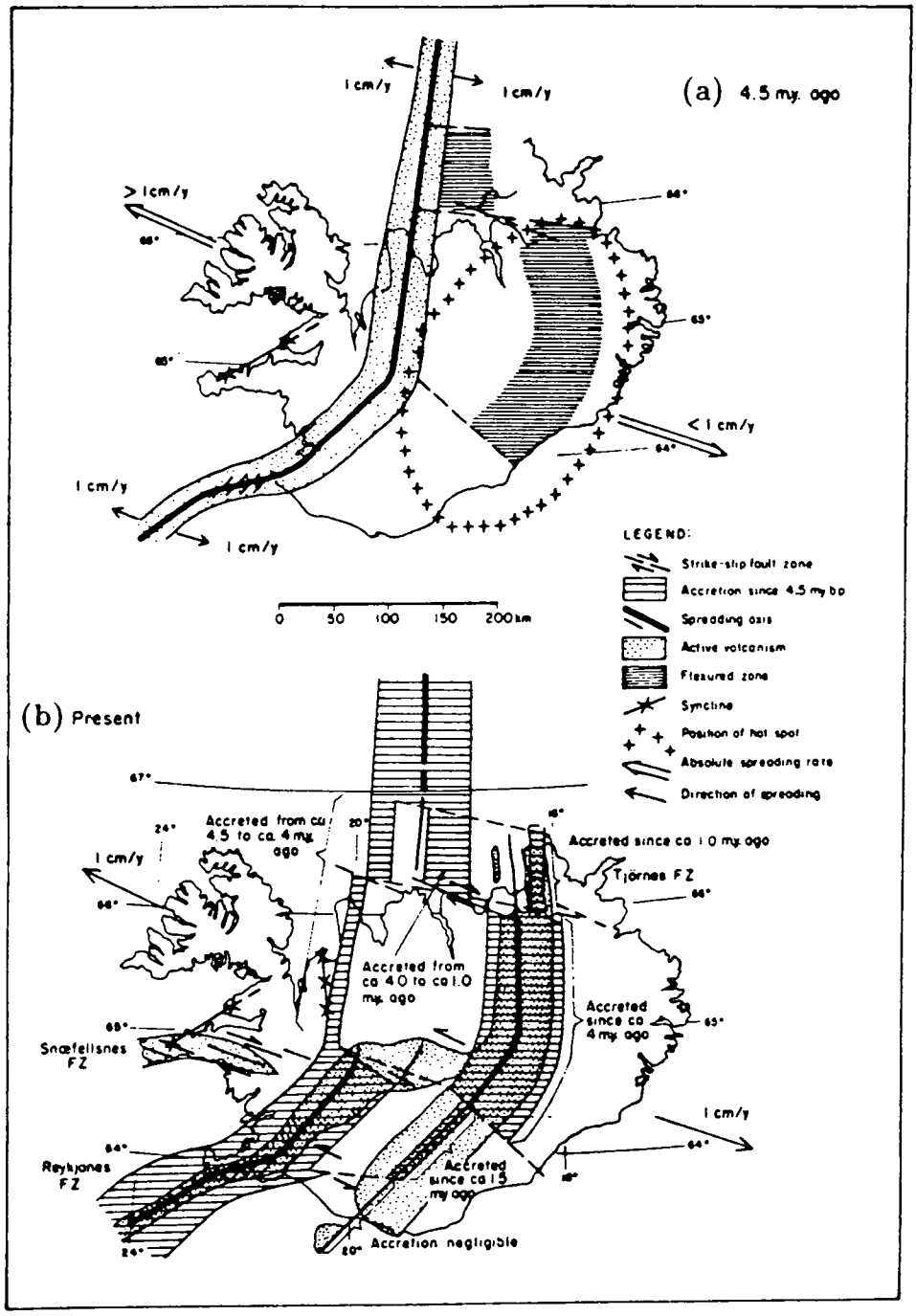

Figure 1.9 : Development of the present pattern of the volcanic zones in Iceland. **(a)** Reconstruction of the rift zones in Iceland before eastward shift to the present position. The axial rifting zone continues north from the Reykjanes Ridge and joins the Kolbeinsey Ridge more or less directly. To the east, new rifting zones have begun to develop as troughs where thick sediment is being deposited. Offset positions of these troughs within and to the south of the TFZ are responsible for the discontinuity of the flexured zone at Vopnafjördur. **(b)** After the shift was completed, the positions of the earlier rifting zones are indicated by synclinal structures in the Tertiary plateau-basalt sequence. Accretion back to 4.5 m.y. should be regarded only as an approximation. Spreading rates are after Talwani et al. (1971) and Vogt et al. (1970), (from Sæmundsson, 1974).

1.5 Summary

The axial rift zones of Iceland are mostly dominated by volcanic systems consisting of extensional fissure swarms which bisect shield–like central volcanoes. These central volcanoes form with siliceous rocks, high temperature geothermal areas, and sometimes calderas. They occur in the vicinity of the most frequent eruptions and maximum lava production. The volcanic pile of Iceland, which lies outside the axial rift zones, grew from volcanic systems similar to those active today. Exposures of deeply eroded extinct central volcanoes in the volcanic pile exhibit large intrusions of dolerite, gabbro and/or granophyre, as well as intrusive sheet swarms and zones of hydrothermal alteration. Active cone–shaped stratovolcanoes are located in the flank zones, well outside the zone of active crustal accretion, and pierce the older volcanic pile.

Seismicity in Iceland is largely associated with the onshore expression of the Mid–Atlantic Ridge. The plate boundary on Iceland is displaced to the east by two major fracture zones, the South Iceland Seismic Zone in the south and the Tjörnes Fracture Zone in the north, to which the most severe earthquakes in Iceland are restricted. Focal mechanisms for these zones are consistent with a transform faulting interpretation. Most clusters of seismic activity outside these areas coincide with the positions of central volcanoes. The small magnitude background seismicity of the central volcanoes results from tectonic movements in response to regional and local stress fields and geothermal processes, whereas bursts of activity may result from the movement of magma in the crust or from seasonal glacial effects. Subsidiary activity occurs outside the active volcanic areas and may be related to extension or differential cooling in the crust.

The Icelandic crust may be divided into an upper crust, in which the seismic velocity increases continuously with depth, and a lower crust which has an almost constant velocity. The thickness of the crust is less than 10 km in the active rift zones and increases to about 15 km beneath the older parts of Iceland. A low resistivity, low seismic velocity, high S–wave attenuation zone exists at the crust–mantle boundary and has been interpreted as a zone of partial melt. This layer becomes shallower towards the axial rift zones and towards the centre of Iceland. Regions of relatively low seismic velocity in this layer of partial melt correlate with

the locations of active volcanic systems. Zones of low seismic reflectivity have also been observed beneath sections of the axial rift zones and support the presence of partial melt at the base of the crust. The whole of Iceland is underlain by an upper mantle which is anomalous relative to that beneath the surrounding oceanic crust. Low seismic velocities have been shown by teleseismic studies to extend to a depth of more than 275 km, and the Bouguer gravity anomaly which characterizes Iceland can only be accounted for by the presence of low density material in the upper mantle.

In addition to the geophysical anomalies mentioned above which distinguish the Icelandic lithosphere from normal oceanic lithosphere, geochemical anomalies indicate that the Icelandic crust is derived from a chemically–distinct mantle source and, in certain areas, from a mantle–derived partial melt into which crustal material has been assimilated. All these anomalies are consistent with the hypothesized presence of a ridge–centred Icelandic hotspot.

Iceland is a topographic high on the Mid–Atlantic Ridge due to excessive volcanism associated with the ridge–centred Icelandic hotspot. When the North Atlantic began to open, the hotspot fed the Mid–Atlantic Ridge with asthenospheric material from its position beneath Greenland, and subsequent spreading caused the formation of the Iceland–Faeroe Ridge. The emergence of the hotspot from beneath Greenland caused the ridge to jump westwards, leading to the formation of the Greenland–Iceland Ridge. Since that time, a series of ridge jumps have periodically repositioned the westward migrating ridge crest over the hotspot throughout the formation of the Iceland platform.

The evolution of the present plate boundary on Iceland is closely linked with the relative drift of the hotspot with respect to the Mid–Atlantic Ridge. Structural and geochemical features indicate that the ridge axis jumped eastwards in response to this drift, causing the reworking of old crust of the hotspot trail by plume–enriched partial melts. The section of the ridge to the north of the hotspot trail jumped first to form the Northern Volcanic Zone, which is connected to the Mid–Atlantic Ridge offshore by the transform Tjörnes Fracture Zone. The section of ridge to the south of the hotspot trail (the Western Volcanic Zone) is presently being replaced by the Eastern Volcanic Zone. The South Iceland Seismic Zone represents an

evolving transform fault zone which is responding to the southward propagation of the Eastern Volcanic Zone.

Chapter II

The Krafla Volcanic System

2.1 The Plate Boundary in Northeast Iceland

The Northern Volcanic Zone (section 1.4.3) contains five *en échelon* volcanic systems, each consisting of a fissure swarm oriented at about N10°E which passes through a central volcano. Figure 2.1 shows the configuration of the volcanic systems in Northeast Iceland. The direction of plate spreading, as deduced from the Charlie–Gibbs Fracture Zone, is N100°E and perpendicular to the trend of the fissure swarms. It is, however, oblique to the plate boundary, if the latter is defined as a line connecting the central volcanoes (Björnsson, 1985). The Northern Volcanic Zone is offset by about 100 km to the east from the Kolbeinsey Ridge by the offshore Tjörnes Fracture Zone. The Tjörnes Fracture Zone is a broad zone of high seismicity (section 1.3.1) which contains several oblique extensional features which been observed by seismic reflection and magnetic profiling (M^{c}Master et al., 1977).

From North to South the volcanic systems are called the Theistareykir, Krafla, Fremrinámur, Askja and Kverkfjöll systems. The fissure swarms display extensional features such as eruptive and open fissures and normal faults. All central volcanoes contain a high temperature geothermal field. The Theistareykir and Femrinámur central volcanoes have no calderas and their systems contain more numerous olivine–tholeiitic lava shields than elsewhere in the rift zone. These factors combined are thought to indicate that the magma for these systems erupts directly from the mantle (Sæmundsson, 1978, 1979; Jakobsson, 1979). However, the presence of high temperature geothermal areas is an indication of the presence, or former presence, of shallow magma. The Krafla, Askja and Kverkfjöll central volcanoes have developed calderas, and their fissure eruptives are more dominantly olivine–poor tholeiites which are thought to have come from crustal magma sources (Sæmundsson, 1979). Major volcano–tectonic activity is episodic in the Northern

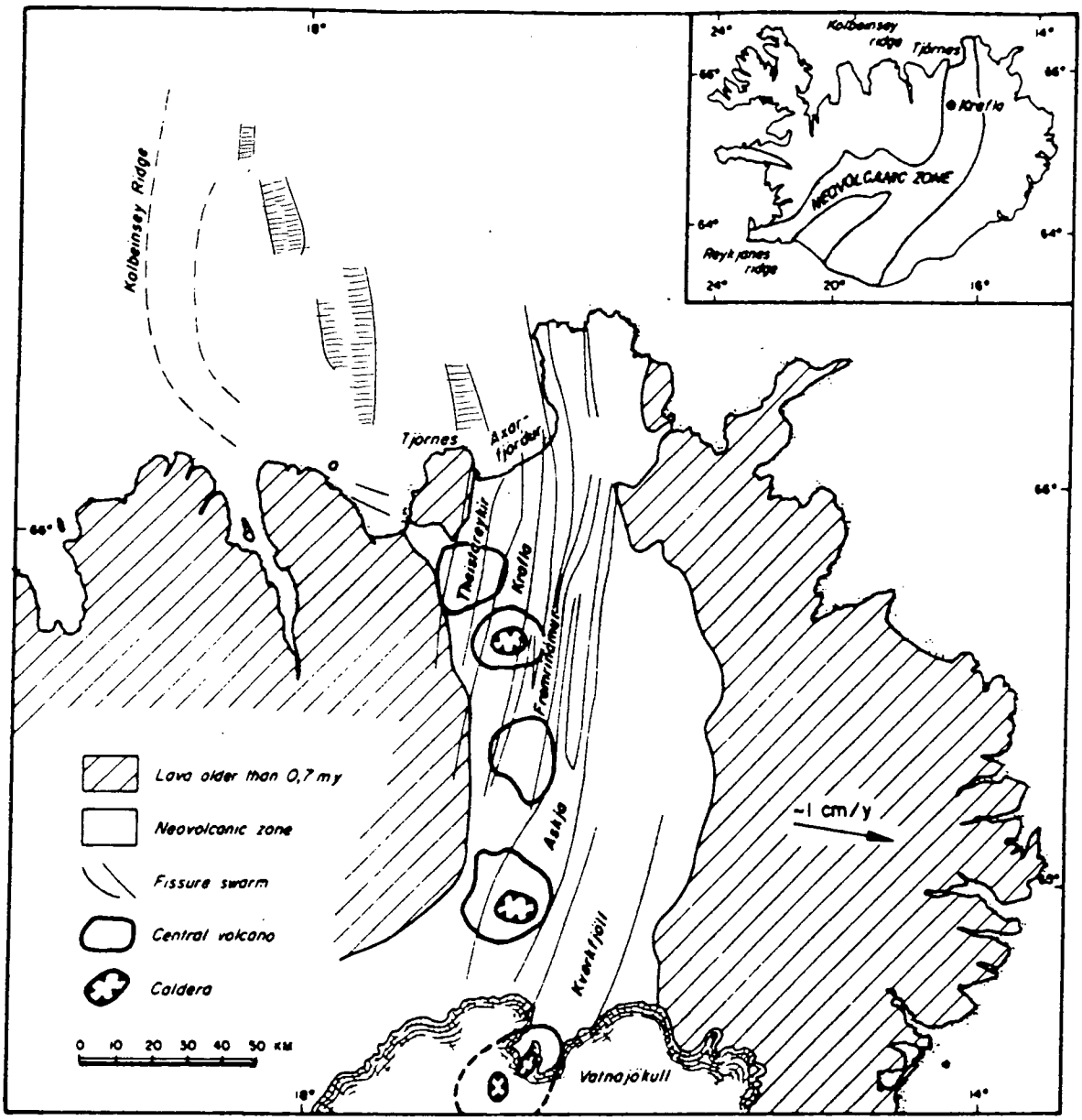

Figure 2.1 : Simplified tectonic map of NE Iceland. The axial rift zone is characterized by five elongated *en échelon* volcanic systems. The inset shows the neovolcanic zone in Iceland divided into an axial rift zone and flank zones, adapted from Sæmundsson (1974). Shaded areas offshore are graben structures, adapted from M^{c}Master et al. (1977). The arrow indicates the spreading direction (from Björnsson, 1985).

Volcanic Zone, occurring every 100–150 years, with a single fissure swarm being active during each episode (Björnsson et al., 1977).

2.2 The Krafla Area

2.2.1 Geology

The Krafla volcanic system consists of a fissure swarm about 10 km wide and 100 km long and a central volcano about 20 km wide, defined by the extent of acidic rocks (figure 2.1). The fissure swarm extends north–northeast from an area immediately to the west of the Fremrinámur central volcano, bisects the Krafla central volcano and terminates offshore in Axarfjördur.

Figure 2.2 shows the main tectonic and geological features of the Krafla volcanic system. The Krafla central volcano contains a fairly inconspicuous low–relief caldera which measures about 10 km in an east–west direction and about 8 km in a north-south direction. Assuming that the caldera was originally circular and that spreading has occurred at the average half–rate deduced from offshore magnetic anomalies of 1 cm/year (Talwani and Eldholm, 1977), this elongation suggests that caldera collapse occurred about 100,000 years ago, during the last interglacial period. It is thought that caldera collapse followed an eruption which formed a sheet of dacite airfall tuff, now welded and exposed around the caldera ring fault, along with sub–parallel dykes and eruptive fissures (Björnsson et al., 1977). The caldera has subsequently been filled almost to the rim with volcanic material. On its eastern and western flanks, low–angle outward dipping lavas and breccias suggest the prior existence of a shield volcano with a diameter of at least 20 km (Björnsson et al., 1977).

Postglacial fissure volcanism has been concentrated mainly within the caldera and to the north and south. Most of the eruptions have been basaltic, but andesite and dacite flows also occurred (Björnsson et al., 1977). The basalts are mostly of olivine normative composition outside the caldera but are dominantly quartz normative within the caldera (Ármannsson et al., 1987). Voluminous silicic eruptions have not occurred in postglacial time but four subglacial silicic eruptions within and around the caldera produced large domes and ridges during the last glacial period (Björnsson et al., 1977). During the last glacial period distinctive hyaloclastite

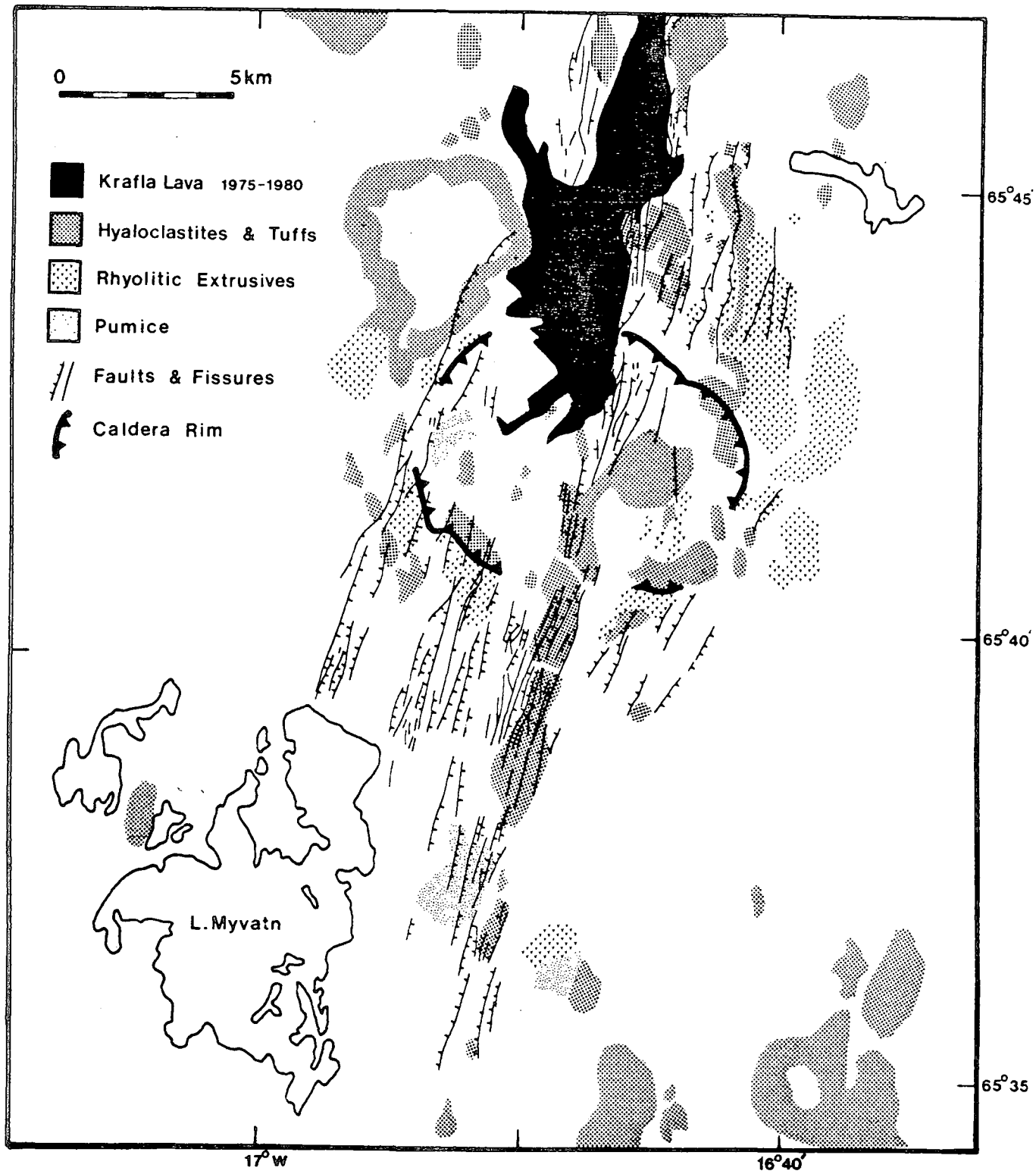

Figure 2.2 : Simplified geological map of the Krafla area (adapted from Sæmundsson, 1977).

ridges parallel to the fissure swarm also developed within the caldera and extended to the north and south (figure 2.2).

The whole chemical range of volcanic rocks from basalt to rhyolite is found in the Krafla area with basic and acid types most abundant, and the $^{87}Sr/^{86}Sr$ ratio of the rhyolites is identical to that of the basalts. These features have been interpreted to indicate that the rhyolites were generated by remelting of basaltic crust (Grönvold, 1976).

Tephra erupted from Hekla and other volcanoes in postglacial times have in some instances covered much of Iceland. An approximate chronology for this succession has made it possible to date other postglacial eruptives by studying their relative positions in the sequence. These tephrachronological studies have been used to determine approximate dates for postglacial eruptives in the Krafla area prior to reliable historical records (Thórarinsson, 1960; Björnsson et al., 1977; Ármannsson et al., 1987). Following an early period of postglacial activity in the Krafla area, there was an eruptive hiatus of more than 4,000 years. Five major volcanic episodes have been recorded within the last 3,000 years, separated by an average interval of about 500 years. The most prolific of these erupted from the Threngslaborgir–Lúdentsborgir crater row to the south of Námafjall (figure 2.3), producing in total 2–3 km^3 of extrusives which covered an area of about 220 km^2. In postglacial times a total of about 35 eruptions have taken place within the Krafla fissure swarm, most of which occurred either within the Krafla caldera or to the south (Björnsson et al., 1977, 1979).

The only historically recorded eruptive events to have occurred in the Krafla area prior to 1975 were the 'Mývatn fires' of 1724–1729 (Björnsson et al., 1977; Grönvold, 1984). The episode began in May 1724 with the formation of a row of explosive craters within the caldera, the most active of which was Víti (figure 2.3). Mud, rock debris, pumice and scoria were ejected from the crater row over a few days, covering large areas of the caldera. Throughout 1725 earthquakes were felt and steam and mud craters were formed in what are now the Krafla and Námafjall geothermal areas (figure 2.2). There then appears to have been a period of volcano–tectonic quiescence until August 1727 when a fissure eruption started at Leirhnjúkur in the centre of the caldera. The fissure extended southwards to

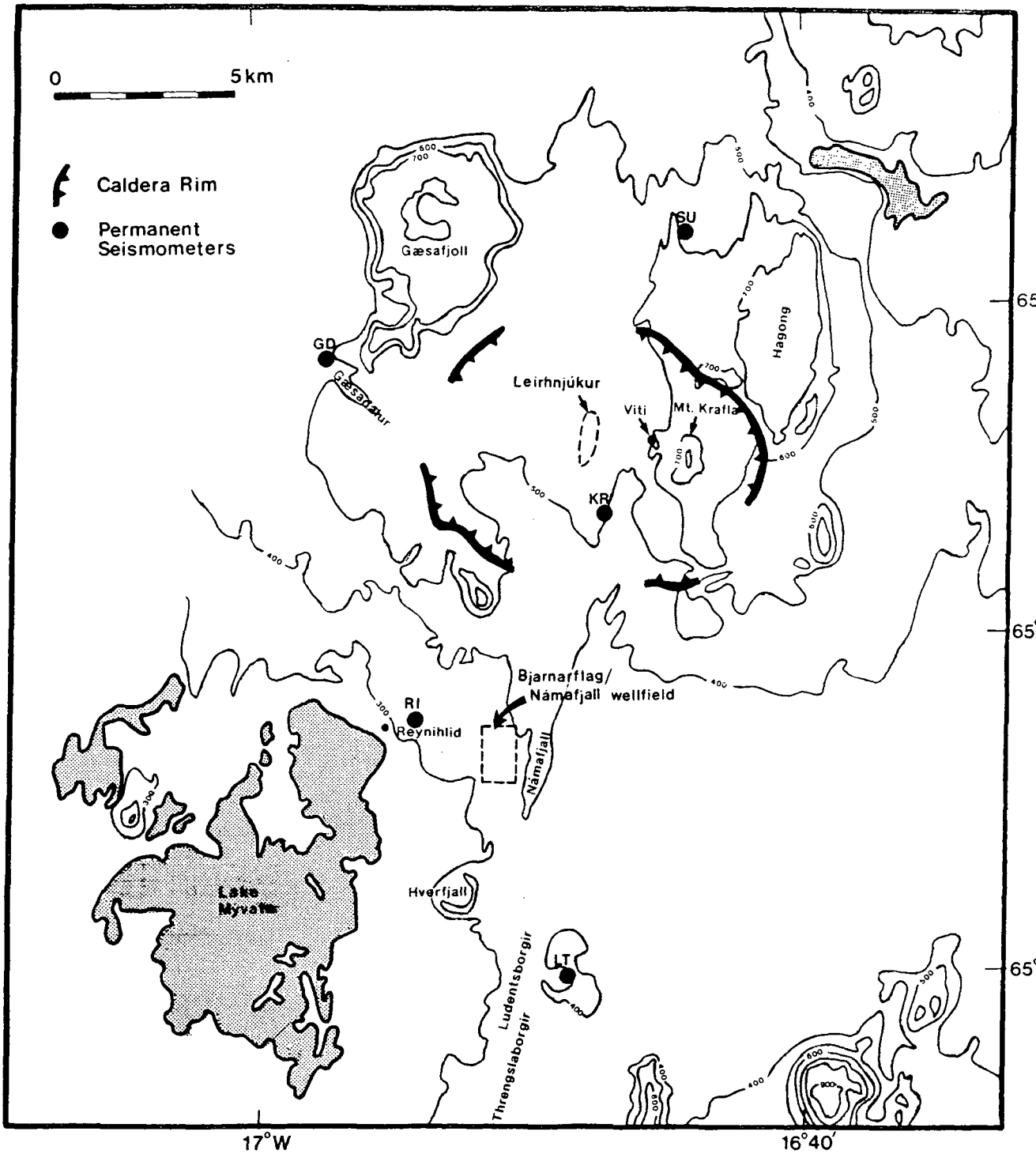

Figure 2.3 : Simplified topographic map of the Krafla area (adapted from Sæmundsson, 1977).

Námafjall in April 1728 and the lava continued to flow until September 1729. Further volcanic and earthquake activity on this fissure is reported to have occurred in 1746. A total of about 0.45 km^3 of basalt was produced during this episode, covering about 35 km^2, and it is thought from their chemical composition that the magma was stored at a shallow depth for a short time prior to eruption (Grönvold, 1984).

2.2.2 Subsurface Geological Investigations

The presence of numerous fumaroles, boiling mudpools and hot and chemically altered ground within the Krafla caldera and in the Námafjall area are obvious indications of geothermal systems. Both these areas have consequently been prime targets for the Icelandic geothermal program.

The Námafjall field is limited to the hyaloclastite hill Námafjall and the low ground to the east and west of it (figures 2.2, 2.3). Industrial exploitation of the high temperature geothermal field began in 1967 for the processing of diatomite deposits from Lake Mývatn (Ragnars et al., 1970), although local people had for a long time used the hot ground for baking bread and the pools of hot water in open fissures for bathing. A 3 MW power station was installed at Bjarnarflag, to the west of Námafjall (figure 2.3), in 1969. Little is known to the author to have been published about the subsurface geology of the Námafjall area. Ragnars et al. (1970) showed that the upper 300–400m of the production boreholes pass through strata dominated by hyaloclastites and basalts. Below this depth, propylitized rock becomes dominant. The main steam discharge into the boreholes was reported to occur at a depth of about 640–680m, with further production horizons at about 1100–1200m.

Systematic geothermal exploration of the Krafla high temperature geothermal field began in 1970 with a series of surface geological and geophysical investigations, and the first exploration wells were drilled in 1974 (Stefánsson, 1981; Ármannsson et al., 1987). .A 60 MW electric power plant was commissioned in 1975, just before the onset of the rifting episode which seriously affected the production characteristics of the field. The main results of recent subsurface geological investigations associated with exploration of the Krafla geothermal field are given by Ármannsson et al. (1987) and are summarized below.

Investigations of subsurface lithology at Krafla are based on the analysis of drill cuttings from 24 wells, all of which lie within the caldera. The locations of two cross–sections based on these well data are shown in figure 2.4, and the geological cross–sections are shown in figure 2.5. At least five stratigraphic horizons have been distinguished in the uppermost 1200–1300m of the field, below which depth intrusives become dominant. The top horizon (B-1) is a postglacial lava formation beneath which is a hyaloclastite formation (M-1) which probably dates from the last glacial period. Below that is a group of lavas dating from the latter part of the last interglacial period (B-2), which is underlain by a hyaloclastite formation (M-2) that is considered to represent the bottom of the caldera fill. This suggests that the throw on the caldera fault is about 1 km, and so it has presumably been reactivated many times. Below this level there are lavas from the early part of the last interglacial period (B-3), followed by basaltic and doleritic intrusions which dominate the strata in the interval 1000–2200m depth below the surface in the centre of the caldera. However, towards the eastern rim of the caldera, gabbro intrusions become dominant below 1800–2000m depth. Some acid intrusions occur at the top of this gabbro and at the base of the hyaloclastite formation M-2. A subsurface horst structure (figure 2.5b) runs west–northwest to east–southeast beneath the main geothermal field and several other major faults are thought to exist in the southern part of the caldera and in the intrusive gabbro formation to the east.

Geothermal alteration zones for the two cross–sections are shown in figure 2.6. The high temperature alteration zones are seen to up–dome beneath the main fields of Sudurhlídar in the east (figure 2.6a), Hvíthólar in the south (figure 2.6b), and Leirbotnar in the centre of the caldera (figure 2.6b). However, the alteration mineral assemblages in the Leirbotnar field have been overprinted by calcite from a more recent invasion of water at a temperature of 190–200°C from the north. At Leirbotnar, the geothermal system is divided into an upper and a lower zone (Stefánsson, 1981), as shown in figure 2.7, with the main aquifers in the lower zone being connected to fissures and intrusion contacts. The upper zone is water dominated at 205°C and the lower zone is boiling at 300–350°C. In the southern part of the field, two main fractures feed the wells and in the northern part the wells draw mainly from the contact zone of a granophyre intrusion at 1900–2100m depth (figure 2.5a). The main aquifers of the Sudurhlídar field in the east are connected

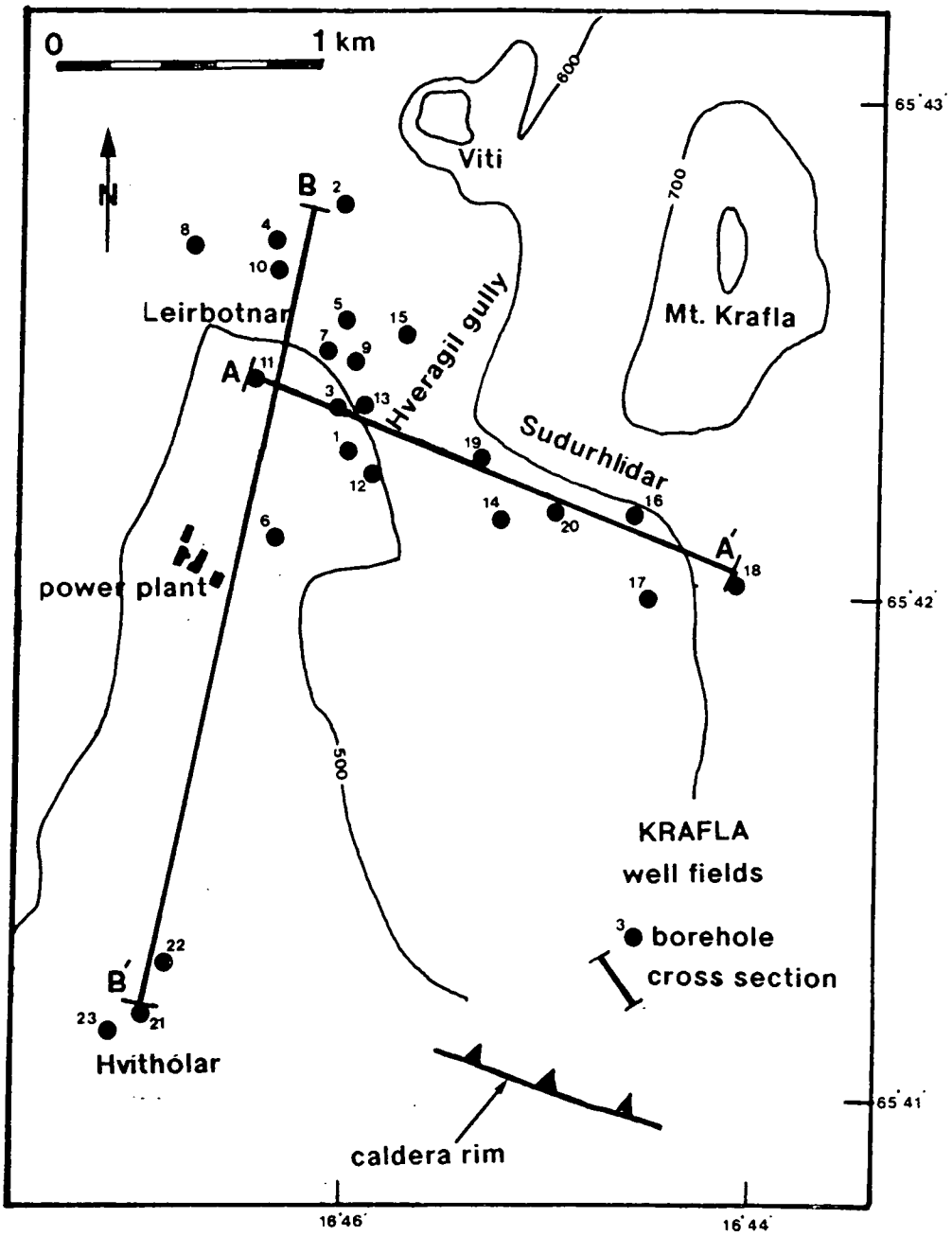

Figure 2.4 : Map of the three geothermal well fields at Krafla. Locations of cross-sections shown in figures 2.5 and 2.6 are marked (adapted from Ármannsson et al., 1987).

(a)

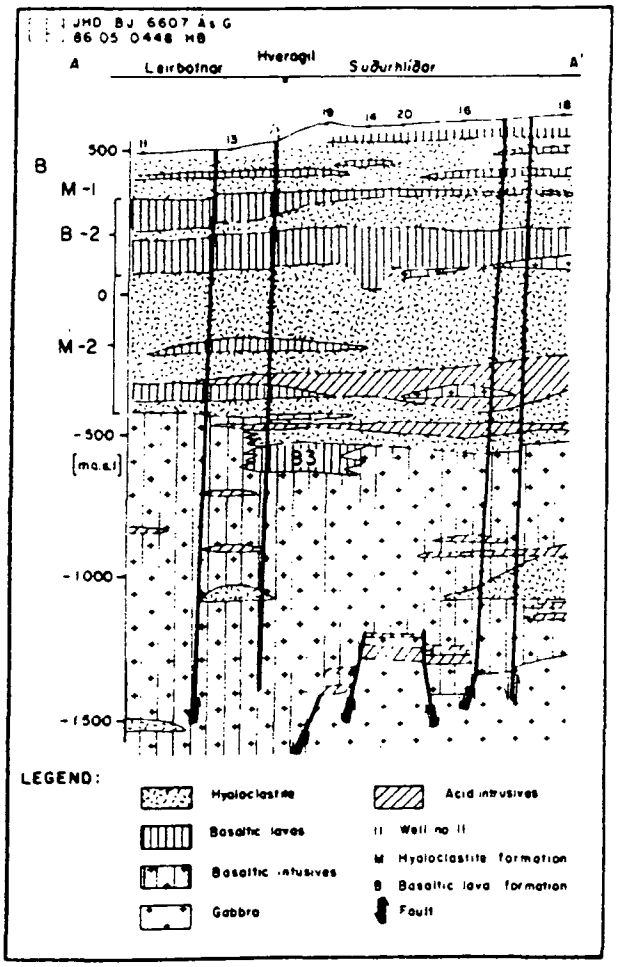

(b)

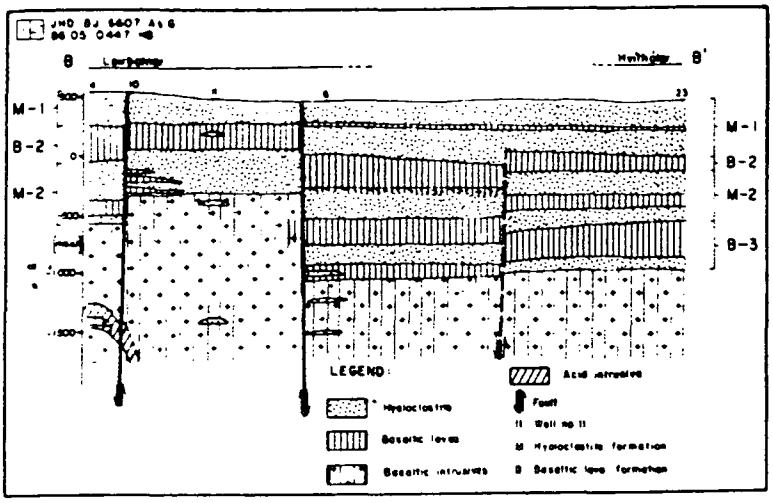

Figure 2.5 : Geological cross-sections of the Krafla caldera, constructed using borehole data. Locations of sections are shown in figure 2.4. **(a)** The Leirbotnar and Sudurhlídar well fields. **(b)** The Leirbotnar and Hvíthólar well fields. (Adapted from Ármannsson et al., 1987).

(a)

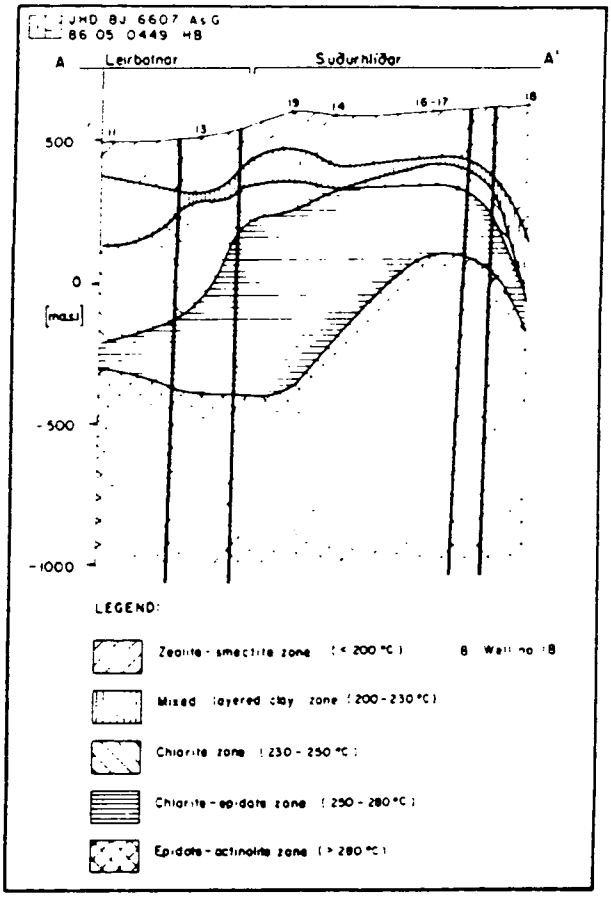

(b)

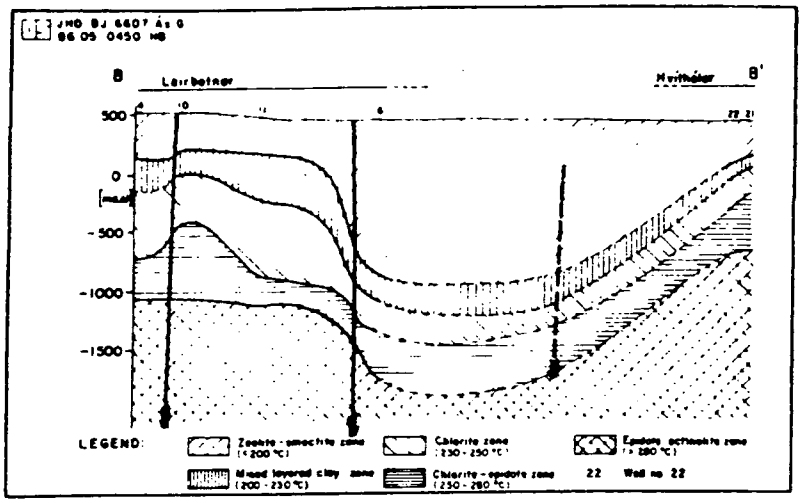

Figure 2.6 : Cross-sections showing alteration zones within the Krafla caldera. Locations of sections are shown in figure 2.4. **(a)** The Leirbotnar and Sudurhlídar well fields. **(b)** The Leirbotnar and Hvíthólar well fields. (Adapted from Ármannsson et al., 1987).

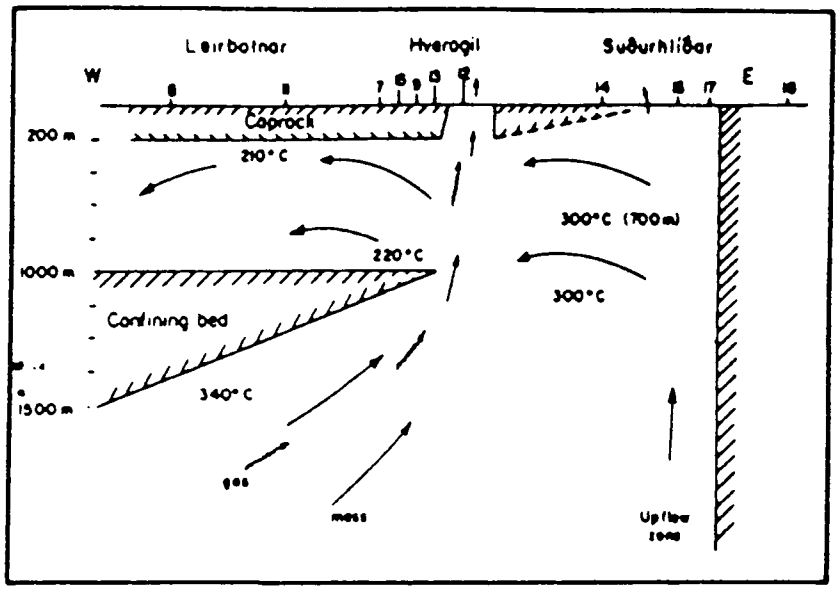

Figure 2.7 : A conceptual model of the Leirbotnar and Sudurhlídar well fields (from Ármannsson et al., 1987).

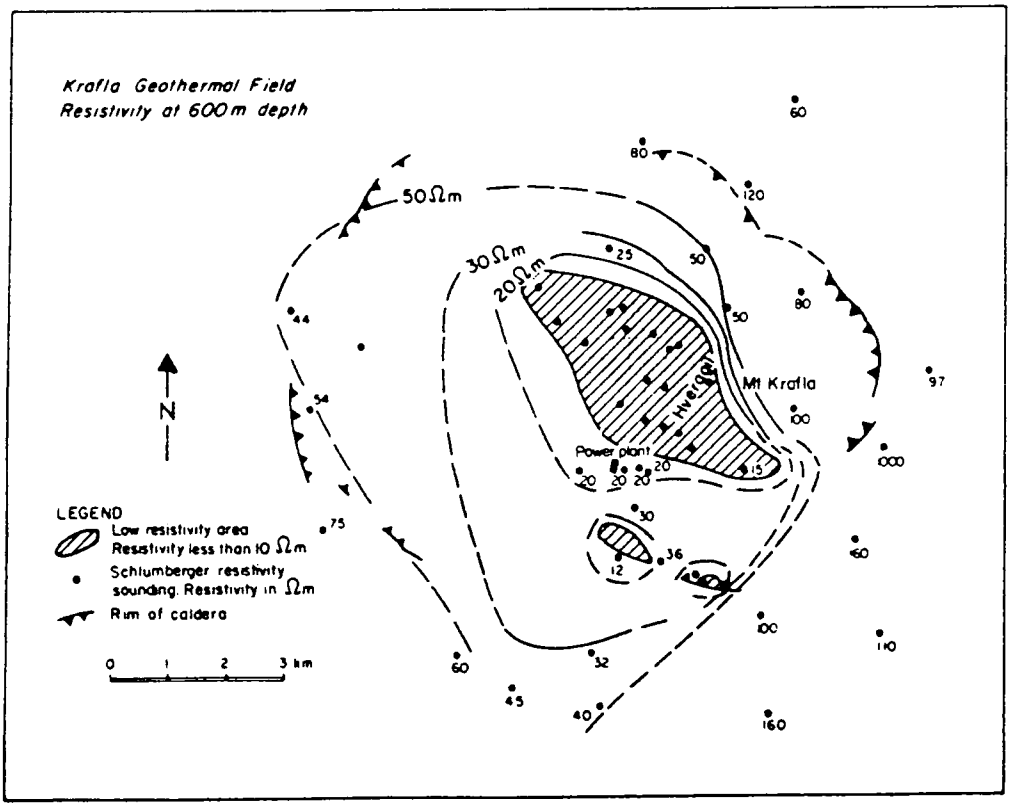

Figure 2.8 : Schlumberger d.c. resistivity at 600m depth in the Krafla geothermal area (from Stefánsson, 1981).

to horizontal acid intrusions at the base of the M-2 hyaloclastite formation at 900–1200m depth, and deeper aquifers are associated with contacts with vertical or subvertical fractures and dykes (figure 2.5a). The reservoir temperature is 300°C. The geothermal fluid in the Hvíthólar field in the south flows laterally from a near–vertical permeability anomaly (which is thought to be a dyke) beneath young volcanics, into a hyaloclastite formation at 300–700m depth. This reservoir has a temperature of 250-260°C.

Extensive numerical modelling of the Krafla geothermal field has been carried out (Bödvarsson et al., 1984a,b,c; Pruess et al., 1984) in order to estimate the generating capacity of the reservoir and to predict its future behaviour. Their conceptual model consists of a cross–section which included the Leirbotnar and Sudurhlidar fields and is shown in figure 2.7. Estimates derived from this modelling suggested that the areas so far exploited could sustain power production of about 55 MW for 30 years (Leirbotnar 30 MW, Sudurhlídar 20 MW and Hvíthólar 5 MW), although the longevity of the field could probably be extended by reinjection.

2.2.3 Geophysical Research

Prior to the onset of the recent rifting episode in Northeast Iceland, most geophysical research carried out in the Krafla area was aimed at geothermal prospecting.

The results of a Schlumberger d.c. survey are shown in figure 2.8. They show that the Krafla geothermal reservoir at 600m depth is characterized by a large resistivity low in the central part of the caldera and two smaller ones near the southern caldera rim. The major anomaly is underlain by a body of higher resistivity which coincides with a change in lithology from hyaloclastites to basaltic lava formations and increased frequency of intrusive rocks (figures 2.5a,b) and high temperature hydrothermal alteration (figures 2.6a,b), (Ármannsson et al., 1987). This picture of shallow local resistivity variations is superimposed on to a deeper image of resistivity which was observed using the magnetotelluric method (figure 2.9). A low resistivity layer (with a resistivity of about 10–20 Ωm) was found to be present beneath the whole of Northeast Iceland, with extremely low resistivities of about 1–5 Ωm present at only 5 km depth beneath the Krafla area (Beblo and Björnsson, 1978,1980; Beblo et al., 1983). This low resistivity layer is thought to indicate basaltic partial melt at the crust–mantle interface. Its peak beneath Krafla is

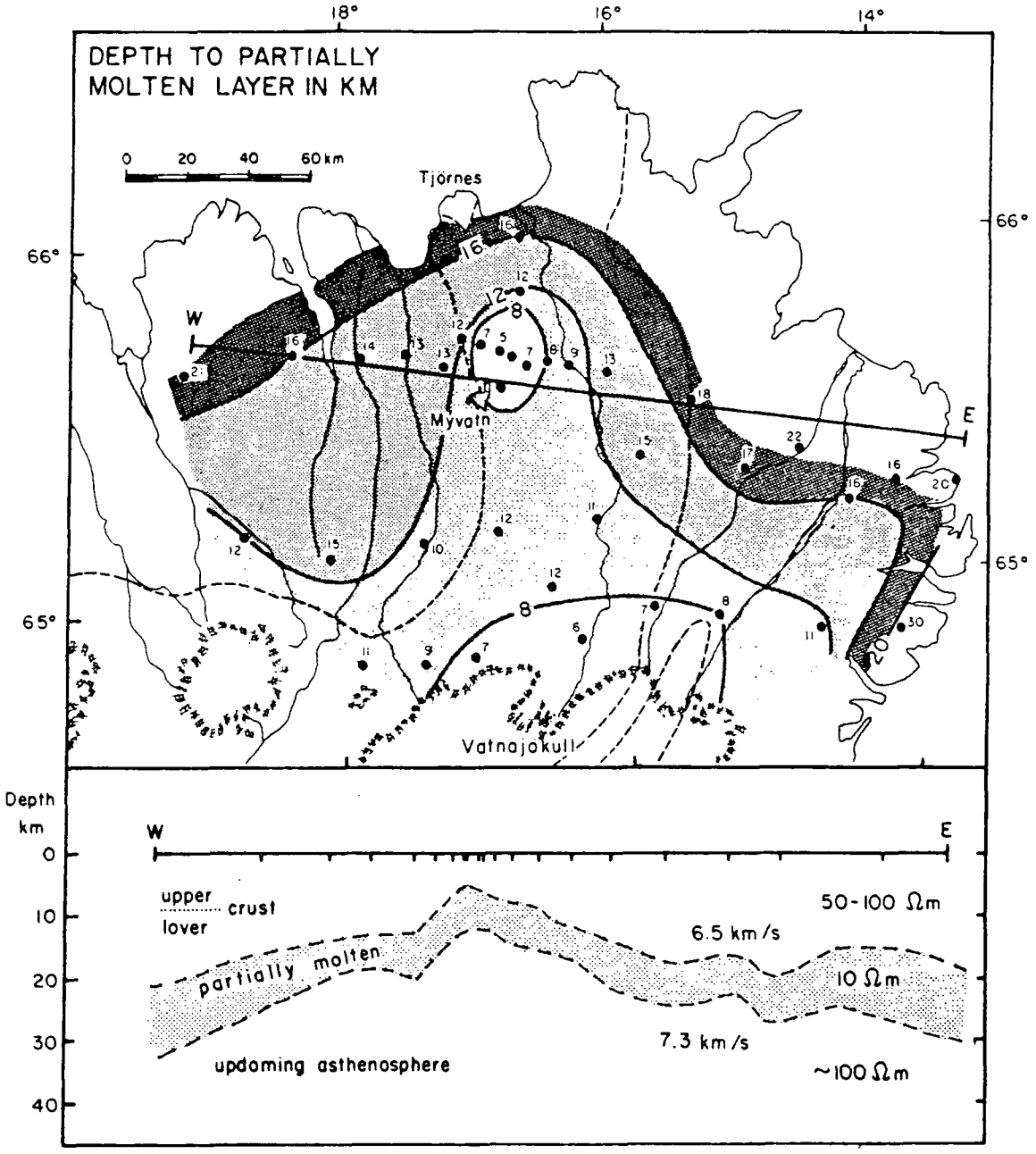

Figure 2.9 : Depth to the low-resistivity, partially molten basaltic layer in NE Iceland. It is thought to correspond to crustal thickness. Depths in kilometres. Below the low-resistivity layer is a broad upwelling asthenosphere. The data are taken from Beblo and Björnsson (1978, 1980) and Beblo et al. (1983). Seismic velocities are taken from Angenheister et al. (1980) and Flóvenz (1980). (From Björnsson, 1985).

interpreted to indicate a shallow magma chamber. This is consistent with the results of Zverev et al. (1980a), who observed a seismically homogeneous body below about 8 km depth (section 1.3.2), and Einarsson (1978), who observed an S–wave shadow zone at a depth of about about 3–7 km beneath the caldera. It is also consistent with large teleseismic delays which were observed within the caldera relative to outside (MacKenzie, 1989).

An aeromagnetic survey of the Krafla area (figure 2.10) demonstrates a strong correlation between the presence of magnetic lows and areas of geothermal activity in both the Krafla and Námafjall areas. This association has been attributed to geothermal alteration of magnetic minerals (Stefánsson, 1981). However, it has not been established whether the broad magnetic low within the caldera is a discrete feature or a side lobe of the large magnetic highs at the caldera rim to the north and east.

A gravity survey covering Northeast Iceland was carried out between 1964 and 1970, and demonstrated the presence of a Bouguer gravity low of about 5 mgal at the central part of the neovolcanic zone, which was attributed to thickening of low density Quaternary volcanics (Schleusener et al., 1976). A more recent residual Bouguer map of the Krafla area (figure 2.11) shows the presence of broad gravity highs near the caldera rim to the northwest, southwest and east, and a northwest–southeast elongated gravity low to the south of the caldera. This pattern suggests that relatively high density material exists at shallow depth beneath sections of the caldera rim compared with that of the caldera fill.

During 1967 and 1968, surveys of microearthquake activity were conducted for the first time in the Krafla area as part of a general reconnaissance of Iceland (Ward et al., 1969; Ward and Björnsson, 1971). In 1967, a tripartite array of geophones and smoked drum recorders was operated. The locations of earthquakes from this tripartite survey are shown in figure 2.12a. An average of 191 events were recorded each day in the vicinity of the Krafla caldera and 86 events on average at a station just to the north of Lake Mývatn. A b–value of 0.83 ± 0.29 was calculated for these events, based on maximum P–wave amplitudes. In contrast, however, an average of only 1.2 events per day were recorded in the Krafla area during the 1968 survey when recorders were operated individually. This dramatic variation in the seismic

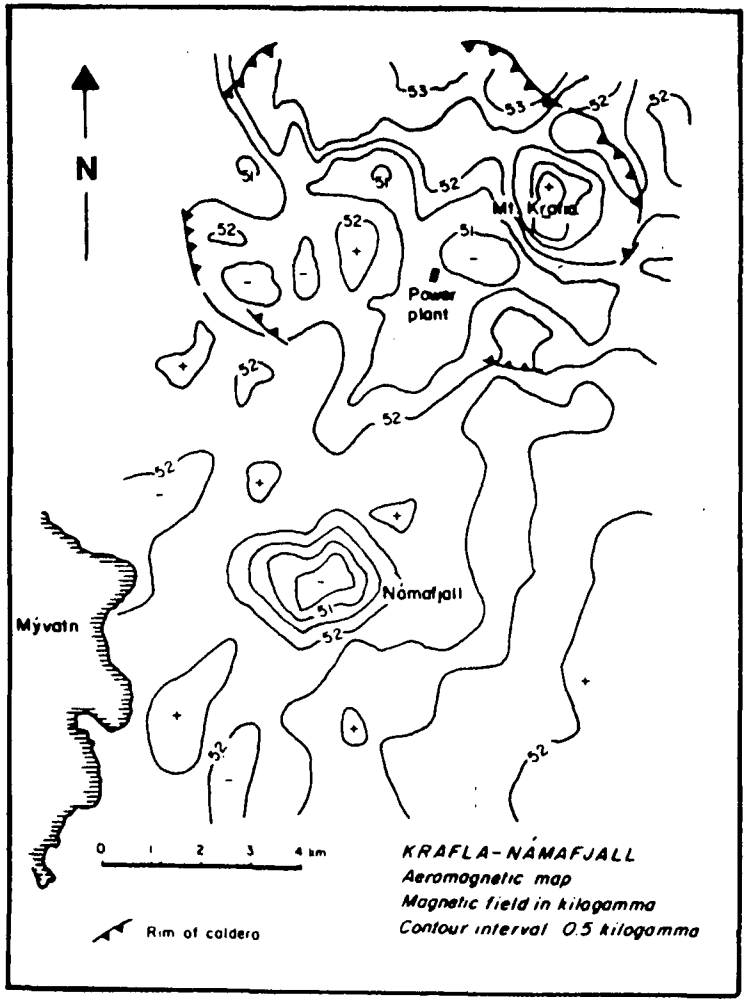

Figure 2.10 : An aeromagnetic map of the Krafla area (from Stefánsson, 1981).

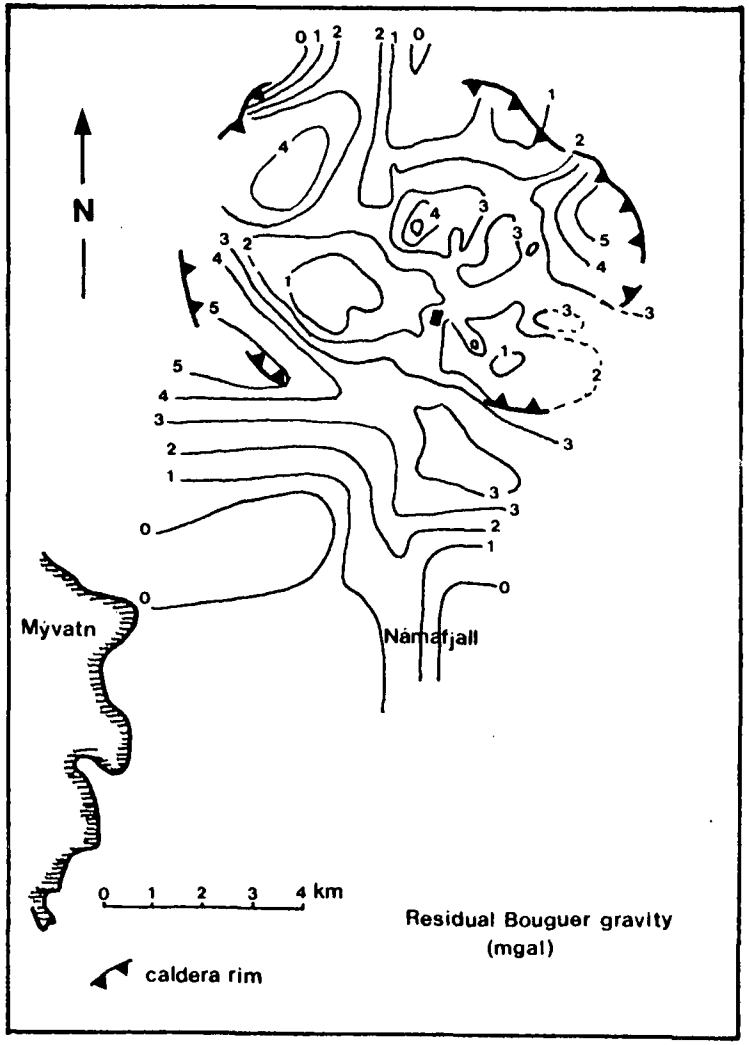

Figure 2.11 : A residual Bouguer gravity map of the Krafla area (adapted from Karlsdóttir et al., 1978)

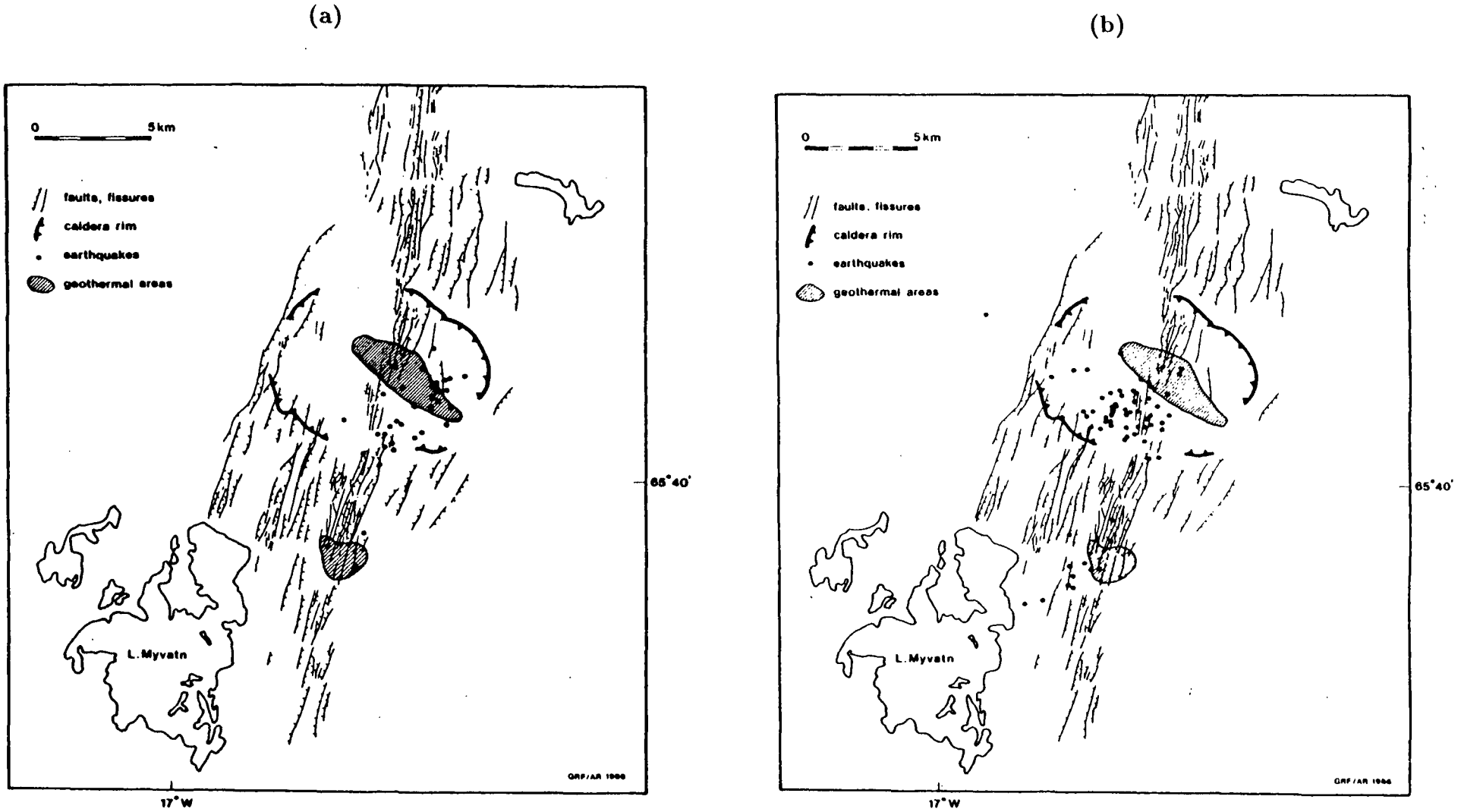

Figure 2.12 : (a) Epicentres of events in the Krafla area recorded in 1967 and 1968 on temporary tripartite arrays, and main areas of surface geothermal activity (compiled by Foulger (1986) using data from Ward et al. (1969); Ward and Björnsson (1971). **(b)** Epicentres of events in the Krafla area located for the period 22 August to 15 October 1982, when the magma chamber was undergoing inflation. Main areas of surface geothermal activity are also shown. (Compiled by Foulger (1986) using data from Einarsson (1982)).

activity of the area was attributed to swarm occurrence during the 1967 survey, due to volcanic or geothermal activity (Ward and Björnsson, 1971). The events occurred between 0–4 km in depth. The precision of location was reported to be about 0.3 km in distance and depth for events within the Krafla caldera and about 0.5 km in distance and 1 km in depth for events beneath Námafjall (Ward and Björnsson, 1971).

A similar distribution of earthquake locations was observed during a phase of slow inflation of the Krafla volcano late in 1982 (figure 2.12b), in which most of the activity was concentrated towards the southern part of the caldera and subsidiary activity occurred in the Námafjall area to the south (Einarsson, 1982). During this period, the level of the caldera began to rise above its previous maximum (section 2.3.3). Einarsson (1990) notes that it was at this stage that seismic activity, which he calls 'inflation earthquakes', would begin in the roof of the caldera. It may be concluded that these 'inflation earthquakes' were dominant within the caldera at this time. However, the activity at Námafjall indicates that background geothermal seismicity occurred there, and probably also in the Krafla geothermal area, simultaneously.

2.3 The Recent Rifting Episode in the Krafla Area

2.3.1 Introduction

A major rifting episode began at the plate boundary in North Iceland in December 1975 and lasted for about 10 years. The episode affected the Krafla fissure swarm between latitudes 65°34′N and 66°18′N. During the episode there were about 20 rifting events, which occurred as short periods of activity at intervals of a few months. Each event involved the rapid flow of magma out of the crustal magma chamber and was accompanied by migrating seismicity, vertical and horizontal ground movements, and sometimes volcanic eruptions. Between the active pulses the caldera inflated steadily as the magma chamber was filled from below, causing earthquake activity in the caldera floor when the land height rose above its previous maximum, and further magmatic outbursts.

This rifting episode provided a rare opportunity for geophysicists to study the crustal accretion mechanism in action, for which the techniques mainly applied were earthquake seismology, gravity and geodesy. Earthquake seismology found its primary use in imaging the subsurface geometry of the dyke injection process, while gravity and geodesy constrained the ground deformation effects and provided contemporaneous observational evidence for plate spreading in Iceland.

A geodetic network in Northeast Iceland was first set up by Niemczyk in 1938 in order to measure tectonic movements in the neovolcanic zone (Möller and Ritter, 1980). Remeasurement of the geodetic network in 1965 showed no significant movement, and a contraction was observed in the same area during the 1965–1971 interval (Gerke, 1974)! Further measurements in 1975, prior to the onset of volcano–tectonic activity, showed that extension of up to 0.3m had occurred in the same area around Krafla (Torge and Drewes, 1977; Möller and Ritter, 1980; Möller et al., 1982).

In early 1975, conspicuous seismic activity was first observed within the Krafla caldera. By the autumn of 1975 the intensity of earthquake occurrence had risen to an unusually high level and a geothermal borehole within the caldera had begun to blow out repeatedly, all of which encouraged the local civil defence committee to prepare for a volcanic eruption (Björnsson et al., 1977). In addition, the enhanced

seismicity prompted the setting up of two more permanent seismometers in the area in October 1975 (Einarsson and Björnsson, 1987). One was set up within the Krafla caldera and the other at Gæsadalur about 9 km to the northwest. They supplemented the existing seismometer at Reynihlid (figure 2.3). With the additional help of other permanent stations of the Icelandic regional network, it was then possible to determine hypocentral locations in the Krafla area with some accuracy.

2.3.2 The First Event

Continuous seismic tremor was first observed on the Krafla seismograph on the morning of 20th December 1975 and was accompanied by an intense earthquake swarm. About an hour later, an eruption started near Leirhnjúkur (figure 2.3) in the centre of the caldera from a fissure about 2 km in length. The seismic activity then propagated northwards, along the fissure swarm, and covered at least 40 km within 2 hours. After a few hours, the activity was mainly confined to the Krafla caldera and the Axarfjördur region (figure 2.1), where the maximum earthquake magnitudes increased until events of magnitude 5.0 and 6.3 occurred respectively in the two areas in mid–January 1976. During this time activity in the caldera was widely distributed, and most earthquakes occurred between 0–4 km depth but a few were as deep as 10 km. In Axarfjördur the epicentres were distributed along the most northern section of the fissure swarm and the adjacent section of the Tjörnes fracture zone (Björnsson et al., 1977). The volcanic eruption at Leirhnjúkur originated from three craters along the fissure which had been active during the 'Mývatn fires' of 1724–1729, and was virtually complete within about 20 minutes, with the exception of minor volcanic explosions. Within a day only water and steam were being ejected from the craters. The lava produced by the eruption was pahoehoe type quartz normative tholeiitic basalt (Björnsson et al., 1977).

The effects of the activity on the geothermal boreholes in the Krafla area were significant. In addition to increased fluid pressure in the boreholes, the CO_2 content of the geothermal fluid increased 100 fold and the pH dropped dramatically. The thermal output of the area increased and new fumaroles appeared (Björnsson et al., 1977).

It was immediately obvious that spreading had taken place across the fissure zone from the stretching and breaking of telephone lines and fences in the Axarfjördur area (Sigurdsson, 1980). Measurements of newly formed cracks revealed a horizontal extension of about 70cm in the Krafla area and 1.0–1.5m in the Axarfjördur area (Björnsson et al., 1977; Sigurdsson, 1980). In addition, relative subsidence of up to 1.5m was estimated to have occurred within the active fissure swarm, with elevation of the flanks of up to 40cm (Sigurdsson, 1980). Levelling in March 1976 showed that subsidence of about 2.1m had occurred near the eruption site since 1974, relative to the north end of Lake Mývatn (Björnsson et al., 1977).

2.3.3 Subsequent Activity

Soon after the earthquake swarm associated with the first rifting event ended, the Krafla volcano started to inflate. This was observed both by optical levelling measurements (Tryggvason, 1978) and tiltmeter readings (Björnsson et al., 1977, 1979). The rate of uplift was greatest near the centre of the caldera, decreasing gradually outwards, and was consistent with the inflation of a spherical body centred at a depth of about 3 km at a rate of about $5 m^3 s^{-1}$ (Tryggvason, 1978). Figure 2.13 shows the correlation between the tilt measured near the centre of the caldera and seismic activity within the caldera from October 1975 to December 1976. By May 1976 there was a noticeable increase in earthquake activity which became more marked until September 28th 1976, when it decreased sharply. At the same time rapid subsidence began within the caldera, followed by seismic tremor when the subsidence rate was at its highest. At about the same time, earthquakes originating from the fault swarm about 15 km north of the caldera were recorded. On October 4th the subsidence stopped and the area began to rise again at a similar rate as before (Björnsson et al., 1977). No widening of the fissure swarm was reported for this event, but widening and subsidence of the active fissure swarm, along with compression and uplift of the flanks, was generally observed for subsequent events (Björnsson et al., 1979).

An episodic pattern of land elevation changes and seismo–tectonic activity similar to the above ensued for about 10 years, during which time a total of about 20 rifting events occurred, 9 of which were accompanied by basaltic fissure eruptions.

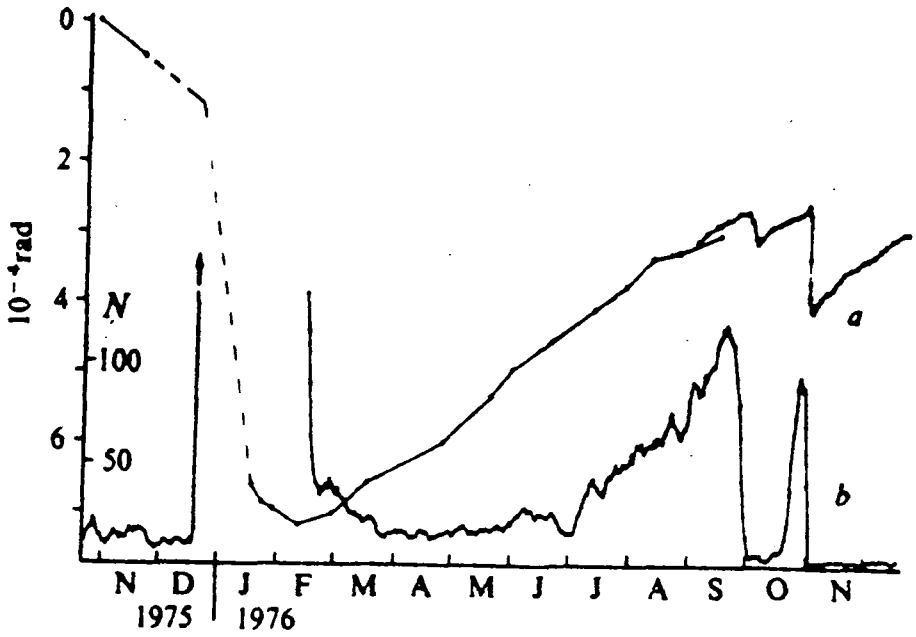

Figure 2.13 : Correlation between (a) the tilt of the Krafla power house and (b) the seismic activity within the caldera. The north–south component of tilt is shown, (increasing numbers mean tilt down towards north). The tilt corresponds well with the land elevation. N is the 5 day running average of the number of earthquakes recorded per day at the seismic station near Reynihlid with amplitude above a certain threshold. From 20 December 1975 to 14 February 1976, N was > 130 and most of that time > 1000. The tilt measurements before 20 August 1976 were done by optical levelling (from Björnsson et al., 1977).

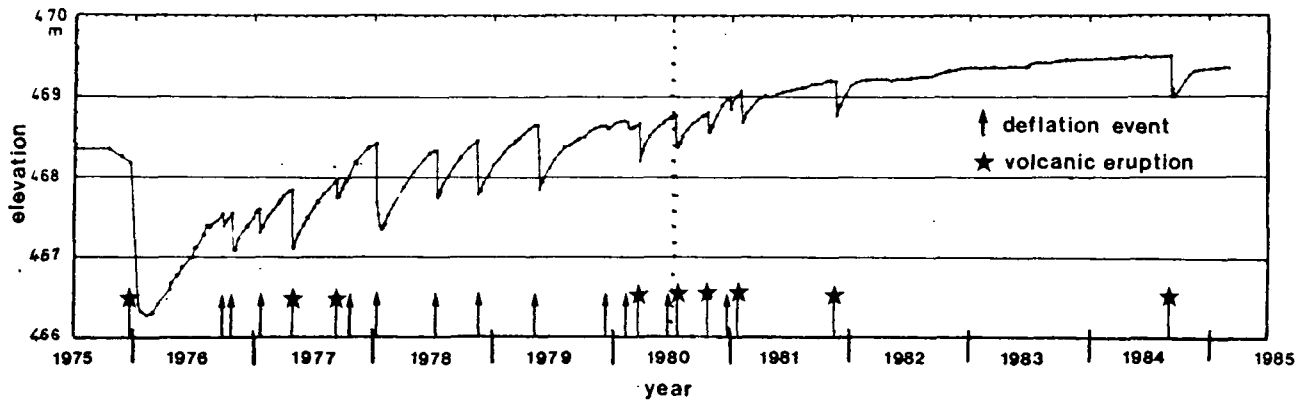

Figure 2.14 : Land elevation changes at bench mark FM5596, about 1 km SE of the centre of the Krafla caldera. The reference bench mark (FM6414) is 20 km away, at the southern end of Lake Mývatn. The crosses are levelling data, and the dots are interpolated values based on tilt measurements at the Krafla power plant. Arrows indicate rifting–deflation events, and stars indicate volcanic eruptions (adapted from Jacoby et al., 1989).

Subsidence–rifting event (time)	Maximum subsidence the apex (cm)	Direction of intrusion (North/South) (of caldera)	Area of extruded lava (km^2)
Dec. 20, 1975 to Feb. 1976	230	N	0.036
Sept. 28 to Oct. 4, 1976	17	N+S	
Oct. 31 to Nov. 1, 1976	51	N	
Jan. 20, 1977	32	N	
April 27–28, 1977	81	S	0.001
Sept. 8–9, 1977	24	S	0.5
Nov. 2, 1977	3	N	
Jan. 7–8, 1978	119	N	
July 10–12, 1978	64	N	
Nov. 12–15, 1978	72	N	
May 13–18, 1979	88	N	
Dec. 6–10, 1979	3	?	
Feb. 10–13, 1980	11	S	
March 16, 1980	53	N+S	1.3
June 20, 1980	2	?	
July 10–18, 1980	43	N	5.3
Oct. 18–23, 1980	29	N	11.5
Dec. 22–27, 1980	16	N	
Jan. 30 to Feb. 4, 1981	44	N	6.3
Nov. 18–23, 1981	47	N	17
Sept. 4–18, 1984	60	S	?
Sum total	10.29 m		42 km^2
Estimated total volume	0.6 km^3		0.1 km^3

Table 2.1 : Magma movements in rifting events (adapted from Björnsson, 1985).

A summary of these rifting–deflation events is given in table 2.1 and land elevation changes for the period are shown in figure 2.14.

Rifting events occurred only after the caldera was elevated to a point beyond its previous maximum level, which was marked by the onset of earthquake activity in the caldera floor. These 'inflation earthquakes' stopped immediately when inflation stopped or deflation began, and earthquake activity in the caldera floor resumed if deflation exceeded about 1m. Deflation was accompanied by volcanic tremor, the amplitude of which was roughly proportional to the rate of deflation, and seismic activity progressed in the same area as that in which the fissure swarm was widening (Einarsson, 1990).

The deflation of the volcano in September 1977 was accompanied by volcanic tremor and the migration of earthquake activity southwards along the fissure swarm (Brandsdóttir and Einarsson, 1979). This activity was monitored by an enlarged local network of eight seismometers, which enabled the seismicity to be studied in more detail and with more accuracy than before. The epicentres for this deflation event are shown in figure 2.15 and demonstrate that the activity was restricted to a narrow linear zone parallel with the fissure swarm and radiating southwards from the centre of the caldera. Figure 2.16 shows the hypocentres of the activity and illustrates their migratory path. Earthquake hypocentres at the beginning of the swarm sequence originated between 0–6 km depth, immediately to the south of Einarsson's S–wave shadow zone (figure 2.16b). The swarm slowly advanced southwards from the magma chamber at a rate of about 0.5 ms^{-1} until the activity culminated about six hours later with 8 earthquakes larger than magnitude 3 near the Námafjall geothermal area and a small basaltic eruption through a geothermal borehole (Larsen et al., 1979). Other brief periods of seismic activity have taken place in this zone to the south of the caldera synchronously with deflation of the magma chamber, as shown in figure 2.17. On each occasion, subsidence within the caldera was accompanied by the migration of earthquake activity southwards along the fissure swarm, terminating the in the Námafjall area. Similarly, an earthquake swarm during the July 1978 deflation of the volcano was observed to propagate northwards along the fissure swarm at a rate of 0.4–0.5 ms^{-1} (Einarsson and Brandsdóttir, 1980).

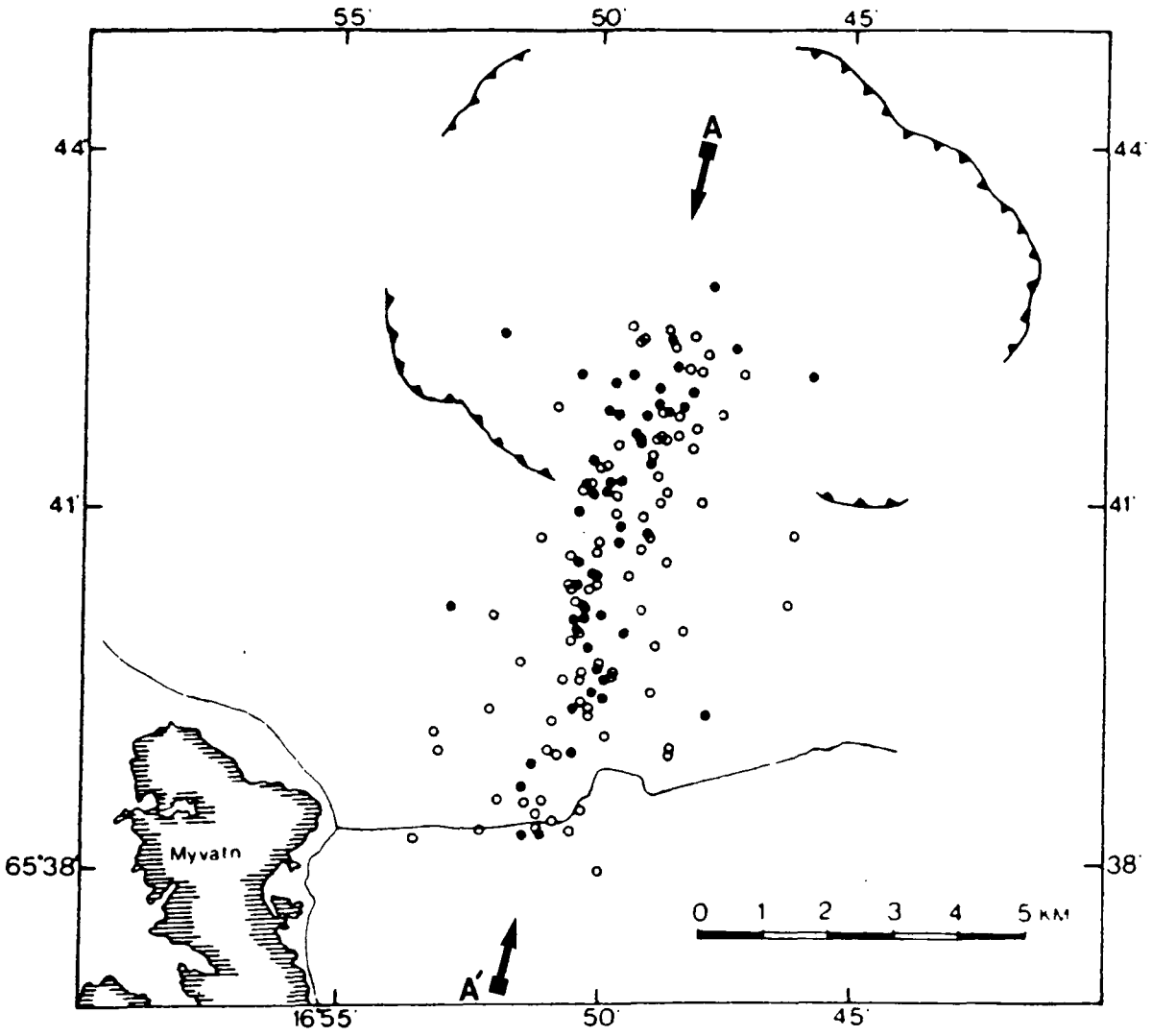

Figure 2.15 : The epicentral zone of events located during the September 1977 deflation of the volcano, as delineated by the most accurately located epicentres. Open circles mark the epicentres located with standard error 0.5–1.0 km in all directions. Closed circles are epicentres located with standard error less than 0.5 km. Roads and the caldera fault are shown for location (from Brandsdóttir and Einarsson, 1979). The line of cross-section in figure 2.16 is marked.

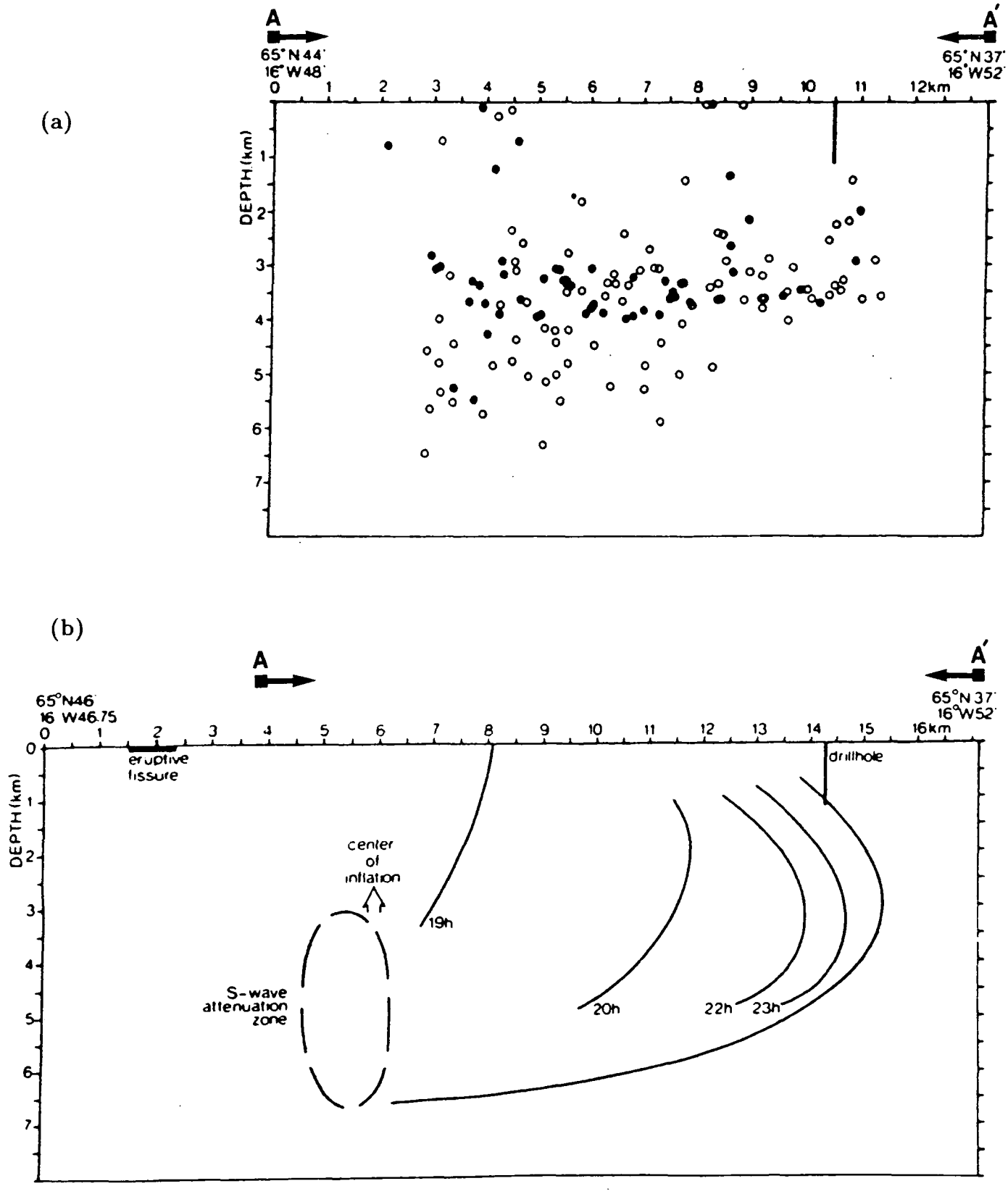

Figure 2.16 : (a) A vertical section across the hypocental zone of events located during the September 1977 deflation of the volcano. Symbols as in figure 2.15. The vertical bar shows the drillhole in the Námafjall geothermal area through which the small pumice eruption took place. **(b)** A vertical section along the Krafla fault swarm, showing the eruptive fissure, the S–wave attenuation zone, the Námafjall drillhole and centre of magma accumulation as determined from elevation and tilt changes. The propagation of the seismic activity along the fault swarm is shown with curved lines. At the time indicated all the seismic activity was north of the line. The final extent of the seismic zone is also shown (from Brandsdóttir and Einarsson, 1979).

(a)

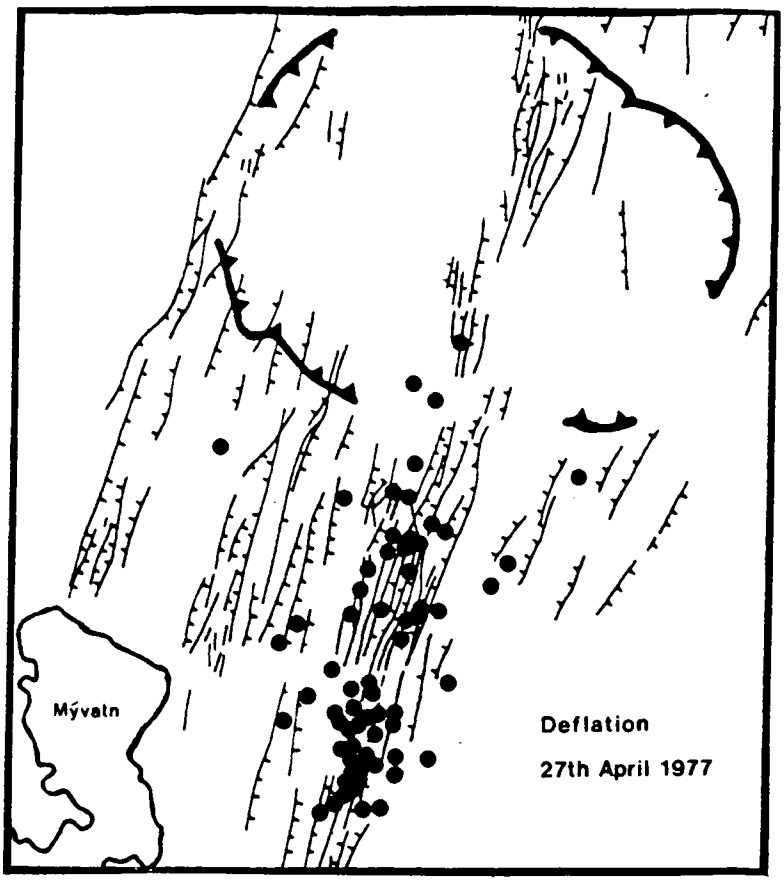

(b)

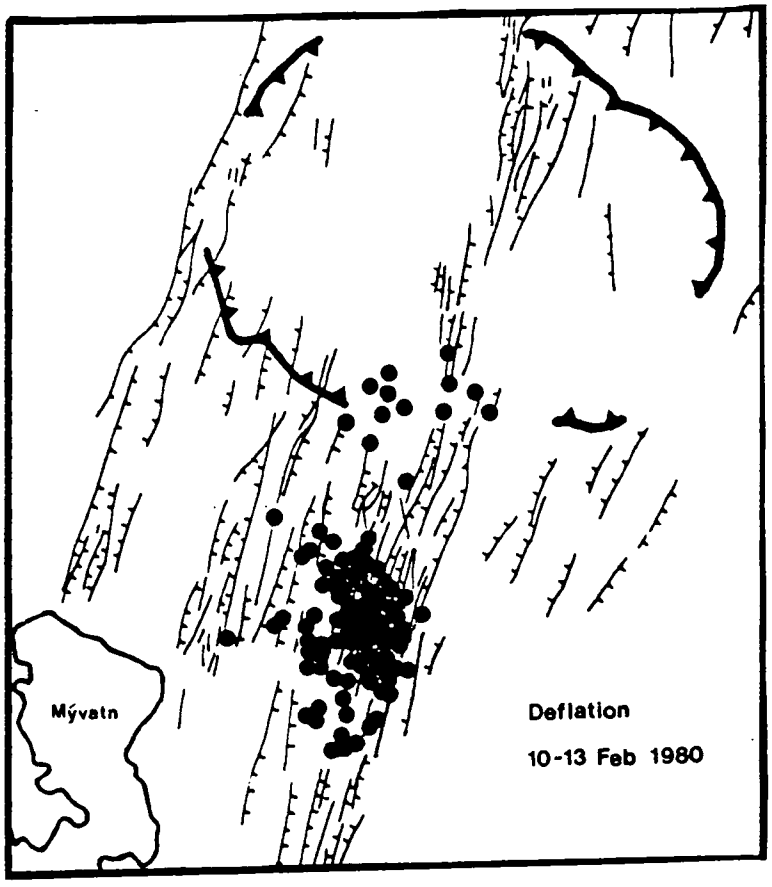

Figure 2.17 : Epicentral distribution of earthquakes south of the caldera during two deflation events. **(a)** 27th April 1977 (adapted from Einarsson, 1977). **(b)** 10–13th February 1980 (adapted from Einarsson and Brands dóttir, 1980).

Widening and subsidence of the central part of the fissure swarm and the contraction and uplift of the flank areas was a reported feature of most of the rifting events (Björnsson et al., 1979; Tryggvason, 1980, 1984). A total of up to 8m of horizontal extension occurred in the central 2–3 km of the rift zone to the north of the caldera (Tryggvason, 1984; Wendt et al., 1985). The flank areas were compressed horizontally (Wendt et al., 1985), reducing the overall extension over a 90 km wide zone to about 10% of that observed in the rift zone (Möller and Ritter, 1980; Möller et al., 1982). Horizontal distance variations along three profiles crossing the fissure swarm are shown for two time periods in figure 2.18. The first includes the rifting event of September 8–9 1977, when earthquake activity was mainly south of the caldera, during which time widening of about 1m took place in the centre of the fissure swarm and contraction of about 0.5m on the flanks. The other includes the rifting events of January and July 1978, when activity took place far to the north of the caldera. Again significant widening occurred in the active fissure swarm, with little movement elsewhere. This is a demonstration of how most land movements outside the central volcano occurred during the short rifting events.

It is evident from table 2.1 that much greater volumes of lava were erupted during later rifting events than earlier events, even though the degree of subsidence was no greater. These later events were characterized by greatly reduced widening in the fissure swarm (Tryggvason, 1984) and a reduction in earthquakes associated with rifting in the fissure swarm. In addition, the interval between the penultimate and final events was much longer than that between the preceding events.

Following the last rifting event in September 1984, the elevation of the caldera increased as before over a period of several months, but then remained almost static at the beginning of 1985 (figure 2.14). It appeared that the rifting episode was over because the elevation was below the previous maximum level. Everything was quiet until November 1986, when inflation started again. Seismic activity increased in February 1986, when the elevation was beyond the previous maximum, indicating that the caldera roof was beginning to respond to the inflation (B. Brandsdóttir, pers. comm.). A further deflation event has been expected ever since.

2.3.4 Dyke Injection

Observations of vertical movements and volcanic tremor in the vicinity of the

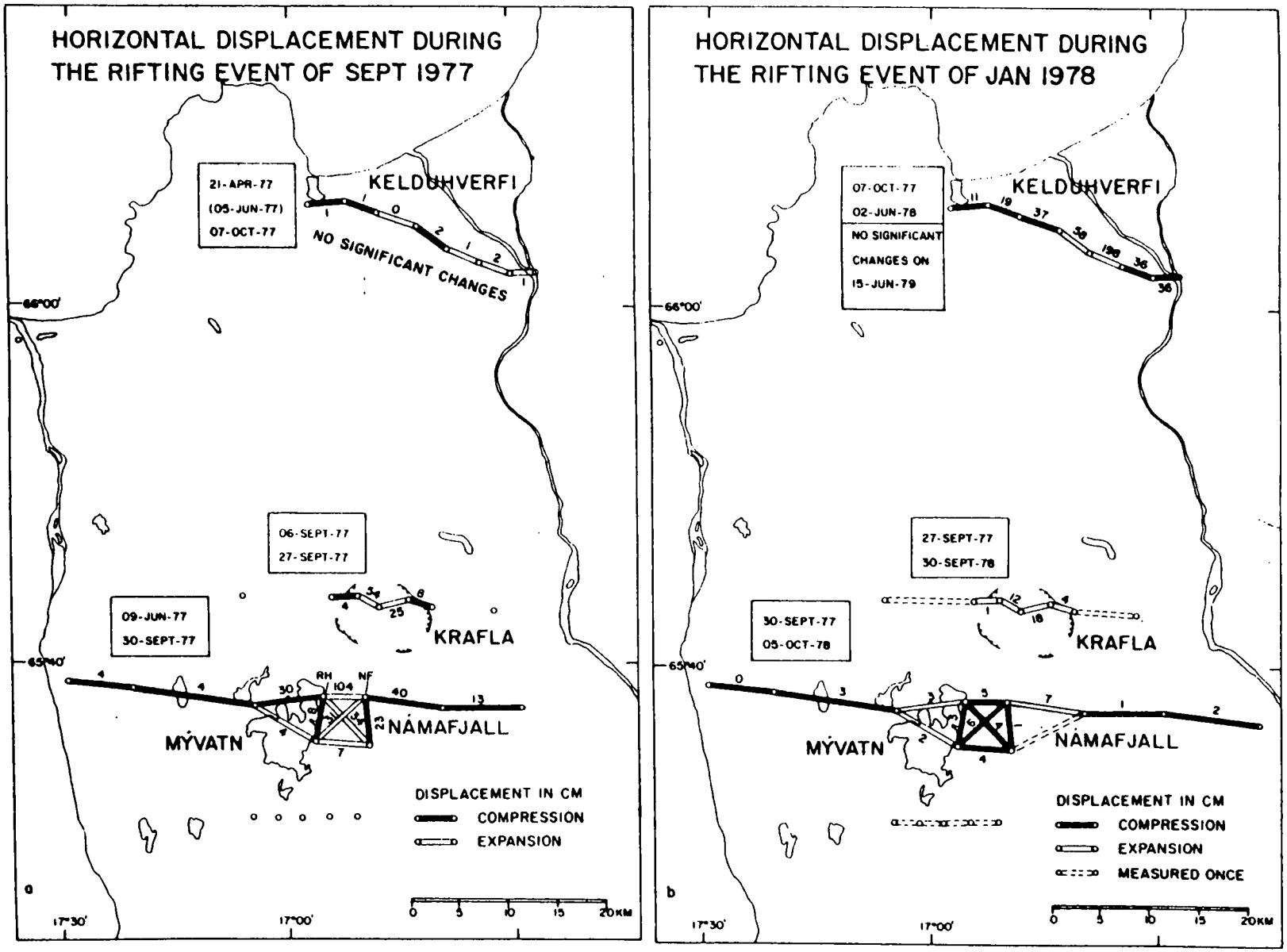

Figure 2.18: Horizontal displacements on three profiles across the Krafla fissure swarm over two time periods (from Björnsson, 1985).

volcano, migrating earthquake swarms, crustal extension, and fissure eruptions strongly suggest that the observed volcano–tectonic events were associated with the movement of magma outwards from beneath the volcano and along the fissure system (Björnsson et al., 1977, 1979; Tryggvason, 1980). Modelling of gravity data suggests that inflation and deflation of the volcano was caused entirely by the flow of magma into and out of a chamber at about 3 km depth (Johnsen et al., 1980). This is also supported by tilt observations (Tryggvason, 1978) and is broadly consistent with S–wave attennuation studies (Einarsson, 1978). It has been estimated from the total accumulated deflation of the Krafla volcano that if the crustal magma chamber could be approximated to a sphere, about 0.5 km^3 of magma was injected into the fissure swarm, (Björnsson, 1985). Total extension across the fissure swarm was on average about 2m along 50 km of its length and about 6m along another 30 km, which suggests that the average height of the injected dykes was about 2 km (Björnsson, 1985). This is in agreement with estimates of dyke height made for single rifting events on the basis of the widening of surface fissures (Tryggvason, 1984), and on the observed length of the dyke tip propagation path (Einarsson and Brandsdóttir, 1980a). However, Marquart and Jacoby (1985) inverted geodetic observations and found that a model in which the widened dykes extended to about 4–6 km in depth was the most consistent with the data. The actual depth extent of the dykes is consequently controversial.

It appears from seismic evidence (figure 2.16) that the dykes may have been injected laterally from the lower levels of the crustal magma chamber. However, the lack of seismic activity below about 4–6 km during the earthquake swarms is not necessarily an indication that no magma was injected at that depth, but could be a result of the onset of viscoelastic rock properties which allow the release of stress by aseismic creep. Björnsson (1985) suggested that dykes injected from the crustal magma chamber were confined to the upper elastic part of the crust, whereas those formed at greater distances from the central volcano may have ascended partially from a deeper layer of partial melt, as illustrated in figure 2.19. This scheme consequently provides a mechanism for the eruption of lavas at great distance from the caldera region which are petrologically less evolved than those erupted close to the caldera. It also helps to explain the apparent inconsistency in the depth extent of emplaced dykes between seismic and geodetic observations.

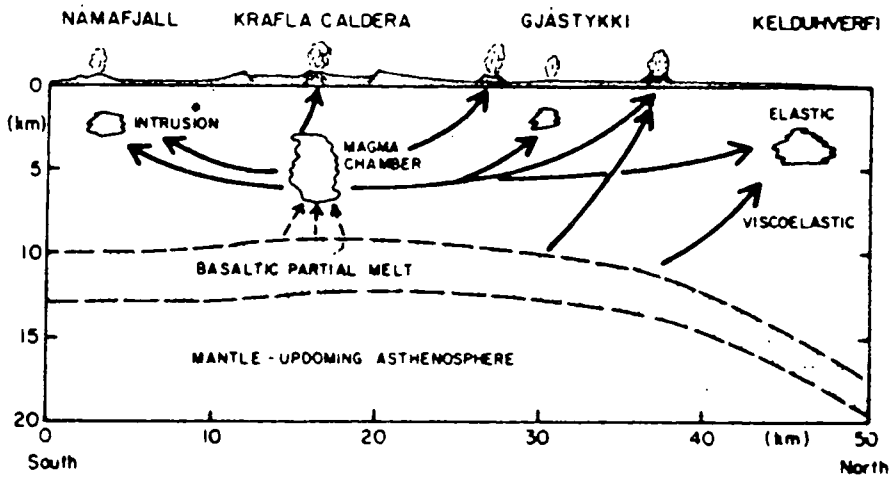

Figure 2.19 : A simplified model of the Krafla volcanic system, showing the partially molten basaltic layer at the base of the crust and the upper crustal magma chamber below the caldera. Arrows indicate magma movements (from Björnsson, 1985).

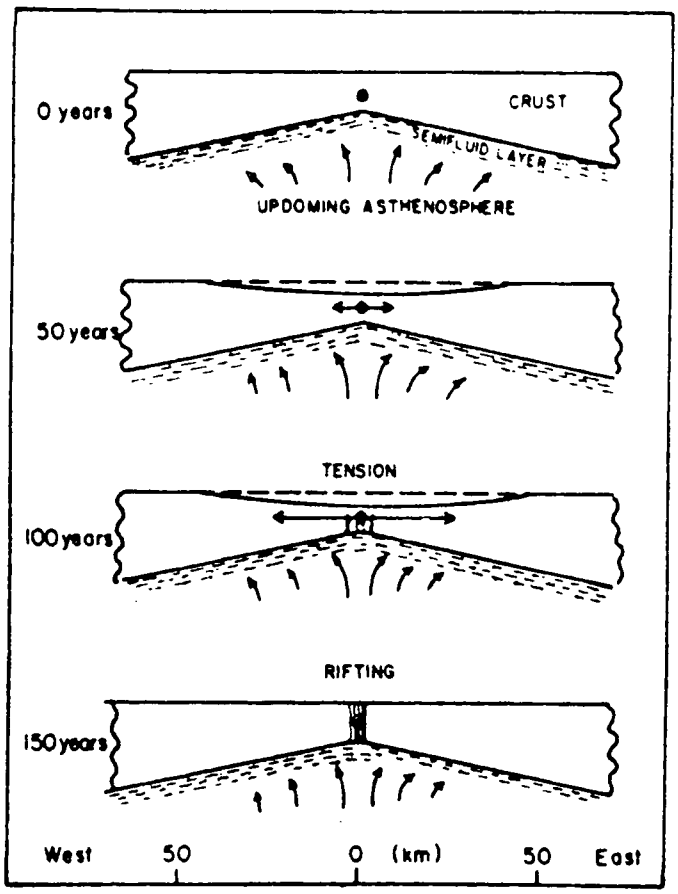

Figure 2.20 : A model of episodic crustal rifting in NE Iceland. Tension is gradually built up in the axial rift zone by ridge push force and is released every few 100 years in a rifting episode. Arrows proportional to deviatoric stress in the crust (from Björnsson, 1985).

2.3.5 Dynamics of Crustal Rifting

The Krafla rifting episode can be explained in terms of the release of extensional stress which had built up gradually over a period of centuries. Figure 2.20 shows a model of episodic crustal rifting in Northeast Iceland. According to this model, slow divergence of the plates leads to the build–up of strain in a narrow zone of the crust near the plate boundary. Gradual crustal thinning and subsidence ensues until the sudden release of extensional stress in a rifting episode (Björnsson, 1985). This may occur first by viscoelastic deformation of the lower crust, permitting the migration of magma from a semi-molten layer or from a deep magma chamber into a shallow crustal magma chamber.

During most of the Krafla episode, magma flowed into the crustal magma chamber at a fairly constant rate of about 5 m^3s^{-1}. This caused the floor of the caldera to rise and fissures near the centre to widen, and continued until the increased extensional stress induced in the caldera floor could no longer be accommodated elastically on existing fractures. At this point, new fractures formed and earthquakes started to occur more frequently above the magma chamber (Björnsson et al., 1979). The magma pressure eventually reached a point at which it triggered the release of tectonic stress in the crust, and magma burst out along the fissure swarm to initiate dyke injection. (Björnsson et al., 1977; Einarsson and Brandsdóttir, 1978). Magma flow caused continuous seismic tremor, and migrating earthquake activity marked the leading edge of injected dykes where seismic opening of fissures was taking place. The dyke tip propagation velocity during the Krafla events was generally about 0.5–1.2 ms^{-1} shortly after the initiation of intrusion, gradually reducing as the dykes lengthened and the pressure in the magma chamber dropped (Einarsson, 1990). Sudden widening of the fissure swarm resulted in elastic contraction on both flanks. Extensive fissuring and normal faulting occurred above the dyke, the central part of the swarm subsided, and the flanks were uplifted. Throughout each deflation event, the magma chamber continued to be fed from below, in preparation for the next event, and outflow from the chamber into the fissure swarm ceased when the pressure fell below some critical value (Björnsson et al., 1979).

Following a rifting event, in which some extensional stress had been released, the

magma chamber had to be further inflated and its pressure had to be slightly greater than it had before in order that seismic activity and dyke injection would be triggered again. The rifting episode came towards an end as the supply of magma to the chamber and the extensional stress in the crust were reduced. The reduction in the rate of magma supply is evident from the reduced rate of inflation of the volcano towards the end of the episode and may have been caused by blockage of the magma passage or by exhaustion of the deeper magma source. Even when most extensional stress in the crust had been released, eruptions occurred. This indicates that the magma supply to the crustal chamber was not controlled by the stresses in the shallow crust. Instead it seems that it was the magma supply which was controlling the tectonic activity, whilst stress in the crust governed the style of volcano–tectonism.

It has been speculated that when one volcanic system undergoes rifting, compressional stresses produced at the flanks of the rift zone result in a decrease in extensional stress in adjacent volcanic systems, preventing them from rifting simultaneously (Björnsson, 1985).

2.3.6 Comparison with other Spreading Systems

2.3.6.1 Other Systems in the Northern Volcanic Zone

A sequence of volcano–tectonic events similar to the Krafla sequence affected the Askja volcanic system (figure 2.1) during 1874–1875 (Björnsson et al., 1977). That period of activity began with increased steam emission from the Askja caldera, which was followed several months later by earthquake activity and fissure movement 50 km to the north. Following a small eruption in the caldera a few months later, activity in the fissures to the north resumed with intermittent basaltic fissure eruptions, intense earthquake activity and fault movements over an 8 month period. During this time, and following a major silicic tephra eruption within the Askja caldera, a smaller caldera collapsed within it. Intense subsidence occurred in the main Askja caldera, resulting in the formation of a new crater lake over 100m deep (Sigurdsson and Sparks, 1978). Further periods of volcanic activity in Askja have been observed in 1921–1926 and 1961, but there was little associated tectonic activity. Tectonic activity was observed in the Theistareykir fissure swarm in 1618

without volcanic activity (Björnsson et al., 1977) and periods of volcanic activity have been reported in the Kverkfjöll volcanic system in 1655, 1711, 1717 and 1729 (Gudmundsson and Sæmundsson, 1980).

2.3.6.2 Afar

In common with Iceland, Afar is one of the few places on Earth where the mid-ocean ridge system comes onto land. In November 1978 a rifting episode began near Lake Asal, where the rift comes ashore, and was marked by seismicity which lasted for two months, and a fissural volcanic eruption which lasted for one week (Abdallah et al., 1979). Crustal deformation was confined to a 3 km wide zone which widened by up to 2.4m over a length of about 25 km, and subsided by up to 70cm. The flank zones were uplifted by up to 18cm and compressed (Tarantola et al., 1979; Tryggvason, 1982). This style of horizontal and vertical ground deformation — extension and subsidence at the rift zone and compression and uplift on the flanks — is strikingly similar to that observed during the events of the recent Krafla episode, and it has been suggested that it may represent a fundamental mode of deformation at the axis of mid-ocean ridges (Abdallah et al., 1979). However, comparable data is lacking from more 'normal' sections of mid-ocean ridge and so the ubiquity of this mode of crustal accretion over the global rift system has not yet been proven.

The Krafla rifting episode was (is ?) much longer than the single-event episode at Afar. This may have been due in part to the critical rôle played by the Krafla magma chamber. At Afar, earthquake activity slowly migrated down the fissure system throughout the episode (Abdallah et al., 1979), and was presumably associated with the injection of magma as crustal extension took place. The fact that this occurred only once and was short-lived may be an indication that the magma supply was also short-lived. In contrast, the supply of magma to the Krafla crustal magma chamber continued steadily for about ten years. The episodic nature of the activity at Krafla was a result of varying pressure in the magma chamber. The release of extensional stress in the crust could only be triggered periodically when the chamber pressure was high enough to pump magma laterally into the fissure swarm.

2.3.6.3 The Sea Floor

The similarities between the mechanism of crustal accretion on Iceland and that on submarine sections of the mid–ocean ridge system are difficult to establish. It is certainly true that segmentation of the axial rift zone on Iceland into discrete *en échelon* volcanic systems appears, with ever increasing clarity, to be echoed offshore. The Reykjanes Ridge southwest of Iceland is strongly oblique to the direction of plate spreading, and segmentation in the form of *en échelon* volcanic ridges shows up with unusual clarity (Laughton et al., 1979). Recent high resolution bathymetric mapping there has shown that ridge segments contain volcanic features similar to some of those observed on Iceland (R.C. Searle, pers.comm.). The Mid–Atlantic Ridge between 24°N and 30°40′N has also been shown to consist of distinct accretionary segments separated by non–transform axial discontinuities (Sempéré et al., 1990). Large gravity anomalies have been observed over some of these segments and are thought to indicate that magmatic accretion is highly focussed at discrete centres along the ridge (Lin et al., 1990). On a section of the East Pacific Rise, the top of an axial magma chamber was imaged by seismic reflection. It was found to be continuous for tens of kilometres along the rise axis and located at a depth of 1.2–2.4 km below the sea floor (Detrick et al., 1987). Gaps in the axial magma chamber coincide with the locations of overlapping spreading centres (Macdonald et al., 1988) and correlate well with geochemical and petrological variations in dredged basalts (Langmuir et al., 1986). A tomographic inversion of P–wave arrival times from explosive and airgun shots was carried out over part of the same section of the East Pacific Rise (Toomey et al., 1990). 3–d variation in an axial low velocity anomaly at depths of 1–3 km was clearly imaged, as was a high velocity anomaly about 1–2 km in width in the upper 1 km of the crust.

Evidence such as this indicates increasingly that segmentation of ridges may be in some way a fundamental process in crustal accretion at mid–ocean ridges. The often regular distribution of accretionary segments has been attributed to gravitational instability in rising partial melt, and the interval of segmentation related to spreading rate (Schouten et al., 1985). Partial melt may therefore ascend and segregate as it feeds axial reservoirs at discrete places along the plate boundary.

If segments of mid–ocean ridge have discrete magma chambers, some of the prin-

ciples learned from Krafla about the lateral flow of magma and the important triggering effect of the magma chamber may find some general application. However, in the absence of observations from a rifting episode (if such occur) in a seafloor spreading segment, the similarities and contrasts in accretionary processes cannot be ascertained.

2.4 Summary

2.4.1 Geology and Geophysics

Krafla is one of five volcanic systems in the Northern Volcanic Zone of Iceland, which connects with the Mid–Atlantic Ridge offshore via the Tjörnes Fracture Zone. The Krafla central volcano is about 20 km wide and is bisected by a fissure swarm which is about 10 km wide, 100 km long and which is orientated in a north–northeast direction — perpendicular to the direction of plate spreading.

Krafla was probably a shield volcano before caldera collapse occurred about 100,000 years ago. Since then the volcano has been very active and has nearly filled the caldera with eruptive products. Acidic volcanism was initiated during the formation of the caldera, as is evident from the presence of a welded rhyolitic airfall tuff around the caldera ring fault. During the last glacial period, four large silicic domes and ridges were formed around the caldera, and distinctive hyaloclastite ridges developed over the active fissure swarm which extended to the north and south from within the caldera. Postglacial volcanism occurred mainly within the caldera and to the south and north. Eruptives were dominantly olivine normative basalts outside the caldera and quartz normative within it. The average period between eruption episodes in postglacial times has been about 500 years. Before 1975, the only series of eruption events in the Krafla area which had been historically observed were the 'Mývatn Fires' of 1724–1729, which were characterized by pulsating volcano–tectonic activity centred within the caldera.

The subsurface geology of parts of the Krafla caldera has been clarified by drilling which was carried out as part of a geothermal exploration programme. Four main stratigraphic units have filled the caldera since its formation. They consist of alternating formations of hyaloclastites and subaerial lavas which were erupted during glacial and interglacial periods respectively. Below a third formation of lava at 1200–1400m depth, the strata are dominated by basaltic and doleritic intrusives. Gabbro intrusions are dominant towards the eastern rim of the caldera below about 1800–2000m depth. A subsurface horst structure affecting most of the sequence is oriented west–northwest to east–southeast beneath the centre of the caldera, and several other major faults exist in the southern part of the caldera and in the intrusive gabbro formation to the east. The subsurface structure of the

Námafjall geothermal area is also dominated by hyaloclastites and basalts in the upper section, and hydrothermally altered rock becomes dominant below about 500m.

Low resistivities characterize the Krafla geothermal reservoir in the upper 700m. At greater depths a zone of low resistivity, low seismic reflectivity and high S–wave attenuation is thought to indicate the presence of partial melt in a crustal magma chamber. Magnetic lows over the Krafla and Námafjall geothermal areas may be a result of the geothermal alteration of magnetic minerals. Broad Bouguer gravity highs over sections of the caldera rim indicate the presence of high density rocks at shallow depth relative to those within the caldera. Local earthquake studies indicate that seismicity within the caldera and in the Námafjall area to the south may be related, at least partially, to geothermal activity.

2.4.2 Crustal Rifting

A major crustal rifting episode centred on the Krafla volcanic system began in December 1975 and lasted for about 10 years. During this time there were about 20 rifting events, 9 of which were accompanied by basaltic fissure eruptions. This episode provided many clues about the nature of the crustal accretion process at spreading plate boundaries.

The Krafla episode can be explained in terms of the release of extensional stress which had built up gradually over a period of centuries as a result of plate divergence. Magma flowed into a crustal magma chamber beneath the Krafla caldera at a fairly constant rate during most of the episode. When the chamber pressure was great enough, dykes were injected into the fissure swarm and some of the extensional stress in the crust was released. Dyke injection stopped when the magma pressure could no longer sustain it. Sudden widening of the fissure swarm resulted in contraction on both flanks. Fissuring and faulting occurred above the dyke, the central part of the swarm subsided and the flanks were uplifted. In order to trigger subsequent rifting, the magma chamber had to become progressively more inflated and its pressure had to be greater than before so that the increased compressional stresses in the fissure swarm could be overcome. The rifting episode petered out with the drop in supply of magma to the chamber.

Observations of crustal rifting episodes are rare and it is therefore difficult to generalize about the tectonic processes at work. However, it seems that the continued supply of magma is fundamental to the longevity of an episode and that the style of deformation at different ridge axes may be similar. Submarine mid–ocean ridges are segmented in a way that is similar to the segmentation of the axial rift zone on Iceland into discrete volcanic systems. If segments of mid–ocean ridge have discrete magma chambers, as some evidence suggests, then some of the tectonic processes observed at Krafla may also occur offshore. However, it is important to realise that spreading in Iceland is influenced additionally by the Icelandic hotspot.

Chapter III

The Seismicity of the Krafla Volcanic System

3.1 The NISE Field Programme

3.1.1 Introduction

This section summarises the North Iceland Seismic Experiment (NISE) field project of 1985 which was carried out by G. Foulger of the University of Durham, in association with the University of Iceland and the Icelandic National Energy Authority (Foulger, 1986).

The main aims of the field project were : -

- To achieve good coverage of the seismically active areas in the region of the Krafla volcano, in order to obtain accurate earthquake three–dimensional locations and focal mechanism solutions.
- To record timed local and regional explosions with good azimuthal coverage in order to detect local variations in crustal structure.
- To record a suite of teleseisms in order to obtain deep crustal/upper mantle structure.

3.1.2 Design

The field programme was designed on the assumption that the earthquake activity in the Krafla region would have a distribution similar to that observed in the past (Foulger, 1986). Figure 3.1 shows the seismometer distribution for the survey. Seismometer locations are given in table 3.1. A zone covering the Krafla caldera, the Námafjall area, and the intermediate zone, between the depths of 0–4 km was targeted.

In order to obtain well constrained focal mechanism solutions from first motions it is desirable to have at least 15 seismometers distributed evenly over the focal

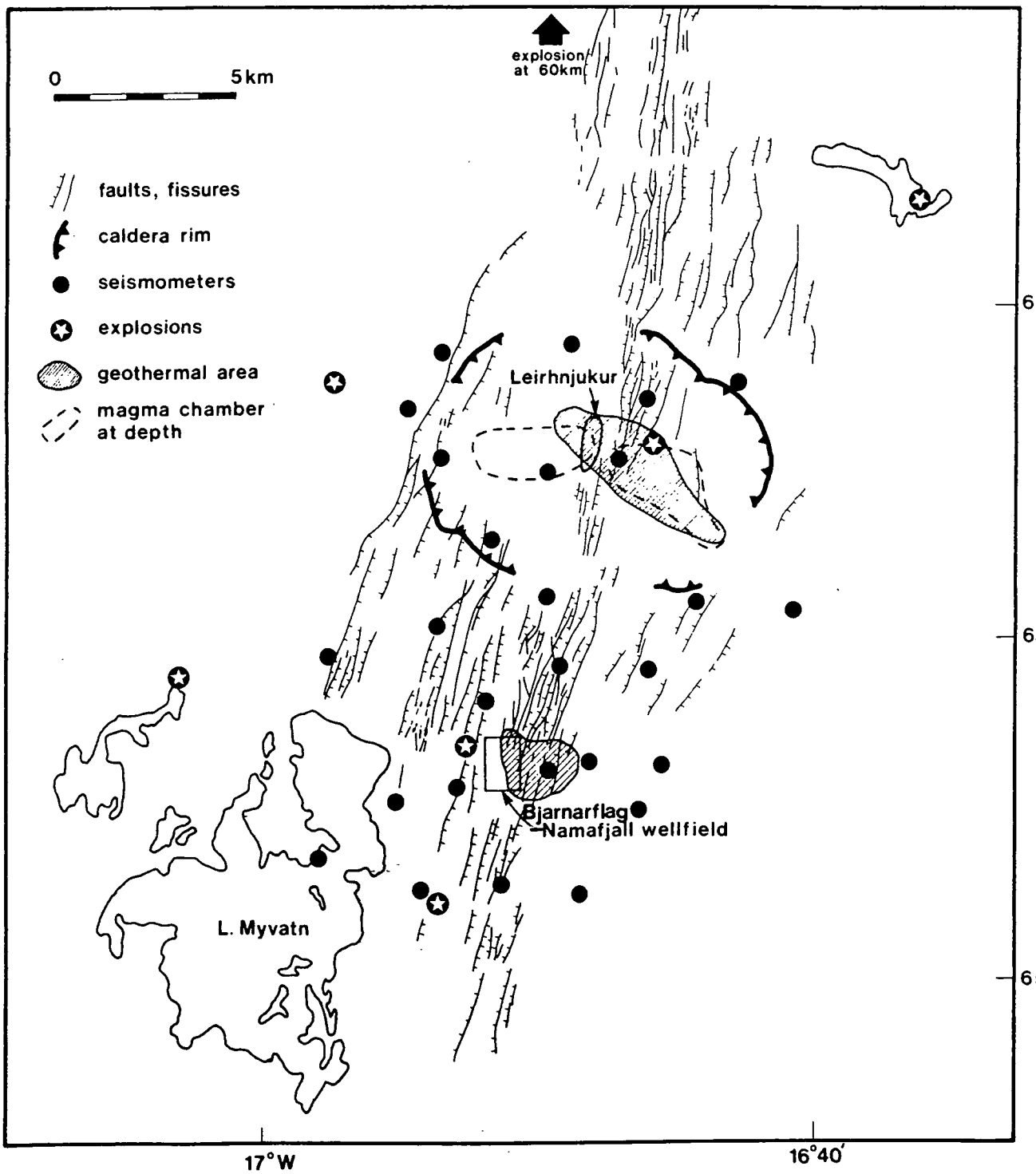

Figure 3.1 : The seismometer network for the NISE–85 experiment. The locations of the seven timed explosions are also shown.

Station	Latitude	Longitude	Height(m)
NBU	65 38.21N	16 45.91W	360
NNO	65 39.64N	16 49.13W	490
NSY	65 36.33N	16 48.44W	380
NGR	65 37.90N	16 52.87W	295
NVO	65 37.76N	16 55.18W	280
NDA	65 39.30N	16 51.76W	360
NSV	65 37.40N	16 50.18W	400
NSK	65 39.86N	16 57.70W	320
NHA	65 39.68N	16 46.17W	400
NHV	65 36.43N	16 51.39W	320
NSA	65 40.49N	16 43.84W	525
NJO	65 40.64N	16 40.99W	500
NRA	65 36.42N	16 54.37W	280
NHE	65 37.32N	16 46.55W	350
NYT	65 37.24N	16 48.44W	380
NSD	65 36.93N	16 57.90W	280
NHR	65 38.33N	16 48.32W	355
NSO	65 40.35N	16 53.30W	420
NNA	65 38.16N	16 49.66W	430
NBI	65 34.32N	16 02.90W	460
RMU	65 44.24N	16 53.23W	600
RNO	65 40.83N	16 49.07W	490
RRA	65 42.58N	16 46.88W	550
RGR	65 43.88N	16 42.32W	720
RKR	65 42.67N	16 53.12W	430
RVI	65 43.72N	16 45.39W	560
RLI	65 43.55N	16 54.52W	600
RLE	65 44.34N	16 48.00W	560
RSA	65 42.70N	16 49.54W	520
RSU	65 41.92N	16 52.00W	520

Table 3.1 : Locations of seismometer stations

Name	Location	Height(m)	Time
Víti	65 43.02N	530	850814 1212 06.986
	16 45.51W		
Eilífsvotn	65 46.53N	350	850814 1639 06.634
	16 39.92W		
Bjarnarflag	65 38.50N	280	850814 2145 07.334
	16 52.44W		
Sandvatn	65 39.50N	280	850815 1215 07.090
	17 03.07W		
Gæsadalur	65 44.22N	430	850815 1645 06.908
	16 57.30W		
Hverfjall	65 36.35N	270	850815 1900 07.125
	16 53.90W		
Oxarfjordur	66 17.12N	-37	850816 1705 06.9
	16 29.73W		

Table 3.2 : Locations of timed explosions

hemisphere for a single earthquake. In practice this means that 15 stations should be closer to the epicentre than about three times the focal depth of the event. Therefore as a result of the relatively shallow earthquake incidence, a high station density was required.

Since line of sight must be maintained between each station and the recording points on a radio-telemetered network, there was a gap in the otherwise good station coverage to the east of Mt. Krafla (figure 2.3). The station coverage was also biased towards the Námafjall area shortly before installation, because of evidence from the five permanent drum recorders operated by the University of Iceland that 80% of the activity was concentrated in that area. The station NBI was maintained some 40km east of the network to provide a regional station to serve as a reference for the reduction of the teleseismic data.

Seven timed explosions were detonated, six locally and one regionally. Shot distribution was good except that none could be fired to the east of the network because

of the absence of lakes and boreholes. The positions of these shots are shown in figure 3.1. Their exact locations and origin times are given in table 3.2.

3.1.3 Equipment

The Krafla radio-telemetered network consisted of the following components : -

Seismometers : 28 Willmore Mk.III vertical component seismometers were used. Each had its natural frequency adjusted to 1 Hz and was used with an amplifier–modulator.

Radio Links : 26 radio links consisting of a transmitter, a receiver and a pair of UHF antennae were used. They transmitted between 458–459 MHz, at frequencies separated by 0.025 MHz.

Tape Recorders : 3 Geostore tape recorders recorded analogue signals on 14 channel, $\frac{1}{2}$ inch magnetic tape at a speed of $\frac{15}{320}$ in.sec^{-1}, giving an upper frequency recording limit of 32 Hz. Seismic signals were recorded on 10 channels. The remaining 4 were used to record two flutter compensation signals, an MSF radio time signal and a time code generated by an internal crystal clock.

Time Code Receivers : MSF Rugby radio time signal receivers and antennae were linked to each Geostore recorder.

Calibration Box : A calibration box was connected to the seismometer and amplifier–modulator in the field. It generated a calibration pulse which was input to the seismometer.

Test Boxes : The small Mk.II type test box with audio output which was used could be connected to the amplifier–modulator, the radio receiver or the tape recorder to check whether they were functioning correctly.

Field Replay Equipment : Recordings were monitored using a 14–channel 'Store 14' tape playback machine, a clock time signal decoder, a stereo audio playback set and a 7–channel Siemens ink jet pen.

3.1.4 Logistics

3.1.4.1 Out–Stations

Of the 25 out–stations, 18 were accessible by jeep and 7 were established and maintained on foot. All seismometers were mounted on bedrock in holes of up to 1m in depth and 0.5m in diameter, lined with a steel paint drum with half of its base cut out. The amplifier–modulator stood in the paint drum on its half–base. The drum was sealed with its lid and covered with polythene sheeting.

A 1.5m length of metal water pipe was used as a mast and was held upright by 3 steel guy–wires. A 30cm length of angle iron was screwed to the base of the mast and covered with boulders to prevent it from moving. A transmitting antenna was then clamped to the top of the mast and the transmitter clamped to the mast below it. All cables on the ground were buried to protect them from sheep.

The 60–70 A.h. lead acid batteries which were used were placed in plastic bags and buried for protection from theft and the weather.

When each out–station had been installed, the seismometer and the amplifier–modulator were checked using the test box. The gains of the amplifier–modulators were put to a setting of 7 at the beginning of the experiment.

3.1.4.2 Recording Stations

All three recording stations were made accessible by jeep because of the weight of the equipment used. 2m high masts accommodated the receiving antennae at the stations. Up to 6 antennae were placed on each mast and these were insulated from their clamps to prevent cross–talk. The receivers were taped to the masts and connected to the recorders by cables running through plastic water piping. The tape recorders were housed in waterproof aluminium boxes and stood on wooden pallets for levelling. Cables were passed into the boxes through small holes cut in their undersides. A seismometer was installed at each recording site and connected directly to the tape recorder. Power was supplied by 12V lead acid batteries — a 60–70 A.h. battery for the tape recorder and a 110 A.h. battery for the radio receivers. Two recording sites were required in order to maintain line of sight from the out–stations. Data from the northern part of the network (10 stations) were

recorded on a tape recorder at Raudholl (R) and signals from the southern part and Biskupshals (18 stations) on the two recorders at Námafjall (NW and NE), (figure 3.1).

3.1.4.3 Maintenance

After installation, out–station maintenance consisted of changing batteries and spare parts every 20–40 days. Tape recorder batteries were changed every 20 days and the receiver batteries every 7 days. Tapes were changed at $3\frac{1}{2}$ day intervals.

Recording took place between July 1st and October 4th 1985, a total of $94\frac{1}{2}$ days of recording.

3.2 Data Playback

The data tapes were played back by the author using a 14–channel 'Store 14' tape recorder. For each tape, two channels some distance from each other were selected for playback at $3\frac{3}{4}$ in.sec^{-1}, which is 80 times the recording speed, through a stereo audio playback set. The range of frequencies expected to be present in local earthquakes (about 1–100 Hz) was therefore brought into the audible range (although the upper recording limit was 32 Hz – see section 3.1.3), whilst the bulk of microseismic noise, whose peak frequency is generally about $\frac{1}{6}$ Hz, remained less audible. More than 500 local earthquakes were thus detected in a process which took about six months to complete.

It was considered that this method of aural detection would be more successful than visual detection for the following reasons : –

- More effective discrimination, by frequency content and wave emergence, between earthquakes and noise bursts.
- Easier detection of very small events, by frequency pattern recognition and stereo enhancement.
- Much quicker
- Less stressful.

The main disadvantage with this method was that only a selection of the most sensitive seismometer channels were examined aurally, which opens up the possibility that some very small events were missed. However, it is likely that such events would only have been detected by two or three stations and therefore could not have been located.

Paper records of each event were produced at scales of 1cm:1sec and 5cm:1sec using a 16 channel Siemens jet pen. The smaller scale was found to be useful for observing the complete waveform of each event, while the larger scale was used to measure arrival times. Jet pen gain was varied for each channel in order to optimize amplitudes yet prevent clipping. Variations in gain were recorded for subsequent magnitude calculations (section 3.4.2). Paper records were produced for data from each recorder, and MSF radio and internal clock codes were written on to the top

and bottom of each record. Records were produced for each detected event at all stations to ensure maximum data extraction. Whenever possible, the MSF radio signal was used to measure phase onset times, but short breaks or degradations in the reception of the signal occurred for intervals of a few minutes or hours throughout the recording period. When this happened, the internal clock signal was interpolated between the closest legible radio signals and used to determine the arrival times. In most cases this process would result in a negligible increase in the error of the phase pick due to internal clock drift (less than one second per week).

P-wave onset times were read from the paper seismograms to an estimated precision of 0.01 sec, using a purpose–made graticule. However, instrument and clock corrections increase the overall uncertainty of the arrival times to about 0.03 sec. S-wave arrival times were read where possible, but were rarely clear.

Apart from the slight repositioning of two stations at the beginning of the experiment and a few short–term breakdowns, the station coverage throughout the recording period was constant (Foulger, 1986). The detection threshold and location accuracy of this data set may therefore be considered to be uniform with time.

3.3 Local Earthquake Locations

3.3.1 The Earthquake Location Problem

A vector of hypocentre coordinates can be given as : -

$$\mathbf{h} = (t, x, y, z)^T \tag{3.1}$$

where t, x, y, z are the coordinates of time and space respectively and T denotes the transpose.

The location of an earthquake using a set of n arrival times τ_k from stations at spatial coordinates (x_k, y_k, z_k), where $k = 1, 2, ..., n$, first requires the assumption of a seismic velocity structure for the Earth. The problem then becomes one of estimating the hypocentral coordinates $\mathbf{h}^*$ for which the differences between the theoretical arrival times t_k and the observed arrival times τ_k are minimised in some way.

The arrival time residual at the kth station, r_k, is given by : -

$$r_k(\mathbf{h}^*) = \tau_k - t_k(\mathbf{h}^*) \tag{3.2}$$

and

$$r_k(\mathbf{h}^*) = \tau_k - T_k(\mathbf{h}^*) - t^* \qquad (k = 1, 2, ..., n) \tag{3.3}$$

where T_k is the theoretical travel-time and t^* is the trial origin time. However, in an over-determined case not all the travel-time residuals can be reduced to zero (even if the assumed velocity model is perfect), because observational errors cause inconsistencies in the data. The trial hypocentre $\mathbf{h}^*$ is adjusted until the sum of the squares of the residuals is minimized, generally by the least-squares method. This method of hypocentral location is one of non-linear optimization, since the travel-time between two points in nearly all media is a non-linear function of the spatial coordinates (Lee and Stewart, 1981).

To overcome the non-linearity of the earthquake problem, the true solution may be approached by iterating through a series of linearized solutions. The $n \times 4$

partial derivative matrix $\mathbf{H}$ is evaluated using the assumed velocity model at the trial hypocentre $\mathbf{h}^*$, where : -

$$H_{kj} = \frac{\partial r_k}{\partial h_j} \qquad (j = 1,2,3,4; \quad k = 1,2,...,n) \tag{3.4}$$

If $\mathbf{r}$ is the vector of the travel-time residuals $r_k(\mathbf{h}^*)$, and $\mathbf{\Delta h}$ is the hypocentral adjustment vector, then : -

$$\mathbf{r} = \mathbf{H\Delta h} \tag{3.5}$$

When n exceeds 4, the true inverse of $\mathbf{H}$ does not exist. The best least-squares solution to the system of linear equations (3.4) satisfies the equation : -

$$\mathbf{H}^T\mathbf{r} = \mathbf{H}^T\mathbf{H\Delta h} \tag{3.6}$$

(e.g. Lee and Stewart, 1981). By computing the travel times and derivatives from a trial hypocentre $\mathbf{h}^*$, equation 3.6 can be solved for the adjustment vector $\mathbf{\Delta h}$. The same process is then repeated using $\mathbf{h}^* + \mathbf{\Delta h}$ as the trial hypocentre and iteration continues until some user-defined cut-off criteria are satisfied. This least-squares solution to the linear problem is known as the Gauss-Newton iterative method of non-linear optimization.

The United States Geological Survey location program HYPOINVERSE (Klein, 1978), which is incorporated into DUEDROPS-HLPS (section 3.3.4), solves the earthquake location problem (equation 3.6) by generalized inversion for hypocentre adjustments $\mathbf{\Delta h}$. Klein's original flow diagram for this program is given in figure 3.2.

HYPOINVERSE begins by choosing a trial earthquake hypocentre, unless it is defined by the user. The trial origin is two seconds before the earliest arrival and the trial epicentre is near the station with the earliest arrival. The trial depth is user-defined and held fixed during early iterations until the horizontal adjustment is less than a specified value. The travel times, travel-time derivatives, and emergence and take-off angles are then calculated for all arrivals by interpolation from a travel-time table. This table is produced using the program TTGEN (Klein, 1978), which traces rays from each of a range of source depths through a user-defined one-dimensional P-wave velocity model to the surface. S-wave velocities

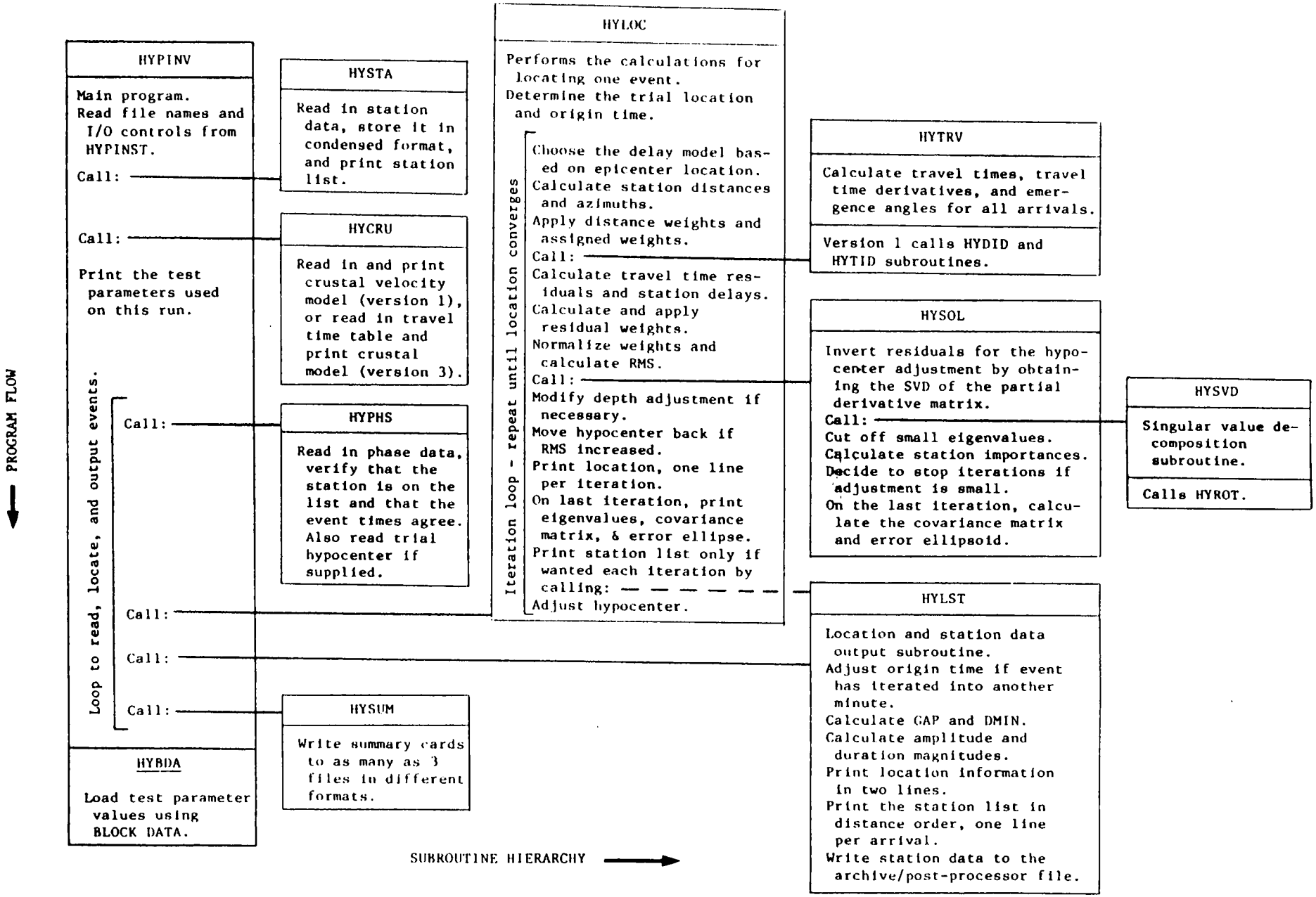

Figure 3.2 : Structure and flow diagram for the hypocentre location program HYPOINVERSE (from Klein, 1978).

are computed using a P–S velocity ratio which is fixed by the user. Parameter residuals are then inverted for hypocentre adjustments, and the hypocentre is adjusted if this will result in a reduction in the r.m.s. travel–time residual. A damping factor is applied to all hypocentre adjustments in order to suppress divergence of the solution.

A maximum number of iterations is specified by the user. However, the iterative location process normally stops earlier than this when the spatial adjustment or the reduction in the r.m.s. travel–time residual becomes smaller than a given value. The covariance matrix, the diagonal members of which are the variances of the hypocentral parameters, is calculated once the iteration process is complete.

The spatial error ellipsoid and the error in origin time are specified by the covariance matrix. The error ellipsoid is centred on the hypocentre solution and has principal axes of lengths equal to the standard errors. The earthquake then has a 32% statistical probability of lying inside this error ellipsoid. The horizontal and vertical projections of the ellipsoid have lengths which are called the horizontal and vertical errors (ERH and ERZ).

3.3.2 Velocity Model

A one–dimensional crustal P–wave velocity model was compiled by P. Einarsson and G. Foulger (unpublished) at the Science Institute, University of Iceland (P. Einarsson, pers. comm.) for earthquake location in the Krafla region. It was derived by making a composite travel–time plot of the first arrivals of profiles observed from explosions carried out in the lakes Víti, Mývatn, Sandvatn and Höskuldsvatn by the Icelandic National Energy Authority (unpublished). They then used the program TTGEN (Klein, 1978) to find a crustal structure which fitted the observed data. The subcrustal halfspace velocity of 7.0 kms^{-1} was taken from the results of the Reykjanes Ridge Iceland Seismic Project (RRISP 77) (Gebrande et al., 1980), (section 1.3.2). The velocity–depth profile for their crustal model is illustrated in figure 3.3.

Flovenz (1980), used secondary refracted arrivals and amplitude data to discriminate between layered and continuously varying velocity models for the Icelandic crust (section 1.3.2). He found that the P–wave velocity increased rapidly with

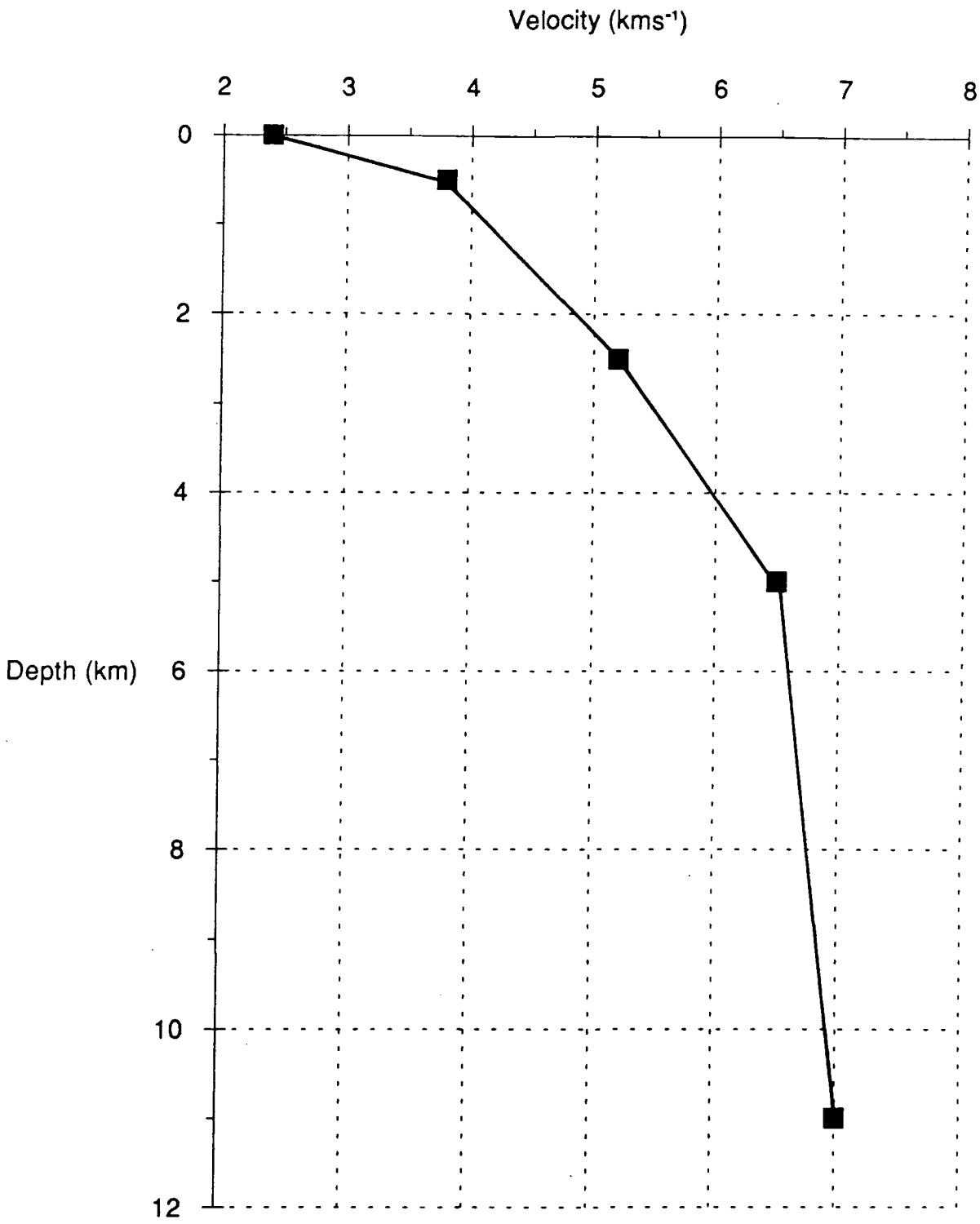

Figure 3.3 : Krafla gross seismic P-wave velocity structure, based on seismic refraction data (Einarsson and Foulger, unpublished).

depth in the velocity interval 2.0–3.5 kms^{-1}, followed by an almost constant gradient of about $0.57s^{-1}$ down to 6.5 kms^{-1}. This is very similar to the sharp gradient of $2.8s^{-1}$ between 2.4–3.8 kms^{-1}, followed by $0.60s^{-1}$ down to 6.5 kms^{-1} of the Einarsson/Foulger model for the Krafla region.

In view of the similarity between these models, the velocity structure of figure 3.3 was adopted for subsequent hypocentral location in this study.

3.3.3 Location Procedure and Pitfalls

HYPOINVERSE (Klein, 1978) was used to calculate the earthquake locations and origin times of the NISE–85 local earthquake data, using a travel–time table which was produced using TTGEN for the one–dimensional velocity structure given in figure 3.3. Both P– and S–waves were used for the location. Phases which were relatively unclear were initially given zero weighting so that their arrival times could be compared with those computed by the program, without influencing the location. If the residual was judged to be small, the observed travel–time was assumed to be correct and its weighting increased. Otherwise, the phase was not incorporated into the location unless an alternative convincing candidate for the phase arrival time was apparent closer to the calculated time. S–waves (when they were clear) were generally emergent, with onset times which were less conspicuous than for P–waves, and were therefore assigned a maximum of half the weighting. 489 events were successfully located in this way, very few of which originated from outside the station network.

The success of the hypocentral location process depends critically on data quality. In theory, the least–squares method should only be applied if errors in arrival times (whatever their source) are random and independent. If not, the solution will be distorted so that errors are spread among the stations (Lee and Stewart, 1981). Consequently, individual station travel–time residuals are only helpful in discovering errors in arrival–time picks or station coordinates when they form a small proportion of the event information. Inaccuracies in the assumed velocity structure can also contribute to observed travel–time residuals, but these errors are not random and may be used to refine the velocity model (chapter 4).

Figure 3.4a shows all the P–wave travel–time residuals as a function of azimuth

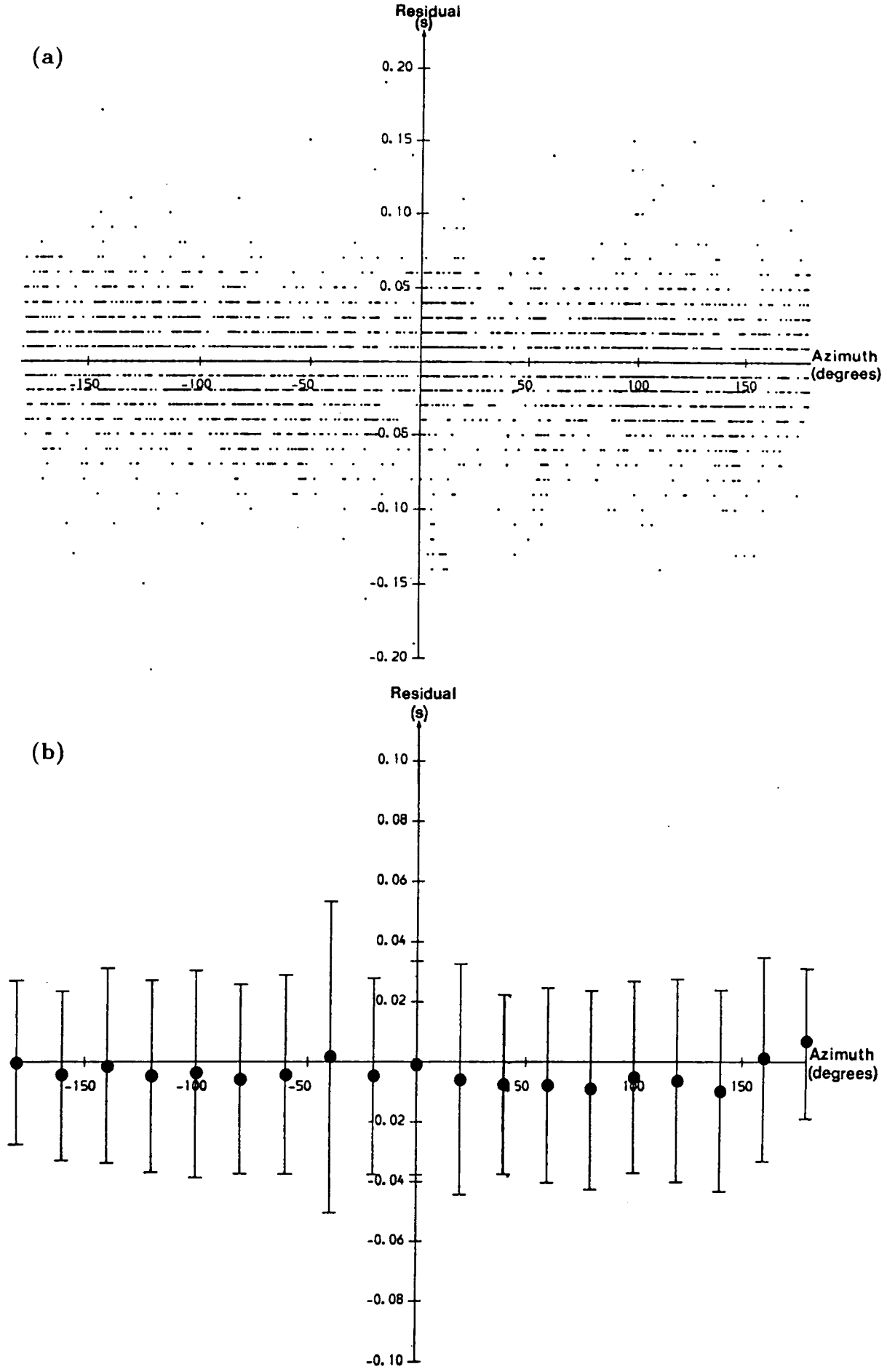

Figure 3.4 : **(a)** Travel-time residuals of all P-phases used for hypocentral location, as a function of azimuth from computed hypocentres. North is 0°, and azimuths are positive to the East. **(b)** The means and standard errors of the travel-time residuals shown in (a) calculated for azimuthal bins of 20°. Note that there is no significant azimuthal variation in mean residual.

from the computed hypocentres. Residual sizes are virtually all $\leq$ 0.15s and are generally $\leq$ 0.07s. Figure 3.4b shows mean residuals, calculated for azimuthal bins of 20°, with their standard errors. There is no significant azimuthal variation in residual. Mean residuals are all < 0.01s, and standard errors vary from $\pm$ 0.02s to $\pm$ 0.07s. This is an indication that errors due to anisotropy–related azimuthal velocity variation, if any, have been absorbed by the hypocentral location procedure.

In areas where station coverage is good, the epicentral location of an earthquake will not be affected very much if it is determined using different one–dimensional velocity models. However, figure 3.5 illustrates why the impact on focal depth can be significant. When S–waves are not clear, only information consisting of P–wave arrival–time differences between stations can be used to estimate the hypocentre position, since the origin time is not well known. The travel–time difference (Δt) between two stations S_A and S_B directly governs the difference in raypath length. Δl increases as the velocity structure becomes faster, resulting in shallower hypocentres. If the velocity structure is slower, hypocentral depths are deeper. However, since an S–wave and a P–wave at the same station have different travel–time derivatives, the estimate of the origin time for an earthquake will be significantly improved if S–waves are available. If the origin time is known accurately, a faster velocity model will result in a deeper focus for a given earthquake. One might therefore expect an earthquake located using only P–waves to be located at shallower depth if the velocity field is increased, while an event located using a large number of S–waves would be relocated at greater depth under the same circumstances. The transition from one case to the other is unclear, however, and will depend on many things including the seismic network geometry, the quality of S–wave arrival–time data and the estimate of the P–S velocity ratio. It *is* clear that the accuracy of the velocity model is of fundamental importance in the determination of the focal depth, but to a lesser extent in that of epicentral location. Consequently, it will also affect the quality of focal mechanism solutions which are calculated using ray take–off and emergence angles (Chapter 5). Furthermore, lateral velocity variations, which cannot be modelled using HYPOINVERSE, will also affect hypocentral location.

Events which originate outside or on the margin of a seismic network may suffer from being 'ill–conditioned', whereby one or more columns in the partial derivative

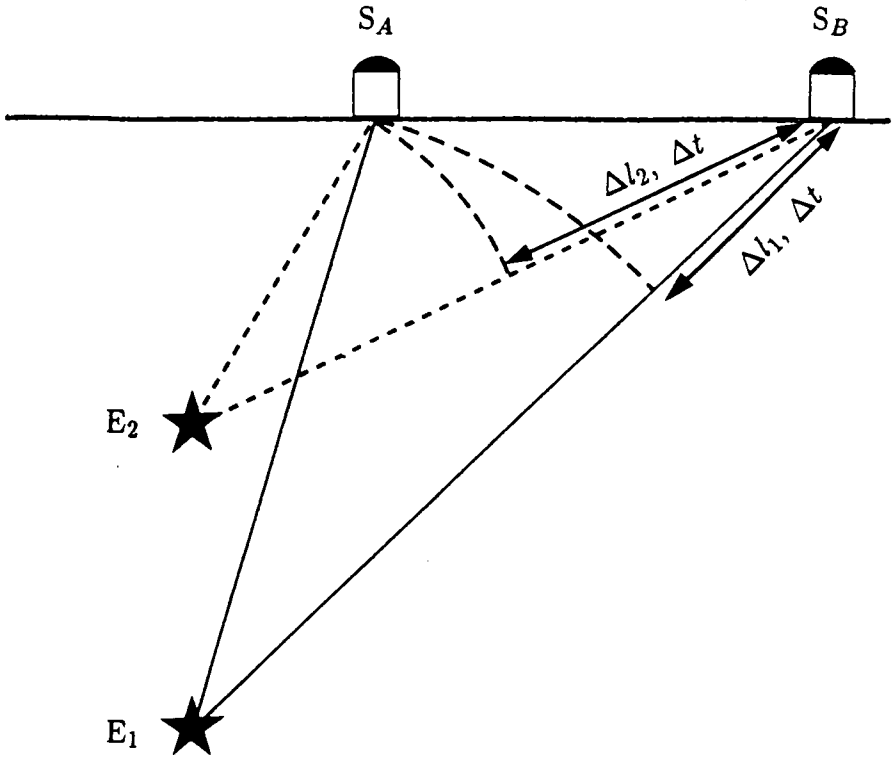

$$v_1 = \frac{\Delta l_1}{\Delta t}$$

$$v_2 = \frac{\Delta l_2}{\Delta t}$$

If $v_2 > v_1 \quad \Longrightarrow$ E_2 shallower (if only P–waves used).

Δt = arrival time difference between seismometers S_A and S_B.

Δl_1, Δl_2 = path length difference between S_A and S_B from hypocentres E_1 and E_2 respectively.

Figure 3.5 : A schematic illustration of the effect on hypocentral depths computed by HYPOINVERSE using P–waves, when the velocity structure is changed.

matrix **H** come close to being multiples of another (e.g. Aki and Richards, 1980). In such cases, the locations are often unstable unless a sufficient number of S–phases are available.

3.3.4 The Hypocentral Locator and Plotting System

The Durham University Earthquake Reduction and Processing System (DUEDROPS) provides software packages for locating (DUEDROPS–HLPS) and plotting (DUEDROPS–HYPOPLOT) earthquake hypocentres (Smith, 1987a).

DUEDROPS–HLPS (Smith and Foulger, 1987) is installed at the University of Newcastle on the Graphics VAX 11/780 running VMS. It is designed to locate earthquake hypocentres and provides a suite of programs and command files to perform all necessary data management. DUEDROPS–HYPOPLOT (Smith, 1987b, c, e) is a graphics system implemented on the Durham University mainframe Amdahl 470 V/8 computer running MTS. It provides a suite of programs and command files to plot earthquake data produced using DUEDROPS–HLPS.

3.3.5 Seismicity

3.3.5.1 Presentation of the Data

Local earthquake data were plotted using the DUEDROPS–HYPOPLOT graphics package. The desired output was achieved by defining plotting constraints in an input control file. No magnitude, or time constraints were used in the plotting. Parameters relating to location accuracy were constrained as follows: –

- RMS $\leq$ 0.08 sec : The final root mean square travel-time residual computed after residual weighting.
- ERH $\leq$ 1.0 km : The horizontal error, defined as the greatest length of the horizontal projection of the 32% error ellipsoid.
- ERZ $\leq$ 1.0 km : The vertical error, defined as the greatest length of the vertical projection of the 32% error ellipsoid.

These constraints were selected qualitatively in an attempt to eliminate from plots those events with poor location accuracies, without distorting the overall earthquake distribution pattern. In order to make some distinction between event locations of differing accuracy, those with a depth error ERZ $\leq$ 0.5 km are plotted as filled circles while those with 0.5 km $<$ ERZ $\leq$ 1.0 km are plotted as unfilled circles. 345 of the 489 located earthquakes are plotted using these criteria. Of these, 153 are plotted as filled circles and 192 as unfilled circles. A complete list of the 489 located earthquakes is given in appendix A.

3.3.5.2 Epicentral Distribution

The epicentral distribution for the Krafla area using the NISE-85 data is shown in figure 3.6.

Local seismicity is most intense beneath Bjarnarflag to the west of the Námafjall geothermal area, where it forms a tight epicentral cluster which appears to be less than 0.8 km in width. Activity extends towards the north–northeast from Bjarnarflag along a narrow linear zone for about 4 km. A more diffuse cluster of activity occurs along the projection of this north-northeast trending line, centred beneath Leirhnjúkur in the middle of the Krafla caldera (figure 3.1). Subsidiary clusters within this area occur about 2 km to the east–southeast of Leirhnjúkur, and about 1.5 km to the north.

Subsidiary activity occurs to the south and west of Leirhnjúkur, and to the south–southwest of Bjarnarflag.

3.3.5.3 Hypocentral Distribution

The distribution of earthquake hypocentres will be described in this section by studying four representative depth cross–sections through the data. The orientations of these sections are shown in figure 3.7.

Three distinct zones of activity have been defined for reference. 'Bjarnarflag' denotes the earthquake cluster beneath Bjarnarflag in the western part of the Námafjall geothermal area, between latitudes 65°37.75′N and 65°38.26′N. The 'Fissure Zone' includes all earthquakes forming the linear zone of activity between latitudes 65°38.26′N and 65°40.97′N. 'Leirhnjúkur' denotes the earthquake cluster

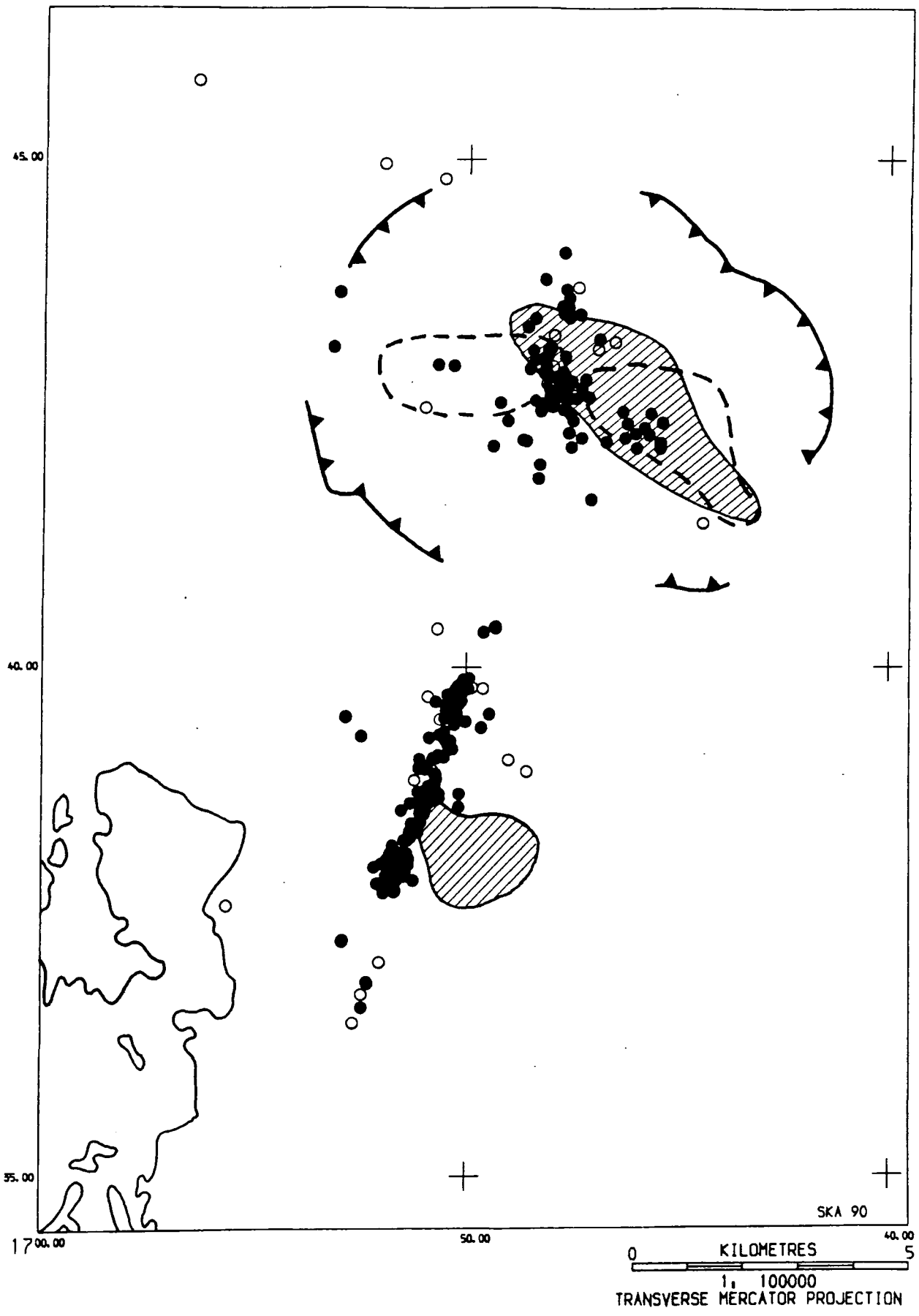

Figure 3.6 : Epicentre map for data collected by the NISE–85 experiment. Events located with an error ERZ $\leq$ 0.5 km are plotted as filled circles, and those located with 0.5 km $<$ ERZ $\leq$ 1.0 km are plotted as open circles.

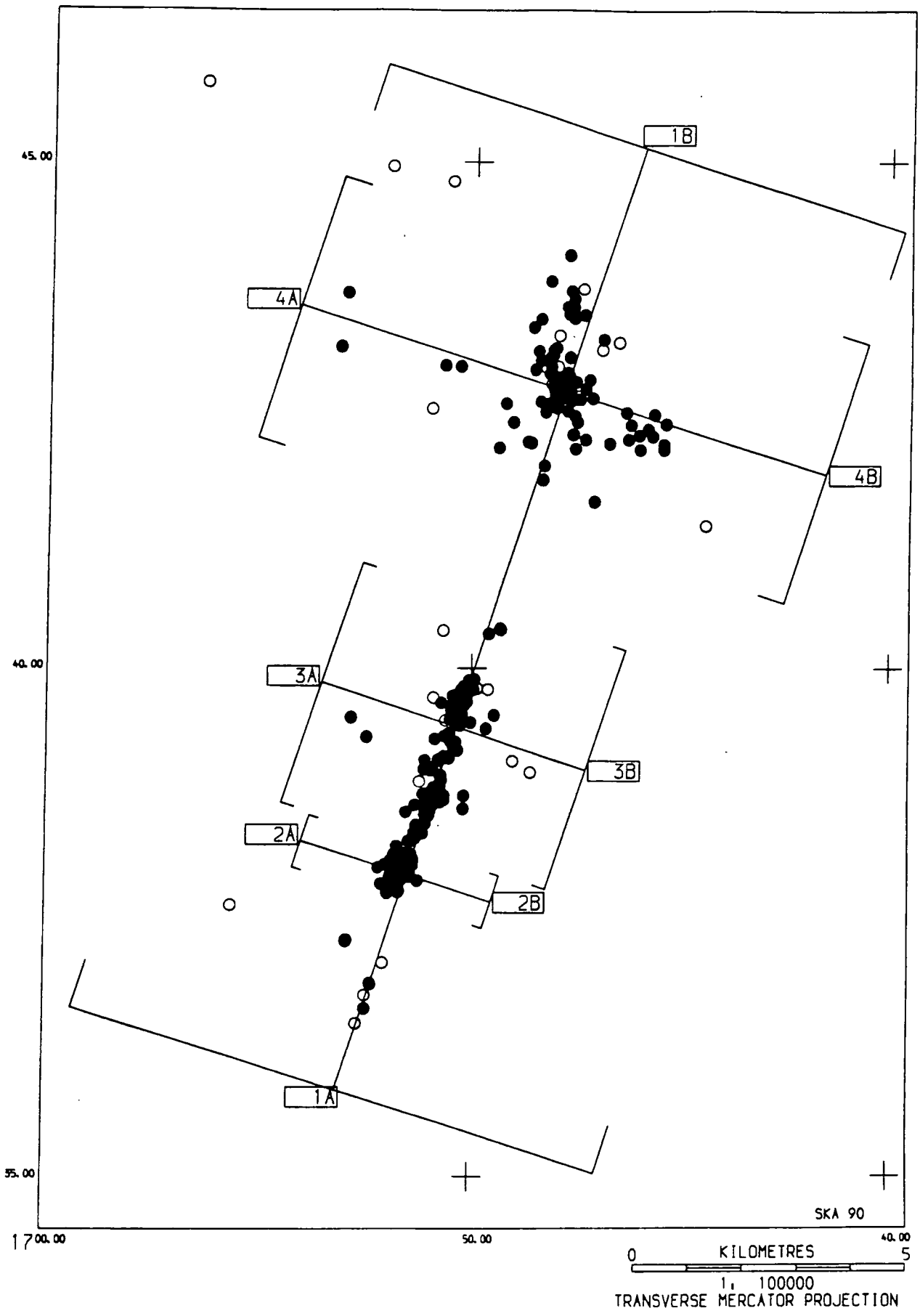

Figure 3.7 : Epicentre map showing the locations of hypocentre cross-sections presented in figures 3.8 and 3.9. Brackets indicate the width of the cross-sections.

beneath the hill Leirhnjúkur, and all others occurring north of 65°40.97′N, within the Krafla caldera.

Figure 3.8 shows cross-section 1 through the main areas of seismic acticity and parallel with the trend of surface fissuring (figure 3.7). Activity has been located between 0–6 km depth, although earthquakes with better constrained locations are restricted to a depth zone of 0.7–4.0 km. The Bjarnarflag cluster lies between 2–4 km depth. It is bounded sharply to the north by a plane which intersects with the surface at Bjarnarflag and dips to the south at about 80°. In cross–section the cluster takes the form of a lens which is convex to the south and has a maximum width of about 0.6 km at 3 km depth. The sharpness of the northerly contact of this zone suggests that the relative location error in this area may be as little as 0.1–0.2 km horizontally. Seismic activity in the fissure zone covers a diffuse elliptical area between about 1.8–3.8 km depth, with major and minor axes of about 3.3 km and 1.5 km in length, respectively. The southern tip of this zone appears to be coincident with the northern tip of the Bjarnarflag cluster. The plane of activity plunges northwards at about 20°. Beyond a seimic gap of about 3 km in width to the north–northeast of the fissure zone lies the Leirhnjúkur cluster, whose centre lies beneath the hyaloclastite hill Leirhnjúkur. Activity is concentrated between about 1.5 km and 3.5 km depth and along a line whose projection intersects the surface near the geothermal area of Hvíthólar, and dips northwards at about 55°.

A cross–section through the Bjarnarflag cluster of activity perpendicular to the fissure swarm (section 2 of figure 3.7) is shown in figure 3.9a. In this section the activity occurs in a strip 0.3–0.4 km in width and displays a sharp easterly edge which dips at about 85° to the west.

Cross-section 3 of figure 3.7 traverses the fissure zone of activity and is shown in figure 3.9b. The width of the main active zone, outlined by the best located events, is 0.3–0.4 km. The plane of activity appears to dip at about 85° to the west.

In cross-section 4 across the Leirhnjúkur cluster (figure 3.9c), activity is found to be concentrated in a circular area centred at 2.5 km depth with a radius of about 0.5 km and enclosed within a triangular wedge which points downwards to a depth of 3.5 km and whose lower sides are defined by relatively poorly constrained events.

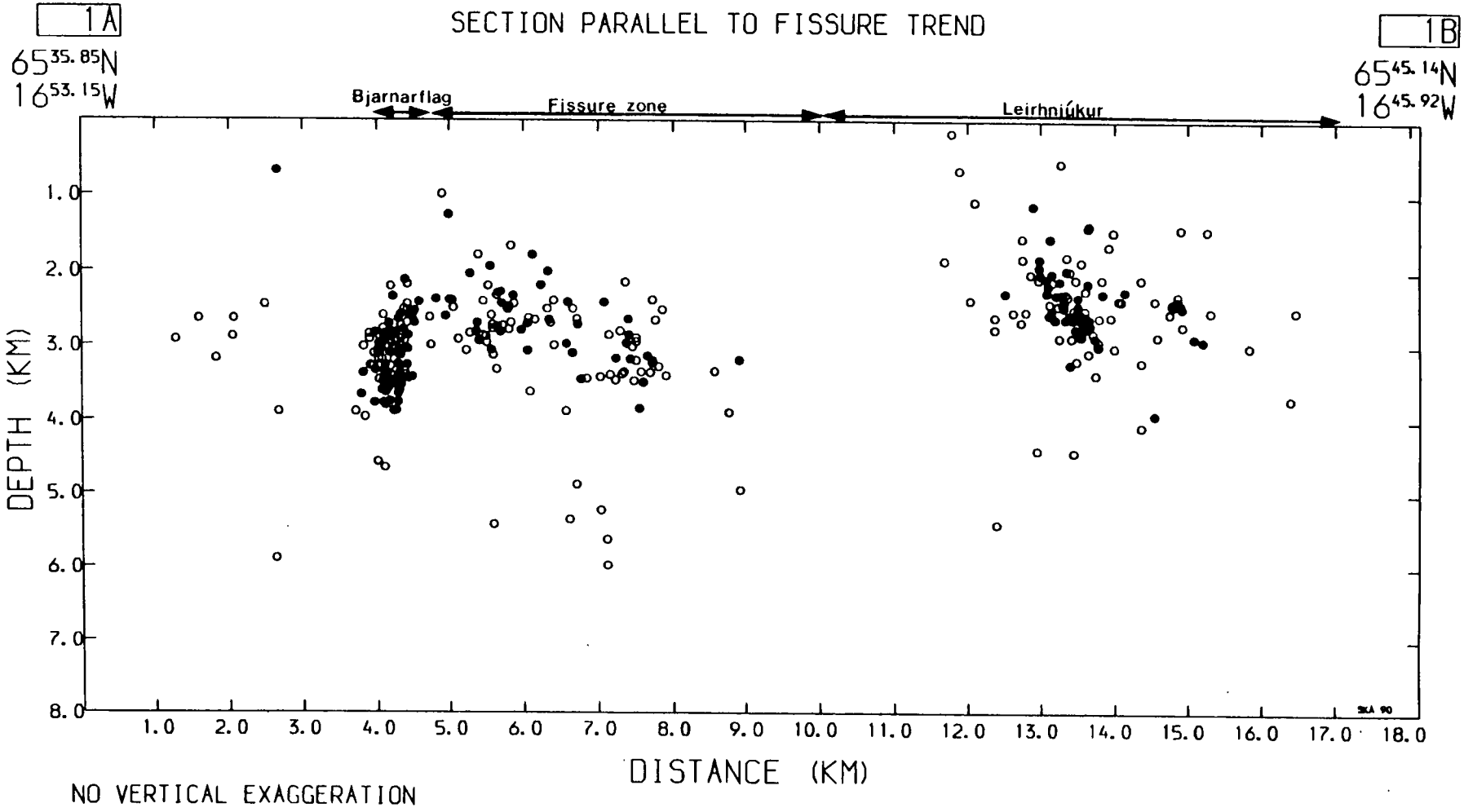

Figure 3.8 : Hypocentres along cross-section 1A–1B of figure 3.7, which is parallel to the trend of the surface fissure swarm.

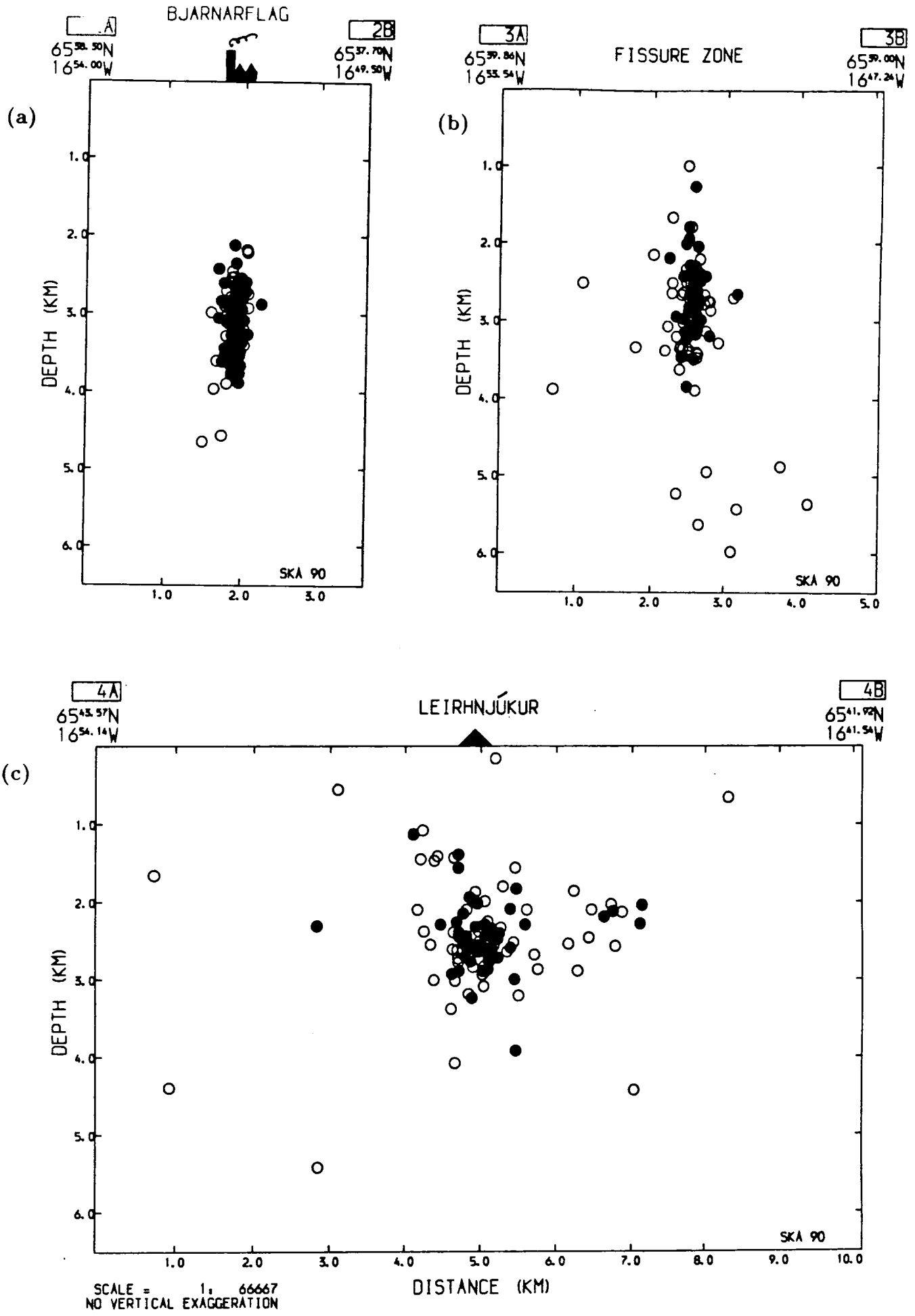

Figure 3.9 : Hypocentres along cross-sections perpendicular to the trend of the surface fissure swarm (figure 3.7). **(a)** Section 2A-2B across the 'Bjarnarflag cluster' of activity. **(b)** Section 3A-3B across the 'fissure zone'. **(c)** Section 4A-4B across the 'Leirhnjúkur cluster'.

The western edge of this triangle dips eastwards at about 80°. The eastern edge dips westwards at about 30°.

3.3.5.4 Temporal Distribution

During the $94\frac{1}{2}$ days when the local network was recording, it was possible to locate 489 of the earthquakes detected within it Figure 3.10 shows the frequency in number of these local earthquakes throughout the survey period. Activity is seen to have been continuous throughout this period, although there were periods of relatively intense and sparse activity.

Figure 3.11 is a plot of activity along a line parallel to the fissure trend (section 1 of figure 3.7) with time. There are few breaks in activity, particularly in the Bjarnarflag cluster and in the fissure zone. However, activity within the Leirhnjúkur cluster does exhibit periods of concentration both in location and in time. Most conspicuous is a relatively intense period of activity within the Leirhnjúkur cluster at the beginning of September 1985, which is discussed further in section 3.4.3.

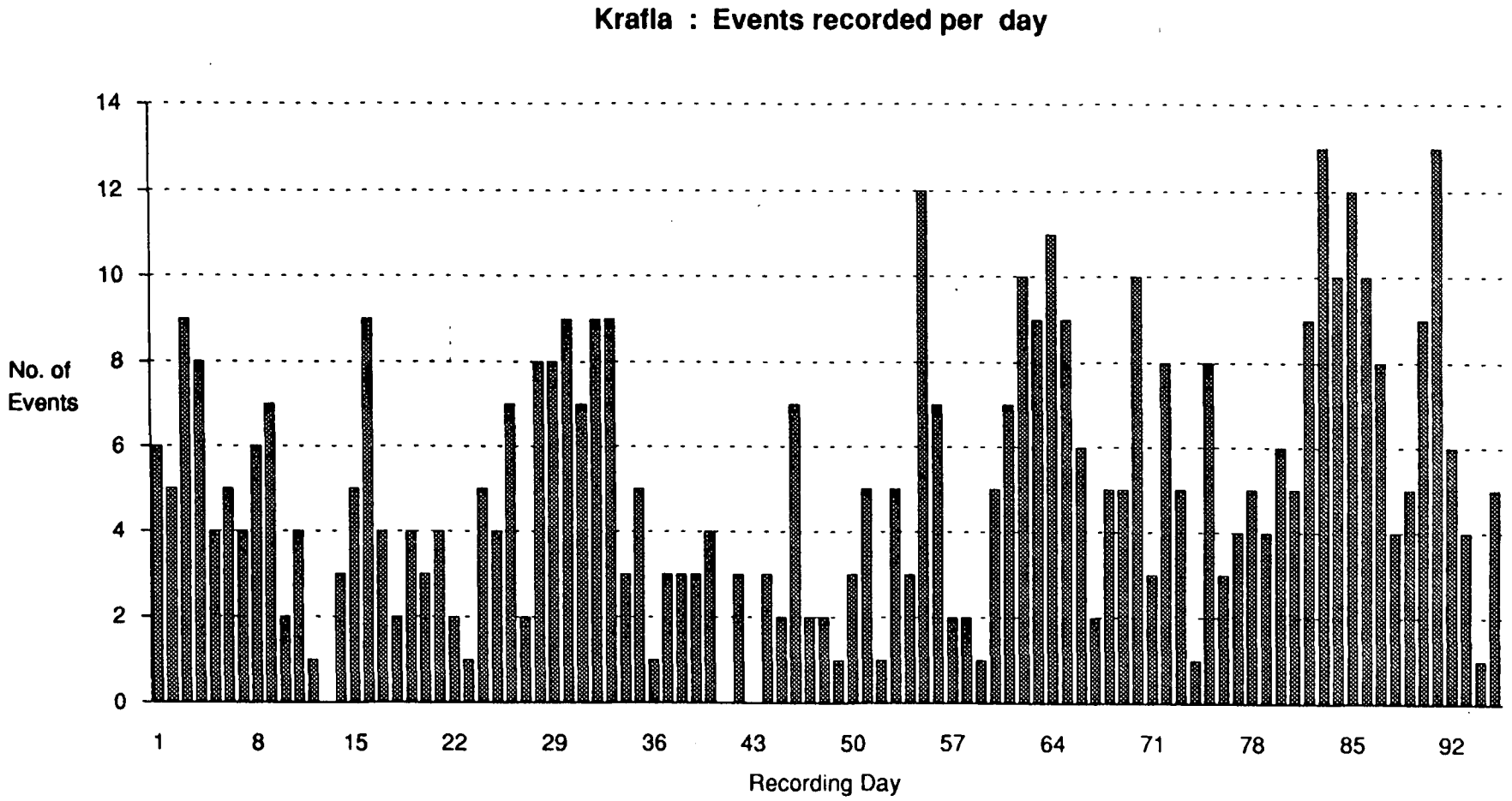

Figure 3.10 : A count of the number of local earthquakes recorded each day by the NISE–85 experiment which could be located.

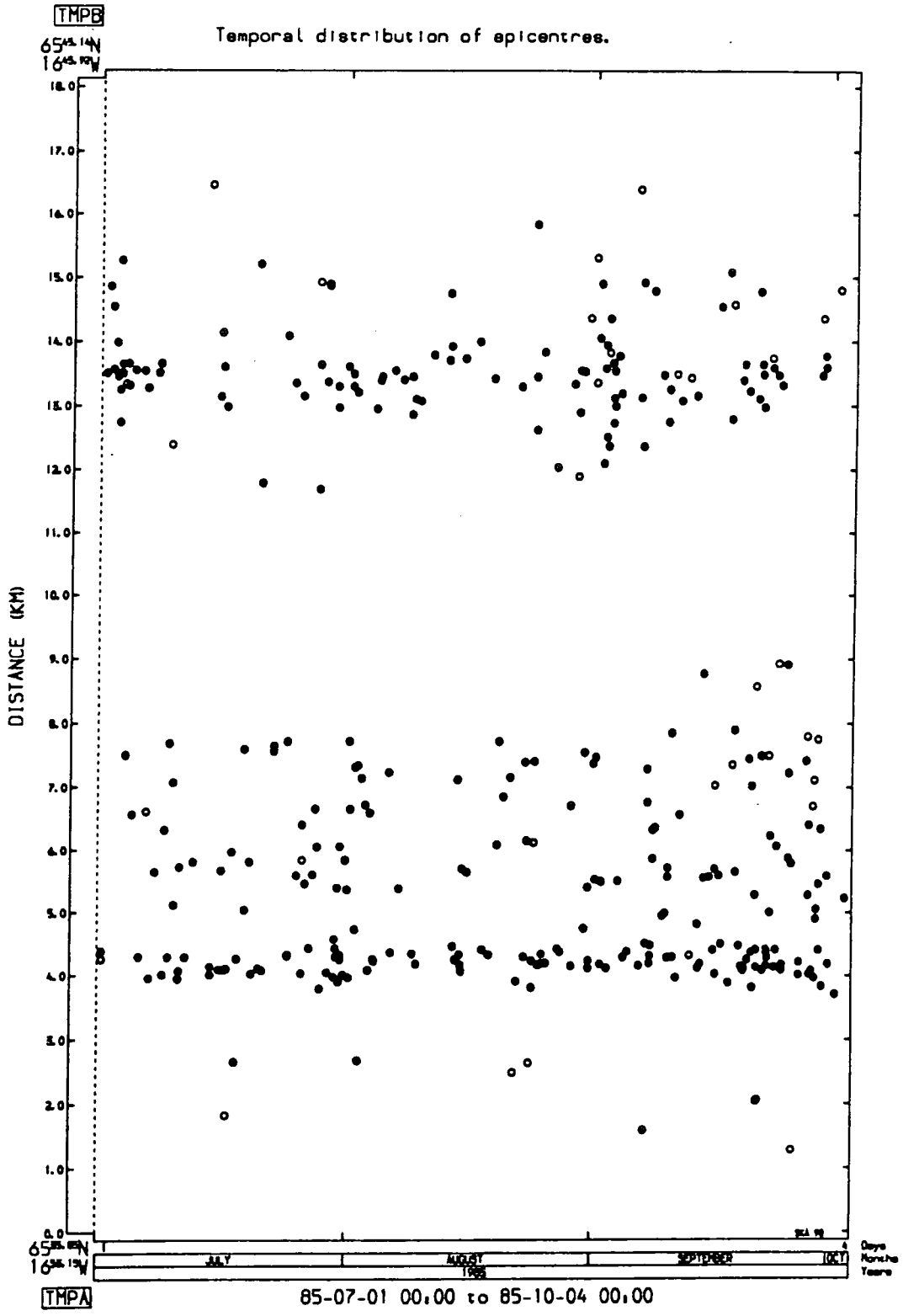

Figure 3.11 : The temporal distribution of epicentres along cross-section 1A–1B of figure 3.7.

3.4 Local Earthquake Magnitudes

3.4.1 Introduction

The best measure of an earthquake's size is the seismic moment M_o, which is a direct measure of the strength of the earthquake generated by a fault rupture (e.g. Aki and Richards, 1980) : -

$$M_o = \mu \tilde{u} S \qquad 3.7$$

where :

μ = Shear modulus of the ruptured medium.

$\tilde{u}$ = Average fault slip.

S = Source Area.

Estimation of the seismic moment can be made by estimating or measuring the shear modulus and the dimensions of the ruptured surface and the extent of the slip. It is more commonly estimated by spectral analysis of the recorded ground motion (e.g. Lee and Stewart, 1981), although ideally this requires broadband, unsaturated digital records from fully calibrated seismic stations.

Richter (1935, 1958) was the first to propose an empirical earthquake magnitude scale based only on the amplitudes of ground motion recorded on seismograms. The Southern California Seismic Network at that time was equipped with Wood-Anderson seismographs which have nearly constant displacement amplification over the frequency range appropriate for local earthquakes. In addition, the depths of moderate strength earthquakes in southern California are approximately constant. Richter recognised that the ratio between the recorded maximum trace amplitudes of two earthquakes observed at equal epicentral distances is related to their relative energy release. He therefore defined a scale for local magnitudes M_L based on this relationship : -

$$M_L = logA - logA_o(\Delta) \qquad 3.8$$

where :

A = Maximum amplitude in mm recorded by a Wood-Anderson short period torsion seismometer at an epicentral distance of Δ km.

A_o = Maximum amplitude at an epicentral distance of Δ km for a 'standard earthquake', taken from a table of the observed amplitudes of accurately located earthquakes.

Richter chose the zero magnitude level to occur when $A_o(\Delta)$ was equal to 1μm at an epicentral distance of 100 km, in order to avoid dealing with negative magnitudes. The local magnitude for any event from southern California could then be determined empirically from a table of $(-logA_o)$ at different epicentral distances for well located 'standard' earthquakes (Richter, 1958 p 342).

The use of signal duration rather than the maximum amplitude is now common practice for microearthquake networks. This is largely due to the considerable additional effort that would be required to calibrate and maintain a network for ground motion calculation (Lee and Stewart, 1981). Duration magnitude for a given station usually takes the form : -

$$M_D = a_1 + a_2 log\tau + a_3\Delta + a_4 h \qquad 3.9$$

where :

τ = signal duration in seconds.

Δ = epicentral distance in km.

a_1, a_2, a_3, a_4 = empirical constants.

The constant a_3 is generally small and so if the focal depth h is approximately constant then the duration magnitude may be given as : -

$$M_D \approx a log\tau + b \qquad 3.10$$

where a and b are empirical constants.

3.4.2 Application to the NISE data

The magnitudes calculated for events recorded by the local earthquake network are local Icelandic magnitudes. They are based on a magnitude scale which was available to the author for the University of Iceland drum seismograph RI (Reynihlid).

This scale was obtained by comparison with the teleseismic surface wave magnitude M_S for the WWSSN station at Akureyri (AKU) and by extrapolation downwards for small magnitudes.

The signal duration was measured manually by the author for each event using the record for one station for each tape recorder operated. A graph of M_{RI} against the logarithm of signal duration was then produced for all the events detected by the drum recorder RI, for each of the stations RRA, NNO and NSO (figure 3.12). The relationships thus derived are given in table 3.3.

Station	Magnitude Relationship	Corr. Coeff.
RRA	$M_{RRA} = 3.35\ log_{10}\ T_{mm} - 7.87$	0.86
NSO	$M_{NSO} = 2.76\ log_{10}\ T_{mm} - 6.32$	0.93
NNO	$M_{NNO} = 3.17\ log_{10}\ T_{mm} - 7.37$	0.91

T_{mm} is the signal duration in mm of a seismogram for which the peak to peak amplitude was $\geq$ 2mm for amplifier-modulator gain 7 and jet pen gain 0.25, corresponding to approximate ground velocities of $\leq 3 \times 10^{-7}$ms^{-1} or approximate ground displacements of $\leq 3 \times 10^{-9}$m. Where a different jet pen gain was used, a corresponding amplitude cut–off was chosen.

Table 3.3: Magnitude relationships.

For events recorded at RI, M_{RI} was adopted as the local Icelandic magnitude M_{IL}, which is consistent with established Icelandic seismological practice (Foulger, 1984). Events which were too small to be given reliable magnitudes were arbitrarily assigned a magnitude of –5. Timed explosions were assigned a magnitude of –9 to distinguish them from natural earthquakes. In every other case the average magnitude from stations RRA, NNO and NSO was calculated to find M_{IL} for each event. Magnitudes M_{IL} are given in the event listing (Appendix A). It should be emphasized, however, that these local Icelandic magnitudes are related to a teleseismic surface–wave scale and not to the Richter local magnitude scale.

(a)

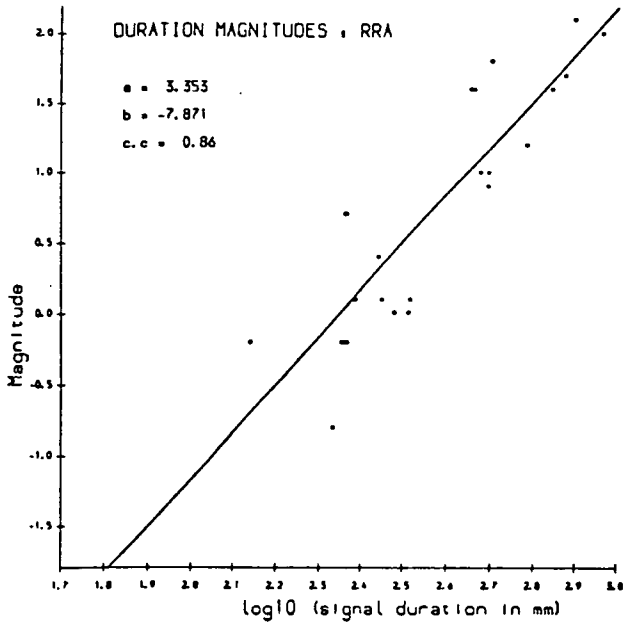

(b)

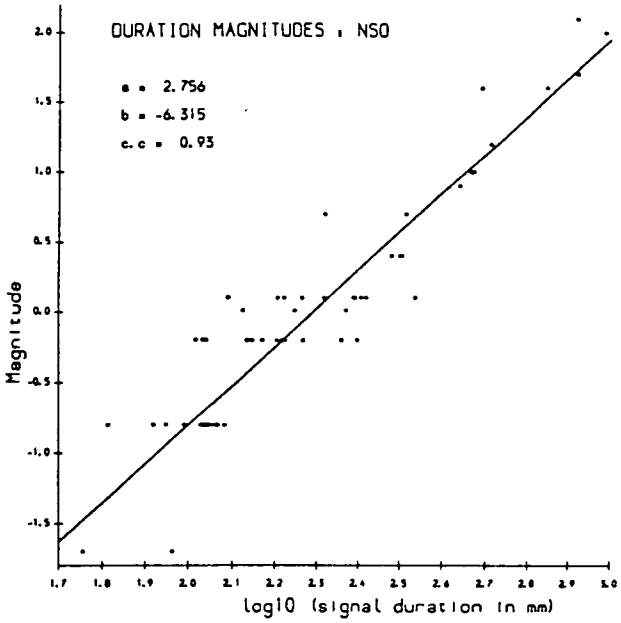

(c)

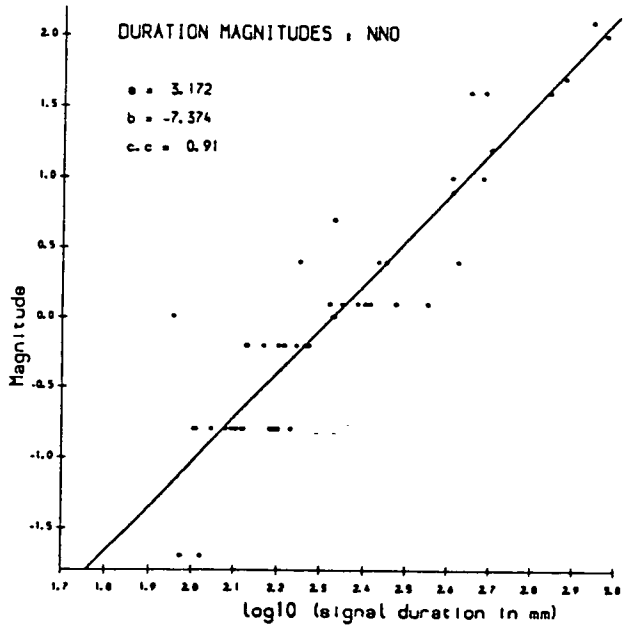

Figure 3.12 : Graphs of local Icelandic magnitude (M_{IL}) at drum station RI against the logarithm of signal duration measured at stations **(a)** RRA, **(b)** NSO, and (c) NNO. The least-squares best fit straight line through each set of points is indicated. a is the gradient, b is the magnitude intercept, and $c.c$ is the correlation coefficient.

3.4.3 Temporal Distribution

The temporal distribution of local earthquake magnitudes is illustrated for the entire data set (figure 3.13a) and for each main area of activity (figures 3.13b, 3.14a,b). In all cases, an earthquake of magnitude $M_{IL} \geq 1.0$ was followed by an event with a magnitude that was at least 1 magnitude unit smaller. Events with $M_{IL} \geq 1.0$ are therefore technically mainshocks (Sykes, 1970). The largest events to occur during the experiment originated in the Bjarnarflag cluster, where two events of $M_{IL} \geq 2.0$ were recorded (figure 3.13b). Other mainshocks ($M_{IL} \geq 1.0$) only occurred in the Bjarnarflag and Leirhnjúkur clusters (figures 3.13b, 3.14b). The largest event to occur in the fissure zone was of $M_{IL} = 0.7$, whereas all other events there were of $M_{IL} \leq 0.1$. Only one temporally coherent earthquake magnitude sequence is apparent throughout the recording period. This occurred between 30th August and 4th September within the Leirhnjúkur cluster (figure 3.15). It takes the form of a mainshock–aftershock sequence which is preceded by a steady reduction in earthquake magnitude, its activity being distributed over a zone 2 km in length in a north–south direction (figure 3.11). Figure 3.16 shows the hypocentres of this mainshock–aftershock sequence. It can be seen that the 'mainshock' (the larger closed circle) occurred in the heart of the Leirhnjúkur cluster of activity, at a depth of 2.6 km (figure 3.16a). There is no clear spatial distribution of 'aftershocks' to suggest that the sequence was associated with, for example, slip on a single fault (figures 3.16a,b).

3.4.4 Frequency–Magnitude Relationships and b–Values

3.4.4.1 Introduction

Gutenberg and Richter (1941) found that N, the frequency of occurrence of earthquakes of magnitude M or greater, is related to magnitude by the relation : –

$$logN = a - bM \qquad 3.11$$

where a and b are numerical constants.

The b–value gives a measure of the rate of increase of earthquake incidence with decreasing magnitude. Variations in b–value are thought to be due to variations in

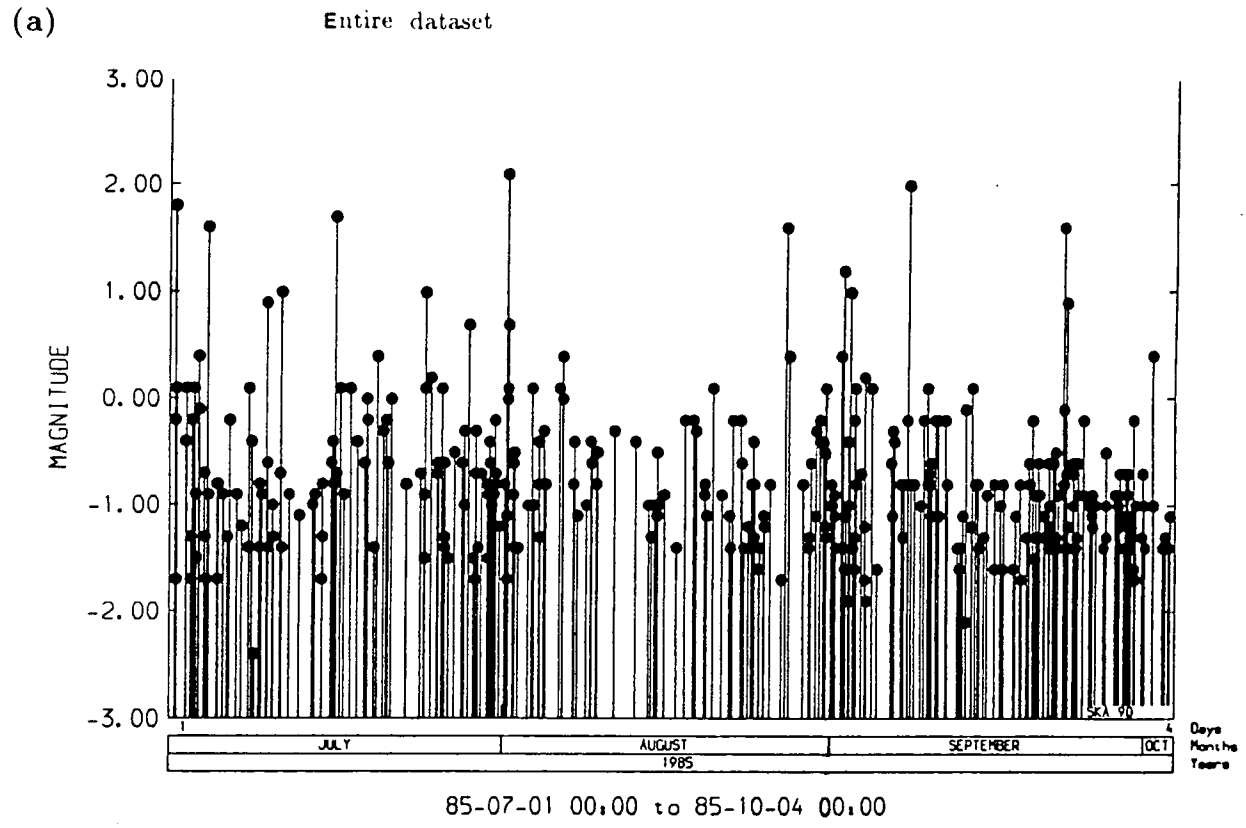

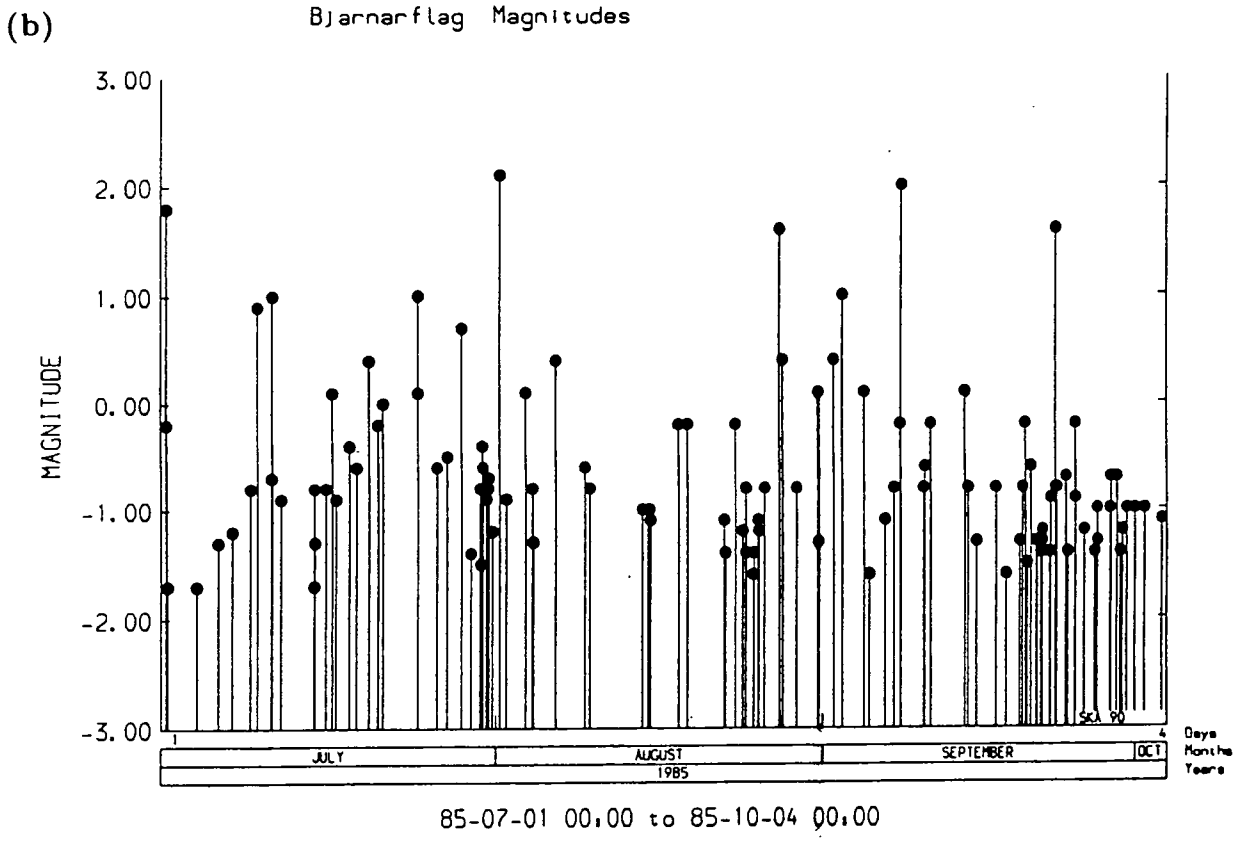

Figure 3.13 : The temporal distribution of local earthquake magnitudes M_{IL} for **(a)** the entire dataset, **(b)** the Bjarnarflag cluster.

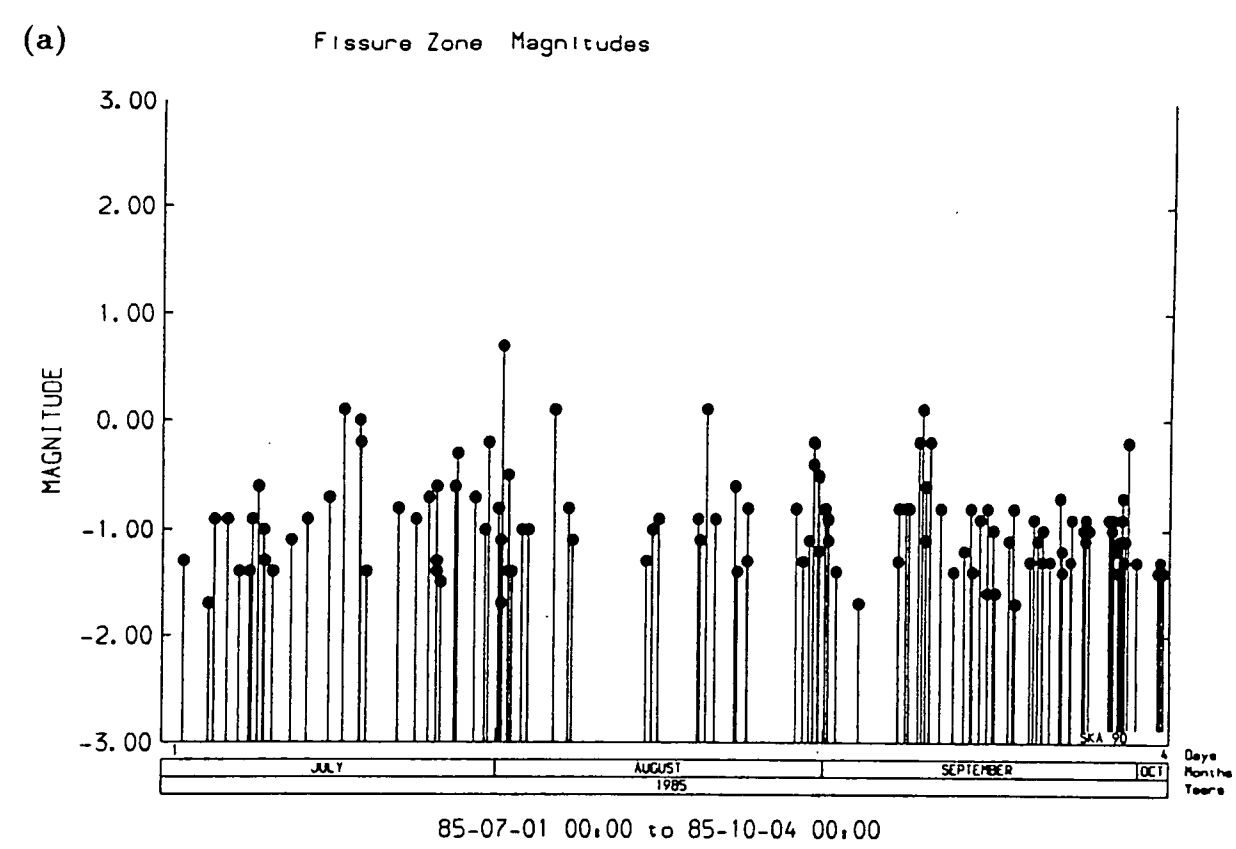

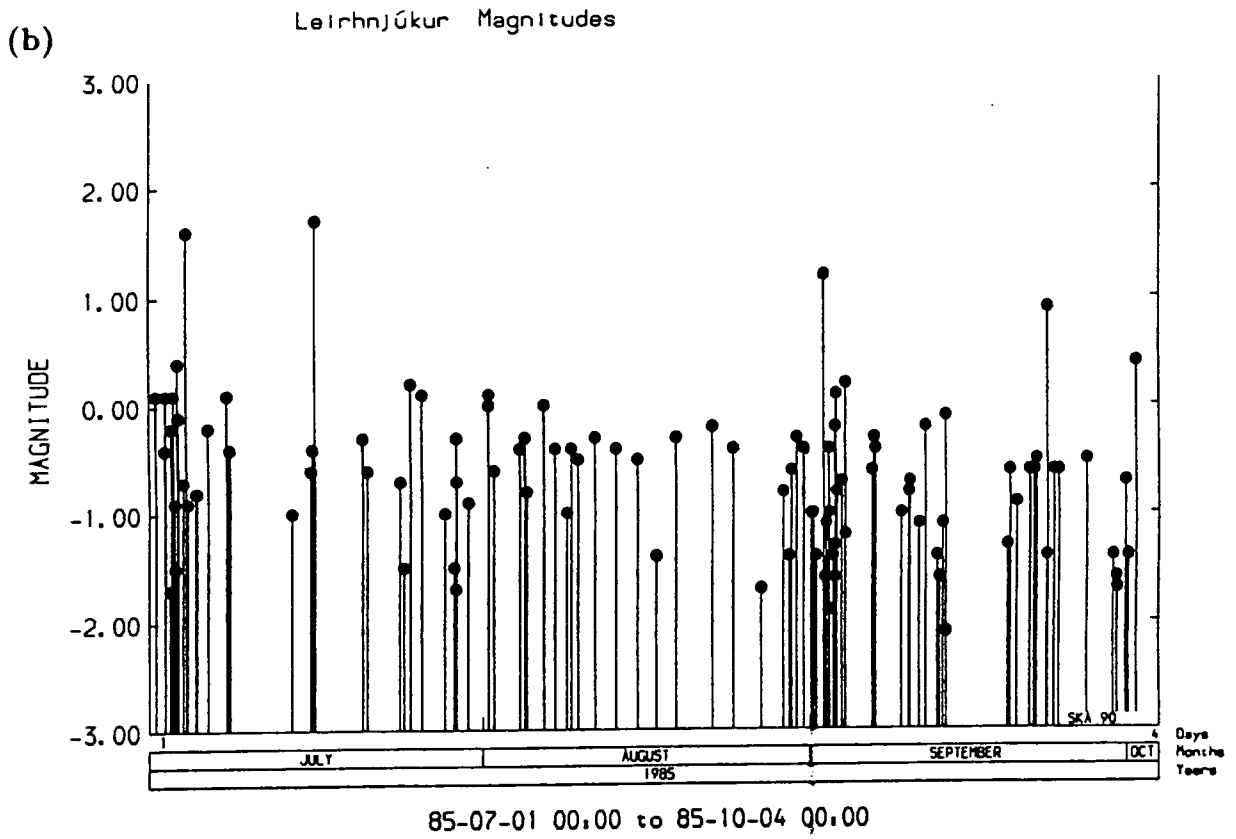

Figure 3.14 : The temporal distribution of local earthquake magnitudes M_{IL} for **(a)** the 'fissure zone', **(b)** the Leirhnjúkur cluster.

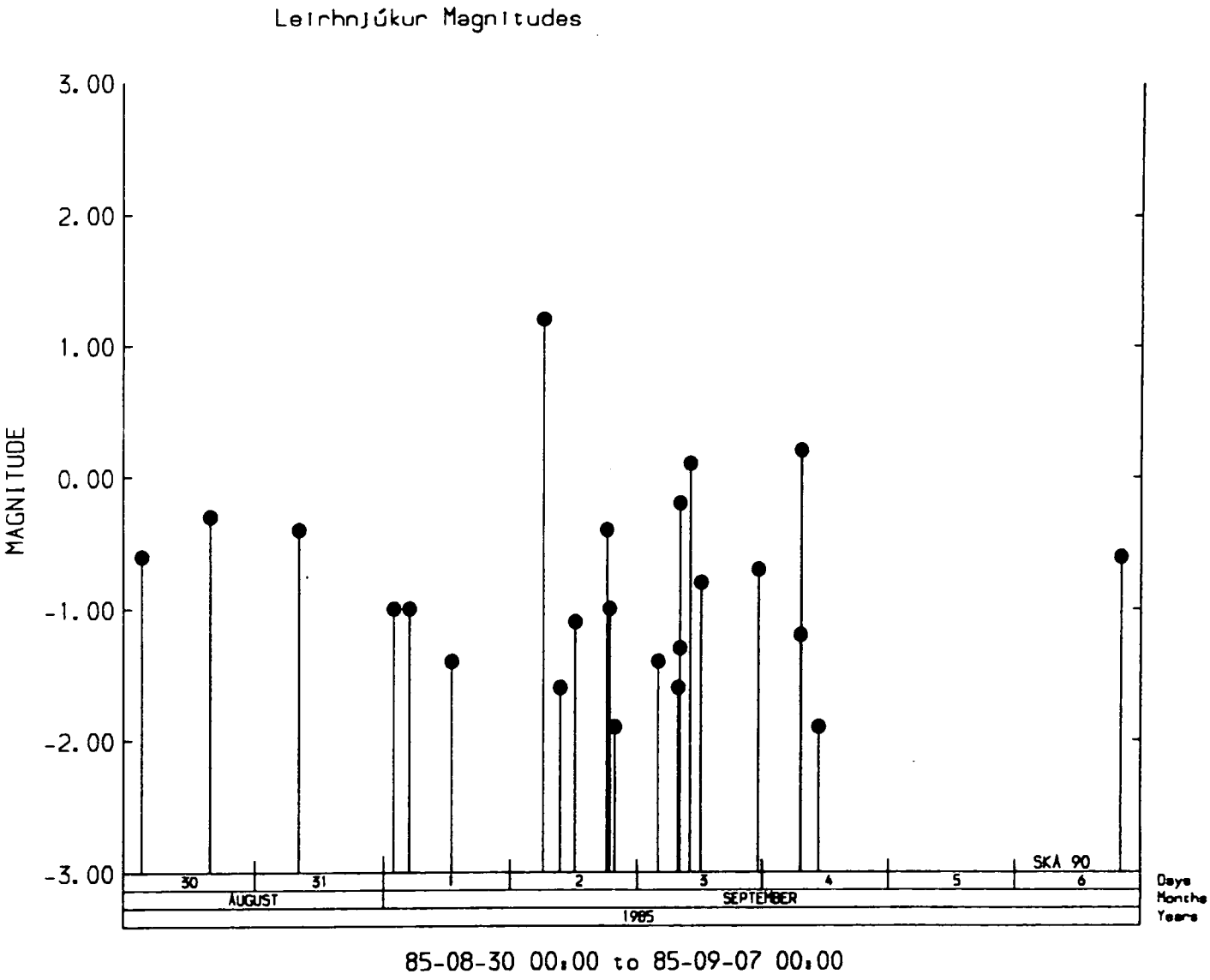

Figure 3.15 : The temporal distribution of local earthquake magnitudes M_{IL} for events originating within the Leirhnjúkur cluster of activity between 30th August and 6th September 1985.

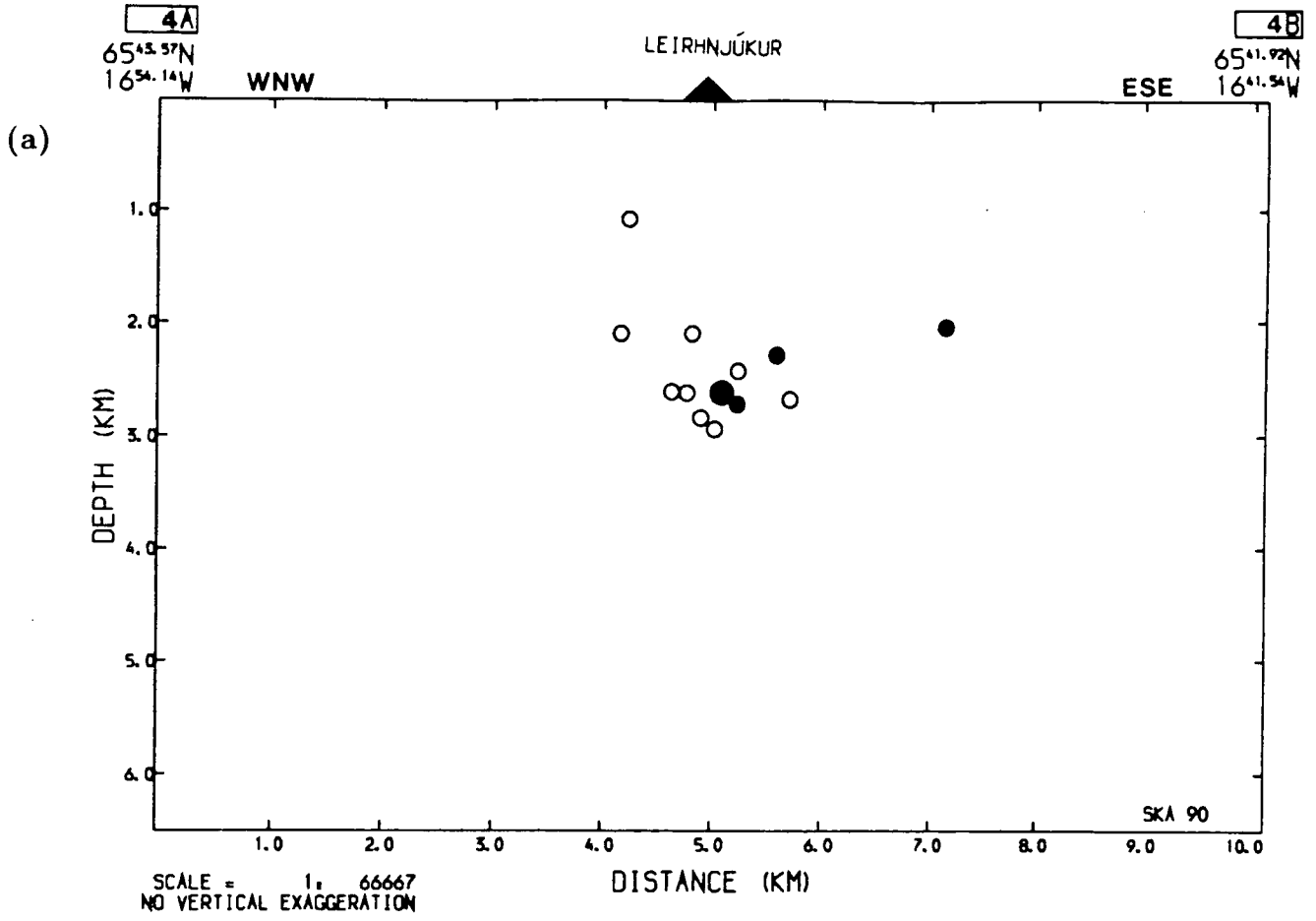

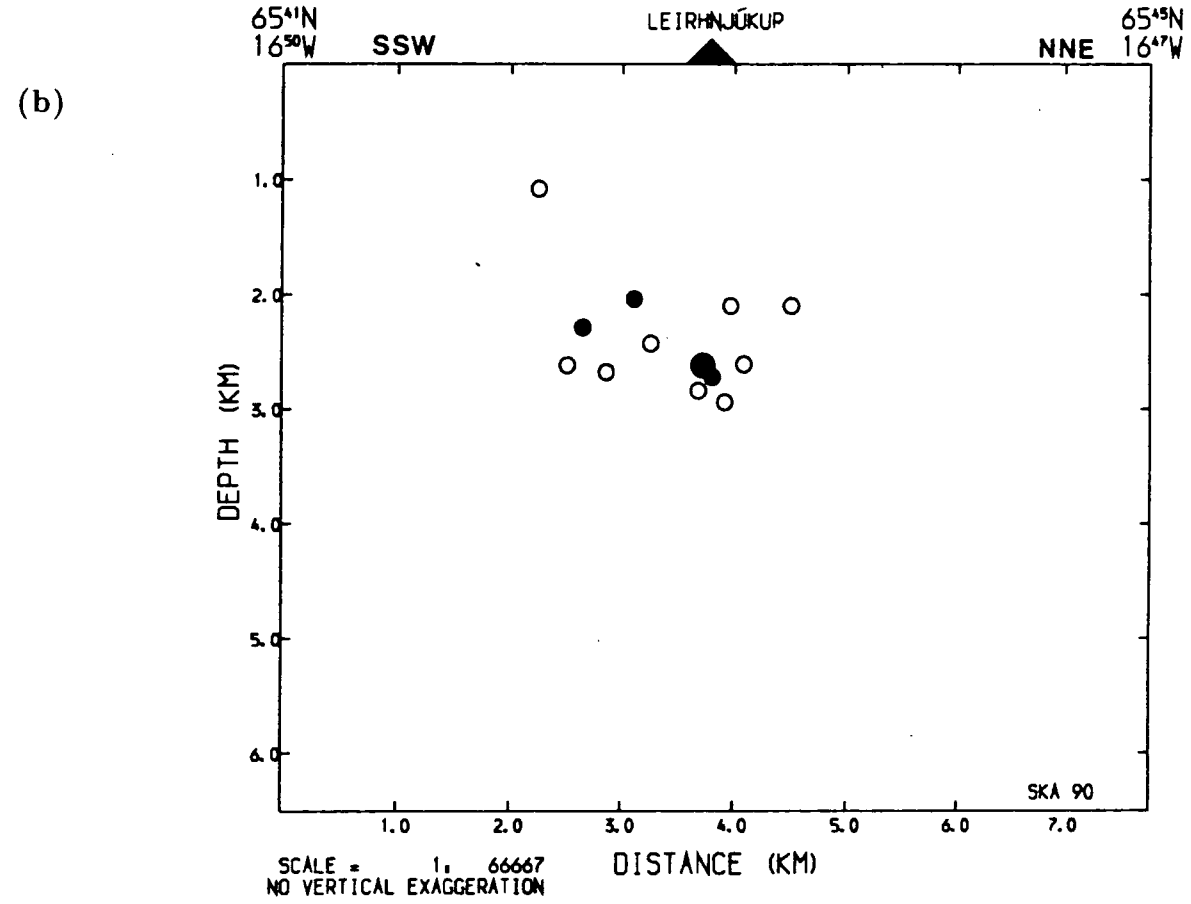

Figure 3.16 : Hypocentral locations of events originating between 2-4th September 1985 within the Leirhnjúkur cluster. The large closed circle represents the 'mainshock' of the sequence (M_{IL} = 1.2). **(a)** Section perpendicular to the trend of the fissure swarm (section 4A-4B of figure 3.7), **(b)** section parallel to the fissure swarm from SSW to NNE.

crustal stress conditions or to the degree of crustal inhomogeneity (Scholz, 1968). The average worldwide value for b is about 1 (Lee and Stewart, 1981). If b–values significantly smaller than 1 are observed, this is thought to indicate that the rock volume is either relatively highly stressed or highly inhomogeneous, or both.

Foreshock–mainshock–aftershock sequences have been related previously to temporal variations in b–value (e.g. Suyehiro et al., 1964; Bufe, 1970; Wyss and Lee, 1973; Udias, 1977). Low b–values are associated with foreshocks and swarms and high b–values with aftershocks. If b is inversely proportional to local stress conditions (Scholz, 1968; Wyss, 1973), then this b–value variation would be compatible with high stress conditions prior to the mainshock and lower stress afterwards.

If the brittle crust is homogeneous then spatial variations in b–value are likely to be due to locally varying stress conditions. Significant variations of this kind have been reported by various observers (e.g. Pfluke and Steppe, 1973; Klein et al., 1977).

3.4.4.2 Application to the NISE data

Frequency–magnitude plots are shown for the entire data set (figure 3.17a) and for the three main seismically active areas (figures 3.17b, 3.18a,b). Each of these plots displays two features characteristic of all frequency-magnitude plots : (a) Incomplete detection of the smallest earthquakes flattens the negative slope of the curves at low magnitude; the break in slope is referred to as the detection threshold, above which detection is complete in the study area. The detection threshold was found to be higher for events beneath Leirhnjúkur than further south due to the lower density of station coverage. (b) At large magnitudes the general increase in the slope of the curves is at least partially due to the decreasing probability of the occurrence of larger and larger events within the study period. This feature is therefore due to having a dataset which is finite. Between these two breaks in slope of the frequency-magnitude plots, b–values were calculated, and points were weighted according to how many earthquakes they represented. Other sharp breaks in the b–slopes evident in the plots may be attributed to the apparent existence of 'preferred' magnitude values for the drum station RI. Inspection of figure 3.19 shows that below magnitude 1, the 80 events detected at RI were given only 8 different magnitude values between them. This is possibly

(a)

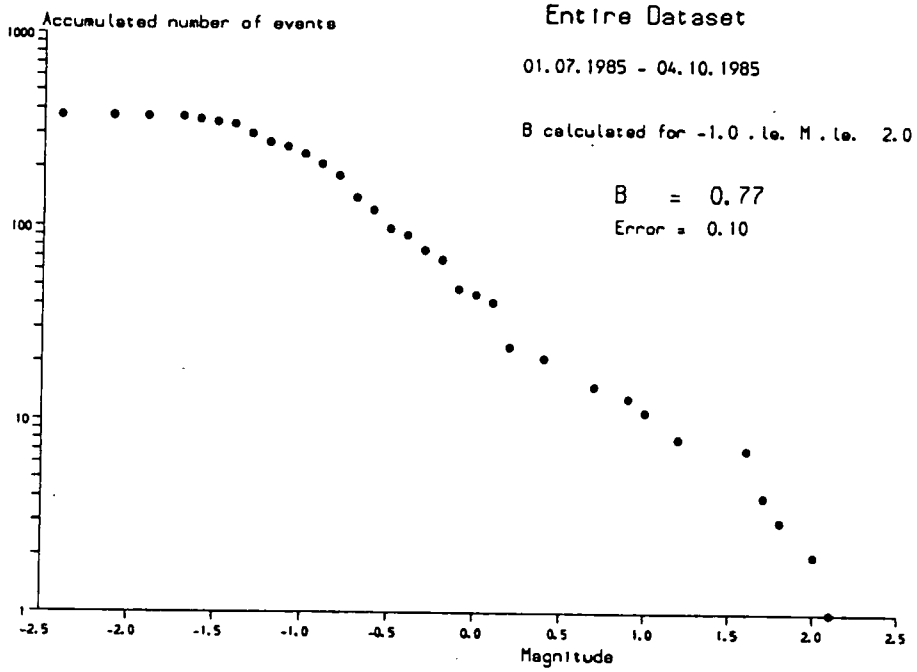

(b)

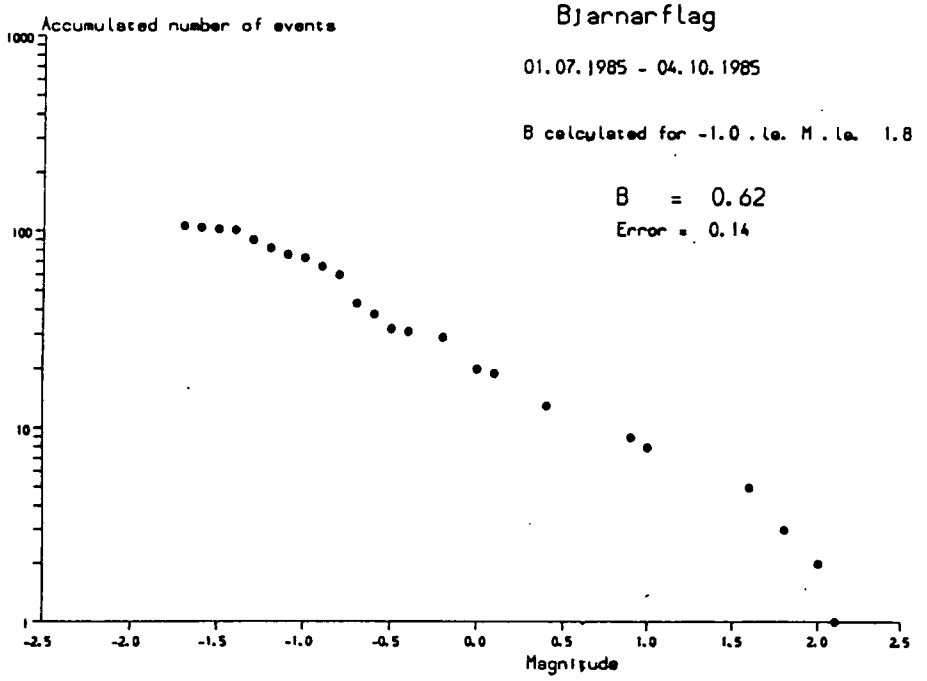

Figure 3.17 : Frequency–magnitude plots for **(a)** the entire dataset, **(b)** the Bjarnarflag cluster.

(a)

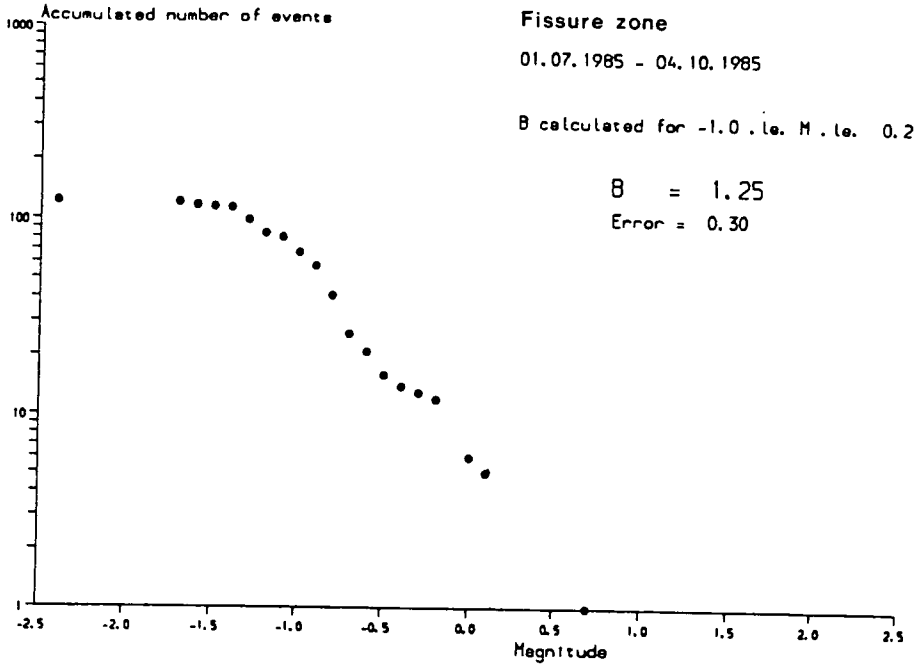

(b)

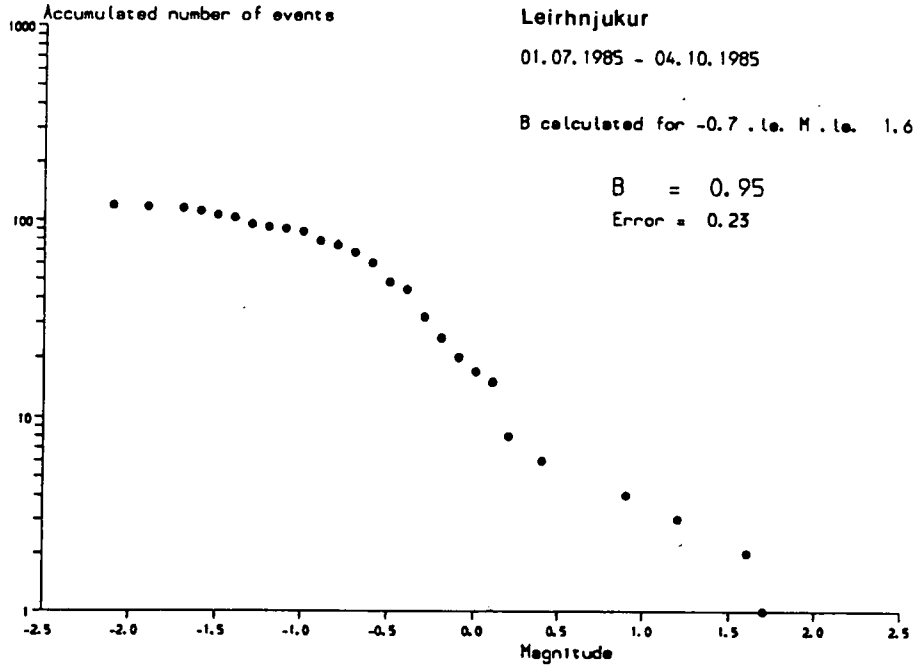

Figure 3.18 : Frequency–magnitude plots for **(a)** the 'fissure zone', **(b)** the Leirhnjúkur cluster.

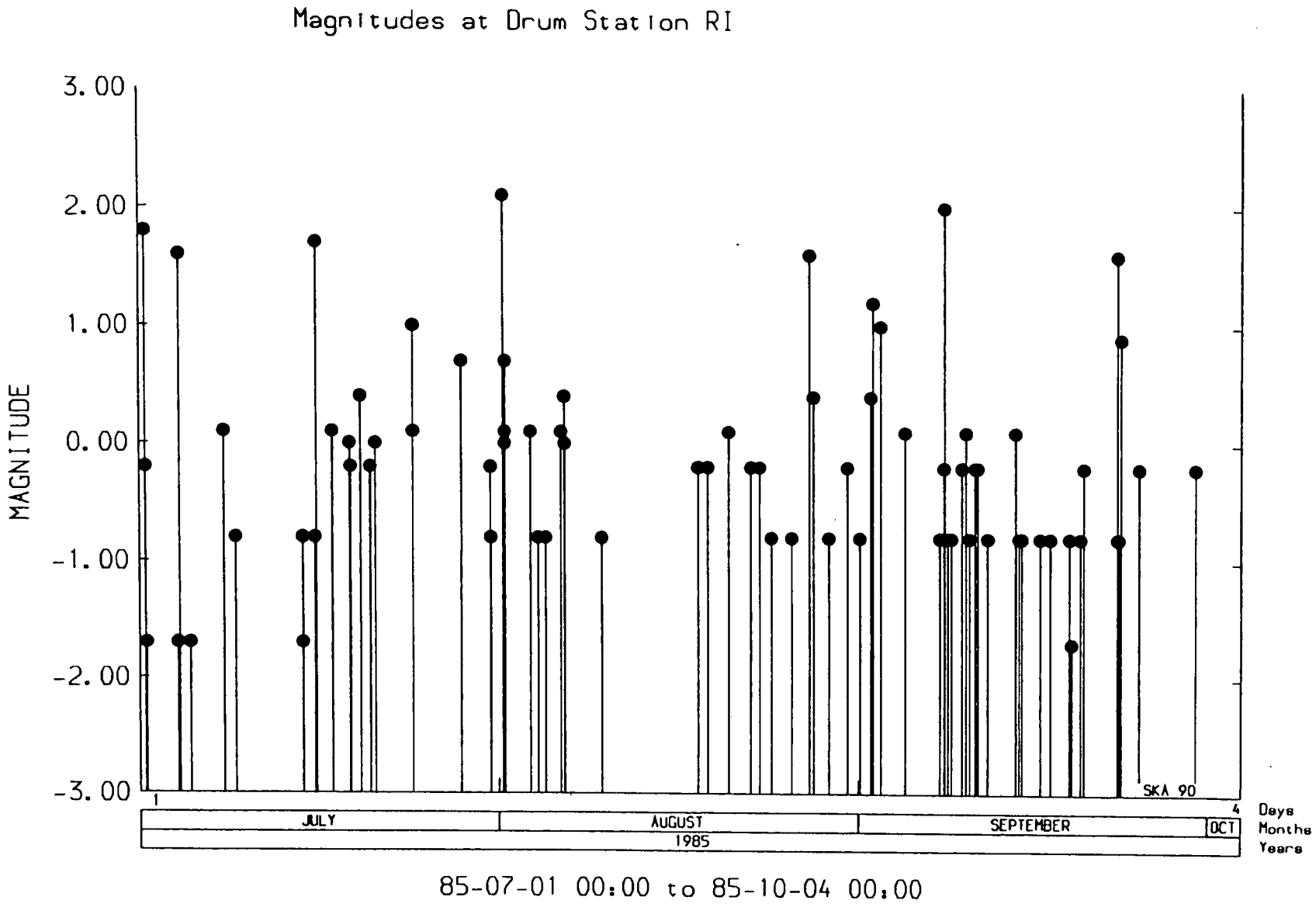

Figure 3.19 : The temporal distribution of magnitudes M_{IL} at the drum station RI throughout the NISE 85 recording period.

due to the significant imprecision inherent in the manual measurement of signal durations on drum recorders. In particular, breaks in the b–slopes which coincide with 'preferred' magnitudes occur at magnitudes –0.8, –0.2, 0.1 and 0.4.

Time Period	b–value	Error
01.07.85 - 22.07.85	0.54	0.15
22.07.85 - 26.07.85	0.62	0.17
26.07.85 - 30.07.85	0.66	0.18
30.07.85 - 01.08.85	0.69	0.19
01.08.85 - 06.08.85	0.73	0.20
06.08.85 - 13.08.85	0.78	0.21
13.08.85 - 20.08.85	0.93	0.25
20.08.85 - 27.08.85	0.94	0.26
27.08.85 - 31.08.85	0.78	0.21
31.08.85 - 03.09.85	0.71	0.19
03.09.85 - 08.09.85	0.71	0.19
08.09.85 - 10.09.85	0.65	0.18
10.09.85 - 16.09.85	0.62	0.17
16.09.85 - 21.09.85	0.75	0.21
21.09.85 - 23.09.85	0.81	0.22
23.09.85 - 25.09.85	0.88	0.24
25.09.85 - 29.09.85	1.10	0.30

The magnitude range for calculations was –1.0 to 2.0, the sample size was 50 and the sample increment was 10.

Table 3.4: Temporal variation in b–value.

3.4.4.3 Variation in b–Values

Using part of the DUEDROPS–HYPOPLOT program package (section 3.3.4), b–values were calculated from the frequency–magnitude distributions (figures 3.17 and 3.18) of events in each of the areas of activity.

For the complete data set a b–value of 0.77±0.10 was obtained. The magnitudes of the 'daily' and 'yearly' events are approximately –0.4 and 3.2 respectively, if it is to be assumed that the seismic rate measured by the experiment is typical for this area. This b–value for the entire dataset is not significantly different from the value of 0.84±0.29 derived by Ward et al. (1969) for the Krafla area using P–wave amplitudes (section 2.2.3).

Figure 3.20 shows the spatial variation in b–value over the main active zones in the Krafla area. The b–value for the Leirhnjúkur events (b = 0.95±0.23) is not significantly different from those of the Bjarnarflag events (b = 0.62±0.14) or the events occurring in the fissure zone (b = 1.25±0.30). However, the b–value for the Bjarnarflag events is significantly lower than the b–value for the adjacent fissure zone events. Therefore if it is assumed that b–value and stress are related, it may be said that the source volume beneath the geothermal area of Bjarnarflag is in a relatively high state of stress compared with that in the central zone of activity.

The temporal variation in b–value for the complete data set is shown in figure 3.21 and table 3.4. No statistically significant variations are observed other than a very slight increase between the first and last calculated values.

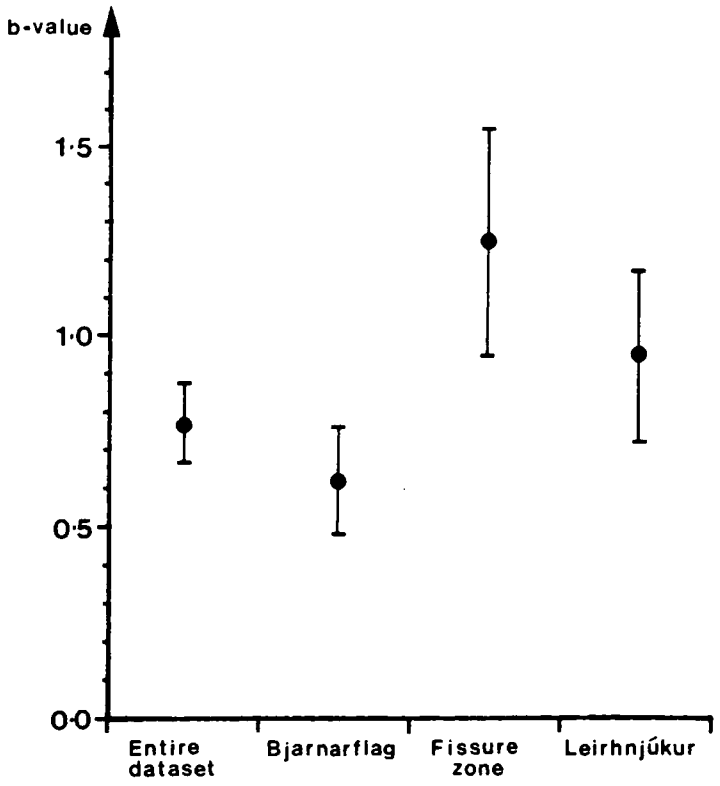

Figure 3.20 : The spatial variation in b-value over the Krafla area. Vertical bars indicate the standard error of each b-value.

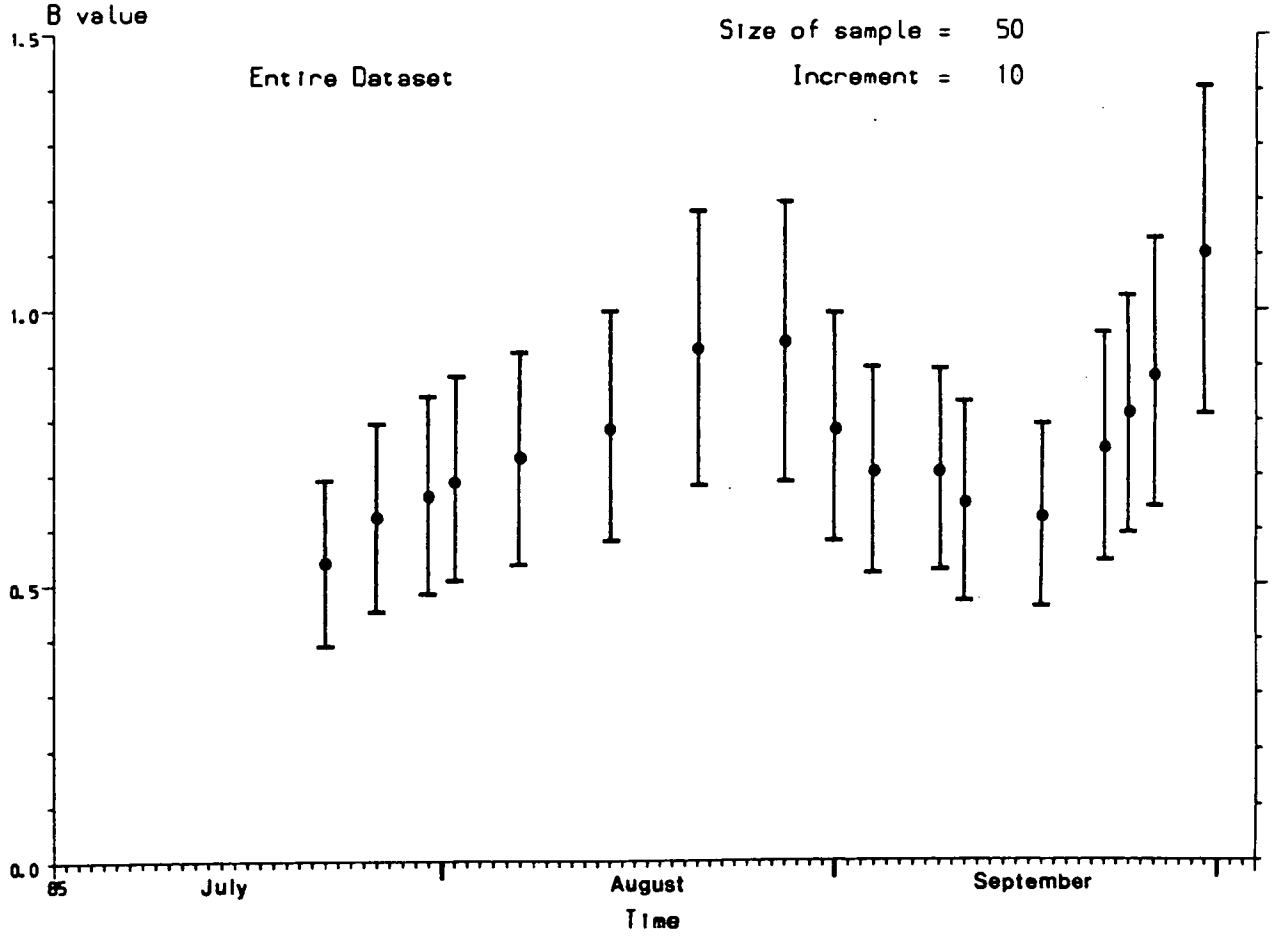

Figure 3.21 : The temporal variation in b-value for the entire dataset. The magnitude range for calculations was -1.0 to 2.0. The sample size was 50 and the sample increment was 10. Vertical bars indicate the standard error of each b-value.

3.5 Summary

The program HYPOINVERSE (Klein, 1978) was used with a 1-d velocity model, based on seismic refraction data, to calculate the locations and origin times of local earthquakes recorded by the NISE-85 experiment. The graphics package DUEDROPS–HYPOPLOT was used for the effective presentation of the best located of these events. Most of the activity is concentrated in three distinct areas.

One dense cluster lies at a depth of about 2–4 km beneath Bjarnarflag, in the Námafjall geothermal field. It has a maximum width of about 0.6 km parallel to the fissure swarm and 0.4 km in a perpendicular direction. To the north the cluster terminates sharply on a steep southward dipping plane. A second area of activity lies immediately to the north of Bjarnarflag, between 1.8–3.8 km depth. This 'fissure zone' consists of a diffuse sub–vertical elliptical plane which plunges to the north–northeast, parallel to the surface fissure trend. The plane appears to be 0.3–0.4 km in thickness, perpendicular to this plunge direction. The third main area of activity appears as a cluster between 1.5–3.5 km depth which is centred beneath the hyaloclastite hill Leirhnjúkur, covering a broad area currently under exploitation for geothermal power. Activity is concentrated on a northward dipping plane.

Local Icelandic duration magnitude values M_{IL} were calculated for events detected by the radio–telemetered network, by comparing them with the same events recorded by an established magnitude–calibrated drum seismograph (RI) nearby. Activity during the recording period was characterized by its relatively continuous nature. There is little evidence of swarm activity. Events of magnitudes –2.4 to 2.1 were located, although the location threshold was found to be about –1.0 in the south and about –0.7 in the north, where station density was lower. Events of magnitude $M_{IL} > 0.7$ were restricted to the Bjarnarflag and Leirhnjúkur clusters. The b–value for events originating beneath the geothermal area of Bjarnarflag is significantly lower than that for events in the adjacent fissure zone. This indicates that, if b–value is related to rock stress, the source volume is in a relatively high state of stress compared with that in the central zone of activity. Statistically significant temporal variations in b–value are very small.

Chapter IV

Simultaneous Tomographic Inversion

4.1 Introduction

Three–dimensional seismic imaging (tomographic) techniques have been used extensively in recent years to tackle some of the most fundamental problems in earth sciences. Global surface–wave inversions have given some insight into the nature of hotspots and the structure beneath mid–ocean ridges (e.g. Dziewonski and Anderson, 1984), and body waves have been used to produce coarse images of lower–mantle structure (e.g. Sengupta et al., 1981). Teleseismic tomography has been used to image lithospheric structure (e.g. Aki et al., 1977; Mitchell et al., 1977) and areas of lithospheric subduction (e.g. Hirahara and Mikumo, 1980; Humphreys et al., 1984). The teleseismic method has been particularly successful at outlining low velocity zones beneath volcanic systems, which are generally interpreted as magma chambers or zones of partial melt within the crust or upper mantle (e.g. Ellsworth and Koyanagi, 1977; Reasenberg et al., 1980; Sharp et al., 1980; Robinson and Iyer, 1981; Oppenheimer and Herkenhoff, 1981; Stauber et al., 1988). See Iyer (1984) for a review. However, because of the low frequency content, these travel–time data are only sufficient to resolve very large crustal structures.

The higher frequency content of local earthquake and explosive phases allows the illumination of smaller scale lateral variations in upper–crustal structure. Volcanic and geothermal complexes have been most frequently targeted by this technique because of the expectation that extreme lateral structural inhomogeneities will be associated with them. Low velocity zones have been interpreted as magma chambers or zones of partial melt when they occur beneath active volcanoes (e.g. Thurber, 1984; M^{c}Nutt and Jacob, 1986; Evans and Zucca, 1988; Achauer et al., 1988; Burnett et al., 1989; Foulger and Toomey, 1989), or have been associated with fractured geothermal reservoirs (e.g. Benz and Smith, 1984; Eberhart–Phillips, 1986; Toomey et al., 1988) or with volumes of tephra and sedimentary fill (e.g. Eberhart–Phillips, 1986; Evans and Zucca, 1988). High velocity zones are commonly linked with (high

density) igneous intrusives (e.g. Achauer et al., 1988; Foulger and Toomey, 1989; Lees and Crosson, 1990).

4.2 Simultaneous Inversion

4.2.1 Introduction

The primary aims of seismologists who study local earthquake data are often those of hypocentral location and focal mechanism determination. In order to locate earthquakes it is necessary to assume some simplified velocity model and then to calculate the travel times of seismic waves propagating between the source and the receivers. The earthquake hypocentre is then estimated by minimizing the difference between the observed and calculated travel times (section 3.3.1) and seismic wave take–off angles are used to plot focal mechanism solutions. However, in areas of significant lateral variation in crustal structure, neither earthquake hypocentres nor focal mechanisms can be determined accurately without more detailed knowledge of the three–dimensional seismic velocity field. The coupled problem of simultaneously locating local earthquakes whilst inverting for three–dimensional velocity structure can be conveniently addressed using the simultaneous inversion method.

4.2.2 The Simultaneous Inversion Algorithm

Several algorithms have been developed in the last 15 years to solve the over–determined simultaneous inversion problem. The principal difference between them has been variation in representation of the Earth's velocity structure, e.g. constant velocity layers (Crosson, 1976), constant velocity blocks (Aki and Lee, 1976), analytical functions defined by a small number of parameters (Spencer and Gubbins, 1980), arbitrarily shaped averaging volumes (Chou and Booker, 1979), continuous functions with *a priori* probability density distributions (Tarantola and Nercessian, 1984), and three–dimensional interpolation between nodes of specified values (Thurber, 1983, 1985). The method of parameterization should be general enough so that no assumption is made *a priori* about the geometry of velocity heterogeneity (such as constant velocity layers). It is also desirable with local earthquake data to have a method for selecting parameters which allows smooth tracing of seismic rays laterally through a model, without encountering sharp boundaries

such as block edges. The interpolative method of Thurber (1983, 1985) satisfies these requirements and is probably one of the better methods suited to imaging small scale lateral inhomogeneities in the shallow crust from local earthquake data.

Given a set of arrival times from an earthquake, an estimate of the hypocentral location and a starting velocity model, each travel–time reduction r can be related to model parameter changes : –

$$r = \Delta t_e + \frac{\partial t}{\partial x_e}\Delta x_e + \frac{\partial t}{\partial y_e}\Delta y_e + \frac{\partial t}{\partial z_e}\Delta z_e + \sum_{n=1}^{N} \frac{\partial t}{\partial v_n}\Delta v_n \qquad 4.1$$

where Δt_e, Δx_e, Δy_e, Δz_e and Δv_n are perturbations to the hypocentral parameters (earthquake origin time and location) and velocity parameters respectively. $\frac{\partial t}{\partial x_e}$, $\frac{\partial t}{\partial y_e}$, $\frac{\partial t}{\partial z_e}$ and $\frac{\partial t}{\partial v_n}$ are partial derivatives of arrival time with respect to these parameters. N is the number of velocity parameters.

Thurber (1983, 1985) adopted an iterative approach to the over–determined simultaneous inversion problem. A flow diagram for his program SIMUL3 is shown in figure 4.1. It has has three principal features : –

- Velocity Model Parameterization
- Approximate Ray Tracing
- Parameter Separation

The velocity at a given point (x, y, z) is interpolated from the eight surrounding nodal values in a 3-d cartesian grid by distance weighting. This results in a realistic and continuous velocity structure. The travel–times for equations 4.1 are calculated using an approximate ray–tracing method (Thurber and Ellsworth, 1980), which is carried out in three dimensions (figure 4.2). The travel time along each of a large number of smooth curves connecting the source and receiver are calculated and the fastest curve adopted as the best estimate of the true ray path. This travel–time estimate agrees well with that calculated by rigorous three–dimensional ray tracing for paths which are shorter than 50 km (Smith, 1987d), so that this method provides a good, computationally inexpensive, alternative.

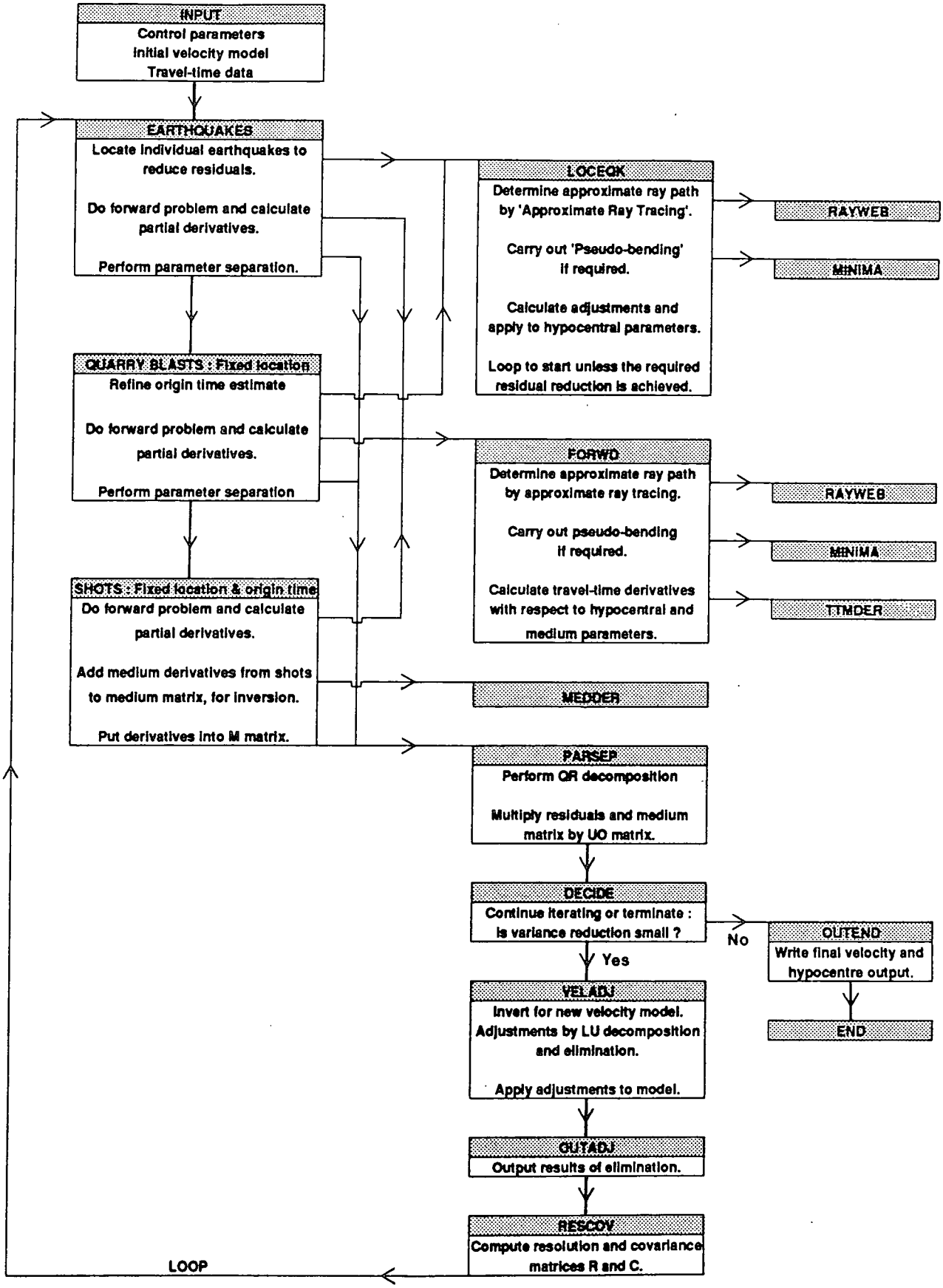

Figure 4.1 : Structure and flow diagram for the simultaneous tomographic inversion program SIMUL3.

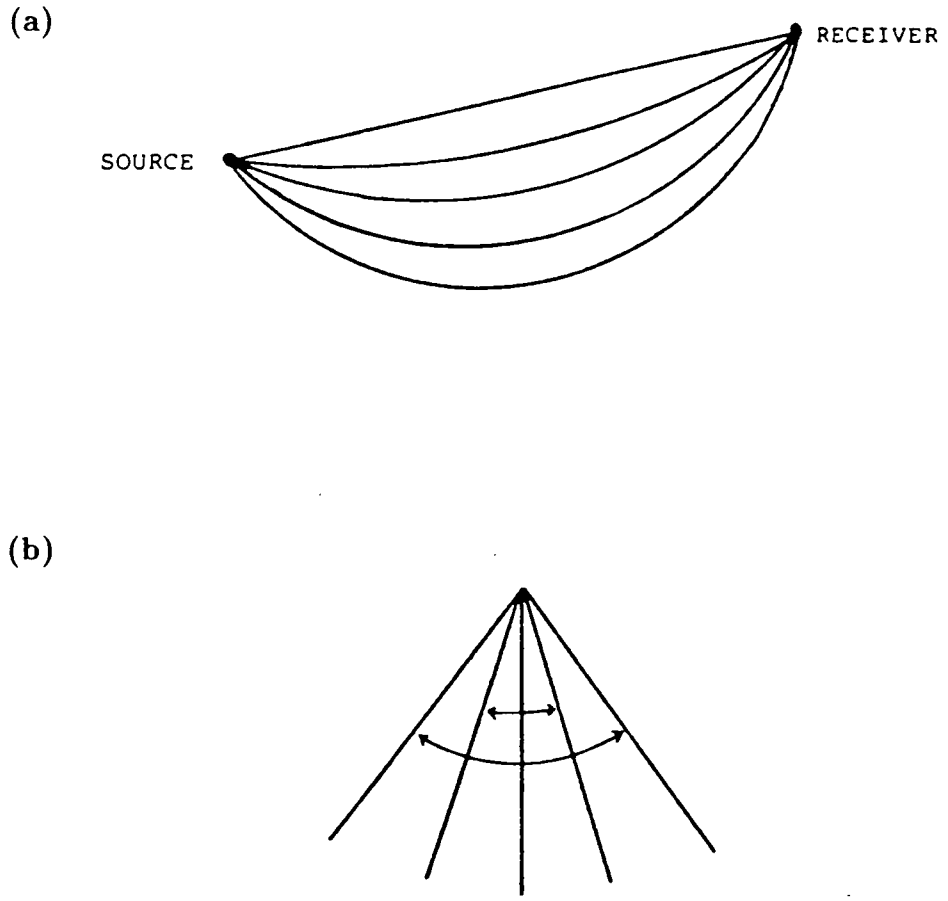

Figure 4.2 : The approximate ray tracing scheme. **(a)** Circular paths of varying radii of curvature are constructed. **(b)** The plane containing the paths is systematically rotated about the source–receiver axis. The path with the shortest travel-time is adopted as the best estimate of the true ray path (from Thurber, 1983).

The coupled inverse problem can be expressed in matrix notation and split into two separate inverse problems (Palvis and Booker, 1980) : -

$$\mathbf{r}_i = \mathbf{H}_i \Delta \mathbf{h}_i + \mathbf{M}_i \Delta \mathbf{m} \qquad 4.2$$

where $\mathbf{H}_i$ and $\mathbf{M}_i$ are matrices of hypocentral and velocity partial derivatives for the ith event, $\mathbf{r}_i$ and $\Delta \mathbf{h}_i$ are vectors containing the L residuals and four unknown hypocentral parameter adjustments, and $\Delta \mathbf{m}$ is the vector of the N velocity parameter adjustments. It should be noted that these travel-time residuals include all errors in the timing of arrivals, which are assumed to be random and independent and therefore eliminated by subsequent application of the least-squares method.

It can be shown (Marquardt, 1963) that the best least-squares solution to the system of linear equations involving travel-time residuals, velocity partial derivatives and velocity parameter adjustments satisfies the normal equations : -

$$(\mathbf{M}'^T \mathbf{M}' + \Theta) \Delta \mathbf{m} = \mathbf{M}'^T \mathbf{r}' \qquad 4.3$$

where the diagonal damping matrix Θ is introduced to suppress strong fluctuations in the solution due to small random errors (e.g. Aki and Lee, 1976).* Then by considering the submatrices $\mathbf{r}'_i$ and $\mathbf{M}'_i$ $(i = 1, ...N_{eq})$, where N_{eq} is the total number of earthquakes, it is possible to accumulate the matrix $\mathbf{M}'^T \mathbf{M}'$ and the vector $\mathbf{M}'^T \mathbf{r}'$ of equation (4.3) sequentially as each event is processed. This circumvents the problem of requiring excessive amounts of computer memory (Thurber, 1983). The solution to the normal equations (4.3) is then found by inverting the symmetrical matrix $\mathbf{M}'^T \mathbf{M}'$, e,g. Aki and Lee (1976), and the best least-squares estimate $\Delta \widetilde{\mathbf{m}}$ of the velocity parameter adjustments $\Delta \mathbf{m}$ is given by : -

$$\Delta \widetilde{\mathbf{m}} = (\mathbf{M}'^T \mathbf{M}' + \Theta)^{-1} \mathbf{M}'^T \mathbf{r}' \qquad 4.4$$

These velocity parameter changes are then applied to the starting model and the earthquakes are each relocated iteratively in the new model. The simultaneous inversion is repeated until the reduction in the travel-time residuals is small, as determined by an F test (DeGroot, 1975) on the variance reduction.

* $\mathbf{r}$ and $\mathbf{M}$ have been transformed into $\mathbf{r}'$ and $\mathbf{M}'$ by the operation of a matrix $\mathbf{Q}_0^T$, which is constructed such that $\mathbf{Q}_0^T \mathbf{H}_i = 0$, on equation 4.2 (see Thurber (1983) for details).

The resolution matrix $\mathbf{R}$ (Backus and Gilbert, 1968) for the inverse solution (equation 4.4) is : -

$$\mathbf{R} = (\mathbf{M'}^T\mathbf{M'} + \Theta)^{-1}\mathbf{M'}^T\mathbf{M'} \qquad 4.5$$

Resolution becomes poorer as $\mathbf{R}$ deviates from the identity matrix $\mathbf{I}$.

The covariance matrix of errors in the model (e.g. Aki and Lee, 1976; Kissling, 1988) is then : -

$$\mathbf{C} = \sigma^2(\mathbf{M'}^T\mathbf{M'} + \Theta)^{-1}\mathbf{R} \qquad 4.6$$

where σ^2 is the variance (or standard deviation) of the travel-time data, which is estimated as the sum of the squared residuals divided by the number of degrees of freedom (Aki and Lee, 1976) : -

$$\sigma^2 = \frac{|\mathbf{r'} - \mathbf{M'}\Delta\widetilde{\mathbf{m}}|^2}{(L.N_{eq} - 4.N_{eq} - N)} \qquad 4.7$$

The diagonal elements of $\mathbf{R}$ and $\mathbf{C}$ are normally cited as the resolution and covariance values of the velocity parameters, since off-diagonal elements are usually small (Wiggins, 1972). However, the off-diagonal elements can be important indicators of the influence on these parameter values by other nodes in the model. Thus, a velocity perturbation at node i will influence the perturbation at node j if R_{ij} is significantly non-zero, and the error in the perturbation will cause an error at node j if C_{ij} is significantly non-zero.

The standard error D_j of the jth model parameter is estimated by : -

$$D_j = \sqrt{C_{jj}} \qquad 4.8$$

where C_{jj} is the diagonal element of the covariance matrix $\mathbf{C}$ corresponding to the jth model parameter.

4.2.3 Software

The simultaneous inversion algorithm SIMUL3 was used in this study (Thurber, 1985). It was implemented at the University of Durham as part of the Durham University Earthquake Data Reduction and Processing System (DUEDROPS-TOMOGRAPHY), (Smith, 1987d,f), with a number of improvements designed

to increase its user–friendliness and compatability with other DUEDROPS software. DUEDROPS-TOMOGRAPHY also contains a program called TOMPLOT which produces contour plots of the velocity field output from SIMUL3DUR (the Durham version of SIMUL3) on a horizontal or vertical plane. Another program, MAPPLOT, allows tomographic output to be superimposed on top of maps or sections produced by HYPOPLOT (section 3.3.4).

4.3 Model Development

4.3.1 Event Selection

Input for the simultaneous inversion was selected from the best located earthquakes. Events were chosen according to their accuracy of location by HYPOINVERSE (section 3.3.5) and to the number of recorded arrivals. The following criteria were used in the selection process : –

- RMS $\leq$ 0.08 sec
- ERH $\leq$ 1.0 km
- ERZ $\leq$ 1.0 km
- GAP $\leq 180°$
- Minimum number of arrivals from event : Bjarnarflag cluster (15), Fissure Zone and Leirhnjúkur cluster (10), and in areas of sparse seismicity (9).

Using these selection criteria, 105 local earthquakes were chosen for the inversion. Six timed local explosion were also included, giving a total of 1771 P–wave arrival times in the dataset. The initial earthquake hypocentral parameters used were those output by HYPOINVERSE using a one–dimensional velocity model. The origin times and locations of explosions were held fixed throughout the inversion process. The minimum number of arrivals for events included in the inversion was varied according to epicentral location, in order to include events from zones of sparse activity and thereby achieve a better distribution of hypocentres.

4.3.2 Velocity Model Parameterization

4.3.2.1 Parameter Values

An initial nodal distribution for velocity parameters of 2 km spacing horizontally and 1 km vertically was chosen on the basis of the scale of surface geological features (figure 2.1). It was using this configuration that tests were carried out to determine the best starting velocity model and the best damping value.

The obvious initial model to be input to the inversion process was the one that was used for hypocentral location (section 3.3.2). This velocity profile needed to be reformulated slightly in order to satisfy the input format requirements of the program. The velocity field output from this first test inversion showed significant increases in average velocity for each layer, and so these averages were input as the model for a further inversion. As this process was repeated, the average layer velocities approached constant values (figure 4.3a) and the reduction in travel-time residuals improved (figure 4.3b). The final average one-dimensional model is hereafter called the 'evolved 1-d' model.

Figure 4.4 shows a comparison between the initial one-dimensional model and the 'evolved 1-d' velocity model. The higher average velocities resulting from these initial inversions may have been a result of using unrealistically low velocities as input. All but two of the explosions used in developing that model were detonated on the flanks of Krafla central volcano and fissure swarm, which were the subjects of the inversion (figure 3.1). Indeed, Zverev et al. (1980) found by refraction and reflection profiling that crustal velocities reached peak values beneath the axis of the Krafla fissure swarm (figure 1.4), and Palmason (1971) and Flovenz (1980) suggested that there is an increase in crustal velocity in the region of central volcanoes. A similar overall increase in local velocity was observed by Toomey and Foulger (1989) for a simultaneous inversion carried out on data from the Hengill-Grensdalur central volcano complex in Southwest Iceland. The 'evolved 1-d' velocity model for the Krafla data was used as a starting model in all subsequent tomographic inversions, so that areas of relatively high and low velocities could be outlined.

Figure 4.5 shows the effect on the variance reduction of using different damping values in the inversion. The maximum variance reduction was achieved with a damping value of 0.2 sec^2, which was used for all subsequent inversions. However, no major difference in the inversion solution was observed by using the different damping values, indicating that the solution was generally stable.

4.3.2.2 Parameter Distribution

Toomey and Foulger (1989) deal in some depth with the problem of velocity model parameterization for the Hengill-Grensdalur local earthquake dataset. They ob-

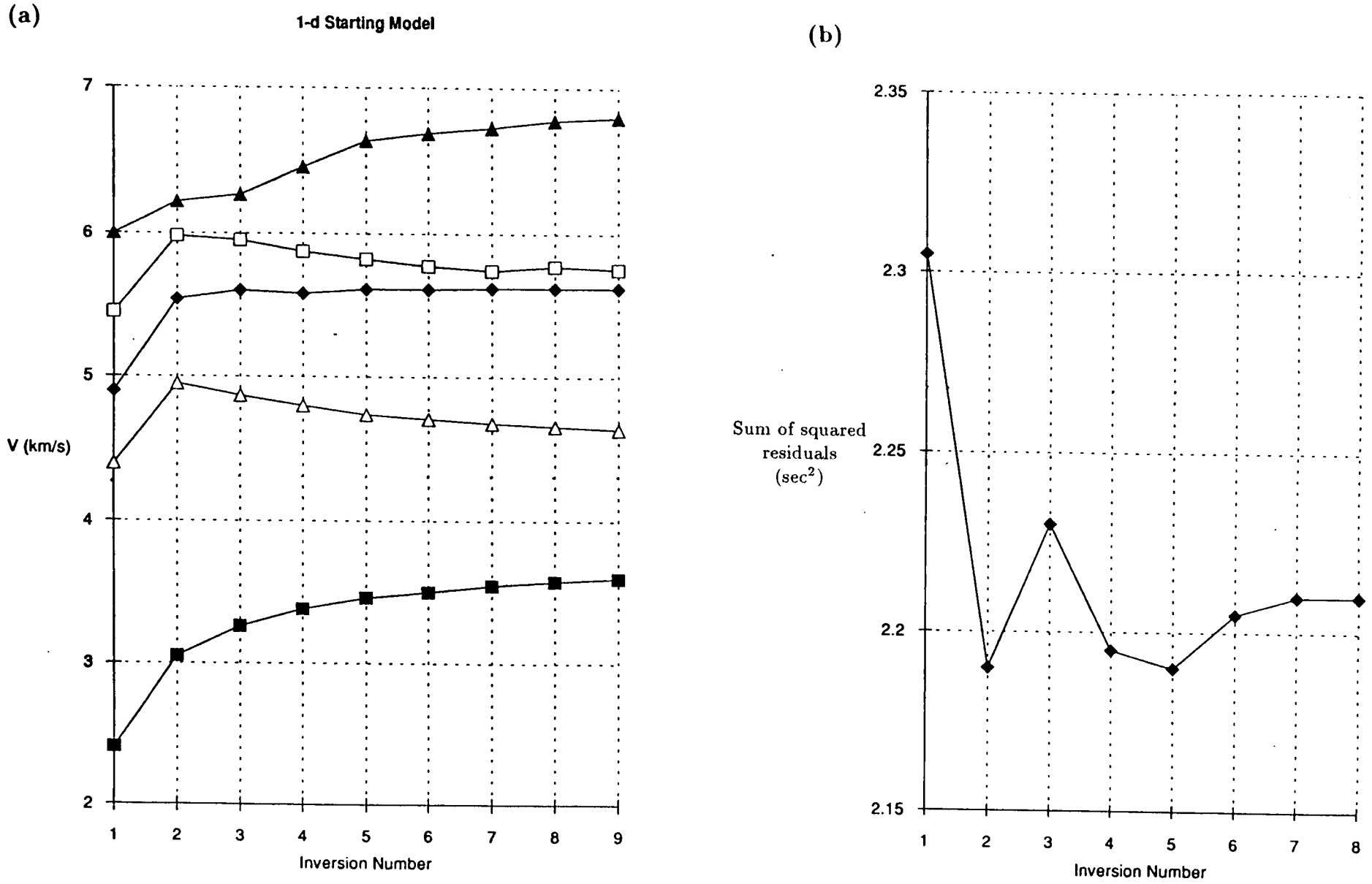

Figure 4.3 : Development of a one-dimensional velocity model for input to SIMUL3. **(a)** The evolution of the average value for each layer of velocity nodes at depths of 0, 1, 2, 3, and 4 km as inversion was repeated. After each inversion, an average was calculated for each layer of nodes. These values were then used as the input 1-d model for the next test inversion. **(b)** The variation in the sum of the squared residuals output by test inversions using velocity models given in (a).

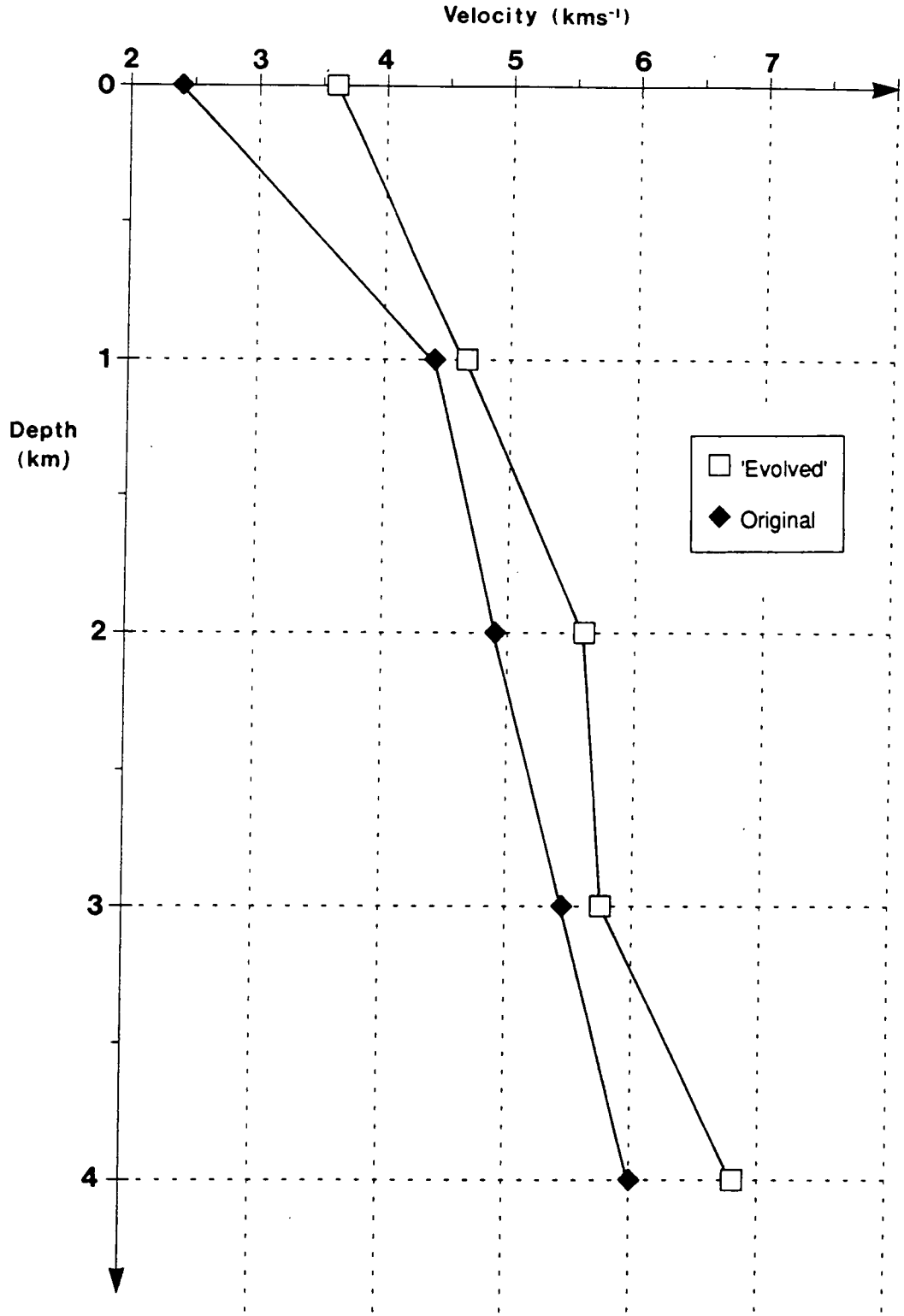

Figure 4.4 : A comparison between the original one–dimensional velocity model used for hypocentral location by HYPOINVERSE, and the 'evolved 1–d' model input to the final simultaneous inversion.

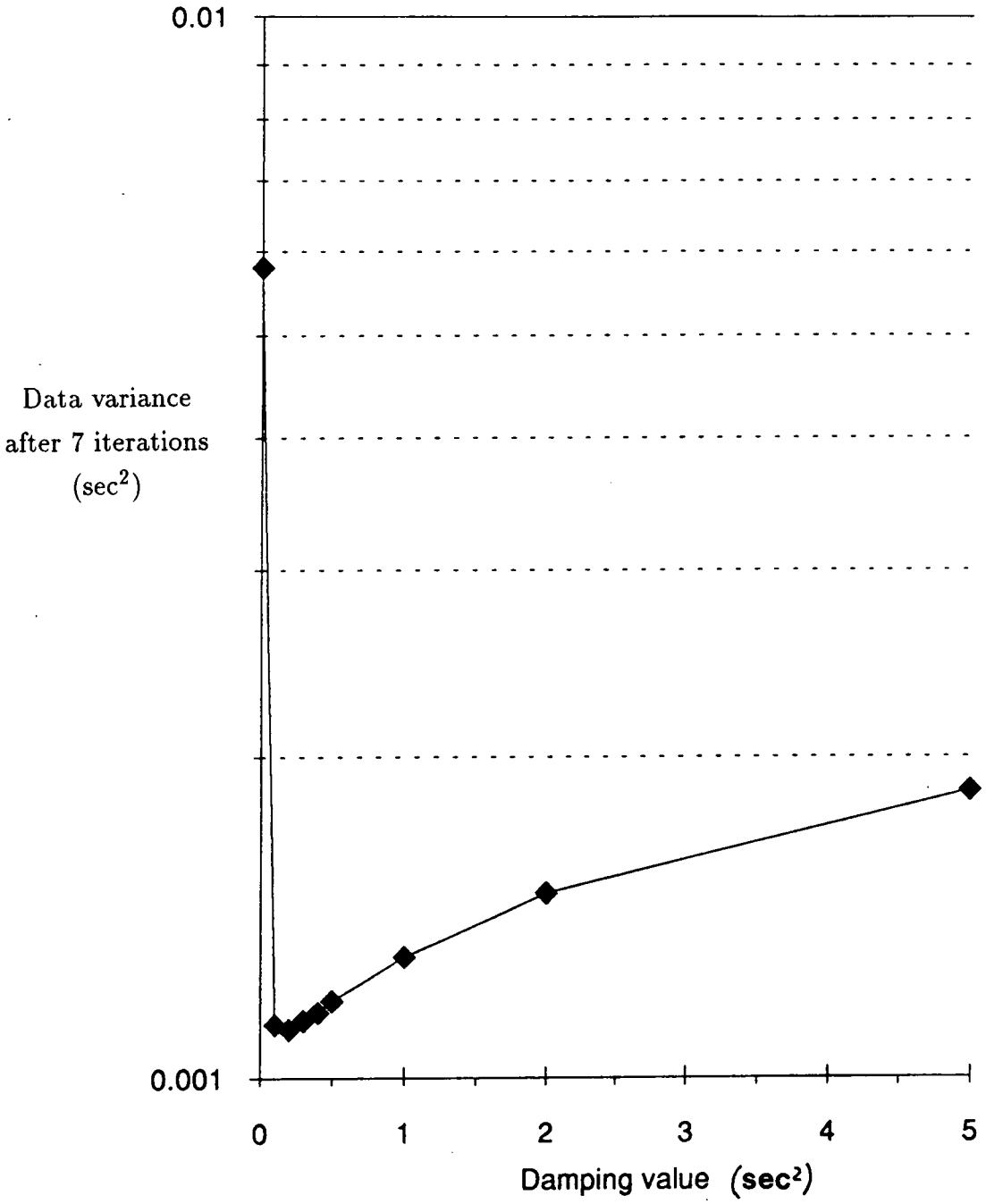

Figure 4.5 : Data variance after 7 iterations, using different values of the damping parameter.

serve that an increase in the density of velocity parameters simultaneously leads to improved image fidelity but a decrease in individual parameter resolution (as measured by the diagonal of the resolution matrix). They also report that a change in the density of parameterization can give significantly different results. In general they find that, for damped least squares inversion, good parameterization maximizes the density of velocity nodes and minimizes the number of poorly sampled nodes, and proposed that good model fidelity is more important than the resolution of an individual parameter. This emphasis on image fidelity differs from that in many other studies (e.g. Aki and Lee, 1976; Thurber, 1983), where little reasoning is given for the choice of model parameterization and the emphasis is placed instead on estimating parameter resolution.

In addition to the initial horizontal and vertical parameter distribution of 2 km and 1 km respectively, two coarser configurations were tested with horizontal separations of 3 km and 4 km, and each with a vertical separation of 2 km. Parameterization in a finer grid (e.g. 1 km horizontally) was not possible since this would have required machine dependent storage allocation limits for arrays and common blocks to have been exceeded (Smith, 1987d). Figures 4.6–4.8 show contour plots of velocity difference from the starting model for the three different parameter densities. Alongside each is shown the diagonal member of the resolution matrix and the number of rays passing close to a node ('hits', from the observation matrix). It should be noted that the crosses representing nodes on the velocity maps are not mapped correct, due to a bug in the plotting routine, but should be reversed in the x–direction.

Although the results are generally similar in their distribution of areas of relatively high and low velocities, significant variations in the exact location, shape and size of the anomalies is evident (figures 4.6–4.8). For example, the two coarse velocity parameterizations have given rise to much broader areas of anomalous velocity than the original dense configuration, which displays a greater number of discrete anomalous zones. This is particularly clear to the south, where the plots for the two coarser models show broad areas of high and low velocities, whereas the denser gridded model features alternating zones high and low velocity.

These differences may be attributed to a combination of sources. The location of

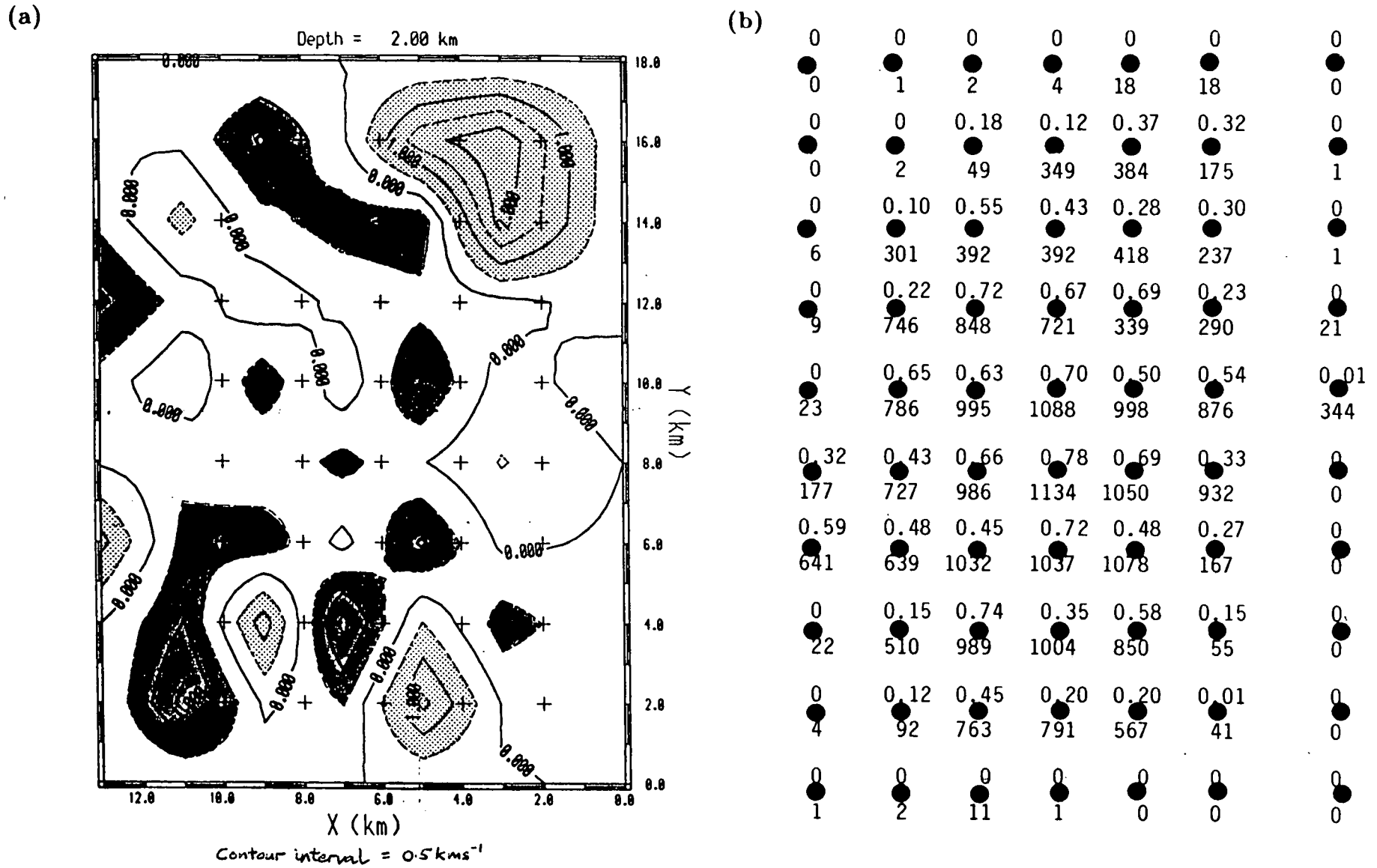

Figure 4.6 : (a) Contoured plot on a plane at 2 km depth of the change in velocity from the 'evolved 1-d' model, using a velocity node spacing of 2 km horizontally and 1 km vertically (the 'dense' model). **(b)** The diagonal member of the resolution matrix (top), and the number of rays passing close to the node (bottom) for each velocity node.

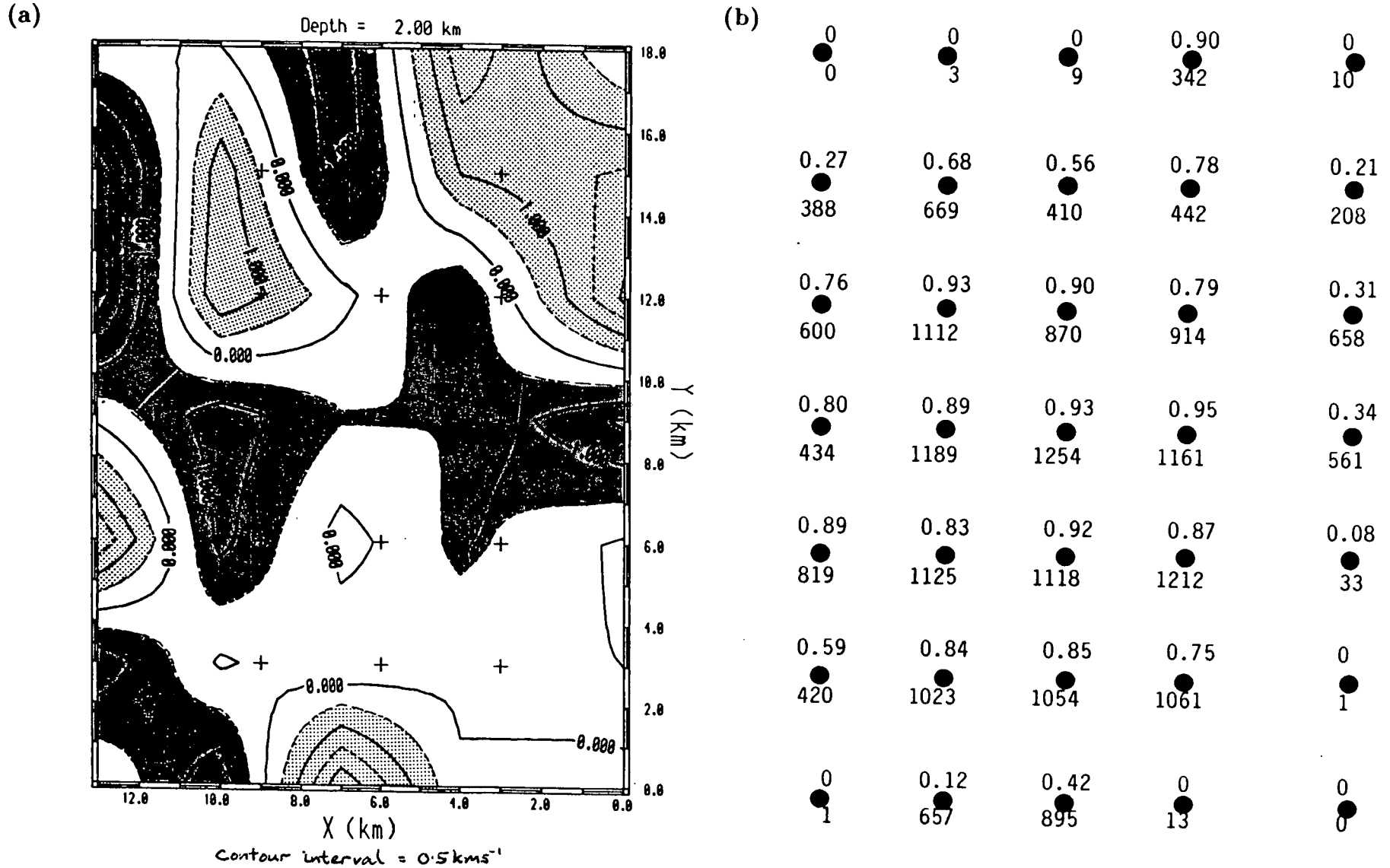

Figure 4.7 : (a) Contoured plot on a plane at 2 km depth of the change in velocity from the 'evolved 1–d' model, using a velocity node spacing of 3 km horizontally and 2 km vertically (the 'coarser' model). **(b)** The diagonal member of the resolution matrix (top), and the number of rays passing close to the node (bottom) for each velocity node.

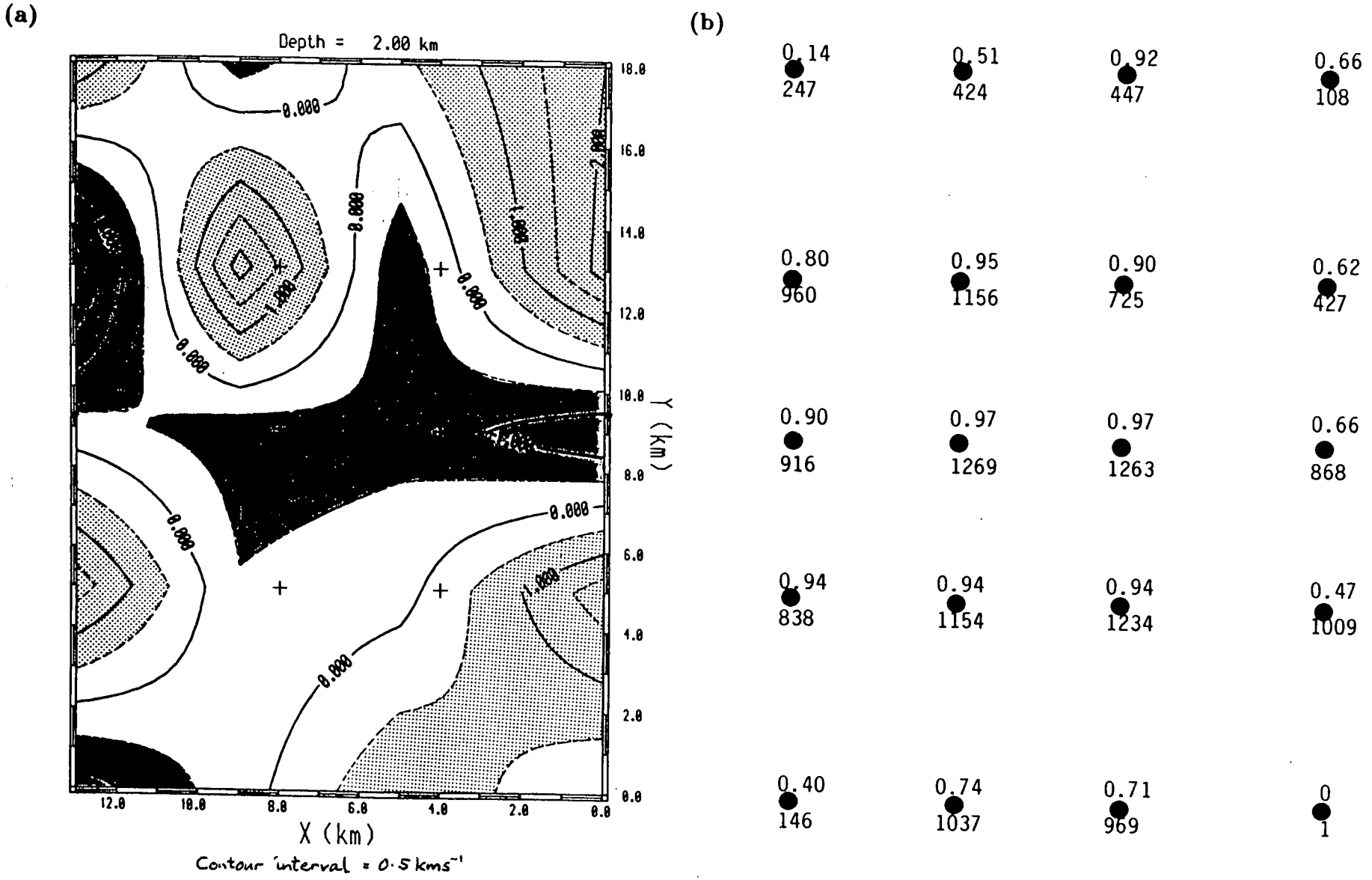

Figure 4.8 : **(a)** Contoured plot on a plane at 2 km depth of the change in velocity from the 'evolved 1-d' model, using a velocity node spacing of 4 km spacing horizontally and 2 km vertically (the 'coarsest' model). **(b)** The diagonal member of the resolution matrix (top), and the number of rays passing close to the node (bottom) for each velocity node.

the grid nodes seems to affect the central location of the anomalies. For example, the high velocity area which is centred on $(x = 10, y = 12, z = 2)$ in figure 4.7a is centred on (9,13,2) in figure 4.8a; in each case the centre is close to the nearest node. Also, where fewer nodes exist, a greater degree of spatial interpolation is required of the contouring program which results in broader and smoother anomalous zones. However, the most important source of variation between the models is likely to be the difference in the volume over which the velocity has been averaged by the inversion process. The reduction in the number of 'hits' towards the edge of each model appears to become more extreme as the parameter density increases. This is a good indication of the difference in the degree to which ray information is averaged in the three models. It also shows up the inadequacy of the 'hit' matrix, which gives no information about the spatial separation between seismic rays and velocity parameters.

4.3.3 Resolution

The two most important problems which now present themselves are (a) which velocity parameterization, if any, yields the most acceptable inversion results ? and (b) which parts of the model are imaged to sufficiently high resolution to enable a reliable geological interpretation ?

Figure 4.9 shows how some indicators of inversion quality have been affected by the different model parameterizations. The densest nodal distribution has resulted in a significant reduction in the mean r.m.s. travel-time residual and travel-time variance compared to the coarser models, indicating that it has best modelled the data. The trace of the resolution matrix, which is a good measure of the total amount of information present in a solution (Wiggins, 1972; Toomey and Foulger, 1989), is significantly larger for the densest parameterization than for the others. This further suggests that the densest model yields the solution with the best total image quality (as well as the best fidelity). However, it is possible that parameterization on a finer grid than any of those tested may have resulted in an even better inversion solution, but this could only be attempted using a computer with greater storage capacity than was available for this study (section 4.3.2.2). It is equally possible, however, that such very dense parameterization would result in significant volumes in the interior of the model being inadequately sampled. The

(a)

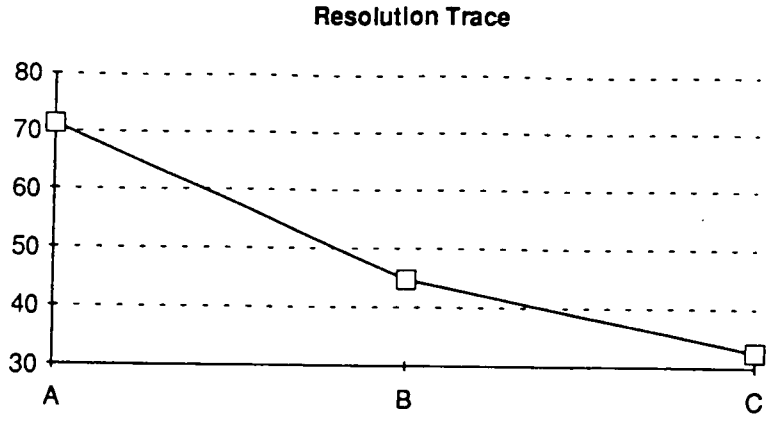

(b)

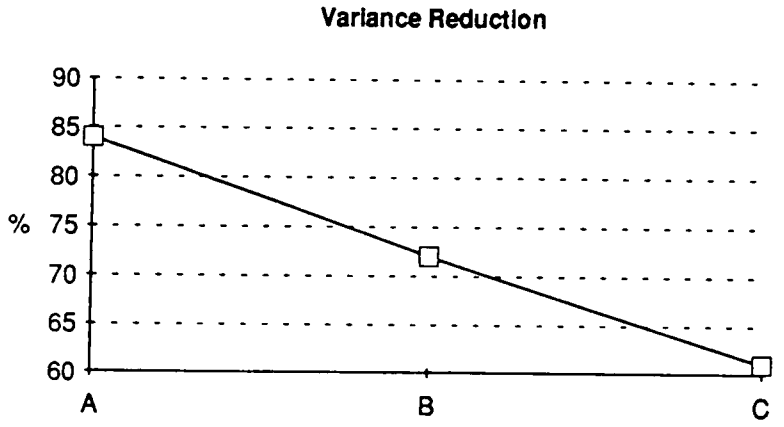

(c)

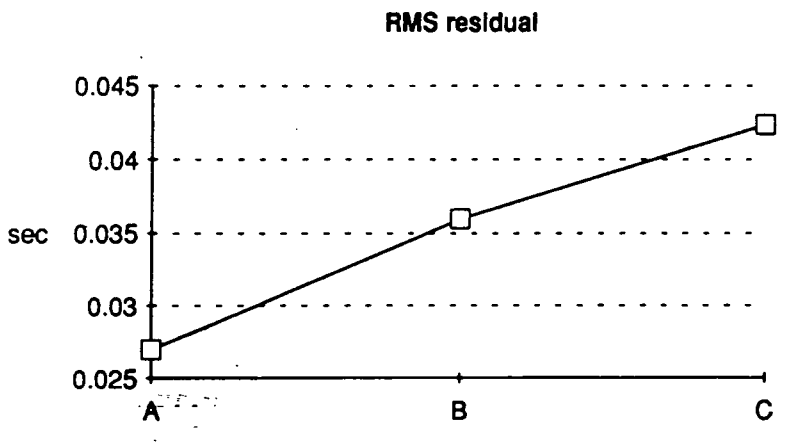

(d)

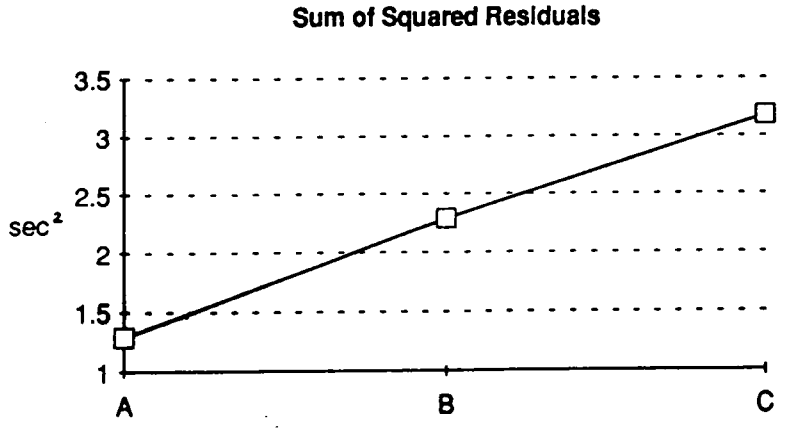

Figure 4.9 : The effect on some indicators of inversion quality of using three different velocity node spacings defined in figures 4.6–4.8. 'A' = the 'dense' model, 'B' = the 'coarser' model, and 'C' = the 'coarsest' model. **(a)** Trace of the resolution matrix, **(b)** variance reduction, **(c)** root mean squared residual, **(d)** sum of the squared residuals. *Note that figures (b), (c), and (d) show essentially the same thing in slightly different forms.*

individual diagonal members of the resolution matrices show the expected decrease in value as parameter density is increased (figures 4.6–4.8). However, this is not as important as the effect of suppressing the image fidelity of excessive volumetric averaging of velocity when too coarse a grid is used (Toomey and Foulger, 1989). Thus the individual diagonal members of the resolution matrix are probably not a good independent measure of the significance of velocity anomalies imaged in the Krafla volcanic system.

Each row of the resolution matrix is an averaging vector for a single model parameter and describes the influence of every other parameter value on its own (e.g. Wiggins, 1972; Menke, 1984). In other words, when the model resolution matrix is not the identity matrix, the estimate of a model parameter is a weighted average of all parameters. Therefore in order to achieve localized averaging of velocity into single parameters, it is important to reduce the influence of other parameter values to an acceptable level.

The spread function (Backus and Gilbert, 1967, 1968) gives a measure of how compact each averaging vector is, or of the 'spread' of the off–diagonal elements of the resolution matrix. It can therefore be useful in determining what scale of features in a model can actually be resolved. Menke (1984) defined it as : –

$$Spread(\mathbf{R}) = \sum_{i=1}^{N} \sum_{j=1}^{N} w(i,j) R_{ij}^2 \qquad 4.9$$

where R_{ij} are elements of the $N \times N$ resolution matrix and $w(i,j)$ is a weighting function defined as the distance between the ith and jth nodes. Therefore a small value of the spread function for a parameter implies that localized averaging of velocity is taking place. The question now becomes : how small is small ?

The calculation of the individual parameter spread functions has not been carried out for this inversion because of the extensive programming complexities involved. Toomey and Foulger (1989) found, by pictorial examination of averaging vectors for the Hengill–Grensdalur system, that a spread value of 2 was an effective upper limit for distinguishing between parameters with compact averaging vectors and those with significant lateral averaging of velocity. Their plot of the spread function for a velocity parameter against its 'derivative weight sum' (DWS) shows quite a

clear relationship (figure 4.10). The DWS provides a useful relative measure of the density of seismic rays near a velocity node. It is a better indicator of ray distribution than the more commonly cited ray observation or 'hit' matrix since it is influenced by the spatial separation of the rays from the velocity node (Toomey and Foulger, 1989). They note that the scatter in the correlation is due to the fact that the averaging vector also depends on the geometry of rays near the grid point.

Since the velocity model parameterizations for the Hengill–Grensdalur volcanic system (Toomey and Foulger, 1989) and for the Krafla volcanic system are very similar, and the DWS is related only to the density of rays near a parameter, it seems reasonable to expect a DWS which approximately corresponds to a spread value of 2 in figure 4.10 to be a fair threshold above which parameters may be considered to be well resolved in the Krafla inversion solution. Velocity nodes with a DWS of 50 or greater are therefore considered to be adequately resolved.

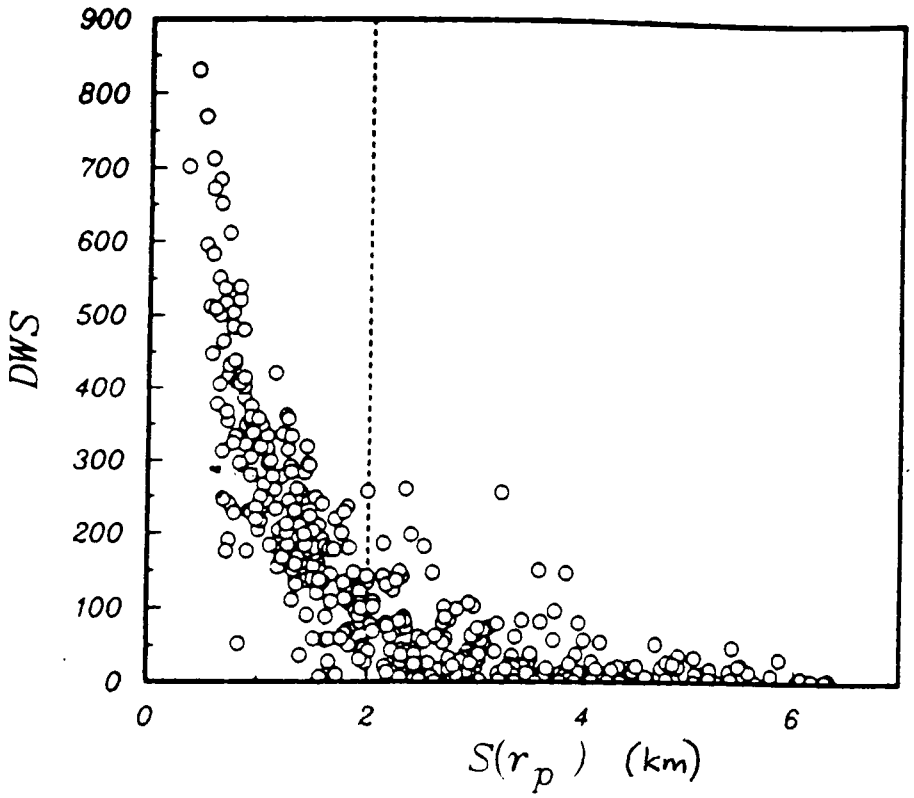

Figure 4.10 : A plot of the derivative weight sum (DWS) versus the spread function of the averaging vector $S(r_p)$ for model parameters used in the inversion of P-wave data from the Hengill-Grensdalur volcanic system in Southwest Iceland. The dashed line at $S(\mathbf{r}_p) = 2$ was considered the upper limit for values of the spread function considered to be acceptable (from Toomey and Foulger, 1989). The DWS provides only a relative measure of ray distribution and its units of distance are unimportant (Toomey and Foulger, 1989).

4.4 Inversion Results

4.4.1 The Final Inversion Solution

The velocity parameter distribution for the final simultaneous inversion had nodes with horizontal separation of 2 km, except for a 3 km spacing at the eastern edge, and with a vertical separation of 1 km from sea level to 4 km depth. This gives a total of 350 nodes sampling a volume of $13 \times 18 \times 4$ km^3 (figure 4.11). The grid was designed to have its y–axis parallel to the axis of the volcanic system, to enclose in a tight envelope all the local telemetered stations (except for NBI, which lay outside the system) and to stop at the (apparent) seismic basement. This volume needed to be surrounded by another layer of nodes displaced from the interior grid by a considerable distance, which acted as bounding nodes. The values of the input velocity parameters were those given by the 'evolved 1-d' model of figure 4.4. A copy of the input control parameters, stations, initial velocity model and event locations are given in appendix B.1. The output event locations, velocity model, observation matrix, DWS matrix, diagonal resolution values and standard errors, as well as statistics for the inversion iterations, are given in appendix B.2.

4.4.2 Presentation of Results

Maps of velocity difference from the starting velocity are shown in figures 4.12a to 4.12e. The limits of good resolution are indicated by the DWS = 50 contour. Vertical cross–sections of velocity are shown in the same way in figures 4.13a to 4.13h.

It is not easy to visualize three–dimensional features by studying a series of two–dimensional maps. Three–dimensional perspective views have therefore been produced using the UNIRAS–GEOPAK mapping package (Uniras, 1985). This package enables the user to produce full colour, high resolution, smooth shaded maps in two and three–dimensions with little computer programming. The Fortran program MOD3D given in appendix C was written by the author to produce three–dimensional plots of P–wave velocity anomalies for the Krafla volcanic system. Nodal velocities output from SIMUL3DUR were interpolated to 0.25 km spacing in three-dimensions (using TOMPLOT, with a slight modification) and converted into blocks. Blocks with a velocity anomaly less than a given threshold (0.65

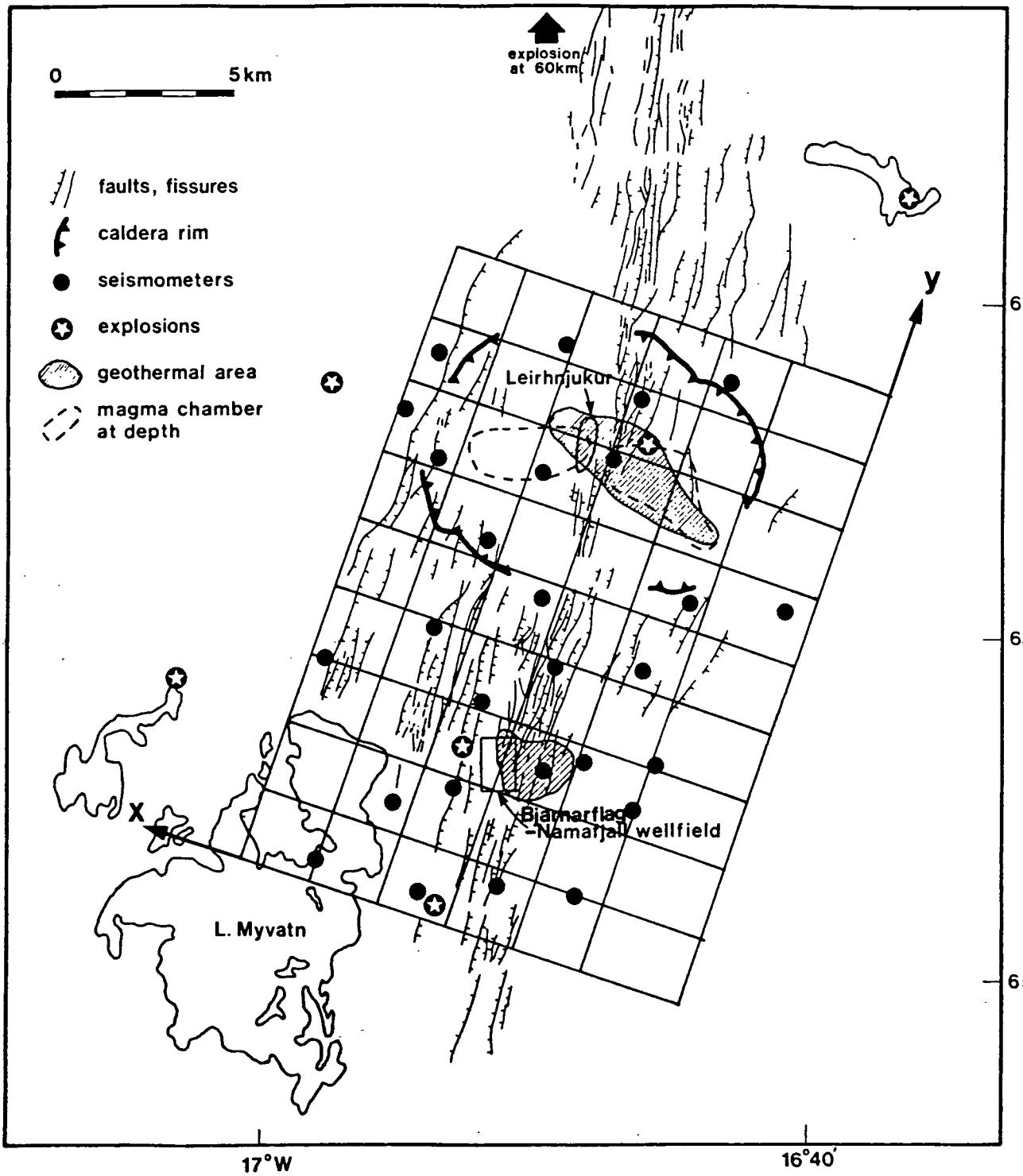

Figure 4.11 : The velocity grid spacing used to produce the final tomography results. Vertical node spacing was 1 km.

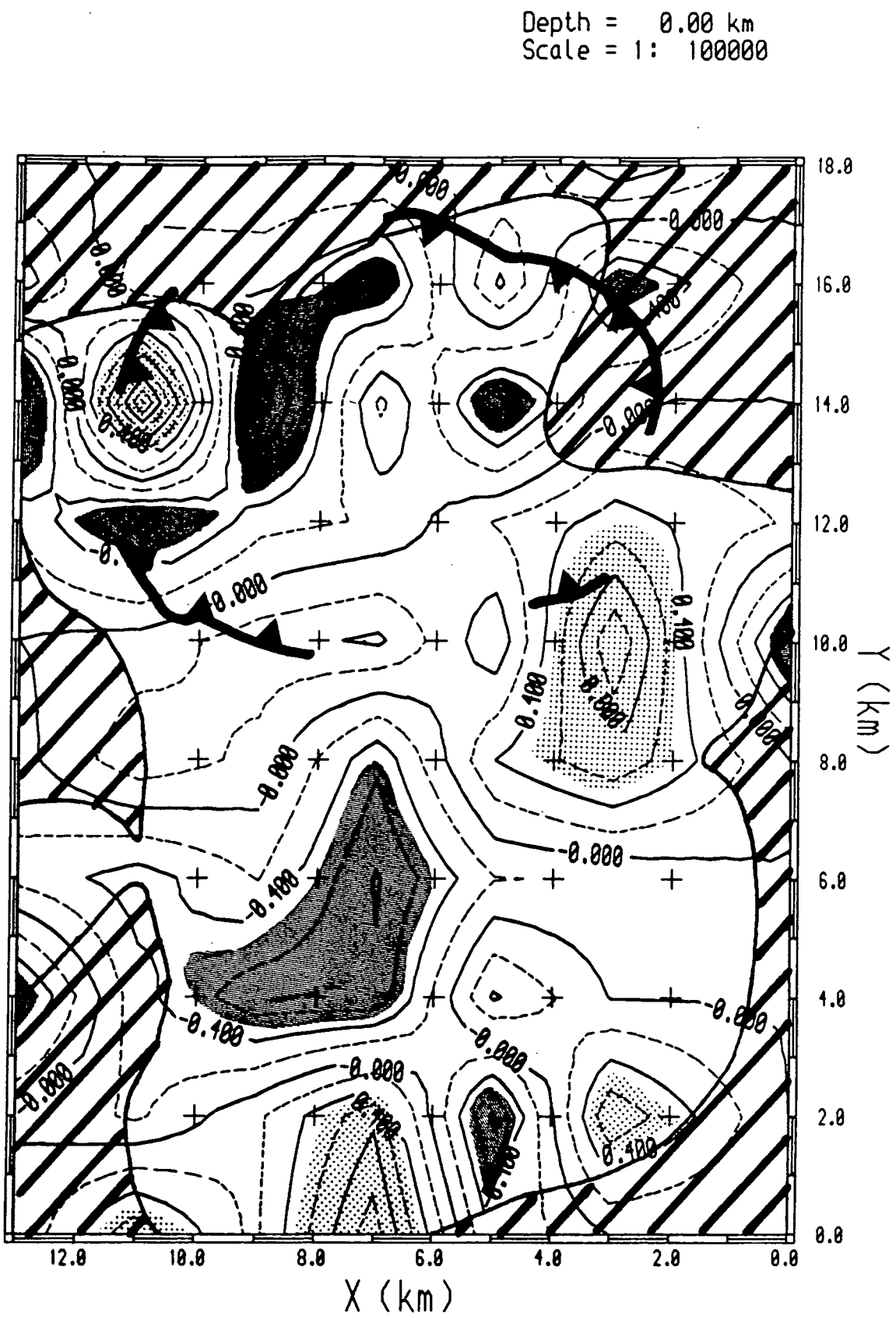

Figure 4.12a : Velocity differences from the 'evolved 1-d' velocity model at a depth of 0 km. The contour interval is 0.2 kms^{-1}. Areas with velocity difference $\geq +0.5$ kms^{-1} are stipled, and areas with velocity difference ≤ -0.5 kms^{-1} are shaded. The poorly resolved areas (DWS ¡ 50) are hatched.

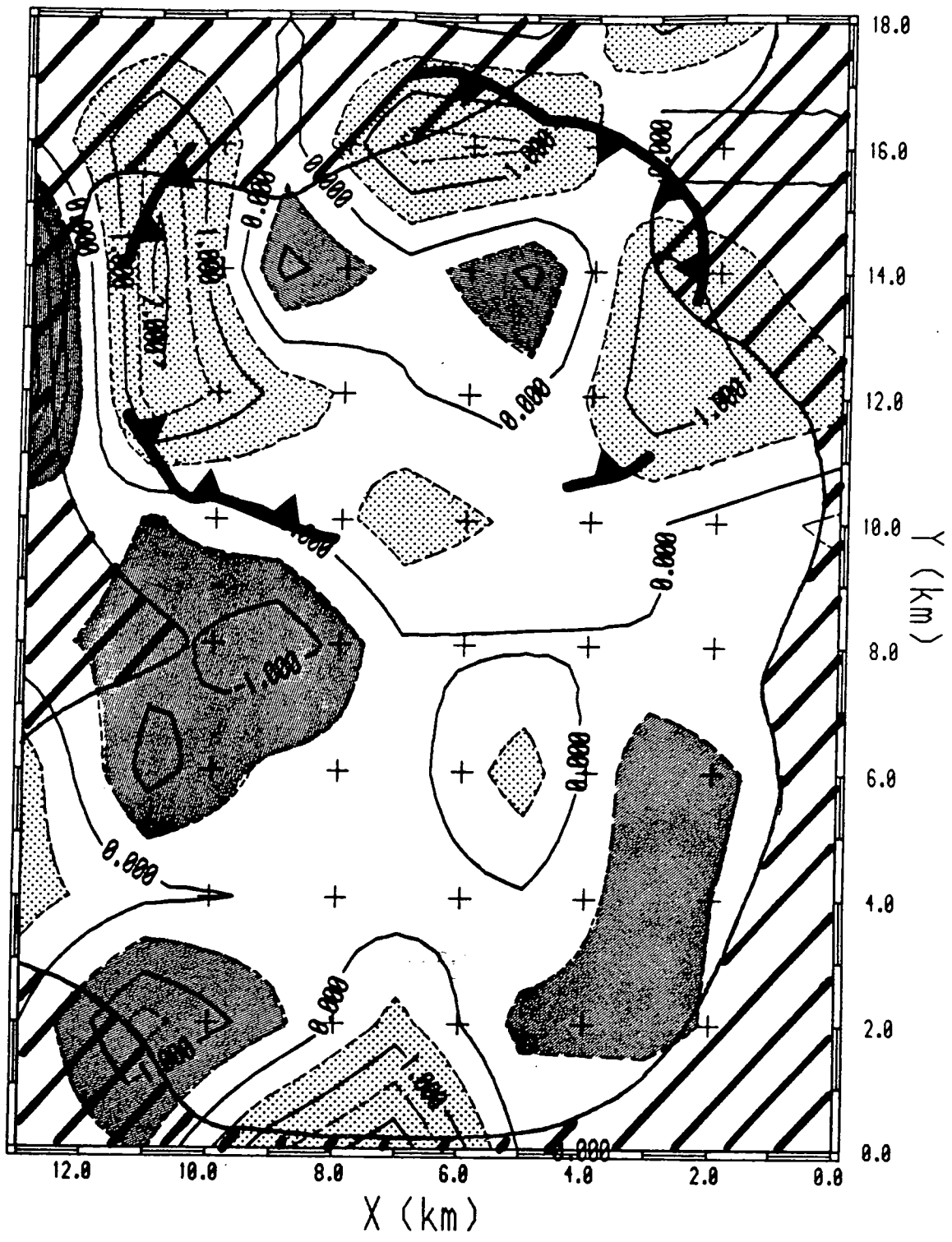

Figure 4.12b : Velocity differences from the 'evolved 1-d' velocity model at a depth of 1 km. The contour interval is 0.5 kms^{-1}. Areas with velocity difference $\geq +0.5$ kms^{-1} are stipled, and areas with velocity difference ≤ -0.5 kms^{-1} are shaded. The poorly resolved areas (DWS ¡ 50) are hatched.

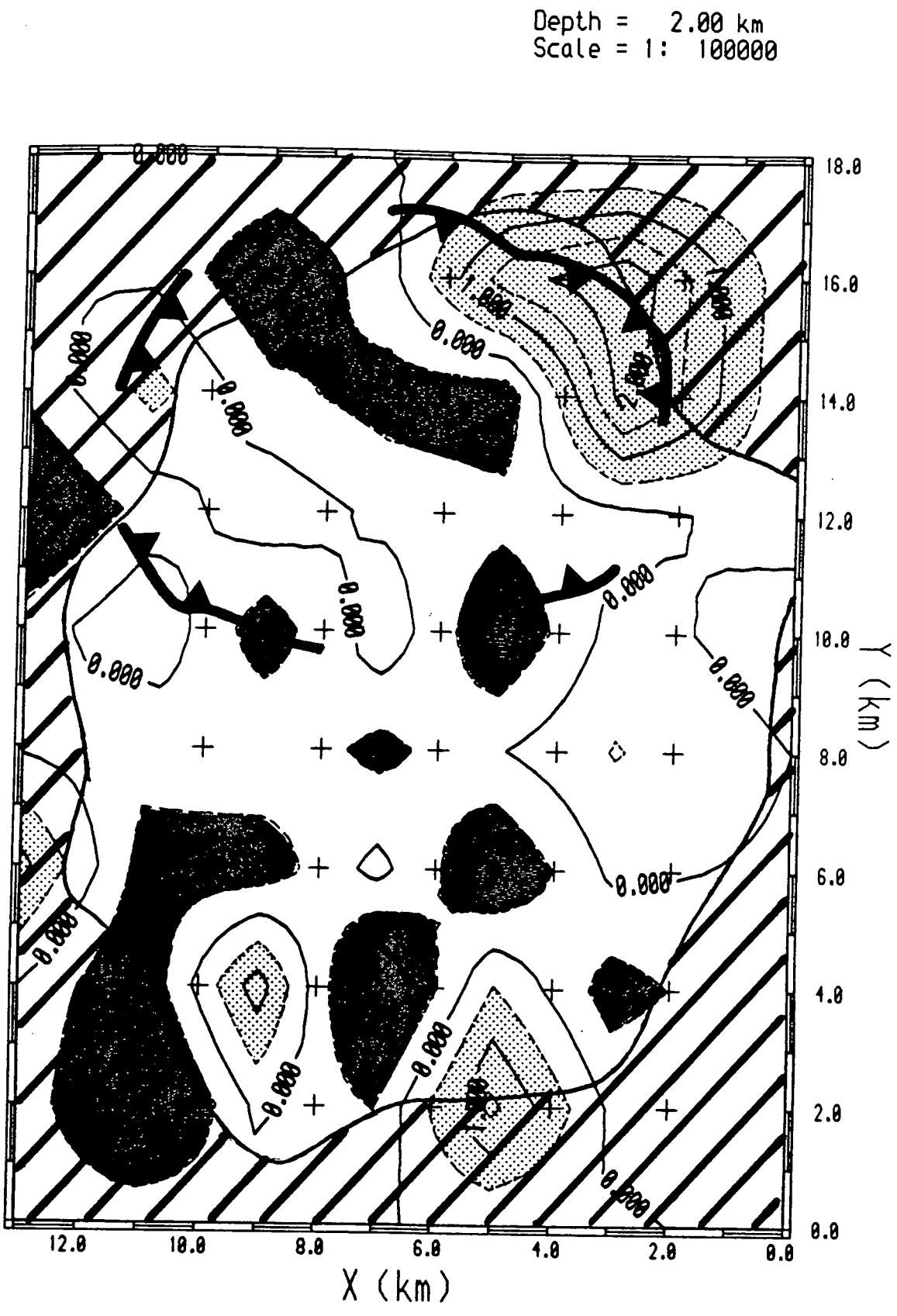

Figure 4.12c : Velocity differences from the 'evolved 1-d' velocity model at a depth of 2 km. The contour interval is 0.5 kms^{-1}. Areas with velocity difference $\geq +0.5$ kms^{-1} are stipled, and areas with velocity difference ≤ -0.5 kms^{-1} are shaded. The poorly resolved areas (DWS ; 50) are hatched.

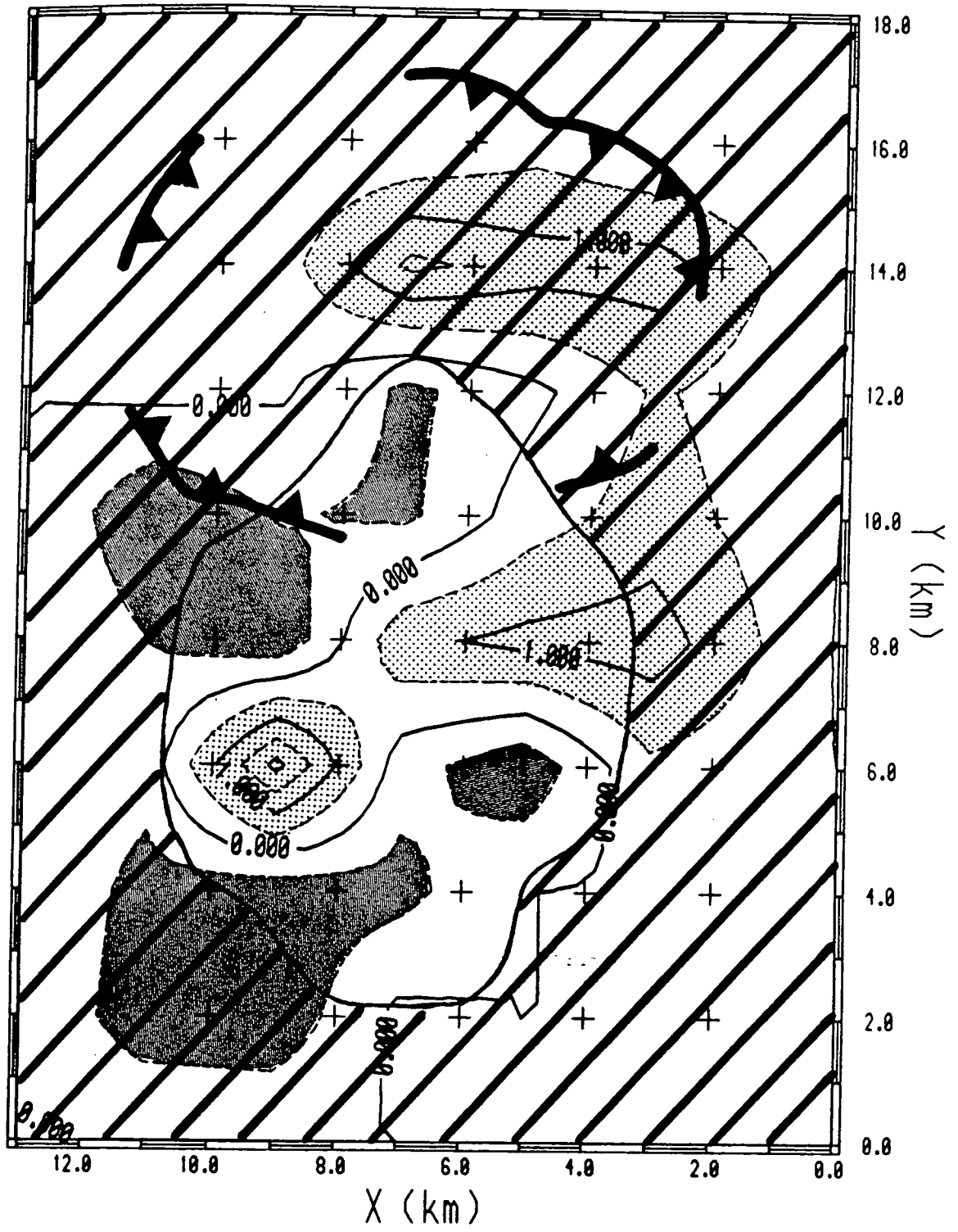

Figure 4.12d : Velocity differences from the 'evolved 1-d' velocity model at a depth of 3 km. The contour interval is 0.5 kms^{-1}. Areas with velocity difference $\geq +0.5$ kms^{-1} are stipled, and areas with velocity difference ≤ -0.5 kms^{-1} are shaded. The poorly resolved areas (DWS ¡ 50) are hatched.

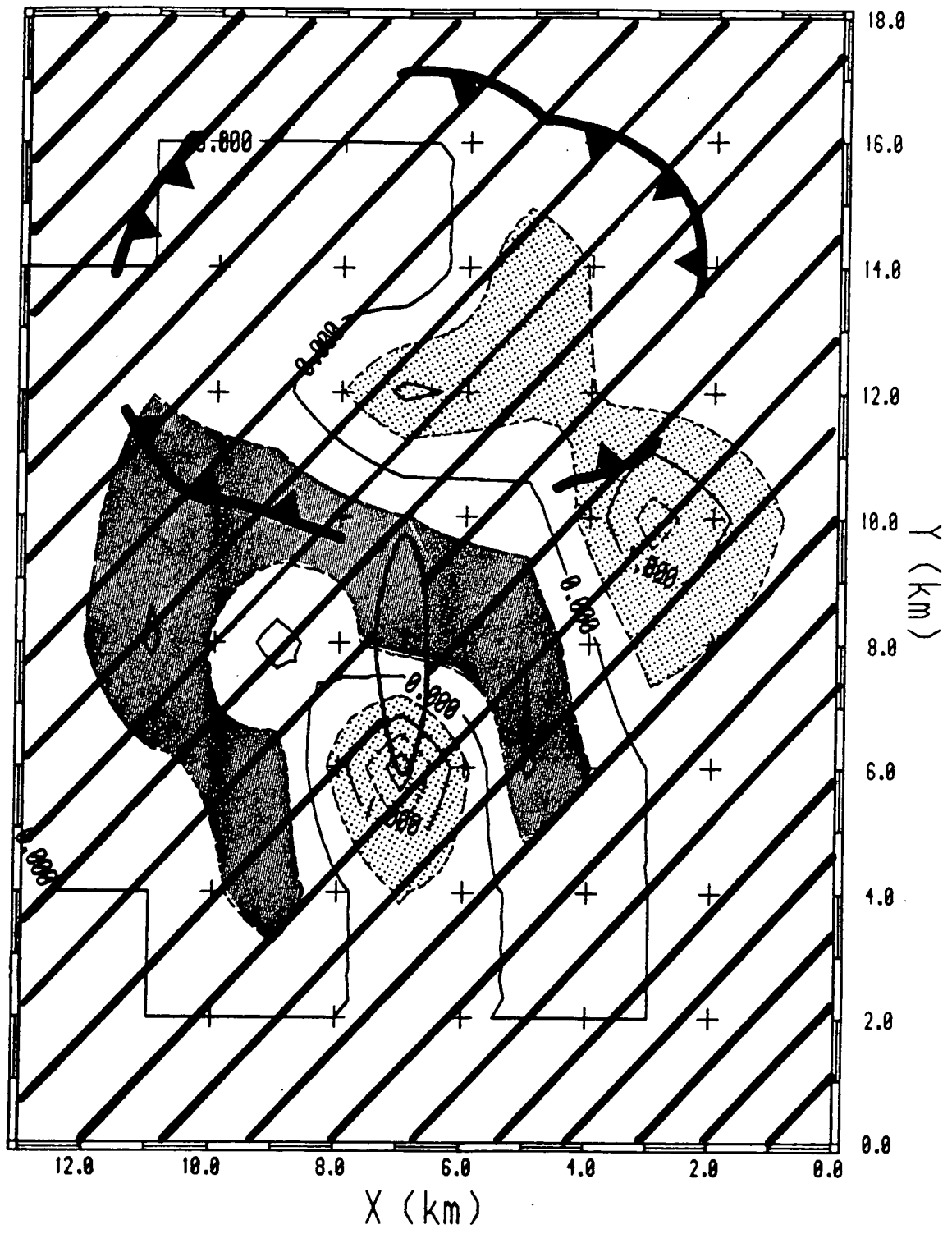

Figure 4.12e : Velocity differences from the 'evolved 1-d' velocity model at a depth of 4 km. The contour interval is 0.5 kms^{-1}. Areas with velocity difference $\geq +0.5$ kms^{-1} are stipled, and areas with velocity difference ≤ -0.5 kms^{-1} are shaded. The poorly resolved areas (DWS ¡ 50) are hatched. Note that very little is well resolved at this depth.

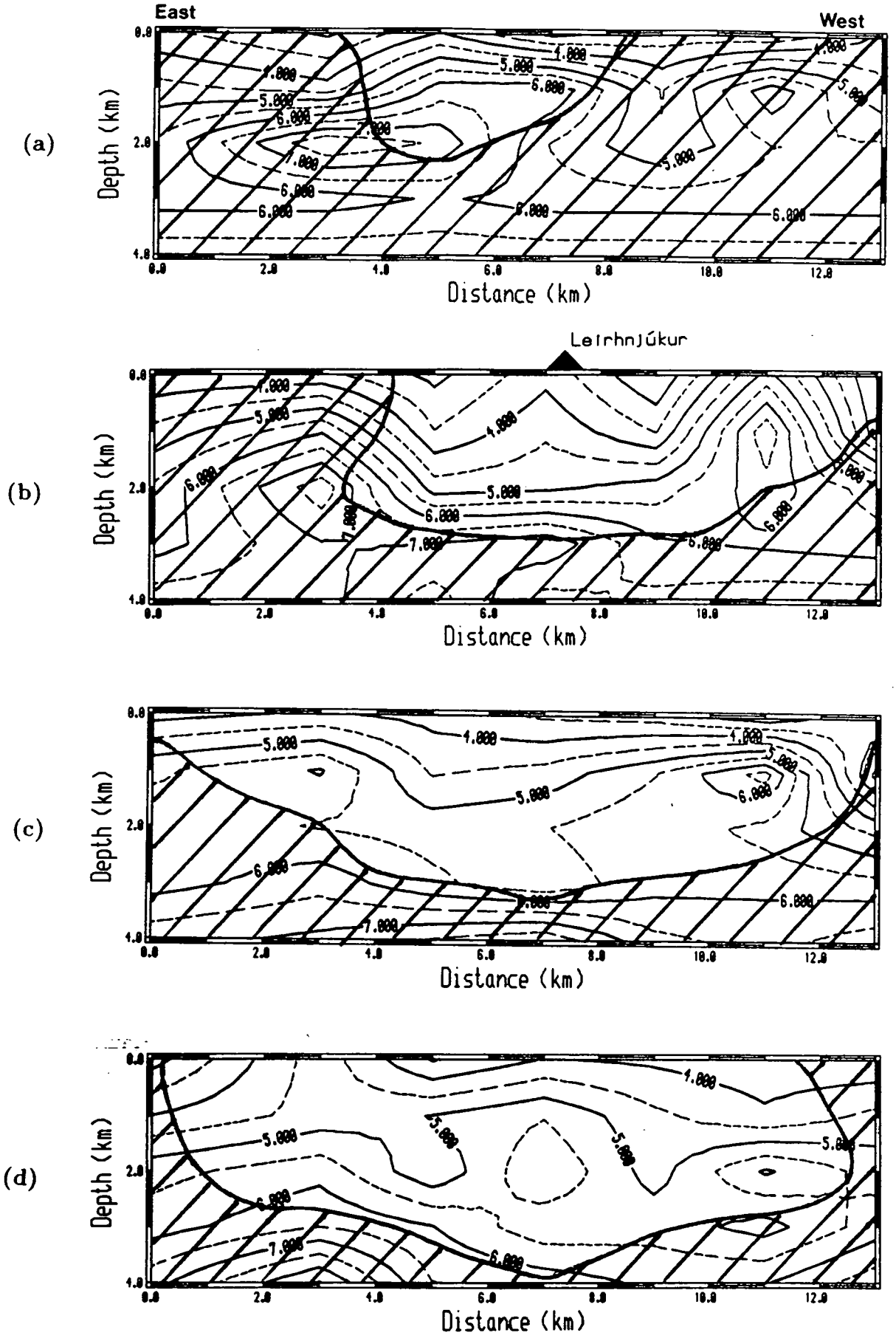

Figures 4.13a–d : Cross-sections from east to west through the final velocity model. The contour interval is 0.5 kms^{-1}. The poorly resolved areas (DWS < 50) are hatched. **(a)** y = 16 km, **(b)** y = 14 km, **(c)** y = 12 km, and **(d)** y = 10 km.

(e)

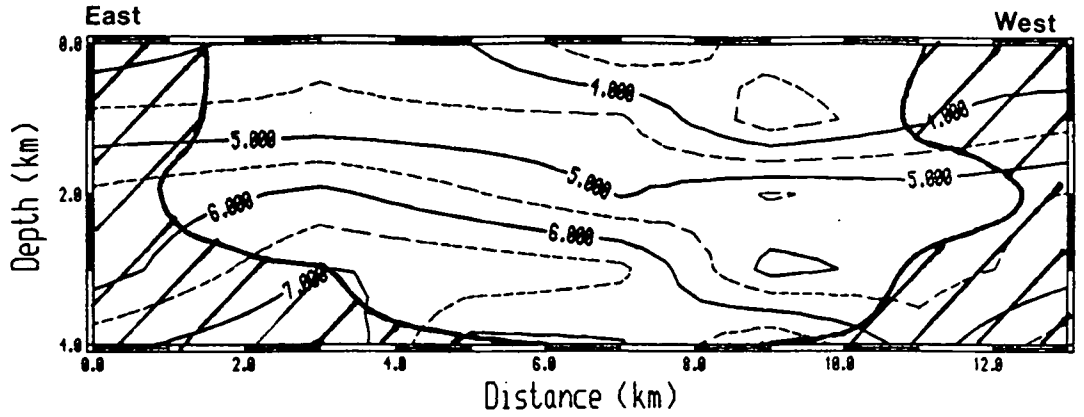

(f)

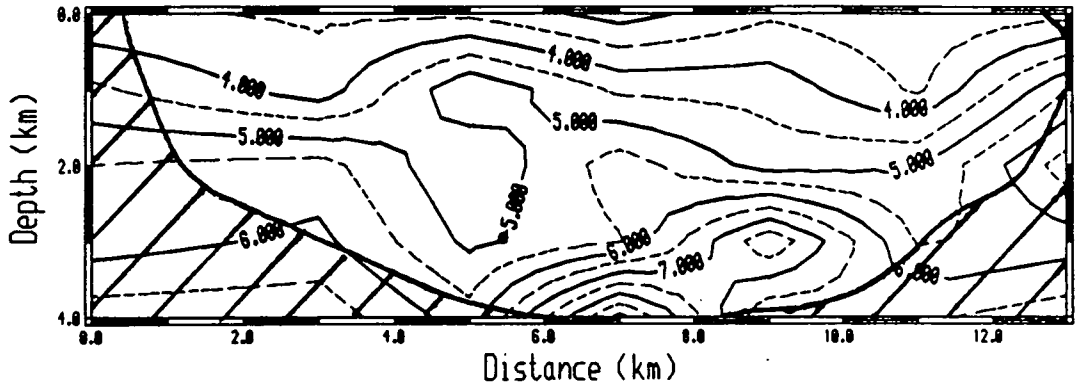

(g)

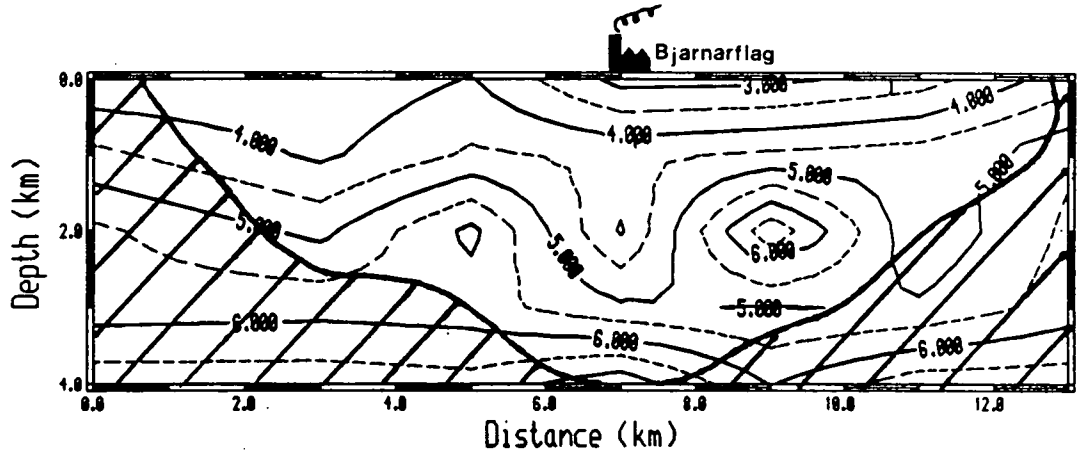

(h)

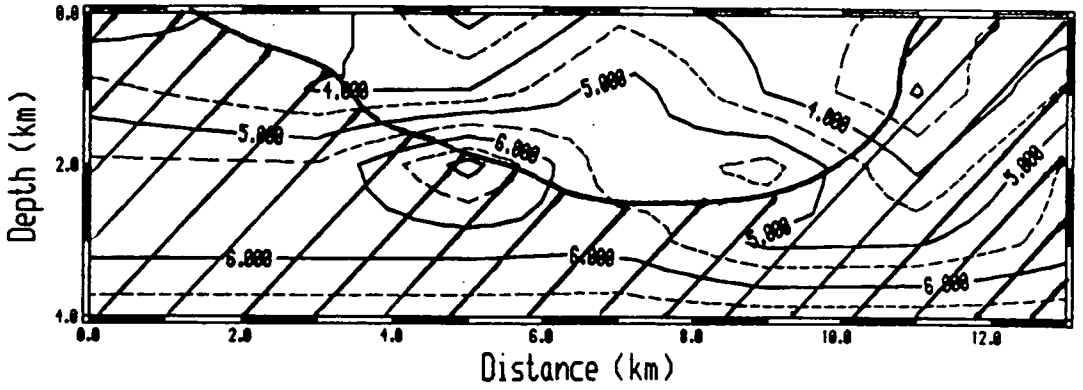

Figures 4.13e–h : Cross-sections from east to west through the final velocity model. The contour interval is 0.5 kms^{-1}. The poorly resolved areas (DWS < 50) are hatched. **(e)** $y = 8$ km, **(f)** $y = 6$ km, **(g)** $y = 4$ km, and **(h)** $y = 2$ km.

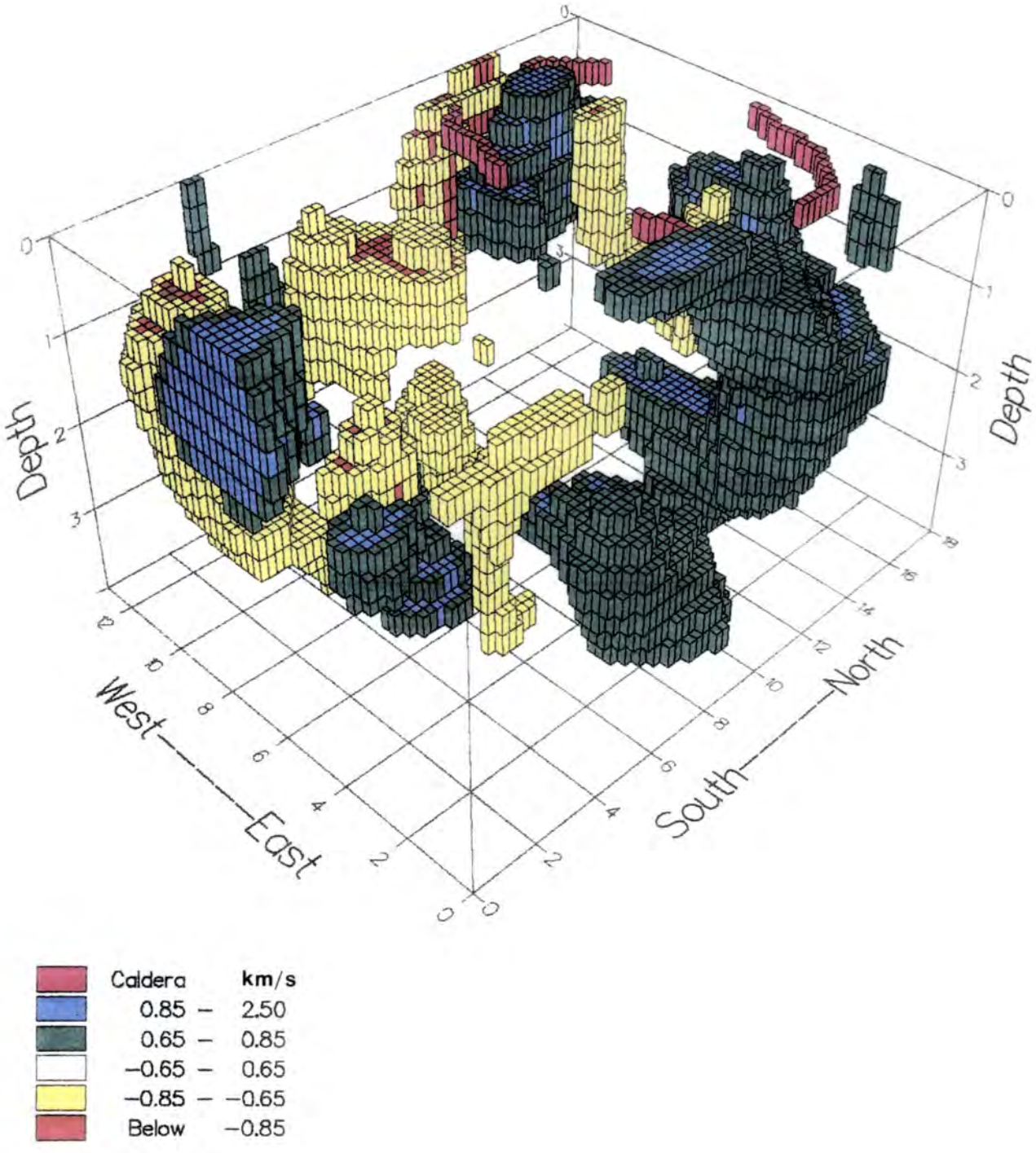

Figure 4.14a : Three–dimensional perspective map of velocity differences from the 'evolved 1–d' model. Viewed from Southeast.

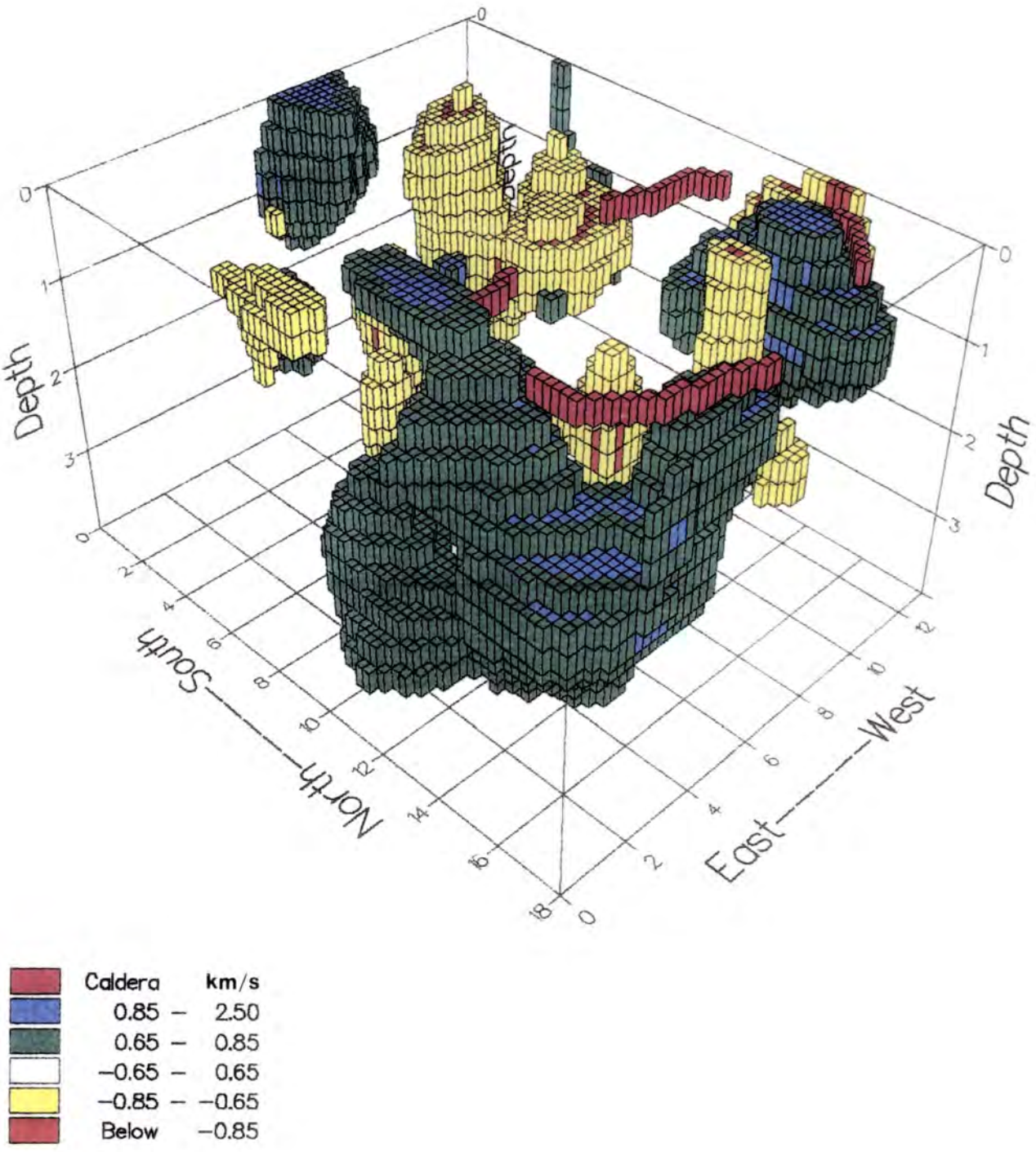

Figure 4.14b : Three–dimensional perspective map of velocity differences from the 'evolved 1–d' model. Viewed from Northeast.

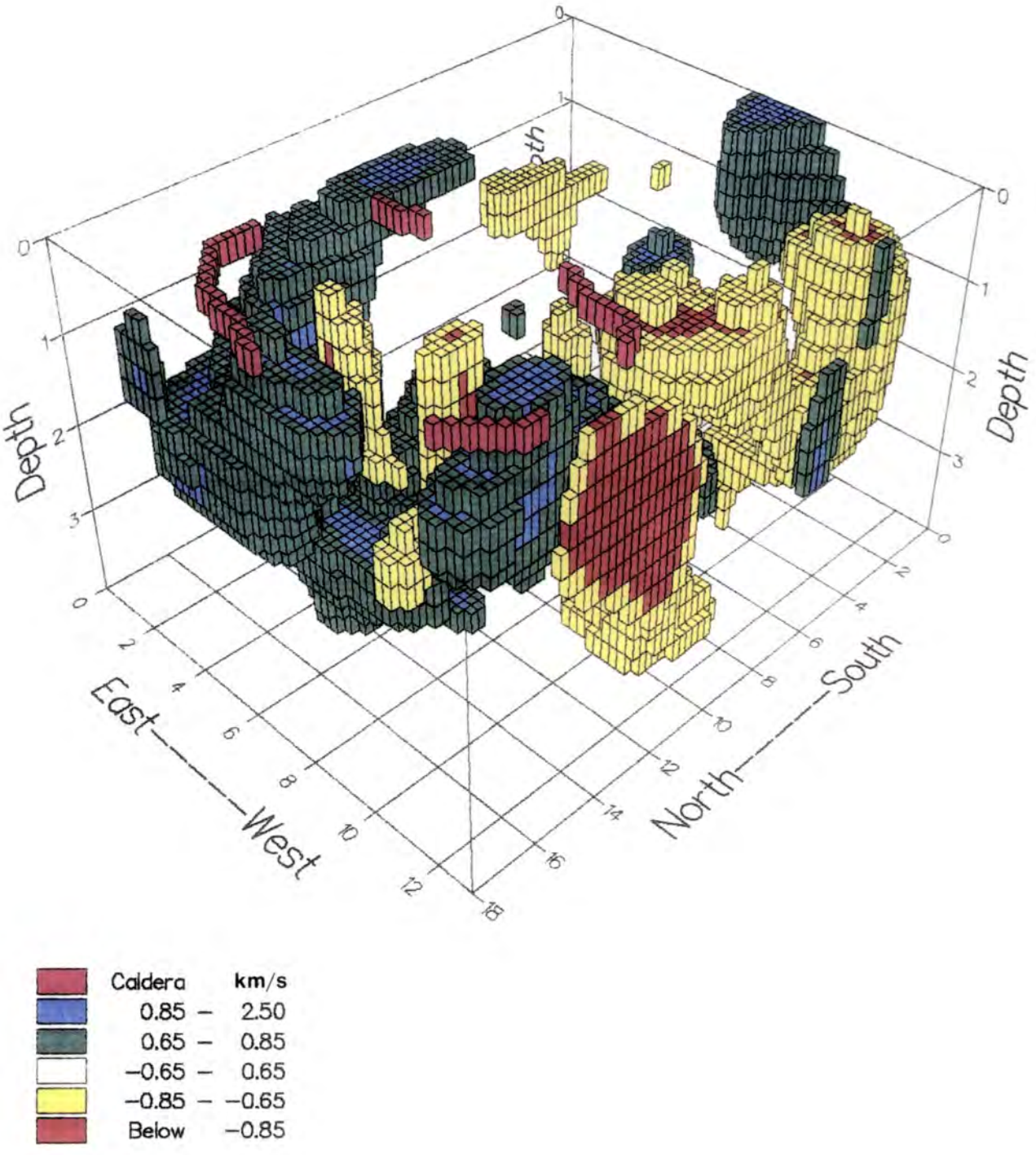

Figure 4.14c : Three–dimensional perspective map of velocity differences from the 'evolved 1–d' model. Viewed from Northwest.

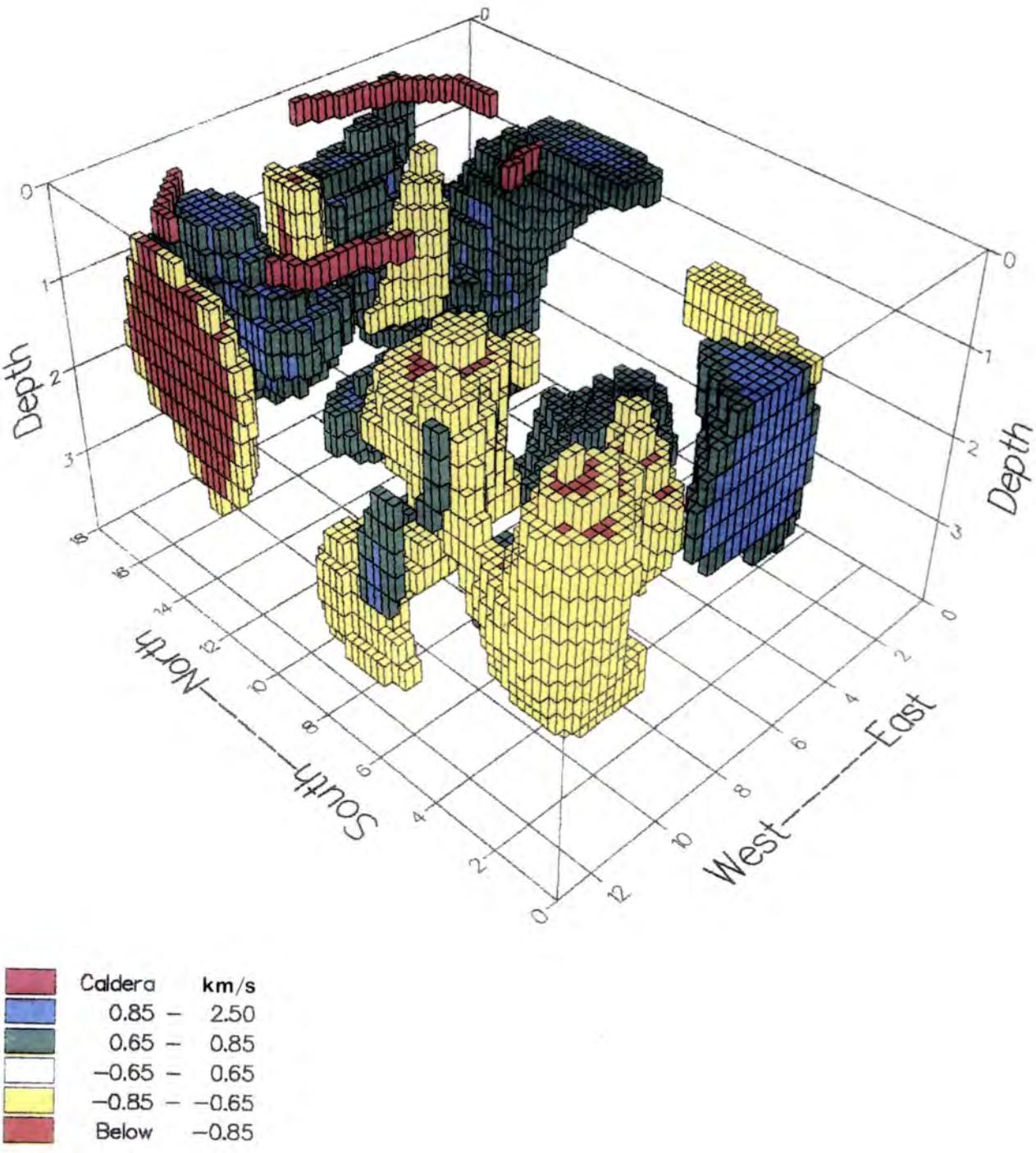

Figure 4.14d : Three–dimensional perspective map of velocity differences from the 'evolved 1–d' model. Viewed from Southwest.

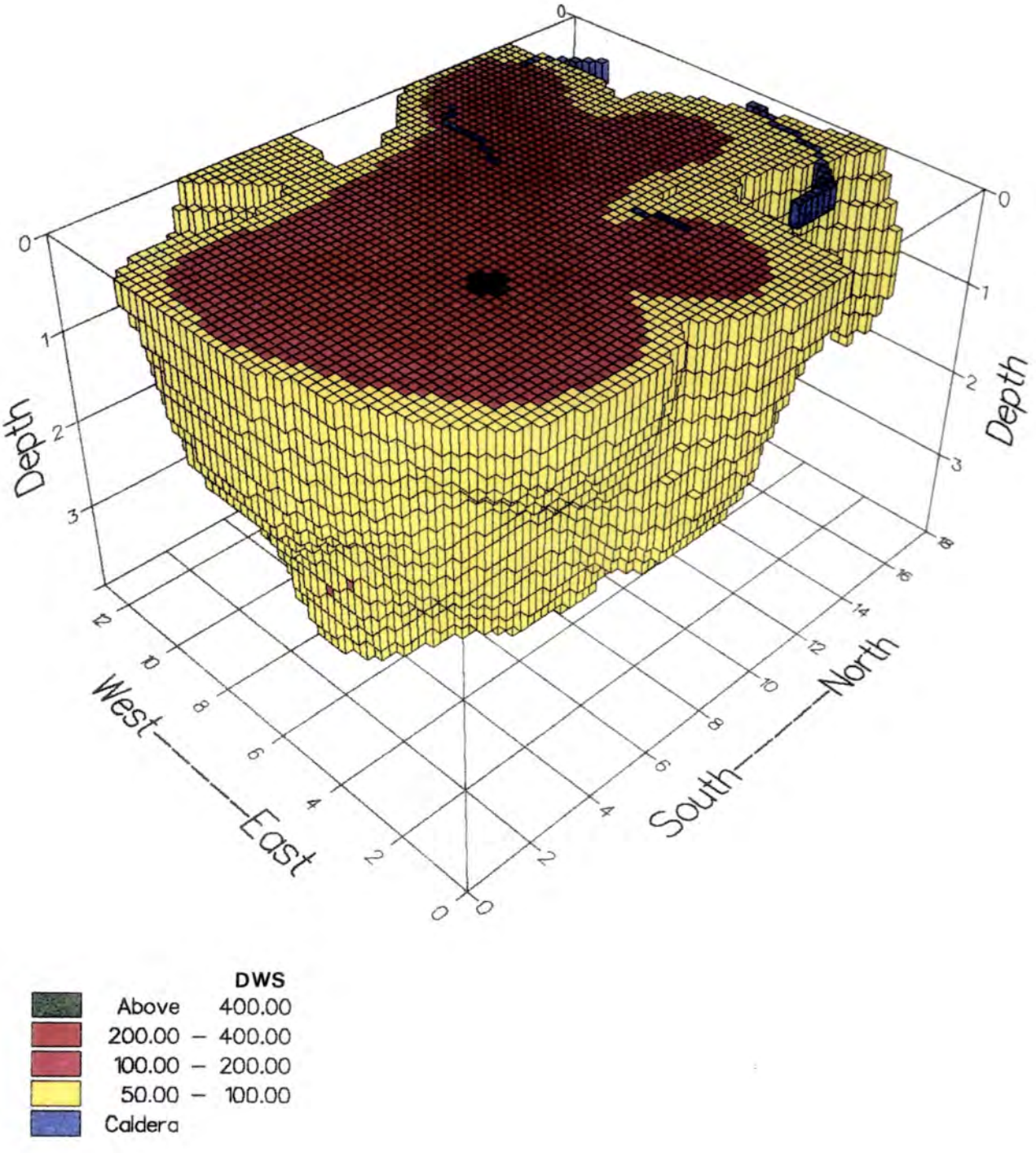

Figure 4.15a : Three-dimensional perspective map of the derivative weight sum (DWS). Only volumes for which DWS $\geq$ 50 are shown. Viewed from the Southeast.

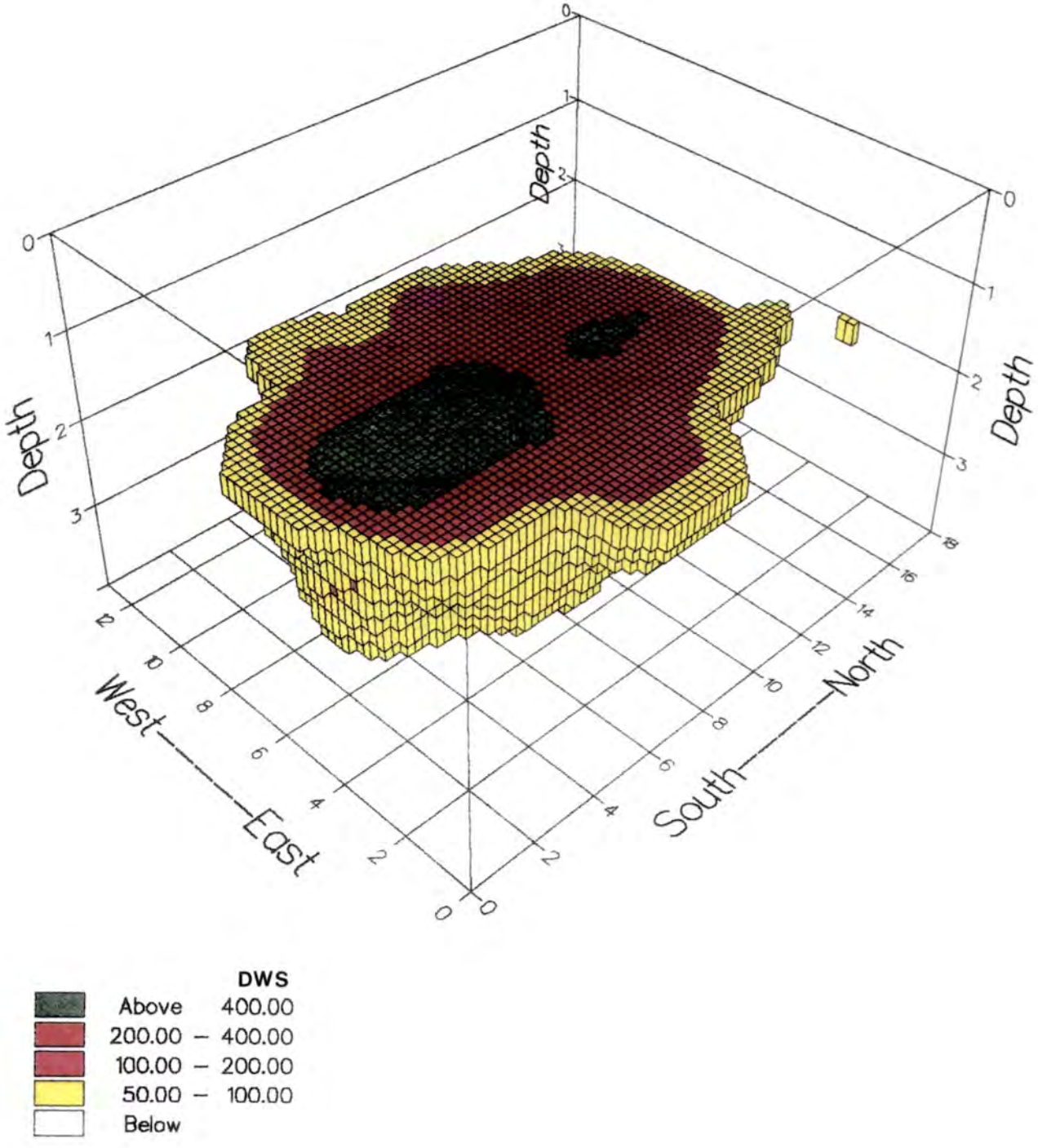

Figure 4.15b : Three–dimensional perspective map of the derivative weight sum (DWS) below 2 km depth. Only volumes for which DWS $\geq$ 50 are shown. Viewed from the Southeast.

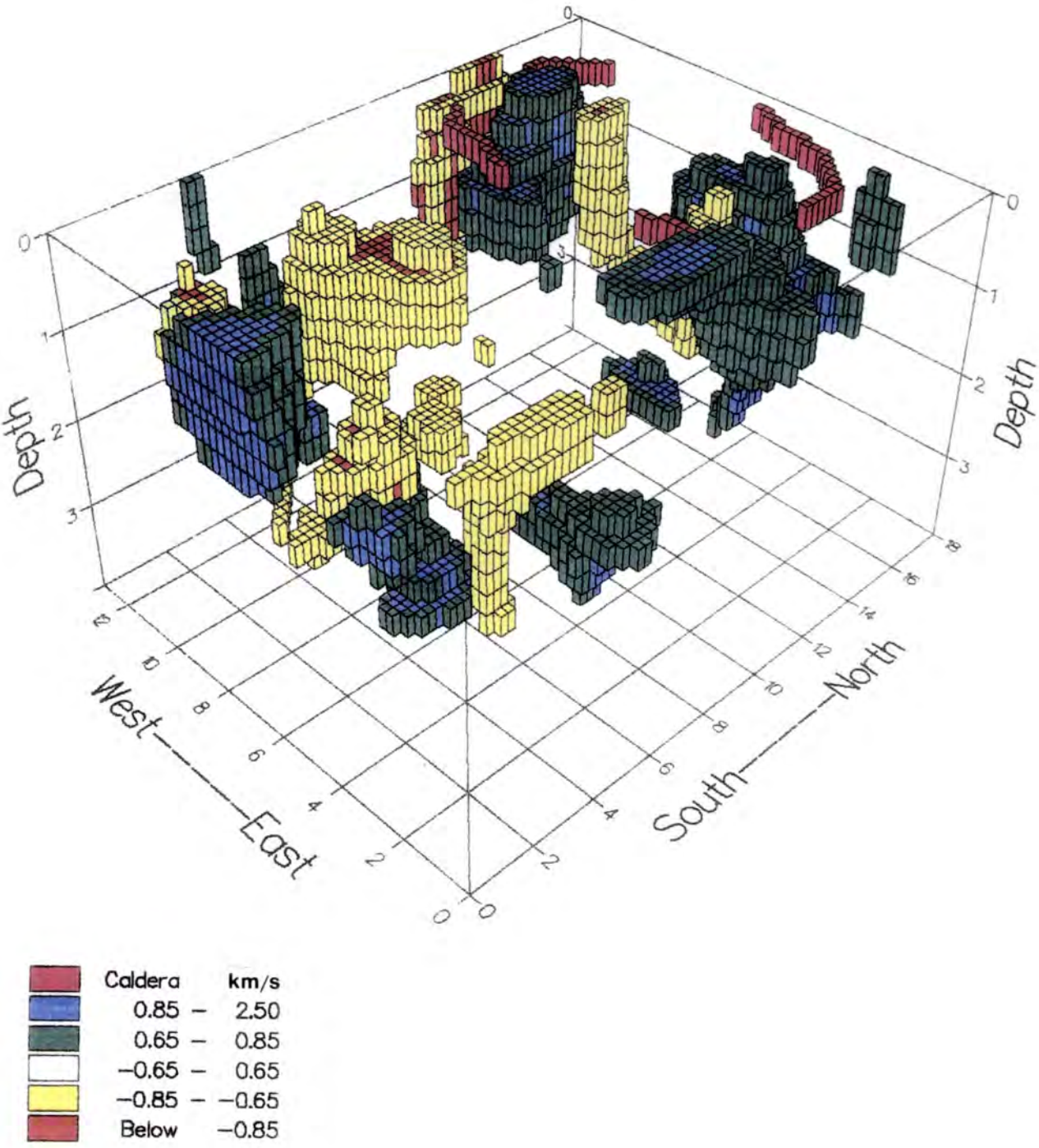

Figure 4.16 : Three–dimensional perspective map of velocity differences from the 'evolved 1–d' model. Only volumes for which DWS $\geq$ 50 are shown. Viewed from the Southeast.

kms^{-1}) were then removed to make the model transparent to all but relatively large anomalies. The three–dimensional model is shown with a variety of perspective views in figures 4.14a to 4.14d. Figures 4.15a and 4.15b show the volume which is considered to be well resolved (DWS $\geq$ 50), as viewed from the southeast. It can clearly be seen that resolution near the surface is good over almost the complete area of study (figure 4.15a). Not surprisingly, there is a close correlation between areas of good resolution and areas of seismometer coverage (figure 4.11). Figure 4.15b illustrates how the resolved volume decreases with depth, and how the heart of the imaged volume is the best resolved (has the highest DWS). As discussed earlier, this distribution in DWS is a result of variation in the density of rays passing through the model. Figure 4.16 is a perspective plot of only those volumes of anomalous velocity which are well resolved (only those volumes in figure 4.14a which have DWS $\geq$ 50 are shown), as viewed from the southeast.

It should be emphasized that smoothing of velocity has not only occurred in the inversion process, but has also been carried out in the mapping interpolation scheme. As a result, seismic discontinuities cannot faithfully be imaged. Furthermore, all imaged volumes are smoothed such that their highest velocity contrast is positioned in their centres, even though they may be of uniform velocity. These factors must be taken into account during the interpretation of the images.

4.4.3 Krafla P–wave Velocity Anomalies

Only those velocity anomalies which are defined by more than one node have been interpreted as being geologically significant. Thus, for an anomaly to be considered important, it must have a volume of at least about 2 km^3 within the bounds of the well resolved volume.

Several distinct bodies of relatively high velocity exist within the Krafla volcanic system. At 1 km depth (figure 4.12b), three significant high velocity volumes are evident which lie beneath the western, northern and eastern outlines of the Krafla caldera. The western anomaly, centred at (11,14,1), is up to 2 kms^{-1} faster than the surrounding crust (i.e. up to about 6.5 kms^{-1}, figure 4.13b) and extends up to the surface and down to about 2 km depth. It is shown clearly in figures 4.14a and 4.16. The eastern anomaly extends from the surface at about (3,10,0) (figure 4.12a) and deepens northward until it reaches its maximum value and areal extent

at about +2 kms^{-1} centred on (3,16,2), although at that point it is not well resolved (figures 4.12c, 4.13a). The northern anomaly extends from about (6,16,1) with a value of up to +1.5 kms^{-1}, and merges with the eastern anomaly at 2 km depth (figures 4.12c, 4.14b). The only other significant zone of high velocity lies in the extreme south of the area and is also anomalous by up to +2 kms^{-1}. It appears to be centred at about (6,0,1) and extends to the surface at the ash cone Hverfjall (figure 2.3) and down to about 2 km depth (figures 4.14a,d, 4.16). However, it may extend further to the south, beyond the imaged volume.

The most coherent zone of low velocity lies within the Krafla caldera. It stretches from about (9,16,2) to (5,13,2) at 2 km depth and extends to the surface in the form of two low velocity pipes (low by up to -1 kms^{-1}) which appear to outcrop at the western flank of Mt. Krafla (5,14,0) and about 2 km west–northwest of Leirhnjúkur (9,14,0), (figures 4.13b, 4.14a,c,d, 4.16). The other volume of low velocity near the surface extends from Bjarnarflag (7,4,0) towards the north at (7,7,0) and towards Reynihlid in the west at (10,4,0); it is anomalous by about -0.7 kms^{-1}.

At about 1 km depth there are two main low velocity zones outside the caldera : one is centred at about (10,8,1), (figures 4.12b, 4.14d), is about 4 km in diameter and is anomalous by up to -1 kms^{-1}; the other is a long narrow zone extending from about (4,2,1) to about (2,6,1) and has a velocity which is low by around -0.7 kms^{-1} (figure 4.12b). Another significant area of low velocity has its peak 2 km beneath Bjarnarflag at (7,4,2), and is an anomaly of up to -1.5 kms^{-1} (figure 4.13g). As depth increases, this zone extends towards the northeast and southwest. The only other reasonably well resolved low velocity zone exists between about (10,9,3) and (7,11,3), with an anomalous velocity of about –0.5 kms^{-1} (figure 4.12d).

There is no indication from the anomalies outlined above of the presence of significant azimuthal P–wave velocity anisotropy. This is consistent with (and a result of) the absence of significant azimuthal variation in travel–time residuals observed earlier (figure 3.4).

It should be noted that the volumes of high and low velocity outlined by this description are anomalous relative to the starting velocity model (the 'evolved 1–d' model), the values of which were effectively averages for the whole imaged volume. The presence of a central volcano, which features higher crustal seismic

velocities than more 'normal' Icelandic crust, has caused the starting model to have higher average values. This has resulted in larger volumes of relatively low velocity being imaged to the south of the model than in the vicinity of the caldera. The maps of velocity values rather than differences may therefore be more useful for outlining volumes of anomalous velocity when compared with regional velocities.

4.5 Earthquake Relocation

4.5.1 The Effects

4.5.1.1 Introduction

The effects of relocating the Krafla local earthquake hypocentres by the simultaneous inversion process are large and varied. They are illustrated in this section using the DUEDROPS program MAPPLOT (Smith, 1987d), which allows the plotting of revised event locations (as solid circles) joined by vectors to the pre–inversion locations. A version of SIMUL3 which carries out the location of events through a given velocity structure without going on to invert for velocity model perturbations was used. In this way, the full dataset presented in figures 3.6–3.9 was relocated through the 'evolved 1–d' and final 3–d velocity structures without perturbations in velocity structure. Appendix D contains the original and final hypocentral locations of the events presented in chapter 3.

4.5.1.2 Relocation Using the 'Evolved 1–d' Model

Figures 4.17–4.19 demonstrate the effects on the calculated hypocentres of increasing the average layer velocities from the original one–dimensional model to the 'evolved 1–d' models. The effect on the epicentres is generally no more than 0.5 km, which is of the same order as the ERH of the original location (section 3.3.5), although a few have been relocated by more than this amount (figure 4.17). Epicentres of events originating within the Bjarnarflag cluster and the 'fissure zone' have generally been relocated to the north by about 0.1–0.2 km (figure 4.18). Relocation also has the effect of reducing the depth of virtually all events by 0.6–0.7 km (figures 4.18, 4.19). This is consistent with the effect discussed in section 3.3.3.

4.5.1.3 Relocation Using the Final 3–d Model

Figures 4.20–4.22 show the effects on the calculated hypocentres between location through the 'evolved 1–d' velocity model and the final 3–d model. The hypocentre maps are shown with contours outlining the extent to which the three–dimensional velocity model is well resolved. Events originally located outside this well–resolved volume are not reliably relocated and are therefore disregarded in this analysis.

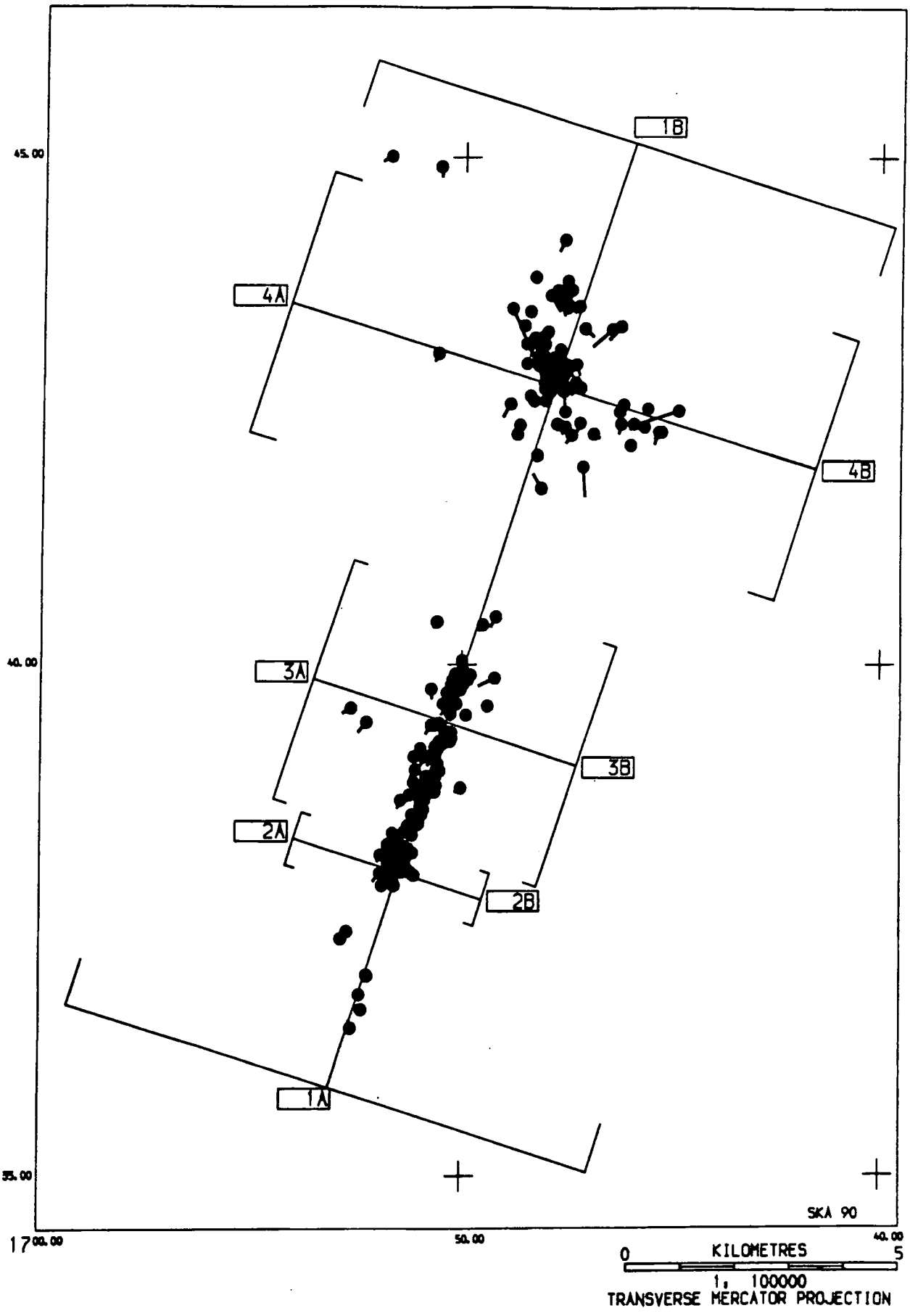

Figure 4.17 : Relocation of epicentres from those computed using the original one–dimensional velocity model and HYPOINVERSE (figure 3.7), to those computed using the 'evolved 1–d' model and SIMUL3. Closed circles represent the new locations, which are joined to the original locations by short lines. The locations of the hypocentre cross–sections in figures 4.18 and 4.19 are shown.

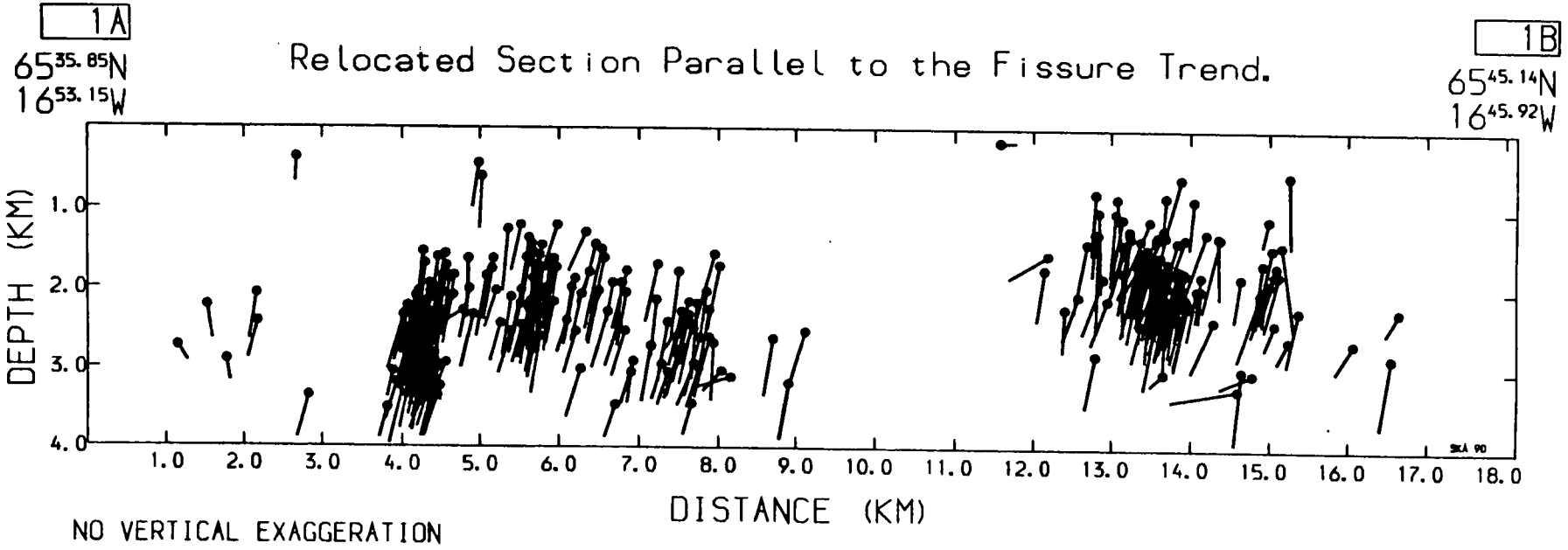

Figure 4.18 : Relocation of hypocentres along cross-section 1A-1B of figure 4.17, from those computed using the original one-dimensional velocity model (figure 3.8) to those computed using the 'evolved 1-d' model. Symbols as defined in figure 4.17.

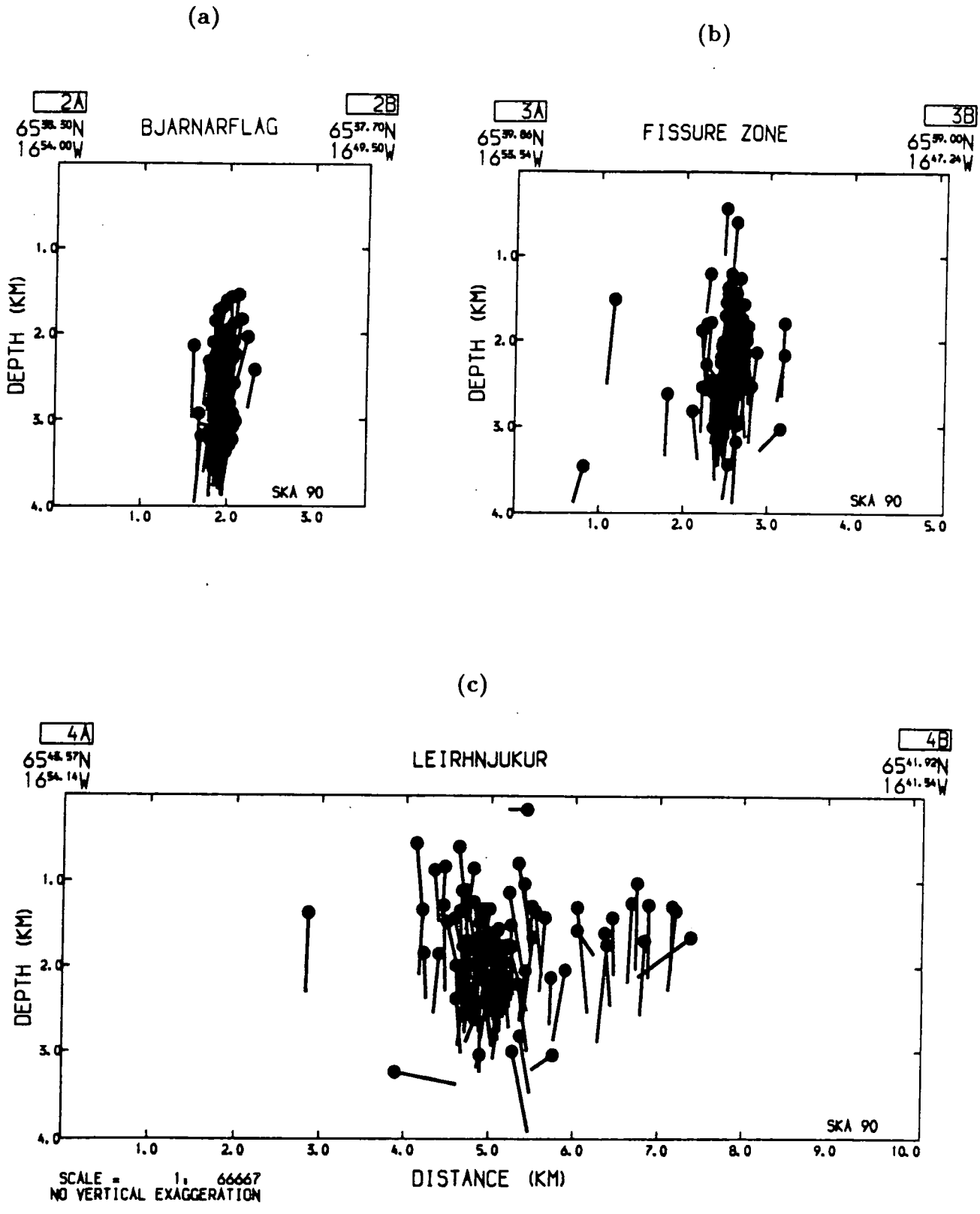

Figure 4.19 : Relocation of hypocentres along cross-sections perpendicular to the trend of the surface fissure swarm, from those computed using the original one-dimensional velocity model (figure 3.9) to those computed using the 'evolved 1-d' model. Symbols as defined in figure 4.17. **(a)** Section 2A-2B across the Bjarnarflag cluster. **(b)** Section 3A-3B across the 'fissure swarm'. **(c)** Section 4A-4B across the Leirhnjúkur cluster.

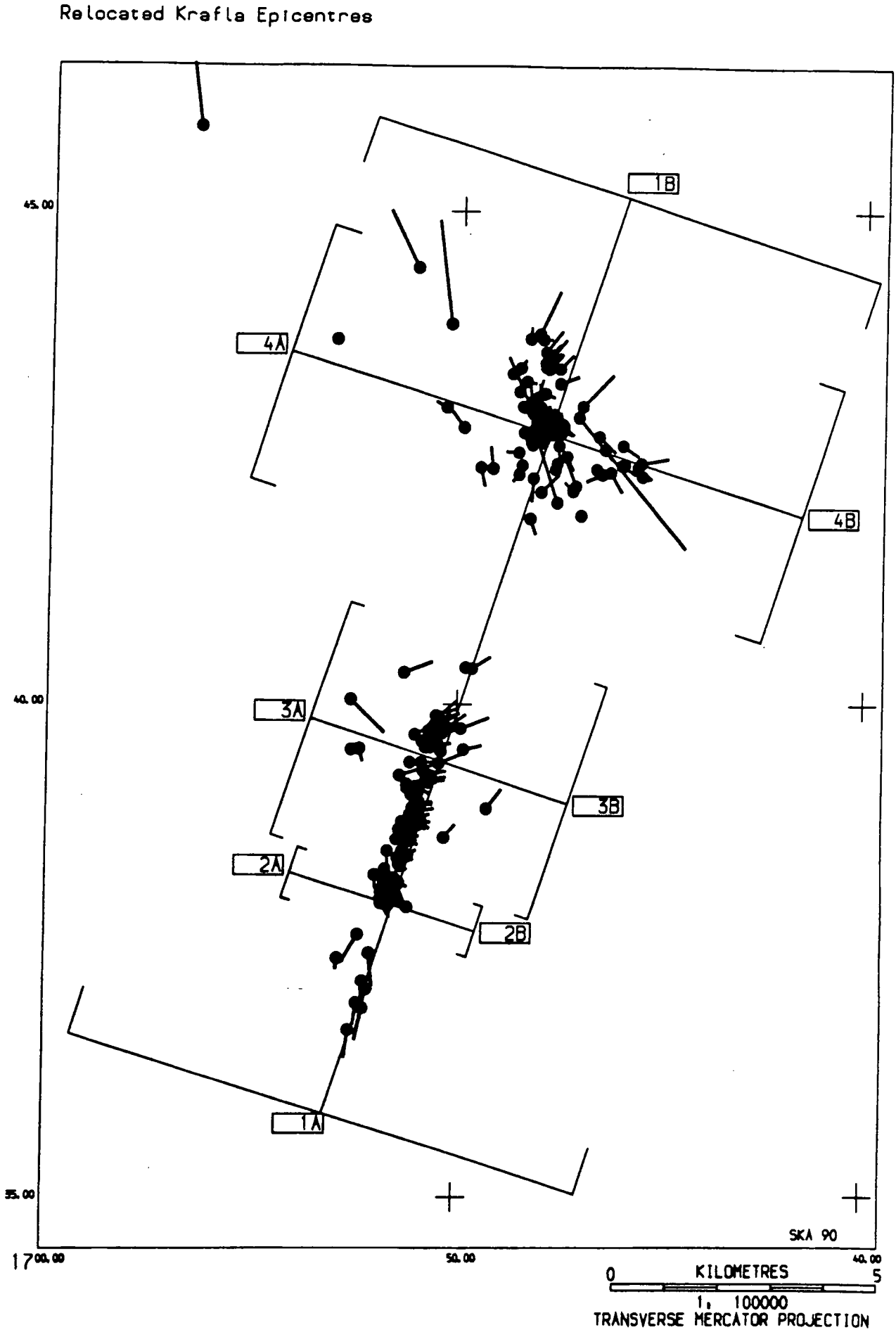

Figure 4.20 : Relocation of epicentres from those computed using the 'evolved 1–d' velocity model (figure 4.17) to those computed using the final 3–d model. Closed circles represent the new locations, which are joined to the original locations by short lines. The locations of the hypocentre cross–sections in figures 4.21 and 4.22 are shown.

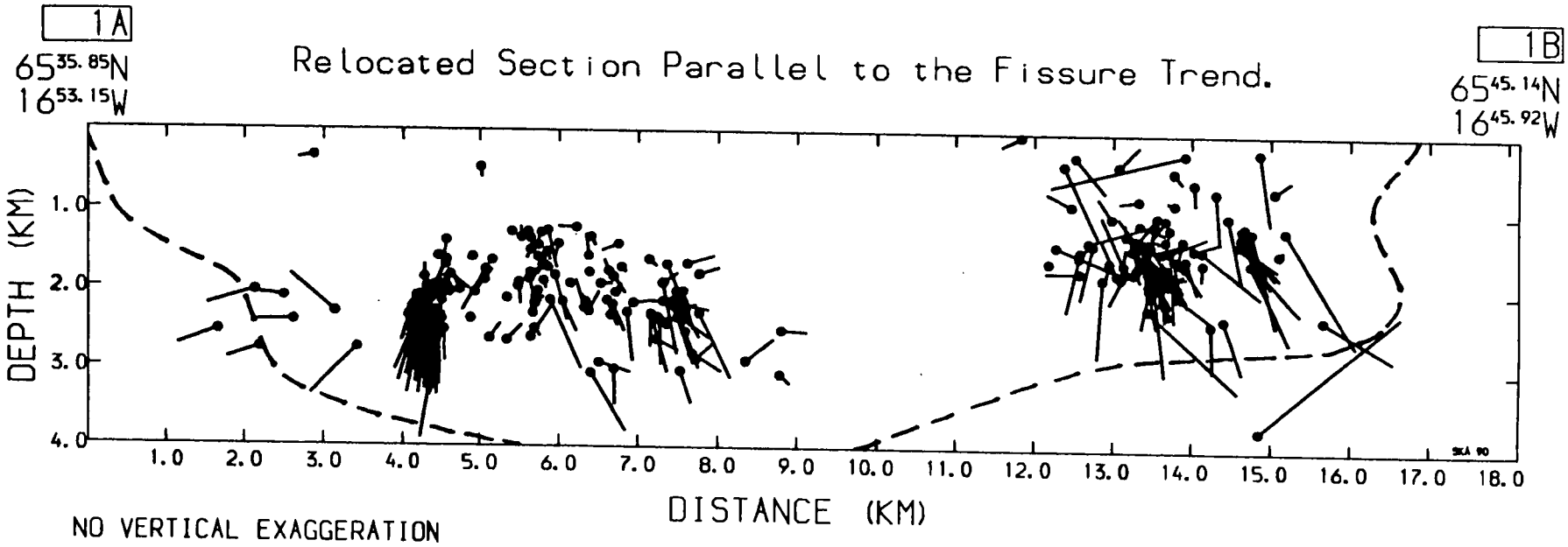

Figure 4.21 : Relocation of hypocentres along cross-section 1A–1B of figure 4.20, from those computed using the 'evolved 1-d' velocity model (figure 4.18) to those computed using the final 3-d model. The DWS = 50 contour is shown to indicate the outer limits of the 3-d velocity model considered to be well resolved. Symbols as defined in figure 4.20.

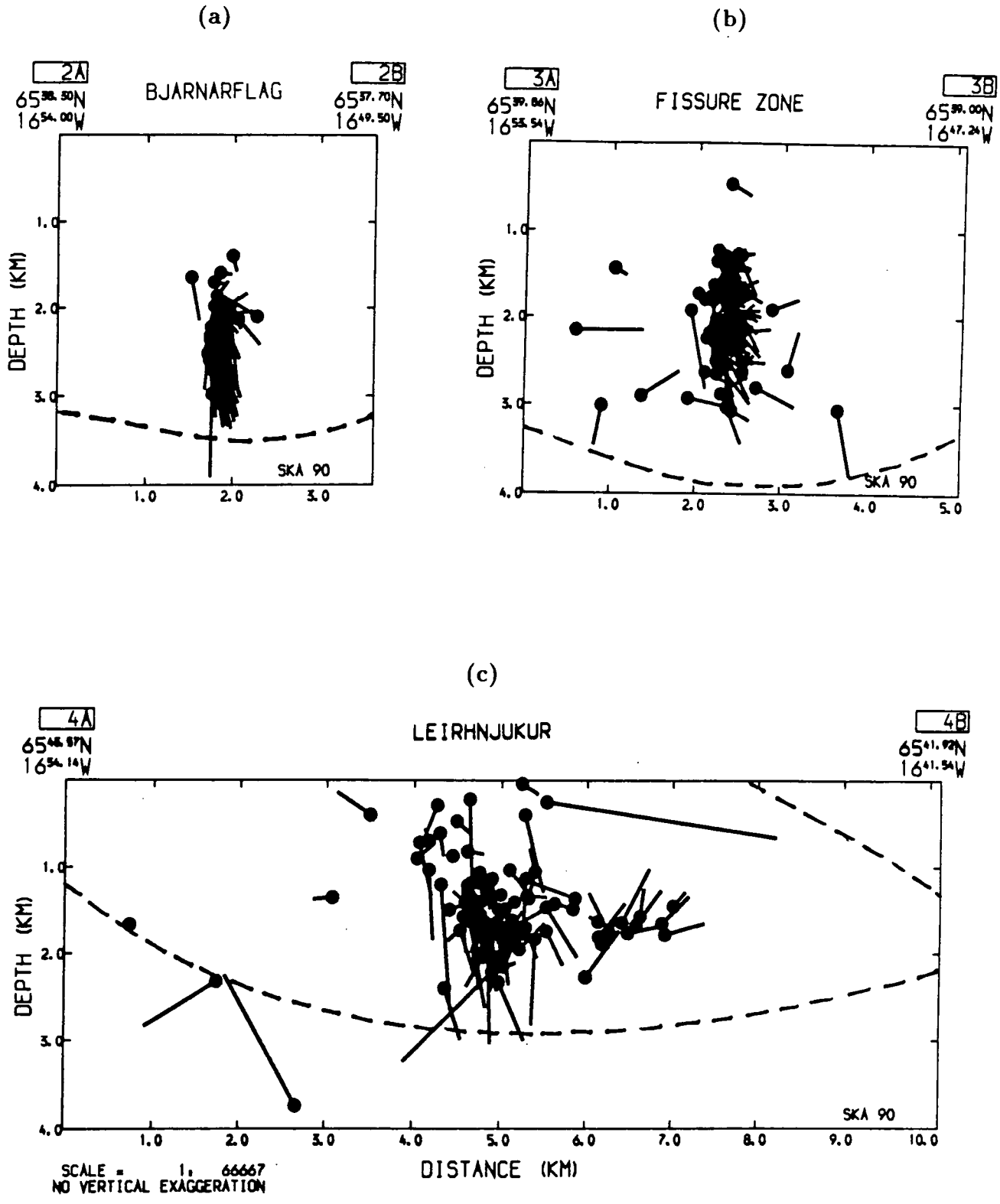

Figure 4.22 : Relocation of hypocentres along cross-sections perpendicular to the trend of the surface fissure swarm, from those computed using the 'evolved 1-d' velocity model (figure 4.19) to those computed using the final 3-d model. The DWS = 50 contour is shown to indicate the outer limits of the 3-d velocity model considered to be well resolved. Symbols as defined in figure 4.20. **(a)** Section 2A-2B across the Bjarnarflag cluster. **(b)** Section 3A-3B across the 'fissure swarm'. **(c)** Section 4A-4B across the Leirhnjúkur cluster.

It can be seen from the epicentre map (figure 4.20) and hypocentre cross-section (figure 4.22a) that events within the Bjarnarflag cluster have largely been relocated westwards by about 0.2 km. Considerable shallowing has affected events within the Bjarnarflag cluster (figures 4.21, 4.22a). Events are shallower by about 0.5 km at the deepest part of the cluster but this effect appears to be smaller at shallower depths. A slight northward migration of these events is also evident (figure 4.21). Events to the south of Bjarnarflag have been relocated to the north by about 0.5 km (figure 4.20).

Events within the 'fissure zone' have also largely been relocated westwards, by about 0.2–0.5 km (figures 4.20, 4.22b). Many events have also been relocated shallower, particularly those further to the north which are shallower by as much as 1 km. Events at the northern part of the 'fissure zone' also tend to be relocated slightly southwards.

Relocation of events in the Leirhnjúkur cluster is considerable and varied. Epicentres can be seen to have been relocated generally towards the centre of the cluster (figure 4.20), the effect being greater for events originally lying towards its fringes. Many events near the centre of the cluster and to the north have been relocated to shallower depths by up to about 0.5–1.0 km (figures 4.21, 4.22c), while those in the subcluster to the east have been moved by about 0.1–0.7 km nearer to the surface (figure 4.22c).

Figures 4.23 to 4.25 show the final locations of the NISE–85 local earthquake data. These maps will now be compared with those discussed in section 3.3.5, which used the original velocity model for location.

4.5.2 Final Epicentral Distribution

The clearest difference between the epicentre maps (figures 3.7 and 4.23) is the slight relocation, by about 0.2–0.3 km, of events in the Bjarnarflag cluster and the 'fissure zone' of activity to the north and west. In addition, all three main areas of activity appear to be slightly narrower in a direction parallel to the fissure swarm. As a result, the distance between the northern edge of the 'fissure zone' and the centre of the Leirhnjúkur cluster has increased by about 0.4 km. The Bjarnarflag cluster and the 'fissure zone' are also slightly narrower in a direction

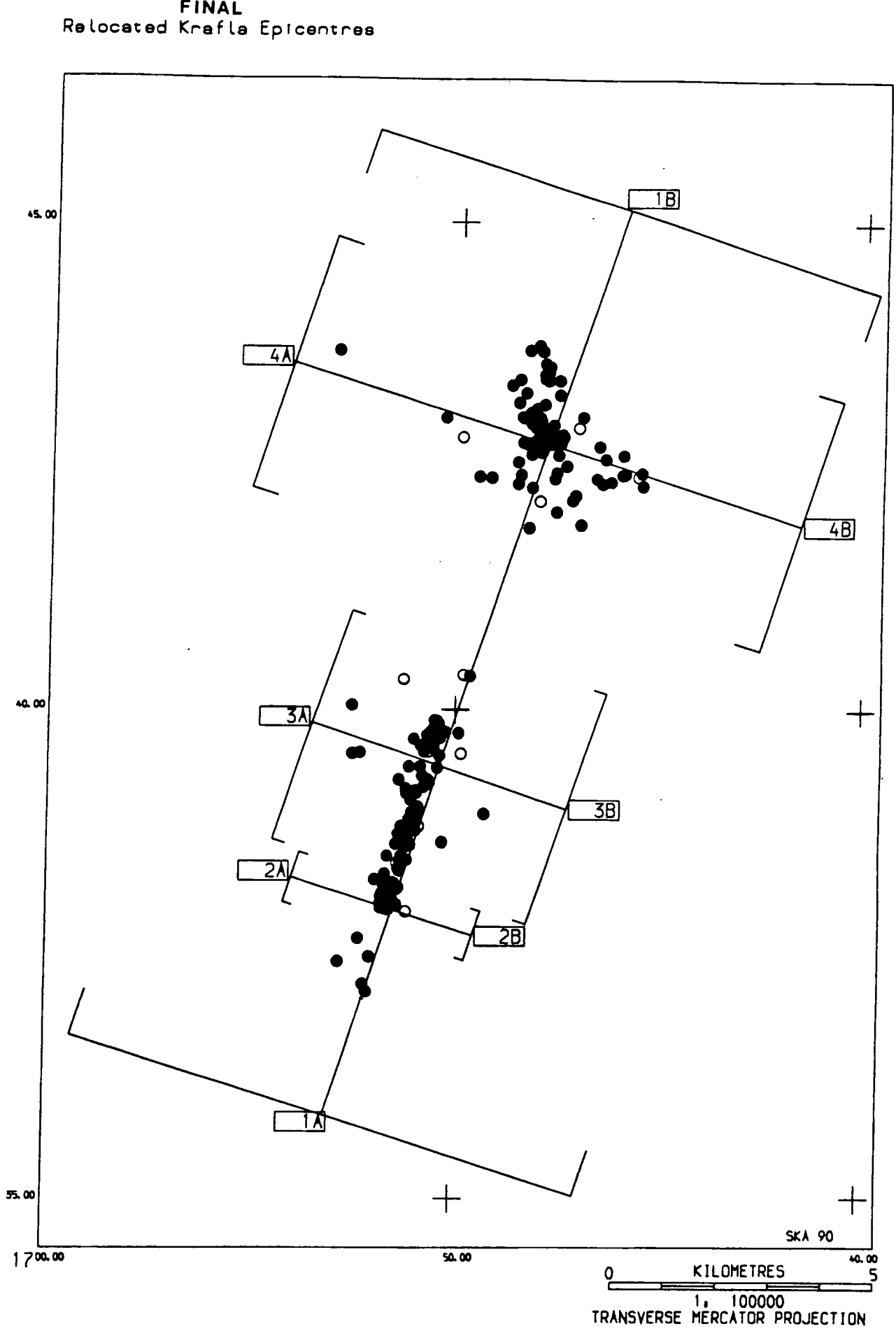

Figure 4.23 : The final epicentre map for data collected by the NISE–85 experiment. Events located with an error ERZ $\leq$ 0.5 km are plotted as filled circles, and those located with 0.5km $<$ ERZ $\leq$ 1.0 km are plotted as open circles. The locations of the hypocentre cross–sections in figures 4.24 and 4.25 are shown.

perpendicular to the fissure swarm. Two subclusters of the Leirhnjúkur cluster are still apparent to the east–southeast and north, the latter of which now appears to be more focussed with a roughly north–northwesterly strike.

4.5.3 Final Hypocentral Distribution

Significant differences are evident between the original and final hypocentral locations.

After relocation the Bjarnarflag cluster appears to be much more compact, lying between about 1.9–2.8 km depth compared with 2–4 km originally (compare figures 3.8 and 4.24). It is still bound to the north by an 80° southward dipping plane which intersects the surface at Bjarnarflag. The cluster still appears convex in shape, with its maximum width changed to about 0.5 km at 2.2 km depth. In a perpendicular direction (figures 3.9a, 4.25a) the cluster now appears to be slightly narrower, at 0.3 km, and is still slightly sub–vertical.

Activity in the 'fissure zone' appears to be less diffuse on the final location plots than on those showing the original locations. The zone now appears to be more rectangular than elliptical in cross–section (figures 3.8 and 4.24), and plunges northwards at about 10°. The roof of the active zone appears more linear than before, reaching a minimum depth of about 1.2 km compared with 1.7 km. The base of the most intense area of activity is also linear, plunging northwards at about 10° from the northernmost tip of the Bjarnarflag cluster. Two sub–vertical earthquake lineations running through the 'fissure zone' are visible. One extends between depths of about 1.3–2.6 km at an offset of about 5.6 km on figure 4.24, and the other is at the northern edge of the zone — at an offset of about 7.7 km — between 1.6–3.0 km depth. In a perpendicular direction (figures 3.9b, 4.25b) the 'fissure zone' still appears to be about 0.3–0.4 km wide, but no longer has a coherent dip to the west.

Activity in the Leirhnjúkur cluster takes on a very different form when events are relocated using the three–dimensional velocity model. The active zone has been relocated to lie between 0–2.3 km depth (figures 4.24, 4.25c) compared with 1.5–3.5 km using the original model (figures 3.8, 3.9c). The previously observed lineation of events up to Hvíthólar at the surface is no longer clear and the densest part

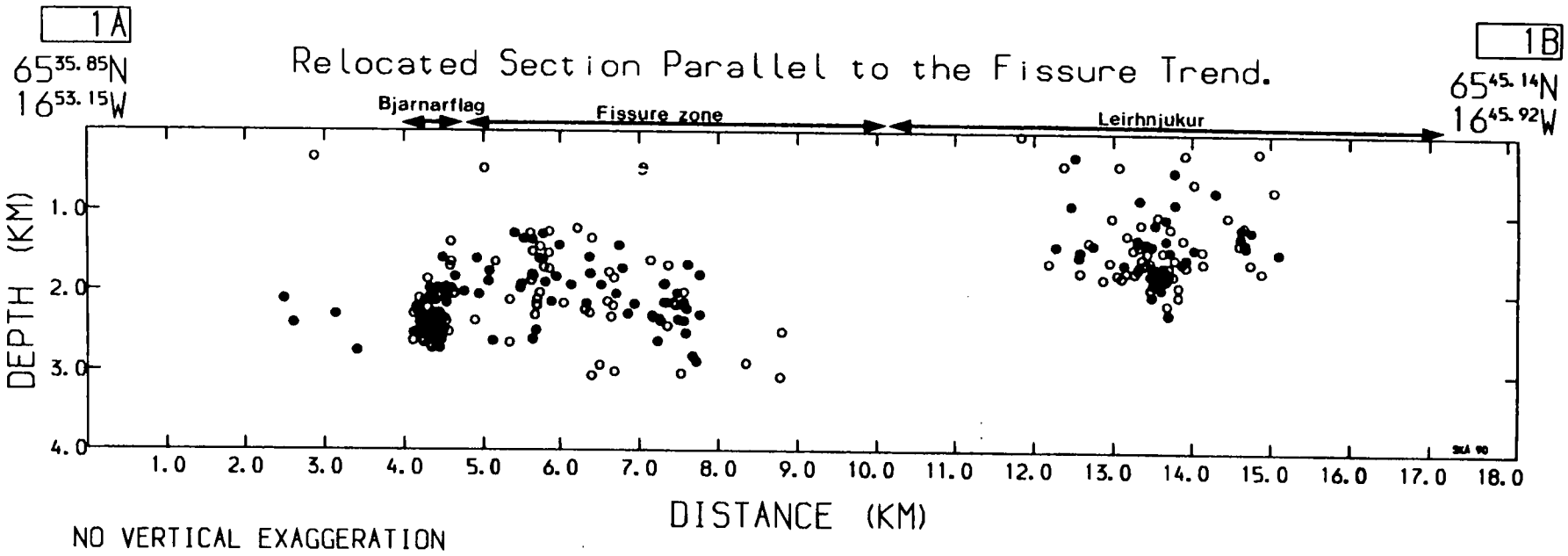

Figure 4.24 : The final hypocentres along cross-section 1A–1B of figure 4.23, which is parallel to the trend of the surface fissure swarm.

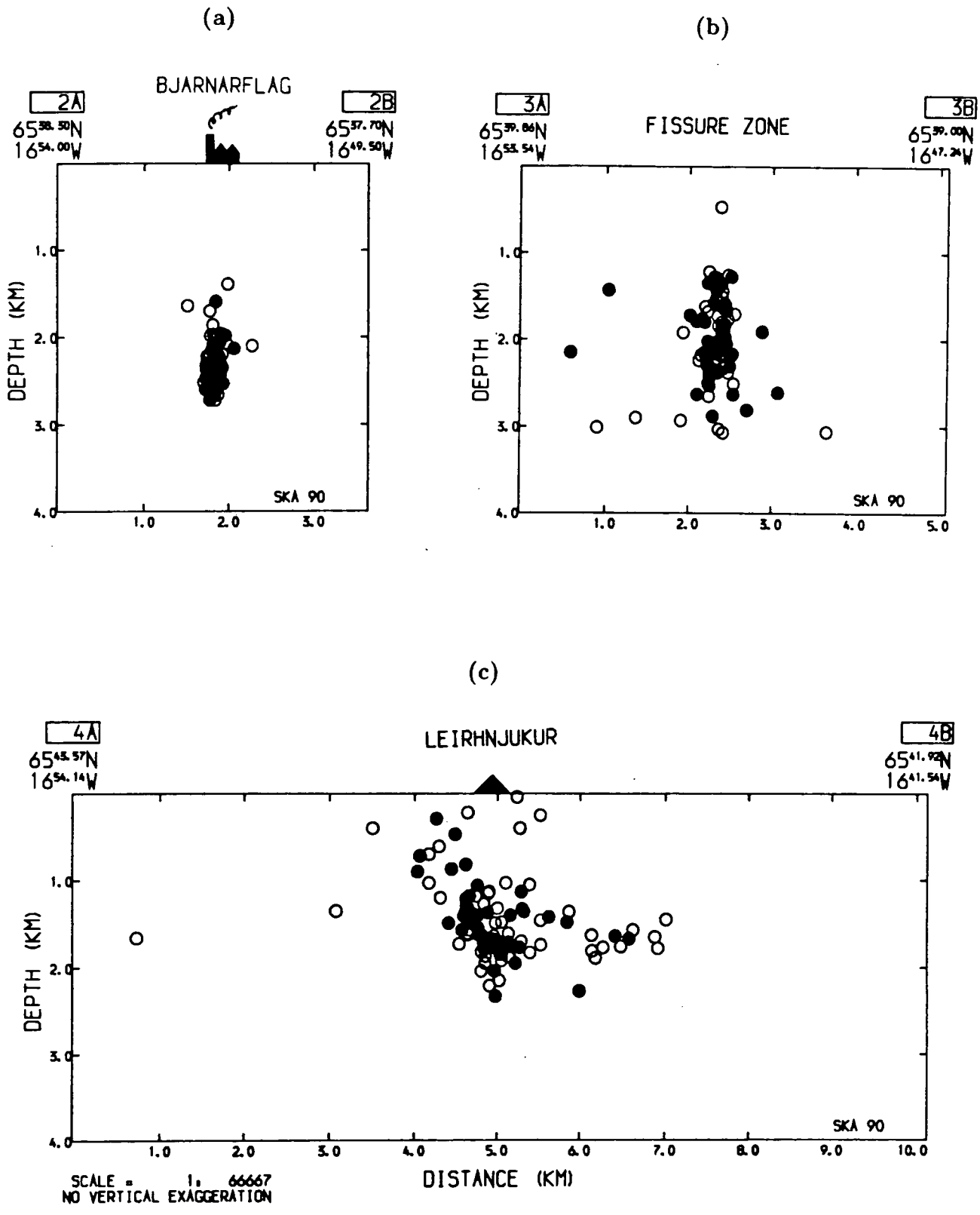

Figure 4.25 : Final hypocentres along cross-sections perpendicular to the trend of the surface fissure swarm. **(a)** Section 2A–2B across the Bjarnarflag cluster. **(b)** Section 3A–3B across the 'fissure swarm'. **(c)** Section 4A–4B across the Leirhnjúkur cluster.

of the cluster now lies in the centre, close to the greatest depth (figure 4.24). At right angles to this (figure 4.25c), activity extending from the north of the cluster projects up to the surface near the hill Leirhnjúkur (figure 2.3), while that to the east occurs at a depth of about 1.7 km beneath the slopes of the Mt. Krafla.

4.6 Summary

The simultaneous tomographic inversion of 1771 P–wave arrival times was carried out using the program SIMUL3 (Thurber, 1985), which performs the iterative simultaneous inversion of earthquake hypocentres and origin times, and three–dimensional P–wave velocity structure by minimizing r.m.s. travel–time residuals. Initial tests were carried out in order to determine the best starting one–dimensional velocity model and damping value. A relatively dense configuration of velocity nodes was found to yield the best inversion solution in terms of variance reduction and image fidelity. A value of the derivative weight sum, which is related to the density of rays passing close to a velocity node, was selected to indicate the volumetric limits of good resolution.

Several significant volumes of relatively high and low velocity have been outlined by this procedure. High–velocity bodies are found to exist at the western, eastern and northern edges of the Krafla caldera, and at the southern part of the seismometer network, beneath the ash cone Hverfjall. Low velocity zones exist within the Krafla caldera on the western flank of Mt. Krafla and slightly west–northwest of Leirhnjúkur. Other volumes of relatively low velocity exist to the north and west of Bjarnarflag near the surface, to the southwest of the caldera, in the southeast of the imaged area at about 1 km depth, and another one plunges to the northeast and southwest from about 2 km depth beneath Bjarnarflag.

The earthquakes have virtually all been relocated to significantly shallower depths with the overall increase in the velocity field. The Bjarnarflag cluster has become tighter and the fissure zone of activity has become more sharply defined compared with the original locations using the original one–dimensional velocity model. The Leirhnjúkur cluster has a clearer core and its subsidiary activity to the north extends to the surface near the hill Leirhnjúkur, while that to the east occurs at about 1.7 km beneath the slopes of the Mt. Krafla.

Chapter V

Focal Mechanisms

5.1 Introduction

Prior to the NISE–85 experiment, very little was known about the type of earthquake focal mechanisms from the Krafla area. Ward et al. (1969) published a composite solution of 14 events which had been observed using a tripartite array. If slip had occurred on a fault plane which was parallel to the fissure swarm then this solution indicates sinistral strike–slip motion with a component of thrust. Composite solutions have also been determined for events which occurred during one of the recent dyke injection events in the Krafla area (Brandsdóttir and Einarsson, 1979). These solutions are consistent with normal faulting which had been observed at the surface during the same period. More detailed studies of local earthquake focal mechanisms have been carried out on other parts of the Icelandic rift axis. On the Reykjanes Peninsula (Klein et al., 1977) and at the Hengill triple junction (Foulger, 1988b), a large proportion of the solutions indicated normal and strike–slip motion in response to a component of minimum compressive stress which was approximately horizontal and orientated perpendicular to the strike of surface extensional features. At Hengill, about half the events studied could not be interpreted using a double couple model but were interpreted as tensile crack earthquakes resulting from geothermal heat loss in an extensional stress field.

If these observations are considered, it might be expected that focal mechanisms observed during this study would be influenced by a variety of geological processes. Regional extensional stresses are likely to be reduced substantially from previous levels at the end of a major rifting episode, and so a reduced proportion of extensional events might be expected. It also seems likely that the influence on the local stress field of the Krafla central volcano would depend on its state of inflation and reduce with distance from it. Superimposed onto this already complex picture is the influence of the Krafla and Námafjall geothermal areas. What mode of

fracturing would be expected in these areas in the presence of a post–rifting stress field ?

The source mechanism of an earthquake is often inferred from the distribution of far field P–wave first motion polarities projected onto a sphere centred on its focus. The upper or lower hemisphere is then mapped onto a plane using a stereographic or equal area projection. The position of a given seismic station on the focal sphere is described by the azimuthal and take–off angles of a ray travelling from the earthquake focus to the station, which are calculated during the hypocentral location process (section 3.3.3). This method of focal mechanism determination is particularly suitable when only vertical component seismograms are available, in which case most of the recoverable polarity information is derived from the initial P–waves. For an earthquake resulting from shear slip on a buried planar fault in an isotropic medium, the P–wave radiation pattern will consist of compressional and dilatational quadrants which, when projected onto the focal sphere, can be separated by two orthogonal planes known as nodal planes (section 5.2.2). One of these nodal planes represents the fault plane.

There are several potential problems with this traditional approach to earthquake source determination. It assumes *a priori* that all earthquakes result from shear slip on planar faults and that other effects do not significantly distort the radiation pattern, and orthogonal nodal planes are typically drawn regardless of whether all the data are consistent with that interpretation. This method has been widely adopted by the seismological community because much observational data fit this theory. However, a significant volume of data cannot be explained in this way.

Non–orthogonal nodal planes are required for many events originating at the Mid–Atlantic Ridge and its continuation onto the Reykjanes Ridge (e.g. Sykes, 1967, 1970; Klein et al., 1977; Einarsson, 1979; Toomey et al., 1985). A reduced dilatational field for these events has been attributed to the focussing of down–going rays through a sub–crestal magma chamber (Solomon and Julian, 1974), small scale lateral heterogeneity (Klein et al., 1977; Einarsson, 1979), interference between P, pP and sP phases (Tréhu et al., 1981; Einarsson, 1987) and to small errors in focal depths or in the assumed velocity model (Toomey et al., 1985). Tréhu and Solomon (1983) accounted for non–orthogonality of nodal planes for

events at the Orozco Transform by studying lateral velocity heterogeneity, and it has been shown that anisotropy in the source medium can have a similar effect (Kawasaki and Tanimoto, 1981).

Other workers have invoked non–double couple earthquake mechanisms to explain unusual seismic radiation patterns. Chouet (1979) attributed a complete field of compressional first arrivals around sources on the crust of the Kilauea Iki lava lake to the opening of tensile cracks due to cooling. At the Hengill ridge-ridge-transform triple junction in Southwest Iceland, about half the seismic events studied could not be interpreted as double couple earthquakes using first motions and were attributed instead to tensile crack formation (Foulger and Long, 1984; Foulger, 1988b). They observed that these non–double couple events were restricted to a high temperature geothermal area and were interspersed with shear events, and concluded that propagation effects could not therefore account for the non–double couple radiation patterns. Shimizu et al. (1987) envisaged a coupled tensile crack/shear faulting mechanism to account for short–period radiation patterns of earthquakes occurring around the Miyakejima volcano, Japan. They found that events originating at a short distance from eruptive fissures showed compressional P–wave first motions, which they related to the sudden opening of tensile/shear cracks due to the excess pressure of intrusive magma. Events originating from the fissures showed dilatation arrivals and were related to tensile/shear crack closure due to a decrease in magmatic pressure in the fissures following an eruption. Wong and M^{c}Garr (1988) reviewed several reports of apparent implosional focal mechanisms associated with coal mining and suggested a mechanism of cavity collapse which would produce the observed S–wave radiation patterns as well as the exclusively dilatational P–wave first motions.

Three large earthquakes which occurred during an intense period of activity at Long Valley, California have received considerable attention because of their unusual seismic radiation patterns. Given et al. (1982) inverted surface–wave data to determine the moment tensor for the largest event and found that their double couple solution was not consistent with that derived by using short–period first motions. Propagation effects (Wallace et al., 1983; Given et al., 1982; Barker and Langston, 1983) and simultaneous multiple ruptures (Barker and Langston, 1983;

Ekström, 1983) have been proposed as possible explanations for the unusual radiation patterns, but seem incompatable with the geology of the area (Julian and Sipkin, 1985). A simpler and perhaps more plausible mechanism of tensile failure under high fluid pressure was invoked by Julian (1983) using the compensated linear vector dipole (CLVD) source model (Knopoff and Randall, 1970), and he suggested that the events were generated by dyke injection. However, by studying the effects of the non–double couple source on body wave synthetics, Wallace (1985) found that the CLVD mechanism was not well resolved in the long–period Long Valley data.

There is controversy associated with the interpretation of events with anomalous radiation patterns as non–shear events, since the motions recorded on a seismometer result from both propagation and source effects. Equation 5.9 (section 5.2.2), which describes the amplitude distribution for P–waves in the far–field, is only valid for simple slip on planar shear faults occurring in isotropic media when observed at far–field distances. It has been shown that serious departures from these requirements can result in amplitude fields which cannot be interpreted by conventional means, e.g. multiple events; non–planar faults; anisotropic media or non–double couple source mechanisms. It is important, but sometimes not easy, to correct for as many sources of bias as possible. The correct identification of phases is essential. Of common concern, particularly in local earthquake studies, are the effects of lateral inhomogeneities in the local seismic velocity structure and of errors in the calculated focal depth. If such effects are not corrected for, the radiation field observed at seismic stations will be incorrectly mapped on to the focal sphere. Furthermore, the double couple representation of a seismic source is only valid for far–field distances, that is at positions that are 'more than a few wavelengths away from the source' (Aki and Richards, 1980; p88), where waves can be treated as though they were plane waves.

5.2 Representation of a Seismic Source

5.2.1 Introduction

The seismic waves generated by fault slip are the same as those generated by a distribution on the fault of certain forces with cancelling moment. For a given fault slip this distribution is not unique, but in an isotropic medium it can always be chosen as a surface distribution of double couples (Aki and Richards, 1980).

The strength of a shear fault source is described by the moment of the constituent couples. The seismic moment is defined as : -

$$M_o = \mu \tilde{u} S \qquad 5.1$$

where μ is the Lamé shear modulus, $\tilde{u}$ is the mean displacement on the fault, and S is the area of the faulting surface (e.g. Aki, 1966).

The seismic moment tensor $\mathbf{M}$, which is a function of space and time, is introduced in order to describe sources which are more general than double couples and to make it easier to deal with coordinate system rotations. $\mathbf{M}$ depends on the source strength and fault orientation, and it characterizes all the information about the source that can be observed (Aki and Richards, 1980). For a shear source, the seismic moment M_o is the absolute value of the (equal) principal moments of $\mathbf{M}$. In general, the equivalent force system corresponding to a dislocation on an infinitesimal surface element $d\Sigma$ can be represented as a combination of the 9 couples illustrated in figure 5.1, the strength of which are given by the elements of the moment density tensor $\mathbf{m}$. Then elements of the seismic moment tensor $\mathbf{M}$ can be expressed as : -

$$M_{ij} = \iint_{\Sigma} m_{ij} d\Sigma \qquad (i,j = x,y,z \ \ directions) \qquad 5.2$$

The idealized displacement field in an isotropic medium is a solution of the elasto-dynamic equation of motion, which can be solved using the Green's function.† It can be shown (e.g. Aki and Richards, 1980) that for a dipolar point source with moment tensor $\mathbf{M}$, the displacement in the n-direction at a point $(\mathbf{X}, t)$ is given by : -

$$u_n(\mathbf{X}, t) = M_{ij} * \frac{\partial G_{ni}}{\partial \xi_j} \qquad 5.3$$

† The Green's function $G_{ij}(X,t)$ is defined as the ith component of the displacement at X caused by an impulsive point force in the j-direction applied at the source.

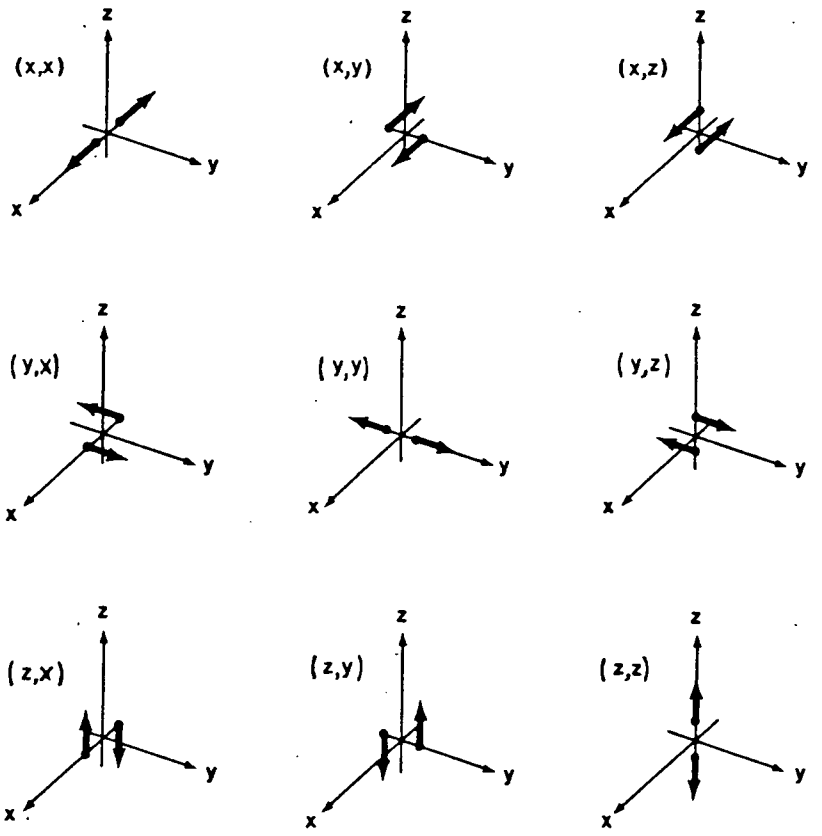

Figure 5.1 : The nine possible couples that are required to obtain equivalent forces for a generally oriented displacement discontinuity in anisotropic media (adapted from Aki and Richards, 1980). Note the symmetry, which reduces the number of independent components of the moment tensor to 6.

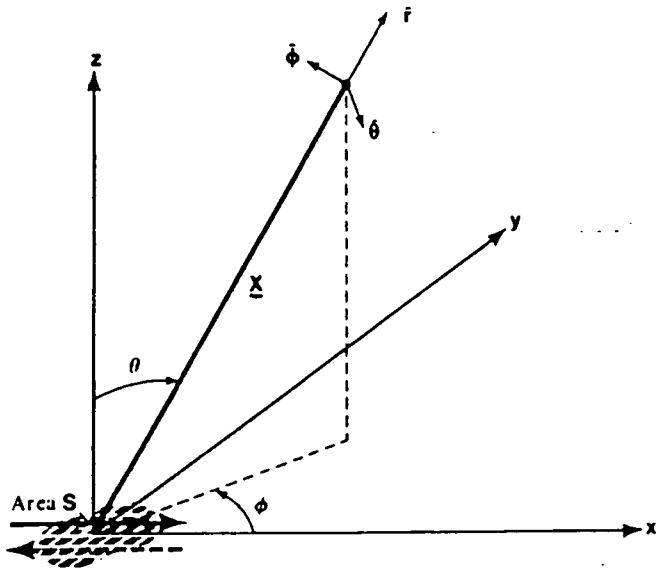

Figure 5.2 : Cartesian and spherical polar coordinates for analysis of radial and transverse components of displacement radiated by a shear dislocation of area S and average slip $\tilde{\mathbf{u}}$ (adapted from Aki and Richards, 1980).

where ξ_j is the jth source coordinate.

A common geophysical problem is that of synthesizing a model of the seismic source using a finite series of displacement measurements which have been observed on the Earth's surface. This is an inverse problem and its solution is non–unique. Any given set of seismograms could be produced by more than one source mechanism.

5.2.2 Moment Tensor Representation

The moment tensor is conventionally expressed in cartesian coordinates. In the frequency domain, let it be given by : –

$$\mathbf{M} = \begin{pmatrix} M_{xx} & M_{xy} & M_{xz} \\ M_{yx} & M_{yy} & M_{yz} \\ M_{zx} & M_{zy} & M_{zz} \end{pmatrix} \tag{5.4}$$

whose six independent components can be arranged as a column vector : –

$$\mathbf{M}' = (\, M_{xx} \quad M_{xy} \quad M_{yy} \quad M_{xz} \quad M_{yz} \quad M_{zz} \,)^T \tag{5.5}$$

Following Julian (1986), equation 5.3 can be written as : –

$$\mathbf{u} = \mathbf{G}^T \mathbf{M}' \tag{5.6}$$

where : –

$$\mathbf{G} = (\, G_{xx} \quad G_{xy} \quad G_{yy} \quad G_{xz} \quad G_{yz} \quad G_{zz} \,)^T \tag{5.7}$$

is a column vector whose components are spectra of Green's functions. $\mathbf{G}$ depends on the type of seismic wave and the positions of the source and receiver. The components of $\mathbf{G}$ (in the time domain) for far–field P–waves in a homogeneous medium are given in table 5.1. The coordinate system used in this analysis is illustrated in figure 5.2.

For a shear dislocation in the x–y plane with motion in the x direction, the moment tensor can be given by : –

$$\mathbf{M}' = M_0 (\, 0 \quad 0 \quad 0 \quad 1 \quad 0 \quad 0 \,)^T \tag{5.8}$$

Component	Green's Function
G_{xx}	$sin^2\theta cos^2\phi$
G_{xy}	$sin^2\theta sin2\phi$
G_{yy}	$sin^2\theta sin^2\phi$
G_{xz}	$sin2\theta cos\phi$
G_{yz}	$sin2\theta sin\phi$
G_{zz}	$cos^2\theta$

The common factor of $\frac{1}{4\pi\rho\alpha^3 r}\frac{\partial}{\partial t}M_o(t-\frac{r}{\alpha})$ has been omitted, where t is time, r is the distance to the observation point, ρ is the density at the source, and α is the P-wave velocity at the source ($\alpha = \sqrt{\frac{\lambda+2\mu}{\rho}}$, where λ and μ are Lamé elastic moduli). A right handed coordinate system is assumed, with the z-axis directed downwards. θ is the angle between the ray direction and the $+z$-axis; ϕ is measured from the $+x$-axis towards the $+y$-axis. If the $+x$-axis is directed northwards then the definitions agree with the conventional definitions of take-off angle and azimuth (adapted from Julian, 1986).

Table 5.1: Green's functions for P-waves.

Seismic radiation patterns are traditionally studied using projections of the focal sphere and it is therefore convenient to use spherical coordinates to express the displacement field. Following Aki and Richards (1980), the displacement field for a P-wave observed in the far field at the position vector $\mathbf{r}$ and time t can be given in spherical coordinates by : -

$$\mathbf{u}(\mathbf{r},t) = \frac{sin2\theta cos\phi}{4\pi\rho\alpha^3 r}\frac{\partial}{\partial t}[M_o(t-\frac{r}{\alpha})]\,\hat{\mathbf{r}} \qquad 5.9$$

The P-wave amplitude distribution varies with $sin2\theta cos\phi$, which equals zero when the ray take-off direction is parallel with the fault plane ($\theta = \frac{\pi}{2}$) or at right angles to it on the so called 'auxiliary' plane ($\phi = \frac{\pi}{2}$). A sphere centred at the effective point source of a shear event will exhibit a P-wave radiation pattern which is split into four sectors of alternating polarity by two perpendicular nodal planes. One of these planes represents the fault plane and the other the auxiliary plane; the two are indistinguishable in the point source approximation. Figure 5.3 illustrates the far-field radiation pattern.

Non-shear sources can also be modelled using the moment tensor. For example, a

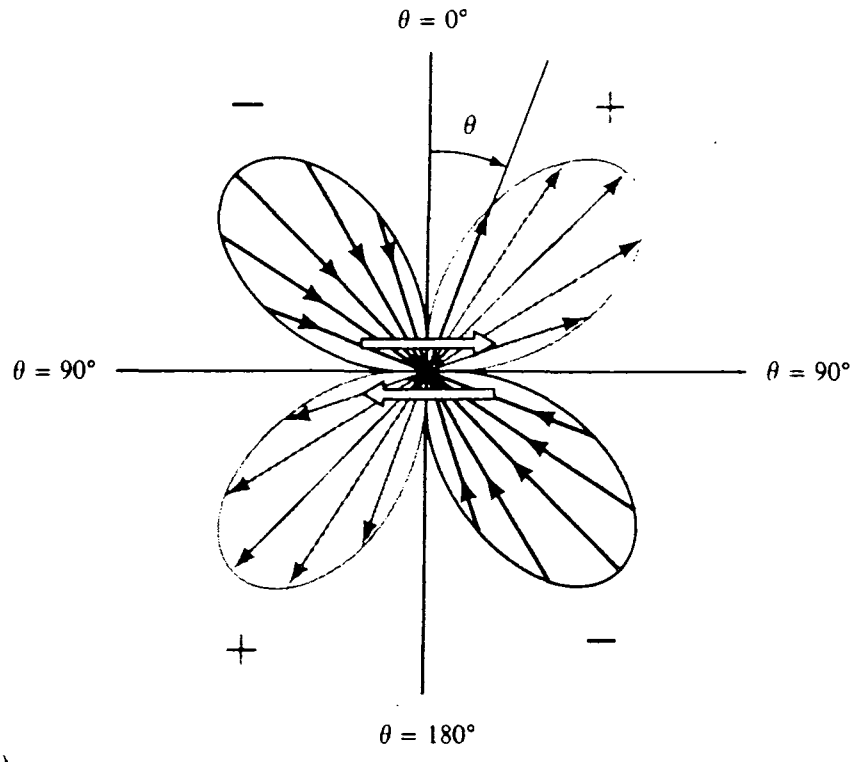

(a)

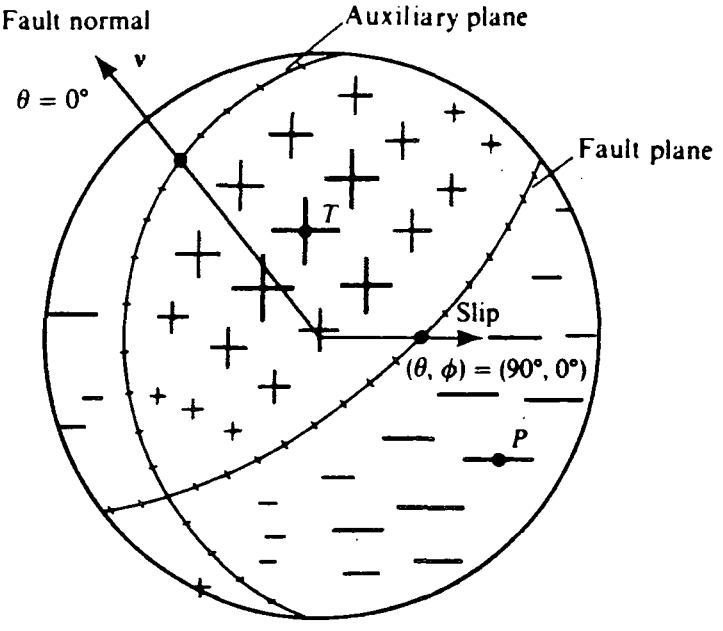

(b)

Figure 5.3 : Diagrams for the radiation pattern of the radial component of displacement due to a double couple, i.e., $sin2\theta cos\phi\hat{\mathbf{r}}$. **(a)** The lobes are a focus of points having a distance from the origin that is proportional to $sin2\theta$. The diagram is for a plane of constant azimuth, and the pair of arrows at the centre denote the shear dislocation. Note the alternating quadrants of inward and outward directions. In terms of far-field P-wave displacement, plus signs denote outward displacement (if $M_o(t - \frac{r}{\alpha})$ is positive), and minus signs denote inward displacement. **(b)** View of the radiation pattern over a sphere centred at the origin. Plus and minus signs of various sizes denote variation (with θ, ϕ) of outward and inward motions. The fault plane and the auxiliary plane are nodal lines (on which $sin2\theta cos\phi = 0$). An equal-area projection has been used. Point P marks the pressure axis, and T the tension axis (from Aki and Richards, 1980).

compensated linear vector dipole (CLVD) equivalent force system acting with its strongest dipole oriented in the z direction has a moment tensor of : -

$$\mathbf{M}' = M_o \, (-1 \quad 0 \quad -1 \quad 0 \quad 0 \quad 2)^T \qquad 5.10$$

The CLVD may be thought of as a point force system without net force or torque that has no explosive, implosive, or double couple component. It has been used to describe unusual seismic radiation patterns observed at Long Valley in 1980 (Julian, 1983), and as the theoretical basis for seismic dyke emplacement. The displacement field for such a source is given by : -

$$\mathbf{u}(\mathbf{r}, t) \; \propto \; 2cos^2\theta - sin^2\theta \qquad 5.11$$

$$\mathbf{u}(\mathbf{r}, t) \; = \; 0 \qquad when \; \theta \approx 55^\circ$$

The P-wave nodal surfaces for such a source form cones which have their axes colinear with the strongest dipole. If the source is generated on a vertical plane, the nodal lines form small circles which are symmetrical on the upper hemisphere of the focal sphere and are separated by about 70°.

Seismic sources can be described generally by using only those couples with force and arm in the same direction (figure 5.1), by an appropriate rotation of the coordinate system. That is, the point source equivalent of any seismic source can be represented by three mutually orthogonal linear vector dipoles (e.g. Aki and Richards, 1980). The ratio of the principal moments may be expressed by : -

$$(a, b, c) \qquad 5.12$$

For a shear source, the ratio of these principal moments is $(1, 0, -1)$. There is no volumetric component because $a + b + c = 0$. The CLVD is an example of a non-double couple source which conserves volume, having its principal moments in the ratio $(-1, -1, 2)$. The tensor representation can be manipulated to model any source, regardless of whether or not it involves a component of volume change, as a linear combination of simpler sources. For example, Foulger and Long (1984)

modelled events which were characterized by a narrow dilatational belt on the focal sphere by combining a tensile crack with a spherically symmetrical implosion : -

$$[(\lambda + 2\mu), \lambda, \lambda] + [-(\lambda + \delta), -(\lambda + \delta), -(\lambda + \delta)] = [(2\mu - \delta), -\delta, -\delta] \qquad 5.13$$

This involves a volume increase ($a+b+c > 0$) and is close to a linear vector dipole. Shimizu et al. (1987) combined a shear slip with an opening or closing tensile crack to account for observations of focal spheres dominated by compressions or dilatations.

5.3 The Data

5.3.1 Introduction

Focal mechanisms have been determined manually for 153 of the best located earthquakes using the method described by Lee and Stewart (1981, p 141–146). Figure 5.4 illustrates the quality of data used for focal mechanism determination. Only polarities from impulsive P–wave first motions were used. The minimum number of data points used to constrain any one solution is 9. The seismometer polarities were tested using both explosions and teleseisms and were therefore reliably known throughout the recording period. The ray take–off and azimuthal angles which were used initially were those computed by HYPOINVERSE using the original velocity structure (chapter 3). Most of the rays were up–going, as shown in appendix A, and so first motions were plotted on upper hemisphere Wulff stereographic nets. However, as a result of the relatively shallow hypocentral depths, down–going rays were quite often the first arrivals at more distant stations, and their polarities have therefore been projected on to the upper hemisphere to contribute to the information used in the solutions. The solutions are shown on the left hand side of each pair of plots in Appendix E. They are split into three sections, according to the epicentral zones in which the events occur : 'Bjarnarflag', the 'fissure zone' and 'Leirhnjúkur' (see section 3.3.5.3 for a definition of these zones). The events for which double couple solutions could not be obtained are discussed fully in section 5.3.4.

5.3.2 Removal of Biases

5.3.2.1 Introduction

The initial focal mechanisms were derived using the azimuthal and take–off angles computed by HYPOINVERSE for location through the original one–dimensional velocity structure. However, the results of the tomographic study (chapter 4) showed that two potentially important sources of bias would affect the first P–wave focal mechanisms determined using this dataset : the use of incorrect hypocentral depths and of incorrect raypaths. Hypocentral depths were found to occur at shallower depths, typically about 0.8–1.0 km nearer the surface, as a result of an overall increase in the average seismic velocity at all depths imaged (appendix D).

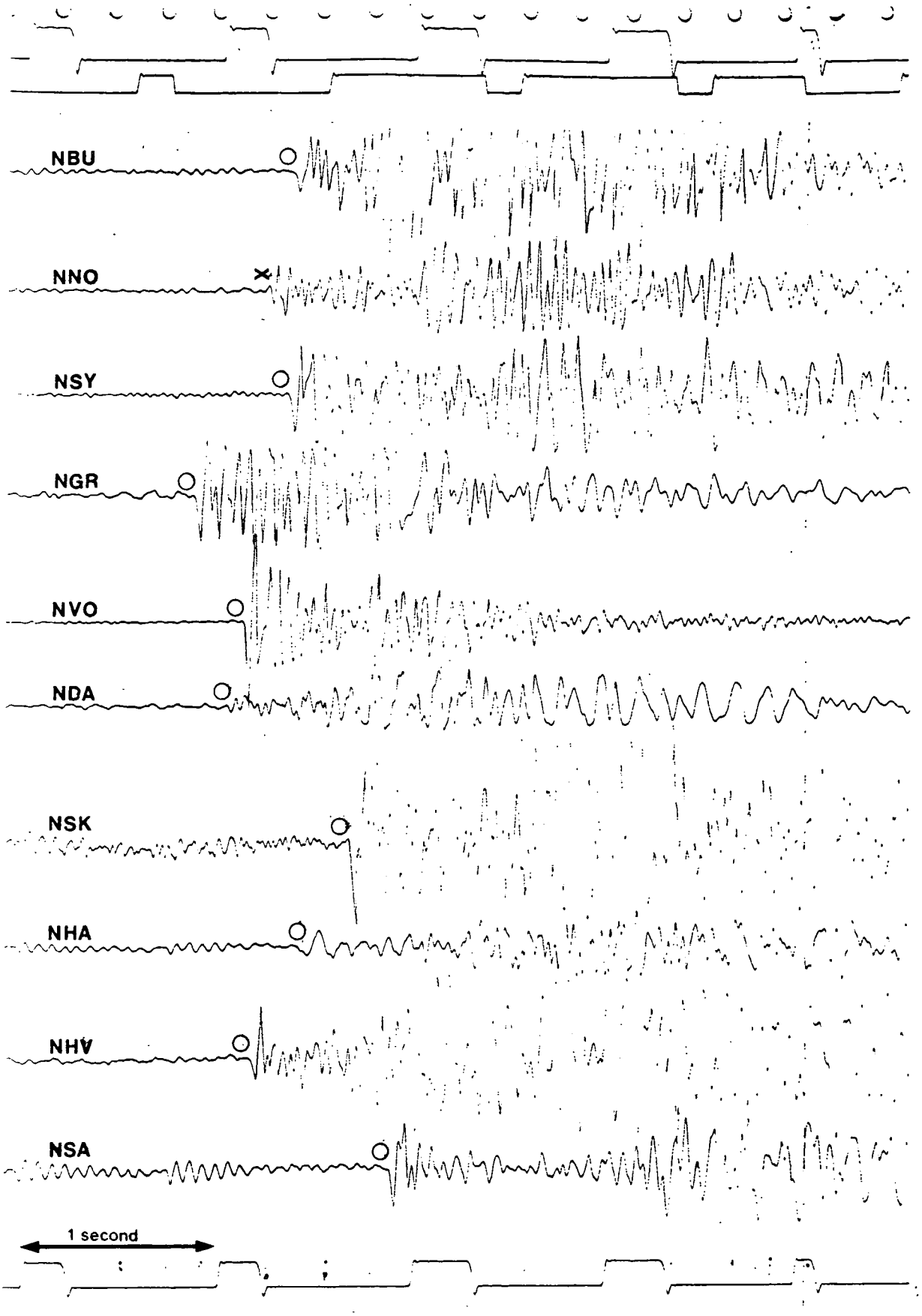

Figure 5.4 : First arrivals at stations recorded by Geostore 'NW' for event 850806 1548 at Bjarnarflag.

In addition, significant lateral inhomogeneity in velocity was discovered. To the author's knowledge, no other first P–wave polarity focal mechanisms have been published with these biases removed.

5.3.2.2 Software

The computer program BENDRAY (B.R. Julian, unpublished) computes the take–off and emergence angles of seismic rays propagating between any two points through a three–dimensional velocity structure. BENDRAY uses the 'bending' method of Julian and Gubbins (1977) to find the optimum (fastest) raypath between the two end points. The program begins by estimating a raypath which is bent until it satisfies the Fermat principle of stationary time with respect to small path variations. The program does sometimes fail to converge on a raypath solution, which happens under several circumstances, e.g. if no raypath exists (i.e. in a shadow zone), or if the initial estimate of the raypath is not close enough (B.R. Julian, pers. comm.). The program RUNNETS (B.R. Julian, unpublished) can then be used to plot the changes in the positions of stations on the upper hemisphere of a stereographic projection obtained using different input models. RUNNETS incorporates the plotting program ONNET (A. Michael, unpublished), which was used to plot all solutions.

5.3.2.3 Application to the Data

Data can be corrected for the biases of using incorrect hypocentres and the incorrect velocity structure by using the software described above, and computing the take–off and azimuthal angles for rays travelling from the relocated hypocentres through the three–dimensional velocity structure. However, it is interesting to consider the individual effect of each source of bias on the data. This is demonstrated for one well–constrained event within the Bjarnarflag cluster in figure 5.5.

Figure 5.5a shows the original double couple solution (all rays shown were up–going). The figure also shows the change in the take–off and azimuthal angles caused by changing the velocity model from the original one–dimensional model used by HYPOINVERSE, to the 'evolved 1–d' model which was the input for the final run of the tomography program (figure 4.4) The effect of changing the one–dimensional model is negligible. Furthermore, the angles computed by BEN-

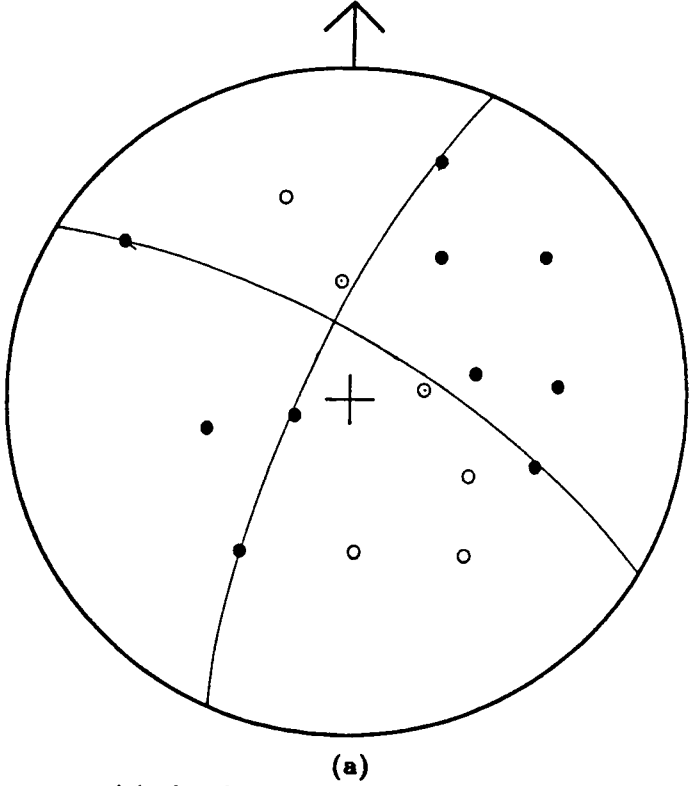

(a)
original 1–d model ⟹ 'evolved 1–d' model
original hypocentre

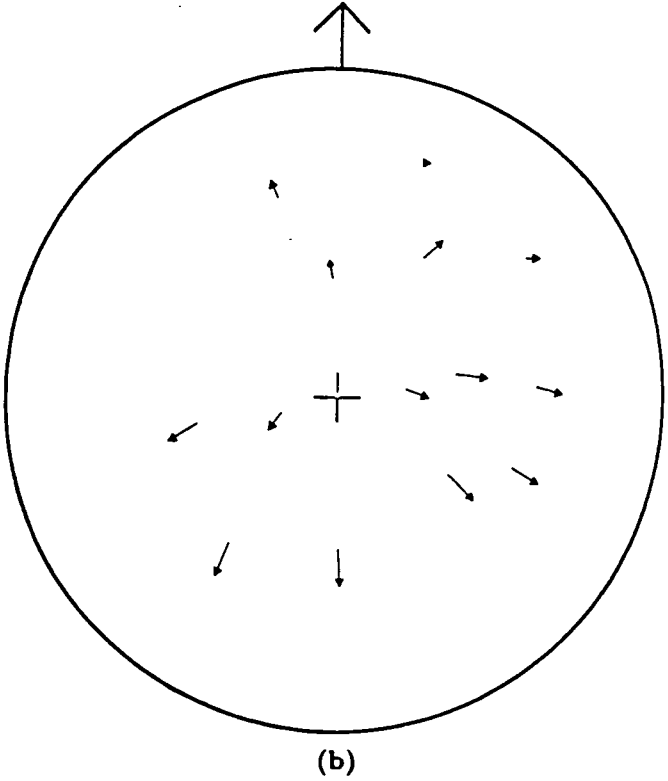

(b)
'evolved 1–d' model
original hypocentre ⟹ final (deeper) hypocentre

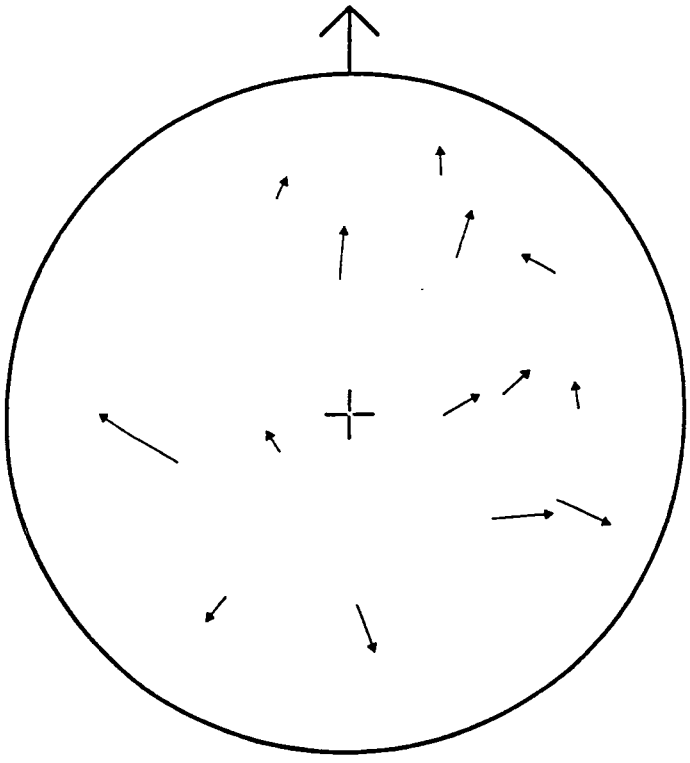

(c)
'evolved 1–d' model ⟹ final 3–d model
final hypocentre

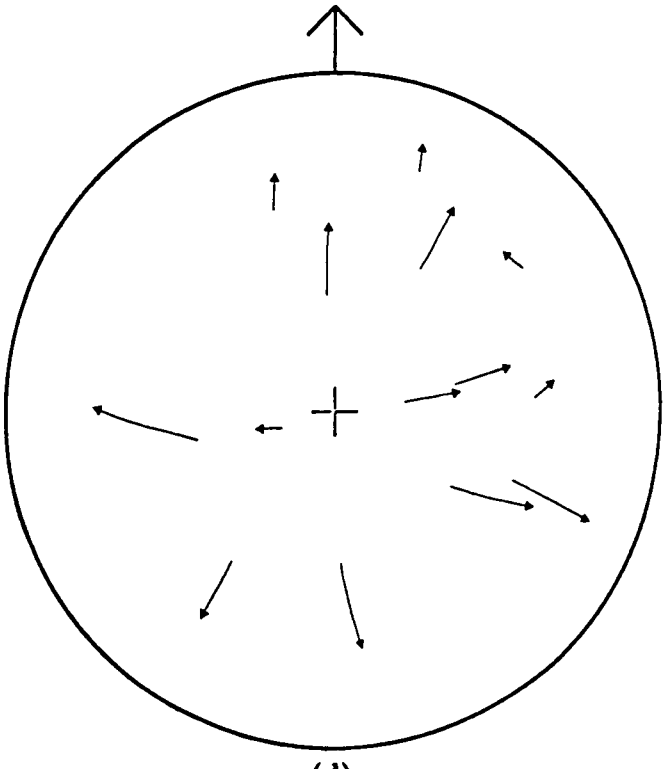

(d)
combined effect
original 1–d model ⟹ final 3–d model
original hypocentre ⟹ final hypocentre

Figure 5.5 : Removal of sources of bias from focal mechanism 850709 1954 at Bjarnarflag. All ray angles were computed by the program BENDRAY. **(a)** The effect of changing the 1–d velocity model used to compute rays from the original hypocentre output by HYPOINVERSE. Open and closed circles represent dilatational and compressional first P–wave motions, for which ray angles were computed using the 'evolved 1–d' model. They are joined by short arcs to the positions on the focal sphere of rays computed using the original one–dimensional model. Note that movement is very slight. **(b)** The effect of shallowing the hypocentre and moving the epicentre. The arrows show the changes in ray angles from the original hypocentre at 3.76 km to the relocated hypocentre at 2.59 km, 0.3 km to the NNW. **(c)** The effect of introducing a 3–d velocity structure. The arrows show the changes in ray angles from the relocated hypocentre when the velocity model was changed from the 'evolved 1–d' model to the final 3–d model. **(d)** The combined effect of removing all sources of bias shown in (a), (b) and (c).

DRAY for the original model are almost exactly the same as those computed by HYPOINVERSE.

Figure 5.5b shows the effect of a shallowing in the hypocentre from 3.76 km to 2.59 km and of moving it about 0.3 km to the north–northwest. All rays were computed using the 'evolved 1–d' velocity structure. The effect is generally greatest for distant stations (shallow take–off angles), and increases away from the direction of epicentral relocation. Changes in take–off angle range between about 0–10°, and changes in azimuth are slight.

Figure 5.5c shows the effect of changing the velocity structure from the 'evolved 1–d' to the final three–dimensional model. All rays originated from the relocated hypocentre at 2.59 km depth. The effects are large and variable. Take–off angles in this case have virtually all decreased, by between about 5–20°, as a result of elocation through the new model, and changes in azimuth vary between 0–15°.

Figure 5.5d shows the total effect of the removal of all sources of bias, and figure 5.6 illustrates the relative magnitudes of the hypocentral and velocity biases. It can be seen that in this case the overall result has been a very significant reduction in take–off angles — data points are pushed towards the edge of the stereographic projection by about 0–30° — and a change in azimuth by about 0–15°. Both individual sources of bias introduce a significant effect, but the bias introduced by the three–dimensional structure is the more serious.

Both sources of bias have been removed from all focal mechanisms. New solutions were then determined manually, and are shown next to the original solutions in appendix E. When data points were lost due to convergence failure, the redetermination of the focal mechanisms was carried out as though the missing arrivals had not moved from their original positions on the focal sphere. Solutions are therefore sometimes better constrained than they may appear. Convergence failure was found to be at its most serious for events occurring within the Krafla caldera, from which rays had to travel through volumes with the strongest velocity inhomogeneity. Only the effect of the velocity bias is demonstrated in each solution, and so the plots are of the same type as that in figure 5.5c.

As can be seen in appendix E, the effect on the ray take–off and azimuthal angles

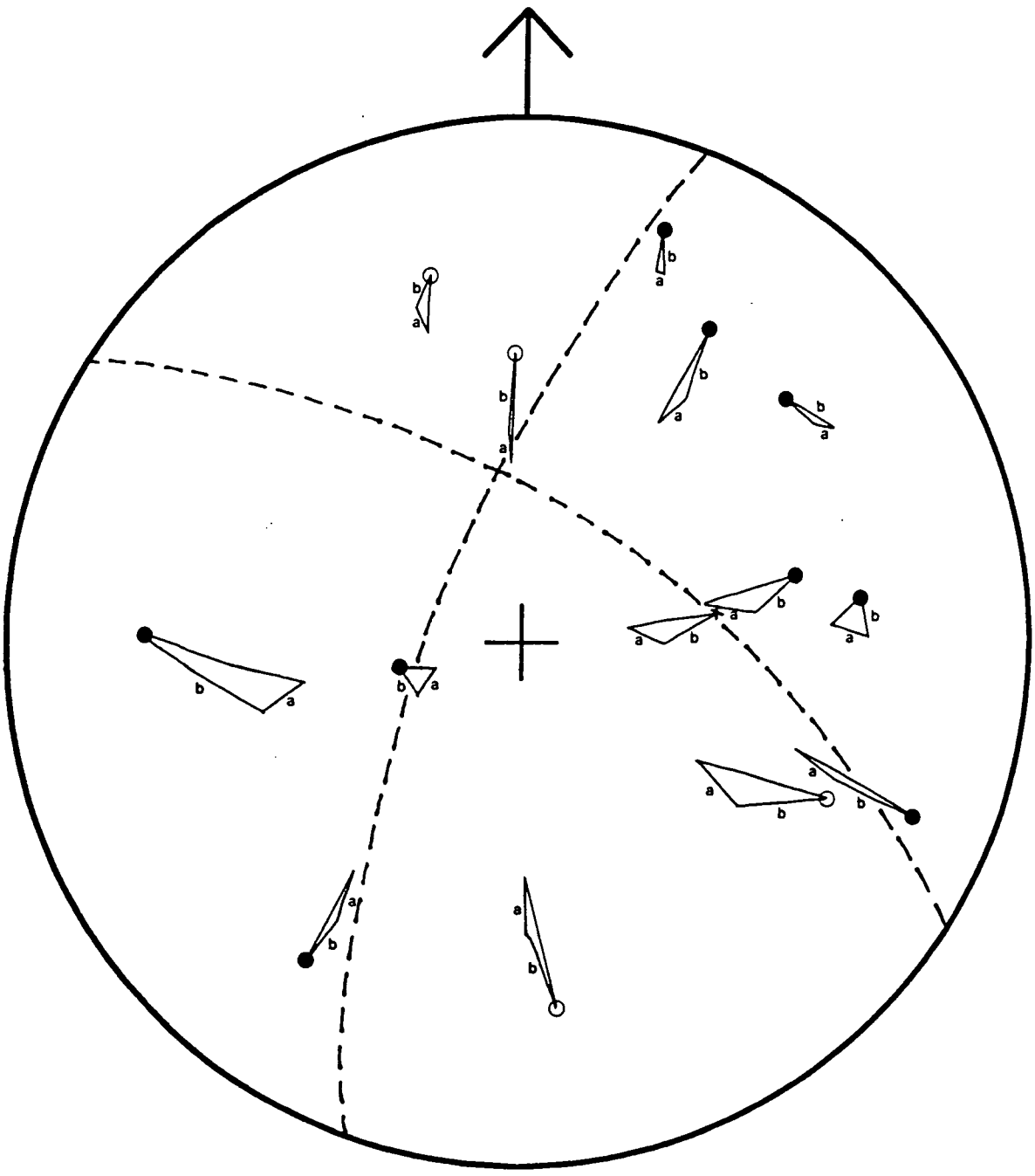

Figure 5.6 : The relative magnitudes of the hypocentral and velocity biases for event 850709 1954 at Bjarnarflag. The changes in ray angles caused by moving the hypocentre from the original to the final (deeper) location are shown by arcs *a*. The effect of changing the velocity model from the 'evolved 1-d' model to the final 3-d model is shown by arcs *b*. Open and closed circles represent the polarities of first P-wave arrivals whose raypaths have been corrected for bias. The new double couple solution is indicated.

of the velocity bias is often large. Typically, the change in take-off angle is about 10°, but can sometimes be as great as 30–40° or more. Take–off angles are more often reduced than increased, but this is by no means universal. The effect on ray azimuth is generally slightly less than that on take–off angle, about 0–10°, but can be as much as 15–20°. Figure 5.7 shows a comparative statistical summary of the focal mechanism interpretations before and after both sources of bias had been removed. It is interesting to note that whereas individual solutions were sometimes changed considerably, the overall picture remained the same.

5.3.3 Double Couple Events

5.3.3.1 Introduction

Over 90% of the polarity distributions could be interpreted by double couple solutions after sources of bias had been removed (figure 5.7). These events are discussed below in three sections, according to their epicentral locations. Figure 5.8 shows a statistical summary of the dominant component of shear slip present in each double couple solution for each epicentral zone, before and after the removal of bias. Small changes in the distribution of double couple types are due almost entirely to slight changes in the dominant components of shear.

For a double couple focal mechanism, the principal axes of the moment tensor are called the pressure (P), tension (T) and null axes. The P–axis projects through the centres of the dilatational quadrants of the focal sphere and the T–axis through the compressional quadrants. It is often assumed that the P– and T– axes are the axes of the principal stress directions. However, M^{c}Kenzie (1969) showed that when slip occurs on pre–existing faults, the principal stress directions can lie anywhere in their corresponding focal sphere quadrants. In the case when slip occurs along a fresh fault in homogeneous rock, the direction of maximum compressive stress lies between the P–axis and the fault plane.

5.3.3.2 Bjarnarflag

More than half the double couple focal mechanisms originated from the Bjarnarflag cluster (figure 5.8). Of the shear events at Bjarnarflag 49 (~70%) had a dominant strike–slip component (e.g. event 850827 1721), 15 events (~20%) resulted from

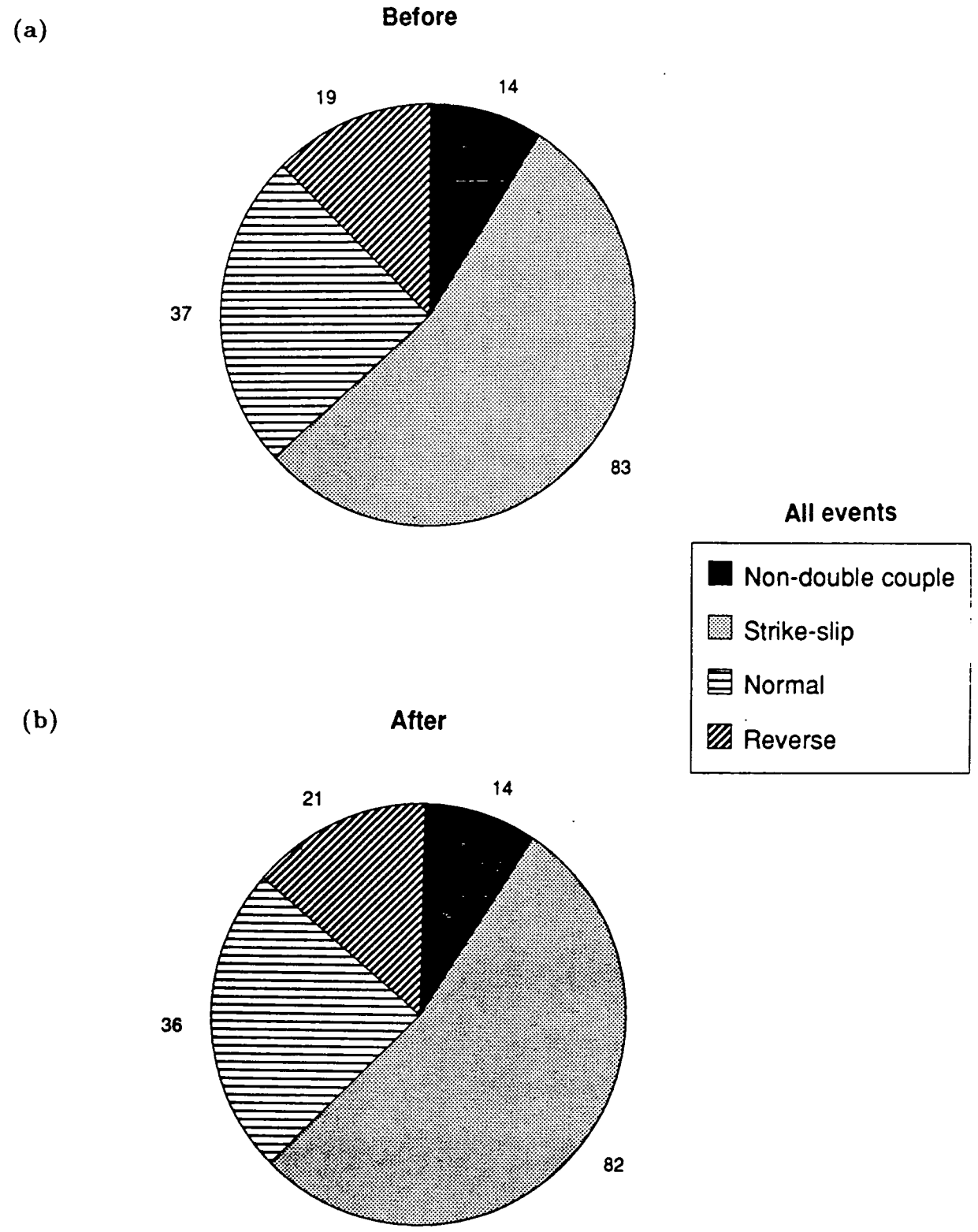

Figure 5.7 : A statistical break–down of all fault plane solutions **(a)** before and **(b)** after the removal of bias.

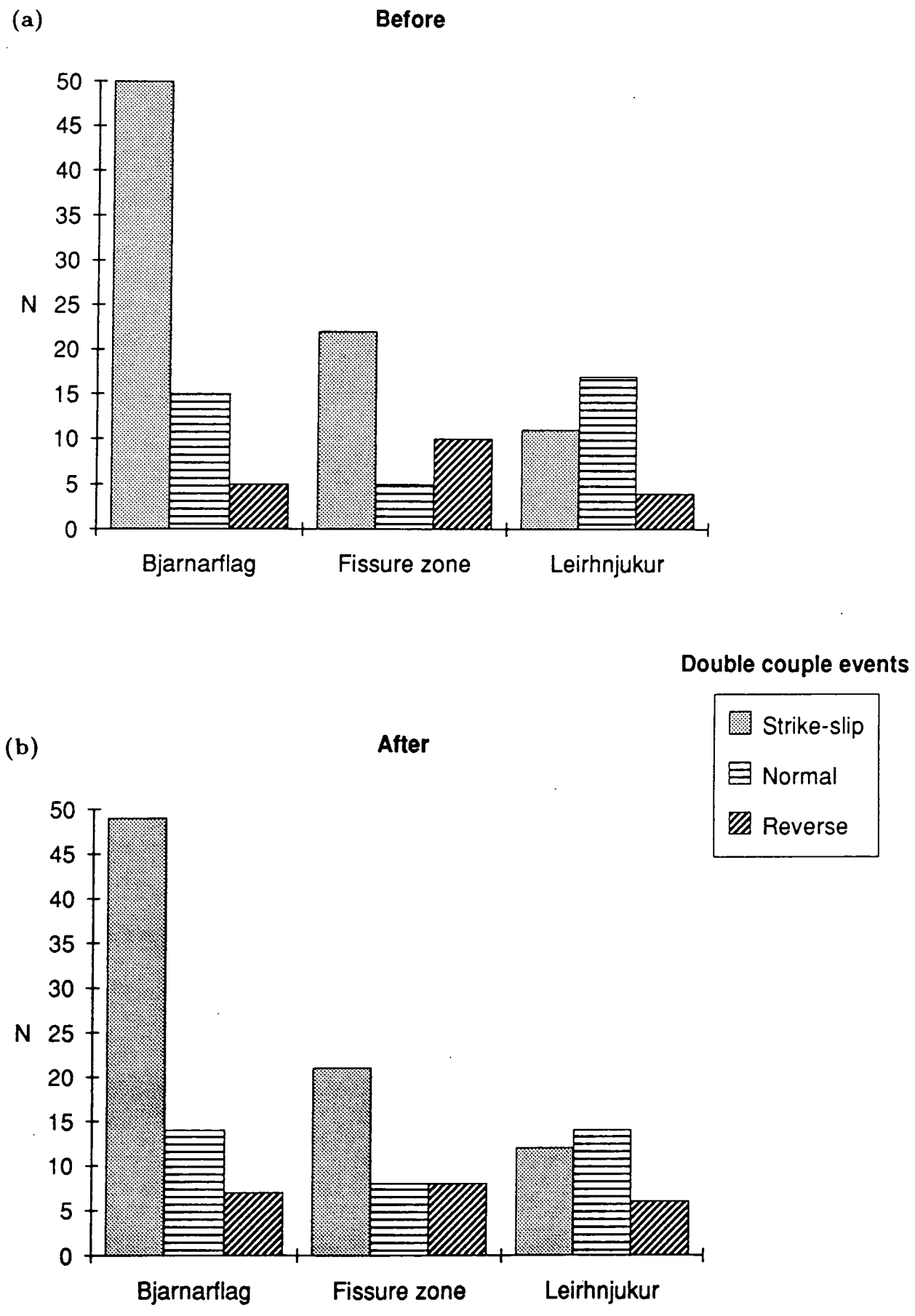

Figure 5.8 : A statistical break-down of double couple focal mechanisms according the epicentral location **(a)** before and **(b)** after the removal of bias.

normal faulting (e.g. event 850828 0120), and the other 7 (~20%) from reverse faulting (e.g. event 850721 0038). However, most strike–slip faults had a significant component of normal or reverse slip (usually normal), and virtually all normal and reverse events had a significant strike–slip component.

Figure 5.9 shows the P– and T–axes for the shear events at Bjarnarflag, with a summary plot of the nodal planes. Strike–slip was largely either on approximately vertical planes striking north to N25°E or on planes which dip steeply towards the north–northeast and strike between about N90°E and N110°E (figure 5.9b), although strike–slip motion along faults with different orientations was not uncommon (Appendix E.1). The sense of motion on these faults was irregular, for example if the north to N25°E striking planes were the fault planes, then approximately the same number of sinistral events occurred along these planes as dextral events (Appendix E.1). The orientation of nodal planes for normal and reverse faulting mechanisms is quite variable. This highly variable nature of the fault and auxiliary plane orientations and of the sense of movement is reflected in the P–T axis plot (figure 5.9a), which displays little coherence in the distribution of the axes. The pressure and tension axes seem to be almost randomly distributed over the focal sphere. The dominant north–northeast striking, approximately vertical, nodal planes are roughly parallel to the orientation of the surface fissures (figure 2.1) and are therefore likely to represent the most active fault orientations within this volume. The almost random orientations of the P–T axes and the variable sense of strike–slip suggests that the orientations of the maximum and minimum axes of compressive stress (σ_1 and σ_3 respectively) were also varying in some complex manner. If this were not the case then the sense of strike–slip motion on a given fault orientation would be expected to be reasonably consistent, whether the faults were fresh or reactivated. However, the predominance of a small normal component in the strike–slip events (appendix E.1) and of normal over reverse motion (figure 5.8) suggests that, if an average is taken over the whole area, σ_3 may have been closer to the horizontal than σ_1. This stress scheme is illustrated in figure 5.10a.

5.3.3.3 Fissure Zone

Activity within the fissure zone accounted for about one quarter of the double

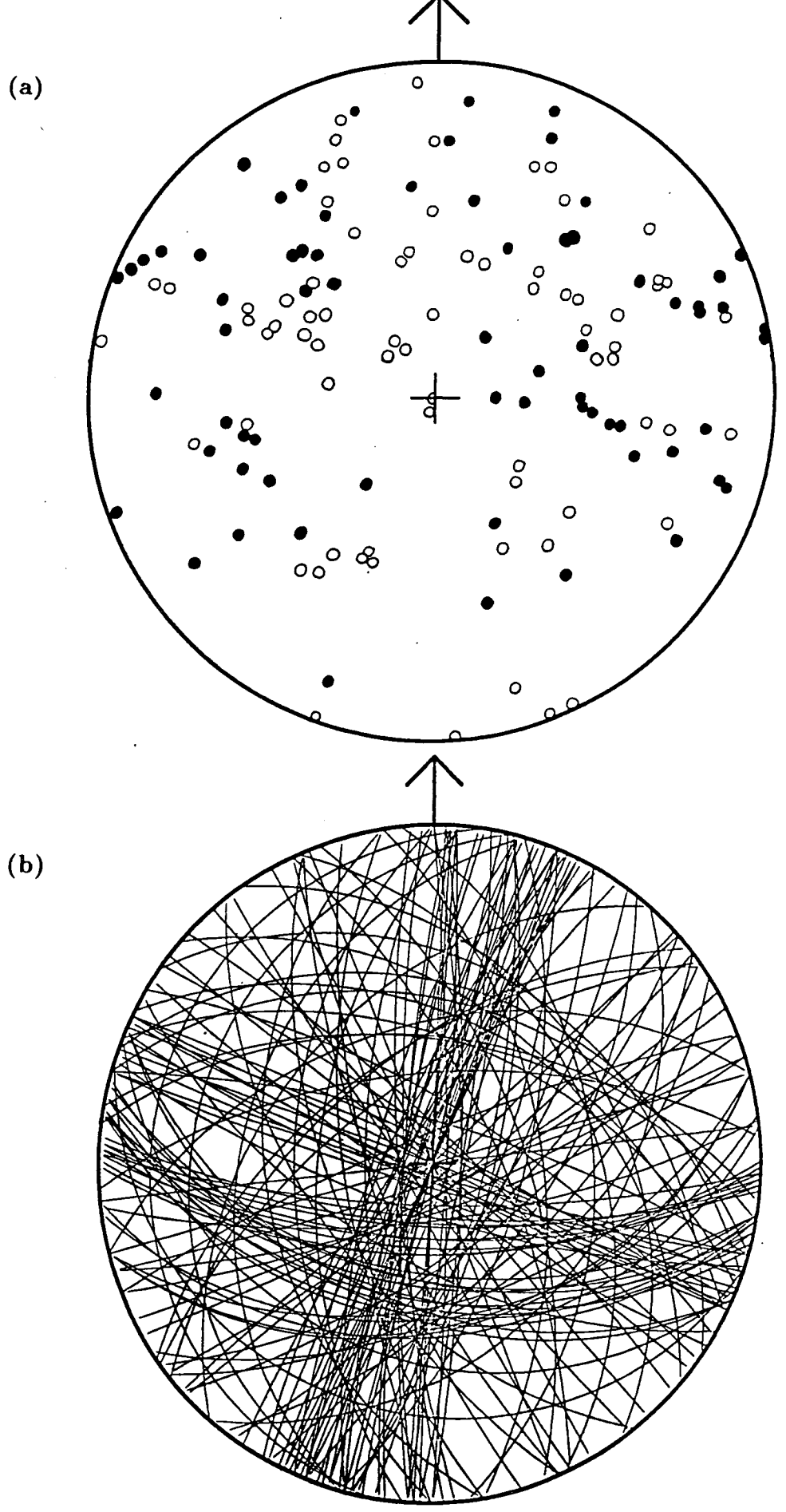

Figure 5.9 : (a) P- and T-axes for all double couple events at Bjarnarflag. Open circles represent the P-axes and closed circles represent the T-axes. **(b)** A summary plot of nodal lines for all double couple events at Bjarnarflag.

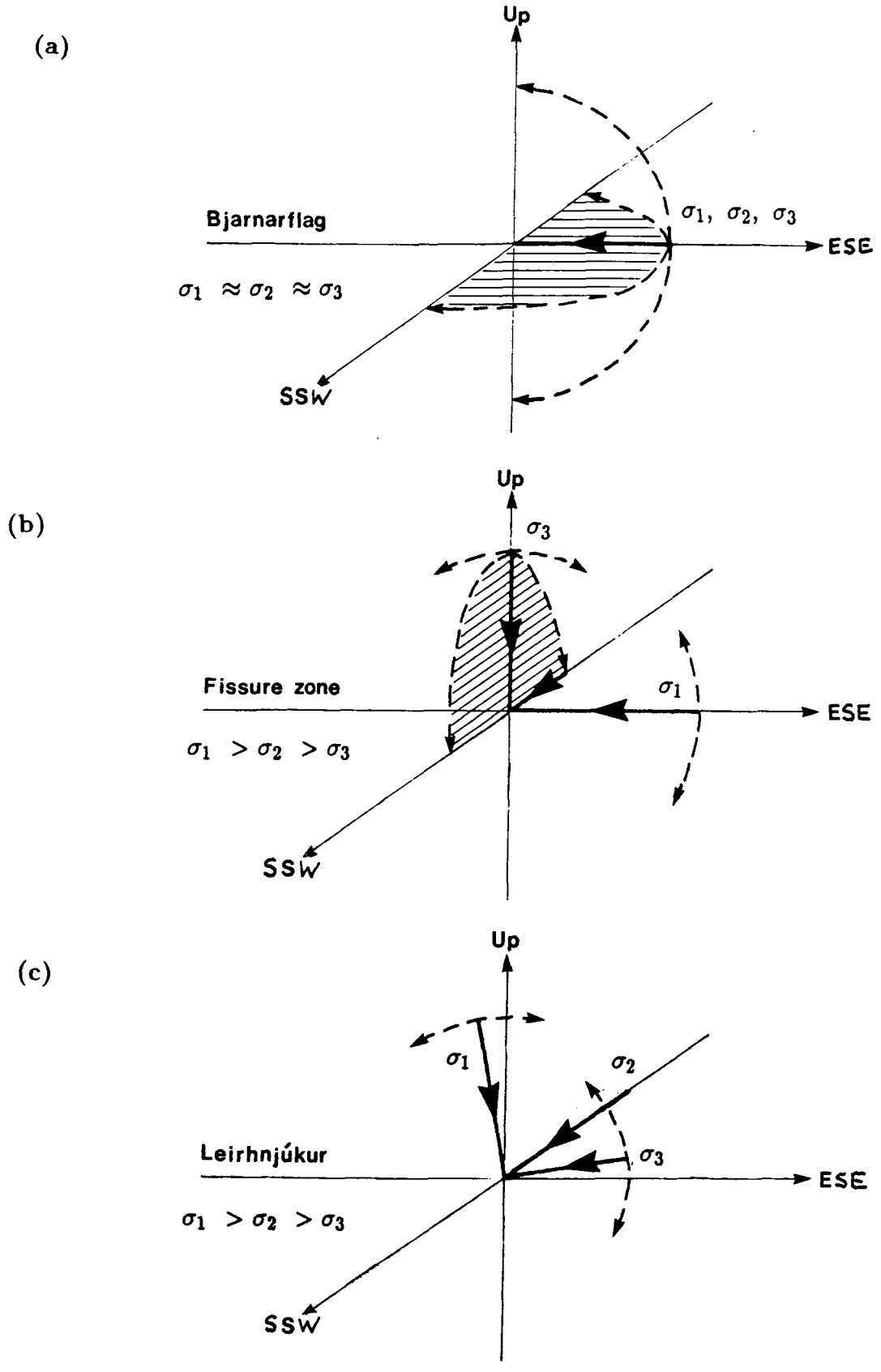

Figure 5.10 : The spatial variation in stress field in the Krafla area. σ_1, σ_2 and σ_3 are the maximum, intermediate and minimum principal stresses respectively. **(a)** Bjarnarflag : the stress field varies almost chaotically. **(b)** Fissure zone : σ_1 has an approximately horizontal northwest–southeast orientation. σ_3 varies between horizontal and vertical in an approximately northeast–southwest direction. **(c)** Leirhnjúkur : σ_3 is closer to horizontal than σ_1, and σ_2 is approximately horizontal and parallel to the trend of surface fissures.

couple events observed (figure 5.8). Of these, 21 (~55%) were strike–slip (e.g. event 850910 1504), 8 (~20%) had a strong normal component (e.g. event 850711 0558) although most of these are not well constrained (e.g. event 850716 1010), and 8 (~20%) had reverse shear mechanisms (e.g. event 850719 0746).

Figure 5.11a illustrates the clear distribution of the P– and T–axes for shear events in the fissure zone of activity. The axes may be separated using small circles which define a full cone within which the P–axes lie. The cone has a half-angle of 50°, with its axis orientated N110°E — N70°W, and dipping by 20° towards N110°E. T–axes thus occupy a broad band across the focal sphere, while P–axes are confined mostly to the western and eastern edges of the plot. The summary of nodal lines (figure 5.11b) shows that although a wide scatter exists, there is a very slight prevalence of steeply dipping planes striking at about N30°W and at about N120°W. These nodal planes arise largely from strike–slip focal mechanisms which were usually sinistral if the N30°W trending planes are taken as the slip surfaces (Appendix E.2). There is, however, no indication of which (if either) of the nodal plane orientations represents the dominant fault surface. Reverse, normal and other strike–slip events account for the remaining nodal lines of variable orientation. This pattern of faulting and of P–T axes is consistent with a stress régime in which the direction of greatest compressive stress (σ_1) was orientated approximately horizontal, perpendicular to the trend of surface fissures, and the perpendicular direction of least compressive stress (σ_3) varied between horizontal and vertical, approximately parallel to the fissure swarm. This is illustrated in 5.10b.

5.3.3.4 Leirhnjúkur

At Leirhnjúkur, shear slip was dominated by normal and strike–slip components (figure 5.8). Twelve events (~35%) were strike–slip (e.g. event 850702 1152), 14 (~45%) were normal (e.g. event 850716 0758), and 6 (~20%) had a strong reverse component which tended to be not well resolved (e.g. event 850802 0055). This zone of activity therefore released a higher proportion of stress by normal faulting than elsewhere.

Strike–slip activity was dominant along steeply dipping planes striking either at about N25°E or N60°W (figure 5.12b) and apparantly have no preferred sense of

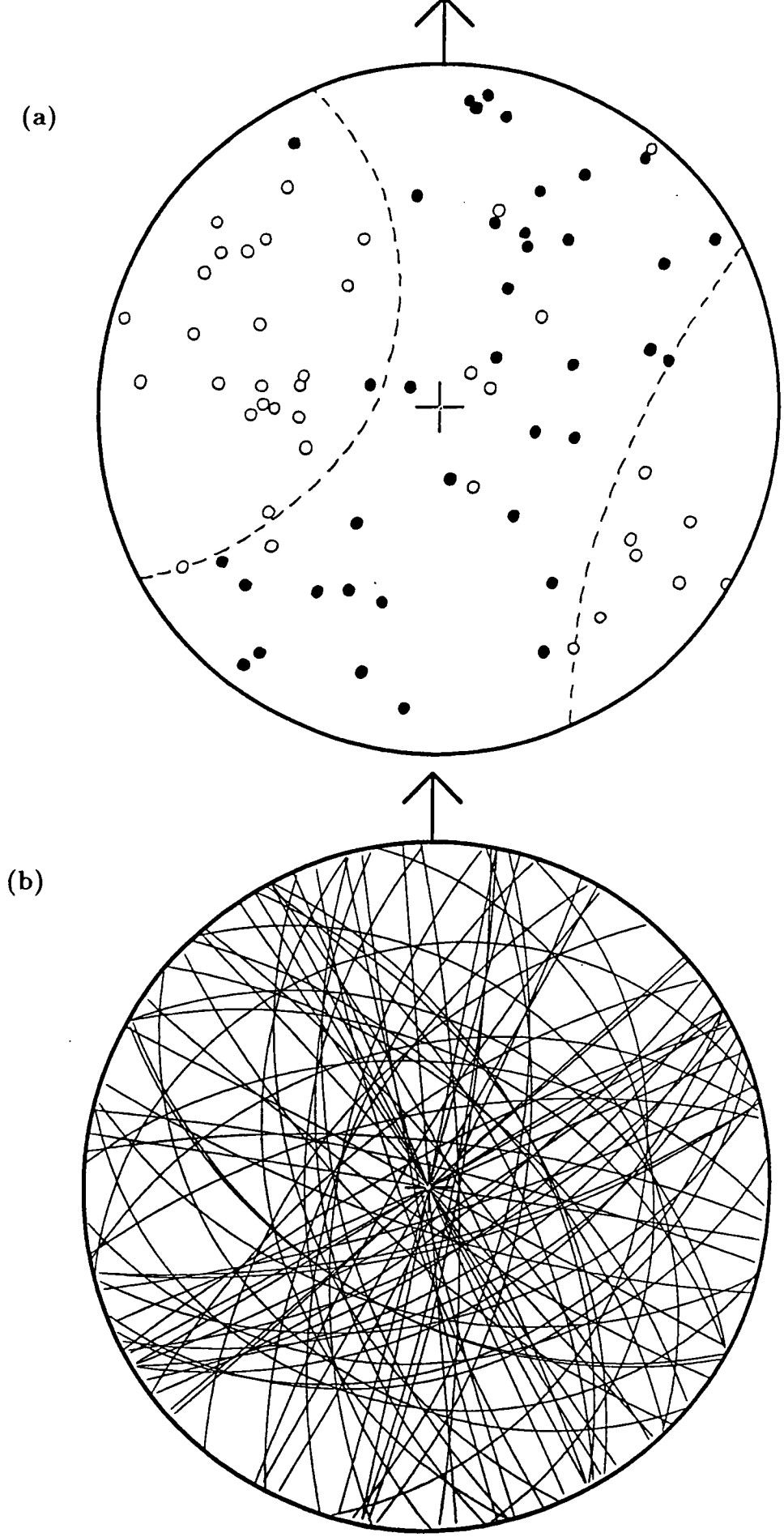

Figure 5.11 : (a) P- and T-axes for all double couple events in the fissure zone. Open circles represent the P-axes and closed circles represent the T-axes. **(b)** A summary plot of nodal lines for all double couple events in the fissure zone.

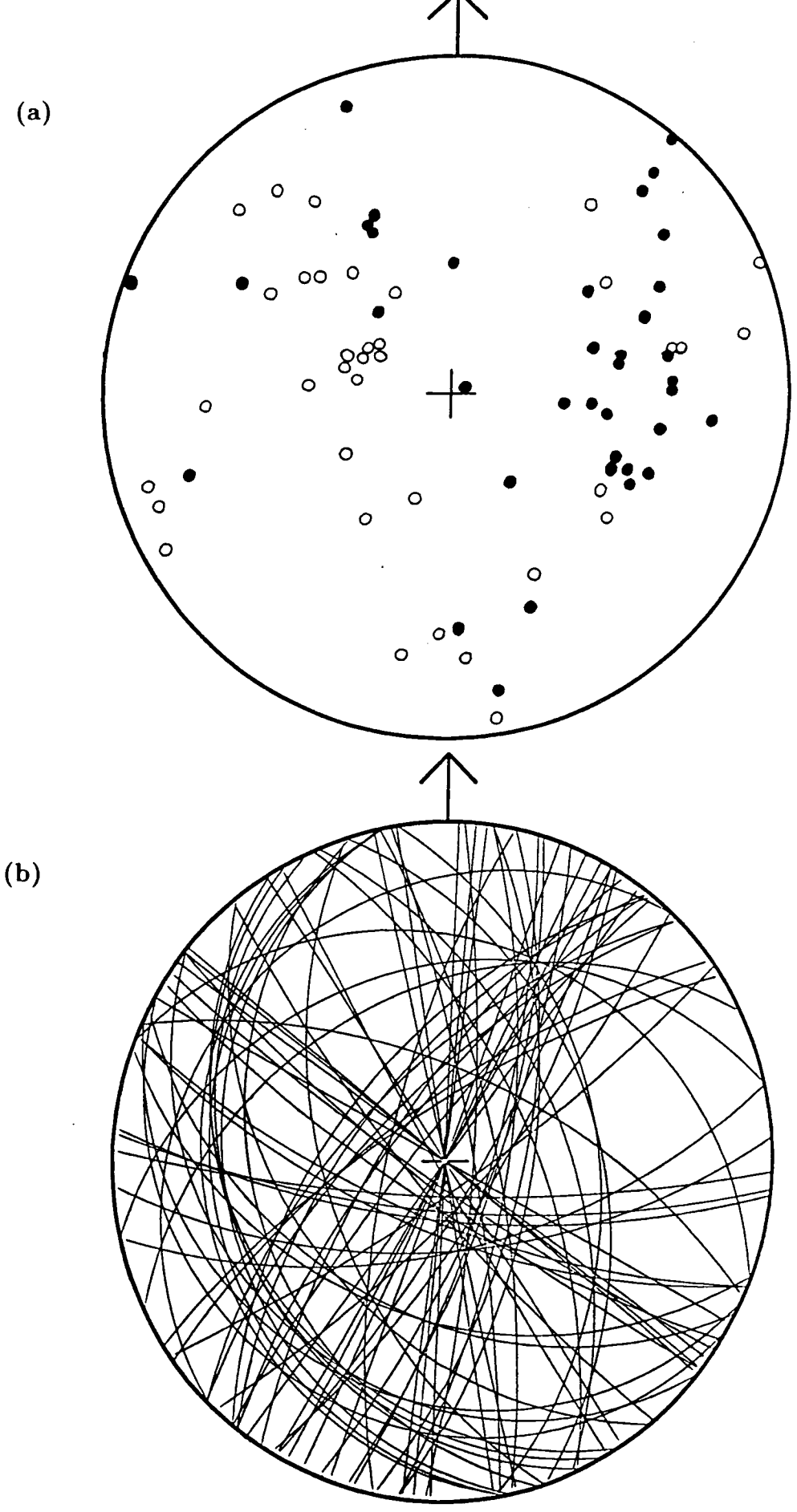

Figure 5.12 : (a) P- and T-axes for all double couple events at Leirhnjúkur. Open circles represent the P-axes and closed circles represent the T-axes. **(b)** A summary plot of nodal lines for all double couple events at Leirhnjúkur.

slip (Appendix E.3). The planes striking approximately parallel to the surface fissure trend are assumed to represent the principal fault planes. Normal faulting usually occurred on planes striking about N30°W and having a dip which was either gentle to the east or steep to the west (Appendix E.3). The distribution of P– and T–axes for the Leirhnjúkur events (figure 5.12a) is fairly widespread but clearly exhibits preferred orientations. The centre of the T–axis field lies at an azimuth of about N90°E and plunges at about 35°, while the centre of the P–axis field lies approximately at an azimuth of N70°W and plunges at about 60°. These average P– and T–axis positions are perpendicular on a plane dipping at 80° to the north and striking at about N95°E. If these average positions are close to those of the principal stress axes then it would appear that σ_3 was closer to the horizontal than σ_1, and that σ_2 was approximately horizontal and parallel to the trend of the surface fissures. This is illustrated in figure 5.10c.

5.3.4 Non–Double Couple Events

5.3.4.1 Introduction

Prior to correcting the data for hypocentral and velocity model errors, fourteen (9%) of the earthquakes could not be interpreted as having double couple focal mechanisms. As outlined in the section 5.1, this could be explained by several effects other than non–shear slip, although most of these explanations can be discarded as being unlikely. The hypocentral depths of all of the anomalous events were all greater than 1.9 km after relocation through the three–dimensional velocity structure. They had (by inspection) first P–wave arrivals with dominant frequencies greater than 10 Hz (e.g. figure 5.4), and therefore were all observed at distances of a least 4 wavelengths, which is in the far–field (Aki and Richards, 1980). A normal quadrantal radiation pattern would therefore be expected if there were no source or medium complexities.

The possibility that phases may have been misidentified is considered unlikely because of the impulsive nature of the first arrivals, as exemplified by the seismogram shown in figure 5.4. It also seems unlikely that anisotropy in the source volume is a significant effect, since these events occurred within the same volume as many events which could be interpreted by conventional means. Furthermore, there was

no evidence for significant anisotropy from travel–time residuals computed by HYPOINVERSE (section 3.3.3). Fault curvature is more difficult to assess because the events are small and the sources have no surface expression. An empirical relationship between earthquake moment M_o and local magnitude M_L such as : –

$$logM_o = 15.1 + 1.7M_L \qquad (Wyss\ and\ Brune,\ 1968) \qquad 5.14$$

can be used with equation 5.1 to estimate the order of the dimensions of a shear fault's slip and size. It is easy to show that for an event of magnitude about –1 in the Krafla area, which is roughly the magnitude of most of the anomalous events, the dimensions of fault slip were probably of the order of metres. Fault curvature on this scale is considered unlikely to be serious if the source volume is fairly homogeneous. The fact that the anomalous events occurred within the same volume as, and had similar magnitudes to, events which could be interpreted as double couple, suggests that this effect is probably slight if it exists.

5.3.4.2 Removal of Bias

Before removing sources of bias from the data, seven of the fourteen anomalous radiation patterns could be separated into compressional and dilatational portions using small circles and the remaining eight could not. This procedure has previously been adopted by several authors (e.g. Julian, 1983; Foulger and Long, 1984; Foulger et al., 1989) as a basis for interpreting such radiation patterns as resulting from non–double couple source mechanisms. The non–double couple events which were interpreted in this way could be divided into two groups : those which exhibited reduced dilatational fields ('explosive' events) and those with reduced compressional fields ('implosive' events).

Figure 5.13 shows the statistical distribution of non–double couple events before and after the removal of hypocentre and velocity biases. The removal of bias reduced the number of implosive events from 4 to 1, but did not affect the number of explosive events. Three 'implosive' events were reinterpreted as shear events, and their solutions before and after the removal of bias are shown in figures 5.14 and 5.15. A common feature in this process has been that data points for each event were pushed out towards the edge of the stereographic projection, which enabled

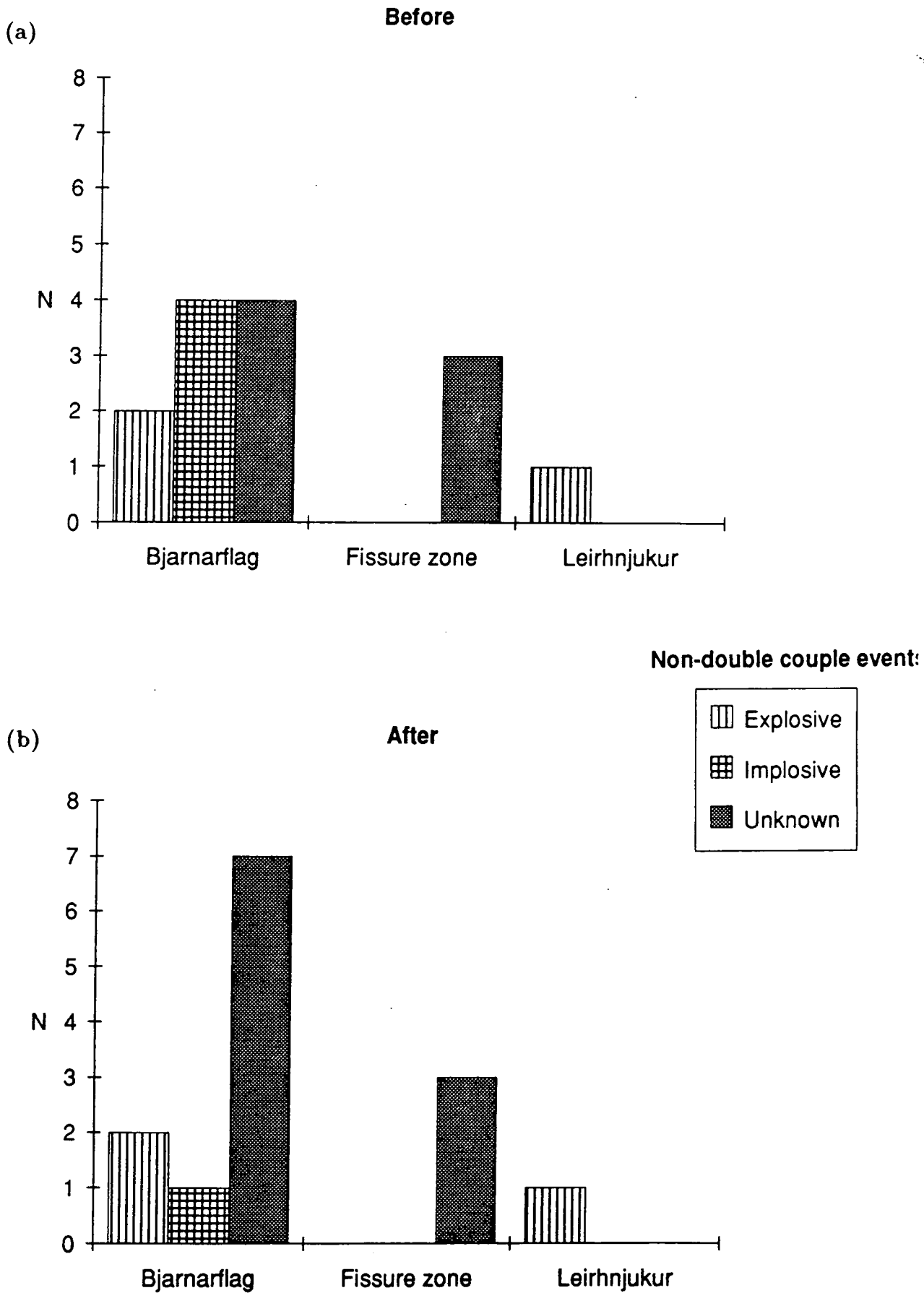

Figure 5.13 : A statistical break-down of non-double couple focal mechanisms **(a)** before and **(b)** after the removal of bias.

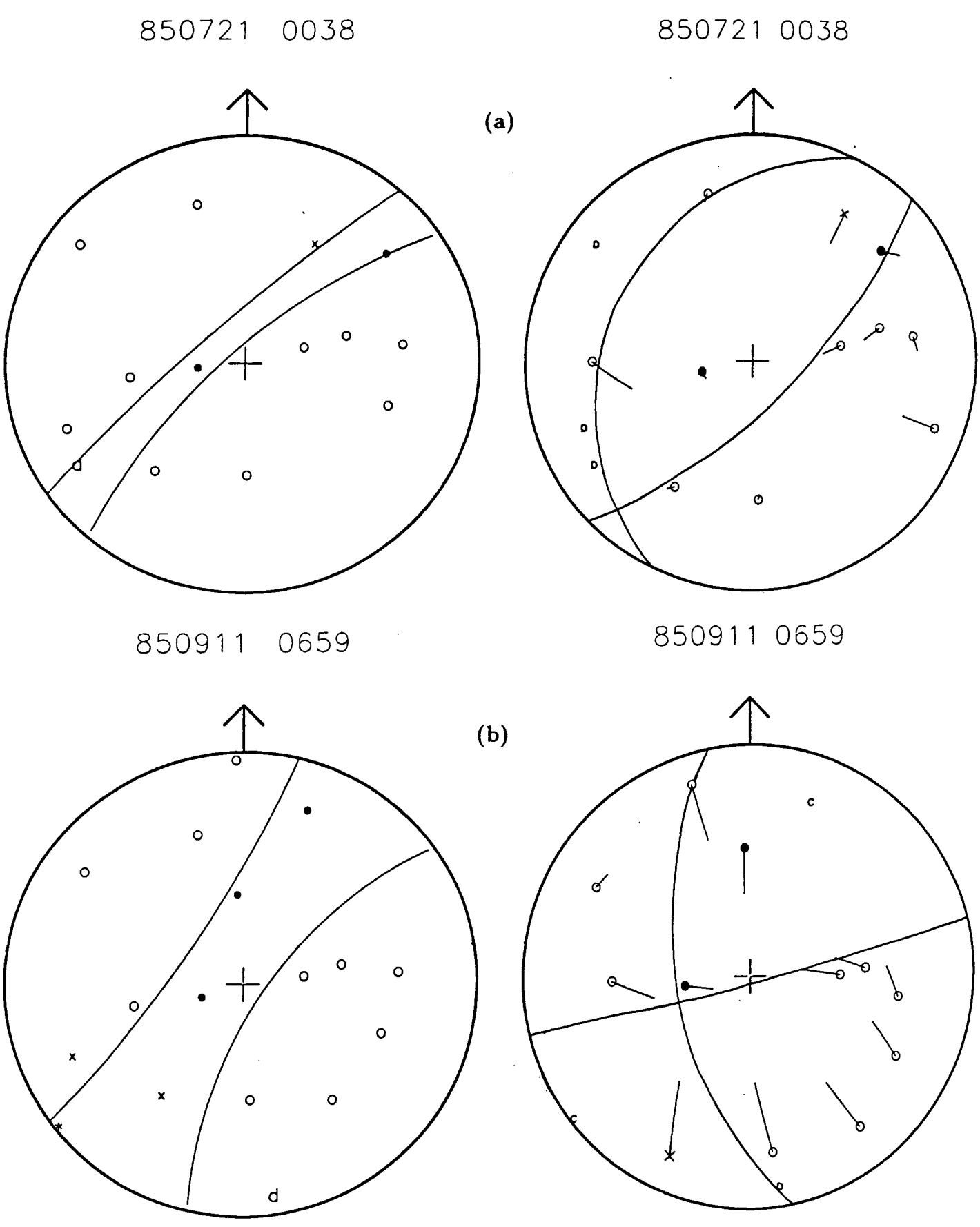

Figure 5.14 : The reinterpretation of two 'implosive' events as shear events after the removal of bias. Compressions and dilatations on the upper hemisphere are denoted by closed and open circles respectively. First P-wave arrivals of nodal character are denoted by ×. Compressions and dilatations projected onto the upper hemisphere from the lower hemisphere are denoted by * and d respectively. Arcs on right-hand plots show the effect of the velocity bias (contribution *b* of figure 5.6). Reinterpretation was carried out as though arrivals whose rays did not converge had not moved from their original positions on the focal sphere. The original positions of such arrivals are denoted by C and D on right-hand plots. **(a)** Event 850721 0038 at Bjarnarflag. **(b)** Event 850911 0659 at Bjarnarflag.

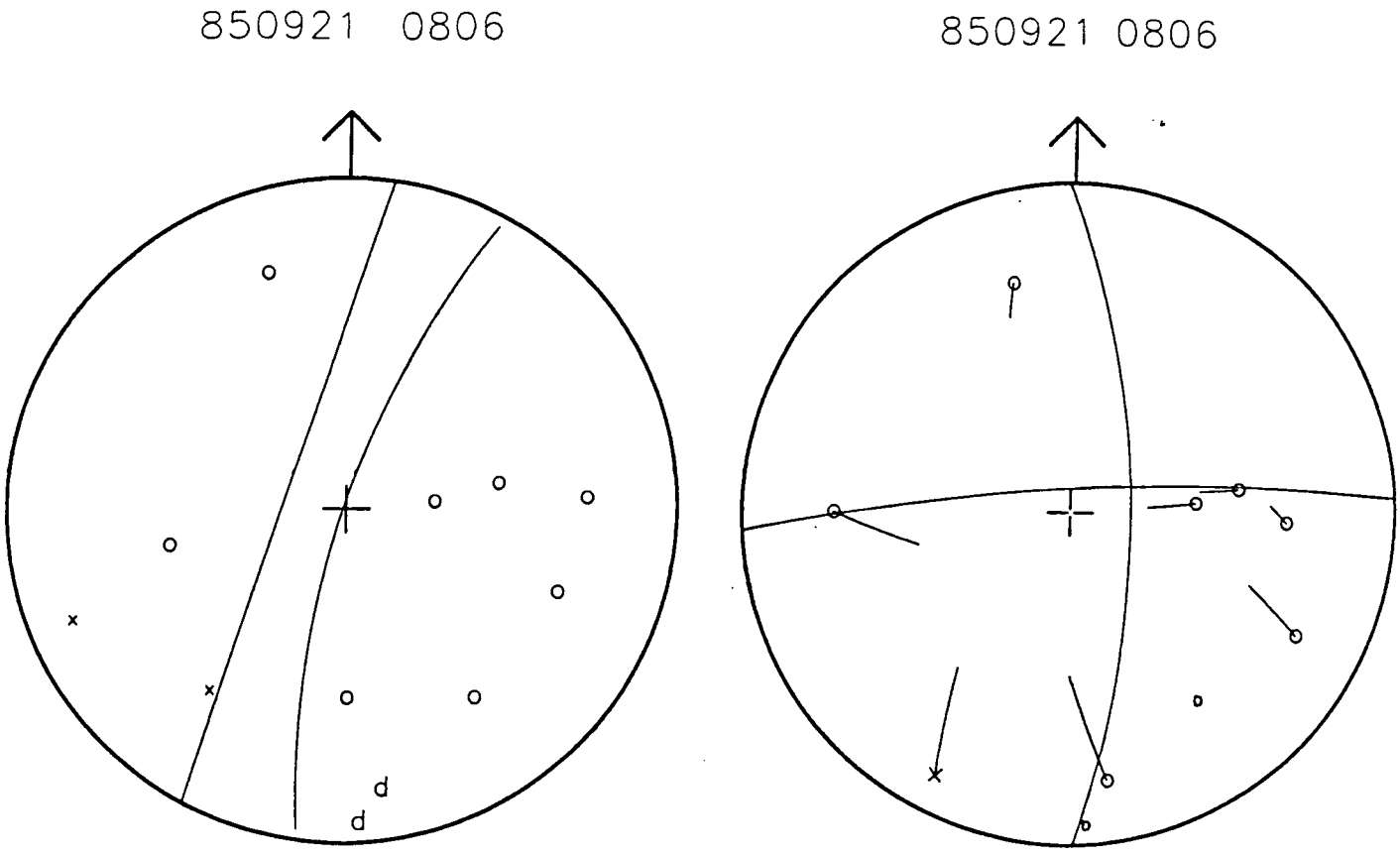

Figure 5.15 : The reinterpretation of 'implosive' event 850921 0806 at Bjarnarflag as a shear event after the removal of bias. Symbols as defined in figure 5.14.

orthogonal nodal planes to be drawn. This demonstrates the critical importance of removing large sources of bias from a dataset before invoking non–double couple source mechanisms. Failure to do so could result in the complete misunderstanding of the fracture processes at work.

The number of radiation patterns which could not be interpreted using either great or small circles rose from 7 to 10 when sources of bias were removed (figure 5.13). The increase was entirely due to three events within the Bjarnarflag cluster which were originally interpreted as thrusts and became non–double couple (figures 5.16 and 5.17). This further demonstrates the importance of ensuring that data are free of bias before drawing conclusions. The remaining 7 anomalous events in this class could not be solved using either great or small circles without significant inconsistencies either before or after removing sources of bias. Most of them are well constrained but display no coherent pattern of first motion polarity (e.g. event 850815 1514 in the fissure zone). However, two events at Bjarnarflag (events 850711 0449 and 850831 1407) have coherent areas on the focal sphere of compressions and dilatations.

5.3.4.3 Source Models

Once sources of bias had been removed, four non–double couple events could be interpreted using small circles. Three of these are explosional in character (figures 5.18a,b, 5.19a) and the other is implosional (figure 5.19b).

When they are interpreted using small circles, events 850815 1404 (Leirhnjúkur), 850925 0211 (Bjarnarflag), and 850929 0508 (Bjarnarflag) are characterized by strongly reduced dilatational fields which form narrow belts across the focal spheres (figures 5.18a,b, 5.19a). This indicates that the sources have a net explosional component (the sum of the principal seismic moments is significantly greater than zero). However, the quality of these solutions must be examined critically. Without first motions which were nodal in character, the first two of these solutions are only constrained by 8 and 9 data points respectively, 2 of which are dilatations in each case. The third 'explosional' event (850929 0508) is better constrained, by 10 compressions and 3 dilatations. However, in common with the other 'explosional' events, this event cannot be given completely unambiguous non–double couple status because of insufficient ray convergence. In spite of these data limitations,

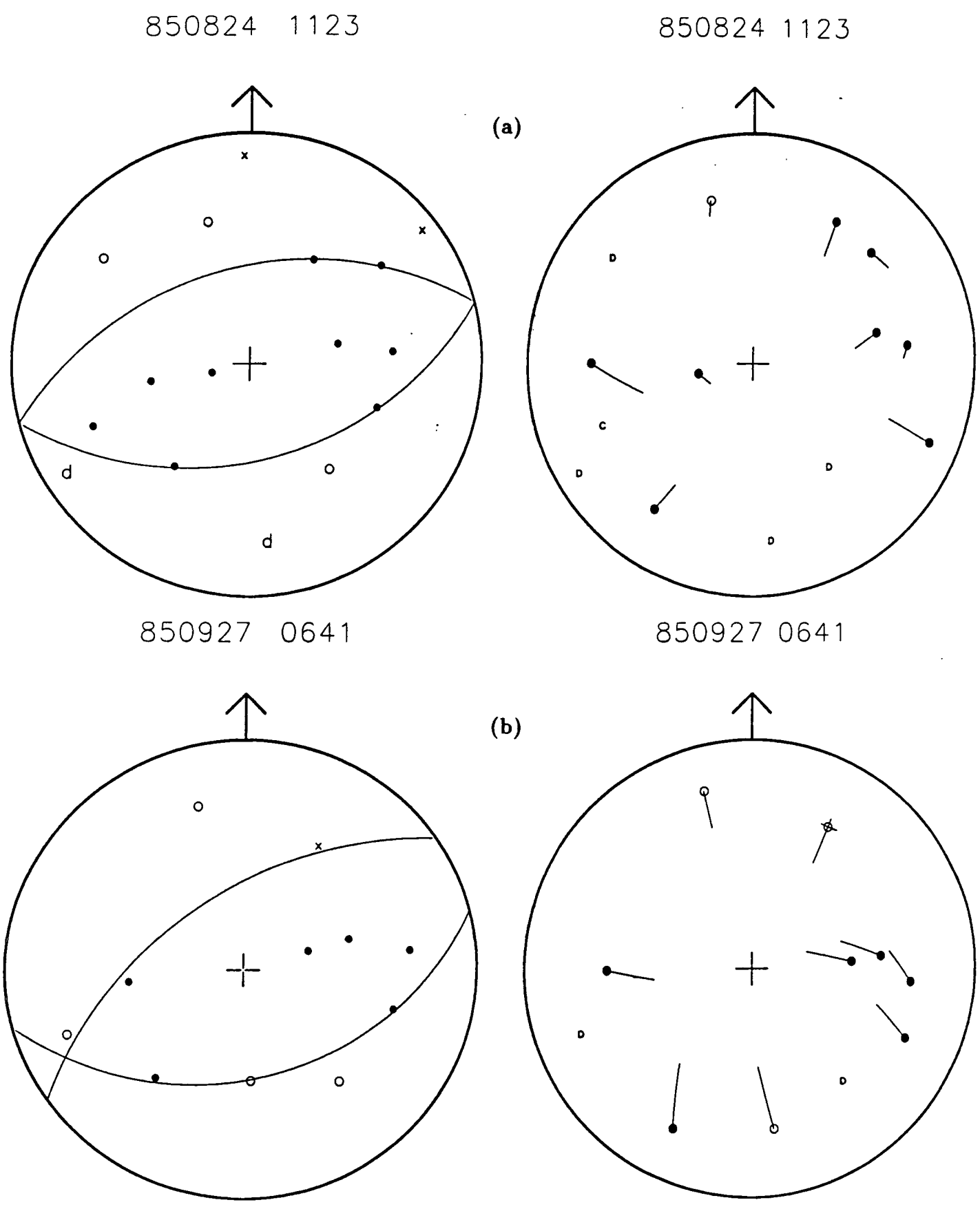

Figure 5.16 : The reinterpretation of 'thrust' events **(a)** 850824 1123 and **(b)** 850927 0641, both at Bjarnarflag, to have no double couple solution after the removal of bias. Symbols as defined in figure 5.14.

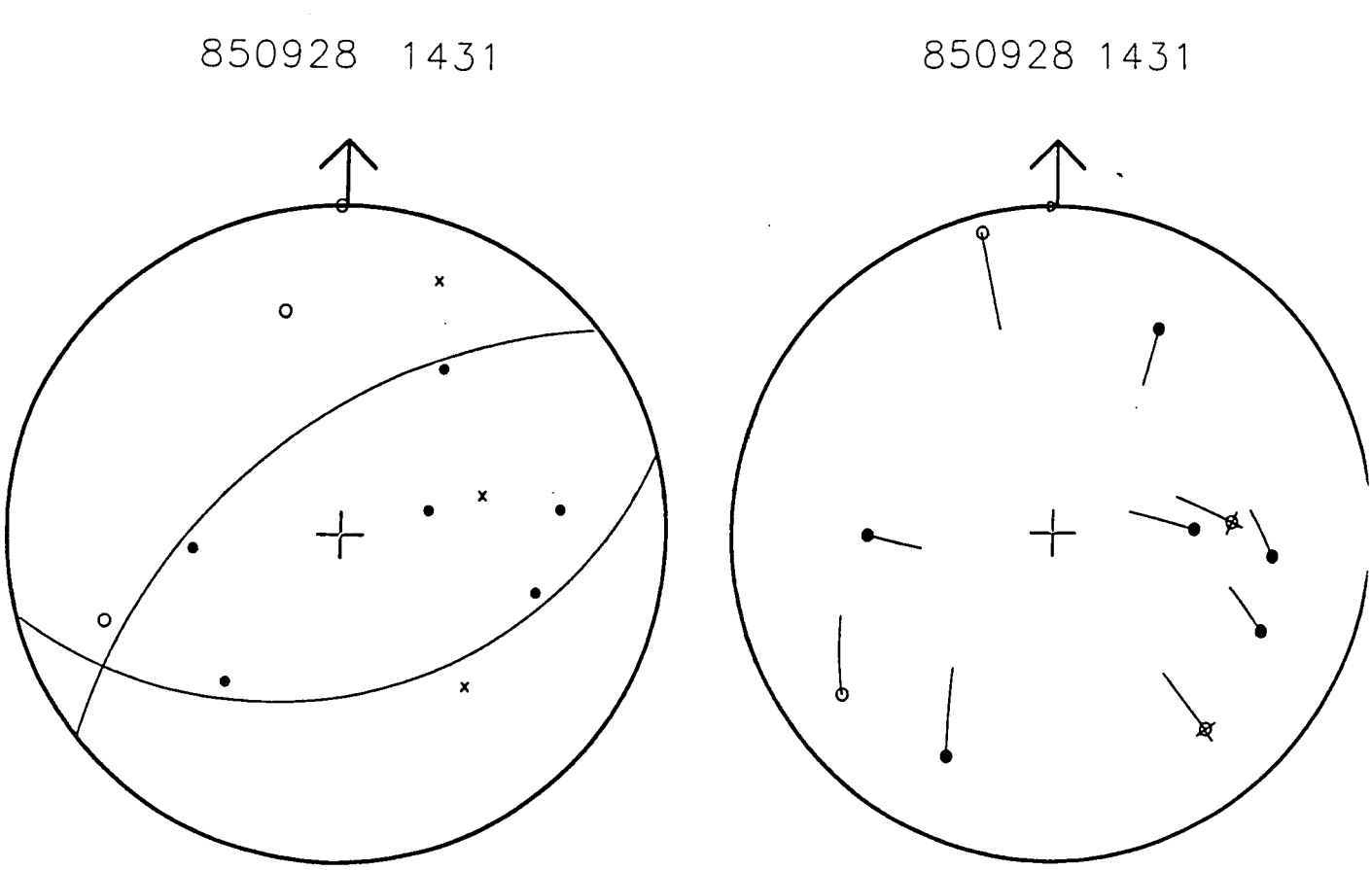

Figure 5.17 : The reinterpretation of 'thrust' event 850928 1431 at Bjarnarflag to have no double couple solution after the removal of bias. Symbols as defined in figure 5.14

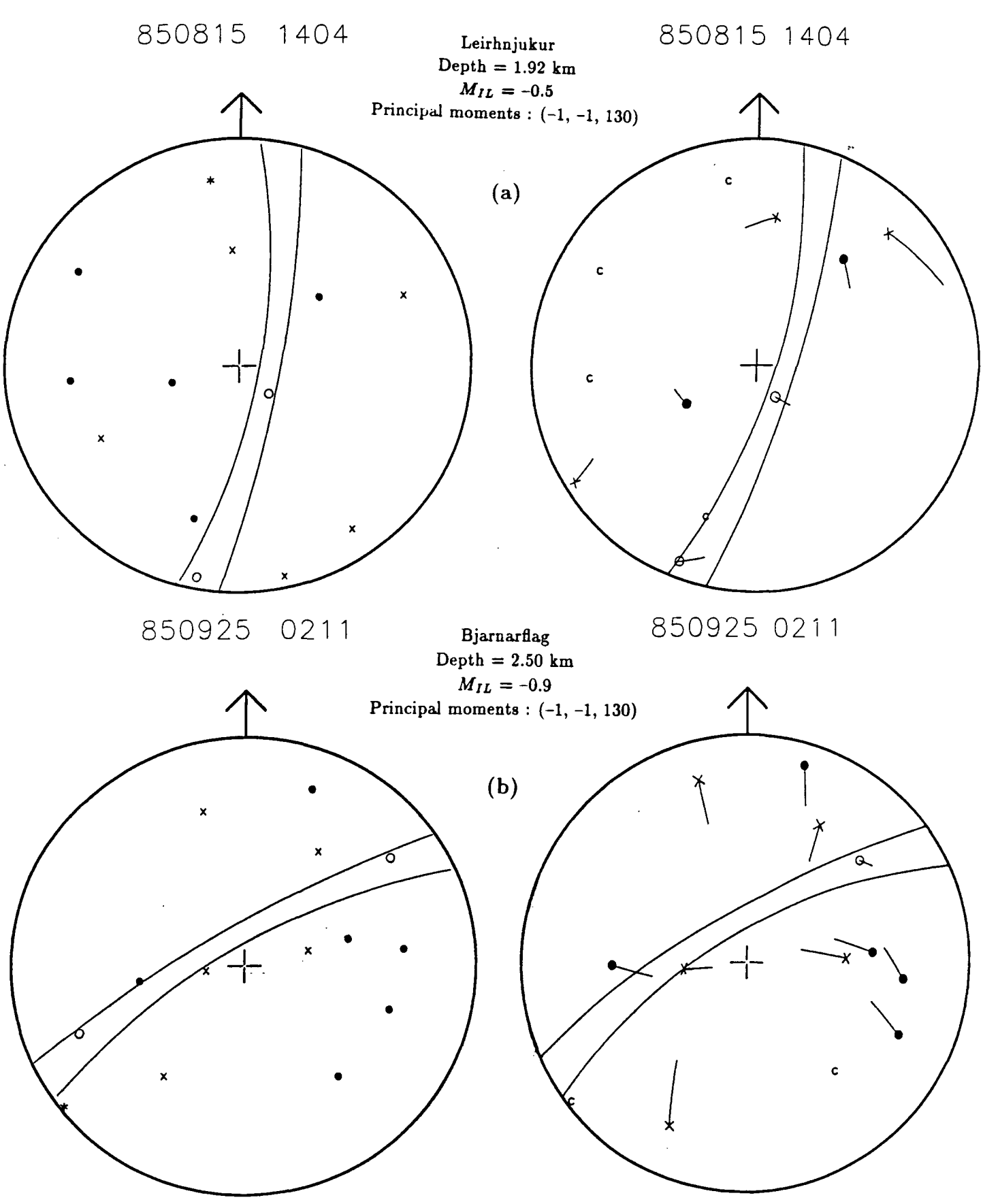

Figure 5.18 : The reinterpretation of 'tensile crack' type non-double couple events after the removal of bias. **(a)** Event 850815 1404 at Leirhnjúkur, and **(b)** event 850925 0211 at Bjarnarflag. The hypocentral depths, local magnitudes, and approximate principal seismic moments are given. Symbols as defined in figure 5.14.

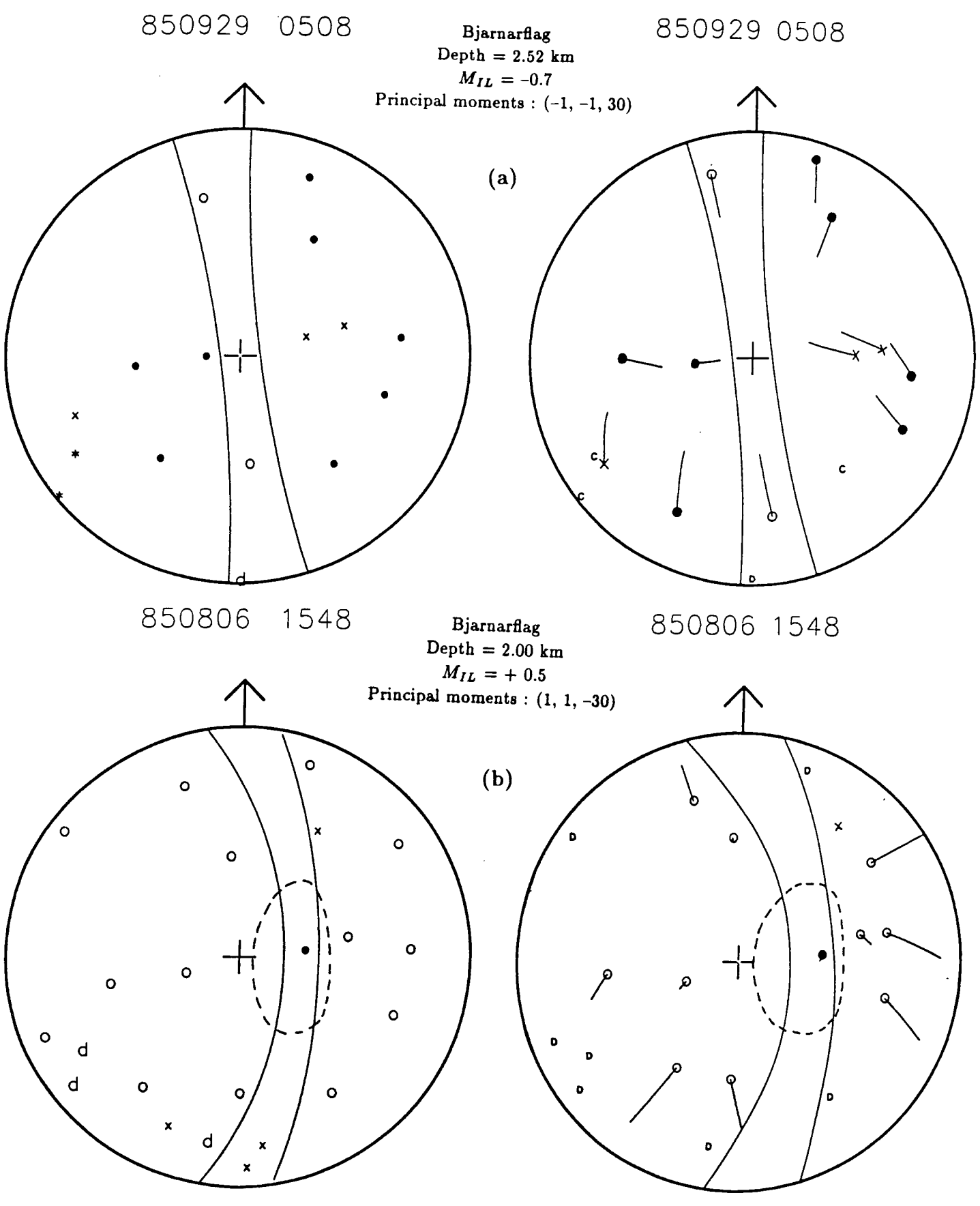

Figure 5.19 : The reinterpretation of **(a)** the 'tensile crack' type non-double couple event 850929 0508, and **(b)** 'implosive' event 850806 1548, both at Bjarnarflag, after the removal of bias. The hypocentral depth, local magnitude, and approximate principal seismic moments are given. Symbols as defined in figure 5.14. Two possible non-double couple interpretations are shown in (b). One is constrained by small circles and could indicate the collapse of a tensile crack. The other has nodal lines which are neither great or small circles, and could indicate closure of a tensile crack by shear failure.

the three 'explosive' events have been interpreted as non–double couple for two main reasons. Firstly, the events occurred within the same volume as many events which could easily be interpreted as having shear sources. In addition, 'explosive' non–double couple mechanisms at the Hengill volcanic system in Southwest Iceland account for about half of the observed seismicity (Foulger, 1988b), and it has been reported that these mechanisms do not revert to double couple after the removal of bias (G. Foulger, pers. comm.). These factors together provide strong evidence that non–double couple sources are operating at Krafla. The remaining ambiguity in the three 'explosive' solutions could be eliminated by considering amplitude information, or by achieving greater ray convergence. The polarity fields have been separated using small circles and approximate moment tensors have been calculated on the basis of their geometry (the moment tensors are given in figures 5.18 and 5.19).

It is possible that these events conform with the model of tensile crack formation proposed by Foulger and Long (1984) in which the opening of a fissure causes an instantaneous spherically symmetrical drop in pore pressure due to the relatively slow movement of fluids into the cavity (equation 5.13). It is a model which is intuitively attractive for an area of crustal accretion such as Krafla, which features open surface fissures and intense geothermal activity. The penetration of fluids into volumes of hot rock is thought to result in the formation of contraction cracks, particularly if a regional extensional stress régime is predominant (Lister, 1974; Foulger, 1984). For this source model in the x–y plane, using the approximation $\lambda \approx \mu$, equation 5.13 can be rewritten as : –

$$A\ (\ 1,\ 1,\ 3) + B\ (-1,-1,-1) = (d_1, d_2, d_3) \qquad 5.15$$

where A and B are numerical constants for a given event which determine the relative strength of each source component and must be positive in the case of an opening tensile crack. Assuming that $A, B > 0$, then there will be a band of dilatations oriented parallel with the x–y plane on the focal sphere when $d_1 = d_2 < 0$ and $d_3 > 0$. This is the case when $\frac{1}{3}B < A < B$. There will be a net increase in volume if $A > \frac{3}{5}B$. The explosional events may be interpreted according to this model, where $A = 64.5, B = 65.5$ (events 850815 1404 and 850925 0211) and $A = 12.5, B = 13.3$ (event 850929 0508), to indicate the opening of tensile cracks

on nearly vertical planes which strike between north and northeast. However, the precise shapes of the nodal surfaces for these events is not known and this is only one possible non–double couple source model.

Event 850806 1548 at Bjarnarflag (figure 5.19b) has a strongly reduced compressional field, with only a single compression out of 22 observations. The event is still well constrained to be unambiguously non–double couple after the sources of bias are remove. This radiation pattern seems to be the reverse of the tensile crack polarity distribution and may be modelled by the closure of a near–vertical crack. In this case, the constants of equation 5.15 are given by $A = -14.5$ and $B = -13.5$. However, as with the tensile crack type events, the ratios of the principal moments for this event are not accurately known. It is likely that more detailed knowledge of the moment tensor (obtained, for example, by moment tensor inversion of the seismic waveform) could lead to an alternative plausible interpretation. To demonstrate this point, it will now be shown that the observed polarity distribution for the implosional event at Bjarnarflag is also consistent with a slightly different non–double couple mechanism.

If a significant shear contribution to crack closure is invoked (figure 5.20) then the source will not approximate a linear vector dipole and small circles will not describe its nodal planes. Shimizu et al. (1987) envisaged the nucleation of a tensile crack coupled with a shear fault as a non–double couple source mechanism, but did not consider the rôle of pore fluid pressure. By combining a shear fracture with the tensile crack and symmetrical implosion of equation 5.15, according to the geometry of figure 5.20, it is possible to describe a tensile/shear crack mechanism by : –

$$A\ (\ 1,\ 1,\ 3) + B\ (-1,-1,-1) + C\ (\ 0,-1,\ 1) = (d_1, d_2, d_3) \qquad 5.16$$

where A, B and C are numerical constants for a given event. For a cavity which is closed by a shear fault and accompanied by an instantaneous spherically symmetrical increase in pore pressure, $A, B, C < 0$ and $d_2 > d_1 > d_3$. This model represents the reverse of that illustrated in figure 5.20, and it could be produced by swapping the directions of maximum and minimum compressive stress. A net volume reduction would result when $A < \frac{3}{5}B$. This source combination would always produce a radiation pattern which had a reduced area of compressions that could not be

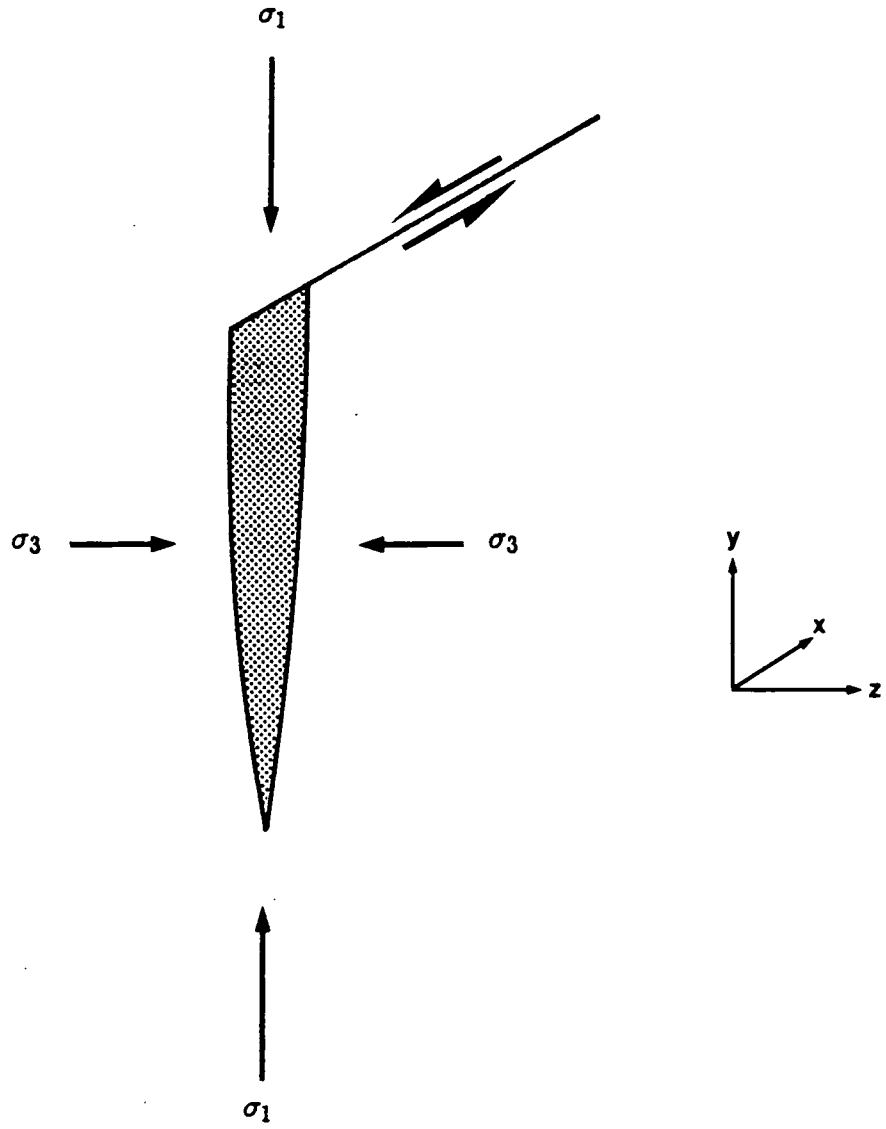

Figure 5.20 : Schematic illustration of a tensile crack coupled with a shear crack (a tensile/shear crack). σ_1 and σ_3 indicate the axes of maximum and minimum compressive stress respectively for an opening tensile/shear crack. In the case of the sudden closure of an open crack, σ_1 and σ_3 are transposed (after Shimizu et al., 1987).

constrained by great or small circles. An alternative interpretation of the nodal lines for the implosional event is shown in figure 5.19b, for which $d_2 > 0 > d_3$, but the polarity of d_1 is unclear. A wide range of shear/crack geometries could produce the observed polarity distribution. However, it should be emphasized that although the shear/crack model is attractive in its conceptual simplicity and its apparent compatibility with other source models which have been invoked, it is just one of many possible non–double couple source models which could be used to explain the observed radiation pattern.

5.3.4.4 Implications for the Stress Field

The two types of non–double couple events which occurred within the Bjarnarflag cluster of activity were very different : one was explosive in character and the other was implosive. This itself is an indication that the local stress field is heterogeneous, which is consistent with the results for this area derived from the double couple events (figure 5.10a). The two explosive polarity distributions are consistent with a model of tensile crack formation on a near–vertical plane striking northeast, which is oblique to the trend of the surface fissures. The implosive pattern is consistent with the closure of a vertical tensile crack striking parallel to the fissure swarm, and also with crack closure by shear slip according to a wide range of geometries.

The single non–double couple event which originated within the Leirhnjúkur cluster of activity has a solution which has small circles orientated approximately parallel to the fissure swarm. This could indicate the approximately co–planar opening of a tensile crack, and is consistent with having σ_3 close to horizontal and roughly perpendicular to the fissure trend (figure 5.10c).

5.4 Summary

Well constrained focal mechanisms were determined manually for 153 of the best located earthquakes using impulsive P–wave polarity data. This was done initially using ray information output by HYPOINVERSE for hypocentral location through the original one–dimensional velocity structure.

The biasing effect of using incorrect hypocentres and an over–simplified velocity structure have been investigated by three–dimensional ray tracing. Relocating hypocentres to shallower depths decreases the take–off angles of P–wave first arrivals at a given set of stations. This effect is reduced in the direction of epicentral relocation and accentuated in the opposite direction. The introduction of the three–dimensional velocity structure derived by tomographic inversion had a major effect on the seismic raypaths for the entire dataset, with typical changes in take–off angle and azimuth of about 10° and 0–10° respectively. These angular changes usually have only a small impact on double couple solutions, but their influence on non–double couple source mechanism interpretations can be critical.

The double couple events were analysed in three groups according to their epicentral locations, after the sources of bias had been removed from the data. Activity in the Bjarnarflag zone was dominantly strike–slip on steeply dipping faults striking either north to N25°E or east - southeast. There was no preferred sense of motion although there was often a small normal component of shear. Pressure and tension axes are almost randomly distributed over the focal sphere, suggesting that the maximum and minimum axes of compressive stress (σ_1 and σ_3) varied in some complex manner within this zone, although σ_3 may have been closer to the horizontal than σ_1.

Within the 'fissure' zone of activity most events also occurred by strike–slip on faults with a wide variety of orientations, but there was a slight predominance of slip on steeply dipping planes with strikes of about N30°W and N120°W. The sense of motion on these faults was almost always the same, although there is no indication of which (if either) of the orientations represents the dominant faulting direction. Some reverse and normal faulting occurred with variable orientation. σ_1 is inferred to have been orientated approximately horizontal, perpendicular to the

trend of surface fissures, and σ_3 varied between horizontal and vertical, parallel to the fissure trend.

At Leirhnjúkur, most of the stress was released by normal and strike–slip faulting. Normal faulting was dominant on planes striking at about N30°W and dipping either steeply to the west or gently to the east. Strike–slip activity was dominant along steeply dipping planes striking either at about N25°E or N60°W and having no preferred sense of slip. It is inferred that σ_3 was closer to horizontal than σ_1, and that σ_2 was approximately horizontal and parallel to the trend of surface fissures.

Reports of non–double couple earthquake mechanisms are rare and so the events which could not be interpreted as resulting from simple–shear slip have been examined critically. Before removing sources of bias from the data, seven of the fourteen anomalous radiation patterns could be separated into compressional and dilatational fields using small circles. This has previously been used as a basis for interpreting such radiation patterns as resulting from non–double couple source mechanisms. Once the sources of bias had been removed, three of these patterns could be given double couple solutions. Seven events had no solution before or after the data had been corrected for bias.

Three different source models have been invoked as possible explanations of the non–double couple events which were solved using small circles. Three events were consistent with a model of tensile crack formation which had previously been used to interpret events observed in a geothermal area in Southwest Iceland. The fourth event was consistent with the reverse model of tensile crack closure, but may also be interpreted as resulting from the closure of a tensile crack by shear failure. All four events originated from within geothermal areas, and their occurrence was consistent with the stress fields implied by the double couple events.

Chapter VI

Synthesis and Conclusions

6.1 Seismicity and Structure

6.1.1 Krafla Caldera

It is clear from the original study of seismicity in the Krafla area by Ward et al. (1969) that earthquake activity within the caldera is not restricted to periods of volcano–tectonic activity associated with periodic crustal rifting episodes. Many high temperature geothermal areas exhibit a higher background seismicity than their surrounding regions (see Foulger (1982) for a review), but the common coincidence in location of a geothermal area and an active volcano can make it difficult to distinguish between tectonically and geothermally driven seismicity. This problem is relevant to all seismic activity observed in the Krafla area during the NISE–85 survey, but particularly to that originating from within the caldera.

Figure 6.1 shows the distribution of earthquake hypocentres within the Krafla caldera in relation to known subsurface geology. Cross–section locations are shown in figure 6.2. The bulk of seismic activity observed within the caldera during this survey forms a tight cluster in the form of a cone which points downwards to a depth of about 2.3 km beneath the hyaloclastite hill Leirhnjúkur. Thus most of the activity occurs in the centre of the caldera, directly above a saddle in the crustal magma chamber (figure 6.2). This is also the location of the maximum uplift of the caldera roof between rifting events. The spatial concentration of this activity contrasts sharply with that observed during periods of inflation, when earthquakes occurred over the whole caldera, and is an indication that the slow inflation of the volcano at the time of the NISE–85 experiment (figure 2.14) was not the primary force behind the activity. This is in agreement with observations that earthquake activity due to inflation of the magma chamber only increased significantly when stress in the chamber roof exceeded the highest previous stress level (Einarsson, 1990). Thus the level of the inflation must exceed the previous maximum level

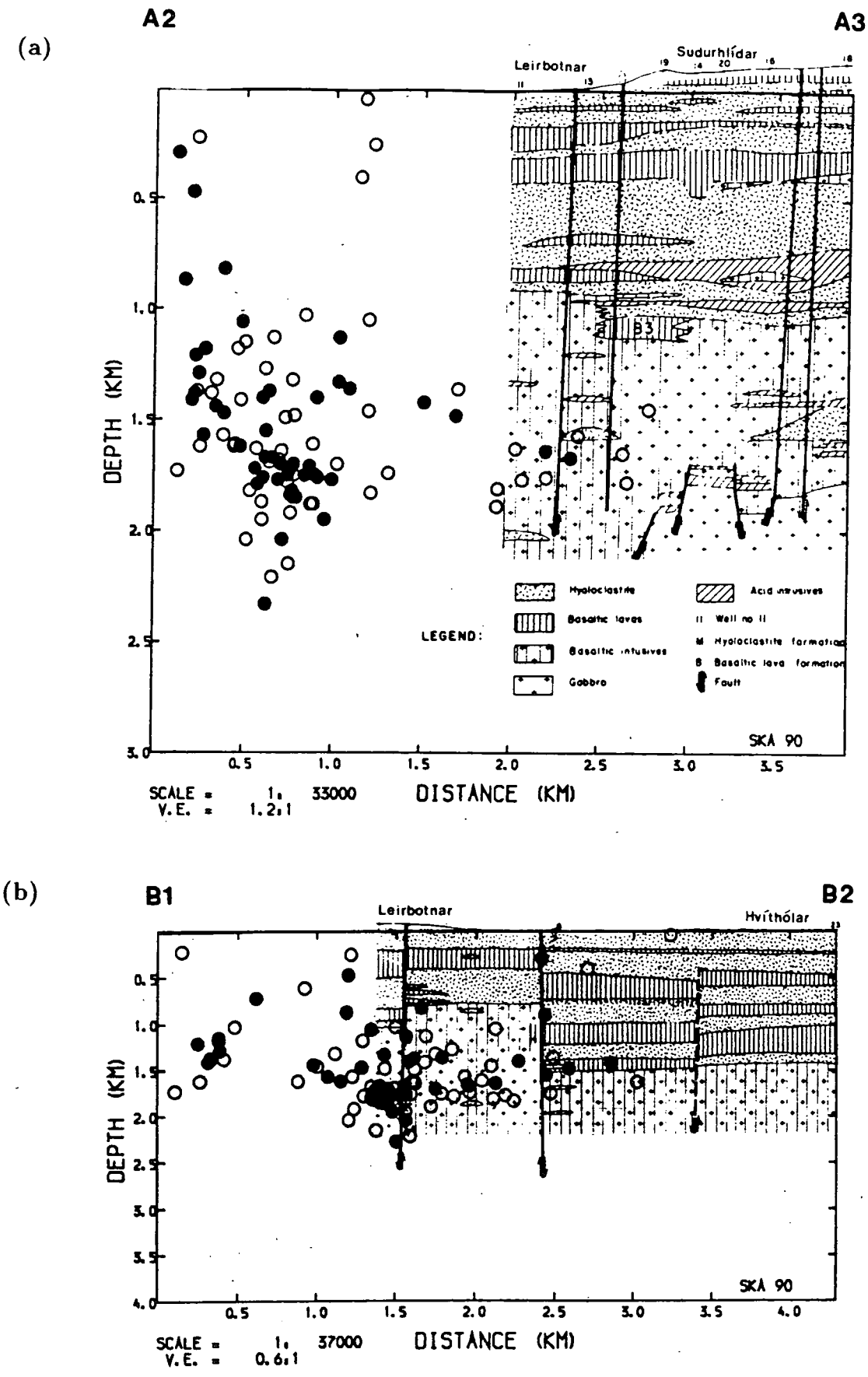

Figure 6.1 : Combined plots of hypocentres within the Krafla caldera and geological cross-sections based on borehole data. Lines of cross-sections are shown in figure 6.2. Hypocentre section widths are 5km. **(a)** Section A2–A3. **(b)** Section B1–B2.

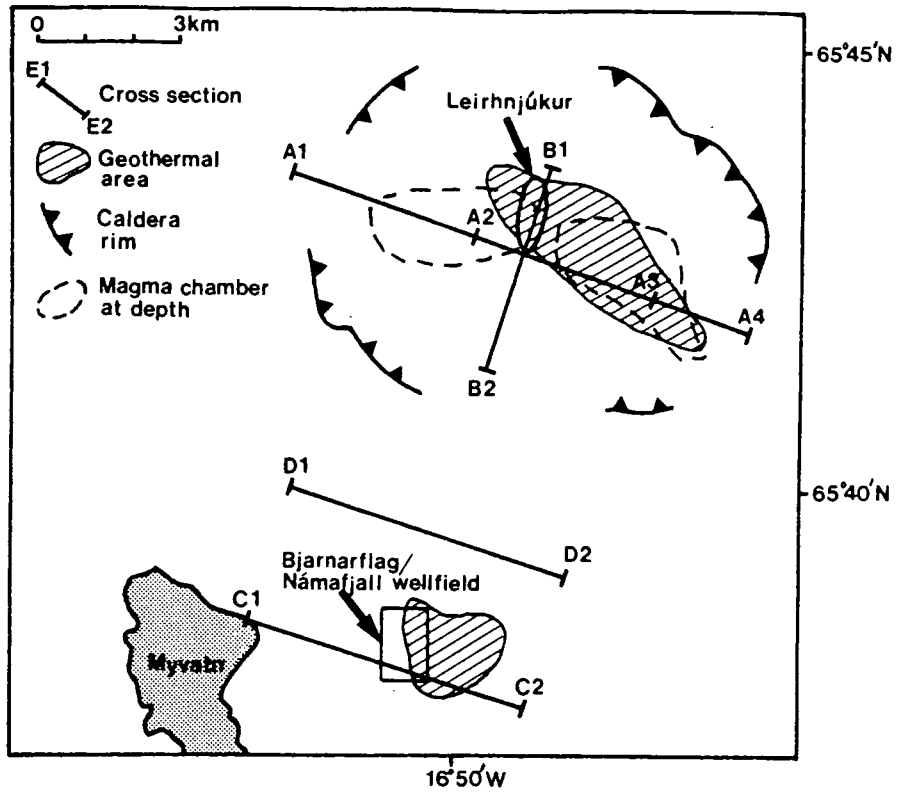

Figure 6.2 : Map showing lines of cross-section for figures 6.1 to 6.5.

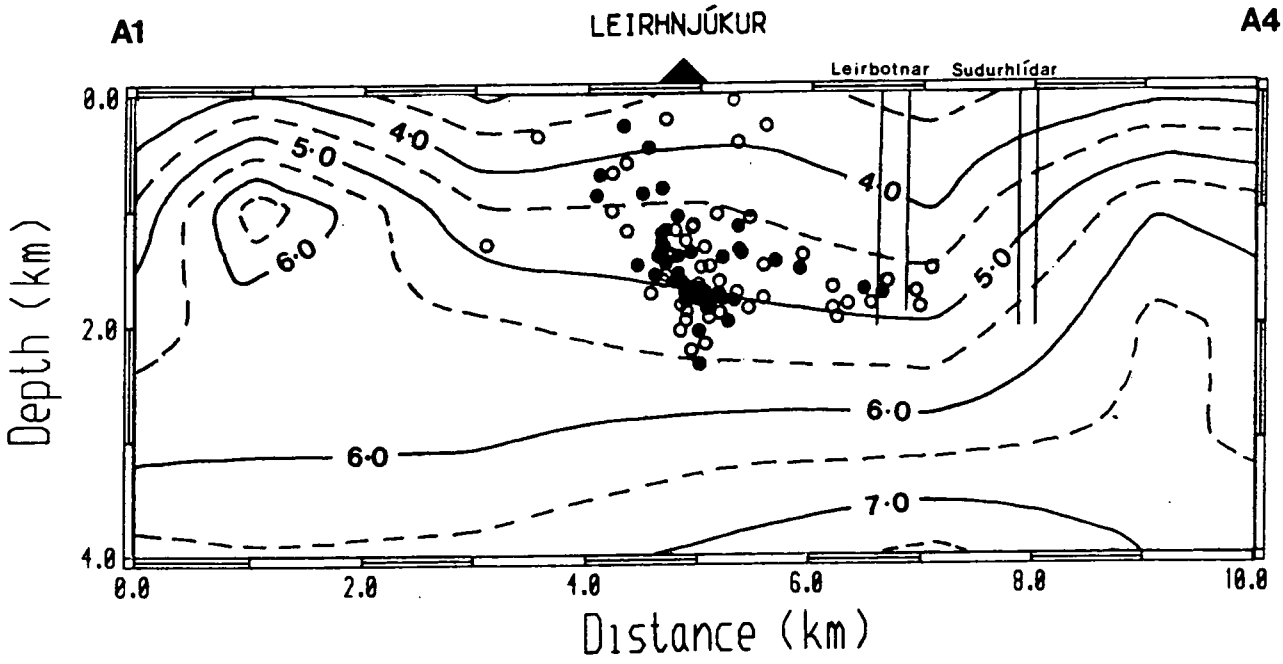

Figure 6.3 : Combined plot of hypocentres within the Krafla caldera and P-wave velocities from the tomography for section A1–A4 of figure 6.2. Hypocentre section width is 5km.

before activity resumes. Leirhnjúkur lies in the centre of the fissure swarm which bisects the caldera and has been a site of fissure eruptions both during the recent episode and during the Mývatn fires of 1724–29. The cluster of earthquakes beneath Leirhnjúkur may therefore lie in the vicinity of a magma conduit which fed the fissure eruptions immediately to the north. The stress field within the caldera, which was inferred from focal mechanism studies, indicates that the area was under extensional stress in a direction perpendicular to the fissure trend and trending approximately horizontally. Some local extensional stress therefore remained in the caldera area, suggesting that the rifting episode may not have been completely over, in accordance with the continued slow inflation of the volcano.

It is proposed that much of the low magnitude seismicity beneath Leirhnjúkur is a result of the extraction of heat from hot rock intrusions at depth, in a process similar to that previously observed in the Hengill area of Southwest Iceland (Foulger and Long, 1984; Foulger, 1984, 1988b). The circulation of groundwater causes intrusive bodies to cool rapidly, and this leads to the seismic formation of small cracks. The residual extensional stress field permits some volumetric extension, as is manifested in the occurrence of tensile crack type earthquakes, but most stress release occurs by strike–slip and normal faulting with little or no volumetric component. There is no preferred sense of strike–slip motion. Reverse faulting also occurs. It is considered likely that the proportion of tensile crack type events within the intrusive volume will increase with the recovery and build–up of the regional extensional stress field following the rifting episode. The steeply–dipping zone of activity which extends from the cluster towards the surface near Leirhnjúkur (figure 6.1a) is interpreted to outline the magma conduit for fissure eruptions in that area.

The northern fault of a west–northwest to east–southeast trending horst block, which was discovered by drilling for geothermal heat (figure 6.1b), projects through the centre of the main cluster of activity at a depth of about 1.5–2.0 km beneath the Leirbotnar geothermal field. This pattern of seismicity may indicate that the fault provides a path for the efficient removal of heat from adjacent intrusive bodies towards the geothermal fields. The southern fault of this horst block also appears to be marked by enhanced seismic activity (figure 6.1b) and may also therefore form an effective geothermal migratory path. Further minor activity immediately

to the south of this fault indicates the presence of an efficient aquifer at the top of the basaltic intrusive series at about 1.5 km depth.

It was shown (section 4.4.3) that within the caldera a coherent volume of relatively low seismic velocity in the form of a U–shaped pipe extends from near the surface on the western flanks of Mt. Krafla down to a depth of about 2 km, west–northwest for about 5 km, and up to an area close to the surface about 2 km west–northwest of Leirhnjúkur (figure 4.16). The eastern section of this low velocity volume is therefore approximately coincident with the proposed migratory path of geothermal fluids from beneath Leirhnjúkur towards the main area of geothermal mining, and is interpreted to have resulted from hydrothermal alteration of geothermal reservoir rocks. The low velocity volume west of Leirhnjúkur may have been formed by the same geothermal process, although the absence of coincident seismicity suggests that the activity may either be progressing with a lower intensity than that to the east, or may have stopped completely. This is consistent with the low surface heat loss to the west of Leirhnjúkur.

The presence of large relatively high velocity bodies at depth near the northern, western and eastern edges of the caldera has clearly been shown by tomographic inversion (chapter 4), although their exact shapes and depth extents are not well resolved. As discussed in section 4.4.2, localized averaging of velocity is a feature of the inversion process and consequently it is not possible to identify the exact positions of seismic discontinuities nor precise values of seismic velocity for individual geological units with confidence. Figure 6.3 shows seismic velocities along a section parallel to that shown in figure 6.1a (figure 6.2). The occurrence of these zones of anomalously high velocity correlates fairly well with the presence of Bouguer gravity highs around the caldera (figure 2.11), which suggest the existence of zones of relatively high density at shallow depth. Boreholes drilled to exploit geothermal heat have shown that gabbro intrusions become dominant beneath the Sudurhlídar field towards the east of the caldera at depths greater than 1.8–2.0 km, although they were found to be absent further west in the centre of the caldera (figure 6.1a). A granular gabbro at a depth of about 2 km (a pressure of about 5×10^6Pa) might be expected to have a seismic P–wave velocity of about 7.1 kms^{-1} (Kroenke et al., 1976), which is higher than that indicated by figure 6.3 for this location. However, inspection of the nodal velocity values within the

resolved volume (Appendix B.2) reveals that this may at least be partially a result of localized averaging and interpolation of velocities, and that the average velocity value within the resolved volume is roughly consistent with that of a gabbro. It is therefore proposed that significant volumes of relatively high velocity, high density intrusives are present at depth beneath sections of the caldera rim and that these intrusives are probably gabbros, similar to those found at sites of deeply eroded Tertiary central volcanoes (section 1.2.4). They may have formed by intrusion at the time of caldera collapse.

6.1.2 Námafjall–Bjarnarflag

Most seismicity located during this study originated within a tight cluster beneath the Námafjall geothermal area. This zone of activity has been accurately outlined to lie between about 2–3 km depth and to have a width of less than about 0.5 km (figure 4.25a). To the north, the zone has a sharply defined planar edge which dips steeply to the south and which projects up to the surface near the geothermal well-field at Bjarnarflag. The b–value for these events was relatively low (0.62 ± 0.14), suggesting that the active volume is in a high state of stress. Most stress is released by shear failure. Figure 6.4 demonstrates a striking coincidence between the seismicity beneath Bjarnarflag and a volume of relatively low seismic velocities.

The Námafjall geothermal area has previously been associated with enhanced background seismicity during periods of volcano–tectonic quiescence (e.g. figure 2.12a). It has been shown (section 5.3.3.2) that focal mechanisms of earthquakes within this zone of activity at the time of observation are consistent with an inhomogeneous stress field, although activity was concentrated on faults with preferred orientations. This stress pattern is distinct from the more coherent patterns observed for events originating within the other seismically active zones and demonstrates that failure was not controlled by a directional stress field. It may be inferred from these observations, and from the coincidence of intense seismicity and geothermal activity, that geothermal processes were the primary (and probably the sole) cause of seismic activity in this area at the time of the survey. It is therefore proposed that the observed seismicity in this area was (and is) a result of the extraction of heat from hot rocks at shallow depth, in a process similar to that which occurs in geothermal areas within the caldera. In this scheme, cooling and contraction of

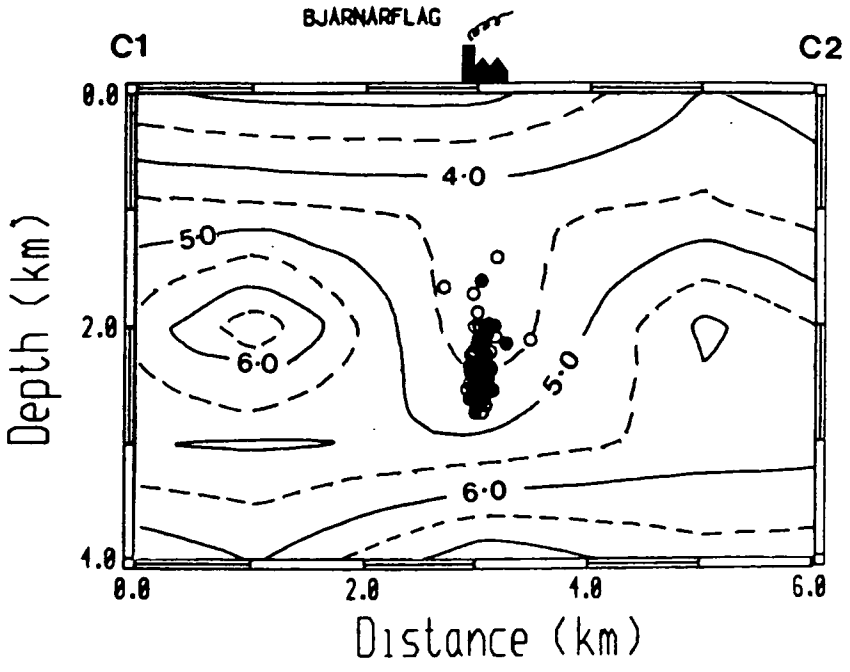

Figure 6.4 : Combined plot of hypocentres beneath Bjarnarflag and P-wave velocities from the tomography for section C1–C2 of figure 6.2. Hypocentre section width is 1 km.

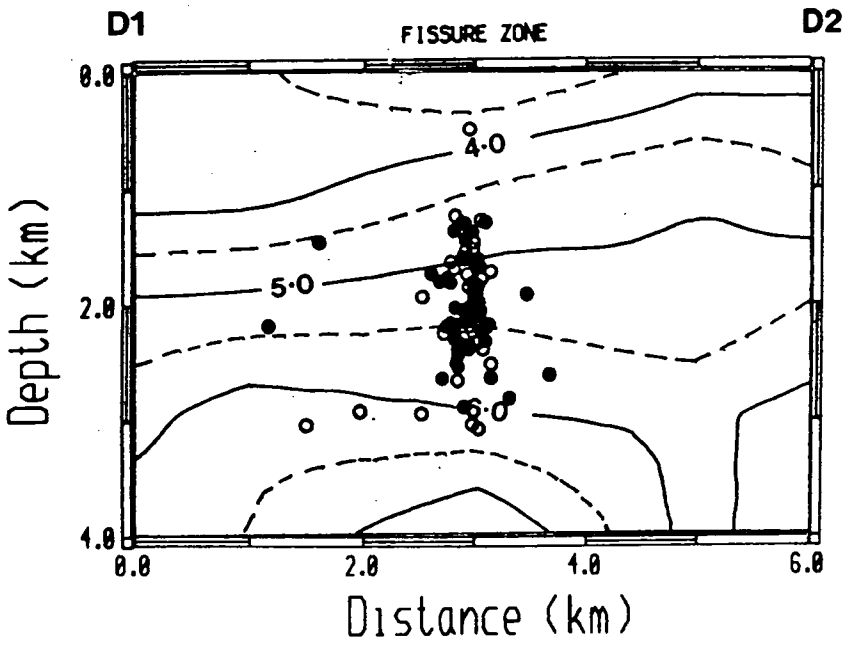

Figure 6.5 : Combined plot of hypocentres within the 'fissure swarm' and P-wave velocities from the tomography for section D1–D2 of figure 6.2. Hypocentre section width is 4.5 km.

hot rock under the influence of groundwater causes a stress distribution which is random on the scale of fracturing; a few metres. However, the fracturing occurs preferentially along pre–existing planes of weakness and is therefore concentrated along fault planes which lie within, and parallel to, the trend of surface fissures. An enhanced normal component in the fracturing results from a residual regional extensional stress field. Pervasive seismic fracturing and hydrothermal alteration of the geothermal reservoir has lowered seismic velocities. The sharp northern edge to the active volume is interpreted as a fault zone which marks the northern limit of the cooling volume. This fault may also provide an efficient migratory path for geothermal fluids between the cooling volume and the well field at Bjarnarflag. The virtual confinement of seismicity to beneath Bjarnarflag, which lies west of the main area of surface heat loss at Námafjall, may indicate that much of the activity is induced by mining. The heat source is unclear, but is likely to lie either directly beneath the Námafjall/Bjarnarflag area or to the south, and may be associated with an intrusive body (of high seismic velocity) beneath the ash cone Hverfjall (figure 2.3).

The presence of a 'chaotic' stress field is further supported by the occurrence within this volume of events which could be modelled as both opening and closing tensile cracks. Both types of non–double couple events occurred along almost vertical planes striking sub–parallel to the fissure trend, and were therefore opening and closing in the same direction. This could not be achieved under a uniform stress field. Tensile crack events require volumetric contraction of the hot rock and an extensional stress field, and would therefore be expected to have occurred more frequently prior to the onset of the rifting episode. Conversely, crack closure occurs under compressive stress and could therefore be characteristic of the post–rift period. It has been shown that closure of cavities within this volume could be driven by shear failure.

6.1.3 Fissure Zone

A narrow blade–like zone of seismic activity was observed to lie immediately to the north of the active volume beneath Námafjall (figure 6.5). It lies within a depth range of about 1.2–3.0 km, extends north–northeast from Námafjall towards the Krafla caldera for about 3 km and plunges northwards at about 10–15° (figure

4.24). The dominant orientations of the activated faults are oblique to the fissure swarm.

Significant seismic activity between Námafjall and the caldera has previously been reported only during the recent rifting episode. Activity was observed to migrate slowly southwards from the caldera as the magma chamber deflated, and to terminate in the Námafjall area (figures 2.15–2.17). These events were associated with lateral injection of magma from the magma chamber, and the activity marked the tips of propagating dykes (section 2.3.5). It is interesting to note that the southern dyke injections did not go much further south than Bjarnarflag. This may have been influenced by the presence of the distinctive fault which marks the northern limit of the geothermal seismicity there (section 6.1.2). Therefore this fault, or zone of faulting, may have acted as a structural barrier to the southward migration of injected magma.

The events observed during this study were not directly associated with a dyke injection event, but the fact that they delineate paths of previously injected dykes suggests that they are associated with that activity. The activity within the dyke injection zone resulted from a very coherent and distinctive stress field (section 5.3.3.3). The direction of greatest compressive stress was orientated approximately perpendicular to the axis of the volcanic system, which is not what one might normally expect at an accretionary plate boundary! However, each dyke injection event resulted in subsidence and extension within the fissure swarm, and uplift and compression at the flanks (section 2.3.5). It is proposed here that the local direction of maximum compressive stress, which is orientated perpendicular to the migratory path of injected dykes, is a result of emplacement of magma into the fissure swarm and is probably the reverse of that which existed prior to 1975.

It is possible that the injected magma is undergoing contraction and fracturing as it cools. However, there is no evidence to support this from surface heat loss (or from the occurrence of non–double couple earthquakes). There is evidence, however, that if this section of the fissure swarm is geothermally active, then it probably has not been so for long, or is not extensive. This is clear from the absence of a low velocity anomaly in the active zone, as shown in figure 6.5, which

provides no evidence for a mature zone of hydrothermal alteration such as that which exists beneath Bjarnarflag.

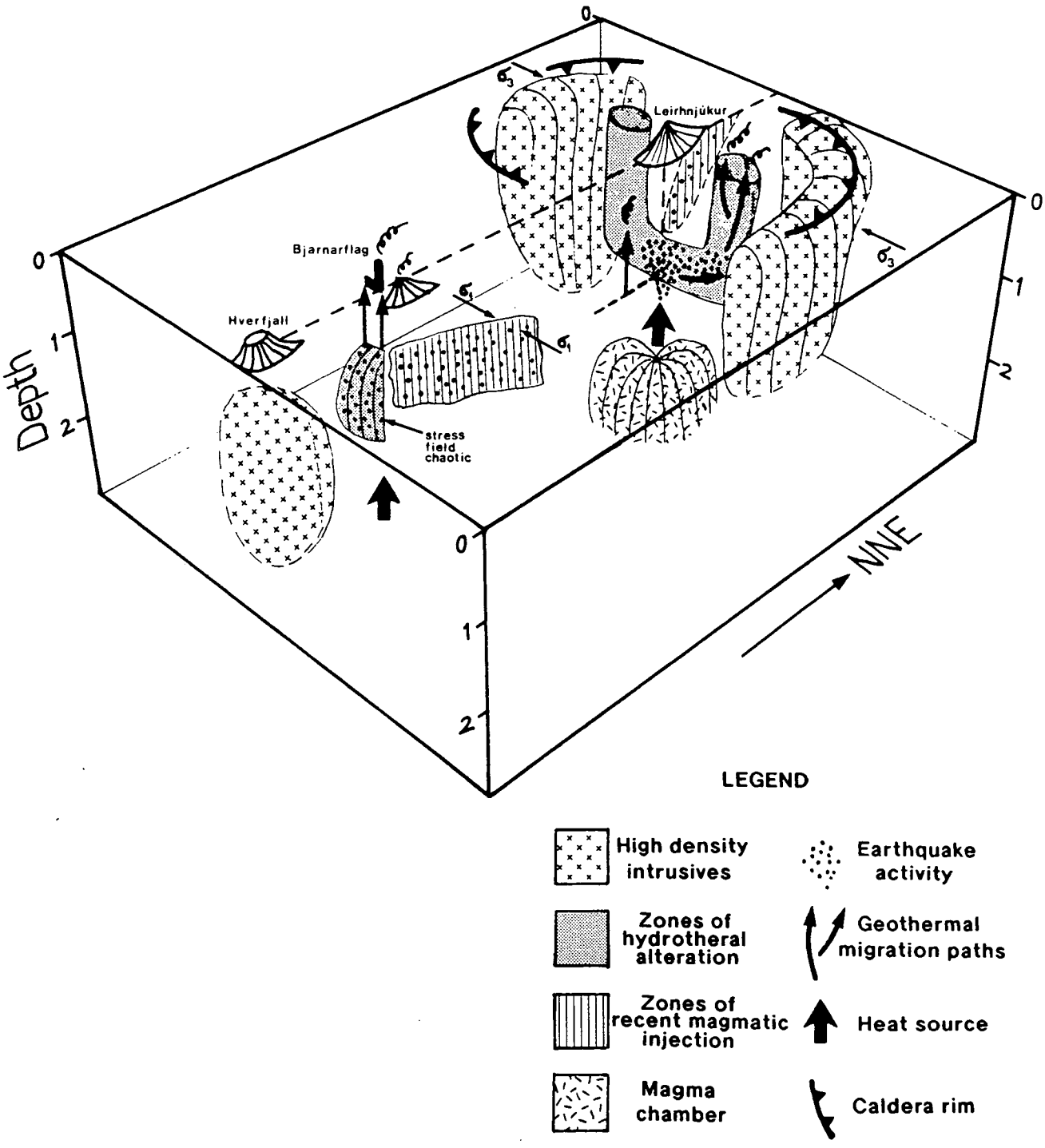

Figure 6.6 : Schematic summary illustration of the main geological features outlined by this study.

6.2 Conclusions

6.2.1 Geology

Figure 6.6 is a schematic summary illustration of the main results of this study. These are : -

- Seismicity in the Krafla–Námafjall area was concentrated in tight clusters beneath the two geothermal areas, and in a narrow planar zone coincident with a site of recent dyke injection. Activity was continuous.
- Large volumes of high velocity, high density intrusives — probably gabbros — are present at depth beneath sections of the caldera rim. A large volume of high velocity also lies beneath the ash cone Hverfjall.
- Geothermal areas under exploitation were characterized by continuous low magnitude seismicity and relatively low seismic velocities. Earthquake activity resulted from cooling and fracturing of hot intrusives at depth, and low velocities from intense fracturing and hydrothermal alteration.
- Explosive and implosive non–double couple events occurred in the geothermal areas.
- Fault surfaces are marked by enhanced seismicity where they provide efficient migratory paths for geothermal fluids.
- Seismicity may have been induced partially by geothermal mining.
- The stress field in the Krafla volcanic system varied significantly along its length, as did the mode of seismic fracturing. Heterogeneity is attributed to variation in regional extensional stress release during the recent rifting episode.
- In the Námafjall/Bjarnarflag geothermal area, the stress field was chaotic and the mode of fracturing random. Extensional and compressional fracturing, including tensile crack formation, cavity collapse, and normal and reverse faulting, occurred within the same volume.
- In the geothermal area within the Krafla caldera the stress field was extensional, resulting in dominantly extensional fracturing including tensile crack formation.

Strike–slip and reverse faulting also occured.

- Dyke injection south of the caldera induced a localized compressional stress régime perpendicular to the plate boundary. There is no evidence from surface heat loss or from a well–developed velocity anomaly, for geothermal activity in this zone.

- The b–value for the entire dataset was 0.77 ± 0.10. It was significantly lower for events at Bjarnarflag than for events in the zone of dyke injection.

6.2.2 Data Limitations

The main problems with the seismic dataset were : –

- The seismic network was too sparse, given the relatively shallow earthquake incidence. It was designed to optimize coverage for events at depths of about 4 km, whereas in fact the deepest hypocentre was at about 2.8 km. This over–estimation resulted from the use of a velocity structure for hypocentral location which was considerably in error (i.e. by about 15%). The principal effect was to reduce the number of polarity data constraining the earthquake focal mechanisms at steep take–off angles.

- The volume resolved by tomography was restricted to that enclosed by the seismic network. Slightly wider station coverage may have enabled the extent of intrusives around the caldera to be more clearly imaged.

6.3 Suggestions for Further Research

- Inversion of P–waveform data for seismic moment tensors. This would be particularly useful to confirm non–double couple earthquake interpretations and to identify the best solution where constraint on the positions of nodal lines is poor.
- Investigate S to P amplitude ratios to confirm focal mechanism solutions and to map variations in Q.
- Re–examine seismograms for reflected and refracted arrivals as a potential tool to clarify the nature and geometry of local crustal seismic discontinuities.
- Gravity and magnetic modelling based on the 3–d seismic velocity structure, particularly in the vicinity of the caldera.

References

Abdallah, A., Courtillot, V., Kasser, M., Le Dain, A., Lépine, J., Robineau, B., Ruegg, J., Tapponnier, P. and Tarantola, A., 1979. Relevance of Afar seismicity and volcanism to the mechanics of accreting plate boundaries. *Nature*, **282**, 17–23.

Achauer, U., Evans, J.R. and Stauber, D.A., 1988. High resolution seismic tomography of compressional wave velocity structure at Newberry volcano, Oregon Cascade Range. *J. Geophys. Res.*, **93**, 10135–10148.

Aki, K., 1966. Generation and propagation of G waves from the Niigata earthquake of June 16, 1964. 2. Estimation of earthquake movement, released energy and stress–strain drop from G wave spectrum. *Bull. Earthquake Res. Inst.*, **44**, 23–88

Aki, K., Cristoffersson, A. and Husebye, E., 1977. Determination of three dimensional seismic structure of the lithosphere. *J. Geophys. Res.*, **82**, 277–296.

Aki, K. and Lee, W.H.K., 1976. Determination of three–dimensional velocity anomalies under a seismic array using first P arrival times from local earthquakes. 1. A homogeneous initial model. *J. Geophys. Res.*, **81**, 4381–4399.

Aki, K. and Richards, P.R., 1980. *Quantitative Seismology, Vol. 1.* W.H. Freeman and Company, New York.

Angenheister, G., Gebrande, H., Miller, H., Goldflam, P., Weigel, W., Jacoby, W., Pálmason, G., Björnsson, S., Einarsson, P., Pavlenkova, N.I., Zverev, S.M., Litvenenko, I.V., Loncarević, B., Solomon, S. and Richard, S., 1980. Reykjanes Ridge seismic experiment (RRISP 77). *J. Geophys.*, **47**, 228–238.

Ármannsson, H., Gudmundsson, Á. and Steingrímsson, B.S. 1987. Exploration and development of the Krafla geothermal area. *Jökull*, **37**, 13–29.

Backus, G.E. and Gilbert, J.F., 1967. Numerical application of a formalism for geophysical inverse problems. *Geophys. J. R. Astron. Soc.*, **13**, 247–276.

Backus, G.E. and Gilbert, J.F., 1968. The resolving power of gross earth data. *Geophys. J. R. Astron. Soc.*, **16**, 169–205.

Barker, J.S. and Langston, C.A. 1983. A teleseismic body–wave analysis of the May 1980 Mammoth Lakes, California, earthquakes. *Bull. Seismol. Soc. Am.*, **73**, 419–434.

Båth, M., 1960. Crustal structure of Iceland. *J. Geophys. Res.*, **65**, 1793–1807.

Beblo, M. and Björnsson, A., 1978. Magnetotelluric investigation of the lower crust and upper mantle beneath Iceland. *J. Geophys.*, **45**, 1–16.

Beblo, M. and Björnsson, A., 1980. A model of electrical resistivity beneath N.E. Iceland, correlation with temperature. *J. Geophys.*, **47**, 184–190.

Beblo, M., Björnsson, A., Arnason, K., Stein, B. and Wolfgram, P., 1983. Electrical conductivity beneath Iceland — constraints imposed by magnetotelluric results on temperature, partial melt, crust– and mantle structure. *J. Geophys.*, **53**, 16–23.

Benz, H.M. and Smith, R.B., 1984. Simultaneous inversion for lateral velocity variations and hypocenters in the Yellowstone region using earthquake and refraction data. *J. Geophys. Res.*, **89**, 1208–1220.

Björnsson, A., 1985. Dynamics of crustal rifting in N.E. Iceland. *J. Geophys. Res.*, **90**, 10151–10162.

Björnsson, A., Johnsen, G., Sigurdsson, S., Thorbergsson, G. and Tryggvason, E., 1979. Rifting of the plate boundary in northern Iceland 1975–1978. *J. Geophys. Res.*, **84**, 3029–3038.

Björnsson, A., Saemundsson, K., Einarsson, P., Tryggvason, E. and Gronvold, K., 1977. Current Rifting episode in North Iceland. *Nature*, **266**, 318–323.

Björnsson, H., Björnsson, S. and Sigurdsson, Th., 1982. Penetration of water into hot rock boundaries of magma at Grímsvötn. *Nature*, **295**, 580–581.

Björnsson, S., 1983. Crust and upper mantle beneath Iceland. in : *Structure and development of the Greenland–Scotland Ridge.* ed. M.H.P. Bott et al., Plenum Press, New York and London, 31–61.

Bödvarsson, G.S., Benson, S.M., Sigurdsson, Ó., Stefánsson, V. and Elíasson, E.T., 1984a. The Krafla geothermal field, Iceland. 1. Analysis of well data. *Water Res. Res.*, **20**, 1515–1530.

Bödvarsson, G.S., Preuss, K., Stefánsson, V. and Elíasson, E.T., 1984b. The Krafla geothermal field, Iceland. 2. The natural state of the system. *Water Res. Res.*, **20**, 1531–1544.

Bödvarsson, G.S., Preuss, K., Stefánsson, V. and Elíasson, E.T., 1984c. The Krafla geothermal field, Iceland. 3. The generating capacity of the field. *Water Res. Res.*, **20**, 1545–1559.

Bott, M.H.P., 1974. Deep structure, evolution and origin of the Icelandic transverse ridge. in. *Geodynamics of Iceland and the North Atlantic Area*, ed. L. Kristjansson. D. Reidel Pub. Co., Dordrecht, 33–47.

Bott, M.H.P., 1983a. Deep structure and geodynamics of the Greenland–Scotland Ridge; an introductory review. in : *Structure and development of the Greenland–Scotland Ridge.* ed. M.H.P. Bott et al., Plenum Press, New York and London

Bott, M.H.P., 1983b. The crust beneath the Iceland–Faeroe Ridge. in : *Structure and development of the Greenland–Scotland Ridge.* ed. M.H.P. Bott et al., Plenum Press, New York and London

Bott, M.H.P., 1985. Plate tectonic evolution of the Icelandic Transverse Ridge and adjacent regions. *J. Geophys. Res.*, **90**, 9953–9960.

Bott, M.H.P. and Gunnarsson, K., 1980. Crustal structure of the Iceland–Faeroe Ridge. *J. Geophys.*, **47**, 221–227.

Brandsdóttir, B. and Einarsson, P., 1979. Seismic activity associated with the September 1977 deflation of the Krafla central volcano in north–eastern Iceland. *J. Volcanol. Geotherm. Res.*, **6**, 197–212.

Bufe, C.G., 1970. Frequency–magnitude variations during the 1970 Demville earthquake swarm. *Earthquake Notes*, **41**, 3–7.

Burnett, M.S., Caress, D.W. and Orcutt, J.A., 1989. Tomographic image of the magma chamber at 12°50′N on the East Pacific Rise. *Nature*, **339**, 206–208.

Chou, C.W. and Booker, J.R., 1979. A Backus–Gilbert approach to inversion of travel–time data for three–dimensional velocity structure. *Geophys. J. R. Astron. Soc.*, **59**, 325–344.

Chouet, B., 1979. Sources of seismic events in the cooling lava lake of Kilauea Iki, Hawaii. *J. Geophys. Res.*, **84**, 2315–2330.

Crosson, R.D., 1976. Crustal structure modelling of earthquake data. 1. Simultaneous least squares estimation of hypocenter and velocity parameters. *J. Geophys. Res.*, **81**, 3036–3046.

Degroot, M.H., 1975. *Probability and Statistics*, Addison–Wesley, Reading, Mass., 607 pp.

Detrick, R.S., Buhl, P., Vera, E., Mutter, J., Orcutt, J., Madsen, J. and Brocher, T., 1987. Multi–channel seismic imaging of a crustal magma chamber along the East Pacific Rise. *Nature*, **326**, 35–41.

Dziewonski, A.M. and Anderson, D.L., 1984. Seismic tomography of the Earth's interior. *Am. Sci.*, **72**, 483–494.

Eberhart–Phillips, D., 1986. Three–dimensional velocity structure in northern California Coast Ranges from inversion of local earthquake arrival times. *Bull. Seismol. Soc. Am.*, **76**, 1025–1032.

Einarsson, P., 1977. Phenomenon in the Krafla area (in Icelandic). *Skjálftabréf*, no. **24**, 6–9.

Einarsson, P., 1978. S–wave shadows in the Krafla caldera in NE–Iceland, evidence for a magma chamber in the crust. *Bull. Volcanol.*, **41-3**, 1–9.

Einarsson, P., 1979. Seismicity and earthquake focal mechanisms along the mid–Atlantic plate boundary between Iceland and the Azores. *Tectonophysics*, **55**, 127–153.

Einarsson, P., 1982. Increase in seismic activity in the Krafla area (in Icelandic). *Skjálftabréf* no. **53**, 6–8.

Einarsson, P., 1987. Compilation of earthquake fault plane solutions in the North Atlantic and Arctic Oceans. in : *Recents Plate Movements and Deformation.* ed. K. Kasahara, Geodynamic series, Vol. 20, Am. Geophys. Union, 47–62.

Einarsson, P., 1989. Intraplate Earthquakes in Iceland. in : *Earthquakes at North Atlantic Passive Margins : Neotectonics and Postglacial Rebound.* ed. S. Gregersen and P.W. Basham, Kluwer Academic Publishers, 329–344.

Einarsson, P., 1990. Earthquakes and present tectonics in Iceland. *Tectonophysics*, in press.

Einarsson, P. and Björnsson, S., 1979. Earthquakes in Iceland. *Jökull*, **29**, 37–43.

Einarsson, P. and Björnsson, S., 1987. Seismological Research at the science institute, University of Iceland (in Icelandic). in : *Í hlutarins edli*, festschrift for Thorbjörn Sigurgeirsson. ed. Thorsteinn Sigússon, Menningarsjódur, Reykjavík, 251–278.

Einarsson, P. and Brandsdóttir, B., 1980a. Seismological evidence for lateral magma intrusion during the July 1978 deflation of the Krafla volcano in NE–Iceland. *J. Geophys.*, **47**, 160–165.

Einarsson, P. and Brandsdóttir, B., 1980b. Magmatic intrusion in February (in Icelandic). *Skjálftabréf* no. **41**, 5–7.

Einarsson, P. and Eiriksson, J., 1982. Earthquake fractures in the districts Land and Rangarvellir in the South Iceland Seismic Zone. *Jökull*, **32**, 113–120.

Einarsson, T., 1954. A survey of gravity in Iceland. *Soc. Sci. Islandica*, Rit **30**.

Ekström, G., 1983. Evidence for source complexities of 1980 Mammoth Lakes earthquakes (abstract). *EOS Trans. AGU*, **64**, 769.

Ellsworth, W.L. and Koyanagi, R.Y., 1977. Three–dimensional crust and mantle structure of Kilauea volcano, Hawaii. *J. Geophys. Res.*, **82**, 5379–5394.

Evans, J.R. and Zucca, J.J., 1988. Active high resolution seismic tomography of compressional wave velocity and attenuation structure at Medicine Lake volcano, northern California Cascade Range. *J. Geophys. Res.*, **93**, 15016–15036.

Flovenz, O.G., 1980. Seismic structure of the Icelandic crust above layer three and the relation between body wave velocity and the alteration of the basaltic crust. *J. Geophys.*, **47**, 211–220.

Foulger, G.R., 1982. Geothermal exploration and reservoir monitoring using earthquakes and the passive seismic method. *Geothermics*, **11**, no. 4, 259–268.

Foulger, G.R., 1984. *Seismological Studies at the Hengill Geothermal Area, SW Iceland.* Ph.D. Thesis, University of Durham, 313 pp.

Foulger, G.R., 1986. *Krafla. The seismological field project of June–October 1985.* Report prepared for National Energy Authority, Iceland, Science Institute, University of Iceland, and University of Durham, U.K. 24 pp.

Foulger, G.R., 1988a. Hengill triple junction, S.W. Iceland. 1. Tectonic structure and the spatial and temporal distribution of local earthquakes. *J. Geophys. Res.*, **93**, 13493–13506.

Foulger, G.R., 1988b. Hengill triple junction, S.W. Iceland. 2. Anomalous focal mechanisms and implications for processes within the geothermal reservoir and at accretionary plate boundaries. *J. Geophys. Res.*, **93**, 13507–13523.

Foulger, G.R. and Long, R.E. 1984. Anomalous focal mechanisms : tensile crack formation on an accreting plate boundary. *Nature*, **310**, 43–45.

Foulger, G.R., Long, R.E., Einarsson, P. and Björnsson, A., 1989. Implosive earthquakes at the active accretionary plate boundary in northern Iceland. *Nature*, **337**, 640–642.

Foulger, G.R. and Toomey, D.R., 1989. Structure and evolution of the Hengill–Grensdalur volcanic complex, Iceland : geology, geophysics and seismic tomography. *J. Geophys. Res.*, **94**, 17511–17522.

Gebrande, H., Miller, H. and Einarsson, P., 1980. Seismic structure of Iceland along RRISP – profile 1. *J. Geophys.*, **47**, 239–249.

Gerke, K., 1974. Crustal movements in the Mývatn and in the Thingvallavatn area, both horizontal and vertical. in : *Geodynamics of Iceland and the North Atlantic Area*, ed. L.Kristjansson, Dordrecht, Holland. D. Reidel Publ. Co, 263–275.

Given, J.W., Wallace, T.C. and Kanamori, H., 1982. Teleseismic analysis of the 1980 Mammoth Lakes earthquake sequence. *Bull. Seismol. Soc. Am.*, **72**, 1093–1110.

Goldflam, P., Wiegel, W. and Loncarevic, B.D., 1980. Seismic structure along RRISP – profile 1 on the Southeast flank of the Reykjanes Ridge. *J. Geophys.*, **47**, 250–260.

Grönvold, K., 1976. Variation and origin of magma types in the Námafjall area, North Iceland. *Bull. Soc. Géol. France*, (**7**), t.XVIII, 869–870.

Grönvold, K., 1984. Mývatn fires 1724–1729. Chemical composition of the lava. *Nordic Volcanological Institute Report 8401.*

Gudmundsson, G. and Sæmundsson, K., 1980. Statistical analysis of damaging earthquakes and volcanic eruptions in Iceland from 1550–1978. *J. Geophys.*, **47**, 99–109.

Gutenberg, B. and Richter, C.F., 1941. Seismicity of the Earth. *Geol. Soc. Am., Spec. Pap.*, **34**, 1–133.

Helgason, J., 1985. Shifts of the plate boundary in Iceland : some aspects of Tertiary volcanism. *J. Geophys. Res.*, **90**, 10084–10092.

Hermance, J.F., 1981. Crustal genesis in Iceland : geophysical constraints on crustal thickening with age. *Geophys. Res. Let.*, **8**, 203–206.

Hirahara, K., Mikumo, T., 1980. Three–dimensional seismic structure of subducting lithospheric plates under the Japan islands. *Phys. Earth Planet. Inter.*, **21**, 109–119.

Humphreys, E., Clayton, R.W. and Hager, B.H., 1984. A tomographic image of mantle structure beneath southern California. *Geophys. Res. Lett.*, **11**, 625–627.

Iyer, H.M., 1984. Geophysical evidence for the locations, shapes and sizes, and internal structures of magma chambers beneath regions of quaternary volcanism. *Phil. Trans. R. Soc. Lond.*, **A310**, 473–510.

Jakobsson, S.P., 1972. Chemistry and distribution pattern of Recent basaltic rocks in Iceland. *Lithos*, **5**, 365–386.

Jakobsson, S.P., 1979. Outline of the petrology of Iceland. *Jökull*, **29**, 57–73.

Jacoby, W.R., Zdarsky, H. and Altmann, U., 1989. Geodetic and geophysical evidence for magma movement and dyke injection during the Krafla rifting episode in North Iceland. in : *Evolution of Mid Ocean Ridges*, IUGG, **8**, Geophysical monograph 57. ed. J.M. Sinton, American Geophysical Union, 65–77.

Johnsen, G.V., Björnsson, A. and Sigurdsson, S., 1980. Gravity and elevation changes caused by magma movement beneath the Krafla caldera, Northeast Iceland. *J. Geophys.*, **47**, 132–140.

Julian, B.R., 1983. Evidence for dyke intrusion earthquake mechanisms near Long Valley caldera, California. *Nature*, **303**, 323–325.

Julian, B.R., 1986. Analysing seismic–source mechanisms by linear–programming methods. *Geophys. J. R. Astron. Soc.*, **84**, 431–443.

Julian, B.R. and Gubbins, D., 1977. Three–dimensional seismic ray tracing. *J. Geophys.*, **43**, 95–113.

Julian, B.R. and Sipkin, S.A., 1985. Earthquake processes in the Long Valley caldera area, California. *J. Geophys. Res.*, **90**, 11155–11169.

Karlsdóttir, R., Johnsen, G., Björnsson, A., Sigurdsson, Ó. and Hauksson, E., 1978. *The geothermal area of Krafla : general report on geophysical research 1976–78* (in Icelandic). Report no. OS/JDH–7847, Orkustofnun, Reykjavík.

Kawasaki, I. and Tanimoto, T., 1981. Radiation patterns of body waves due to seismic dislocation occurring in an anisotropic source medium. *Bull. Seismol. Soc. Am.*, **71**, 37–50.

Kissling, E., 1988. Geotomography with local earthquake data. *Rev. Geophys.*, **26**, 659–698.

Klein, F.W., 1978. *Hypocenter location program – HYPOINVERSE : users guide to versions 1, 2, 3, and 4.*, U.S. Geol. Surv. Open–File Report 78–694.

Klein, F.W., Einarsson, P. and Wyss, M., 1977. The Reykjanes Peninsula, Iceland, earthquake swarm of September 1972 and its tectonic significance. *J. Geophys. Res.*, **82**, 865–888.

Knopoff, L. and Randall, M.J., 1970. The compensated linear vector dipole : a possible mechanism for deep earthquakes. *J. Geophys. Res.*, **75**, 4957–4963.

Kroenke, L.W., Maughnani, M.H., Rai, C.S., Fryer, P. and Ramananantoandro, R., 1976. Elastic properties of selected ophiolitic rocks from Papua New Guinea :nature and composition

of oceanic lower crust and upper mantle. in : *The Geophysics of the Pacific Ocean Basin and its Margin*, Geophysical Monograph **19**, American Geophysical Union, 407–421.

Langmuir, C.H., Bender, J.F., Batiza, R., 1986. Petrological and tectonic segmentation of the East Pacific Rise, 5°30′–14°30′N. *Nature*, **322**, 422–429.

Larsen, G., Grönvold, K. and Thorarinsson, S., 1979. Volcanic eruption through a geothermal borehole at Námafjall, Iceland. *Nature*, **278**, 707–710.

Laughton, A.S., Searle, R.C. and Roberts, D.G., 1979. The Reykjanes Ridge crest and the transition between its rifted and non-rifted regions. *Tectonophysics*, **55**, 173–177.

Lees, J.M. and Crosson, R.S., 1990. Tomographic imaging of local earthquake delay times for three–dimensional velocity variation in western Washington. *J. Geophys. Res.*, **95**, 4763–4776.

Lee, W.H.K. and Stewart, S.W., 1981. *Principles and Applications of Microearthquake Networks.* Academic Press, New York.

Lin, J., Purdy, G.M., Schouten, H., Sempéré, J.C. and Zervas, C., 1990. Evidence from gravity data for focussed magmatic accretion along the Mid–Atlantic Ridge. *Nature*, **344**, 627–632.

Lister, C.R.B., 1974. On the penetration of water into hot rock. *Geophys. J. R. Astron. Soc.*, **39**, 465–509.

Long, R.E. and Mitchell, M.G., 1970. Teleseismic P–wave delay times in Iceland. *Geophys. J. R. Astron. Soc.*, **20**, 41–48.

Macdonald, K.C., Fox, P.J., Perram, L.J., Eisen, M.F., Haymon, R.M., Miller, S.P., Carbotte, S.M., Cornier, M.H. and Shor, A.N., 1988. A new view of the mid–ocean ridge from the behaviour of ridge–axis discontinuities. *Nature*, **335**, 217–225.

MacKenzie, R., 1989. *An analysis of teleseismic arrivals at the Krafla seismic array, Iceland.* M.Sc. thesis, University of Durham, U.K., 99pp.

Marquart, G. and Jacoby, W., 1985. On the mechanism of magma injection and plate divergence during the Krafla rifting episode in N.E. Iceland. *J. Geophys. Res.*, **90**, 10178–10192.

M^{c}Kenzie, D.P., 1969. The relation between fault plane solutions for earthquakes and directions of the principal stresses. *Bull. Seismol. Soc. Am.*, **59**, 591–601.

M^{c}Master, R.L., Schilling, J.G.E. and Pinet, P.R., 1977. Plate boundary within the Tjörnes Fracture Zone on northern Iceland's insular margin. *Nature*, **269**, 663–668.

M^{c}Nutt, S.R. and Jacob, H.H., 1986. Determination of large scale structures of the crust and upper mantle in the vicinity of Pavlov volcano, Alaska. *J. Geophys. Res.*, **91**, 5013–5022.

Menke, W., 1984. *Geophysical Data Analysis : Discrete Inversion Theory.* Academic Press, San Diego, California, 260 pp.

Mitchell, B.J., Stauder, W. and Cheng, C.C., 1977. The New Madrid seismic zone as a laboratory for earthquake prediction research. *J. Phys. Earth*, **255**, 43–49.

Möller, D. and Ritter, B., 1980. Geodetic measurements and horizontal crustal movements in the rift zone of NE–Iceland. *J. Geophys.*, **47**, 110–119.

Möller, D., Ritter, B. and Wendt, K., 1982. Geodetic measurement of horizontal deformations in Northeast Iceland. *Earth Evolution Sciences*, **2**, 149–154.

Nunns, A.G., 1983. Plate tectonic evolution of the Greenland-Scotland Ridge and surrounding regions. in : *Structure and development of the Greenland-Scotland Ridge.* ed. M.H.P. Bott et al., Plenum Press, New York and London, 11–29.

Oppenheimer, D.H. and Herkenhoff, K.E., 1981. Velocity–density properties of the lithosphere from three–dimensional modelling at Geysers–Clear Lake region, California. *J. Geophys. Res.*, **86**, 6057–6065.

Oskarsson, N., Steinthorsson, S. and Sigvaldason, G.E., 1985. Iceland geochemical anomaly : origin, volcanotectonics, chemical fractionation and isotope evolution of the crust. *J. Geophys. Res.*, **90**, 10011–10025.

Pálmason, G., 1963. Seismic refraction investigation of the basalt lavas in northern and eastern Iceland. *Jökull*, **13**, 40–60.

Pálmason, G., 1971. Crustal structure of Iceland from explosion seismology. *Soc. Sci. Islandica*, **40**, 187 pp.

Pálmason, G., 1980. A continuum model of crustal generation in Iceland; kinematic aspects. *J. Geophys.*, **47**, 7–18.

Palvis, G.L. and Booker, J.R., 1980. The mixed discrete–continuous inverse problem : application to the simultaneous determination of earthquake hypocenters and velocity structure. *J. Geophys. Res.*, **85**, 4801–4810.

Pfluke, J.H. and Steppe, J.A., 1983. Magnitude–frequency statistics of small earthquakes from San Francisco Bay to Parkfield. *Stanford Univ. Publ., Geol. Sci.*, **13**, 13–23.

Pruess, K., Bödvarsson, G.S., Stefánsson, V. and Elíasson, E.T., 1984. The Krafla geothermal field, Iceland. 4. History match and prediction of individual well performance. *Water Res. Res.*, **20**, 1561–1584.

Ragnars, K., Sæmundsson, K., Benediktsson, S. and Einarsson, S.S., 1970. Development of the Námafjall area, Northern Iceland. *Geothermics, Special Issue 2*, **2**(1), 925–935.

Reasenberg, P., Ellsworth, W. and Walter, A., 1980. Teleseismic evidence for a low–velocity body under the Coso geothermal area. *J. Geophys. Res.*, **85**, 2471–2483.

Richter, C.F., 1935. An instrumental earthquake magnitude scale. *Bull. Seismol. Soc. Am.*, **25**, 1–32.

Richter, C.F., 1958. *Elementary Seismology.* Freeman, San Francisco, California.

Robinson, R. and Iyer, H.M., 1981. Delineation of a low–velocity body under the Roosevelt Hot Springs area, Utah, using teleseismic P–wave data. *Geophysics*, **46**, 1456–1466.

Sæmundsson, K., 1974. Evolution of the axial rifting zone in northern Iceland and the Tjörnes Fracture Zone. *Geol. Soc. Am. Bull.*, **85**, 495–504.

Sæmundsson, K., 1978. Fissure swarms and central volcanoes of the neovolcanic zones of Iceland. *Geol. J., Spec. Issue*, **10**, 415–432.

Sæmundsson, K., 1979. Outline of the geology of Iceland. *Jökull*, **29**, 7–28.

Schilling, J.G., 1973. Iceland mantle plume, geochemical evidence along Reykjanes Ridge. *Nature*, **242**, 565–578.

Schleusener, A., Torge, W. and Drewes, H., 1976. The gravity field of northeastern Iceland. *J. Geophys.*, **42**, 27–45.

Scholz, C., 1968. The frequency–magnitude relation of microfracturing in rock and its relation to earthquakes. *Bull. Seismol. Soc. Am.*, **58**, 399–415.

Schouten, H., Klitgord, K.D. and Whitehead, J.A., 1985. Segmentation of mid–ocean ridges. *Nature,* **317**, 225–229.

Sempéré, J.C., Purdy, G.M. and Schouten, H., 1990. Segmentation of the Mid–Atlantic Ridge between 24°N and 30°40′N. *Nature,* **344**, 427–431.

Sengupta, M.K., Hassel, R.E. and Ward, R.W., 1981. Three–dimensional seismic velocity structure of the Earth's mantle using body wave travel times from intra–plate and deep–focus earthquakes. *J. Geophys. Res.,* **86**, 3913–3934.

Sharp, A.D.L., Davis, P.M. and Gray, F., 1980. A low velocity zone beneath Mount Etna and magma storage. *Nature,* **287**, 587–591.

Shimizu, H., Ueki, S. and Koyama, J., 1987. A tensile–shear crack model for the mechanism of volcanic earthquakes. *Tectonophysics,* **144**, 287–300.

Sigurdsson, O., 1980. Surface deformation of the Krafla fissure swarm in two rifting events. *J. Geophys.,* **47**, 154–159.

Sigurdsson, H. and Sparks, R.S.J., 1978. Rifting episode in North Iceland, 1874–1875 and the eruption of Askja and Sveinagja. *Bull. Volc.,* **41**, 149–167.

Sigvaldason, G.E., Steinthorsson, S., Oskarsson, N. and Imsland, P., 1974. Compositional variation in recent Icelandic tholeiites and the Kverkfjöll hotspot. *Nature,* **251**, 579–582.

Smith, M.J., 1987a. *DUEDROPS. Durham University Earthquake Data Reduction and Processing System. System Guide.* Dept. Geol. Sci., Univ. of Durham internal report 87–01, 28 pp.

Smith, M.J., 1987b. *DUEDROPS–HYPOPLOT. Hypocentre plotting system. User manual.* Dept. Geol. Sci., Univ. of Durham internal report 87–03, 82 pp.

Smith, M.J., 1987c. *DUEDROPS–HYPOPLOT. Hypocentre plotting system. HYPOPLOT program documentation.* Dept. Geol. Sci., Univ. of Durham internal report 87–04, 83 pp.

Smith, M.J., 1987d. *DUEDROPS–TOMOGRAPHY. Tomographic inversion system. User manual.* Dept. Geol. Sci., Univ. of Durham internal report 87–05, 65 pp.

Smith, M.J., 1987e. *DUEDROPS–HYPOPLOT. An example run of HYPOPLOT.* Dept. Geol. Sci., Univ. of Durham internal report 87–06, 36 pp.

Smith, M.J., 1987f. *DUEDROPS–TOMOGRAPHY. Tomographic inversion system. User update manual.* Dept. Geol. Sci., Univ. of Durham internal report 87–07, 6 pp.

Smith, M.J. and Foulger, G.R., 1987. *DUEDROPS–HLPS. Hypocentre locator system. User manual.* Dept. Geol. Sci., Univ. of Durham internal report 87–02, 47 pp.

Solomon, S.C and Julian, B.R., 1974. Seismic constraints on ocean–ridge mantle structure : anomalous fault–plane solutions from first motions. *Geophys. J. R. Astron. Soc.,* **38**, 265–285.

Spencer, C. and Gubbins, D., 1980. Travel time inversion for simultaneous earthquake location and velocity structure determination in laterally varying media. *Geophys. J. R. Astron. Soc.,* **63**, 95–116.

Stauber, D.A., Green, S.M. and Iyer, H.M., 1988. Three–dimensional P–velocity structure of the crust below Newberry Volcano, Oregon. *J. Geophys. Res.,* **93**, 10095–10109.

Stefánsson, V., 1981. The Krafla Geothermal Field, Northeast Iceland. in : *Geothermal Systems : Principles and Case Histories.* ed. L. Rybach and L.J.P. Muffler. John Wiley and Sons Ltd, 273–294.

Steinthorsson, S. and Jacoby, W., 1985. Crustal accretion in and around Iceland. *J. Geophys. Res.*, **90**, 9951–9952.

Suyehiro, S., Asada, T. and Ohtake, M., 1964. Foreshocks and aftershocks accompanying a perceptible earthquake in central Japan : on the peculiar nature of aftershocks. *Pap. Meteorol. Geophys.*, **15**, 71–88.

Sykes, L.R., 1967. Mechanism of earthquakes and nature of faulting on the mid–ocean ridges. *J. Geophys. Res.*, **72**, 2131–2153.

Sykes, L.R., 1970. Earthquake swarms and seafloor spreading. *J. Geophys. Res.*, **75**, 6598–6611.

Talwani, M. and Eldholm, O., 1977. Evolution of the Norwegian–Greenland Sea. *Bull. Geol. Soc. Am.*, **88**, 969–999.

Talwani, M., Windisch, C.C. and Langseth, M.G.Jr., 1971. Reykjanes Ridge crest. A detailed geophysical study. *J. Geophys. Res.*, **76**, 473–517.

Tarantola, A. and Nercessian, A., 1984. Three–dimensional inversion without blocks. *Geophys. J. R. Astron. Soc.*, **76**, 299–306.

Tarantola, A., Ruegg, J. and Lépine, J., 1979. Geodetic evidence for rifting in Afar : a brittle–elastic model of the behaviour of the lithosphere. *Earth Plan. Sci. Lett.*, **45**, 435–444.

Thorarinsson, S., 1960. *On the Geology and Geophysics of Iceland.* Guide to Excursions 60, Int. Geol. Congr., Reykjavík.

Thurber, C.H., 1983. Earthquake locations and three dimensional crustal structure in the Coyote Lake area, central California. *J. Geophys. Res.*, **88**, 8226–8236.

Thurber, C.H., 1984. Seismic detection of the summit magma complex of the Kilauea Volcano, Hawaii. *Science,* **223**, 165–167.

Thurber, C.H., 1985. *SIMUL3 User Manual, Third Edition.* Internal Report, Dept. Earth and Space Sciences, State University of New York. 10 pp.

Thurber, C.H. and Ellsworth, W.L., 1980. Rapid solution of ray tracing problems in heterogeneous media. *Bull. Seismol. Soc. Am.*, **70**, 1137–1148.

Toomey, D.R. and Foulger, G.R., 1989. Tomographic inversion of local earthquake data from the Hengill–Grensdalur central volcano complex, Iceland. *J. Geophys. Res.*, **94**, 17497–17510.

Toomey, D.R., Purdy, G.M., Solomon, S.C. and Wilcock, S.D., 1990. The three–dimensional seismic velocity structure of the East Pacific Rise near latitude 9°30'N. *Nature,* **347**, 639–645.

Toomey, D.R., Solomon, S.C. and Purdy, G.M., 1988. Microearthquakes beneath median valley of Mid–Atlantic Ridge near 23°N : tomography and tectonics. *J. Geophys. Res.*, **93**, 9093–9112.

Toomey, D.R., Solomon, S.C., Purdy, G.M. and Murray, M.H., 1985. Microearthquakes beneath the median valley of the Mid–Atlantic Ridge near 23°N : hypocenters and focal mechanisms. *J. Geophys. Res.*, **90**, 5443–5458.

Torge, W. and Drewes, H., 1977. Gravity changes in connection with the volcanic and earthquake activity in northern Iceland 1975/1976. *Jökull,* **27**, 60–70.

Tréhu, A.M., Nábělek, J.L. and Solomon, S.C., 1981. Source characterization of two Reykjanes Ridge earthquakes : surface waves and moment tensors; P waveforms and nonorthogonal nodal planes. *J. Geophys. Res.*, **86**, 1710–1724.

Tréhu, A.M. and Solomon, S.C., 1983. Earthquakes in the Orozco Transform Zone : seismicity, source mechanisms and tectonics. *J. Geophys. Res.*, **88**, 8203–8225.

Tryggvason, E., 1964. Arrival times of P–waves and upper mantle structure. *Bull. Seismol. Soc. Am.*, **54**, 727–736.

Tryggvason, E., 1978. Tilt observations in the Krafla–Mývatn area 1976–1977. *Nordic Volcanological Institute Report 7802.*

Tryggvason, E., 1980. Subsidence events in the Krafla area, northern Iceland, 1975–1979. *J. Geophys.*, **47**, 141–153.

Tryggvason, E., 1982. Recent ground deformation in continental and oceanic rift zones. in : *Continental and Oceanic Rifts.* ed. G. Pálmason, Geodynamic series **8**, Am. Geophys. Union, 17–30.

Tryggvason, E., 1984. Widening of the Krafla fissure swarm during the 1975–1981 volcano–tectonic episode. *Bull. Volcanol.*, **47**, 47–69.

Tryggvason, E. and Båth, M., 1961. Upper crustal structure of Iceland. *J. Geophys. Res.*, **66**, 1913–1925.

Tryggvason, K., Husebye, E.S. and Stefánsson, R., 1984. Seismic image of the hypothesised Icelandic hotspot. *Tectonophysics,* **100**, 97–119.

Udias, A., 1977. Time and magnitude relations for three microaftershock series near Hollister, California. *Bull. Seismol. Soc. Am.*, **67**, 173–185.

Uniras, 1987. *GEOPAK reference manual, version 5.4.* Uniras Document no. 050, Denmark.

Vine, F.J. and Matthews, D.H., 1963. Magnetic anomalies over ocean ridges. *Nature,* **199**, 947–949.

Vink, G.E., 1984. A hotspot model for Iceland and the Vøring plateau. *J. Geophys. Res.*, **89**, 9949–9959.

Vogt, P.R., 1970. Magnetic and Bathymetric data bearing on sea–floor spreading north of Iceland. *J. Geophys. Res.*, **75**, 903–920.

Vogt, P.R., 1971. Asthenosphere flow recorded by the ocean floor South of Iceland. *Earth Planet. Sci. Lett.*, **13**, 153–160.

Vogt, P.R., 1983. The Iceland mantle plume : status of the hypothesis after a decade of new work. in : *Structure and development of the Greenland–Scotland Ridge.* ed. M.H.P. Bott et al., Plenum Press, New York and London, 191–213.

Walker, G.P.L., 1974. The structure of eastern Iceland. in : *Geodynamics of Iceland and the North Atlantic Area,* ed. L. Kristjansson., Dordrecht, Holland, D.Reidel Publ. Co, 177–188.

Wallace, T.C., 1985. A re-examination of the moment tensor solutions of the 1980 Mammoth Lakes earthquakes. *J. Geophys. Res.*, **90**, 11171–11176.

Wallace, T.C., Burdick, L.J. and Kanamori, H., 1983. Faulting and structure complexity : a possible explanation for the moment tensor solutions of the 1980 Mammoth Lakes earthquakes, (abstract). *EOS Trans. AGU,* **64**, 769.

Ward, P.L. and Björnsson, S., 1971. Microearthquakes, swarms, and the geothermal areas of Iceland. *J. Geophys. Res.*, **76**, 3953–3982.

Ward, P.L., Pálmason, G. and Drake, C., 1969. Microearthquake survey and the Mid–Atlantic Ridge in Iceland. *J. Geophys. Res.*, **74**, 665–684.

Wegener, A., 1912. Die entstehung der kontinente. *Petermanns Geogr. Mitt.*, **58**, 305–309.

Wendt, K., Möller, D. and Ritter, B., 1985. Geodetic measurements of surface deformations during the present rifting episode in N.E. Iceland. *J. Geophys. Res.*, **90**, 10163–10172.

Wiggins, R.A., 1972. The general linear inverse problem : implication of surface waves and free oscillations for earth structure. *Rev. Geophys.*, **10**, 251–285.

Wong, I.G. and M^{c}Garr, A., 1988. Implosional failure in mining–induced seismicity : a critical review. Preprinted papers, *2nd Int. Symp. Rockbursts and Seismicity in Mines*, Minneapolis, Minn., June 8–10, 1988, pp 13–28. Univ. of Minnesota, Minneapolis.

Wyss, M., 1973. Towards a physical understanding of the earthquake frequency distribution. *Geophys. J. R. Astron. Soc.*, **31**, 341–359.

Wyss, M. and Lee, W.H.K., 1973. Time variations of the average earthquake magnitude in central California. *Stanford Univ. Publ., Geol. Sci.*, **13**, 24–42.

Zverev, S.M., Litvinenko, I.V., Pálmason, G., Yarashevskaya, G.A., Osokin, N.N. and Akhmetjev, M.A., 1980a. A seismic study of the rift zone in northern Iceland. *J. Geophys.*, **47**, 191–201.

Zverev, S.M., Litvinenko, I.V., Pálmason, G., Yarashevskaya, G.A. and Osokin, N.N., 1980b. A seismic crustal study of the axial rift zone in Southwest Iceland. *J. Geophys.*, **47**, 202–210.

Marquardt, D.W., 1963. An algorithm for least squares estimation of non-linear parameters. J. Soc. Indust. App. Math., 11, 431-441.

Appendix A

Earthquake Locations Using HYPOINVERSE

Date	Origin time	Latitude	Longitude	Depth	M_{IL}	N	Gap	D	RMS	ERH	ERZ
85 7 1	1219 23.37	65 38.10	16 51.41	3.40	1.80	14	168	2.0	0.03	0.4	0.9
85 7 1	1222 21.90	65 38.06	16 51.66	2.97	-0.20	8	182	2.0	0.02	0.6	1.0
85 7 1	1416 25.30	65 37.77	16 50.99	3.36	-1.70	4	186	1.0	0.00	0.9	1.6
85 7 1	1448 29.19	65 42.76	16 47.69	2.46	0.10	9	136	1.0	0.02	0.3	0.4
85 7 1	18 4 4.23	65 37.58	16 51.80	4.88	-5.00	4	173	1.0	0.02	10.8	10.5
85 7 1	2332 43.03	65 46.77	16 47.67	7.77	-0.40	7	325	8.0	0.03	1.9	2.0
85 7 2	1 6 34.44	65 43.48	16 47.35	2.32	-5.00	8	90	2.0	0.01	0.4	0.6
85 7 2	1015 10.97	65 43.24	16 46.89	3.92	-0.40	12	168	1.0	0.03	0.5	0.3
85 7 2	1152 33.85	65 42.80	16 47.73	2.74	0.10	16	61	1.0	0.03	0.2	0.5
85 7 2	2152 21.50	65 43.13	16 48.46	1.47	-1.70	6	124	1.0	0.03	0.4	0.6
85 7 2	22 3 13.64	65 38.70	16 51.38	3.76	-1.30	9	117	2.0	0.02	0.4	1.1
85 7 3	040 26.78	65 42.76	16 47.93	2.51	-0.20	10	141	1.0	0.02	0.4	0.6
85 7 3	123 58.47	65 42.31	16 45.83	1.31	-5.00	9	114	3.0	0.04	0.2	1.1
85 7 3	457 56.79	65 42.76	16 47.71	2.34	0.10	9	100	1.0	0.02	0.3	0.4
85 7 3	749 51.50	65 42.65	16 47.95	2.89	-0.90	8	129	1.0	0.01	0.3	0.6
85 7 3	9 5 0.26	65 42.32	16 47.62	1.56	-1.50	7	120	1.0	0.02	0.3	0.6
85 7 3	10 4 12.09	65 43.82	16 48.18	1.45	-5.00	5	172	2.0	0.04	0.5	0.9
85 7 3	1322 9.00	65 39.46	16 50.19	5.65	-5.00	8	154	3.0	0.02	0.7	1.2
85 7 3	1435 54.44	65 42.89	16 48.08	2.71	0.40	13	110	1.0	0.03	0.3	0.5
85 7 3	1556 1.21	65 42.76	16 47.73	2.53	-0.10	9	136	1.0	0.01	0.3	0.6
85 7 4	155 0.62	65 42.69	16 47.88	2.29	-0.70	6	133	1.0	0.01	0.6	0.7
85 7 4	321 36.22	65 41.06	16 48.78	2.88	-1.30	6	214	1.0	0.00	1.2	0.5
85 7 4	535 8.99	65 38.16	16 51.64	2.50	-1.70	4	194	1.0	0.01	0.8	1.3
85 7 4	852 53.96	65 42.87	16 47.89	2.64	1.60	21	108	1.0	0.04	0.2	0.4
85 7 4	926 30.49	65 39.70	16 50.21	2.95	-5.00	11	115	2.0	0.02	0.3	0.8
85 7 4	1144 53.60	65 42.65	16 47.68	2.48	-0.90	11	126	1.0	0.03	0.3	0.4
85 7 4	1554 31.42	65 42.62	16 47.49	2.09	-5.00	6	121	2.0	0.03	0.9	1.5
85 7 4	2033 9.91	65 43.73	16 47.65	2.38	-5.00	4	163	2.0	0.02	0.8	1.4
85 7 5	6 0 20.71	65 42.82	16 47.96	1.87	-0.80	6	149	1.0	0.02	0.5	0.7
85 7 5	621 48.74	65 39.52	16 52.85	3.88	-1.70	8	138	2.0	0.05	0.5	1.0
85 7 5	757 9.07	65 43.52	16 47.70	0.72	-0.80	7	192	2.0	0.04	0.4	1.2
85 7 5	1911 38.28	65 40.29	16 49.59	4.52	-0.90	5	123	1.0	0.01	1.5	1.9
85 7 6	333 29.44	65 40.79	16 50.98	0.10	-5.00	4	149	1.0	0.03	0.4	2.3
85 7 6	5 2 47.99	65 38.11	16 51.88	3.60	-1.30	10	90	2.0	0.02	0.3	0.8
85 7 6	822 44.06	65 38.99	16 51.47	3.68	-5.00	6	124	4.0	0.04	0.5	2.0
85 7 6	1011 41.85	65 42.51	16 45.66	2.57	-0.20	14	114	1.0	0.04	0.3	0.6
85 7 6	2058 3.81	65 42.98	16 50.34	0.56	-5.00	4	113	1.0	0.01	0.3	0.9
85 7 7	0 7 17.56	65 45.47	16 47.29	1.84	-1.20	4	326	5.0	0.02	28.5	9.9
85 7 7	118 33.52	65 38.98	16 48.57	5.36	-0.90	9	159	1.0	0.04	0.6	0.9
85 7 7	1154 28.19	65 37.89	16 51.68	3.11	-1.20	16	73	1.0	0.03	0.2	0.6
85 7 7	1434 31.52	65 42.99	16 47.59	2.27	-5.00	4	161	1.0	0.00	1.2	1.2
85 7 8	337 40.68	65 38.76	16 51.06	2.33	-1.40	8	90	2.0	0.01	0.3	0.8
85 7 8	4 2 9.32	65 42.79	16 47.91	2.63	0.10	20	55	1.0	0.03	0.2	0.4
85 7 8	1010 36.70	65 42.91	16 48.19	1.39	-0.40	13	111	1.0	0.03	0.2	0.4
85 7 8	1021 11.29	65 40.36	16 51.13	0.32	-5.00	5	134	2.0	0.04	0.3	2.1
85 7 8	1637 32.12	65 40.78	16 50.35	1.09	-2.40	4	174	1.0	0.01	1.3	1.1
85 7 8	1649 29.89	65 32.50	16 40.94	8.49	-5.00	9	313	9.0	0.03	9.3	4.4
85 7 9	3 2 55.52	65 40.17	16 50.88	0.30	-1.40	6	138	2.0	0.04	0.3	1.1
85 7 9	4 4 43.91	65 37.94	16 51.82	3.07	-0.80	20	94	2.0	0.03	0.2	0.5
85 7 9	824 18.41	65 39.33	16 52.48	2.51	-0.90	11	230	2.0	0.06	0.5	0.6
85 7 9	1954 15.02	65 38.06	16 51.52	3.76	0.90	32	47	1.0	0.04	0.2	0.3
85 7 9	22 0 4.67	65 39.80	16 50.17	3.36	-0.60	14	52	1.0	0.03	0.3	0.6
85 7 9	2246 34.47	65 42.57	16 51.01	5.42	-5.00	7	119	1.0	0.02	0.7	0.9
85 7 9	2311 44.99	65 37.00	16 47.91	6.32	-1.40	5	271	3.0	0.03	3.9	2.1
85 710	936 6.12	65 39.50	16 50.51	2.42	-1.00	16	52	1.0	0.03	0.2	0.5
85 710	1214 0.60	65 38.47	16 51.08	2.92	-1.30	13	95	2.0	0.03	0.3	0.9
85 711	237 13.21	65 37.91	16 51.87	3.28	-0.70	11	68	3.0	0.02	0.3	0.8
85 711	449 8.25	65 37.97	16 51.81	3.60	1.00	25	47	1.0	0.04	0.2	0.4
85 711	558 55.86	65 38.75	16 50.64	2.74	-1.40	13	51	1.0	0.03	0.2	0.6
85 711	2317 28.46	65 38.05	16 51.45	3.08	-0.90	18	70	1.0	0.02	0.2	0.5
85 712	2231 53.59	65 38.81	16 50.74	2.48	-1.10	19	77	1.0	0.03	0.2	0.4
85 714	450 23.74	65 42.86	16 47.62	2.79	-1.00	5	147	1.0	0.02	1.3	1.0
85 714	1023 6.51	65 38.03	16 49.47	4.27	-0.90	10	249	0.0	0.04	1.4	0.6
85 714	1738 25.68	65 44.81	16 50.58	2.53	-5.00	8	273	2.0	0.02	0.7	0.7
85 715	231 24.55	65 38.00	16 51.72	3.48	-1.70	19	84	2.0	0.03	0.2	0.5
85 715	247 33.19	65 37.95	16 51.90	4.57	-0.80	19	85	2.0	0.03	0.3	0.6
85 715	359 49.18	65 38.14	16 51.60	3.27	-1.30	9	87	3.0	0.01	0.3	1.7
85 715	557 19.30	65 45.18	16 56.42	3.75	-5.00	6	306	4.0	0.02	1.0	0.6
85 715	2246 59.47	65 42.62	16 48.19	2.55	-0.60	12	98	1.0	0.02	0.2	0.3
85 716	226 39.33	65 43.16	16 48.03	2.26	-0.40	16	125	1.0	0.04	0.2	0.3
85 716	459 26.10	65 37.91	16 51.25	2.87	-0.80	19	76	1.0	0.05	0.2	0.4
85 716	623 35.40	65 36.91	16 54.33	8.56	-5.00	6	226	2.0	0.04	3.3	5.7
85 716	758 53.17	65 42.82	16 47.73	2.60	1.70	31	63	1.0	0.04	0.2	0.3
85 716	1010 9.63	65 38.75	16 50.89	2.29	-0.70	14	102	1.0	0.03	0.3	0.4
85 716	18 4 37.99	65 42.44	16 47.51	1.83	-5.00	11	104	1.0	0.03	0.2	0.5
85 716	1914 1.69	65 37.96	16 51.63	3.77	0.10	20	87	1.0	0.03	0.3	0.5
85 716	2023 19.94	65 37.06	16 51.86	6.95	-0.70	10	267	4.0	0.04	1.3	1.6
85 716	2257 36.38	65 37.74	16 52.23	4.53	-5.00	5	167	2.0	0.01	1.1	4.8
85 717	019 30.70	65 37.42	16 41.05	0.77	-5.00	6	311	4.0	0.02	0.8	1.1
85 717	316 36.87	65 36.79	16 52.46	3.18	-5.00	9	116	1.0	0.03	0.7	0.9
85 717	323 19.45	65 38.04	16 52.17	4.65	-0.90	12	91	2.0	0.04	0.4	1.0
85 717	1734 55.34	65 38.90	16 50.71	2.80	0.10	23	50	1.0	0.05	0.2	0.3
85 718	310 57.00	65 37.32	16 52.92	0.68	-5.00	14	82	1.0	0.04	0.2	0.5
85 718	9 9 26.57	65 38.05	16 51.55	3.87	-0.40	16	84	1.0	0.03	0.3	0.6
85 719	1 0 33.71	65 37.95	16 51.59	1.76	-0.60	9	86	3.0	0.05	0.3	1.1
85 719	540 57.69	65 39.74	16 50.11	3.49	0.00	23	52	1.0	0.03	0.2	0.4
85 719	746 39.93	65 38.44	16 51.20	2.40	-0.20	15	50	1.0	0.03	0.2	0.4
85 719	2152 37.71	65 38.83	16 50.89	2.79	-1.40	10	96	2.0	0.04	0.3	0.6
85 720	432 12.85	65 37.94	16 51.76	2.98	0.40	24	50	1.0	0.03	0.2	0.4
85 720	531 34.59	65 42.92	16 56.45	3.58	-5.00	7	215	2.0	0.02	0.8	1.1
85 720	1744 29.01	65 43.72	16 47.68	2.93	-0.30	13	98	1.0	0.05	0.4	0.5
85 721	038 4.49	65 37.95	16 51.46	3.26	-0.20	22	72	1.0	0.04	0.2	0.4
85 721	111 27.66	65 38.14	16 50.36	3.58	-5.00	7	173	1.0	0.01	1.4	1.1
85 721	420 32.38	65 41.87	16 48.33	0.16	-0.60	9	183	2.0	0.03	0.3	0.8
85 721	1133 12.90	65 37.97	16 51.75	2.78	0.00	9	97	1.0	0.02	0.4	0.7
85 722	2045 42.93	65 39.75	16 50.31	3.35	-0.80	12	70	1.0	0.02	0.3	0.6
85 722	2133 43.06	65 39.79	16 50.25	3.14	-0.80	12	82	1.0	0.03	0.3	0.5
85 723	1926 42.22	65 43.91	16 55.49	5.32	-5.00	5	299	1.0	0.01	1.7	2.1
85 724	536 35.72	65 43.14	16 48.10	2.39	-0.70	8	124	1.0	0.03	0.3	0.7
85 724	1358 47.35	65 39.82	16 50.19	3.20	-0.90	10	139	1.0	0.02	0.4	0.5
85 724	1432 49.11	65 42.98	16 49.56	2.25	-1.50	6	247	1.0	0.04	1.3	0.5
85 724	1612 28.63	65 38.08	16 51.59	3.61	1.00	28	48	1.0	0.04	0.2	0.4
85 724	1615 39.31	65 38.08	16 51.50	3.53	0.10	28	46	1.0	0.04	0.2	0.4
85 725	514 8.77	65 42.72	16 48.06	1.98	0.20	13	101	1.0	0.03	0.2	0.3
85 725	15 4 44.53	65 43.64	16 50.63	6.45	-5.00	7	190	2.0	0.01	2.2	1.5
85 725	1846 25.84	65 38.69	16 50.76	2.78	-0.70	11	108	1.0	0.02	0.3	0.7
85 725	2117 26.69	65 37.72	16 52.31	5.75	-0.60	5	115	2.0	0.00	1.6	6.9
85 726	556 22.85	65 42.61	16 48.08	2.02	0.10	21	96	1.0	0.04	0.2	0.3
85 726	11 0 41.63	65 37.94	16 51.73	3.10	-0.60	15	79	1.0	0.03	0.3	0.6
85 726	12 3 55.05	65 39.12	16 50.53	2.40	-0.60	10	82	1.0	0.02	0.3	0.6
85 726	1215 47.98	65 38.89	16 51.22	1.67	-1.40	5	215	2.0	0.01	0.8	0.9
85 726	1218 22.83	65 39.88	16 50.41	3.31	-1.30	5	156	1.0	0.01	0.9	1.7
85 726	1356 40.83	65 37.97	16 51.81	3.36	-5.00	11	85	3.0	0.04	0.3	1.1
85 726	21 0 42.98	65 38.65	16 51.01	2.41	-1.50	10	88	2.0	0.02	0.2	0.9
85 727	1017 26.85	65 38.12	16 51.36	2.59	-0.50	14	87	1.0	0.03	0.3	0.4
85 727	2015 48.17	65 38.62	16 50.18	5.43	-5.00	16	75	3.0	0.03	0.3	0.7
85 728	343 38.89	65 39.31	16 50.87	2.51	-0.60	17	92	2.0	0.06	0.2	0.6
85 728	641 58.97	65 43.56	16 47.69	2.73	-5.00	6	140	1.0	0.01	0.6	0.9
85 728	9 9 13.56	65 42.89	16 48.12	2.15	-1.00	10	110	1.0	0.03	0.4	0.3
85 728	910 18.27	65 41.65	16 47.08	1.86	-1.00	9	180	2.0	0.07	0.4	0.7

85	728	911	55.19	65	38.95	16	50.74	2.71	-0.30	17	61	1.0	0.02	0.2	0.5
85	728	920	28.40	65	48.85	16	49.09	6.81	-5.00	5	309	8.0	0.04	10.3	5.0
85	728	1847	39.35	65	37.80	16	51.70	3.66	0.70	26	72	1.0	0.03	0.2	0.4
85	728	2311	55.78	65	37.77	16	51.69	3.21	-5.00	10	93	3.0	0.02	0.4	1.3
85	729	553	8.69	65	43.62	16	48.75	0.49	-1.50	8	202	2.0	0.05	0.4	1.1
85	729	631	2.53	65	42.67	16	47.61	2.33	-5.00	5	159	1.0	0.01	0.5	0.9
85	729	944	4.01	65	41.85	16	47.79	3.03	-1.70	8	246	1.0	0.06	1.3	0.6
85	729	1048	39.48	65	43.54	16	47.66	2.43	-0.70	10	89	1.0	0.02	0.3	0.6
85	729	11 8	37.12	65	43.53	16	47.70	2.39	-0.30	16	86	2.0	0.02	0.2	0.4
85	729	1613	30.95	65	37.90	16	52.02	4.09	-1.40	6	116	2.0	0.02	0.8	3.0
85	729	1614	18.20	65	37.94	16	51.68	3.26	-1.40	9	109	2.0	0.02	0.3	1.0
85	729	2338	7.12	65	38.65	16	51.11	2.99	-0.70	7	136	2.0	0.04	0.4	1.1
85	730	1229	28.45	65	37.91	16	51.75	2.83	-0.80	15	81	2.0	0.02	0.2	0.5
85	730	1353	48.62	65	38.25	16	51.74	2.42	-1.50	15	104	1.0	0.02	0.2	0.4
85	730	15 8	37.12	65	42.67	16	47.91	2.30	-0.90	17	53	1.0	0.04	0.2	0.4
85	730	1627	28.04	65	42.27	16	46.28	2.10	-5.00	9	199	3.0	0.03	0.5	1.0
85	730	1752	12.44	65	38.13	16	51.47	2.87	-0.40	23	84	1.0	0.04	0.2	0.3
85	730	1848	53.88	65	38.08	16	51.68	3.41	-0.60	22	86	1.0	0.03	0.2	0.5
85	730	2139	26.28	65	40.72	16	49.80	3.28	-5.00	4	108	1.0	0.01	1.2	3.6
85	730	2218	51.71	65	38.62	16	51.07	1.79	-1.00	7	121	2.0	0.03	0.4	0.9
85	730	2330	0.92	65	46.80	16	42.84	3.88	-5.00	4	311	12.0	0.00	10.8	6.2
85	731	320	57.45	65	37.88	16	51.84	2.92	-0.90	13	85	1.0	0.03	0.3	0.6
85	731	620	45.48	65	38.95	16	50.72	3.07	-0.20	20	80	1.0	0.03	0.2	0.4
85	731	714	16.15	65	38.08	16	51.54	2.59	-0.80	16	58	1.0	0.03	0.2	0.4
85	731	822	1.29	65	38.05	16	51.62	3.49	-0.70	21	47	1.0	0.03	0.2	0.5
85	731	1648	50.70	65	37.92	16	51.68	3.12	-1.20	15	47	1.0	0.03	0.2	0.7
85	731	2113	27.35	65	42.82	16	47.73	2.25	-5.00	6	140	1.0	0.03	0.5	0.6
85	731	2156	39.34	65	38.75	16	50.17	2.70	-5.00	10	102	1.0	0.02	0.3	0.6
85	8	1	146	29.20	65	38.07	16	52.00	4.85	-5.00	7	190	3.0	0.01	0.9	2.4
85	8	1	414	41.87	65	38.60	16	51.04	2.82	-0.80	18	92	1.0	0.04	0.2	0.4
85	8	1	854	40.99	65	37.91	16	51.78	3.77	2.10	27	42	1.0	0.04	0.2	0.4
85	8	1	936	52.70	65	39.79	16	49.96	2.39	-1.10	7	142	1.0	0.02	0.4	0.7
85	8	1	10 6	18.09	65	39.18	16	50.77	3.74	-1.70	7	108	2.0	0.02	0.5	1.1
85	8	1	1044	28.49	65	38.11	16	51.69	3.45	-5.00	5	213	1.0	0.01	1.0	2.0
85	8	1	1218	1.34	65	42.67	16	47.90	2.44	0.00	22	71	1.0	0.04	0.2	0.4
85	8	1	1227	47.41	65	42.78	16	47.93	2.56	0.10	22	103	1.0	0.05	0.2	0.4
85	8	1	1256	24.37	65	39.25	16	50.44	3.10	0.70	31	43	1.0	0.04	0.2	0.3
85	8	2	0 4	13.64	65	38.32	16	52.41	3.59	-0.90	11	106	2.0	0.02	0.3	1.2
85	8	2	055	21.47	65	42.99	16	50.71	2.31	-0.60	12	110	1.0	0.05	0.3	0.5
85	8	2	312	12.39	65	39.66	16	50.72	3.18	-1.40	13	78	1.0	0.03	0.3	0.7
85	8	2	337	31.50	65	38.30	16	51.47	2.63	-0.50	10	144	1.0	0.03	0.4	0.6
85	8	2	338	55.50	65	38.10	16	51.46	2.45	-5.00	7	133	2.0	0.01	0.4	1.6
85	8	2	933	54.26	65	42.14	16	56.29	2.41	-5.00	4	283	3.0	0.01	3.0	0.9
85	8	2	1113	16.98	65	39.64	16	50.46	3.35	-1.40	8	155	1.0	0.03	0.5	0.8
85	8	2	1329	37.97	65	37.33	16	52.91	3.89	-5.00	10	89	1.0	0.04	0.4	0.8
85	8	2	2230	50.02	65	39.47	16	50.02	2.86	-5.00	6	135	3.0	0.02	0.5	1.0
85	8	3	948	56.64	65	39.28	16	50.38	2.72	-1.00	16	52	1.0	0.04	0.2	0.5
85	8	3	1837	13.20	65	37.95	16	51.59	3.48	0.10	24	71	1.0	0.03	0.2	0.5
85	8	3	2325	51.31	65	39.20	16	50.33	2.42	-1.00	14	70	1.0	0.03	0.2	0.5
85	8	4	1011	17.97	65	38.05	16	51.60	2.83	-0.80	18	80	1.0	0.02	0.2	0.4
85	8	4	1032	13.05	65	43.17	16	53.18	4.40	-0.40	12	108	1.0	0.03	0.5	0.7
85	8	4	1217	55.15	65	38.02	16	51.48	3.20	-1.30	15	58	1.0	0.04	0.3	0.6
85	8	4	1556	0.35	65	43.02	16	47.74	2.71	-5.00	6	130	2.0	0.04	0.5	1.1
85	8	4	2131	59.96	65	42.66	16	47.44	2.59	-0.30	16	80	0.0	0.04	0.2	0.4
85	8	5	1 9	22.12	65	42.75	16	47.86	2.63	-0.80	17	54	1.0	0.04	0.2	0.5
85	8	6	843	8.60	65	39.55	16	50.23	3.17	0.10	18	50	1.0	0.04	0.2	0.5
85	8	6	1548	55.18	65	38.09	16	51.44	2.79	0.40	27	47	1.0	0.03	0.2	0.3
85	8	6	1614	14.65	65	42.83	16	48.07	2.60	0.00	15	57	1.0	0.03	0.2	0.5
85	8	7	1625	41.29	65	38.60	16	50.97	2.70	-0.80	13	100	1.0	0.03	0.3	0.5
85	8	7	1657	25.74	65	43.17	16	44.04	0.03	-5.00	5	318	5.0	0.06	1.5	1.1
85	8	7	1833	10.86	65	42.75	16	48.07	3.24	-0.40	16	56	1.0	0.04	0.3	0.5
85	8	8	151	47.08	65	38.36	16	50.35	4.83	-1.10	10	75	3.0	0.02	0.4	1.1
85	8	8	22 1	26.04	65	42.17	16	46.00	2.03	-1.00	9	143	1.0	0.03	0.4	0.7
85	8	8	2213	1.24	65	42.42	16	45.38	4.43	-5.00	9	238	1.0	0.03	0.5	0.7
85	8	9	756	17.36	65	42.31	16	46.02	2.19	-0.40	17	110	1.0	0.03	0.2	0.4
85	8	9	953	4.25	65	38.10	16	51.60	3.06	-0.60	15	85	1.0	0.03	0.3	0.5
85	8	9	2059	22.49	65	38.01	16	51.62	2.82	-0.80	15	83	1.0	0.03	0.2	0.5
85	8	9	2332	15.57	65	42.50	16	47.57	2.09	-0.50	9	161	1.0	0.03	0.5	0.3
85	811	622	7.97	65	43.58	16	47.44	2.93	-5.00	6	145	1.0	0.02	0.7	1.5
85	811	1414	22.81	65	43.68	16	47.34	3.34	-5.00	4	136	1.0	0.01	0.9	2.2
85	811	1417	23.86	65	42.98	16	48.15	2.62	-0.30	9	114	1.0	0.03	0.4	0.7
85	813	1328	24.84	65	42.88	16	47.75	2.83	-0.40	12	66	1.0	0.03	0.3	0.6
85	813	16 3	19.77	65	43.45	16	47.60	2.56	-5.00	7	148	2.0	0.03	0.4	0.7
85	813	1938	7.68	65	43.70	16	53.04	1.66	-5.00	6	191	1.0	0.01	0.5	0.9
85	814	12 1	27.75	65	38.14	16	51.39	2.58	-5.00	15	84	1.0	0.04	0.2	0.5
85	814	1212	6.90	65	42.99	16	45.50	0.49	-9.00	28	60	1.0	0.05	0.2	0.5
85	814	1639	7.24	65	45.64	16	37.93	2.14	-9.00	23	230	5.0	0.07	0.7	0.8
85	814	1838	16.34	65	38.04	16	51.57	2.93	-1.00	15	83	1.0	0.04	0.2	0.7
85	814	2145	7.35	65	38.59	16	52.27	0.00	-9.00	22	64	1.0	0.10	0.2	1.0
85	815	025	54.95	65	37.72	16	52.93	4.73	-1.50	8	122	2.0	0.02	0.7	1.1
85	815	058	18.51	65	39.41	16	49.65	5.98	-1.30	10	114	1.0	0.01	0.5	1.0
85	815	810	40.93	65	38.06	16	51.37	2.92	-1.00	13	81	1.0	0.03	0.3	0.7
85	815	11 2	51.64	65	37.98	16	51.47	2.71	-1.00	16	80	1.0	0.03	0.2	0.5
85	815	1215	7.46	65	39.57	17	3.12	1.73	-9.00	22	261	4.0	0.05	1.1	0.7
85	815	1319	20.92	65	37.95	16	51.67	3.19	-1.10	15	80	1.0	0.04	0.3	0.7
85	815	14 4	47.94	65	42.89	16	47.71	2.89	-0.50	19	68	1.0	0.04	0.2	0.5
85	815	1514	30.05	65	38.78	16	50.99	2.82	-1.00	18	87	1.0	0.04	0.3	0.4
85	815	1645	6.76	65	44.57	16	57.41	0.00	-9.00	18	271	3.0	0.08	1.2	1.8
85	815	19 0	7.48	65	36.70	16	53.95	1.21	-9.00	21	174	2.0	0.06	0.3	0.4
85	816	147	29.68	65	42.75	16	47.24	3.36	-5.00	9	260	2.0	0.04	1.2	0.7
85	816	555	27.51	65	38.77	16	51.14	3.32	-0.90	10	94	2.0	0.01	0.3	0.9
85	817	917	30.19	65	43.09	16	48.11	3.02	-1.40	9	121	1.0	0.03	0.3	0.6
85	817	20 1	30.56	65	37.65	16	52.51	4.87	-5.00	5	117	2.0	0.02	3.9	8.9
85	818	429	15.75	65	38.12	16	51.47	3.26	-0.20	16	87	1.0	0.04	0.3	0.5
85	819	0 4	20.92	65	38.08	16	51.51	3.13	-0.20	19	46	1.0	0.04	0.2	0.5
85	819	559	5.89	65	42.53	16	46.33	2.89	-0.30	12	103	0.0	0.05	0.3	0.6
85	819	825	38.53	65	37.93	16	51.90	4.93	-5.00	5	172	2.0	0.01	1.1	2.1
85	820	041	33.87	65	39.00	16	50.97	3.62	-0.90	9	174	2.0	0.03	0.4	0.8
85	820	118	52.41	65	37.75	16	52.40	6.36	-0.80	10	124	2.0	0.04	0.6	1.4
85	820	513	3.05	65	39.82	16	50.19	3.23	1.10	11	92	1.0	0.03	0.3	0.5
85	820	8 8	3.39	65	41.86	16	48.46	1.22	5.00	5	153	2.0	0.03	4.9	8.3
85	820	1919	50.30	65	39.37	16	50.52	3.44	0.10	10	146	2.0	0.02	0.4	0.6
85	821	1546	35.31	65	39.53	16	50.40	3.39	-0.90	8	122	3.0	0.02	0.5	0.9
85	822	346	23.13	65	37.11	16	52.04	2.46	-5.00	6	151	2.0	0.00	0.6	0.9
85	822	9 6	52.69	65	37.76	16	51.68	3.37	-1.10	5	126	2.0	0.01	0.4	1.4
85	822	12 8	25.25	65	37.88	16	51.80	3.27	-1.40	9	113	2.0	0.02	0.3	0.9
85	822	1640	27.29	65	42.69	16	48.06	2.32	-0.20	12	68	1.0	0.04	0.3	0.5
85	822	2248	18.50	65	41.85	16	42.85	1.56	-5.00	7	194	4.0	0.03	0.6	2.3
85	823	1045	37.13	65	38.07	16	51.57	3.42	-0.20	18	53	1.0	0.02	0.3	0.5
85	823	13 1	40.32	65	39.54	16	49.46	2.65	-0.60	11	63	0.0	0.03	0.3	0.5
85	823	1811	26.33	65	39.03	16	50.92	2.66	-1.40	9	87	1.0	0.03	0.4	0.8
85	824	335	52.50	65	37.67	16	55.64	5.89	-1.50	9	222	0.0	0.05	0.6	1.0
85	824	340	16.21	65	37.84	16	51.76	2.80	-1.20	11	95	3.0	0.02	0.3	1.1
85	824	1059	7.61	65	37.81	16	51.68	3.37	-0.80	16	81	1.0	0.03	0.2	0.5
85	824	11 1	28.48	65	37.78	16	51.96	3.74	-1.40	9	82	2.0	0.03	0.3	1.3
85	824	1123	39.00	65	38.03	16	51.55	3.88	-0.80	20	73	1.0	0.04	0.2	0.5
85	824	12 7	17.45	65	44.08	16	47.73	3.01	-5.00	8	119	1.0	0.03	0.4	0.7
85	824	1351	24.44	65	34.86	16	55.58	11.46	-5.00	7	300	5.0	0.04	10.9	12.2
85	824	1525	39.92	65	42.73	16	47.72	2.60	-0.40	17	54	1.0	0.05	0.2	0.5
85	824	1639	4.83	65	42.44	16	49.06	2.55	-5.00	9	154	1.0	0.03	0.3	0.6

85	824	1647	40.36	65	39.00	16	50.82	1.79	-1.30	6	176	1.0	0.01	0.6	0.5
85	824	1718	16.22	65	48.40	16	50.21	3.00	-5.00	7	317	8.0	0.04	1.1	1.5
85	824	1746	32.72	65	39.64	16	50.17	2.86	-0.80	14	61	1.0	0.03	0.3	0.5
85	825	335	44.30	65	39.95	16	51.44	3.95	-5.00	4	285	4.0	0.01	8.2	2.1
85	825	4 8	53.58	65	38.08	16	51.64	3.39	-1.60	6	97	3.0	0.02	0.4	1.9
85	825	539	35.49	65	38.01	16	51.67	3.10	-1.40	11	93	2.0	0.02	0.3	0.7
85	825	14 4	40.41	65	43.04	16	48.41	2.29	-5.00	8	160	1.0	0.03	0.4	0.4
85	825	1434	9.70	65	38.02	16	51.67	3.28	-1.10	10	132	2.0	0.02	0.4	0.7
85	825	1637	51.96	65	38.10	16	51.62	2.88	-1.20	11	86	2.0	0.02	0.3	0.9
85	825	1923	32.41	65	36.77	16	52.87	3.12	-5.00	6	148	1.0	0.04	2.0	1.8
85	826	3 7	53.80	65	38.38	16	51.36	2.82	-5.00	7	203	1.0	0.02	0.7	1.1
85	826	539	45.49	65	38.04	16	51.79	3.53	-0.80	21	86	1.0	0.03	0.2	0.5
85	827	8 0	55.27	65	42.01	16	48.30	2.39	-1.70	8	108	2.0	0.07	0.4	0.8
85	827	1721	48.66	65	38.16	16	51.70	3.44	1.60	28	50	1.0	0.06	0.2	0.3
85	828	120	54.18	65	38.11	16	51.54	3.34	0.40	16	85	1.0	0.03	0.3	0.6
85	829	836	55.09	65	39.29	16	50.50	2.65	-0.80	10	107	1.0	0.03	0.4	0.6
85	829	913	48.23	65	42.68	16	47.81	2.64	-0.80	11	86	1.0	0.03	0.3	0.4
85	829	1015	20.53	65	38.01	16	51.75	3.58	-0.80	14	85	2.0	0.03	0.3	0.7
85	829	19 8	55.05	65	43.13	16	48.37	2.02	-5.00	4	167	1.0	0.00	1.6	0.9
85	829	2259	36.42	65	41.41	16	44.41	0.66	-1.40	7	307	3.0	0.05	1.0	0.8
85	830	038	59.77	65	40.08	16	51.42	0.02	-1.30	7	122	2.0	0.04	0.3	1.3
85	830	132	25.43	65	42.62	16	49.24	1.13	-5.00	5	146	0.0	0.01	0.3	0.5
85	830	325	51.76	65	42.79	16	47.75	2.87	-0.60	12	58	1.0	0.04	0.3	0.5
85	830	1253	42.41	65	43.76	16	49.21	2.80	-5.00	6	229	2.0	0.01	1.1	0.5
85	830	1454	25.25	65	39.39	16	50.58	3.86	-1.10	7	119	1.0	0.01	0.6	1.6
85	830	1553	1.15	65	42.80	16	47.89	2.60	-0.30	11	74	1.0	0.03	0.3	0.5
85	830	1630	40.78	65	37.38	16	48.61	0.29	-1.30	4	345	10.0	0.05	60.5	78.3
85	831	023	18.38	65	38.30	16	51.39	3.00	-0.40	13	106	1.0	0.03	0.3	0.6
85	831	029	13.74	65	39.73	16	50.25	3.84	-0.20	22	66	1.0	0.04	0.3	0.4
85	831	524	36.29	65	40.30	16	58.29	6.06	-5.00	7	319	5.0	0.04	12.5	7.5
85	831	8 7	19.41	65	43.28	16	47.96	4.08	-0.40	7	196	2.0	0.03	1.0	0.9
85	831	1137	20.71	65	38.66	16	51.32	2.94	-0.50	15	54	1.0	0.03	0.3	0.5
85	831	1218	21.24	65	39.74	16	50.06	4.62	-1.20	9	106	1.0	0.06	0.8	1.3
85	831	1221	27.01	65	42.14	16	45.54	2.72	-5.00	5	191	3.0	0.01	0.7	1.9
85	831	1314	57.61	65	39.54	16	50.17	2.78	-5.00	4	258	3.0	0.00	2.5	1.5
85	831	1349	52.30	65	38.04	16	51.60	3.47	0.10	24	46	1.0	0.03	0.2	0.4
85	831	14 7	12.53	65	37.98	16	51.67	3.63	-1.30	12	82	2.0	0.03	0.3	0.9
85	9	1	045	26.23	65	44.08	16	45.99	4.39	-1.60	4	325	3.0	0.01	19.2	11.3
85	9	1	157	47.77	65	43.74	16	47.39	2.54	-1.00	6	193	1.0	0.01	0.6	0.7
85	9	1	254	41.44	65	39.65	16	50.39	2.97	-0.80	11	69	1.0	0.02	0.4	0.5
85	9	1	455	3.35	65	42.66	16	47.58	1.80	-1.00	4	140	1.0	0.01	1.0	0.8
85	9	1	950	10.68	65	38.67	16	50.87	2.20	-0.90	7	120	2.0	0.02	0.3	0.9
85	9	1	1017	14.36	65	39.67	16	50.11	3.47	-1.10	11	77	1.0	0.02	0.3	0.7
85	9	1	1258	41.99	65	43.07	16	47.70	2.38	-1.40	8	155	1.0	0.03	0.4	0.7
85	9	1	1658	18.21	65	43.56	16	47.77	1.43	-5.00	5	139	1.0	0.05	0.5	0.9
85	9	1	1754	9.22	65	38.04	16	51.63	2.50	-5.00	7	88	2.0	0.01	0.3	1.4
85	9	2	145	29.71	65	38.02	16	51.69	3.75	0.40	27	47	1.0	0.04	0.2	0.4
85	9	2	337	26.53	65	42.19	16	49.40	1.08	-5.00	5	186	1.0	0.01	0.4	0.7
85	9	2	453	8.04	65	38.67	16	51.01	2.88	-1.40	10	88	1.0	0.02	0.3	0.6
85	9	2	6 4	44.26	65	42.81	16	47.75	2.62	1.20	29	61	1.0	0.04	0.2	0.4
85	9	2	911	56.60	65	43.07	16	48.17	2.61	-1.60	8	120	1.0	0.03	0.3	0.9
85	9	2	12 3	10.62	65	42.18	16	47.55	2.29	-1.10	12	154	1.0	0.04	0.3	0.4
85	9	2	18 5	20.38	65	42.24	16	48.62	2.62	-0.40	11	99	1.0	0.04	0.3	0.6
85	9	2	1827	44.02	65	44.50	16	45.96	3.95	-2.10	5	328	4.0	0.01	2.0	1.0
85	9	2	1838	46.97	65	42.98	16	47.99	2.10	-1.00	4	168	1.0	0.01	1.0	1.0
85	9	2	1941	29.59	65	43.36	16	48.59	2.10	-1.90	8	139	1.0	0.06	0.4	0.9
85	9	2	2149	19.62	65	37.98	16	51.66	3.80	1.00	26	46	1.0	0.04	0.2	0.5
85	9	3	4 4	34.26	65	42.83	16	47.54	2.72	-1.40	13	72	1.0	0.04	0.3	0.5
85	9	3	439	49.27	65	43.18	16	47.93	2.50	-5.00	5	223	2.0	0.01	1.6	1.4
85	9	3	755	58.48	65	42.27	16	47.31	2.68	-1.60	6	158	1.0	0.04	0.5	0.7
85	9	3	813	23.16	65	42.27	16	47.62	3.48	-1.30	6	215	1.0	0.01	1.3	1.3
85	9	3	813	27.78	65	42.55	16	47.75	2.43	-0.20	8	163	1.0	0.04	0.4	0.6
85	9	3	1012	11.67	65	42.82	16	48.00	2.84	0.10	11	73	1.0	0.04	0.4	0.6
85	9	3	1220	3.62	65	42.17	16	45.43	2.04	-0.80	16	94	1.0	0.04	0.2	0.5
85	9	3	1234	28.57	65	37.30	16	54.21	3.99	-1.60	5	299	4.0	0.02	2.3	1.3
85	9	3	2311	13.33	65	42.92	16	47.75	2.94	-0.70	7	109	1.0	0.03	0.5	0.9
85	9	4	246	52.10	65	43.57	16	47.19	3.34	-5.00	5	152	1.0	0.03	1.0	1.7
85	9	4	6 2	51.85	65	42.19	16	45.57	2.18	-5.00	5	263	3.0	0.01	1.5	1.6
85	9	4	716	57.66	65	38.67	16	50.96	2.96	-1.70	12	117	1.0	0.02	0.3	0.6
85	9	4	718	52.46	65	41.91	16	47.77	3.23	-1.20	6	243	1.0	0.01	1.5	0.8
85	9	4	724	2.63	65	42.63	16	48.04	2.64	0.20	16	52	1.0	0.03	0.2	0.4
85	9	4	1049	57.22	65	44.24	16	49.86	0.00	-1.90	5	264	3.0	0.02	0.9	1.6
85	9	5	0 1	7.20	65	38.08	16	51.67	3.65	0.10	25	48	1.0	0.04	0.2	0.4
85	9	5	1159	27.19	65	38.12	16	51.57	2.12	-1.60	15	85	1.0	0.04	0.2	0.4
85	9	6	953	51.66	65	39.34	16	50.13	0.62	-5.00	5	143	2.0	0.02	1.0	6.1
85	9	6	11 7	21.39	65	44.96	16	52.01	3.71	-5.00	10	248	2.0	0.02	0.6	0.6
85	9	6	2015	50.83	65	42.64	16	48.40	1.56	-0.60	7	130	1.0	0.04	0.3	0.4
85	9	6	2322	53.71	65	38.03	16	51.86	2.83	-1.10	17	87	1.0	0.03	0.2	0.5
85	9	6	2331	7.80	65	42.58	16	46.82	2.69	-5.00	6	164	2.0	0.02	0.4	1.3
85	9	7	050	21.93	65	43.55	16	47.62	2.49	-0.30	12	90	1.0	0.02	0.3	0.5
85	9	7	340	27.55	65	42.25	16	48.70	2.78	-0.40	10	79	1.0	0.05	0.3	0.7
85	9	7	17 2	45.40	65	36.66	16	52.46	2.65	-5.00	10	136	1.0	0.05	0.5	0.7
85	9	7	1914	1.40	65	38.17	16	51.40	2.54	-0.80	16	64	1.0	0.03	0.2	0.5
85	9	7	2320	44.62	65	39.59	16	50.30	2.81	-1.30	7	149	2.0	0.02	0.4	1.0
85	9	8	042	36.06	65	39.34	16	50.64	3.45	-0.80	19	49	1.0	0.05	0.3	0.5
85	9	8	256	4.43	65	37.91	16	51.79	4.09	-5.00	7	111	3.0	0.01	0.5	1.9
85	9	8	4 7	47.50	65	37.49	16	53.04	7.49	-1.30	13	80	2.0	0.05	0.8	1.5
85	9	8	737	56.37	65	38.07	16	52.01	2.98	-5.00	12	103	2.0	0.05	0.3	0.6
85	9	8	921	26.20	65	38.07	16	51.50	3.36	-0.20	22	83	1.0	0.03	0.2	0.4
85	9	8	928	5.89	65	43.49	16	47.73	2.42	-5.00	10	137	2.0	0.03	0.3	0.6
85	9	8	1045	39.91	65	38.18	16	51.61	3.42	2.00	30	49	1.0	0.05	0.2	0.3
85	9	8	1712	39.35	65	38.85	16	50.79	2.33	-0.80	13	87	2.0	0.03	0.2	0.4
85	9	8	1716	13.23	65	39.11	16	50.78	2.01	-0.80	17	58	1.0	0.03	0.2	0.4
85	9	8	21 1	42.25	65	44.94	16	47.77	3.23	-0.70	5	321	4.0	0.04	10.7	0.8
85	9	9	1 0	6.98	65	39.12	16	50.71	2.70	-0.80	10	116	2.0	0.02	0.3	0.7
85	9	9	1449	3.40	65	42.67	16	47.14	2.10	-1.00	9	122	0.0	0.03	0.4	0.6
85	9	9	2231	56.68	65	38.38	16	51.14	2.61	-0.20	16	52	1.0	0.02	0.2	0.5
85	910		310	29.42	65	38.64	16	51.19	2.92	-5.00	6	219	1.0	0.03	1.7	0.8
85	910		651	58.87	65	38.41	16	51.18	1.26	0.10	18	51	1.0	0.04	0.2	0.4
85	910		747	13.06	65	42.32	16	47.60	1.83	-0.80	7	182	1.0	0.02	0.4	0.6
85	910		1022	58.62	65	42.37	16	45.81	2.12	-0.70	13	180	1.0	0.03	0.4	0.4
85	910		1343	24.89	65	38.08	16	51.69	3.12	-0.80	18	86	1.0	0.03	0.2	0.5
85	910		1459	21.79	65	38.71	16	50.99	2.60	-1.10	11	111	1.0	0.03	0.3	0.6
85	910		15 4	25.87	65	38.77	16	50.83	2.44	-0.60	21	51	1.0	0.03	0.2	0.4
85	910		1650	15.28	65	38.07	16	51.60	2.65	-0.60	19	54	1.0	0.03	0.2	0.4
85	911		120	27.71	65	39.88	16	50.07	2.52	-0.20	18	53	2.0	0.03	0.2	0.6
85	911		659	53.89	65	38.07	16	51.56	3.44	-0.20	19	47	1.0	0.05	0.3	0.5
85	911		733	9.26	65	42.81	16	48.14	2.56	-1.10	8	170	1.0	0.03	0.6	0.6
85	911		1641	24.16	65	37.91	16	51.76	2.83	-5.00	12	81	2.0	0.03	0.3	0.8
85	911		23 1	8.77	65	42.22	16	45.43	2.28	-0.20	16	94	1.0	0.04	0.2	0.5
85	912		256	13.05	65	39.20	16	50.41	2.98	-0.80	20	46	1.0	0.03	0.2	0.4
85	913		130	46.97	65	42.69	16	47.48	2.64	-1.40	7	128	1.0	0.04	1.0	0.6
85	913		139	59.28	65	43.99	16	48.76	2.00	-5.00	6	239	2.0	0.02	1.7	0.7
85	913		634	9.11	65	42.75	16	47.63	2.09	-1.60	4	136	1.0	0.01	1.1	0.9
85	913		9 6	54.87	65	40.55	16	50.92	1.64	-1.40	5	188	2.0	0.02	0.8	1.5
85	913		1032	4.71	65	38.06	16	51.37	2.74	-5.00	8	178	1.0	0.03	0.7	0.9
85	913		14 4	20.87	65	43.60	16	47.38	3.23	-1.10	9	114	1.0	0.02	0.5	1.1
85	913		2117	58.44	65	42.30	16	45.70	2.13	-0.10	16	127	1.0	0.03	0.3	0.6
85	913		2140	48.11	65	43.66	16	47.89	3.69	-2.10	5	221	2.0	0.03	1.6	1.1
85	914		934	2.48	65	38.33	16	51.31	2.38	-1.20	10	134	1.0	0.03	0.3	0.5

85	914	12	9	52.11	65	38.01	16	51.86	3.61	0.10	21	95	1.0	0.03	0.3	0.4
85	914	19	0	15.10	65	38.03	16	51.73	3.40	-0.80	12	184	2.0	0.02	0.4	0.7
85	915		052	24.33	65	40.34	16	49.60	3.89	-0.80	18	66	1.0	0.03	0.3	0.7
85	915		428	23.66	65	38.71	16	51.05	1.94	-1.40	10	107	1.0	0.03	0.3	0.5
85	915	1440		20.92	65	37.79	16	52.23	4.03	-1.30	8	92	2.0	0.02	0.4	1.1
85	915	2150		50.13	65	38.71	16	50.98	3.06	-0.90	15	64	1.0	0.03	0.2	0.5
85	916	1048		16.08	65	38.15	16	51.68	2.70	-5.00	9	102	2.0	0.01	0.3	0.8
85	916	1447		12.14	65	38.78	16	50.97	2.28	-0.80	19	55	1.0	0.03	0.2	0.4
85	916	15	4	46.90	65	39.49	16	50.62	5.23	-1.60	10	178	1.0	0.02	0.6	1.0
85	916	1734		41.02	65	37.94	16	51.74	2.88	-5.00	11	93	1.0	0.04	0.4	0.6
85	916	2120		41.40	65	43.44	16	48.41	2.38	-5.00	6	135	2.0	0.02	0.4	0.9
85	917		426	11.72	65	38.69	16	50.73	3.13	-1.00	11	107	1.0	0.05	0.3	0.7
85	917		915	32.18	65	39.92	16	49.98	5.01	-1.60	6	277	1.0	0.02	1.8	1.3
85	917	1130		30.62	65	38.18	16	51.49	2.70	-0.80	15	102	1.0	0.02	0.2	0.5
85	917	2011		22.38	65	37.02	16	53.47	8.80	-5.00	4	233	2.0	0.03	5.4	10.4
85	918		0	7 23.97	65	43.64	16	47.61	2.89	-5.00	9	137	1.0	0.02	0.4	0.5
85	918		913	35.51	65	42.23	16	46.73	2.54	-5.00	7	192	2.0	0.02	0.5	0.9
85	918	1055		41.98	65	37.86	16	51.71	2.85	-1.60	15	70	1.0	0.02	0.2	0.6
85	918	12	7	27.53	65	43.21	16	46.52	2.87	-5.00	8	227	3.0	0.03	0.8	1.0
85	918	16	5	38.86	65	38.68	16	50.72	4.05	-1.10	8	114	4.0	0.02	0.5	1.5
85	918	20	7	38.95	65	39.71	16	50.91	2.15	-5.00	7	290	3.0	0.01	0.8	0.9
85	919		228	18.68	65	39.89	16	49.94	3.40	-0.80	11	112	1.0	0.02	0.4	0.7
85	919		631	23.07	65	38.71	16	50.64	2.75	-1.70	12	82	1.0	0.04	0.3	0.6
85	919	1753		9.02	65	42.72	16	47.86	1.99	-1.30	7	136	1.0	0.01	0.3	0.6
85	919	1813		51.49	65	38.19	16	51.69	2.60	-1.30	11	96	1.0	0.03	0.3	0.5
85	919	2259		38.01	65	42.85	16	47.78	3.09	-0.60	12	142	1.0	0.04	0.3	0.6
85	920		050	22.60	65	37.99	16	51.60	3.03	-0.80	13	82	2.0	0.03	0.3	0.9
85	920		717	55.41	65	37.95	16	51.56	2.94	-0.20	20	79	1.0	0.04	0.2	0.4
85	920	11	0	6.23	65	38.00	16	51.80	3.03	-5.00	7	121	2.0	0.01	0.4	0.9
85	920	1157		32.94	65	37.87	16	51.70	2.54	-1.50	8	91	3.0	0.02	0.4	1.3
85	920	14	0	0.76	65	42.41	16	46.22	2.46	-0.90	15	139	3.0	0.05	0.3	0.8
85	920	1533		49.89	65	39.83	16	50.13	4.78	-1.30	4	269	2.0	0.01	6.1	7.8
85	920	2019		26.82	65	38.06	16	51.68	2.94	-0.60	15	85	2.0	0.03	0.3	0.7
85	920	2337		55.58	65	43.54	16	47.40	2.52	-5.00	4	153	2.0	0.00	1.3	2.5
85	920	2342		23.71	65	39.69	16	50.36	3.02	-0.90	9	91	1.0	0.03	0.4	0.8
85	921		8	6 10.10	65	38.10	16	51.45	2.94	-1.30	14	83	1.0	0.03	0.2	0.6
85	921		848	45.71	65	39.44	16	50.28	3.42	-1.10	8	96	1.0	0.01	0.3	0.6
85	921	1130		24.37	65	37.83	16	51.81	3.02	-1.30	11	115	2.0	0.04	0.4	0.9
85	921	18	4	21.26	65	43.73	16	47.31	2.33	-5.00	6	168	1.0	0.01	0.7	1.4
85	921	1853		55.81	65	42.58	16	48.01	2.58	-0.60	15	52	1.0	0.04	0.2	0.4
85	921	1856		44.21	65	38.25	16	51.56	4.51	-1.40	13	104	1.0	0.09	0.6	0.8
85	921	1858		28.29	65	38.55	16	51.00	2.04	-1.30	14	86	1.0	0.03	0.2	0.5
85	921	2025		55.68	65	40.37	16	50.69	3.34	-1.00	5	132	2.0	0.02	0.8	1.0
85	921	2027		44.61	65	37.79	16	51.89	3.75	-5.00	6	167	2.0	0.03	0.8	1.4
85	921	2113		12.21	65	43.47	16	47.61	2.44	-0.60	11	84	2.0	0.02	0.3	0.5
85	921	22	9	58.99	65	38.00	16	51.73	2.88	-1.30	14	84	2.0	0.03	0.2	0.6
85	921	2211		54.05	65	37.94	16	51.88	3.67	-1.40	8	132	2.0	0.02	0.5	1.1
85	921	2234		45.73	65	38.14	16	51.59	2.45	-1.20	8	145	1.0	0.02	0.3	0.8
85	922		057	47.83	65	36.90	16	52.33	2.89	-1.20	12	100	1.0	0.02	0.5	0.8
85	922		419	41.63	65	42.95	16	48.54	1.41	-0.60	9	67	1.0	0.07	0.3	0.7
85	922		449	3.04	65	36.91	16	52.34	2.65	-5.00	7	118	1.0	0.03	0.7	1.0
85	922		651	24.05	65	42.80	16	48.09	3.19	-0.60	11	105	1.0	0.04	0.3	0.6
85	922		7	1 53.34	65	35.18	16	51.73	14.41	-5.00	4	275	3.0	0.04	45.4	88.0
85	922		711	10.96	65	43.57	16	47.32	2.82	-5.00	6	148	2.0	0.01	0.7	1.3
85	922	1118		17.01	65	42.54	16	48.28	1.94	-0.50	13	80	1.0	0.05	0.3	0.4
85	922	1226		39.77	65	39.73	16	50.45	3.20	-1.30	6	152	1.0	0.01	0.5	0.8
85	922	1514		19.59	65	37.91	16	51.92	3.35	-1.40	7	93	2.0	0.01	0.4	1.2
85	922	1715		52.84	65	37.99	16	51.86	2.85	-0.90	17	85	2.0	0.03	0.2	0.6
85	923		057	22.27	65	43.62	16	47.25	3.18	-5.00	4	147	1.0	0.01	1.7	3.1
85	923		423	58.59	65	38.17	16	51.80	3.05	1.60	29	51	1.0	0.06	0.2	0.3
85	923		433	51.81	65	38.02	16	51.80	2.90	-0.80	17	48	1.0	0.03	0.2	0.6
85	923		526	19.37	65	38.11	16	51.58	2.52	-5.00	6	105	1.0	0.02	0.4	1.0
85	923		636	31.60	65	43.07	16	54.85	3.79	-0.10	7	210	1.0	0.02	0.9	1.2
85	923		727	39.46	65	38.06	16	51.54	3.25	-0.80	23	84	1.0	0.04	0.2	0.4
85	923		8	1 33.94	65	38.41	16	51.52	3.64	-5.00	8	207	1.0	0.02	1.3	1.2
85	923		930	38.81	65	42.97	16	48.27	3.38	-1.40	10	155	1.0	0.05	0.8	0.7
85	923	11	0	9.39	65	39.69	16	50.14	2.90	-0.70	5	149	1.0	0.01	0.6	0.8
85	923	12	4	53.32	65	42.81	16	47.71	2.77	0.90	30	63	1.0	0.04	0.2	0.3
85	923	1520		37.68	65	38.42	16	51.20	2.39	-1.20	10	130	1.0	0.02	0.3	0.6
85	923	1636		14.86	65	39.10	16	51.10	2.19	-1.40	8	120	1.0	0.01	0.3	0.5
85	924		3	8 14.49	65	42.79	16	48.06	2.77	-0.60	13	55	1.0	0.03	0.3	0.5
85	924		411	40.03	65	41.12	16	48.52	5.62	-1.00	6	160	1.0	0.02	0.9	1.5
85	924		432	25.08	65	38.00	16	51.72	3.38	-0.70	19	84	2.0	0.04	0.3	0.5
85	924		8	5 37.60	65	37.97	16	51.47	2.83	-1.40	8	101	3.0	0.02	0.3	2.1
85	924		9	1 18.85	65	38.11	16	51.36	2.18	-1.40	12	83	1.0	0.05	0.2	0.7
85	924	1051		53.98	65	39.01	16	51.12	2.64	-1.30	8	127	2.0	0.04	0.4	0.8
85	924	1150		10.92	65	43.05	16	46.82	2.56	-5.00	5	201	2.0	0.01	0.7	1.5
85	924	1425		33.11	65	40.39	16	49.33	4.95	-0.90	8	134	1.0	0.01	0.9	0.7
85	924	15	3	39.79	65	42.65	16	47.65	2.40	-0.60	13	82	1.0	0.03	0.3	0.5
85	924	18	1	39.42	65	37.90	16	51.98	4.11	-5.00	6	134	3.0	0.01	0.5	2.6
85	925		211	32.74	65	37.97	16	51.68	3.35	-0.90	17	82	1.0	0.03	0.3	0.5
85	925		3	6 31.73	65	38.03	16	51.77	3.10	-0.20	18	47	1.0	0.04	0.2	0.5
85	925		459	36.89	65	43.65	16	47.47	4.85	-0.70	4	277	2.0	0.01	32.6	28.0
85	925		718	30.71	65	38.79	16	50.96	2.96	-5.00	5	161	2.0	0.02	0.8	1.4
85	925	1625		35.05	65	40.38	16	49.31	3.19	-1.00	11	74	1.0	0.03	0.3	0.5
85	925	2131		41.69	65	38.85	16	50.74	2.44	-1.10	9	93	2.0	0.02	0.3	0.9
85	925	2213		38.79	65	39.58	16	50.48	3.46	-0.90	17	63	3.0	0.03	0.2	0.6
85	925	23	9	51.70	65	37.96	16	51.87	3.31	-1.20	9	84	2.0	0.02	0.3	1.1
85	926		627	50.32	65	38.82	16	50.87	2.52	-1.00	13	87	2.0	0.04	0.3	0.5
85	926		726	48.67	65	38.47	16	51.09	2.57	-5.00	7	209	2.0	0.01	1.1	1.0
85	926		814	12.07	65	38.51	16	50.33	2.82	-5.00	7	133	2.0	0.02	0.6	1.2
85	926	1133		2.94	65	36.51	16	52.66	2.93	-0.80	9	164	1.0	0.03	0.6	0.7
85	927		032	17.59	65	37.89	16	51.85	4.24	-1.40	6	131	3.0	0.03	0.5	2.0
85	927		6	9 31.60	65	42.22	16	44.82	4.15	-0.50	7	300	2.0	0.02	1.1	0.8
85	927		641	14.85	65	37.92	16	51.63	3.19	-1.00	15	80	2.0	0.04	0.3	0.6
85	927		7	0 56.71	65	38.03	16	51.61	2.35	-1.30	10	84	1.0	0.03	0.3	0.5
85	927	1226		34.74	65	43.09	16	50.47	3.96	-5.00	6	179	1.0	0.03	1.0	1.5
85	928		246	23.14	65	39.66	16	50.25	3.18	-0.90	14	91	1.0	0.02	0.3	0.4
85	928		632	2.13	65	39.79	16	49.61	3.28	-0.90	6	116	0.0	0.05	0.9	1.0
85	928	10	7	7.66	65	38.56	16	51.09	2.84	-1.00	14	88	1.0	0.03	0.3	0.6
85	928	12	3	21.74	65	39.14	16	50.66	3.00	-0.90	12	84	2.0	0.02	0.3	0.6
85	928	1232		26.00	65	37.98	16	49.81	4.31	-1.00	5	320	3.0	0.01	1.4	1.4
85	928	1431		11.19	65	37.93	16	51.67	3.46	-0.70	14	81	2.0	0.03	0.3	0.6
85	928	1447		10.39	65	38.72	16	51.17	2.91	-1.20	7	142	2.0	0.01	0.4	1.1
85	928	1957		44.82	65	37.97	16	51.73	2.60	-5.00	8	83	1.0	0.02	0.3	0.7
85	928	2348		46.47	65	39.09	16	49.00	4.88	-1.40	6	307	1.0	0.03	1.0	1.0
85	929		354	27.38	65	39.48	16	50.20	5.63	1.10	12	114	1.0	0.02	0.6	0.7
85	929		5	8 42.91	65	37.91	16	51.75	3.33	-0.70	19	77	1.0	0.04	0.2	0.5
85	929		847	42.69	65	38.38	16	51.34	0.99	-0.90	10	116	1.0	0.02	0.2	0.7
85	929	1050		35.35	65	38.46	16	51.29	2.50	-0.70	12	90	1.0	0.03	0.3	0.7
85	929	1116		21.70	65	37.95	16	51.97	3.40	-5.00	7	84	3.0	0.02	0.4	1.6
85	929	13	3	57.38	65	37.92	16	51.67	2.93	-1.40	9	127	2.0	0.04	0.5	1.1
85	929	1411		57.32	65	39.80	16	49.87	2.66	-1.30	6	157	1.0	0.01	0.6	0.8
85	929	1444		3.65	65	42.74	16	47.68	2.56	-5.00	7	89	1.0	0.03	0.4	0.7
85	929	17	7	18.63	65	43.14	16	46.92	3.21	-1.40	9	246	1.0	0.03	0.7	0.6
85	929	1714		7.33	65	38.66	16	51.09	2.87	-1.10	11	95	1.0	0.04	0.3	0.6
85	929	18	9	54.47	65	38.14	16	51.60	2.53	-1.20	10	102	1.0	0.02	0.3	0.6
85	929	1811		20.32	65	39.07	16	51.08	3.15	-5.00	8	119	2.0	0.02	0.3	1.1
85	929	2340		40.72	65	39.11	16	50.71	2.66	-0.20	22	58	1.0	0.05	0.2	0.4
85	930		031	53.79	65	42.85	16	47.22	3.00	-1.60	9	134	1.0	0.03	0.4	0.5

85	930	245	44.23	65	42.76	16	47.31	2.52	-1.70	7	108	1.0	0.02	0.5	0.7
85	930	4 7	28.40	65	37.88	16	52.10	3.96	-1.00	9	84	2.0	0.05	0.4	0.9
85	930	1848	0.46	65	38.71	16	50.92	2.73	-1.30	11	87	1.0	0.03	0.3	0.6
85	930	2058	31.43	65	41.88	16	48.02	0.12	-0.70	5	159	2.0	0.01	0.4	2.4
85	930	2314	6.05	65	37.99	16	51.44	2.21	-1.00	13	80	1.0	0.03	0.2	0.6
8510	1	222	13.36	65	43.73	16	47.13	2.20	-1.40	4	253	2.0	0.00	1.2	1.9
8510	1	743	52.89	65	44.61	16	37.41	13.89	0.20	11	294	6.0	0.07	2.1	1.2
8510	1	2021	54.96	65	43.50	16	47.72	2.45	0.40	8	231	2.0	0.02	0.8	0.5
8510	1	2139	17.75	65	37.79	16	51.95	3.89	-1.00	9	134	2.0	0.03	0.4	0.9
8510	2	1917	37.65	65	38.59	16	51.58	3.32	-1.40	9	121	2.0	0.03	0.4	1.1
8510	3	123	6.30	65	38.59	16	51.53	3.07	-1.30	10	121	2.0	0.04	0.4	0.7
8510	3	422	33.17	65	37.66	16	51.94	2.58	-5.00	4	146	2.0	0.00	1.0	2.5
8510	3	914	42.19	65	39.21	16	51.13	2.38	-1.40	7	244	2.0	0.02	1.5	0.7
8510	3	1121	12.21	65	37.83	16	53.69	5.87	-1.10	10	119	1.0	0.10	0.8	0.9
8510	3	1245	31.66	65	38.38	16	53.23	6.19	-1.10	9	126	2.0	0.06	0.7	1.7

Appendix B

Tomography Final Run

B.1 Input

- Input control parameters.
- Seismometer stations.
- Initial ('evolved') 1–d velocity model.
- Locations of 105 earthquakes and 6 timed explosions used in the inversion.

MACHINE CONSTANTS ETA AND TOL: 0.953674E-06 0.565980E-72

PROGRAM SIMUL3M (JAN 1985)
* FAST ART *
* PSEUDO-BENDING *

CONTROL PARAMETERS

NEQS	NQRY	NSHT	NITLOC	EIGTOL	RMSCUT	NHITCT	DVMAX	VDAMP	IRES	I3D	NITMAX
105	0	6	6	0.020	0.020	25	0.40	0.200	1	1	7

ITS. FOR 1-D VEL. MODEL = 1
RMS FOR TERM. = 0.010
FIX LOCATIONS FOR ITERATIONS = 0
DISTANCE WEIGHTING: 200.00 700.00 RESIDUAL WEIGHTING: 0.30 1.20
STEP LENGTH FOR PAR. DER.: 0.500; SHOT WEIGHT: 1.00
PARAMETERS FOR APPROXIMATE RAY TRACER

NDIP	ISKIP	SCALE1	SCALE2
9	3	0.50	1.50

PARAMETERS FOR PSEUDO-BENDING:

XFAC	TLIM	NITPB
1.20	0.0020	7

ORIGIN : LATITUDE LONGITUDE ROTATION
65 34.69 16 44.84 -19.00
SHORT DISTANCE CONVERSION FACTORS
ONE MIN LAT 1.8584 KM
ONE MIN LON 0.7692 KM

STATION		LATITUDE	LONGITUDE	ELEV	X	Y	Z
1	NBU	65 38.21	16 45.91	360	2.91	5.92	-0.36
2	NNO	65 39.64	16 49.13	490	6.11	7.62	-0.49
3	NSY	65 36.33	16 48.44	380	3.61	1.98	-0.38
4	NGR	65 37.90	16 52.87	295	7.78	3.63	-0.29
5	NVO	65 37.76	16 55.18	280	9.37	2.81	-0.28
6	NDA	65 39.30	16 51.76	360	7.81	6.37	-0.36
7	NSV	65 37.40	16 50.18	400	5.52	3.43	-0.40
8	NSK	65 39.86	16 57.70	320	12.47	5.87	-0.32
9	NHA	65 39.68	16 46.17	400	3.98	8.44	-0.40
10	NHV	65 36.43	16 51.39	320	5.81	1.42	-0.32
11	NSA	65 40.49	16 43.84	525	2.78	10.44	-0.52
12	NJO	65 40.64	16 40.99	500	0.81	11.42	-0.50
13	NRA	65 36.42	16 54.37	280	7.97	0.65	-0.28
14	NHE	65 37.32	16 46.55	350	2.83	4.19	-0.35
15	NYT	65 37.24	16 48.44	380	4.16	3.58	-0.38
16	NSD	65 36.93	16 57.90	280	10.85	0.67	-0.28
17	NHR	65 38.33	16 48.32	355	4.73	5.53	-0.35
18	NSO	65 40.35	16 53.30	420	9.57	7.83	-0.42
19	NNA	65 38.16	16 49.66	430	5.60	4.89	-0.43
20	RMU	65 44.24	16 53.23	600	11.86	14.69	-0.60
21	RNO	65 40.83	16 49.07	490	6.79	9.73	-0.49
22	RRA	65 42.58	16 46.88	550	6.25	13.35	-0.55
23	RGK	65 43.88	16 42.32	720	3.73	16.78	-0.72
24	RKR	65 42.67	16 53.12	430	10.83	11.95	-0.43
25	RVI	65 43.72	16 45.39	560	5.86	15.73	-0.56
26	RLI	65 43.55	16 54.52	600	12.38	13.15	-0.60
27	RLE	65 44.34	16 48.00	560	8.13	16.17	-0.56
28	RSA	65 42.70	16 49.54	520	8.26	12.90	-0.52
29	RSU	65 41.92	16 52.00	520	9.57	10.91	-0.52

VELOCITY GRID SIZE:

NX = 9 NY = 12 NZ = 7

XGRID
-100.00 0.00 3.00 5.00 7.00 9.00 11.00 13.00 100.00

YGRID
-100.00 0.00 2.00 4.00 6.00 8.00 10.00 12.00 14.00 16.00 18.00 100.00

ZGRID
-50.00 0.00 1.00 2.00 3.00 4.00 50.00

VELOCITY VALUES ON THREE-DIMENSIONAL GRID

LAYER 1

3.00	3.00	3.00	3.00	3.00	3.00	3.00	3.00	3.00
3.00	3.00	3.00	3.00	3.00	3.00	3.00	3.00	3.00
3.00	3.00	3.00	3.00	3.00	3.00	3.00	3.00	3.00
3.00	3.00	3.00	3.00	3.00	3.00	3.00	3.00	3.00
3.00	3.00	3.00	3.00	3.00	3.00	3.00	3.00	3.00
3.00	3.00	3.00	3.00	3.00	3.00	3.00	3.00	3.00
3.00	3.00	3.00	3.00	3.00	3.00	3.00	3.00	3.00
3.00	3.00	3.00	3.00	3.00	3.00	3.00	3.00	3.00
3.00	3.00	3.00	3.00	3.00	3.00	3.00	3.00	3.00
3.00	3.00	3.00	3.00	3.00	3.00	3.00	3.00	3.00
3.00	3.00	3.00	3.00	3.00	3.00	3.00	3.00	3.00

LAYER 2

3.60	3.60	3.60	3.60	3.60	3.60	3.60	3.60	3.60
3.60	3.60	3.60	3.60	3.60	3.60	3.60	3.60	3.60
3.60	3.60	3.60	3.60	3.60	3.60	3.60	3.60	3.60
3.60	3.60	3.60	3.60	3.60	3.60	3.60	3.60	3.60
3.60	3.60	3.60	3.60	3.60	3.60	3.60	3.60	3.60
3.60	3.60	3.60	3.60	3.60	3.60	3.60	3.60	3.60
3.60	3.60	3.60	3.60	3.60	3.60	3.60	3.60	3.60
3.60	3.60	3.60	3.60	3.60	3.60	3.60	3.60	3.60
3.60	3.60	3.60	3.60	3.60	3.60	3.60	3.60	3.60
3.60	3.60	3.60	3.60	3.60	3.60	3.60	3.60	3.60
3.60	3.60	3.60	3.60	3.60	3.60	3.60	3.60	3.60

LAYER 3

4.65	4.65	4.65	4.65	4.65	4.65	4.65	4.65	4.65
4.65	4.65	4.65	4.65	4.65	4.65	4.65	4.65	4.65
4.65	4.65	4.65	4.65	4.65	4.65	4.65	4.65	4.65
4.65	4.65	4.65	4.65	4.65	4.65	4.65	4.65	4.65
4.65	4.65	4.65	4.65	4.65	4.65	4.65	4.65	4.65
4.65	4.65	4.65	4.65	4.65	4.65	4.65	4.65	4.65
4.65	4.65	4.65	4.65	4.65	4.65	4.65	4.65	4.65
4.65	4.65	4.65	4.65	4.65	4.65	4.65	4.65	4.65
4.65	4.65	4.65	4.65	4.65	4.65	4.65	4.65	4.65
4.65	4.65	4.65	4.65	4.65	4.65	4.65	4.65	4.65
4.65	4.65	4.65	4.65	4.65	4.65	4.65	4.65	4.65

LAYER 4

5.60	5.60	5.60	5.60	5.60	5.60	5.60	5.60	5.60
5.60	5.60	5.60	5.60	5.60	5.60	5.60	5.60	5.60
5.60	5.60	5.60	5.60	5.60	5.60	5.60	5.60	5.60
5.60	5.60	5.60	5.60	5.60	5.60	5.60	5.60	5.60

5.60	5.60	5.60	5.60	5.60	5.60	5.60	5.60	5.60
5.60	5.60	5.60	5.60	5.60	5.60	5.60	5.60	5.60
5.60	5.60	5.60	5.60	5.60	5.60	5.60	5.60	5.60
5.60	5.60	5.60	5.60	5.60	5.60	5.60	5.60	5.60
5.60	5.60	5.60	5.60	5.60	5.60	5.60	5.60	5.60
5.60	5.60	5.60	5.60	5.60	5.60	5.60	5.60	5.60
5.60	5.60	5.60	5.60	5.60	5.60	5.60	5.60	5.60
5.60	5.60	5.60	5.60	5.60	5.60	5.60	5.60	5.60

LAYER 5

5.75	5.75	5.75	5.75	5.75	5.75	5.75	5.75	5.75
5.75	5.75	5.75	5.75	5.75	5.75	5.75	5.75	5.75
5.75	5.75	5.75	5.75	5.75	5.75	5.75	5.75	5.75
5.75	5.75	5.75	5.75	5.75	5.75	5.75	5.75	5.75
5.75	5.75	5.75	5.75	5.75	5.75	5.75	5.75	5.75
5.75	5.75	5.75	5.75	5.75	5.75	5.75	5.75	5.75
5.75	5.75	5.75	5.75	5.75	5.75	5.75	5.75	5.75
5.75	5.75	5.75	5.75	5.75	5.75	5.75	5.75	5.75
5.75	5.75	5.75	5.75	5.75	5.75	5.75	5.75	5.75
5.75	5.75	5.75	5.75	5.75	5.75	5.75	5.75	5.75
5.75	5.75	5.75	5.75	5.75	5.75	5.75	5.75	5.75

LAYER 6

6.80	6.80	6.80	6.80	6.80	6.80	6.80	6.80	6.80
6.80	6.80	6.80	6.80	6.80	6.80	6.80	6.80	6.80
6.80	6.80	6.80	6.80	6.80	6.80	6.80	6.80	6.80
6.80	6.80	6.80	6.80	6.80	6.80	6.80	6.80	6.80
6.80	6.80	6.80	6.80	6.80	6.80	6.80	6.80	6.80
6.80	6.80	6.80	6.80	6.80	6.80	6.80	6.80	6.80
6.80	6.80	6.80	6.80	6.80	6.80	6.80	6.80	6.80
6.80	6.80	6.80	6.80	6.80	6.80	6.80	6.80	6.80
6.80	6.80	6.80	6.80	6.80	6.80	6.80	6.80	6.80
6.80	6.80	6.80	6.80	6.80	6.80	6.80	6.80	6.80
6.80	6.80	6.80	6.80	6.80	6.80	6.80	6.80	6.80

LAYER 7

7.00	7.00	7.00	7.00	7.00	7.00	7.00	7.00	7.00
7.00	7.00	7.00	7.00	7.00	7.00	7.00	7.00	7.00
7.00	7.00	7.00	7.00	7.00	7.00	7.00	7.00	7.00
7.00	7.00	7.00	7.00	7.00	7.00	7.00	7.00	7.00
7.00	7.00	7.00	7.00	7.00	7.00	7.00	7.00	7.00
7.00	7.00	7.00	7.00	7.00	7.00	7.00	7.00	7.00
7.00	7.00	7.00	7.00	7.00	7.00	7.00	7.00	7.00
7.00	7.00	7.00	7.00	7.00	7.00	7.00	7.00	7.00
7.00	7.00	7.00	7.00	7.00	7.00	7.00	7.00	7.00
7.00	7.00	7.00	7.00	7.00	7.00	7.00	7.00	7.00
7.00	7.00	7.00	7.00	7.00	7.00	7.00	7.00	7.00

TRIAL EVENT LOCATIONS:

N	ORIGIN TIME	LATITUDE	LONGITUDE	DEPTH	X	Y	Z
1	85 7 2 1152 33.85	65N42.80	16W47.73	2.74	7.00	13.53	2.74
*	NUMBER OF OBSERVATIONS FOR EVENT = 14						
2	85 7 3 1435 54.44	65N42.89	16W48.08	2.71	7.31	13.60	2.71
*	NUMBER OF OBSERVATIONS FOR EVENT = 12						
3	85 7 4 852 53.96	65N42.87	16W47.89	2.64	7.16	13.61	2.64
*	NUMBER OF OBSERVATIONS FOR EVENT = 18						
4	85 7 9 1954 15.02	65N38.06	16W51.52	3.76	6.89	4.25	3.76
*	NUMBER OF OBSERVATIONS FOR EVENT = 22						
5	85 710 936 6.12	65N39.50	16W50.51	2.42	7.03	7.03	2.42
*	NUMBER OF OBSERVATIONS FOR EVENT = 11						
6	85 710 1214 0.60	65N38.47	16W51.08	2.92	6.82	5.08	2.92
*	NUMBER OF OBSERVATIONS FOR EVENT = 10						
7	85 711 449 8.25	65N37.97	16W51.81	3.60	7.05	4.02	3.60
*	NUMBER OF OBSERVATIONS FOR EVENT = 21						
8	85 711 558 55.86	65N38.75	16W50.64	2.74	6.67	5.68	2.74
*	NUMBER OF OBSERVATIONS FOR EVENT = 11						
9	85 712 2231 53.59	65N38.81	16W50.74	2.48	6.78	5.76	2.48
*	NUMBER OF OBSERVATIONS FOR EVENT = 14						
10	85 716 226 39.33	65N43.16	16W48.03	2.26	7.44	14.09	2.26
*	NUMBER OF OBSERVATIONS FOR EVENT = 11						
11	85 716 758 53.17	65N42.82	16W47.73	2.60	7.02	13.56	2.60
*	NUMBER OF OBSERVATIONS FOR EVENT = 27						
12	85 716 1010 9.63	65N38.75	16W50.89	2.29	6.85	5.62	2.29
*	NUMBER OF OBSERVATIONS FOR EVENT = 10						
13	85 717 1734 55.34	65N38.90	16W50.71	2.80	6.81	5.93	2.80
*	NUMBER OF OBSERVATIONS FOR EVENT = 18						
14	85 719 540 57.69	65N39.74	16W50.11	3.49	6.88	7.56	3.49
*	NUMBER OF OBSERVATIONS FOR EVENT = 14						
15	85 719 746 39.93	65N38.44	16W51.20	2.40	6.89	5.00	2.40
*	NUMBER OF OBSERVATIONS FOR EVENT = 11						
16	85 720 432 12.85	65N37.94	16W51.76	2.98	6.99	3.98	2.98
*	NUMBER OF OBSERVATIONS FOR EVENT = 17						
17	85 721 038 4.49	65N37.95	16W51.46	3.26	6.78	4.07	3.26
*	NUMBER OF OBSERVATIONS FOR EVENT = 16						
18	85 722 2133 43.06	65N39.79	16W50.25	3.14	7.01	7.61	3.14
*	NUMBER OF OBSERVATIONS FOR EVENT = 9						
19	85 724 1612 28.63	65N38.08	16W51.59	3.61	6.96	4.27	3.61
*	NUMBER OF OBSERVATIONS FOR EVENT = 24						
20	85 724 1615 39.31	65N38.08	16W51.50	3.53	6.89	4.29	3.53
*	NUMBER OF OBSERVATIONS FOR EVENT = 22						
21	85 726 556 22.85	65N42.61	16W48.08	2.02	7.14	13.11	2.02
*	NUMBER OF OBSERVATIONS FOR EVENT = 15						
22	85 728 911 55.19	65N38.95	16W50.74	2.71	6.86	6.01	2.71
*	NUMBER OF OBSERVATIONS FOR EVENT = 13						
23	85 728 1847 39.35	65N37.80	16W51.70	3.66	6.87	3.75	3.66
*	NUMBER OF OBSERVATIONS FOR EVENT = 22						
24	85 729 11 8 37.12	65N43.53	16W47.70	2.39	7.42	14.82	2.39
*	NUMBER OF OBSERVATIONS FOR EVENT = 13						
25	85 730 15 8 37.12	65N42.67	16W47.91	2.30	7.06	13.25	2.30
*	NUMBER OF OBSERVATIONS FOR EVENT = 12						
26	85 730 1752 12.44	65N38.13	16W51.47	2.87	6.90	4.39	2.87
*	NUMBER OF OBSERVATIONS FOR EVENT = 18						
27	85 730 1848 53.88	65N38.08	16W51.68	3.41	7.02	4.25	3.41
*	NUMBER OF OBSERVATIONS FOR EVENT = 17						
28	85 731 620 45.48	65N38.95	16W50.72	3.07	6.85	6.01	3.07
*	NUMBER OF OBSERVATIONS FOR EVENT = 16						
29	85 731 822 1.29	65N38.05	16W51.62	3.49	6.96	4.21	3.49
*	NUMBER OF OBSERVATIONS FOR EVENT = 16						
30	85 8 1 854 40.99	65N37.91	16W51.78	3.77	6.99	3.92	3.77
*	NUMBER OF OBSERVATIONS FOR EVENT = 26						
31	85 8 1 1218 1.34	65N42.67	16W47.90	2.44	7.05	13.26	2.44
*	NUMBER OF OBSERVATIONS FOR EVENT = 17						
32	85 8 1 1227 47.41	65N42.78	16W47.93	2.56	7.14	13.44	2.56
*	NUMBER OF OBSERVATIONS FOR EVENT = 16						
33	85 8 1 1256 24.37	65N39.25	16W50.44	3.10	6.83	6.61	3.10
*	NUMBER OF OBSERVATIONS FOR EVENT = 24						
34	85 8 2 055 21.47	65N42.99	16W50.71	2.31	9.28	13.12	2.31

```
* NUMBER OF OBSERVATIONS FOR EVENT =  11
 35 85 8 3  948 56.64 65N39.28  16W50.38   2.72   6.80   6.68   2.72
* NUMBER OF OBSERVATIONS FOR EVENT =  13
 36 85 8 3 1837 13.20 65N37.95  16W51.59   3.48   6.88   4.04   3.48
* NUMBER OF OBSERVATIONS FOR EVENT =  18
 37 85 8 3 2325 51.31 65N39.20  16W50.33   2.42   6.72   6.55   2.42
* NUMBER OF OBSERVATIONS FOR EVENT =  10
 38 85 8 4 2131 59.96 65N42.66  16W47.44   2.59   6.71  13.35   2.59
* NUMBER OF OBSERVATIONS FOR EVENT =  12
 39 85 8 6  843  8.60 65N39.55  16W50.23   3.17   6.85   7.19   3.17
* NUMBER OF OBSERVATIONS FOR EVENT =  16
 40 85 8 6 1548 55.18 65N38.09  16W51.44   2.79   6.85   4.32   2.79
* NUMBER OF OBSERVATIONS FOR EVENT =  22
 41 85 8 6 1614 14.65 65N42.83  16W48.07   2.60   7.27  13.50   2.60
* NUMBER OF OBSERVATIONS FOR EVENT =  14
 42 85 8 7 1833 10.86 65N42.75  16W48.07   3.24   7.22  13.36   3.24
* NUMBER OF OBSERVATIONS FOR EVENT =  13
 43 85 815 14 4 47.94 65N42.89  16W47.71   2.89   7.04  13.69   2.89
* NUMBER OF OBSERVATIONS FOR EVENT =  14
 44 85 815 1514 30.05 65N38.78  16W50.99   2.82   6.94   5.65   2.82
* NUMBER OF OBSERVATIONS FOR EVENT =  15
 45 85 819  0 4 20.92 65N38.08  16W51.51   3.13   6.90   4.29   3.13
* NUMBER OF OBSERVATIONS FOR EVENT =  17
 46 85 822 1640 27.29 65N42.69  16W48.06   2.32   7.18  13.25   2.32
* NUMBER OF OBSERVATIONS FOR EVENT =  11
 47 85 823 1045 37.13 65N38.07  16W51.57   3.42   6.93   4.26   3.42
* NUMBER OF OBSERVATIONS FOR EVENT =  16
 48 85 823 13 1 40.32 65N39.54  16W49.46   2.65   6.29   7.37   2.65
* NUMBER OF OBSERVATIONS FOR EVENT =  10
 49 85 824 1059  7.61 65N37.81  16W51.68   3.37   6.86   3.77   3.37
* NUMBER OF OBSERVATIONS FOR EVENT =  11
 50 85 824 1123 39.00 65N38.03  16W51.55   3.88   6.90   4.19   3.88
* NUMBER OF OBSERVATIONS FOR EVENT =  17
 51 85 824 1525 39.92 65N42.73  16W47.72   2.60   6.95  13.41   2.60
* NUMBER OF OBSERVATIONS FOR EVENT =  15
 52 85 824 1746 32.72 65N39.64  16W50.17   2.86   6.87   7.36   2.86
* NUMBER OF OBSERVATIONS FOR EVENT =  12
 53 85 826  539 45.49 65N38.04  16W51.79   3.53   7.08   4.15   3.53
* NUMBER OF OBSERVATIONS FOR EVENT =  18
 54 85 827 1721 48.66 65N38.16  16W51.70   3.44   7.08   4.38   3.44
* NUMBER OF OBSERVATIONS FOR EVENT =  24
 55 85 828  120 54.18 65N38.11  16W51.54   3.34   6.94   4.33   3.34
* NUMBER OF OBSERVATIONS FOR EVENT =  16
 56 85 830  325 51.76 65N42.79  16W47.75   2.87   7.01  13.51   2.87
* NUMBER OF OBSERVATIONS FOR EVENT =  10
 57 85 831  023 18.38 65N38.30  16W51.39   3.00   6.94   4.70   3.00
* NUMBER OF OBSERVATIONS FOR EVENT =  10
 58 85 831  029 13.74 65N39.73  16W50.25   3.84   6.98   7.50   3.84
* NUMBER OF OBSERVATIONS FOR EVENT =  19
 59 85 831 1137 20.71 65N38.66  16W51.32   2.94   7.11   5.35   2.94
* NUMBER OF OBSERVATIONS FOR EVENT =  13
 60 85 831 1349 52.30 65N38.04  16W51.60   3.47   6.94   4.19   3.47
* NUMBER OF OBSERVATIONS FOR EVENT =  21
 61 85 9 2  145 29.71 65N38.02  16W51.69   3.75   6.99   4.14   3.75
* NUMBER OF OBSERVATIONS FOR EVENT =  24
 62 85 9 2  6 4 44.26 65N42.81  16W47.75   2.62   7.02  13.54   2.62
* NUMBER OF OBSERVATIONS FOR EVENT =  26
 63 85 9 2 2149 19.62 65N37.98  16W51.66   3.80   6.95   4.07   3.80
* NUMBER OF OBSERVATIONS FOR EVENT =  24
 64 85 9 3  4 4 34.26 65N42.83  16W47.54   2.72   6.88  13.63   2.72
* NUMBER OF OBSERVATIONS FOR EVENT =  12
 65 85 9 3 1012 11.67 65N42.82  16W48.00   2.84   7.21  13.50   2.84
* NUMBER OF OBSERVATIONS FOR EVENT =  10
 66 85 9 3 1220  3.62 65N42.17  16W45.43   2.04   4.95  13.00   2.04
* NUMBER OF OBSERVATIONS FOR EVENT =  13
 67 85 9 4  724  2.63 65N42.63  16W48.04   2.64   7.13  13.15   2.64
* NUMBER OF OBSERVATIONS FOR EVENT =  13
 68 85 9 5  0 1  7.20 65N38.08  16W51.67   3.65   7.01   4.25   3.65
* NUMBER OF OBSERVATIONS FOR EVENT =  23
 69 85 9 7  050 21.93 65N43.55  16W47.62   2.49   7.38  14.87   2.49
* NUMBER OF OBSERVATIONS FOR EVENT =  11
 70 85 9 8  042 36.06 65N39.34  16W50.64   3.45   7.03   6.72   3.45
* NUMBER OF OBSERVATIONS FOR EVENT =  14
 71 85 9 8  921 26.20 65N38.07  16W51.50   3.36   6.88   4.27   3.36
* NUMBER OF OBSERVATIONS FOR EVENT =  18
 72 85 9 8 1045 39.91 65N38.18  16W51.61   3.42   7.03   4.44   3.42
* NUMBER OF OBSERVATIONS FOR EVENT =  27
 73 85 9 8 1716 13.23 65N39.11  16W50.78   2.01   6.99   6.28   2.01
* NUMBER OF OBSERVATIONS FOR EVENT =  14
 74 85 9 9 2231 56.68 65N38.38  16W51.14   2.61   6.81   4.91   2.61
* NUMBER OF OBSERVATIONS FOR EVENT =  14
 75 85 910 1343 24.89 65N38.08  16W51.69   3.12   7.03   4.24   3.12
* NUMBER OF OBSERVATIONS FOR EVENT =  16
 76 85 910 1459 21.79 65N38.71  16W50.99   2.60   6.90   5.53   2.60
* NUMBER OF OBSERVATIONS FOR EVENT =  11
 77 85 910 15 4 25.87 65N38.77  16W50.83   2.44   6.82   5.67   2.44
* NUMBER OF OBSERVATIONS FOR EVENT =  18
 78 85 911  120 27.71 65N39.88  16W50.07   2.52   6.94   7.81   2.52
* NUMBER OF OBSERVATIONS FOR EVENT =  15
 79 85 911  659 53.89 65N38.07  16W51.56   3.44   6.93   4.26   3.44
* NUMBER OF OBSERVATIONS FOR EVENT =  17
 80 85 911 23 1  8.77 65N42.22  16W45.43   2.28   4.98  13.08   2.28
* NUMBER OF OBSERVATIONS FOR EVENT =  14
 81 85 912  256 13.05 65N39.20  16W50.41   2.98   6.77   6.53   2.98
* NUMBER OF OBSERVATIONS FOR EVENT =  17
 82 85 913 2117 58.44 65N42.30  16W45.70   2.13   5.23  13.16   2.13
* NUMBER OF OBSERVATIONS FOR EVENT =  14
 83 85 914 12 9 52.11 65N38.01  16W51.86   3.61   7.11   4.08   3.61
* NUMBER OF OBSERVATIONS FOR EVENT =  18
 84 85 915  052 24.33 65N40.34  16W49.60   3.89   6.87   8.74   3.89
* NUMBER OF OBSERVATIONS FOR EVENT =  15
 85 85 915 2150 50.13 65N38.71  16W50.98   3.06   6.89   5.53   3.06
* NUMBER OF OBSERVATIONS FOR EVENT =  13
 86 85 916 1447 12.14 65N38.78  16W50.97   2.28   6.93   5.65   2.28
* NUMBER OF OBSERVATIONS FOR EVENT =  15
 87 85 919  631 23.07 65N38.71  16W50.64   2.75   6.65   5.61   2.75
* NUMBER OF OBSERVATIONS FOR EVENT =  10
 88 85 920  717 55.41 65N37.95  16W51.56   2.94   6.85   4.05   2.94
* NUMBER OF OBSERVATIONS FOR EVENT =  16
 89 85 921 1853 55.81 65N42.58  16W48.01   2.58   7.07  13.07   2.58
* NUMBER OF OBSERVATIONS FOR EVENT =  13
 90 85 922 1118 17.01 65N42.54  16W48.28   1.94   7.25  12.93   1.94
* NUMBER OF OBSERVATIONS FOR EVENT =  11
 91 85 923  423 58.59 65N38.17  16W51.80   3.05   7.16   4.37   3.05
* NUMBER OF OBSERVATIONS FOR EVENT =  25
 92 85 923  727 39.46 65N38.06  16W51.54   3.25   6.91   4.25   3.25
* NUMBER OF OBSERVATIONS FOR EVENT =  17
 93 85 923 12 4 53.32 65N42.81  16W47.71   2.77   6.99  13.55   2.77
* NUMBER OF OBSERVATIONS FOR EVENT =  25
 94 85 924  3 8 14.49 65N42.79  16W48.06   2.77   7.24  13.43   2.77
```

```
* NUMBER OF OBSERVATIONS FOR EVENT =   12
 95 85 924  432 25.08 65N38.00  16W51.72   3.38   7.00   4.09   3.38
* NUMBER OF OBSERVATIONS FOR EVENT =   16
 96 85 924 15 3 39.79 65N42.65  16W47.65   2.40   6.85  13.28   2.40
* NUMBER OF OBSERVATIONS FOR EVENT =   11
 97 85 925  211 32.74 65N37.97  16W51.68   3.35   6.95   4.05   3.35
* NUMBER OF OBSERVATIONS FOR EVENT =   15
 98 85 925  3 6 31.73 65N38.03  16W51.77   3.10   7.06   4.13   3.10
* NUMBER OF OBSERVATIONS FOR EVENT =   17
 99 85 925 2213 38.79 65N39.58  16W50.48   3.46   7.05   7.18   3.46
* NUMBER OF OBSERVATIONS FOR EVENT =   12
100 85 926  627 50.32 65N38.82  16W50.87   2.52   6.88   5.75   2.52
* NUMBER OF OBSERVATIONS FOR EVENT =   11
101 85 928  246 23.14 65N39.66  16W50.25   3.18   6.94   7.38   3.18
* NUMBER OF OBSERVATIONS FOR EVENT =   10
102 85 928 10 7  7.66 65N38.56  16W51.09   2.84   6.88   5.24   2.84
* NUMBER OF OBSERVATIONS FOR EVENT =   13
103 85 929  5 8 42.91 65N37.91  16W51.75   3.33   6.97   3.93   3.33
* NUMBER OF OBSERVATIONS FOR EVENT =   16
104 85 929 1050 35.35 65N38.46  16W51.29   2.50   6.97   5.01   2.50
* NUMBER OF OBSERVATIONS FOR EVENT =   11
105 85 929 2340 40.72 65N39.11  16W50.71   2.66   6.94   6.30   2.66
* NUMBER OF OBSERVATIONS FOR EVENT =   18
LAST EARTHQUAKE - REMAINING EVENTS ARE SHOTS
106 85 814 1212  6.99 65N43.02  16W45.51   0.01   5.53  14.47   0.01
* NUMBER OF OBSERVATIONS FOR EVENT =   27
107 85 814 1639  6.63 65N46.53  16W39.92   0.01   3.60  22.03   0.01
* NUMBER OF OBSERVATIONS FOR EVENT =   22
108 85 814 2145  7.33 65N38.50  16W52.44   0.01   7.83   4.79   0.01
* NUMBER OF OBSERVATIONS FOR EVENT =   22
109 85 815 1215  7.09 65N39.50  17W 3.07   0.01  16.15   3.89   0.01
* NUMBER OF OBSERVATIONS FOR EVENT =   22
110 85 815 1645  6.91 65N44.22  16W57.30   0.01  14.80  13.63   0.01
* NUMBER OF OBSERVATIONS FOR EVENT =   18
111 85 815 19 0  7.12 65N36.35  16W53.90   0.01   7.59   0.65   0.01
* NUMBER OF OBSERVATIONS FOR EVENT =   20
```

B.2 Output

- Relocated hypocentres of earthquakes used in the inversion.
- Final 3–d velocity model.
- Observation Matrix.
- Derivative Weight Sum (DWS) matrix.
- Node index map.
- Diagonal resolution values and standard errors for parameter values.
- Iteration summary.
- Inversion summary.

1 FINAL HYPOCENTERS

OYRMODY	HRMN	SEC	LATITUDE	LONGITUDE	DEPTH
85 7 2	1152	33.92	65 42.81	16 47.71	1.69
85 7 3	1435	54.50	65 42.89	16 48.00	1.75
85 7 4	852	54.02	65 42.83	16 47.79	1.76
85 7 9	1954	15.10	65 38.16	16 51.58	2.58
85 710	936	6.15	65 39.57	16 50.75	1.63
85 710	1214	0.62	65 38.47	16 51.20	2.49
85 711	449	8.33	65 38.09	16 51.74	2.43
85 711	558	55.92	65 38.85	16 51.03	1.89
85 712	2231	53.64	65 38.84	16 51.07	1.61
85 716	226	39.37	65 43.07	16 48.16	1.31
85 716	758	53.22	65 42.85	16 47.74	1.80
85 716	1010	9.66	65 38.81	16 51.08	1.43
85 717	1734	55.41	65 38.92	16 50.95	1.83
85 719	540	57.76	65 39.77	16 50.49	2.55
85 719	746	39.94	65 38.47	16 51.33	1.89
85 720	432	12.89	65 38.03	16 51.79	2.19
85 721	038	4.52	65 38.09	16 51.64	2.41
85 722	2133	43.11	65 39.80	16 50.55	2.23
85 724	1612	28.70	65 38.16	16 51.65	2.54
85 724	1615	39.38	65 38.16	16 51.64	2.39
85 726	556	22.87	65 42.73	16 48.05	1.38
85 728	911	55.24	65 39.02	16 50.90	1.92
85 728	1847	39.42	65 37.99	16 51.79	2.62
85 729	11 8	37.18	65 43.46	16 47.95	1.33
85 730	15 8	37.15	65 42.71	16 47.84	1.55
85 730	1752	12.47	65 38.18	16 51.54	2.08
85 730	1848	53.93	65 38.16	16 51.69	2.55
85 731	620	45.55	65 38.97	16 50.92	2.17
85 731	822	1.34	65 38.16	16 51.71	2.59
85 8 1	854	41.08	65 38.04	16 51.77	2.56
85 8 1	1218	1.37	65 42.77	16 48.06	1.66
85 8 1	1227	47.47	65 42.79	16 48.03	1.77
85 8 1	1256	24.45	65 39.29	16 50.71	1.99
85 8 2	055	21.54	65 43.02	16 50.36	1.34
85 8 3	948	56.69	65 39.31	16 50.75	1.84
85 8 3	1837	13.26	65 38.08	16 51.67	2.54
85 8 3	2325	51.34	65 39.22	16 50.75	1.94
85 8 4	2131	59.99	65 42.81	16 47.54	1.95
85 8 6	843	8.66	65 39.61	16 50.52	2.34
85 8 6	1548	55.21	65 38.14	16 51.56	2.00
85 8 6	1614	14.71	65 42.88	16 48.05	1.64
85 8 7	1833	10.95	65 42.78	16 47.92	2.07
85 815	14 4	48.00	65 42.93	16 47.69	1.90
85 815	1514	30.13	65 38.81	16 51.11	1.78
85 819	0 4	20.96	65 38.16	16 51.62	2.33
85 822	1640	27.35	65 42.74	16 48.07	1.34
85 823	1045	37.18	65 38.15	16 51.64	2.53
85 823	13 1	40.36	65 39.55	16 49.84	1.91
85 824	1059	7.66	65 37.97	16 51.61	2.53
85 824	1123	39.09	65 38.13	16 51.64	2.64
85 824	1525	39.97	65 42.74	16 47.69	1.70
85 824	1746	32.77	65 39.70	16 50.48	2.15
85 826	539	45.54	65 38.12	16 51.78	2.60
85 827	1721	48.70	65 38.14	16 51.66	2.64
85 828	120	54.22	65 38.15	16 51.62	2.52
85 830	325	51.82	65 42.79	16 47.66	1.86
85 831	023	18.41	65 38.37	16 51.34	2.39
85 831	029	13.82	65 39.71	16 50.43	2.86
85 831	1137	20.71	65 38.65	16 51.44	2.65
85 831	1349	52.35	65 38.14	16 51.68	2.56
85 9 2	145	29.78	65 38.12	16 51.72	2.62
85 9 2	6 4	44.31	65 42.82	16 47.78	1.80
85 9 2	2149	19.70	65 38.10	16 51.71	2.65
85 9 3	4 4	34.32	65 42.82	16 47.48	1.73
85 9 3	1012	11.75	65 42.87	16 48.03	1.60
85 9 3	1220	3.62	65 42.40	16 45.66	1.65
85 9 4	724	2.70	65 42.67	16 47.97	1.64
85 9 5	0 1	7.27	65 38.19	16 51.67	2.51
85 9 7	050	22.00	65 43.47	16 47.89	1.33
85 9 8	042	36.16	65 39.44	16 50.76	2.14
85 9 8	921	26.24	65 38.14	16 51.62	2.55
85 9 8	1045	39.95	65 38.16	16 51.60	2.63
85 9 8	1716	13.25	65 39.18	16 50.96	1.34
85 9 9	2231	56.69	65 38.40	16 51.34	2.06
85 910	1343	24.92	65 38.14	16 51.69	2.45
85 910	1459	21.84	65 38.77	16 51.09	1.80
85 910	15 4	25.89	65 38.77	16 51.13	1.79
85 911	120	27.74	65 39.89	16 50.51	1.79
85 911	659	53.97	65 38.20	16 51.47	2.21
85 911	23 1	8.80	65 42.41	16 45.60	1.65
85 912	256	13.11	65 39.26	16 50.66	2.14
85 913	2117	58.47	65 42.43	16 45.99	1.66
85 914	12 9	52.18	65 38.05	16 51.78	2.47
85 915	052	24.40	65 40.36	16 49.87	3.14
85 915	2150	50.19	65 38.80	16 51.13	2.16
85 916	1447	12.18	65 38.83	16 51.09	1.48
85 919	631	23.13	65 38.79	16 51.00	1.61
85 920	717	55.44	65 38.01	16 51.60	2.20
85 921	1853	55.86	65 42.65	16 47.98	1.68
85 922	1118	17.04	65 42.64	16 48.22	1.21
85 923	423	58.62	65 38.12	16 51.69	2.38
85 923	727	39.51	65 38.14	16 51.62	2.32
85 923	12 4	53.38	65 42.80	16 47.67	1.85
85 924	3 8	14.55	65 42.82	16 48.05	1.78
85 924	432	25.12	65 38.08	16 51.74	2.50
85 924	15 3	39.82	65 42.74	16 47.81	1.70
85 925	211	32.79	65 38.06	16 51.70	2.50
85 925	3 6	31.77	65 38.09	16 51.80	2.31
85 925	2213	38.84	65 39.62	16 50.62	2.45
85 926	627	50.36	65 38.89	16 51.11	1.53
85 928	246	23.22	65 39.71	16 50.35	2.01
85 928	10 7	7.70	65 38.62	16 51.18	2.02
85 929	5 8	42.95	65 38.01	16 51.75	2.52
85 929	1050	35.37	65 38.56	16 51.30	1.97
85 929	2340	40.78	65 39.11	16 50.89	1.74

1 FINAL MODEL

SUM OF SQUARED RESIDUALS = 1.287; TOTAL NUMBER OF OBSERVATIONS = 1771

RMS RESIDUAL = 0.02695

FINAL VELOCITY MODEL

LAYER 1

3.00	3.00	3.00	3.00	3.00	3.00	3.00	3.00	3.00
3.00	3.00	3.00	3.00	3.00	3.00	3.00	3.00	3.00
3.00	3.00	3.00	3.00	3.00	3.00	3.00	3.00	3.00
3.00	3.00	3.00	3.00	3.00	3.00	3.00	3.00	3.00
3.00	3.00	3.00	3.00	3.00	3.00	3.00	3.00	3.00
3.00	3.00	3.00	3.00	3.00	3.00	3.00	3.00	3.00

3.00	3.00	3.00	3.00	3.00	3.00	3.00	3.00	3.00
3.00	3.00	3.00	3.00	3.00	3.00	3.00	3.00	3.00
3.00	3.00	3.00	3.00	3.00	3.00	3.00	3.00	3.00
3.00	3.00	3.00	3.00	3.00	3.00	3.00	3.00	3.00
3.00	3.00	3.00	3.00	3.00	3.00	3.00	3.00	3.00
3.00	3.00	3.00	3.00	3.00	3.00	3.00	3.00	3.00

LAYER 2

3.60	3.60	3.60	3.60	3.60	3.60	3.60	3.60	3.60
3.60	3.60	3.60	3.20	4.72	3.75	4.34	3.60	3.60
3.60	3.60	4.37	2.77	4.35	3.75	3.36	3.60	3.60
3.60	3.58	3.59	4.03	2.83	2.86	3.28	4.31	3.60
3.60	3.60	3.43	3.39	2.78	3.41	3.10	3.33	3.60
3.60	3.60	4.36	4.00	3.04	3.74	3.95	3.53	3.60
3.60	2.79	4.79	3.45	4.04	3.91	3.68	3.60	3.60
3.60	3.77	4.09	3.82	3.43	3.32	2.77	3.37	3.60
3.60	3.60	3.62	2.85	3.85	2.48	5.21	2.47	3.60
3.60	3.60	2.92	4.04	2.91	3.25	3.21	4.11	3.60
3.60	3.60	4.17	3.60	3.60	3.60	3.60	3.60	3.60
3.60	3.60	3.60	3.60	3.60	3.60	3.60	3.60	3.60

LAYER 3

4.65	4.65	4.65	4.65	4.65	4.65	4.65	4.65	4.65
4.65	4.65	4.65	4.65	7.05	5.98	4.08	4.65	4.65
4.65	4.65	3.96	4.00	5.35	3.96	2.95	4.65	4.65
4.65	4.63	3.90	4.58	4.37	4.60	4.76	5.41	4.65
4.65	4.61	3.70	5.45	4.39	4.32	3.41	5.48	4.65
4.65	4.65	4.63	4.60	4.58	3.16	3.90	4.31	4.65
4.65	4.01	4.70	5.02	5.47	4.62	4.10	4.65	4.65
4.65	5.39	6.05	4.43	4.69	5.46	6.71	2.38	4.65
4.65	4.65	5.92	3.51	4.41	3.47	6.88	2.70	4.65
4.65	4.65	4.18	6.22	6.41	4.47	6.35	4.65	4.65
4.65	4.65	5.77	4.43	4.65	4.65	4.65	4.65	4.65
4.65	4.65	4.65	4.65	4.65	4.65	4.65	4.65	4.65

LAYER 4

5.60	5.60	5.60	5.60	5.60	5.60	5.60	5.60	5.60
5.60	5.60	5.60	5.60	5.60	5.30	5.60	5.60	5.60
5.60	5.60	5.55	7.23	5.08	5.70	3.91	5.60	5.60
5.60	5.60	4.86	6.13	3.94	6.87	4.58	5.60	5.60
5.60	5.51	5.70	4.53	5.77	4.76	4.95	6.76	5.60
5.60	5.60	6.13	5.56	4.93	5.55	5.25	5.52	5.60
5.60	5.32	5.82	4.58	5.98	4.78	6.07	5.30	5.60
5.60	5.80	5.46	5.28	5.47	5.93	5.30	4.40	5.60
5.60	5.60	7.83	4.74	4.87	5.25	6.28	5.24	5.60
5.60	5.60	8.00	7.40	5.47	4.54	5.49	5.60	5.60
5.60	5.60	5.60	5.60	5.60	5.60	5.60	5.60	5.60
5.60	5.60	5.60	5.60	5.60	5.60	5.60	5.60	5.60

LAYER 5

5.75	5.75	5.75	5.75	5.75	5.75	5.75	5.75	5.75
5.75	5.75	5.75	5.75	5.75	5.75	5.75	5.75	5.75
5.75	5.75	5.75	5.75	5.87	4.85	4.95	5.75	5.75
5.75	5.75	5.82	5.74	5.08	4.96	5.07	5.75	5.75
5.75	5.75	6.14	4.88	5.46	7.91	5.45	5.75	5.75
5.75	5.71	7.01	6.89	6.63	4.80	5.24	5.75	5.75
5.75	5.75	6.49	6.02	5.14	5.30	4.79	5.75	5.75
5.75	5.75	6.31	5.62	5.14	5.82	5.90	5.75	5.75
5.75	5.75	6.98	6.98	7.38	6.07	5.91	5.75	5.75
5.75	5.75	5.75	6.07	5.75	5.75	5.75	5.75	5.75
5.75	5.75	5.75	5.75	5.75	5.75	5.75	5.75	5.75
5.75	5.75	5.75	5.75	5.75	5.75	5.75	5.75	5.75

LAYER 6

6.80	6.80	6.80	6.80	6.80	6.80	6.80	6.80	6.80
6.80	6.80	6.80	6.80	6.80	6.80	6.80	6.80	6.80
6.80	6.80	6.80	6.80	6.80	6.80	6.80	6.80	6.80
6.80	6.80	6.80	6.68	7.35	5.97	6.80	6.80	6.80
6.80	6.80	6.83	5.72	9.15	6.02	6.40	6.80	6.80
6.80	6.80	7.54	5.83	5.96	7.00	5.74	6.80	6.80
6.80	6.80	8.55	6.52	6.29	5.89	5.95	6.80	6.80
6.80	6.80	7.11	7.52	7.91	6.66	6.31	6.80	6.80
6.80	6.80	6.80	7.74	6.31	6.63	6.80	6.80	6.80
6.80	6.80	6.80	6.80	6.80	6.80	6.80	6.80	6.80
6.80	6.80	6.80	6.80	6.80	6.80	6.80	6.80	6.80
6.80	6.80	6.80	6.80	6.80	6.80	6.80	6.80	6.80

LAYER 7

7.00	7.00	7.00	7.00	7.00	7.00	7.00	7.00	7.00
7.00	7.00	7.00	7.00	7.00	7.00	7.00	7.00	7.00
7.00	7.00	7.00	7.00	7.00	7.00	7.00	7.00	7.00
7.00	7.00	7.00	7.00	7.00	7.00	7.00	7.00	7.00
7.00	7.00	7.00	7.00	7.00	7.00	7.00	7.00	7.00
7.00	7.00	7.00	7.00	7.00	7.00	7.00	7.00	7.00
7.00	7.00	7.00	7.00	7.00	7.00	7.00	7.00	7.00
7.00	7.00	7.00	7.00	7.00	7.00	7.00	7.00	7.00
7.00	7.00	7.00	7.00	7.00	7.00	7.00	7.00	7.00
7.00	7.00	7.00	7.00	7.00	7.00	7.00	7.00	7.00
7.00	7.00	7.00	7.00	7.00	7.00	7.00	7.00	7.00
7.00	7.00	7.00	7.00	7.00	7.00	7.00	7.00	7.00

1 OBSERVATION MATRIX

LAYER 2

0	0	0	747	951	852	515	1	0
0	0	771	887	1010	1053	982	4	0
0	0	1042	1083	1041	1034	979	488	0
0	0	1199	1197	1122	986	800	803	0
0	0	1092	1149	1209	1128	1076	170	0
0	640	1137	1195	1026	1128	1123	4	0
0	640	999	561	744	1159	1159	497	0
0	0	1	581	768	741	633	646	0
0	0	373	452	399	249	608	608	0
0	0	394	394	1	2	0	0	0

LAYER 3

0	0	0	1	742	645	482	1	0
0	0	705	889	944	1020	518	7	0
0	0	1040	1081	1023	1037	651	435	0
0	0	1181	1203	1068	1015	797	811	0
0	0	974	1204	1128	1142	182	171	0
0	485	982	971	1124	1141	888	4	0
0	640	774	532	746	1130	948	325	0
0	2	181	438	559	447	661	177	0
0	0	355	421	387	259	205	1	0
0	0	41	291	2	1	0	0	0

LAYER 4

0	0	0	0	1	11	2	1	0
0	0	41	567	791	763	92	4	0
0	0	55	850	1004	989	510	22	0

0	0	167	1078	1037	1032	639	641	0
0	0	932	1050	1134	986	727	177	0
0	344	876	998	1088	995	786	23	0
0	21	290	339	721	848	746	9	0
0	1	237	418	392	392	301	6	0
0	1	175	384	349	49	2	0	0
0	0	18	18	4	2	1	0	0

LAYER 5

0	0	0	0	0	1	2	1	0
0	0	0	1	77	3	2	3	0
0	0	2	492	776	799	354	5	0
0	0	18	639	937	893	607	13	0
0	0	631	861	951	867	372	7	0
0	0	331	548	676	651	232	10	0
0	0	70	349	342	213	20	6	0
0	0	91	271	238	64	1	5	0
0	0	8	89	14	3	1	0	0
0	0	7	9	4	2	0	0	0

LAYER 6

0	0	0	0	0	0	0	0	0
0	0	0	0	1	1	1	1	0
0	0	0	1	185	68	2	1	0
0	0	1	123	224	128	3	2	0
0	0	2	130	223	129	5	3	0
0	0	2	119	211	119	7	5	0
0	0	2	110	190	105	4	5	0
0	0	2	90	68	1	0	0	0
0	0	3	5	2	1	0	0	0
0	0	2	5	1	0	0	0	0

1 DERIVATIVE WEIGHT SUM

LAYER 2

0.00	0.00	0.00	13.85	87.82	69.31	47.07	0.28	0.00
0.00	0.00	101.04	191.23	226.56	198.59	55.03	1.69	0.00
0.00	0.00	274.38	231.48	167.85	180.65	8.87	51.93	0.00
0.00	0.00	359.54	399.56	215.79	145.59	51.04	102.18	0.00
0.00	0.00	101.76	280.18	202.62	252.62	43.09	12.95	0.00
0.00	37.68	262.22	77.02	233.91	268.02	65.43	12.76	0.00
0.00	74.26	96.30	27.06	159.51	263.49	254.54	68.86	0.00
0.00	0.00	0.11	80.82	166.70	48.54	163.89	109.41	0.00
0.00	0.00	42.61	98.79	81.97	36.34	24.67	9.02	0.00
0.00	0.00	51.60	32.75	1.02	0.53	0.00	0.00	0.00

LAYER 3

0.00	0.00	0.00	0.13	23.84	20.75	9.40	0.41	0.00
0.00	0.00	22.18	159.09	314.35	254.65	34.89	9.90	0.00
0.00	0.00	81.34	524.31	557.80	282.29	28.96	91.79	0.00
0.00	0.00	134.08	749.22	802.25	195.90	95.98	92.40	0.00
0.00	0.00	105.48	298.36	352.09	118.53	39.28	25.07	0.00
0.00	32.83	232.91	141.05	231.00	348.80	115.75	5.62	0.00
0.00	26.87	105.56	127.11	422.67	306.92	280.75	27.20	0.00
0.00	0.90	15.22	83.68	375.02	116.49	171.23	25.48	0.00
0.00	0.00	21.79	101.60	76.01	18.86	10.51	1.95	0.00
0.00	0.00	82.97	61.30	6.87	0.12	0.00	0.00	0.00

LAYER 4

0.00	0.00	0.00	0.00	0.33	2.71	3.77	1.06	0.00
0.00	0.00	0.79	29.30	100.49	90.55	7.47	12.78	0.00
0.00	0.00	5.41	283.14	1367.14	311.23	33.19	31.21	0.00
0.00	0.00	21.17	293.79	1300.23	278.62	136.85	64.23	0.00
0.00	0.00	178.34	443.29	653.00	410.80	94.29	33.71	0.00
0.00	4.10	174.35	246.15	358.02	388.52	211.51	18.70	0.00
0.00	0.05	42.10	213.59	567.77	268.42	81.80	20.15	0.00
0.00	0.53	36.81	131.32	493.30	210.82	37.72	11.01	0.00
0.00	0.05	34.34	69.34	25.82	8.18	2.52	0.00	0.00
0.00	0.00	59.08	47.67	11.20	3.98	0.34	0.00	0.00

LAYER 5

0.00	0.00	0.00	0.00	0.00	0.18	1.29	0.70	0.00
0.00	0.00	0.80	1.37	3.34	1.07	2.94	4.63	0.00
0.00	0.00	0.43	25.23	520.26	80.85	8.29	3.75	0.00
0.00	0.00	5.24	188.34	680.78	356.00	41.04	6.96	0.00
0.00	0.00	34.80	197.87	299.25	258.02	16.66	11.96	0.00
0.00	0.00	14.31	64.35	89.32	60.95	8.76	8.76	0.00
0.00	0.00	7.59	36.19	65.66	18.50	6.44	22.95	0.00
0.00	0.00	11.11	19.40	16.99	2.44	1.00	2.59	0.00
0.00	0.00	8.45	6.50	2.89	2.84	0.14	0.00	0.00
0.00	0.00	11.40	16.25	9.70	2.81	0.00	0.00	0.00

LAYER 6

0.00	0.00	0.00	0.00	0.00	0.00	0.00	0.00	0.00
0.00	0.00	0.00	0.00	1.42	2.79	2.09	0.50	0.00
0.00	0.00	0.00	0.12	7.65	2.87	3.60	1.00	0.00
0.00	0.00	0.13	4.00	52.16	10.81	6.78	0.80	0.00
0.00	0.00	3.45	12.67	58.29	26.38	12.34	6.41	0.00
0.00	0.00	9.65	21.95	49.15	18.02	13.09	13.25	0.00
0.00	0.00	10.80	22.61	20.06	11.49	4.60	4.35	0.00
0.00	0.00	10.27	12.87	7.81	3.90	0.00	0.00	0.00
0.00	0.00	8.04	10.18	7.13	0.55	0.00	0.00	0.00
0.00	0.00	1.79	3.00	1.79	0.00	0.00	0.00	0.00

1 NODE INDEX MAP

LAYER 2

0	1	2	3	4	5	6	7	0
0	8	9	10	11	12	13	14	0
0	15	16	17	18	19	20	21	0
0	22	23	24	25	26	27	28	0
0	29	30	31	32	33	34	35	0
0	36	37	38	39	40	41	42	0
0	43	44	45	46	47	48	49	0
0	50	51	52	53	54	55	56	0
0	57	58	59	60	61	62	63	0
0	64	65	66	67	68	69	70	0

LAYER 3

0	71	72	73	74	75	76	77	0
0	78	79	80	81	82	83	84	0
0	85	86	87	88	89	90	91	0
0	92	93	94	95	96	97	98	0
0	99	100	101	102	103	104	105	0
0	106	107	108	109	110	111	112	0
0	113	114	115	116	117	118	119	0
0	120	121	122	123	124	125	126	0
0	127	128	129	130	131	132	133	0
0	134	135	136	137	138	139	140	0

LAYER 4

0	141	142	143	144	145	146	147	0
0	148	149	150	151	152	153	154	0
0	155	156	157	158	159	160	161	0
0	162	163	164	165	166	167	168	0
0	169	170	171	172	173	174	175	0
0	176	177	178	179	180	181	182	0
0	183	184	185	186	187	188	189	0

```
     0    190    191    192    193    194    195    196      0
     0    197    198    199    200    201    202    203      0
     0    204    205    206    207    208    209    210      0
LAYER  5
     0    211    212    213    214    215    216    217      0
     0    218    219    220    221    222    223    224      0
     0    225    226    227    228    229    230    231      0
     0    232    233    234    235    236    237    238      0
     0    239    240    241    242    243    244    245      0
     0    246    247    248    249    250    251    252      0
     0    253    254    255    256    257    258    259      0
     0    260    261    262    263    264    265    266      0
     0    267    268    269    270    271    272    273      0
     0    274    275    276    277    278    279    280      0
LAYER  6
     0    281    282    283    284    285    286    287      0
     0    288    289    290    291    292    293    294      0
     0    295    296    297    298    299    300    301      0
     0    302    303    304    305    306    307    308      0
     0    309    310    311    312    313    314    315      0
     0    316    317    318    319    320    321    322      0
     0    323    324    325    326    327    328    329      0
     0    330    331    332    333    334    335    336      0
     0    337    338    339    340    341    342    343      0
     0    344    345    346    347    348    349    350      0
1 RESOLUTION AND ERROR CALCULATIONS

 NODE NUMBER   3: RESOLUTION:  0.0651  ERROR (%):  0.0140
 NODE NUMBER   4: RESOLUTION:  0.3588  ERROR (%):  0.0291
 NODE NUMBER   5: RESOLUTION:  0.3403  ERROR (%):  0.0303
 NODE NUMBER   6: RESOLUTION:  0.3083  ERROR (%):  0.0233
 NODE NUMBER   9: RESOLUTION:  0.5966  ERROR (%):  0.0265
 NODE NUMBER  10: RESOLUTION:  0.4997  ERROR (%):  0.0285
 NODE NUMBER  11: RESOLUTION:  0.7225  ERROR (%):  0.0272
 NODE NUMBER  12: RESOLUTION:  0.5935  ERROR (%):  0.0297
 NODE NUMBER  13: RESOLUTION:  0.2461  ERROR (%):  0.0224
 NODE NUMBER  16: RESOLUTION:  0.8159  ERROR (%):  0.0209
 NODE NUMBER  17: RESOLUTION:  0.6348  ERROR (%):  0.0303
 NODE NUMBER  18: RESOLUTION:  0.6988  ERROR (%):  0.0266
 NODE NUMBER  19: RESOLUTION:  0.5595  ERROR (%):  0.0297
 NODE NUMBER  20: RESOLUTION:  0.0420  ERROR (%):  0.0129
 NODE NUMBER  21: RESOLUTION:  0.5956  ERROR (%):  0.0285
 NODE NUMBER  23: RESOLUTION:  0.8649  ERROR (%):  0.0186
 NODE NUMBER  24: RESOLUTION:  0.7378  ERROR (%):  0.0257
 NODE NUMBER  25: RESOLUTION:  0.7606  ERROR (%):  0.0272
 NODE NUMBER  26: RESOLUTION:  0.6610  ERROR (%):  0.0298
 NODE NUMBER  27: RESOLUTION:  0.0950  ERROR (%):  0.0133
 NODE NUMBER  28: RESOLUTION:  0.4834  ERROR (%):  0.0233
 NODE NUMBER  30: RESOLUTION:  0.3394  ERROR (%):  0.0252
 NODE NUMBER  31: RESOLUTION:  0.7148  ERROR (%):  0.0238
 NODE NUMBER  32: RESOLUTION:  0.6485  ERROR (%):  0.0286
 NODE NUMBER  33: RESOLUTION:  0.8574  ERROR (%):  0.0201
 NODE NUMBER  34: RESOLUTION:  0.2301  ERROR (%):  0.0245
 NODE NUMBER  35: RESOLUTION:  0.0110  ERROR (%):  0.0054
 NODE NUMBER  36: RESOLUTION:  0.0731  ERROR (%):  0.0118
 NODE NUMBER  37: RESOLUTION:  0.7767  ERROR (%):  0.0227
 NODE NUMBER  38: RESOLUTION:  0.2605  ERROR (%):  0.0255
 NODE NUMBER  39: RESOLUTION:  0.8164  ERROR (%):  0.0232
 NODE NUMBER  40: RESOLUTION:  0.7591  ERROR (%):  0.0261
 NODE NUMBER  41: RESOLUTION:  0.4785  ERROR (%):  0.0300
 NODE NUMBER  43: RESOLUTION:  0.3674  ERROR (%):  0.0236
 NODE NUMBER  44: RESOLUTION:  0.3854  ERROR (%):  0.0273
 NODE NUMBER  45: RESOLUTION:  0.3183  ERROR (%):  0.0263
 NODE NUMBER  46: RESOLUTION:  0.5016  ERROR (%):  0.0295
 NODE NUMBER  47: RESOLUTION:  0.6365  ERROR (%):  0.0263
 NODE NUMBER  48: RESOLUTION:  0.7512  ERROR (%):  0.0252
 NODE NUMBER  49: RESOLUTION:  0.7830  ERROR (%):  0.0237
 NODE NUMBER  52: RESOLUTION:  0.5082  ERROR (%):  0.0275
 NODE NUMBER  53: RESOLUTION:  0.7017  ERROR (%):  0.0280
 NODE NUMBER  54: RESOLUTION:  0.2473  ERROR (%):  0.0270
 NODE NUMBER  55: RESOLUTION:  0.5860  ERROR (%):  0.0217
 NODE NUMBER  56: RESOLUTION:  0.8019  ERROR (%):  0.0260
 NODE NUMBER  58: RESOLUTION:  0.1597  ERROR (%):  0.0190
 NODE NUMBER  59: RESOLUTION:  0.6838  ERROR (%):  0.0295
 NODE NUMBER  60: RESOLUTION:  0.5433  ERROR (%):  0.0305
 NODE NUMBER  61: RESOLUTION:  0.5235  ERROR (%):  0.0294
 NODE NUMBER  62: RESOLUTION:  0.0847  ERROR (%):  0.0180
 NODE NUMBER  63: RESOLUTION:  0.0446  ERROR (%):  0.0120
 NODE NUMBER  65: RESOLUTION:  0.6903  ERROR (%):  0.0257
 NODE NUMBER  66: RESOLUTION:  0.1460  ERROR (%):  0.0127
 NODE NUMBER  74: RESOLUTION:  0.1133  ERROR (%):  0.0186
 NODE NUMBER  75: RESOLUTION:  0.1793  ERROR (%):  0.0255
 NODE NUMBER  76: RESOLUTION:  0.0397  ERROR (%):  0.0118
 NODE NUMBER  79: RESOLUTION:  0.0965  ERROR (%):  0.0159
 NODE NUMBER  80: RESOLUTION:  0.5087  ERROR (%):  0.0294
 NODE NUMBER  81: RESOLUTION:  0.7394  ERROR (%):  0.0241
 NODE NUMBER  82: RESOLUTION:  0.5903  ERROR (%):  0.0288
 NODE NUMBER  83: RESOLUTION:  0.1640  ERROR (%):  0.0209
 NODE NUMBER  86: RESOLUTION:  0.2106  ERROR (%):  0.0220
 NODE NUMBER  87: RESOLUTION:  0.7316  ERROR (%):  0.0253
 NODE NUMBER  88: RESOLUTION:  0.7887  ERROR (%):  0.0250
 NODE NUMBER  89: RESOLUTION:  0.7342  ERROR (%):  0.0267
 NODE NUMBER  90: RESOLUTION:  0.5391  ERROR (%):  0.0315
 NODE NUMBER  91: RESOLUTION:  0.7810  ERROR (%):  0.0236
 NODE NUMBER  93: RESOLUTION:  0.2940  ERROR (%):  0.0260
 NODE NUMBER  94: RESOLUTION:  0.8439  ERROR (%):  0.0204
 NODE NUMBER  95: RESOLUTION:  0.8318  ERROR (%):  0.0248
 NODE NUMBER  96: RESOLUTION:  0.7056  ERROR (%):  0.0286
 NODE NUMBER  97: RESOLUTION:  0.3039  ERROR (%):  0.0254
 NODE NUMBER  98: RESOLUTION:  0.4326  ERROR (%):  0.0262
 NODE NUMBER 100: RESOLUTION:  0.5024  ERROR (%):  0.0294
 NODE NUMBER 101: RESOLUTION:  0.7600  ERROR (%):  0.0261
 NODE NUMBER 102: RESOLUTION:  0.7942  ERROR (%):  0.0261
 NODE NUMBER 103: RESOLUTION:  0.3362  ERROR (%):  0.0312
 NODE NUMBER 104: RESOLUTION:  0.2276  ERROR (%):  0.0241
 NODE NUMBER 105: RESOLUTION:  0.3291  ERROR (%):  0.0269
 NODE NUMBER 106: RESOLUTION:  0.0978  ERROR (%):  0.0154
 NODE NUMBER 107: RESOLUTION:  0.4894  ERROR (%):  0.0299
 NODE NUMBER 108: RESOLUTION:  0.7396  ERROR (%):  0.0253
 NODE NUMBER 109: RESOLUTION:  0.7232  ERROR (%):  0.0275
 NODE NUMBER 110: RESOLUTION:  0.7426  ERROR (%):  0.0262
 NODE NUMBER 111: RESOLUTION:  0.3486  ERROR (%):  0.0294
 NODE NUMBER 113: RESOLUTION:  0.0909  ERROR (%):  0.0150
 NODE NUMBER 114: RESOLUTION:  0.4625  ERROR (%):  0.0271
 NODE NUMBER 115: RESOLUTION:  0.6614  ERROR (%):  0.0304
 NODE NUMBER 116: RESOLUTION:  0.7732  ERROR (%):  0.0254
 NODE NUMBER 117: RESOLUTION:  0.6944  ERROR (%):  0.0268
 NODE NUMBER 118: RESOLUTION:  0.7309  ERROR (%):  0.0264
 NODE NUMBER 119: RESOLUTION:  0.4686  ERROR (%):  0.0263
 NODE NUMBER 121: RESOLUTION:  0.2902  ERROR (%):  0.0293
```

NODE NUMBER 122: RESOLUTION: 0.3616 ERROR (%): 0.0264
NODE NUMBER 123: RESOLUTION: 0.6483 ERROR (%): 0.0302
NODE NUMBER 124: RESOLUTION: 0.2584 ERROR (%): 0.0279
NODE NUMBER 125: RESOLUTION: 0.4674 ERROR (%): 0.0243
NODE NUMBER 126: RESOLUTION: 0.5600 ERROR (%): 0.0283
NODE NUMBER 128: RESOLUTION: 0.0505 ERROR (%): 0.0123
NODE NUMBER 129: RESOLUTION: 0.4922 ERROR (%): 0.0288
NODE NUMBER 130: RESOLUTION: 0.4658 ERROR (%): 0.0314
NODE NUMBER 131: RESOLUTION: 0.1995 ERROR (%): 0.0238
NODE NUMBER 132: RESOLUTION: 0.3439 ERROR (%): 0.0303
NODE NUMBER 135: RESOLUTION: 0.6182 ERROR (%): 0.0238
NODE NUMBER 136: RESOLUTION: 0.6794 ERROR (%): 0.0273
NODE NUMBER 149: RESOLUTION: 0.0021 ERROR (%): 0.0030
NODE NUMBER 150: RESOLUTION: 0.2021 ERROR (%): 0.0242
NODE NUMBER 151: RESOLUTION: 0.1952 ERROR (%): 0.0238
NODE NUMBER 152: RESOLUTION: 0.4533 ERROR (%): 0.0292
NODE NUMBER 153: RESOLUTION: 0.1204 ERROR (%): 0.0217
NODE NUMBER 156: RESOLUTION: 0.1464 ERROR (%): 0.0198
NODE NUMBER 157: RESOLUTION: 0.5848 ERROR (%): 0.0309
NODE NUMBER 158: RESOLUTION: 0.3534 ERROR (%): 0.0314
NODE NUMBER 159: RESOLUTION: 0.7366 ERROR (%): 0.0260
NODE NUMBER 160: RESOLUTION: 0.1499 ERROR (%): 0.0210
NODE NUMBER 163: RESOLUTION: 0.2666 ERROR (%): 0.0201
NODE NUMBER 164: RESOLUTION: 0.4817 ERROR (%): 0.0318
NODE NUMBER 165: RESOLUTION: 0.7247 ERROR (%): 0.0282
NODE NUMBER 166: RESOLUTION: 0.4506 ERROR (%): 0.0305
NODE NUMBER 167: RESOLUTION: 0.4847 ERROR (%): 0.0249
NODE NUMBER 168: RESOLUTION: 0.5922 ERROR (%): 0.0275
NODE NUMBER 170: RESOLUTION: 0.3337 ERROR (%): 0.0271
NODE NUMBER 171: RESOLUTION: 0.6912 ERROR (%): 0.0275
NODE NUMBER 172: RESOLUTION: 0.7811 ERROR (%): 0.0259
NODE NUMBER 173: RESOLUTION: 0.6649 ERROR (%): 0.0280
NODE NUMBER 174: RESOLUTION: 0.4301 ERROR (%): 0.0289
NODE NUMBER 175: RESOLUTION: 0.3156 ERROR (%): 0.0224
NODE NUMBER 176: RESOLUTION: 0.0087 ERROR (%): 0.0058
NODE NUMBER 177: RESOLUTION: 0.5350 ERROR (%): 0.0283
NODE NUMBER 178: RESOLUTION: 0.4959 ERROR (%): 0.0286
NODE NUMBER 179: RESOLUTION: 0.7032 ERROR (%): 0.0252
NODE NUMBER 180: RESOLUTION: 0.6255 ERROR (%): 0.0291
NODE NUMBER 181: RESOLUTION: 0.6481 ERROR (%): 0.0250
NODE NUMBER 184: RESOLUTION: 0.2254 ERROR (%): 0.0232
NODE NUMBER 185: RESOLUTION: 0.6850 ERROR (%): 0.0282
NODE NUMBER 186: RESOLUTION: 0.6740 ERROR (%): 0.0276
NODE NUMBER 187: RESOLUTION: 0.7220 ERROR (%): 0.0282
NODE NUMBER 188: RESOLUTION: 0.2237 ERROR (%): 0.0247
NODE NUMBER 191: RESOLUTION: 0.3006 ERROR (%): 0.0233
NODE NUMBER 192: RESOLUTION: 0.2760 ERROR (%): 0.0254
NODE NUMBER 193: RESOLUTION: 0.4317 ERROR (%): 0.0313
NODE NUMBER 194: RESOLUTION: 0.5506 ERROR (%): 0.0309
NODE NUMBER 195: RESOLUTION: 0.1006 ERROR (%): 0.0167
NODE NUMBER 198: RESOLUTION: 0.3154 ERROR (%): 0.0243
NODE NUMBER 199: RESOLUTION: 0.3737 ERROR (%): 0.0274
NODE NUMBER 200: RESOLUTION: 0.1178 ERROR (%): 0.0200
NODE NUMBER 201: RESOLUTION: 0.1821 ERROR (%): 0.0263
NODE NUMBER 221: RESOLUTION: 0.0869 ERROR (%): 0.0186
NODE NUMBER 227: RESOLUTION: 0.1171 ERROR (%): 0.0202
NODE NUMBER 228: RESOLUTION: 0.2513 ERROR (%): 0.0262
NODE NUMBER 229: RESOLUTION: 0.3117 ERROR (%): 0.0279
NODE NUMBER 230: RESOLUTION: 0.1253 ERROR (%): 0.0222
NODE NUMBER 234: RESOLUTION: 0.4823 ERROR (%): 0.0285
NODE NUMBER 235: RESOLUTION: 0.5497 ERROR (%): 0.0298
NODE NUMBER 236: RESOLUTION: 0.7262 ERROR (%): 0.0252
NODE NUMBER 237: RESOLUTION: 0.2999 ERROR (%): 0.0279
NODE NUMBER 240: RESOLUTION: 0.2505 ERROR (%): 0.0193
NODE NUMBER 241: RESOLUTION: 0.4372 ERROR (%): 0.0277
NODE NUMBER 242: RESOLUTION: 0.5491 ERROR (%): 0.0286
NODE NUMBER 243: RESOLUTION: 0.4569 ERROR (%): 0.0299
NODE NUMBER 244: RESOLUTION: 0.1037 ERROR (%): 0.0182
NODE NUMBER 247: RESOLUTION: 0.1275 ERROR (%): 0.0191
NODE NUMBER 248: RESOLUTION: 0.3340 ERROR (%): 0.0267
NODE NUMBER 249: RESOLUTION: 0.2566 ERROR (%): 0.0257
NODE NUMBER 250: RESOLUTION: 0.2675 ERROR (%): 0.0275
NODE NUMBER 251: RESOLUTION: 0.0859 ERROR (%): 0.0164
NODE NUMBER 254: RESOLUTION: 0.1462 ERROR (%): 0.0214
NODE NUMBER 255: RESOLUTION: 0.2258 ERROR (%): 0.0225
NODE NUMBER 256: RESOLUTION: 0.3049 ERROR (%): 0.0268
NODE NUMBER 257: RESOLUTION: 0.0937 ERROR (%): 0.0193
NODE NUMBER 261: RESOLUTION: 0.1078 ERROR (%): 0.0184
NODE NUMBER 262: RESOLUTION: 0.1845 ERROR (%): 0.0226
NODE NUMBER 263: RESOLUTION: 0.0972 ERROR (%): 0.0175
NODE NUMBER 264: RESOLUTION: 0.0220 ERROR (%): 0.0099
NODE NUMBER 269: RESOLUTION: 0.0781 ERROR (%): 0.0161
NODE NUMBER 298: RESOLUTION: 0.0194 ERROR (%): 0.0080
NODE NUMBER 299: RESOLUTION: 0.0412 ERROR (%): 0.0129
NODE NUMBER 304: RESOLUTION: 0.0086 ERROR (%): 0.0056
NODE NUMBER 305: RESOLUTION: 0.3514 ERROR (%): 0.0245
NODE NUMBER 306: RESOLUTION: 0.0425 ERROR (%): 0.0121
NODE NUMBER 311: RESOLUTION: 0.0739 ERROR (%): 0.0122
NODE NUMBER 312: RESOLUTION: 0.2827 ERROR (%): 0.0206
NODE NUMBER 313: RESOLUTION: 0.3614 ERROR (%): 0.0281
NODE NUMBER 318: RESOLUTION: 0.2322 ERROR (%): 0.0203
NODE NUMBER 319: RESOLUTION: 0.2912 ERROR (%): 0.0219
NODE NUMBER 320: RESOLUTION: 0.2042 ERROR (%): 0.0230
NODE NUMBER 325: RESOLUTION: 0.2058 ERROR (%): 0.0199
NODE NUMBER 326: RESOLUTION: 0.1831 ERROR (%): 0.0211
NODE NUMBER 327: RESOLUTION: 0.2048 ERROR (%): 0.0249
NODE NUMBER 332: RESOLUTION: 0.1987 ERROR (%): 0.0231
NODE NUMBER 333: RESOLUTION: 0.1023 ERROR (%): 0.0177
1 *** SUMMARY INFO ***

'+' = Quarry blasts, '*' = Explosions

EVENT	NOBS	IT# 1 WRMS	NIT	IT# 2 WRMS	NIT	IT# 3 WRMS	NIT	IT# 4 WRMS	NIT	IT# 5 WRMS	NIT	IT# 6 WRMS	NIT	IT# 7 WRMS	NIT	WRMS RATIO *100
1	14	0.043	6	0.024	6	0.019	2	0.019	2	0.018	2	0.020	6	0.020	6	47.256
2	12	0.036	6	0.027	6	0.021	6	0.018	2	0.020	1	0.019	1	0.018	2	49.156
3	18	0.055	6	0.036	6	0.020	2	0.018	2	0.019	1	0.019	1	0.016	2	29.689
4	22	0.041	6	0.021	6	0.018	2	0.017	1	0.019	1	0.017	1	0.017	1	41.691
5	11	0.032	6	0.028	6	0.025	6	0.024	6	0.023	6	0.022	6	0.023	6	73.067
6	10	0.023	6	0.017	2	0.017	2	0.016	1	0.013	1	0.014	1	0.012	1	52.081
7	21	0.036	6	0.018	3	0.016	2	0.019	1	0.015	2	0.018	1	0.017	1	45.650
8	11	0.032	6	0.023	6	0.021	6	0.021	6	0.019	2	0.020	4	0.020	1	62.225
9	14	0.028	6	0.025	6	0.019	2	0.018	1	0.017	1	0.017	1	0.017	1	61.739
10	11	0.050	6	0.037	6	0.034	6	0.033	6	0.035	6	0.035	6	0.035	6	70.103
11	27	0.055	6	0.034	6	0.024	6	0.020	6	0.021	6	0.020	1	0.018	2	32.391
12	10	0.030	6	0.025	6	0.021	6	0.020	1	0.022	6	0.023	6	0.023	6	78.958
13	18	0.047	6	0.031	6	0.026	6	0.019	2	0.018	1	0.018	1	0.017	1	36.854
14	14	0.032	6	0.019	2	0.017	2	0.018	1	0.017	1	0.017	1	0.018	1	55.618

15	11	0.028	6	0.023	6	0.019	2	0.018	2	0.019	1	0.019	1	0.019	1	69.049
16	17	0.036	6	0.022	6	0.021	6	0.020	2	0.021	6	0.021	6	0.021	6	58.675
17	16	0.033	6	0.022	6	0.022	6	0.023	6	0.022	6	0.023	6	0.022	6	67.709
18	9	0.026	6	0.023	6	0.023	6	0.022	6	0.023	6	0.022	6	0.022	6	83.840
19	24	0.039	6	0.020	3	0.017	2	0.017	1	0.019	1	0.017	1	0.015	1	39.421
20	22	0.039	6	0.018	3	0.017	2	0.019	1	0.017	2	0.019	1	0.016	1	41.490
21	15	0.062	6	0.041	6	0.024	6	0.019	1	0.020	1	0.019	1	0.018	1	28.684
22	13	0.022	6	0.021	6	0.020	2	0.020	1	0.019	1	0.020	2	0.018	1	82.692
23	22	0.032	6	0.024	6	0.023	6	0.018	2	0.019	1	0.019	1	0.018	1	57.548
24	13	0.043	6	0.025	6	0.021	6	0.022	6	0.019	2	0.019	1	0.020	1	45.535
25	12	0.038	6	0.018	2	0.017	1	0.021	6	0.024	6	0.025	6	0.026	6	66.572
26	18	0.032	6	0.018	2	0.018	2	0.019	1	0.016	2	0.018	2	0.017	1	52.805
27	17	0.029	6	0.017	3	0.015	2	0.015	1	0.018	1	0.015	1	0.015	1	51.430
28	16	0.030	6	0.015	2	0.017	2	0.018	1	0.018	1	0.019	1	0.019	1	62.868
29	16	0.032	6	0.018	3	0.018	2	0.018	1	0.020	1	0.019	1	0.016	1	50.908
30	26	0.039	6	0.021	6	0.017	3	0.019	1	0.016	2	0.019	1	0.017	1	44.003
31	17	0.058	6	0.035	6	0.024	6	0.025	6	0.023	6	0.025	6	0.024	6	41.208
32	16	0.055	6	0.032	6	0.021	6	0.020	2	0.018	2	0.019	2	0.019	2	35.180
33	24	0.045	6	0.033	6	0.028	6	0.021	6	0.020	6	0.019	2	0.020	1	43.760
34	11	0.058	6	0.038	6	0.028	6	0.028	6	0.026	6	0.025	6	0.025	6	42.701
35	13	0.035	6	0.023	6	0.020	6	0.018	2	0.020	1	0.019	1	0.020	6	58.368
36	18	0.032	6	0.019	3	0.017	2	0.018	2	0.020	1	0.018	2	0.018	1	57.546
37	10	0.024	6	0.013	2	0.012	2	0.015	1	0.009	1	0.011	1	0.012	1	47.644
38	12	0.055	6	0.032	6	0.027	6	0.026	6	0.026	6	0.028	6	0.028	6	51.160
39	16	0.037	6	0.027	6	0.020	6	0.020	3	0.020	6	0.019	1	0.020	1	53.951
40	22	0.029	6	0.017	2	0.017	2	0.019	1	0.018	2	0.021	6	0.019	1	66.896
41	14	0.045	6	0.029	6	0.020	6	0.020	1	0.018	1	0.016	1	0.018	1	38.735
42	13	0.045	6	0.033	6	0.031	6	0.027	6	0.028	6	0.027	6	0.028	6	61.561
43	14	0.044	6	0.031	6	0.027	6	0.019	3	0.018	2	0.017	1	0.016	2	37.839
44	15	0.048	6	0.033	6	0.027	6	0.021	6	0.020	2	0.020	2	0.020	2	41.974
45	17	0.036	6	0.019	2	0.014	2	0.015	1	0.016	1	0.014	1	0.012	1	35.047
46	11	0.049	6	0.042	6	0.037	6	0.034	6	0.034	6	0.033	6	0.033	6	67.781
47	16	0.026	6	0.020	2	0.020	2	0.020	1	0.018	2	0.019	1	0.018	1	70.494
48	10	0.042	6	0.028	6	0.025	6	0.026	6	0.027	6	0.027	6	0.028	6	67.882
49	11	0.027	6	0.024	6	0.025	6	0.024	6	0.025	6	0.024	6	0.025	6	90.258
50	17	0.037	6	0.018	2	0.019	1	0.018	1	0.017	1	0.017	1	0.013	1	34.244
51	15	0.059	6	0.038	6	0.031	6	0.024	6	0.023	6	0.022	6	0.022	6	38.182
52	12	0.028	6	0.015	2	0.015	2	0.017	1	0.018	1	0.016	1	0.017	1	60.355
53	18	0.031	6	0.023	6	0.022	6	0.021	6	0.023	6	0.022	6	0.022	6	71.744
54	24	0.041	6	0.021	6	0.018	2	0.018	1	0.018	1	0.017	1	0.015	1	37.474
55	16	0.023	6	0.012	2	0.019	1	0.016	1	0.017	1	0.015	1	0.012	1	50.745
56	10	0.038	6	0.032	6	0.031	6	0.023	6	0.024	6	0.023	6	0.023	6	59.686
57	10	0.021	6	0.019	2	0.016	1	0.014	1	0.014	1	0.016	1	0.013	1	59.407
58	19	0.039	6	0.027	6	0.027	6	0.021	6	0.024	6	0.021	6	0.021	6	54.284
59	13	0.027	6	0.035	6	0.036	6	0.036	6	0.034	6	0.033	6	0.033	6	119.754
60	21	0.030	6	0.017	2	0.019	1	0.015	1	0.016	1	0.014	1	0.012	1	39.880
61	24	0.042	6	0.023	6	0.019	2	0.016	2	0.016	1	0.015	1	0.015	1	35.950
62	26	0.052	6	0.029	6	0.018	2	0.019	1	0.017	1	0.013	1	0.017	1	32.320
63	24	0.040	6	0.022	6	0.019	3	0.017	2	0.017	1	0.017	1	0.016	1	40.635
64	12	0.043	6	0.025	6	0.022	6	0.020	2	0.019	1	0.019	1	0.017	2	39.788
65	10	0.039	6	0.036	6	0.031	6	0.032	6	0.030	6	0.031	6	0.030	6	76.108
66	13	0.063	6	0.032	6	0.024	6	0.022	6	0.021	6	0.022	6	0.021	6	33.654
67	13	0.052	6	0.029	6	0.019	1	0.017	2	0.017	1	0.019	1	0.019	1	35.731
68	23	0.040	6	0.020	3	0.018	2	0.016	1	0.018	1	0.015	1	0.013	1	33.887
69	11	0.028	6	0.020	3	0.019	2	0.020	1	0.018	1	0.016	1	0.017	1	59.097
70	14	0.047	6	0.036	6	0.030	6	0.019	2	0.020	1	0.018	1	0.017	1	37.186
71	18	0.026	6	0.014	2	0.019	1	0.018	1	0.019	1	0.017	1	0.015	1	58.009
72	27	0.038	6	0.020	6	0.020	2	0.020	1	0.017	2	0.020	1	0.018	1	48.243
73	14	0.025	6	0.021	6	0.026	6	0.025	6	0.026	6	0.026	6	0.027	6	107.063
74	14	0.023	6	0.018	2	0.013	2	0.019	1	0.017	1	0.018	1	0.016	1	67.358
75	16	0.027	6	0.016	2	0.015	2	0.014	1	0.016	1	0.014	1	0.013	1	49.336
76	11	0.030	6	0.018	2	0.020	1	0.011	1	0.012	1	0.013	1	0.012	1	40.342
77	18	0.031	6	0.022	6	0.023	6	0.023	6	0.022	6	0.023	6	0.023	6	73.345
78	15	0.032	6	0.030	6	0.030	6	0.030	6	0.031	6	0.029	6	0.031	6	96.223
79	17	0.046	6	0.027	6	0.025	6	0.022	6	0.021	6	0.021	6	0.020	1	42.882
80	14	0.060	6	0.035	6	0.027	6	0.023	6	0.023	6	0.023	6	0.022	6	36.202
81	17	0.029	6	0.014	2	0.014	2	0.018	1	0.017	1	0.018	1	0.017	1	59.756
82	14	0.052	6	0.033	6	0.031	6	0.028	6	0.030	6	0.028	6	0.029	6	56.897
83	18	0.029	6	0.019	2	0.014	2	0.014	1	0.018	1	0.018	1	0.015	1	53.685
84	15	0.037	6	0.030	6	0.031	6	0.032	6	0.031	6	0.032	6	0.033	6	89.605
85	13	0.029	6	0.014	2	0.008	2	0.012	1	0.012	1	0.014	1	0.013	1	43.734
86	15	0.031	6	0.022	6	0.019	2	0.019	1	0.019	1	0.020	1	0.020	6	65.583
87	10	0.025	6	0.032	6	0.034	6	0.033	6	0.034	6	0.034	6	0.034	6	133.543
88	16	0.039	6	0.028	6	0.027	6	0.027	6	0.027	6	0.027	6	0.027	6	68.302
89	13	0.055	6	0.029	6	0.020	6	0.020	3	0.020	1	0.019	2	0.019	2	34.834
90	11	0.072	6	0.049	6	0.034	6	0.028	6	0.022	6	0.022	6	0.020	6	28.285
91	25	0.042	6	0.027	6	0.024	6	0.023	6	0.023	6	0.024	6	0.024	6	57.711
92	17	0.041	6	0.031	6	0.030	6	0.030	6	0.031	6	0.031	6	0.031	6	76.261
93	25	0.051	6	0.030	6	0.026	6	0.021	6	0.021	6	0.019	2	0.020	6	39.939
94	12	0.044	6	0.028	6	0.025	6	0.025	6	0.024	6	0.024	6	0.027	6	62.709
95	16	0.040	6	0.031	6	0.029	6	0.027	6	0.028	6	0.029	6	0.029	6	72.548
96	11	0.041	6	0.027	6	0.021	6	0.018	1	0.018	2	0.019	1	0.017	2	40.643
97	15	0.032	6	0.018	3	0.020	3	0.019	3	0.021	6	0.022	6	0.021	6	66.358
98	17	0.041	6	0.030	6	0.031	6	0.032	6	0.030	6	0.031	6	0.031	6	73.850
99	12	0.026	6	0.025	6	0.029	6	0.031	6	0.030	6	0.031	6	0.032	6	121.123
100	11	0.041	6	0.045	6	0.048	6	0.049	6	0.048	6	0.049	6	0.049	6	118.996
101	10	0.026	6	0.028	6	0.029	6	0.031	6	0.031	6	0.031	6	0.031	6	122.748
102	13	0.033	6	0.034	6	0.036	6	0.036	6	0.035	6	0.035	6	0.035	6	105.646
103	16	0.040	6	0.035	6	0.035	6	0.035	6	0.034	6	0.035	6	0.035	6	87.787
104	11	0.028	6	0.034	6	0.040	6	0.040	6	0.040	6	0.040	6	0.039	6	140.153
105	18	0.043	6	0.037	6	0.034	6	0.028	6	0.027	6	0.029	6	0.027	6	61.634
106*	27	0.083	0	0.052	0	0.036	0	0.029	0	0.024	0	0.025	0	0.025	0	29.802
107*	22	0.200	0	0.150	0	0.112	0	0.085	0	0.067	0	0.045	0	0.037	0	18.481
108*	22	0.188	0	0.145	0	0.110	0	0.107	0	0.097	0	0.107	0	0.099	0	52.950
109*	22	0.085	0	0.079	0	0.047	0	0.044	0	0.041	0	0.040	0	0.039	0	45.889
110*	18	0.378	0	0.293	0	0.218	0	0.142	0	0.097	0	0.072	0	0.062	0	16.358
111*	20	0.163	0	0.131	0	0.123	0	0.110	0	0.110	0	0.099	0	0.098	0	60.320

*** FINAL INVERSION SUMMARY ***

	IT# 1	IT# 2	IT# 3	IT# 4	IT# 5	IT# 6	IT# 7
Sum resids sq.	7.7334	4.1939	2.6473	1.8349	1.4935	1.3707	1.2866
No. of observations	1771	1771	1771	1771	1771	1771	1771
Total RMS	0.06608	0.04866	0.03866	0.03219	0.02904	0.02782	0.02695
Variance	0.00674	0.00365	0.00230	0.00160	0.00130	0.00119	0.00111
Degrees of freedom	1148	1149	1149	1144	1153	1148	1160
Variance ratio	0.000	1.846	1.584	1.437	1.238	1.085	1.077
Cumulative CPU (s)	209.804	451.821	674.788	876.370	1080.363	1273.968	1473.282

A total of 105 earthquakes, 0 quarry blasts and 6 explosions were used in the inversion. 0 earthquakes were not used.

Appendix C

Program MOD3D

```
      PROGRAM MOD3D
C
C
C  *  A computer programme written in FORTRAN77 to produce a
C  *  three-dimensional perspective plot of seismic P-wave
C  *  velocity data derived from the tomographic inversion
C  *  programme SIMUL and interpolated using TOMPLOT.
C  *  The programme uses subroutines of the 'UNIRAS v5'
C  *  graphics library to perform the plotting.
C  *  This version removes volumes for which DWS < 50.
C
C  -  Author : Stuart Arnott
C  -  Date   : Sept. 1989
C
C
C          Define block dimensions and colour range
      DIMENSION Z(72,52,16),Z2(72,52,16),KOLOR(6),ZCL(5)
C          Data Range
      DATA XMIN,XMAX,YMIN,YMAX,ZMIN,ZMAX/0.,18.,0.,13.,4.,0./
C          Values on key
      DATA ZCL/-0.850,-0.650,0.650,0.850,2.500/
C          Colour definition
      DATA KOLOR/2,7,0,3,5,6/
C          Number of boxes
      DATA NPX,NPY,NPZ/72,52,16/
C
C          Open file statement
C
      LU1=1
      OPEN (LU1,file='mod8.65.dat',status='old')
      REWIND (LU1)
      LU2=2
      OPEN (LU2,file='dws.dat',status='old')
      REWIND (LU2)
C
C          Give each block in the volume an unassigned value
C
      DO 10 I=1,NPX
         DO 10 J=1,NPY
            DO 10 K=1,NPZ
               Z(I,J,K)=999.999
10    CONTINUE
C
C     Read in data and eliminate bugs
C
      DO 15 M=1,29592
         READ (LU2,999) I,J,K,Z2(I,J,K)
15    CONTINUE
      DO 20 L=1,7807
         READ (LU1,999) I,J,K,Z(I,J,K)
999      FORMAT (3(I4,1X),F8.3)
         IF (Z(I,J,K) .LT. 0.660 .AND. Z(I,J,K) .GT. 0.000) THEN
            Z(I,J,K) = 0.660
         ELSEIF (Z(I,J,K) .GT. -0.660 .AND. Z(I,J,K) .LT. 0.000) THEN
            Z(I,J,K) = -0.660
         ENDIF
         IF (Z(I,J,K) .EQ. 3.000 ) THEN
            GO TO 20
         ENDIF
         IF (Z2(I,J,K) .LT. 50.000) THEN
```

```
            Z(I,J,K) = 999.999
          ENDIF
 20     CONTINUE
 C
 C         Select Device
        CALL GROUTE('LIST')
 C         Initiate UNIRAS
        CALL GOPEN
 C         Outputs lengths of plot area (mm)
 C      CALL GRPSIZ(XSI,YSI)
 C      SCA=AMIN1((XSI/310.0),(YSI/240.0))
 C         User Coordinates
        CALL GLIMIT(XMIN,XMAX,YMIN,YMAX,ZMIN,ZMAX)
 C         Workbox size
        CALL GWBOX( 1.,0.8,0.6)
 C         Viewport:portion of plot area
        CALL GVPORT(60.,80.,160.,160.)
 C         Viewpoint
        CALL GEYE(-1.5,-1.5,1.5)
 C         Class Colours and Intervals
        CALL GSHADE(KOLOR,6)
        CALL GZCL(ZCL,5,0)
 C         Plot Axes
        CALL GAXIS3(0,'South-----North$','West-----East$','Depth$')
        CALL GAXORI(0.,0.)
        CALL GAXIS(1,0.,2.,18.,'North-----South$')
        CALL GAXORI(0.,0.)
        CALL GAXIS(2,0.,2.,13.,'East-----West$')
        CALL GAXORI(0.,0.)
        CALL GAXEND(1)
        CALL GAXIS(3,0.,0.5,4.,'Depth$')
        CALL GAXORI(0.,0.)
        CALL GAXEND(1)
        CALL GAXIS(3,0.,0.5,4.,'Depth$')
        CALL GAXORI(0.,0.)
        CALL GAXEND(1)
        CALL GAXIS(3,0.,0.5,4.,'$')
        CALL GGRID(1,1)
        CALL GGRID3(0,1)
C         Plot all edges of box
        CALL G3DBOX(-1)
C         Plot 3-D block diagram
        CALL GBLKR3(Z,NPX,NPY,NPZ)
C         Define the colour scale and head lines
        CALL GSCSCO('Below$Caldera$$',4.,2,0,1)
        CALL GCOSCL(60.,40.)
        CALL GHEAD('Krafla 3-D Structure$')
C         Terminate UNIRAS
        CALL GCLOSE
        STOP
        END
```

Appendix D

Relocated and Original Hypocentres

	RELOCATED HYPOCENTRE					ORIGINAL HYPOCENTRE				
Date	h	m	s	Latitude	Longitude	Depth	s	Latitude	Longitude	Depth
85 7 1	12	19	23.41	65 38.14	16 51.70	2.30	23.37	65 38.10	16 51.41	3.40
85 7 1	12	22	22.01	65 37.95	16 51.16	2.10	21.90	65 38.06	16 51.66	2.97
85 7 1	14	48	29.22	65 42.88	16 47.79	1.75	29.19	65 42.76	16 47.69	2.46
85 7 2	1	6	34.51	65 43.40	16 47.57	1.15	34.44	65 43.48	16 47.35	2.32
85 7 2	10	15	11.13	65 43.25	16 47.56	2.33	10.97	65 43.24	16 46.89	3.92
85 7 2	11	52	33.92	65 42.82	16 47.68	1.71	33.85	65 42.80	16 47.73	2.74
85 7 2	21	52	21.51	65 43.17	16 48.56	0.61	21.50	65 43.13	16 48.46	1.47
85 7 3	0	40	26.81	65 42.90	16 48.07	1.82	26.78	65 42.76	16 47.93	2.51
85 7 3	4	57	56.85	65 42.75	16 47.70	1.40	56.79	65 42.76	16 47.71	2.34
85 7 3	7	49	51.56	65 42.79	16 48.09	1.95	51.50	65 42.65	16 47.95	2.89
85 7 3	9	5	0.27	65 42.45	16 47.61	1.05	0.26	65 42.32	16 47.62	1.56
85 7 3	10	4	12.08	65 43.71	16 48.31	0.70	12.09	65 43.82	16 48.18	1.45
85 7 3	14	35	54.50	65 42.90	16 48.01	1.79	54.44	65 42.89	16 48.08	2.71
85 7 3	15	56	1.25	65 42.89	16 47.85	1.68	1.21	65 42.76	16 47.73	2.53
85 7 4	1	55	0.63	65 42.77	16 48.16	1.63	0.62	65 42.69	16 47.88	2.29
85 7 4	8	52	54.02	65 42.85	16 47.80	1.84	53.96	65 42.87	16 47.89	2.64
85 7 4	9	26	30.56	65 39.68	16 50.63	1.68	30.49	65 39.70	16 50.21	2.95
85 7 4	11	44	53.63	65 42.78	16 47.76	1.75	53.60	65 42.65	16 47.68	2.48
85 7 5	6	0	20.73	65 42.94	16 48.13	1.18	20.71	65 42.82	16 47.96	1.87
85 7 5	6	21	48.84	65 39.55	16 52.55	3.01	48.74	65 39.52	16 52.85	3.88
85 7 6	5	2	48.05	65 38.23	16 51.72	2.52	47.99	65 38.11	16 51.88	3.60
85 7 6	10	11	41.86	65 42.63	16 45.98	1.76	41.85	65 42.51	16 45.66	2.57
85 7 7	11	54	28.23	65 38.02	16 51.61	2.32	28.19	65 37.89	16 51.68	3.11
85 7 8	3	37	40.73	65 38.85	16 51.15	1.29	40.68	65 38.76	16 51.06	2.33
85 7 8	4	2	9.37	65 42.84	16 47.89	1.70	9.32	65 42.79	16 47.91	2.63
85 7 8	10	10	36.68	65 43.01	16 48.42	0.47	36.70	65 42.91	16 48.19	1.39
85 7 9	4	4	43.95	65 38.03	16 51.80	2.23	43.91	65 37.94	16 51.82	3.07
85 7 9	8	24	18.49	65 39.56	16 52.36	1.43	18.41	65 39.33	16 52.48	2.51
85 7 9	19	54	15.10	65 38.16	16 51.56	2.59	15.02	65 38.06	16 51.52	3.76
85 7 9	22	0	4.74	65 39.78	16 50.52	2.38	4.67	65 39.80	16 50.17	3.36
85 710	9	36	6.15	65 39.57	16 50.76	1.62	6.12	65 39.50	16 50.51	2.42
85 710	12	14	0.62	65 38.48	16 51.16	2.63	0.60	65 38.47	16 51.08	2.92
85 711	2	37	13.26	65 38.09	16 51.77	2.36	13.21	65 37.91	16 51.87	3.28
85 711	4	49	8.33	65 38.09	16 51.74	2.43	8.25	65 37.97	16 51.81	3.60
85 711	5	58	55.92	65 38.85	16 51.03	1.90	55.86	65 38.75	16 50.64	2.74
85 711	23	17	28.49	65 38.19	16 51.55	2.39	28.46	65 38.05	16 51.45	3.08
85 712	22	31	53.64	65 38.84	16 51.07	1.61	53.59	65 38.81	16 50.74	2.48
85 714	17	38	26.15	65 43.86	16 50.27	3.74	25.68	65 44.81	16 50.58	2.53
85 715	2	31	24.60	65 38.11	16 51.73	2.52	24.55	65 38.00	16 51.72	3.48
85 715	22	46	59.45	65 42.05	16 47.60	1.42	59.47	65 42.62	16 48.19	2.55
85 716	2	26	39.37	65 43.11	16 48.12	1.44	39.33	65 43.16	16 48.03	2.26
85 716	4	59	26.14	65 38.02	16 51.40	2.13	26.10	65 37.91	16 51.25	2.87
85 716	7	58	53.22	65 42.85	16 47.79	1.82	53.17	65 42.82	16 47.73	2.60
85 716	10	10	9.66	65 38.82	16 51.07	1.45	9.63	65 38.75	16 50.89	2.29
85 716	18	4	37.98	65 42.63	16 47.57	1.36	37.99	65 42.44	16 47.51	1.83
85 716	19	14	1.77	65 38.12	16 51.69	2.63	1.69	65 37.96	16 51.63	3.77
85 717	3	16	36.96	65 36.98	16 52.35	2.76	36.87	65 36.79	16 52.46	3.18
85 717	17	34	55.41	65 38.92	16 50.95	1.83	55.34	65 38.90	16 50.71	2.80
85 718	3	10	57.06	65 37.43	16 52.83	0.33	57.00	65 37.32	16 52.92	0.68
85 718	9	9	26.64	65 38.16	16 51.68	2.72	26.57	65 38.05	16 51.55	3.87
85 719	5	40	57.77	65 39.79	16 50.51	2.53	57.69	65 39.74	16 50.11	3.49
85 719	7	46	39.94	65 38.47	16 51.33	1.89	39.93	65 38.44	16 51.20	2.40
85 719	21	52	37.73	65 38.89	16 51.10	1.73	37.71	65 38.83	16 50.89	2.79
85 720	4	32	12.89	65 38.03	16 51.79	2.19	12.85	65 37.94	16 51.76	2.98
85 720	17	44	29.10	65 43.57	16 47.92	1.73	29.01	65 43.72	16 47.68	2.93
85 721	0	38	4.52	65 38.08	16 51.63	2.43	4.49	65 37.95	16 51.46	3.26
85 721	4	20	32.44	65 41.89	16 48.26	0.04	32.38	65 41.87	16 48.33	0.16

85	721	1133	12.93	65	38.09	16	51.69	2.09	12.90	65	37.97	16	51.75	2.78
85	722	2045	43.02	65	39.77	16	50.60	2.17	42.93	65	39.75	16	50.31	3.35
85	722	2133	43.11	65	39.80	16	50.54	2.23	43.06	65	39.79	16	50.25	3.14
85	724	536	35.77	65	43.01	16	48.03	1.62	35.72	65	43.14	16	48.10	2.39
85	724	1358	47.41	65	39.74	16	50.69	2.18	47.35	65	39.82	16	50.19	3.20
85	724	1612	28.71	65	38.16	16	51.65	2.40	28.63	65	38.08	16	51.59	3.61
85	724	1615	39.38	65	38.15	16	51.59	2.47	39.31	65	38.08	16	51.50	3.53
85	725	514	8.81	65	42.72	16	48.08	1.13	8.77	65	42.72	16	48.06	1.98
85	725	1846	25.90	65	38.76	16	51.13	1.88	25.84	65	38.69	16	50.76	2.78
85	726	556	22.88	65	42.68	16	47.97	1.32	22.85	65	42.61	16	48.08	2.02
85	726	11 0	41.66	65	38.03	16	51.69	2.36	41.63	65	37.94	16	51.73	3.10
85	726	12 3	55.08	65	39.26	16	50.63	1.77	55.05	65	39.12	16	50.53	2.40
85	726	1215	48.02	65	39.09	16	51.08	1.22	47.98	65	38.89	16	51.22	1.67
85	726	21 0	43.03	65	38.77	16	51.12	1.51	42.98	65	38.65	16	51.01	2.41
85	727	1017	26.86	65	38.21	16	51.41	1.98	26.85	65	38.12	16	51.36	2.59
85	728	343	38.91	65	39.42	16	51.13	1.72	38.89	65	39.31	16	50.87	2.51
85	728	641	59.08	65	43.49	16	47.87	1.21	58.97	65	43.56	16	47.69	2.73
85	728	9 9	13.57	65	42.75	16	47.95	1.49	13.56	65	42.89	16	48.12	2.15
85	728	910	18.30	65	41.92	16	47.00	1.63	18.27	65	41.65	16	47.08	1.86
85	728	911	55.24	65	39.02	16	50.90	1.93	55.19	65	38.95	16	50.74	2.71
85	728	1847	39.42	65	37.99	16	51.79	2.63	39.35	65	37.80	16	51.70	3.66
85	729	631	2.59	65	42.75	16	47.52	1.13	2.53	65	42.67	16	47.61	2.33
85	729	1048	39.55	65	43.45	16	47.92	1.38	39.48	65	43.54	16	47.66	2.43
85	729	11 8	37.18	65	43.46	16	47.93	1.41	37.12	65	43.53	16	47.70	2.39
85	729	1614	18.21	65	38.10	16	51.71	2.68	18.20	65	37.94	16	51.68	3.26
85	730	1229	28.47	65	38.00	16	51.69	2.21	28.45	65	37.91	16	51.75	2.83
85	730	1353	48.62	65	38.34	16	51.70	2.02	48.62	65	38.25	16	51.74	2.42
85	730	15 8	37.15	65	42.74	16	47.74	1.61	37.12	65	42.67	16	47.91	2.30
85	730	1627	28.08	65	42.39	16	46.63	1.81	28.04	65	42.27	16	46.28	2.10
85	730	1752	12.47	65	38.18	16	51.54	2.08	12.44	65	38.13	16	51.47	2.87
85	**730**	**1848**	**53.92**	**65**	**38.16**	**16**	**51.71**	**2.56**	**53.88**	**65**	**38.08**	**16**	**51.68**	**3.41**
85	730	2218	51.71	65	38.74	16	51.38	1.35	51.71	65	38.62	16	51.07	1.79
85	731	320	57.47	65	38.04	16	51.72	2.31	57.45	65	37.98	16	51.84	2.92
85	731	620	45.55	65	38.97	16	50.92	2.16	45.48	65	38.95	16	50.72	3.07
85	731	714	16.16	65	38.18	16	51.52	2.09	16.15	65	38.08	16	51.54	2.59
85	731	822	1.34	65	38.16	16	51.71	2.58	1.29	65	38.05	16	51.62	3.49
85	731	1648	50.72	65	38.08	16	51.62	2.43	50.70	65	37.92	16	51.68	3.12
85	731	2113	27.37	65	42.84	16	47.78	1.48	27.35	65	42.82	16	47.73	2.25
85	731	2156	39.33	65	38.66	16	50.29	2.61	39.34	65	38.75	16	50.17	2.70
85	8	1	414	41.93	65	38.69	16	51.16	1.92	41.87	65	38.60	16	51.04	2.82
85	8	1	854	41.07	65	38.04	16	51.77	2.55	40.99	65	37.91	16	51.78	3.77
85	8	1	936	52.74	65	39.77	16	50.24	1.67	52.70	65	39.79	16	49.96	2.39
85	8	1	1218	1.37	65	42.75	16	47.98	1.64	1.34	65	42.67	16	47.90	2.44
85	**8**	**1**	**1227**	**47.47**	**65**	**42.82**	**16**	**48.00**	**1.69**	**47.41**	**65**	**42.78**	**16**	**47.93**	**2.56**
85	8	1	1256	24.44	65	39.29	16	50.66	2.19	24.37	65	39.25	16	50.44	3.10
85	8	2	055	21.54	65	43.01	16	50.36	1.35	21.47	65	42.99	16	50.71	2.31
85	8	2	312	12.49	65	39.70	16	51.02	1.92	12.39	65	39.66	16	50.72	3.38
85	8	2	337	31.54	65	38.25	16	51.50	1.83	31.50	65	38.30	16	51.47	2.63
85	8	2	1113	17.02	65	39.63	16	50.84	2.63	16.98	65	39.64	16	50.46	3.35
85	8	2	1329	38.07	65	37.67	16	52.34	2.75	37.97	65	37.33	16	52.91	3.89
85	8	2	2230	50.07	65	39.41	16	50.43	2.17	50.02	65	39.47	16	50.02	2.86
85	8	3	948	56.69	65	39.31	16	50.75	1.84	56.64	65	39.28	16	50.38	2.72
85	8	3	1837	13.26	65	38.09	16	51.69	2.57	13.20	65	37.95	16	51.59	3.48
85	8	3	2325	51.34	65	39.22	16	50.76	1.93	51.31	65	39.20	16	50.33	2.42
85	8	4	1011	17.98	65	38.14	16	51.55	2.31	17.97	65	38.05	16	51.60	2.83
85	8	4	1217	55.20	65	38.10	16	51.58	2.35	55.15	65	38.02	16	51.48	3.20
85	8	4	2131	59.99	65	42.80	16	47.58	1.95	59.96	65	42.66	16	47.44	2.59
85	8	5	1	9	22.17	65	42.83	16	47.92	1.77	22.12	65	42.75	16	47.86	2.63
85	8	6	843	8.66	65	39.60	16	50.52	2.35	8.60	65	39.55	16	50.23	3.17
85	8	6	1548	55.21	65	38.14	16	51.57	1.99	55.18	65	38.09	16	51.44	2.79

85	8	6	1614	14.70	65	42.89	16	48.04	1.72	14.65	65	42.83	16	48.07	2.60
85	8	7	1625	41.33	65	38.68	16	51.14	1.97	41.29	65	38.60	16	50.97	2.70
85	8	7	1833	10.95	65	42.78	16	47.94	2.04	10.86	65	42.75	16	48.07	3.24
85	8	8	22	1	26.05	65	42.36	16	46.28	1.64	26.04	65	42.17	16	46.00	2.03
85	8	9		756	17.37	65	42.44	16	45.93	1.57	17.36	65	42.31	16	46.02	2.19
85	8	9		953	4.29	65	38.11	16	51.66	2.28	4.25	65	38.10	16	51.60	3.06
85	8	9	2059		22.52	65	38.11	16	51.60	2.10	22.49	65	38.01	16	51.62	2.82
85	8	9	2332		15.55	65	42.22	16	47.14	1.36	15.57	65	42.50	16	47.57	2.09
85	811		1417		23.92	65	42.98	16	48.20	1.57	23.86	65	42.98	16	48.15	2.62
85	813		1328		24.90	65	42.91	16	47.76	1.78	24.84	65	42.88	16	47.75	2.83
85	813		16	3	19.85	65	43.42	16	47.87	1.18	19.77	65	43.45	16	47.60	2.56
85	814		12	1	27.78	65	38.18	16	51.43	1.96	27.75	65	38.14	16	51.39	2.58
85	814		1838		16.36	65	38.15	16	51.52	2.43	16.34	65	38.04	16	51.57	2.93
85	815		810		40.99	65	38.18	16	51.42	1.98	40.93	65	38.06	16	51.37	2.92
85	815		11	2	51.67	65	38.07	16	51.50	1.98	51.64	65	37.98	16	51.47	2.71
85	815		1319		20.96	65	38.05	16	51.70	2.51	20.92	65	37.95	16	51.67	3.19
85	815		14	4	48.00	65	42.94	16	47.70	1.92	47.94	65	42.89	16	47.71	2.89
85	815		1514		30.11	65	38.81	16	51.04	2.03	30.05	65	38.78	16	50.99	2.82
85	816		535		27.58	65	38.82	16	51.31	2.50	27.51	65	38.77	16	51.14	3.32
85	817		917		30.25	65	42.98	16	48.01	2.04	30.19	65	43.09	16	48.11	3.02
85	818		429		15.78	65	38.17	16	51.57	2.49	15.75	65	38.12	16	51.47	3.26
85	819		0	4	20.96	65	38.17	16	51.63	2.36	20.92	65	38.08	16	51.51	3.13
85	819		559		5.92	65	42.72	16	46.58	2.27	5.89	65	42.53	16	46.33	2.89
85	820		041		33.98	65	38.90	16	51.07	2.14	33.87	65	39.00	16	50.97	3.62
85	820		513		3.12	65	39.88	16	50.45	2.30	3.05	65	39.82	16	50.19	3.23
85	820		1919		50.31	65	39.29	16	51.38	2.93	50.30	65	39.37	16	50.52	3.44
85	821		1546		35.39	65	39.61	16	50.52	2.38	35.31	65	39.53	16	50.40	3.39
85	822		12	8	25.29	65	38.05	16	51.74	2.48	25.25	65	37.88	16	51.30	3.27
85	822		1640		27.35	65	42.76	16	48.07	1.37	27.29	65	42.69	16	48.06	2.32
85	823		1045		37.17	65	38.16	16	51.64	2.56	37.13	65	38.07	16	51.57	3.42
85	823		13	1	40.36	65	39.55	16	49.84	1.91	40.32	65	39.54	16	49.46	2.65
85	823		1811		26.35	65	39.15	16	51.04	2.16	26.33	65	39.03	16	50.92	2.66
85	824		1059		7.66	65	37.97	16	51.61	2.53	7.61	65	37.81	16	51.68	3.37
85	824		1123		39.09	65	38.13	16	51.64	2.64	39.00	65	38.03	16	51.55	3.88
85	824		12	7	17.61	65	43.76	16	48.08	1.20	17.45	65	44.08	16	47.73	3.01
85	824		1525		39.97	65	42.76	16	47.68	1.76	39.92	65	42.73	16	47.72	2.60
85	824		1639		4.90	65	42.56	16	48.56	1.61	4.83	65	42.44	16	49.06	2.55
85	824		1647		40.35	65	39.16	16	50.94	1.58	40.36	65	39.00	16	50.82	1.79
85	824		1746		32.77	65	39.70	16	50.49	2.15	32.72	65	39.64	16	50.17	2.86
85	825		539		35.49	65	38.10	16	51.71	2.63	35.49	65	38.01	16	51.67	3.10
85	825		14	4	40.43	65	42.95	16	48.23	1.47	40.41	65	43.04	16	48.41	2.29
85	825		1434		9.72	65	38.11	16	51.63	2.60	9.70	65	38.02	16	51.67	3.28
85	825		1637		51.96	65	38.16	16	51.66	2.54	51.96	65	38.10	16	51.62	2.88
85	826		539		45.54	65	38.12	16	51.78	2.60	45.49	65	38.04	16	51.79	3.53
85	827		8	0	55.32	65	42.30	16	48.20	1.75	55.27	65	42.01	16	48.30	2.39
85	827		1721		48.70	65	38.13	16	51.65	2.65	48.66	65	38.16	16	51.70	3.44
85	828		120		54.21	65	38.15	16	51.66	2.54	54.18	65	38.11	16	51.54	3.34
85	829		836		55.13	65	39.33	16	50.80	2.04	55.09	65	39.29	16	50.50	2.65
85	829		913		48.29	65	42.79	16	48.01	1.67	48.23	65	42.68	16	47.81	2.64
85	829		1015		20.60	65	38.15	16	51.75	2.47	20.53	65	38.01	16	51.75	3.58
85	830		325		51.82	65	42.80	16	47.67	1.88	51.76	65	42.79	16	47.75	2.87
85	830		1553		1.19	65	42.85	16	47.81	1.73	1.15	65	42.80	16	47.89	2.60
85	831		023		18.41	65	38.37	16	51.34	2.38	18.38	65	38.30	16	51.39	3.00
85	831		029		13.81	65	39.74	16	50.39	3.03	13.74	65	39.73	16	50.25	3.84
85	831		1137		20.71	65	38.64	16	51.44	2.65	20.71	65	38.66	16	51.32	2.94
85	831		1349		52.34	65	38.14	16	51.68	2.56	52.30	65	38.04	16	51.60	3.47
85	831		14	7	12.60	65	38.12	16	51.63	2.57	12.53	65	37.98	16	51.67	3.63
85	9	1	157		47.84	65	43.70	16	47.99	1.49	47.77	65	43.74	16	47.39	2.54
85	9	1	254		41.47	65	39.67	16	50.61	2.44	41.44	65	39.65	16	50.39	2.97
85	9	1	950		18.71	65	38.77	16	51.13	1.36	18.68	65	38.67	16	50.87	2.20

85	9	1	1017	14.47	65	39.73	16	50.47	2.36	14.36	65	39.67	16	50.11	3.47
85	9	1	1258	42.02	65	43.15	16	47.93	1.62	41.99	65	43.07	16	47.70	2.38
85	9	1	1658	18.23	65	43.54	16	47.81	0.22	18.21	65	43.56	16	47.77	1.43
85	9	2	145	29.78	65	38.12	16	51.72	2.62	29.71	65	38.02	16	51.69	3.75
85	9	2	453	8.09	65	38.81	16	51.18	2.11	8.04	65	38.67	16	51.01	2.98
85	9	2	6	4	44.31	65	42.83	16	47.80	1.85	44.26	65	42.81	16	47.75	2.62
85	9	2	911	56.67	65	43.07	16	48.26	1.57	56.60	65	43.07	16	48.17	2.61
85	9	2	12	3	10.64	65	42.17	16	47.21	1.48	10.62	65	42.18	16	47.55	2.29
85	9	2	18	5	20.47	65	42.43	16	48.48	1.40	20.38	65	42.24	16	48.62	2.62
85	9	2	1941	29.62	65	43.35	16	48.74	0.72	29.59	65	43.36	16	48.59	2.10
85	9	2	2149	19.70	65	38.09	16	51.69	2.63	19.62	65	37.98	16	51.66	3.80
85	9	3	4	4	34.32	65	42.84	16	47.48	1.77	34.26	65	42.83	16	47.54	2.72
85	9	3	755	58.55	65	42.52	16	47.37	1.74	58.48	65	42.27	16	47.31	2.68
85	9	3	813	23.32	65	42.39	16	47.65	1.83	23.16	65	42.27	16	47.62	3.48
85	9	3	1012	11.74	65	42.87	16	47.98	1.67	11.67	65	42.82	16	48.00	2.84
85	9	3	1220	3.63	65	42.32	16	45.49	1.45	3.62	65	42.17	16	45.43	2.04
85	9	3	2311	13.41	65	42.86	16	47.76	1.84	13.33	65	42.92	16	47.75	2.94
85	9	4	716	57.72	65	38.78	16	51.08	2.31	57.66	65	38.67	16	50.96	2.96
85	9	4	724	2.69	65	42.68	16	47.96	1.70	2.63	65	42.63	16	48.04	2.64
85	9	5	0	1	7.27	65	38.19	16	51.66	2.49	7.20	65	38.08	16	51.67	3.65
85	9	5	1159	27.19	65	38.17	16	51.59	1.59	27.19	65	38.12	16	51.57	2.12
85	9	6	11	7	21.61	65	44.43	16	51.10	2.32	21.39	65	44.96	16	52.01	3.71
85	9	6	2015	50.83	65	42.76	16	48.44	0.82	50.83	65	42.64	16	48.40	1.56
85	9	6	2322	53.72	65	38.09	16	51.78	2.22	53.71	65	38.03	16	51.86	2.83
85	9	7	050	22.00	65	43.45	16	47.90	1.37	21.93	65	43.55	16	47.62	2.49
85	9	7	340	27.65	65	42.34	16	48.55	1.55	27.55	65	42.25	16	48.70	2.78
85	9	7	17	2	45.50	65	36.93	16	52.21	2.04	45.40	65	36.66	16	52.46	2.65
85	9	7	1914	1.40	65	38.23	16	51.46	2.05	1.40	65	38.17	16	51.40	2.54
85	9	7	2320	44.65	65	39.62	16	50.63	2.37	44.62	65	39.59	16	50.30	2.81
85	9	8	042	36.15	65	39.42	16	50.85	2.29	36.06	65	39.34	16	50.64	3.45
85	9	8	737	56.45	65	38.28	16	51.95	1.64	56.37	65	38.07	16	52.01	2.98
85	9	8	921	26.24	65	38.15	16	51.63	2.57	26.20	65	38.07	16	51.50	3.36
85	9	8	928	5.96	65	43.42	16	47.92	1.29	5.89	65	43.49	16	47.73	2.42
85	9	8	1045	39.95	65	38.16	16	51.59	2.62	39.91	65	38.18	16	51.61	3.42
85	9	8	1712	39.38	65	38.96	16	51.06	1.43	39.35	65	38.85	16	50.79	2.33
85	9	8	1716	13.25	65	39.18	16	50.96	1.34	13.23	65	39.11	16	50.78	2.01
85	9	9	1	0	7.01	65	39.16	16	50.94	2.28	6.98	65	39.12	16	50.71	2.70
85	9	9	1449	3.43	65	42.82	16	47.45	1.33	3.40	65	42.67	16	47.14	2.10
85	9	9	2231	56.69	65	38.40	16	51.34	2.05	56.68	65	38.38	16	51.14	2.61
85	910		651	58.81	65	38.45	16	51.40	0.47	58.87	65	38.41	16	51.18	1.26
85	910		747	13.16	65	42.16	16	48.00	0.40	13.06	65	42.32	16	47.60	1.83
85	910		1022	58.59	65	42.45	16	45.52	1.78	58.62	65	42.37	16	45.81	2.12
85	910		1343	24.92	65	38.15	16	51.69	2.48	24.89	65	38.08	16	51.69	3.12
85	910		1459	21.84	65	38.77	16	51.09	1.82	21.79	65	38.71	16	50.99	2.60
85	910		15	4	25.89	65	38.77	16	51.13	1.80	25.87	65	38.77	16	50.83	2.44
85	910		1650	15.30	65	38.14	16	51.64	1.97	15.28	65	38.07	16	51.60	2.65
85	911		120	27.74	65	39.89	16	50.51	1.80	27.71	65	39.88	16	50.07	2.52
85	911		659	53.95	65	38.15	16	51.61	2.28	53.89	65	38.07	16	51.56	3.44
85	911		733	9.35	65	42.74	16	48.32	1.41	9.26	65	42.81	16	48.14	2.56
85	911		1641	24.18	65	38.01	16	51.65	2.22	24.16	65	37.91	16	51.76	2.83
85	911		23	1	8.80	65	42.41	16	45.60	1.65	8.77	65	42.22	16	45.43	2.28
85	912		256	13.11	65	39.25	16	50.65	2.14	13.05	65	39.20	16	50.41	2.98
85	913		130	47.02	65	42.79	16	47.49	1.70	46.97	65	42.69	16	47.48	2.64
85	913		1032	4.75	65	38.18	16	51.40	2.07	4.71	65	38.06	16	51.37	2.74
85	913		2117	58.47	65	42.43	16	46.00	1.67	58.44	65	42.30	16	45.70	2.13
85	914		934	2.52	65	38.39	16	51.37	1.60	2.48	65	38.33	16	51.31	2.38
85	914		12	9	52.19	65	38.06	16	51.77	2.47	52.11	65	38.01	16	51.86	3.61
85	914		19	0	15.13	65	38.10	16	51.64	2.72	15.10	65	38.03	16	51.73	3.40
85	915		052	24.41	65	40.37	16	49.81	3.07	24.33	65	40.34	16	49.60	3.89
85	915		428	23.68	65	38.77	16	51.25	1.28	23.66	65	38.71	16	51.05	1.94

85	915	2150	50.19	65	38.80	16	51.14	2.18	50.13	65	38.71	16	50.98	3.06
85	916	1048	16.10	65	38.20	16	51.62	2.16	16.08	65	38.15	16	51.68	3.70
85	916	1447	12.17	65	38.83	16	51.18	1.60	12.14	65	38.78	16	50.97	2.28
85	916	1734	41.04	65	38.01	16	51.70	2.26	41.02	65	37.94	16	51.74	2.88
85	916	2120	41.44	65	43.41	16	48.54	1.03	41.40	65	43.44	16	48.41	2.38
85	917	426	11.78	65	38.78	16	50.96	2.19	11.72	65	38.69	16	50.73	3.13
85	917	1130	30.65	65	38.24	16	51.46	2.04	30.62	65	38.18	16	51.49	2.70
85	918	0	7 24.06	65	43.48	16	47.84	1.62	23.97	65	43.64	16	47.61	2.89
85	918	913	35.51	65	42.34	16	46.49	1.77	35.51	65	42.23	16	46.73	2.54
85	918	1055	41.99	65	37.98	16	51.68	2.29	41.98	65	37.86	16	51.71	2.85
85	918	12	7 27.64	65	43.02	16	46.99	1.46	27.53	65	43.21	16	46.52	2.87
85	919	228	18.70	65	39.85	16	50.40	2.88	18.68	65	39.89	16	49.94	3.40
85	919	631	23.14	65	38.82	16	50.87	1.71	23.07	65	38.71	16	50.64	2.75
85	919	1813	51.50	65	38.18	16	51.66	1.98	51.49	65	38.19	16	51.69	2.60
85	919	2259	38.07	65	42.87	16	47.79	2.15	38.01	65	42.85	16	47.78	3.09
85	920	050	22.60	65	38.12	16	51.58	2.66	22.60	65	37.99	16	51.60	3.03
85	920	717	55.44	65	38.01	16	51.60	2.20	55.41	65	37.95	16	51.56	2.94
85	920	11	0 6.24	65	38.08	16	51.74	2.38	6.23	65	38.00	16	51.80	3.03
85	920	14	0 0.78	65	42.59	16	46.42	1.89	0.76	65	42.41	16	46.22	2.46
85	920	2019	26.85	65	38.13	16	51.67	2.13	26.82	65	38.06	16	51.68	2.94
85	920	2342	23.78	65	39.76	16	50.39	2.02	23.71	65	39.69	16	50.36	3.02
85	921	8	6 10.12	65	38.17	16	51.47	2.35	10.10	65	38.10	16	51.45	2.94
85	921	848	45.80	65	39.53	16	50.38	2.31	45.71	65	39.44	16	50.28	3.42
85	921	1130	24.37	65	38.05	16	51.75	2.61	24.37	65	37.83	16	51.91	3.02
85	921	1853	55.85	65	42.66	16	47.98	1.75	55.81	65	42.58	16	48.01	2.58
85	921	1858	28.32	65	38.63	16	51.08	1.28	28.29	65	38.55	16	51.00	2.04
85	921	2025	55.69	65	40.32	16	51.30	2.90	55.68	65	40.37	16	50.69	3.34
85	921	2113	12.27	65	43.40	16	47.84	1.38	12.21	65	43.47	16	47.61	2.44
85	921	22	9 59.00	65	38.09	16	51.65	2.35	58.99	65	38.00	16	51.73	2.88
85	921	2234	45.76	65	38.23	16	51.63	1.70	45.73	65	38.14	16	51.59	2.45
85	922	057	47.90	65	37.20	16	52.21	2.41	47.83	65	36.90	16	52.33	2.89
85	922	419	41.62	65	43.02	16	48.47	0.87	41.63	65	42.95	16	48.54	1.41
85	922	449	3.11	65	37.12	16	52.12	2.11	3.04	65	36.91	16	52.34	2.65
85	922	651	24.15	65	42.82	16	48.06	1.87	24.05	65	42.80	16	48.09	3.19
85	922	1118	17.03	65	42.64	16	48.23	1.27	17.01	65	42.54	16	48.28	1.94
85	922	1226	39.84	65	39.66	16	50.70	2.15	39.77	65	39.73	16	50.45	3.20
85	922	1715	52.85	65	38.07	16	51.73	2.32	52.84	65	37.99	16	51.86	2.85
85	923	423	58.62	65	38.12	16	51.69	2.37	58.59	65	38.17	16	51.80	3.05
85	923	433	51.82	65	38.13	16	51.76	2.37	51.81	65	38.02	16	51.80	2.90
85	923	526	19.37	65	38.52	16	51.65	1.76	19.37	65	38.11	16	51.58	2.52
85	923	727	39.51	65	38.14	16	51.62	2.32	39.46	65	38.06	16	51.54	3.25
85	923	930	38.91	65	42.77	16	48.03	2.21	38.81	65	42.97	16	48.27	3.38
85	923	11	0 9.42	65	39.65	16	50.53	2.15	9.39	65	39.69	16	50.14	2.90
85	923	12	4 53.38	65	42.80	16	47.69	1.88	53.32	65	42.81	16	47.71	2.77
85	923	1520	37.71	65	38.52	16	51.30	1.64	37.68	65	38.42	16	51.20	2.39
85	923	1636	14.87	65	39.20	16	51.20	1.79	14.86	65	39.10	16	51.10	2.19
85	924	3	8 14.55	65	42.83	16	48.04	1.76	14.49	65	42.79	16	48.06	2.77
85	924	432	25.12	65	38.08	16	51.75	2.50	25.08	65	38.00	16	51.72	3.38
85	924	9	1 18.89	65	38.20	16	51.36	1.39	18.85	65	38.11	16	51.36	2.18
85	924	1051	54.00	65	39.16	16	51.19	2.24	53.98	65	39.01	16	51.12	2.64
85	924	15	3 39.81	65	42.79	16	47.82	1.85	39.79	65	42.65	16	47.65	2.40
85	925	211	32.79	65	38.06	16	51.70	2.50	32.74	65	37.97	16	51.68	3.35
85	925	3	6 31.77	65	38.10	16	51.79	2.32	31.73	65	38.03	16	51.77	3.10
85	925	1625	35.11	65	40.36	16	49.65	2.51	35.05	65	40.38	16	49.31	3.19
85	925	2131	41.75	65	38.87	16	50.94	1.26	41.69	65	38.85	16	50.74	2.44
85	925	2213	38.85	65	39.57	16	50.65	2.33	38.79	65	39.58	16	50.48	3.46
85	926	627	50.36	65	38.89	16	51.12	1.53	50.32	65	38.82	16	50.87	2.52
85	926	1133	3.03	65	36.71	16	52.54	2.54	2.94	65	36.51	16	52.66	2.93
85	927	641	14.88	65	38.02	16	51.66	2.40	14.85	65	37.92	16	51.63	3.19
85	927	7	0 56.71	65	38.08	16	51.70	1.86	56.71	65	38.03	16	51.61	2.35

85	928	246	23.22	65	39.71	16	50.37	2.03	23.14	65	39.66	16	50.25	3.18
85	928	632	2.16	65	39.76	16	49.91	2.81	2.13	65	39.79	16	49.61	3.28
85	928	10 7	7.69	65	38.61	16	51.20	2.12	7.66	65	38.56	16	51.09	2.84
85	928	12 3	21.76	65	39.28	16	50.68	2.33	21.74	65	39.14	16	50.66	3.00
85	928	1431	11.23	65	38.05	16	51.69	2.65	11.19	65	37.93	16	51.67	3.46
85	928	1957	44.84	65	38.11	16	51.64	1.99	44.82	65	37.97	16	51.73	2.60
85	929	5 8	42.95	65	38.01	16	51.76	2.52	42.91	65	37.91	16	51.75	3.33
85	929	847	42.65	65	38.46	16	51.41	0.40	42.69	65	38.38	16	51.34	0.99
85	929	1050	35.37	65	38.56	16	51.30	1.97	35.35	65	38.46	16	51.29	2.50
85	929	1411	57.34	65	39.72	16	50.30	1.97	57.32	65	39.80	16	49.87	2.66
85	929	1444	3.70	65	42.75	16	47.75	1.69	3.65	65	42.74	16	47.68	2.56
85	929	17 7	18.83	65	42.96	16	47.79	1.67	18.63	65	43.14	16	46.92	3.21
85	929	1714	7.38	65	38.72	16	51.26	1.96	7.33	65	38.66	16	51.09	2.37
85	929	18 9	54.49	65	38.19	16	51.54	2.02	54.47	65	38.14	16	51.60	2.53
85	929	2340	40.78	65	39.11	16	50.88	1.79	40.72	65	39.11	16	50.71	2.66
85	930	031	53.85	65	42.88	16	47.34	2.02	53.79	65	42.85	16	47.22	3.00
85	930	245	44.30	65	43.05	16	47.85	1.41	44.23	65	42.76	16	47.31	2.52
85	930	4 7	28.50	65	38.08	16	51.86	2.64	28.40	65	37.88	16	52.10	3.96
85	930	1048	0.52	65	38.83	16	51.07	1.67	0.46	65	38.71	16	50.92	2.73
85	930	2314	6.06	65	38.09	16	51.45	1.73	6.05	65	37.99	16	51.44	2.21
8510	1	2021	55.04	65	43.38	16	47.91	1.58	54.96	65	43.50	16	47.72	2.45
8510	1	2139	17.80	65	37.96	16	51.87	2.93	17.75	65	37.79	16	51.95	3.89
8510	3	123	6.23	65	38.87	16	51.23	3.75	6.30	65	38.59	16	51.53	3.07

Appendix E

Focal Mechanisms

- Upper hemisphere polarity plots in stereographic projection. Each event has two different. The solutions on the left hand side were derived using ray angles computed by HYPOINVERSE with the original 1–d velocity model. The others were derived using angles computed by BENDRAY with the final 3–d velocity model. Arcs on the latter plots show the effect of using the 3–d model. See text for details.

- **Symbols :** upper hemisphere compressions (●), upper hemisphere dilatations (○), upper hemisphere nodal arrivals (×), lower hemisphere compressions (∗), lower hemisphere dilatations (d).

E.1 Bjarnarflag Focal Mechanisms

850701 1219

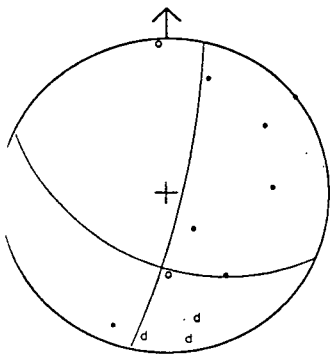

850701 1219

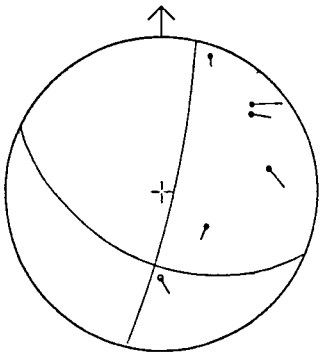

850711 0237

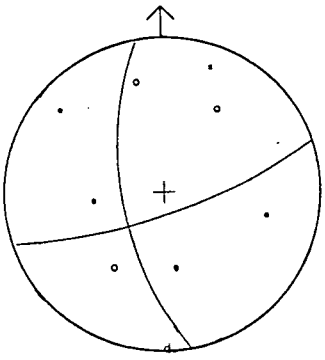

850711 0237

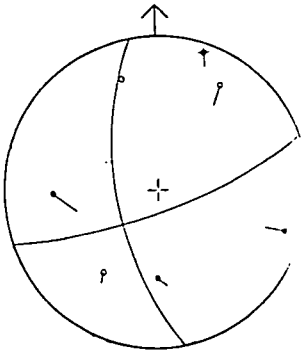

850707 1154

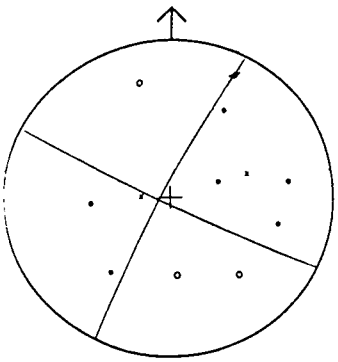

850707 1154

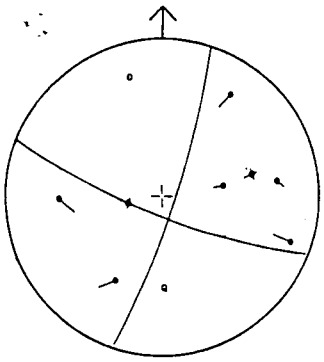

850711 0449

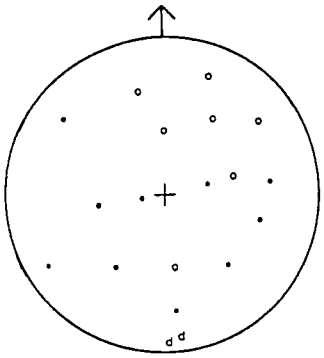

850711 0449

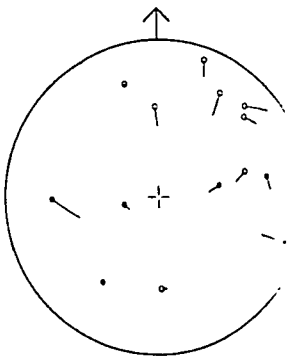

850709 0404

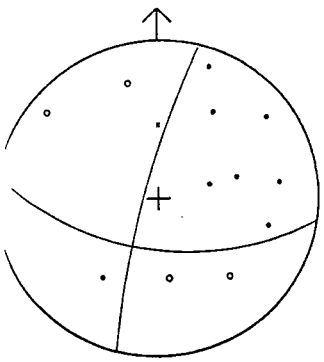

850709 0404

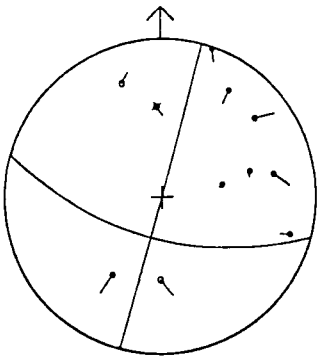

850711 2317

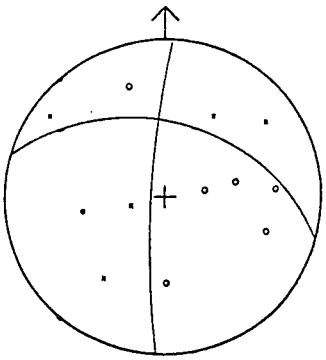

850711 2317

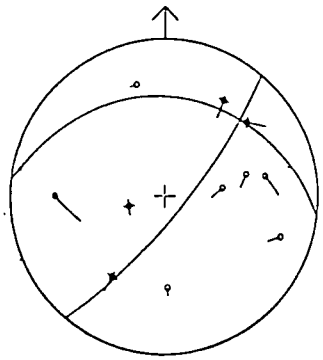

850709 1954

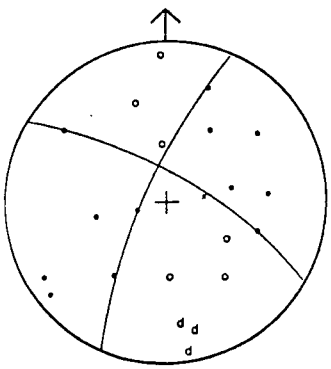

850709 1954

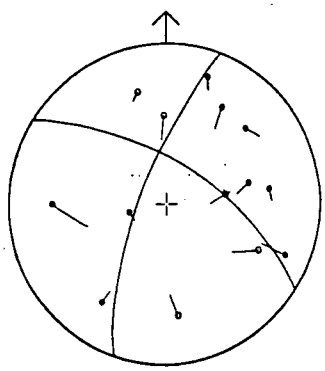

850715 0231

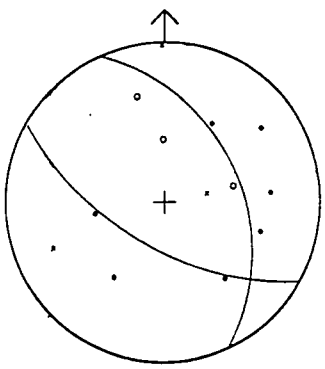

850715 0231

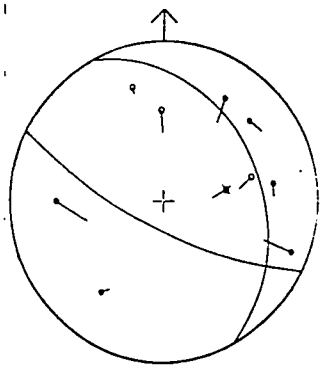

850715 0247

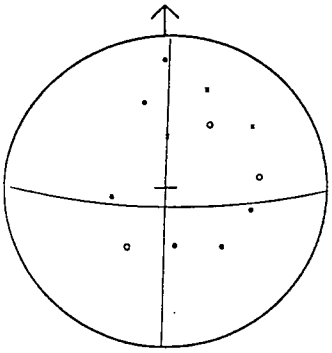

850715 0247

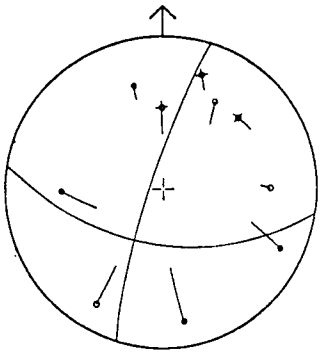

850720 0432

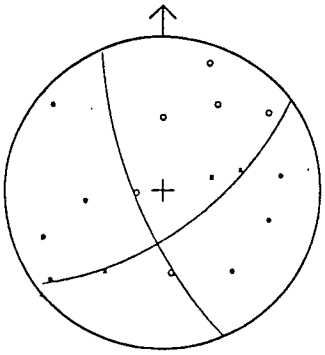

850720 0432

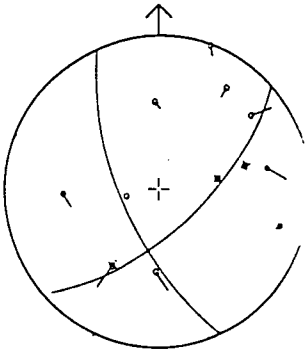

850716 0459

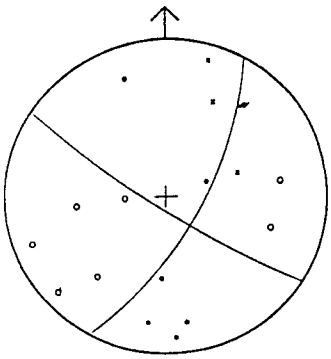

850716 0459

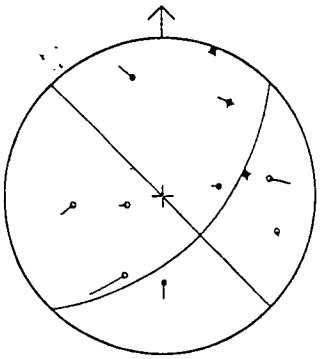

850721 0038

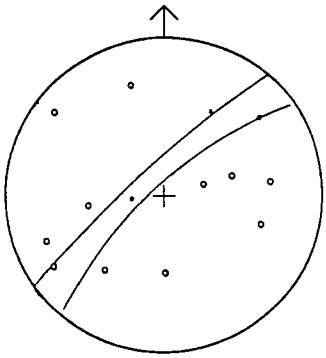

850721 0038

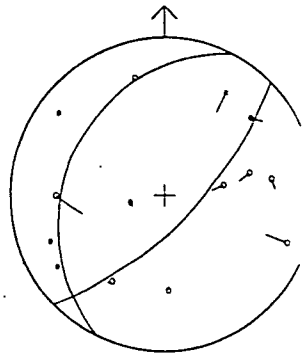

850716 1914

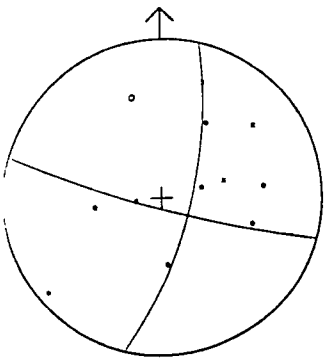

850716 1914

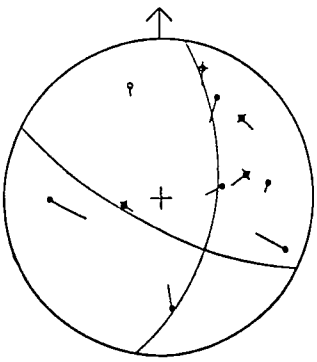

850724 1612

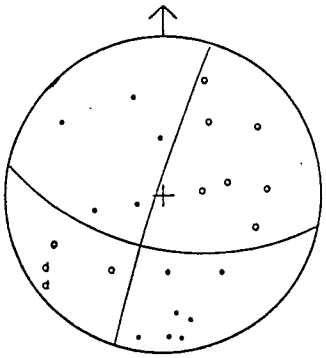

850724 1612

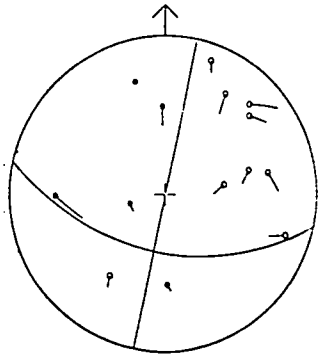

850718 0909

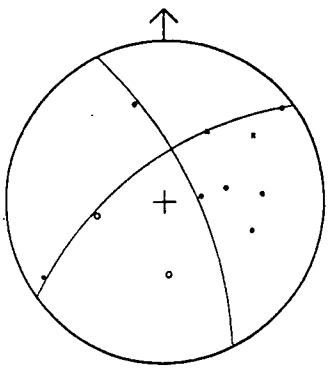

850718 0909

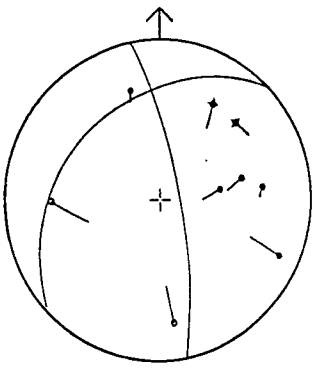

850724 1615

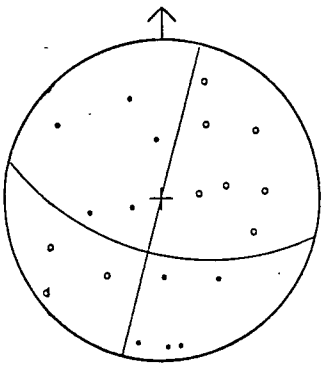

850724 1615

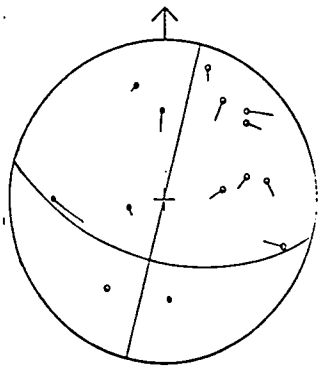

850726 1100

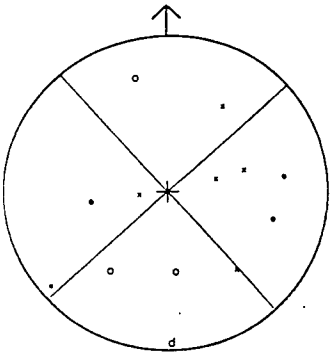

850726 1100

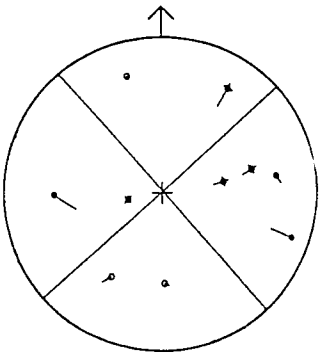

850730 1848

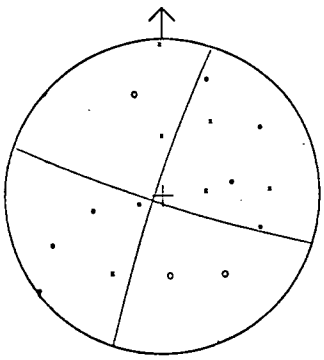

850730 1848

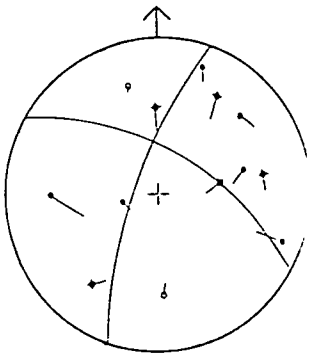

850728 1847

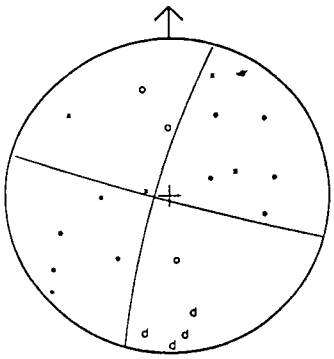

850728 1847

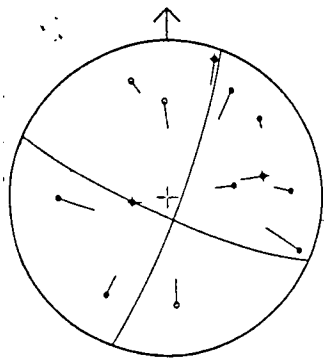

850731 0320

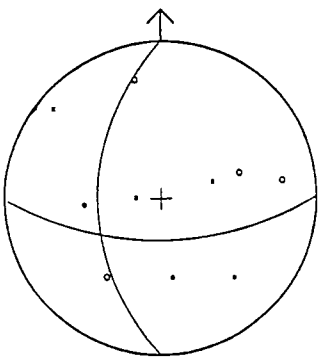

850731 0320

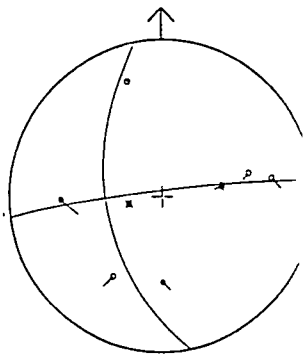

850730 1229

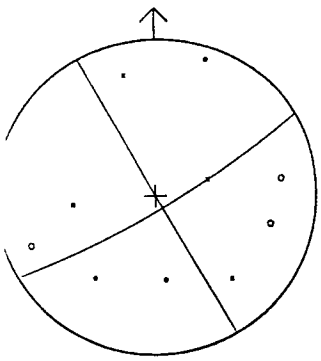

850730 1229

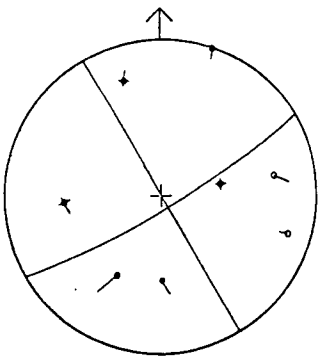

850731 0714

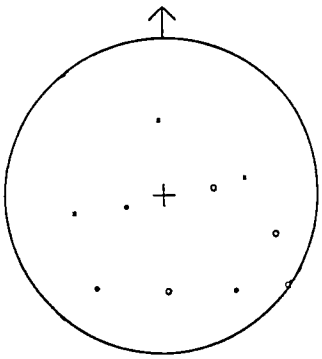

850731 0714

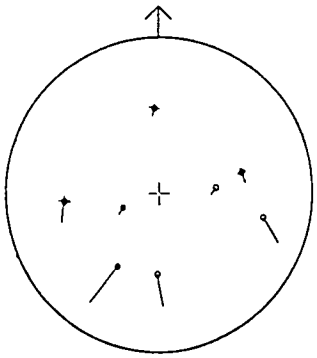

850730 1752

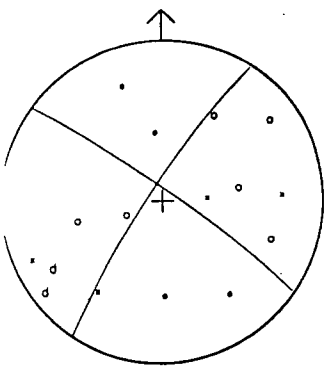

850730 1752

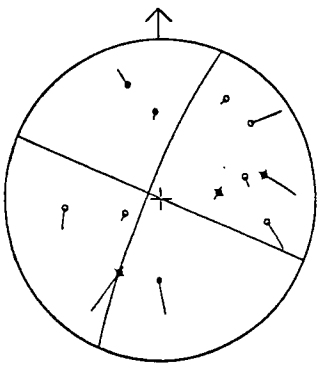

850731 0822

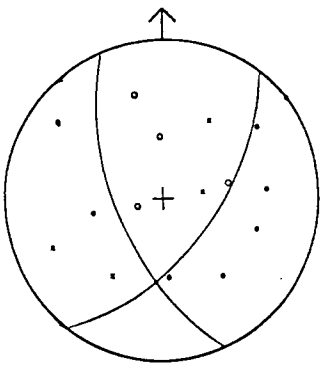

850731 0822

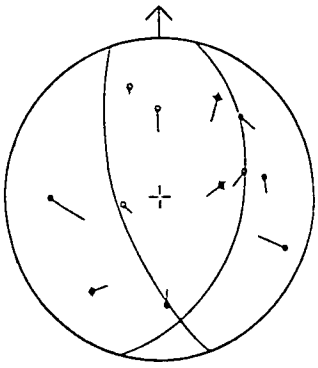

850731 1648

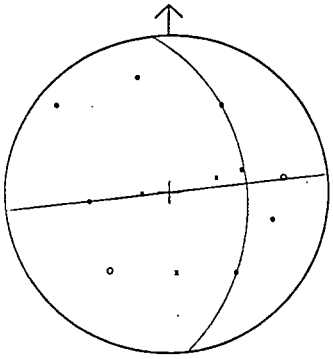

850731 1648

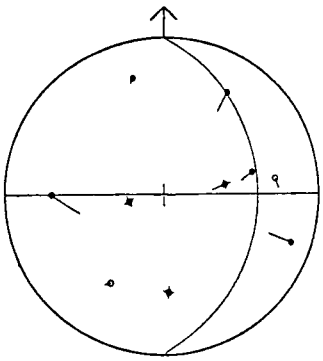

850804 1217

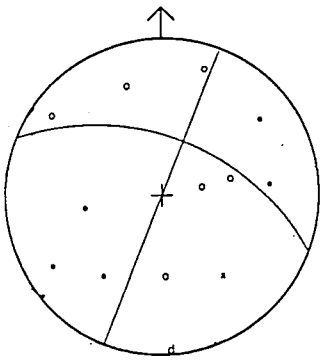

850804 1217

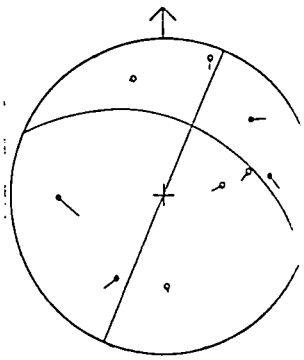

850801 0854

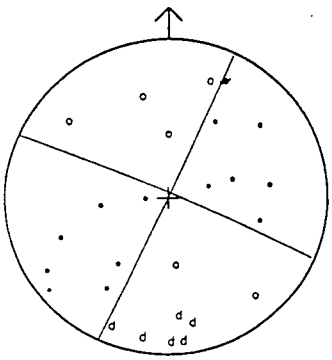

850801 0854

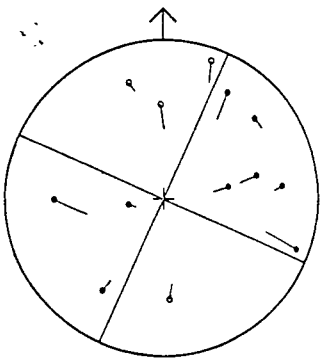

850806 1548

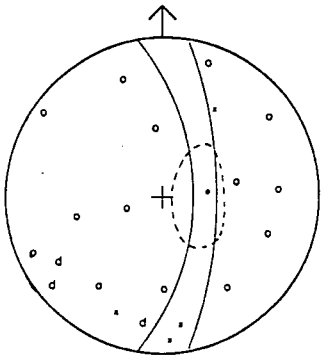

850806 1548

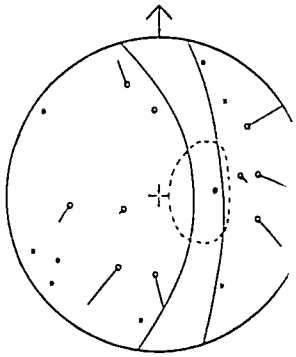

850803 1837

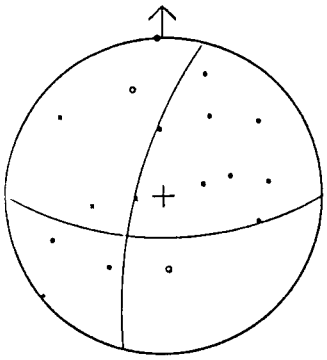

850803 1837

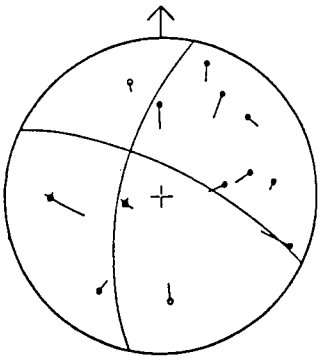

850809 0953

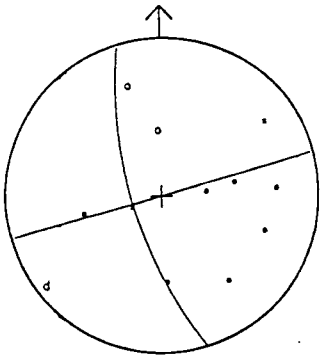

850809 0953

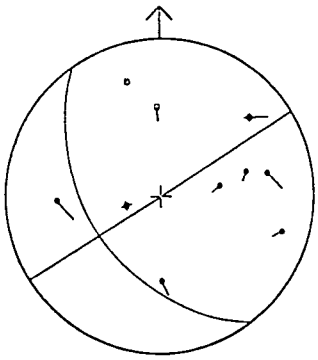

850804 1011

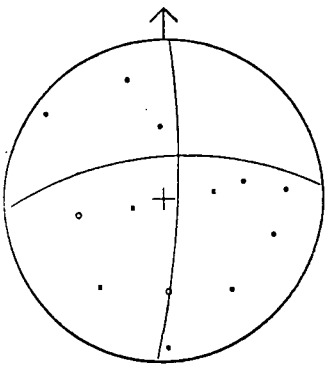

850804 1011

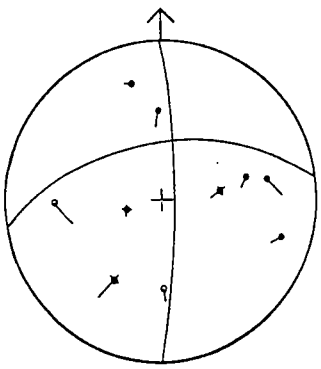

850809 2059

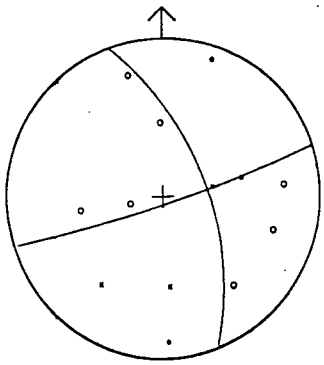

850809 2059

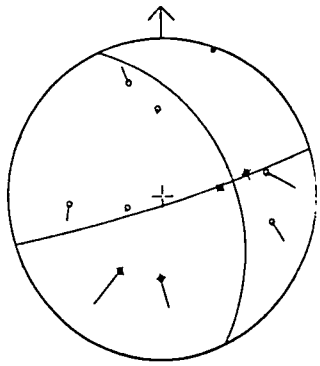

850814 1201

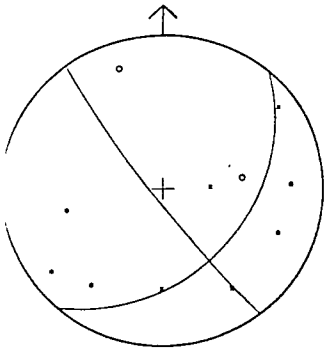

850814 1201

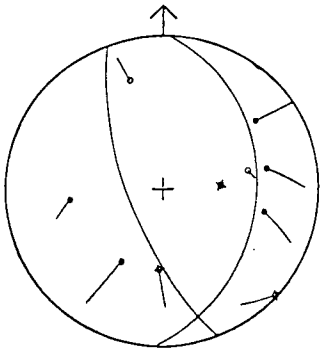

850815 1319

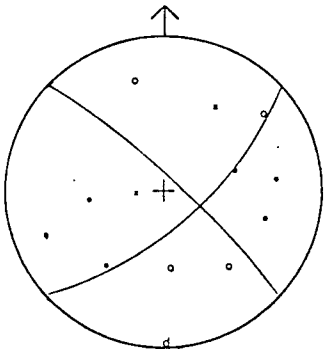

850815 1319

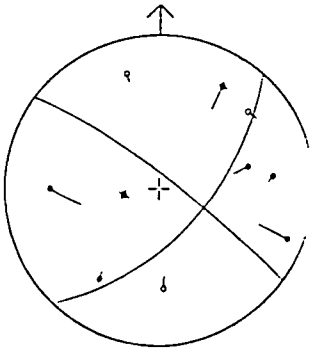

850814 1838

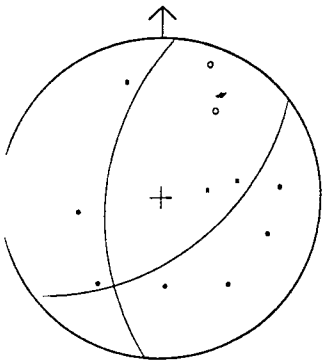

850814 1838

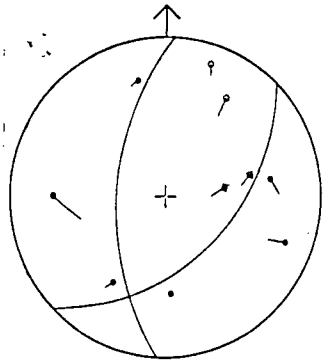

850818 0429

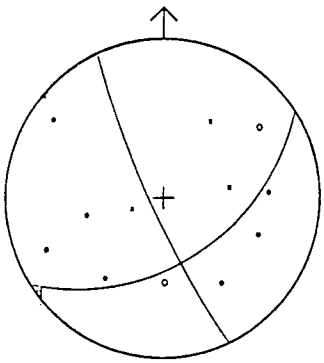

850818 0429

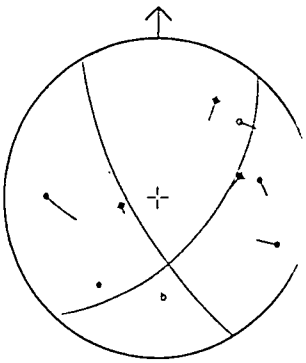

850815 0810

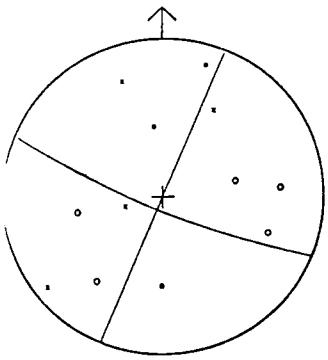

850815 0810

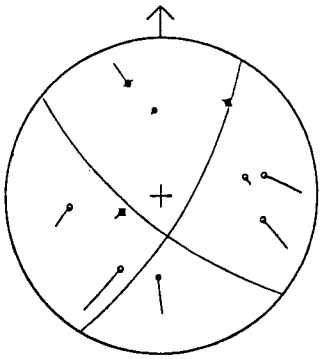

850819 0004

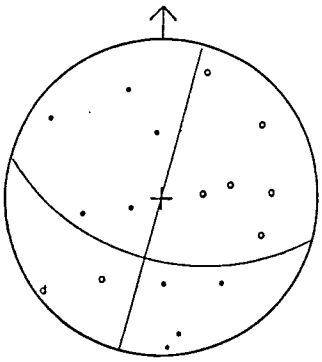

850819 0004

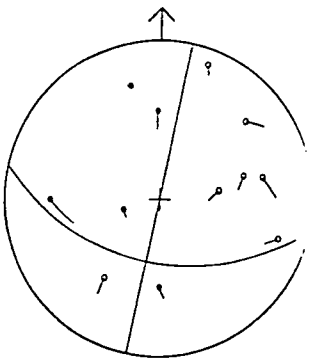

850815 1102

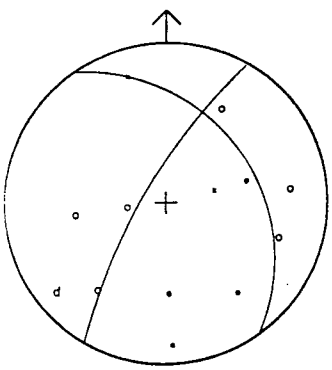

850815 1102

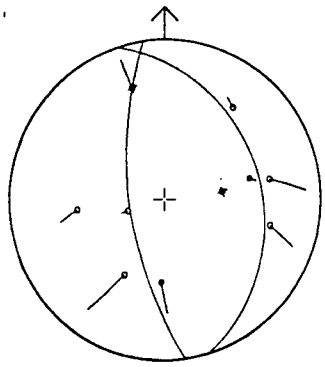

850823 1045

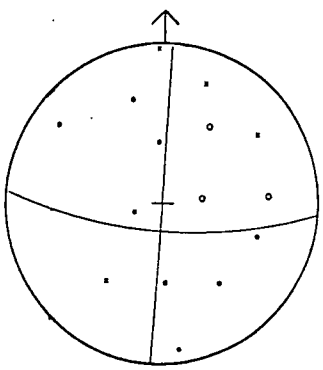

850823 1045

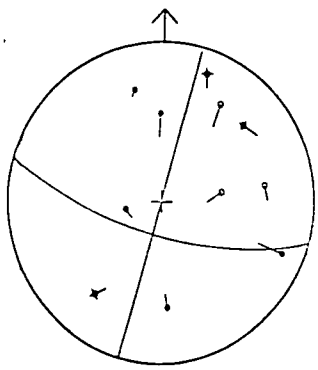

850824 1059

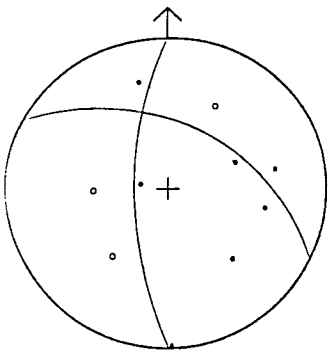

850824 1059

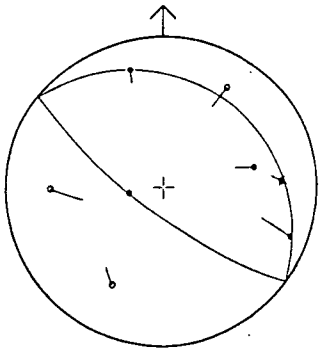

850828 0120

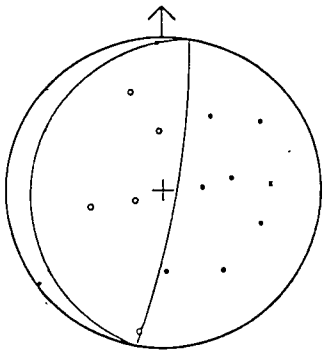

850828 0120

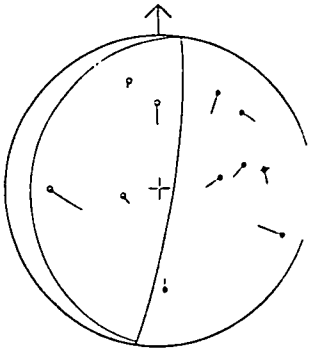

850824 1123

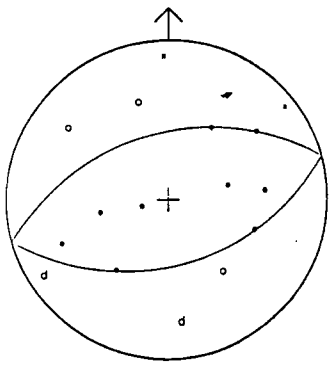

850824 1123

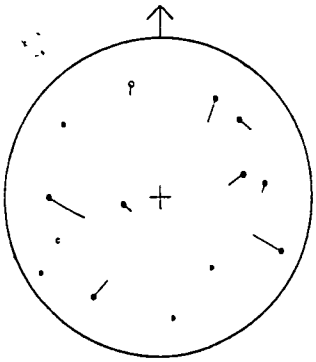

850829 1015

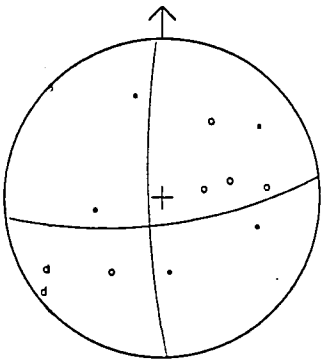

850829 1015

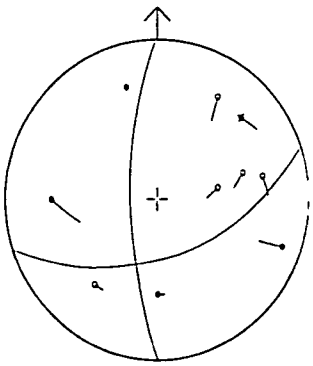

850826 0539

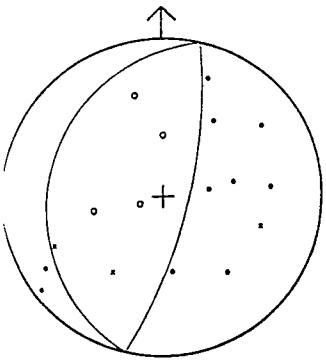

850826 0539

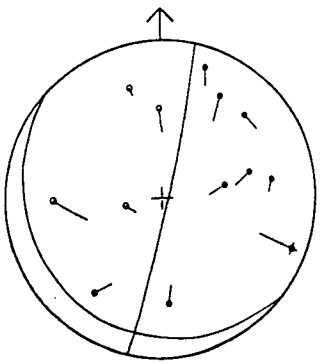

850831 1349

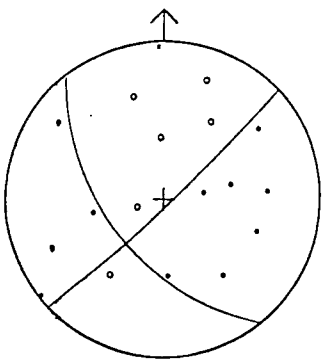

850831 1349

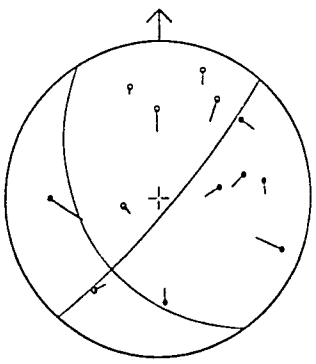

850827 1721

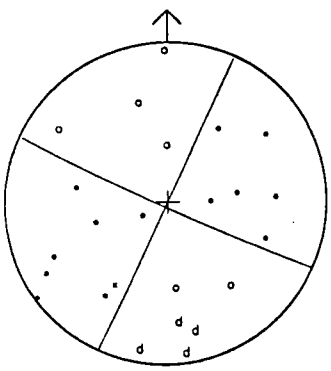

850827 1721

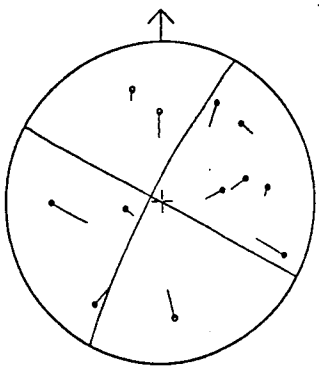

850831 1407

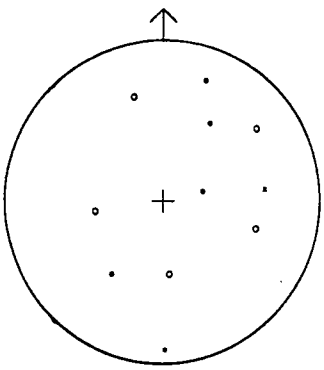

850831 1407

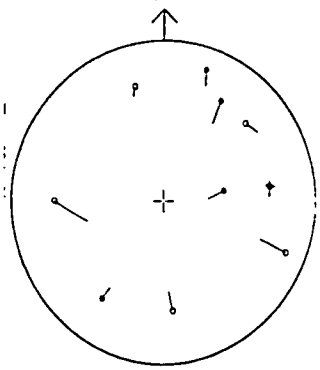

850902 0145

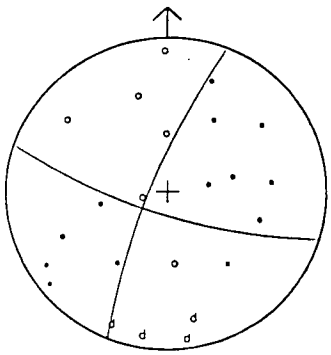

850902 0145

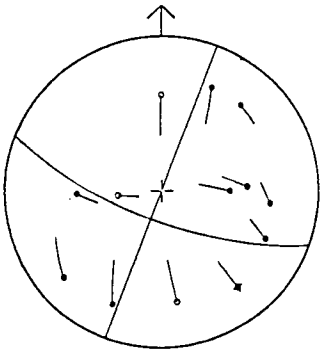

850906 2322

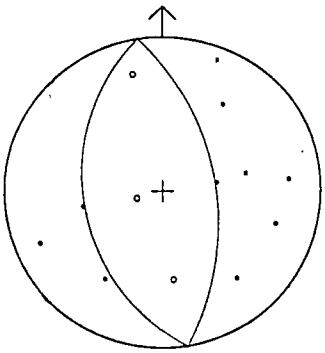

850906 2322

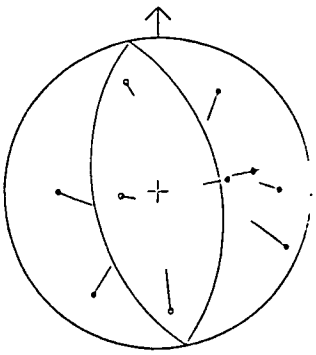

850902 2149

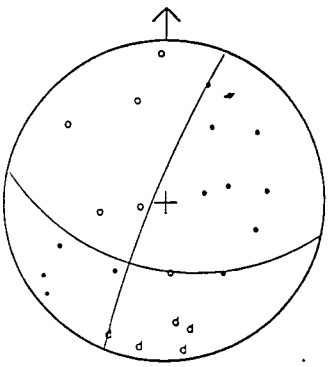

850902 2149

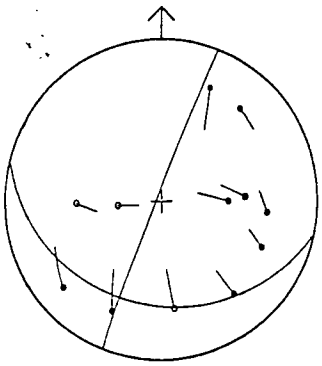

850908 0737

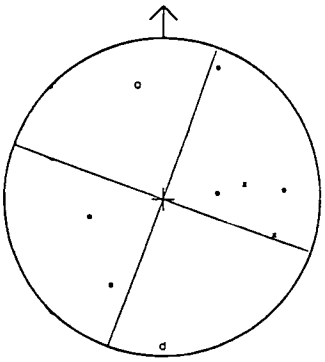

850908 0737

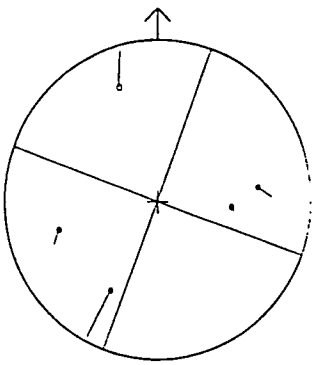

850905 0001

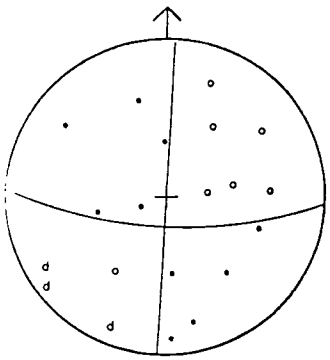

850905 0001

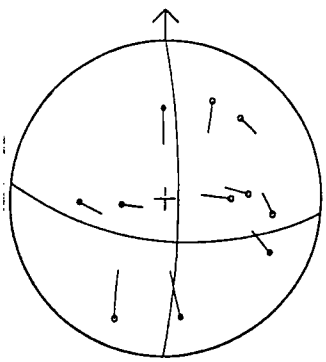

850908 0921

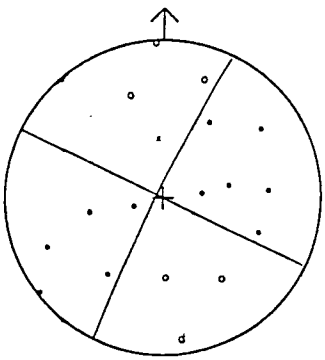

850908 0921

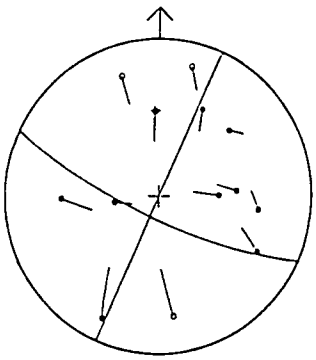

850905 1159

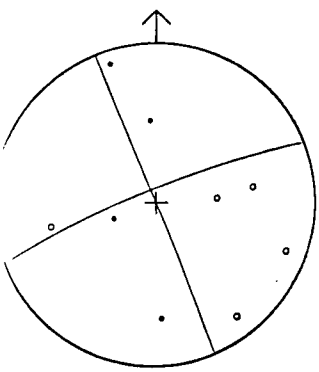

850905 1159

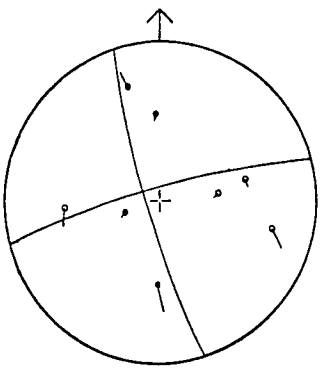

850908 1045

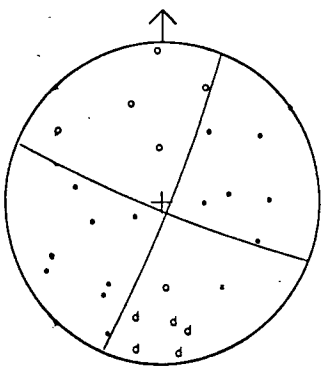

850908 1045

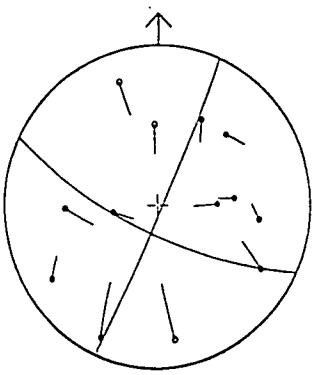

850910 1343

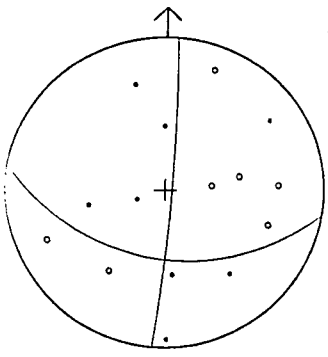

850910 1343

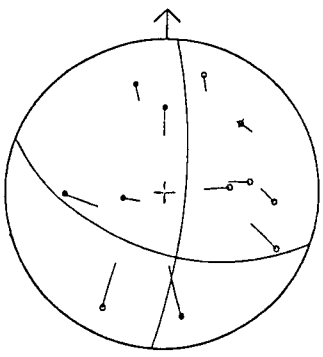

850914 1209

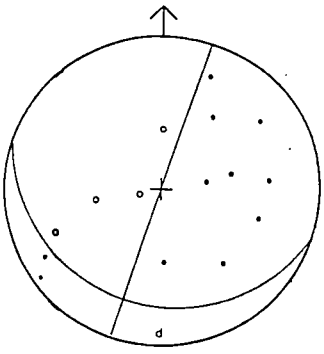

850914 1209

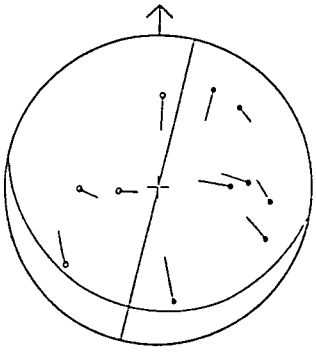

850910 1650

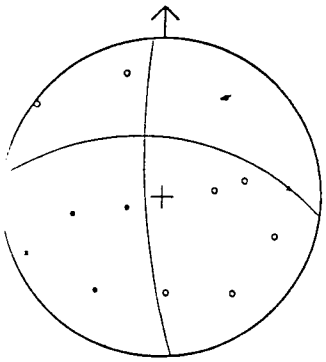

850910 1650

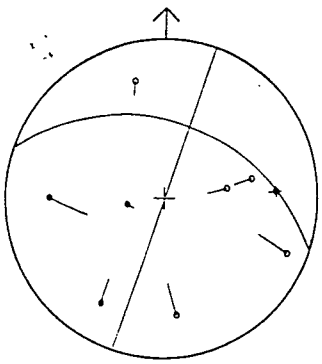

850916 1734

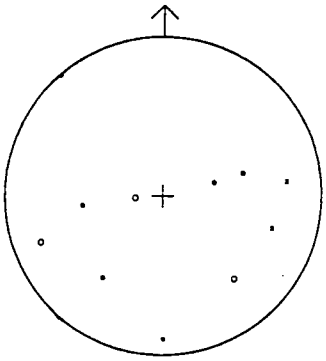

850916 1734

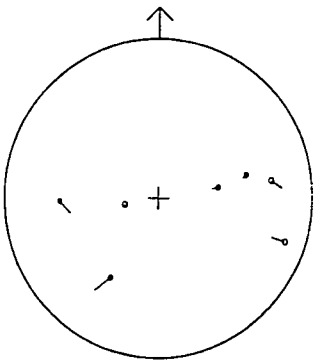

850911 0659

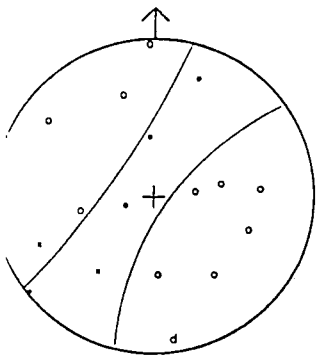

850911 0659

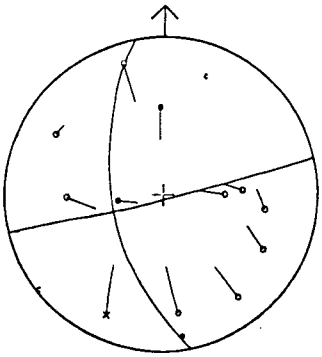

850917 1130

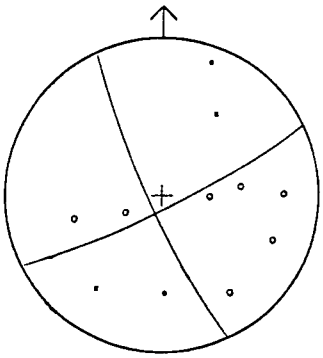

850917 1130

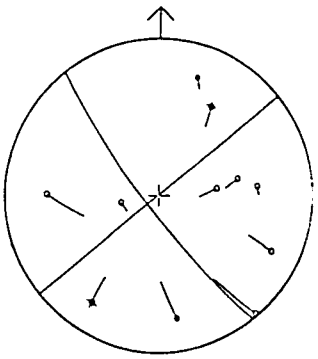

850911 1641

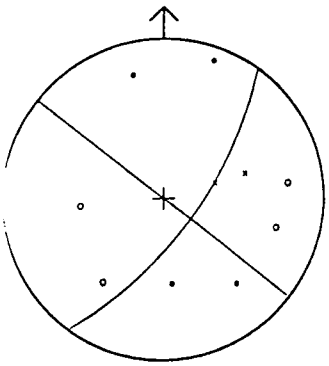

850911 1641

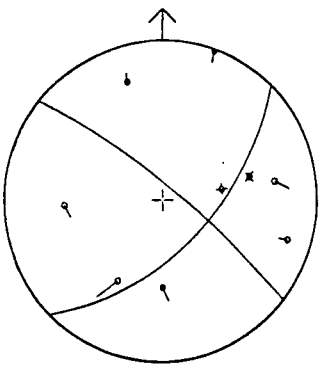

850920 0050

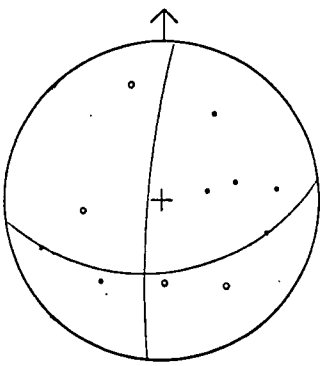

850920 0050

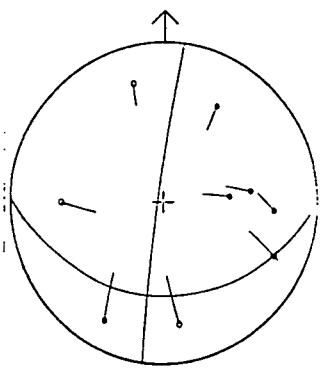

850920 0717

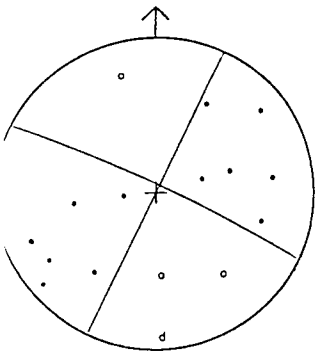

850920 0717

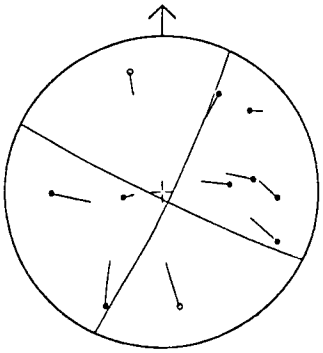

850922 1715

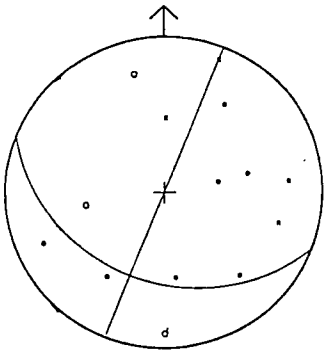

850922 1715

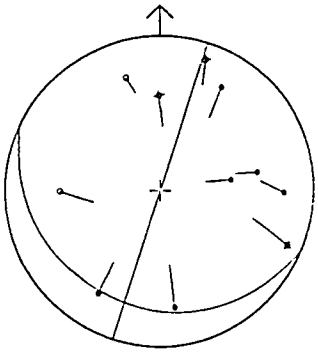

850920 2019

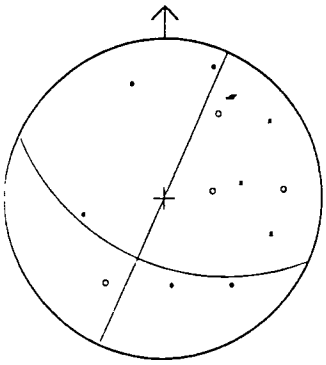

850920 2019

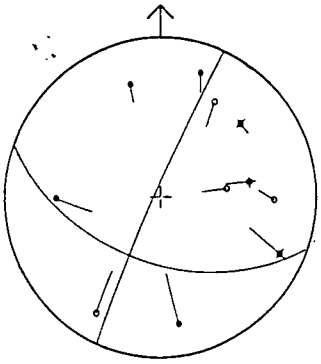

850923 0423

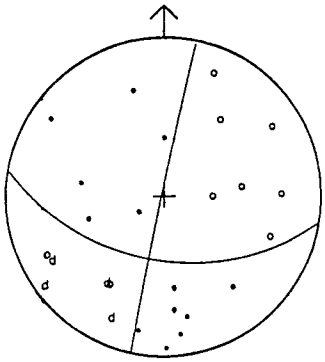

850923 0423

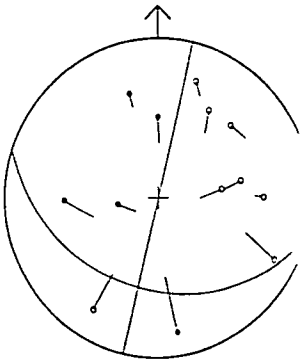

850921 0806

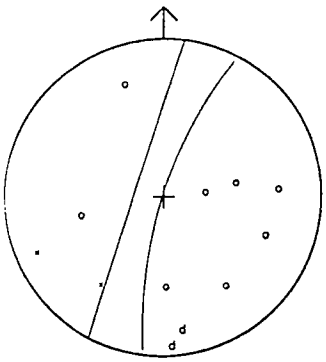

850921 0806

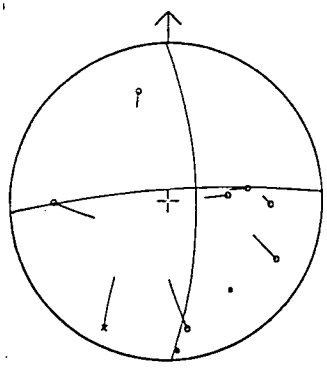

850923 0433

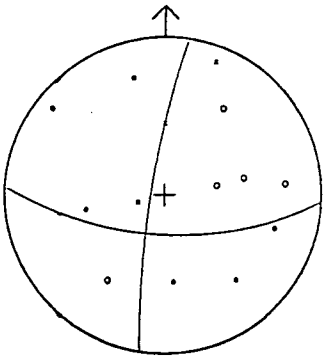

850923 0433

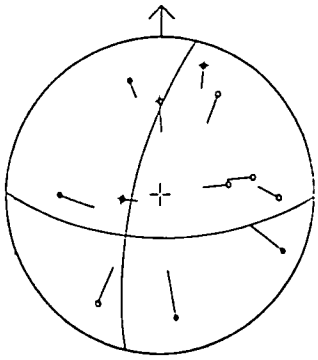

850921 2209

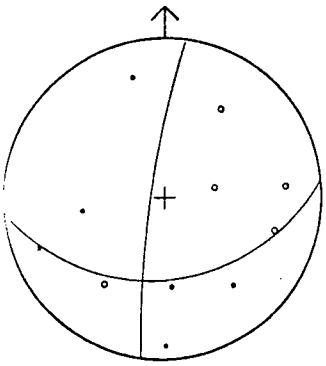

850921 2209

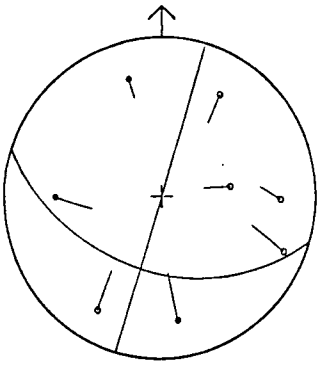

850923 0727

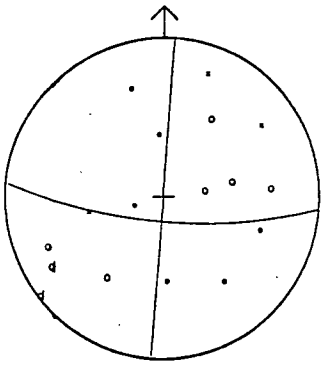

850923 0727

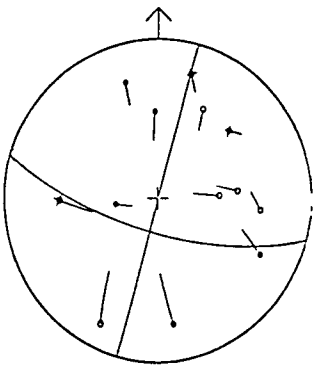

850924 0432

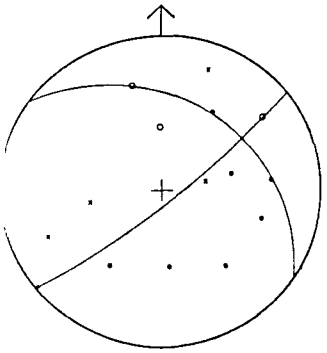

850924 0432

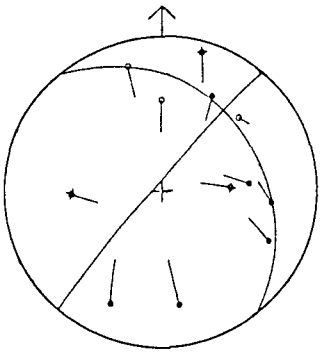

850927 0700

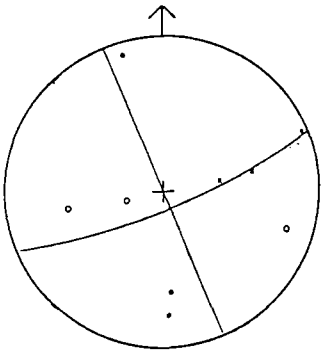

850927 0700

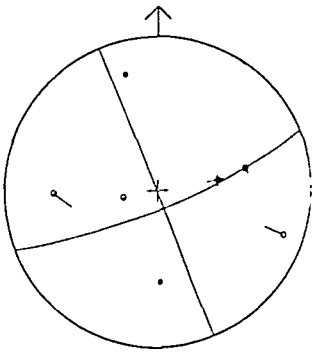

850925 0211

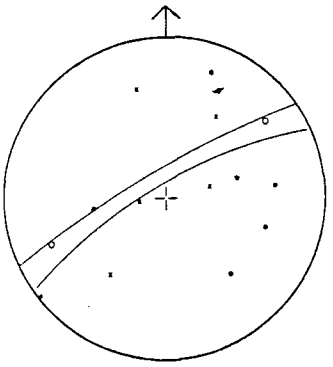

850925 0211

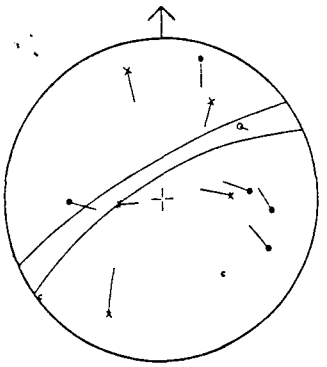

850928 1431

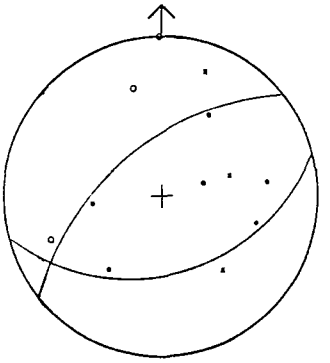

850928 1431

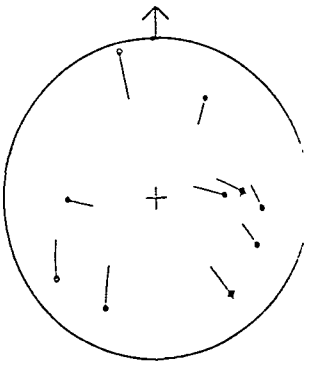

850925 0306

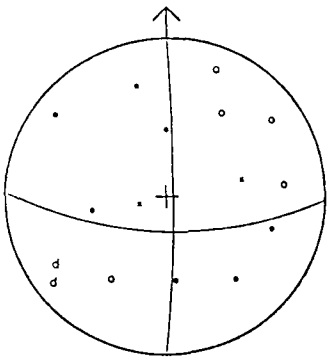

850925 0306

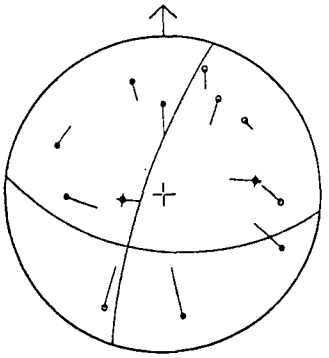

850929 0508

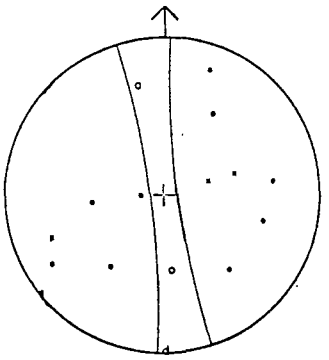

850929 0508

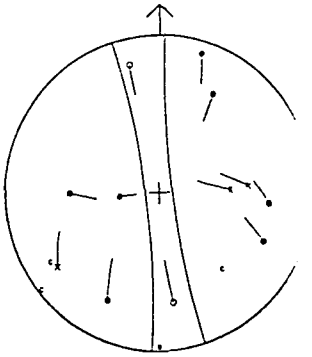

850927 0641

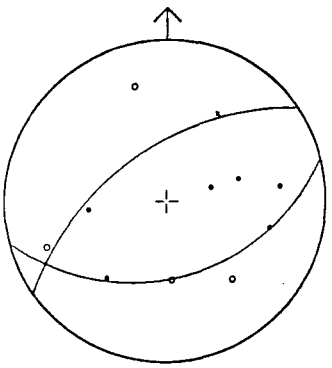

850927 0641

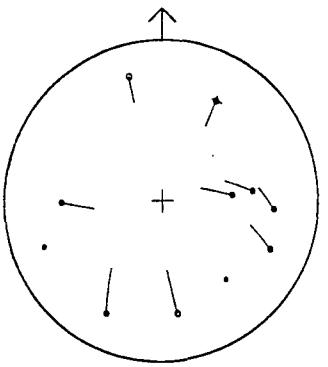

850930 2314

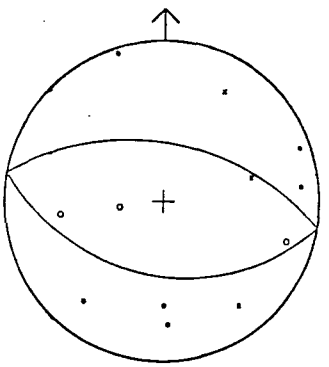

850930 2314

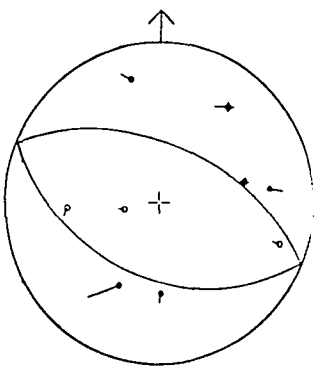

E.2 Fissure Zone Focal Mechanisms

850709 2200

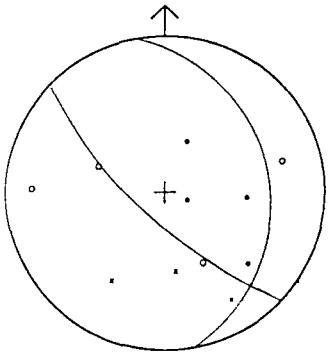

850709 2200

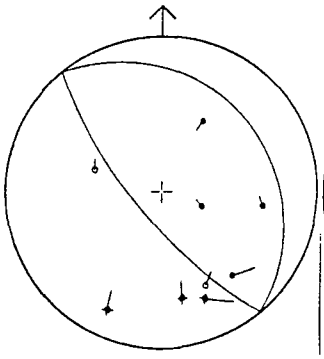

850717 1734

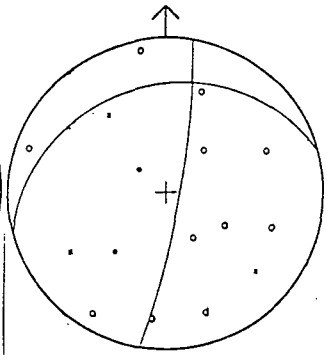

850717 1734

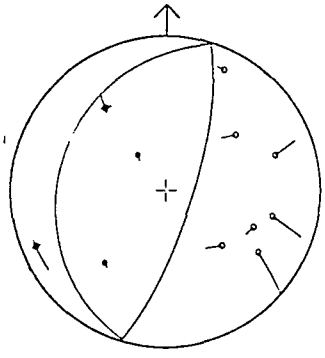

850711 0558

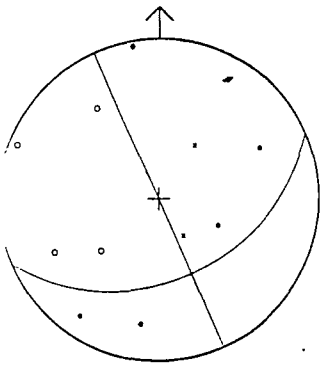

850711 0558

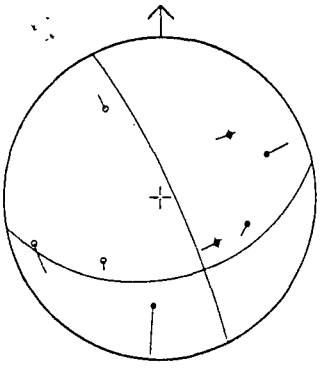

850719 0540

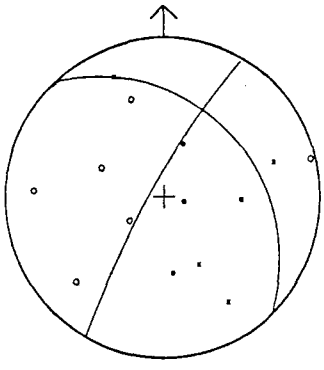

850719 0540

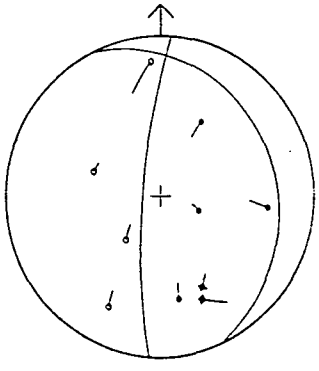

850712 2231

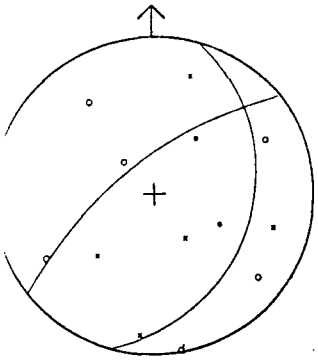

850712 2231

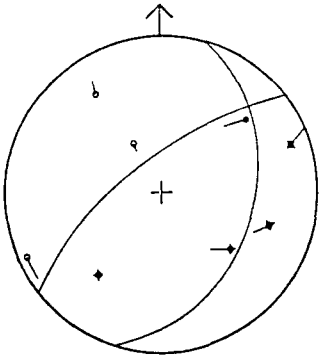

850719 0746

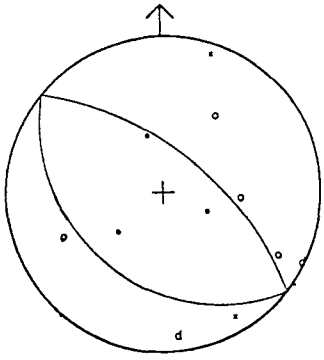

850719 0746

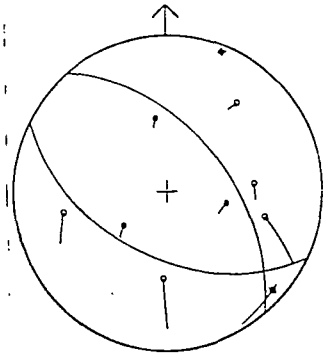

850716 1010

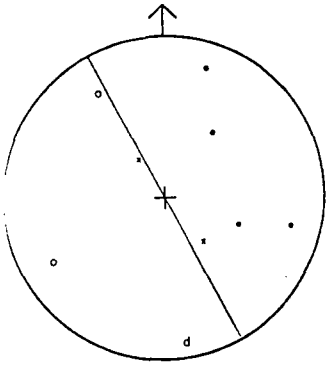

850716 1010

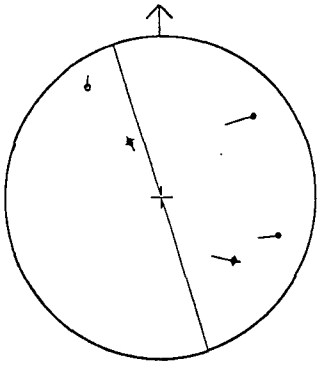

850727 2015

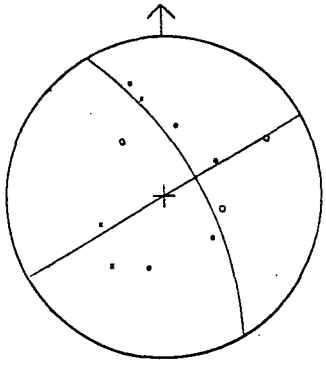

850727 2015

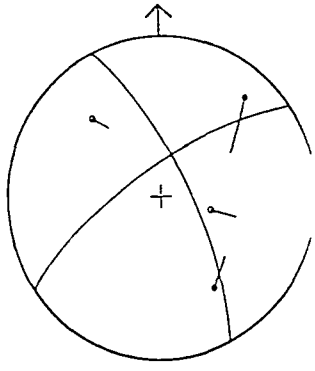

850728 0911

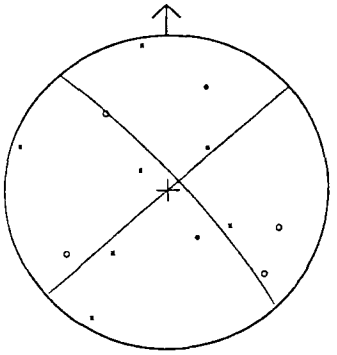

850728 0911

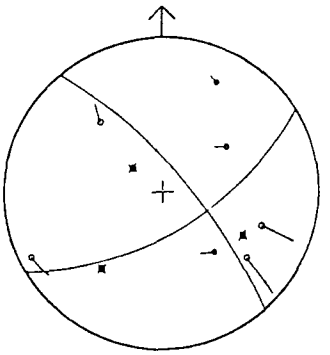

850803 0948

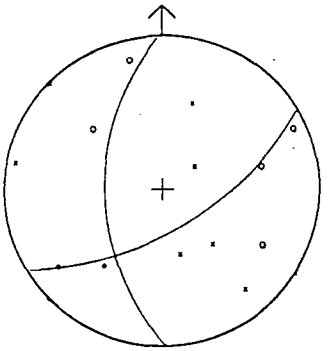

850803 0948

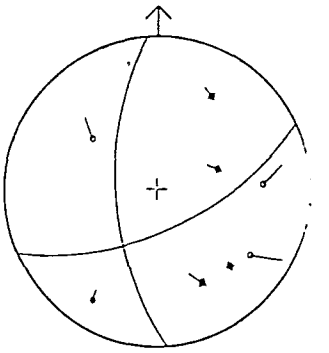

0731 0620

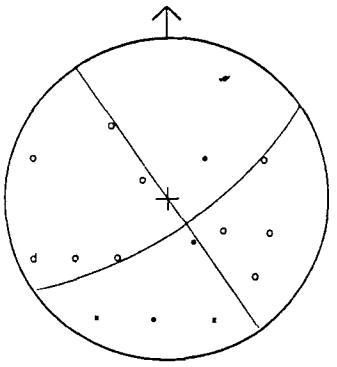

850731 0620

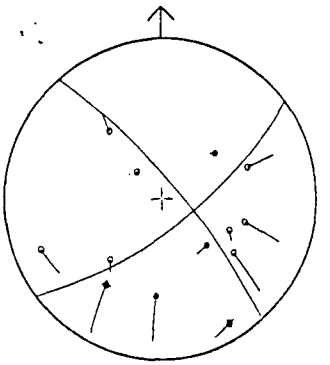

850803 2325

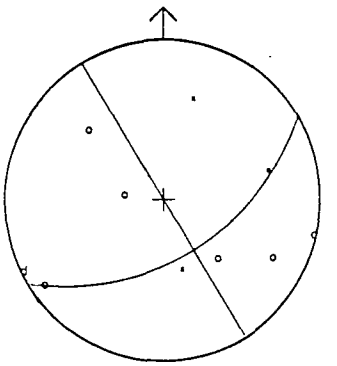

850303 2325

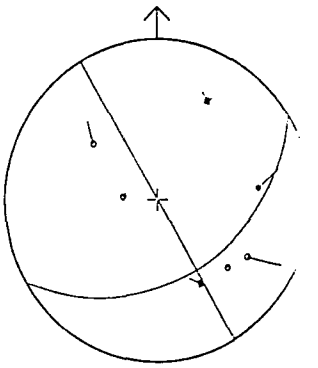

850801 0414

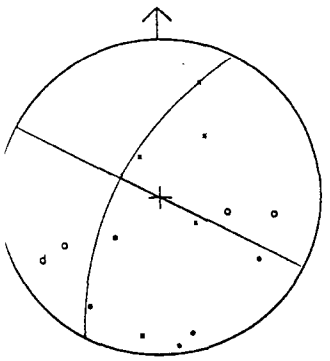

850801 0414

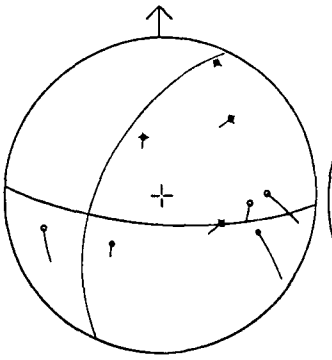

850806 0843

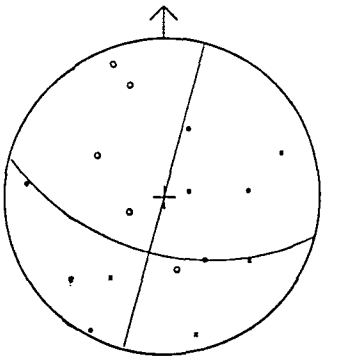

850806 0843

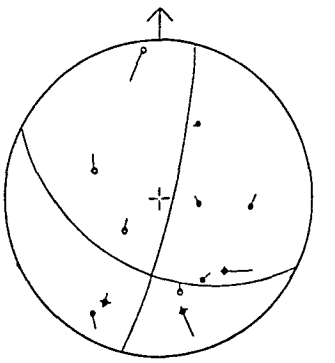

850801 1256

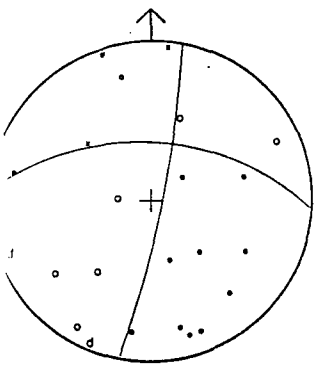

850801 1256

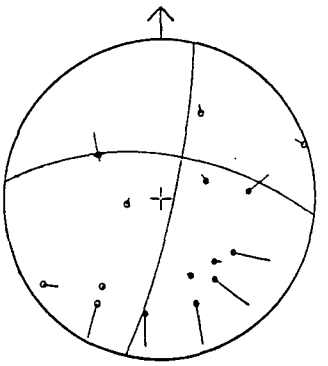

850815 1514

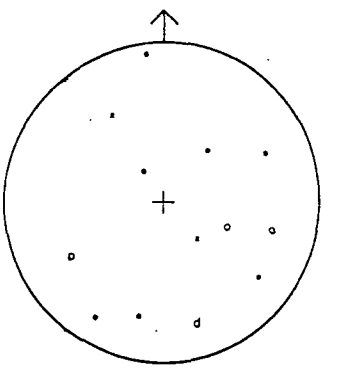

850815 1514

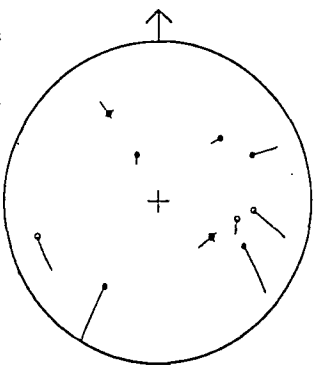

850820 0513

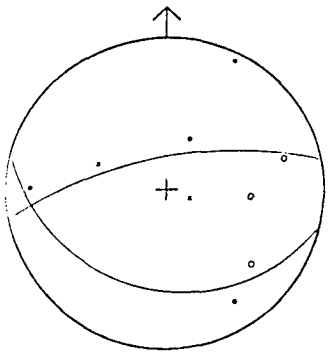

850820 0513

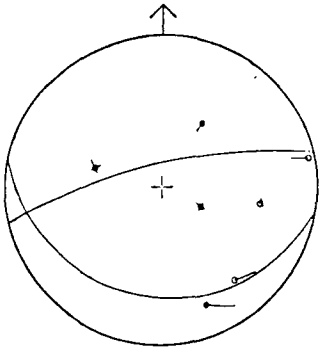

850831 1137

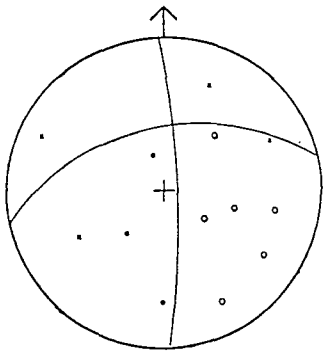

850831 1137

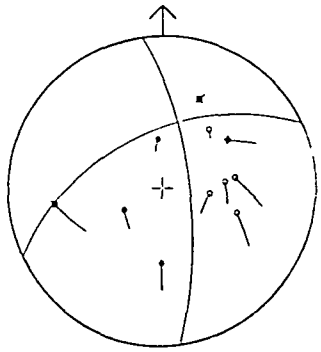

850823 1301

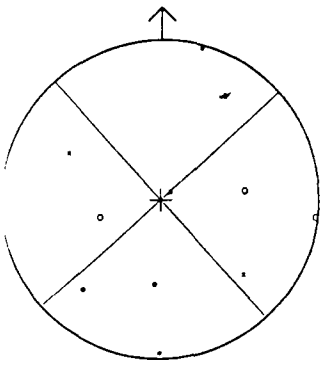

850823 1301

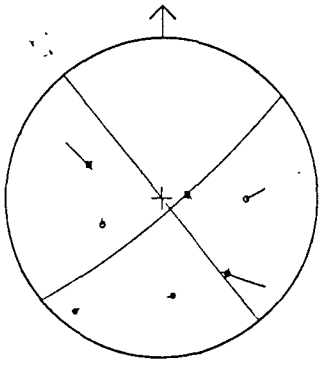

850907 1914

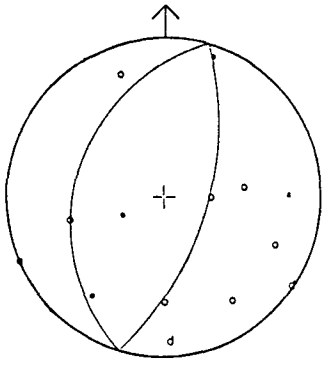

850907 1914

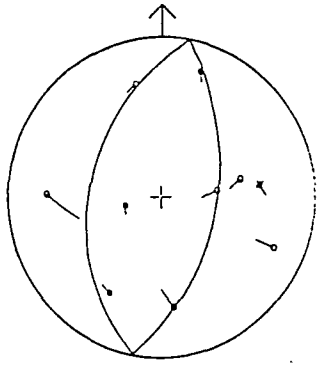

850824 1746

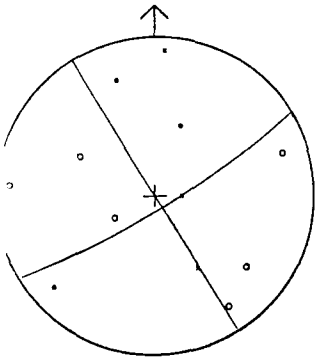

850824 1746

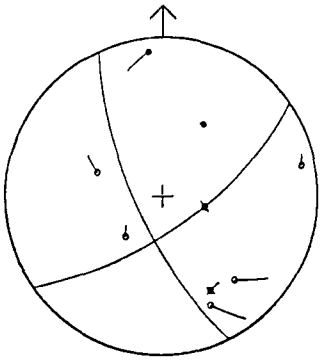

850908 0042

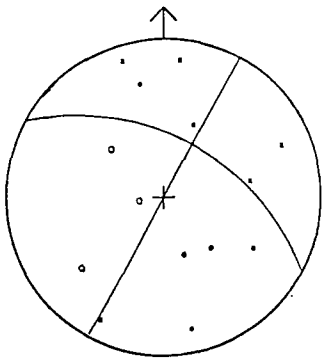

850908 0042

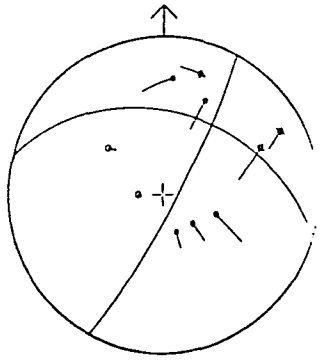

850831 0029

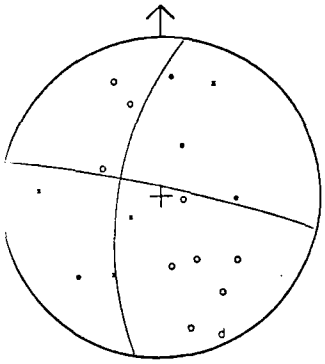

850831 0029

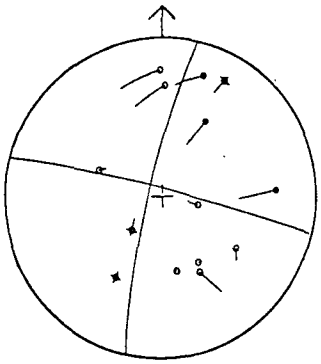

850908 1716

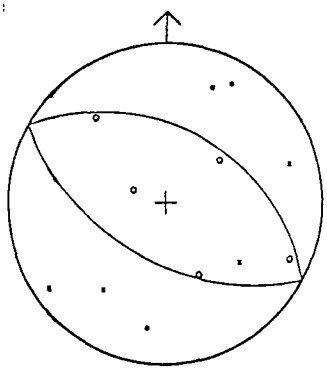

850908 1716

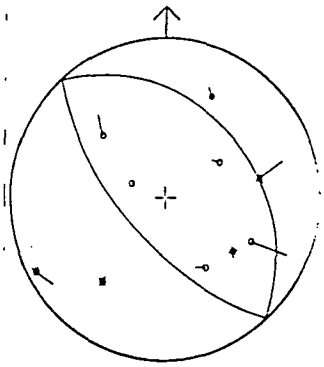

850909 2231

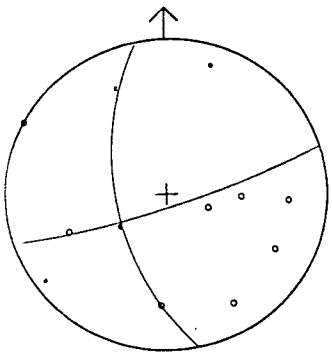

850909 2231

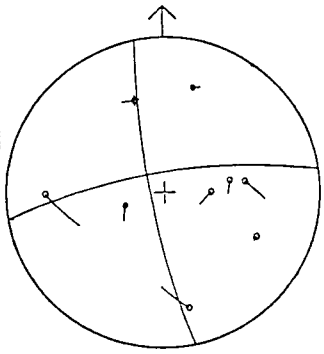

850912 0256

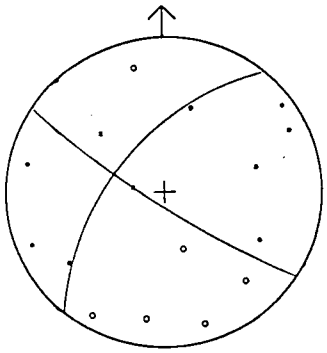

850912 0256

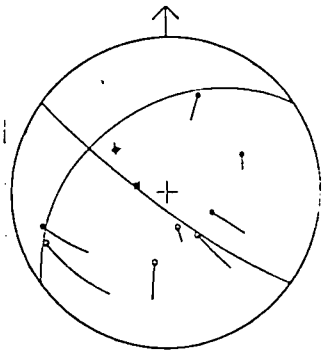

850910 0651

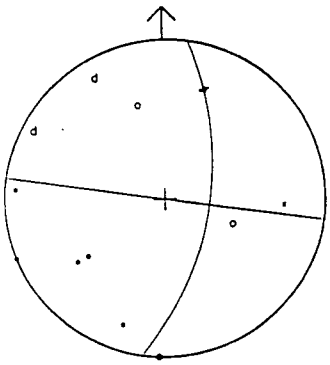

850910 0651

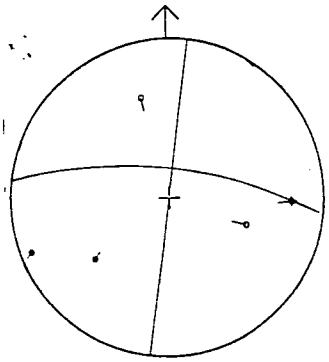

850915 0052

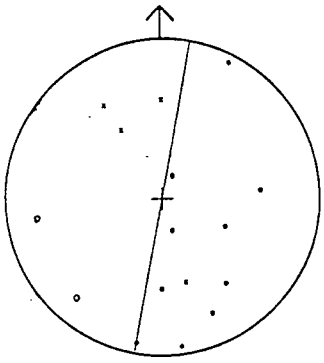

850915 0052

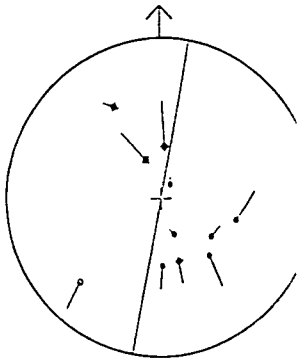

850910 1504

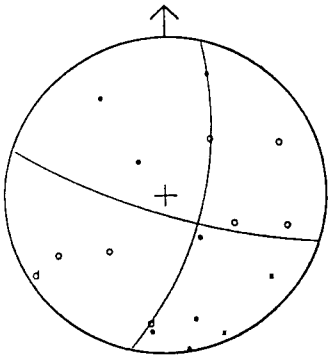

850910 1504

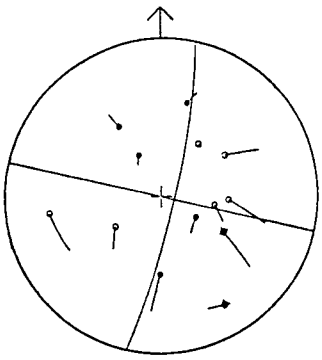

850915 2150

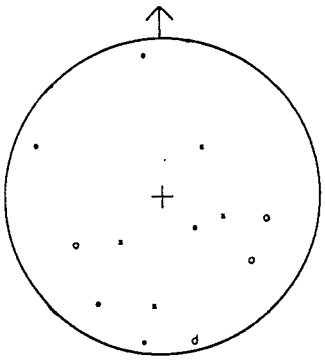

850915 2150

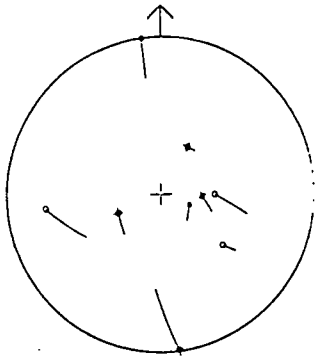

850911 0120

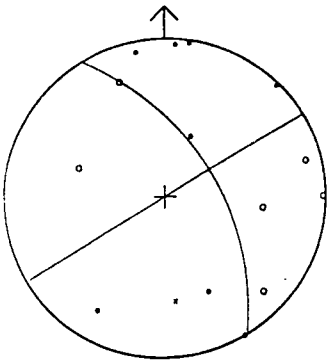

850911 0120

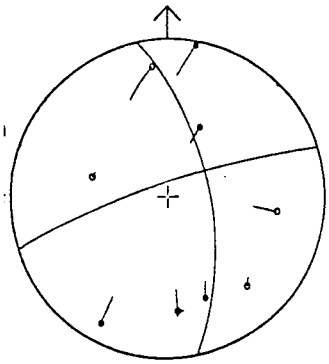

850916 1447

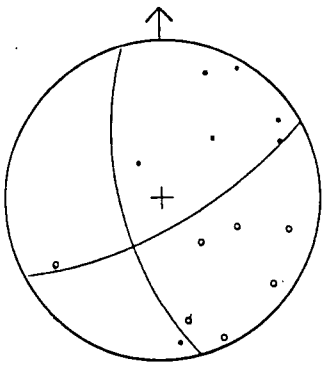

850916 1447

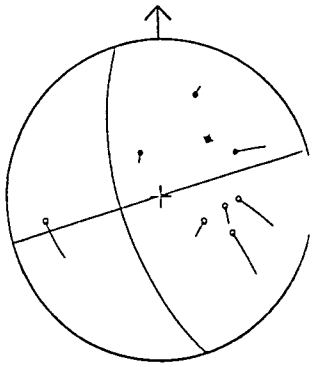

850916 1504

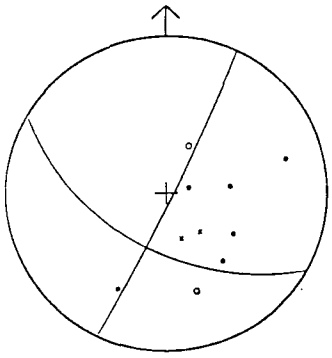

850916 1504

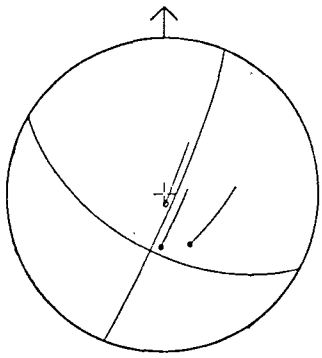

850925 2213

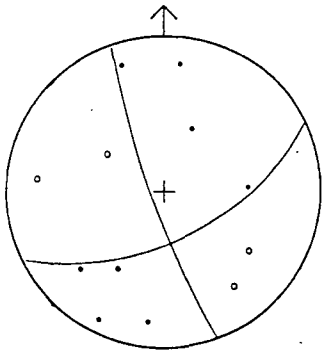

850925 2213

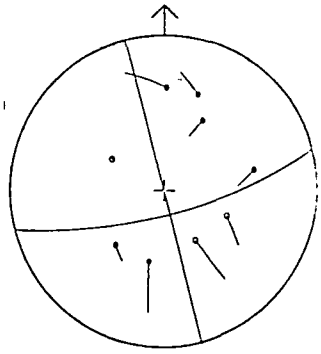

850919 0228

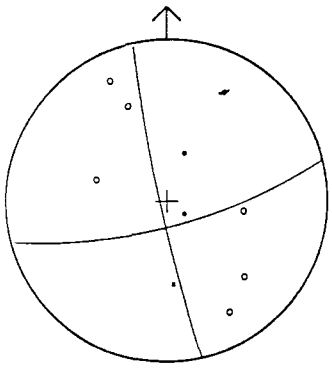

850919 0228

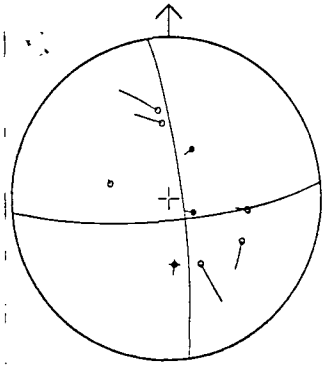

850928 1007

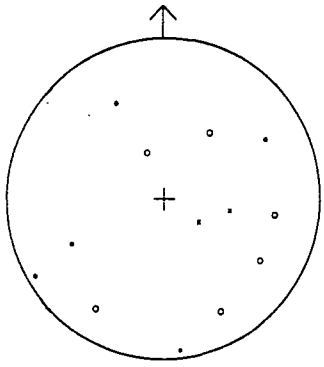

850928 1007

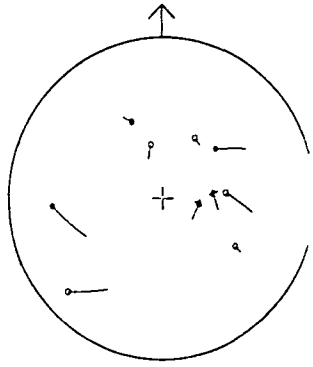

850919 0631

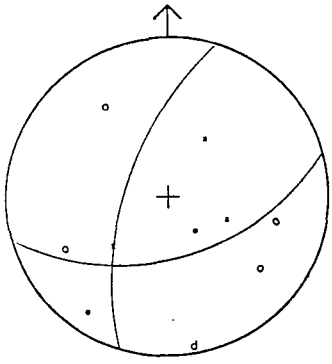

850919 0631

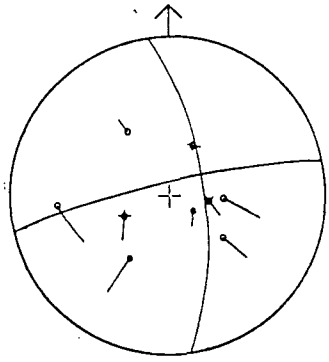

850929 1050

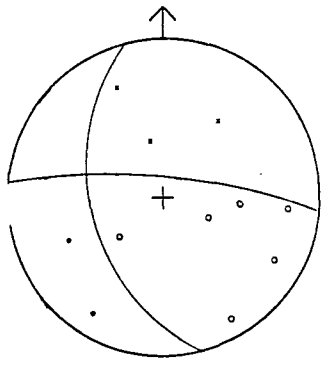

850929 1050

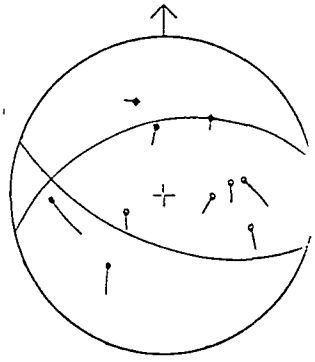

850921 1858

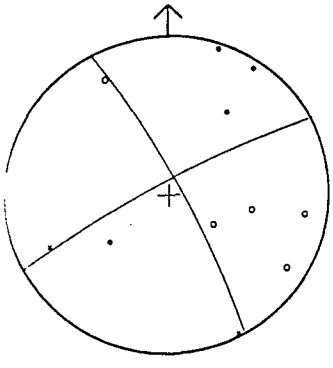

850921 1858

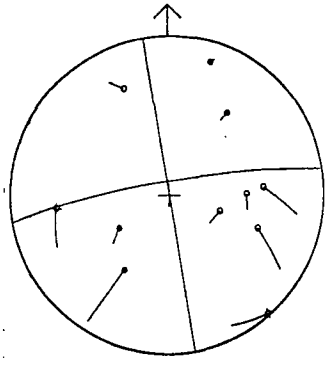

850929 2340

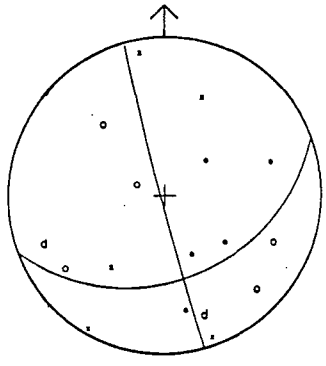

850929 2340

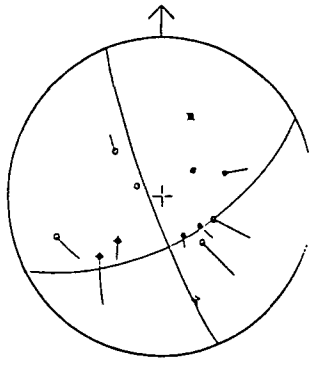

E.3 Leirhnjúkur Focal Mechanisms

850702 1152

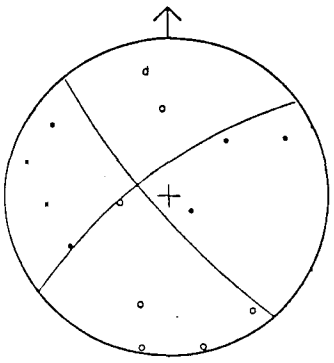

850702 1152

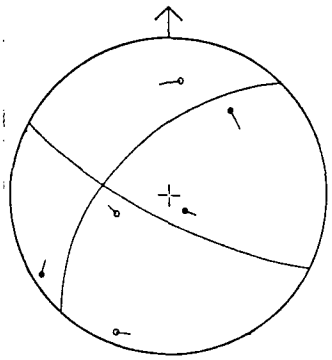

850708 0402

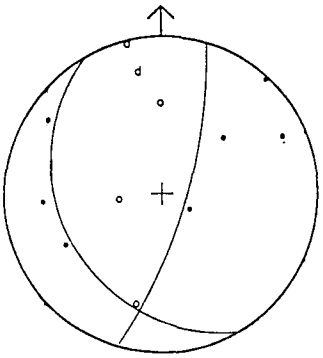

850708 0402

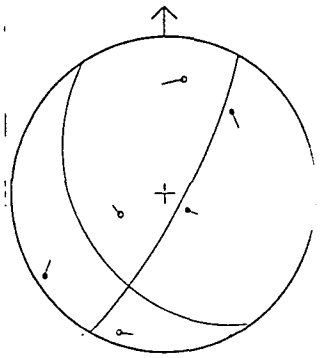

850703 1435

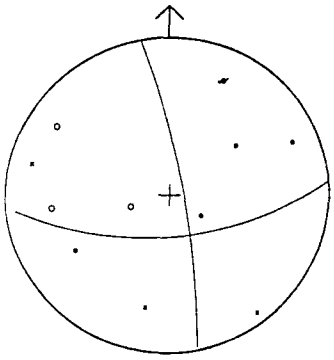

850703 1435

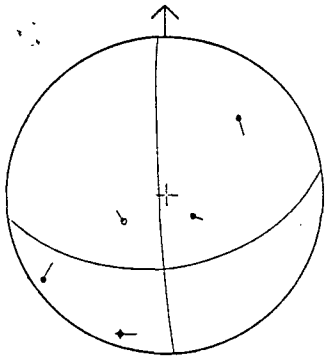

850716 0758

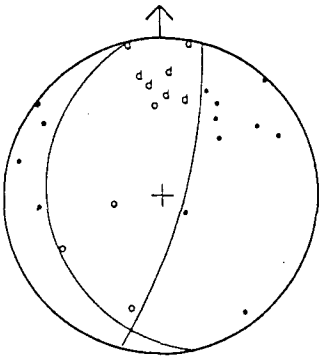

850716 0758

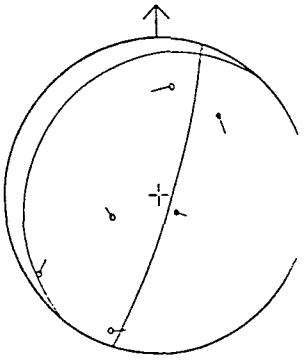

850704 0852

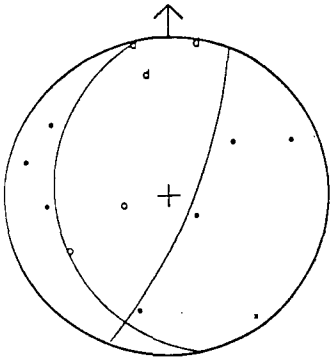

850704 0852

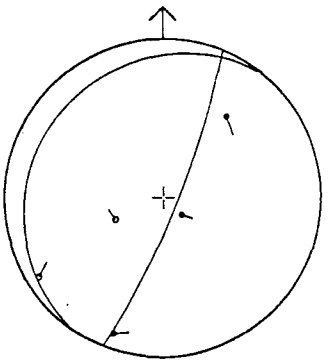

850726 0556

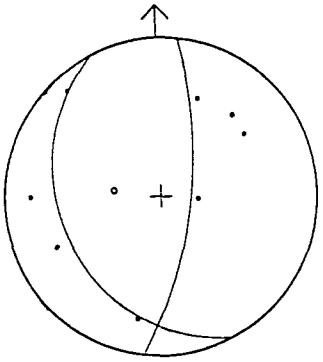

850726 0556

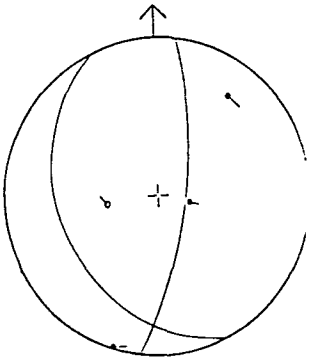

850704 1144

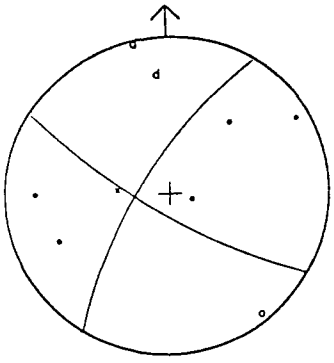

850704 1144

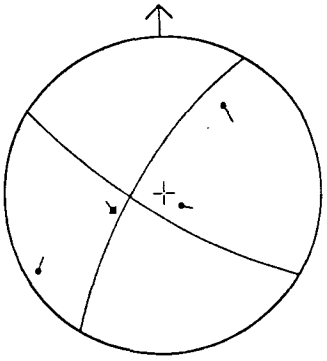

850729 1108

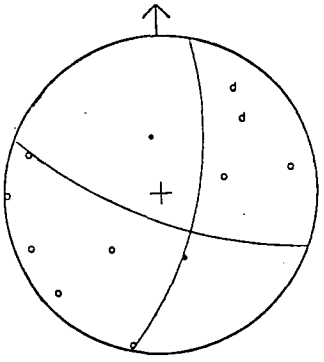

850729 1108

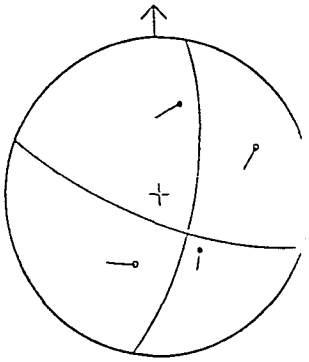

850801 1218

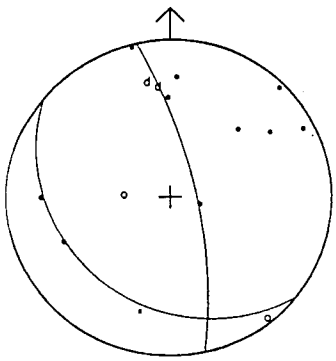

850801 1218

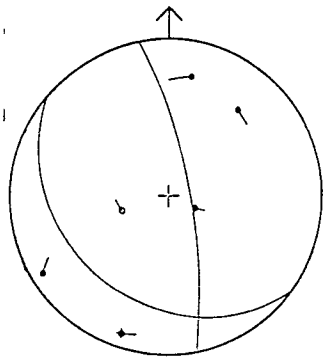

850805 0109

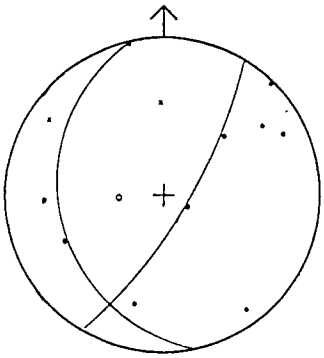

850805 0109

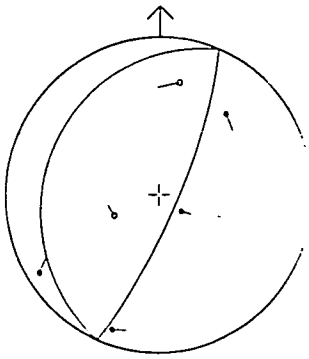

850801 1227

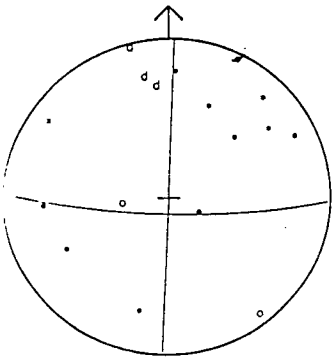

850801 1227

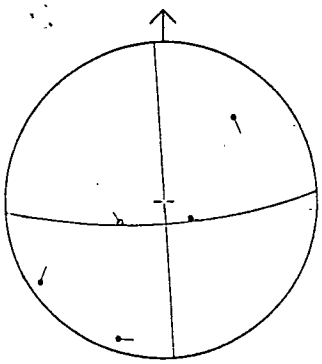

850806 1614

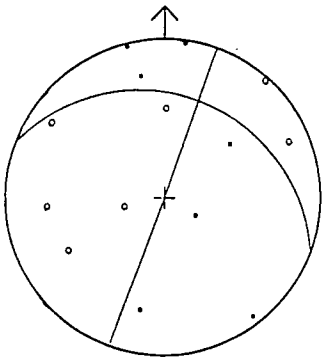

850806 1614

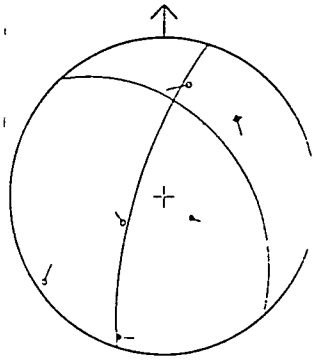

850802 0055

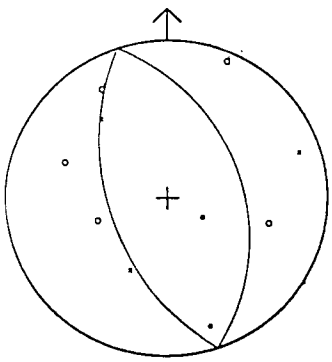

850802 0055

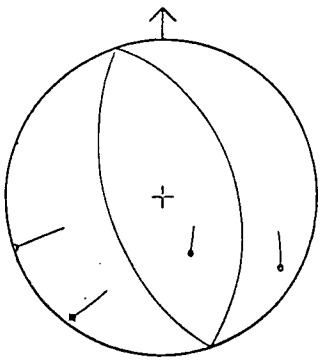

850807 1833

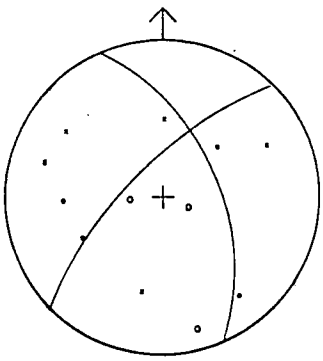

850807 1833

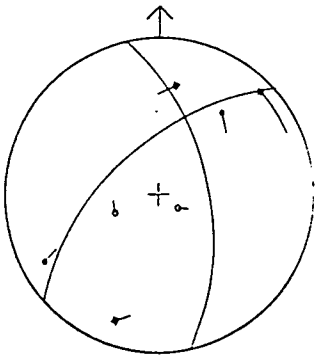

850804 2131

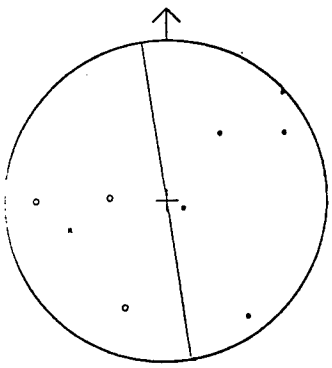

850804 2131

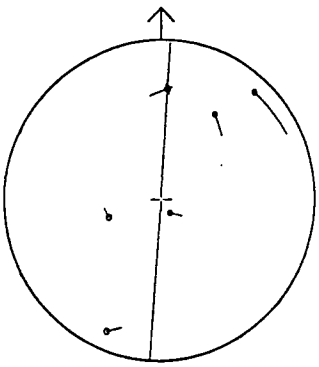

850809 0756

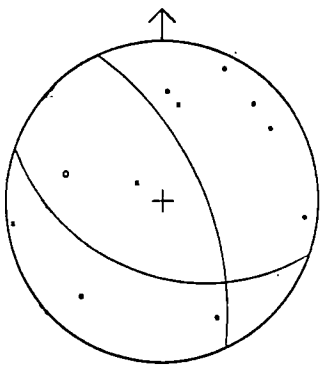

850809 0756

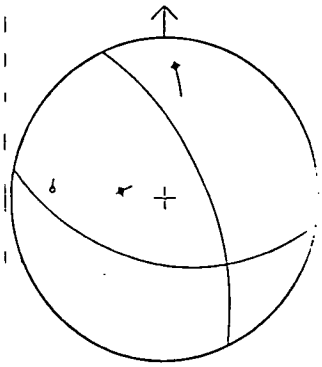

850813 1328

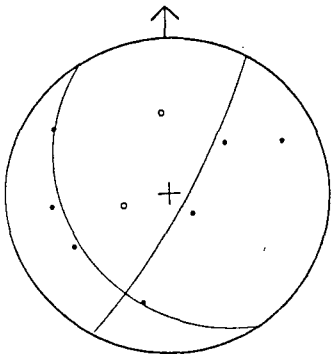

850813 1328

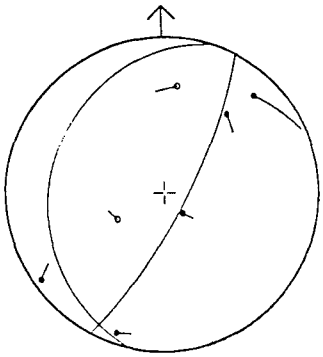

850830 0325

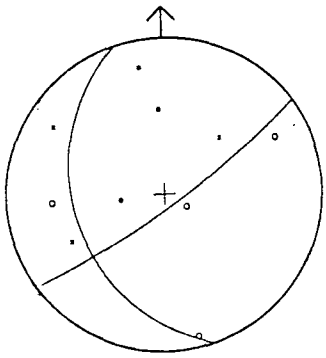

850830 0325

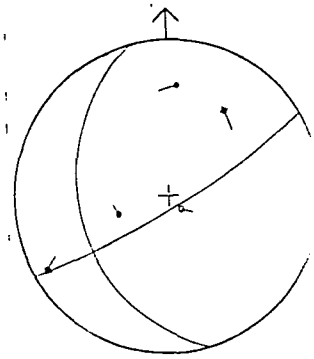

850815 1404

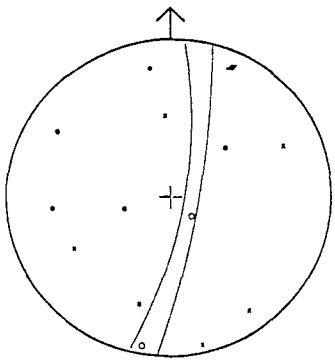

850815 1404

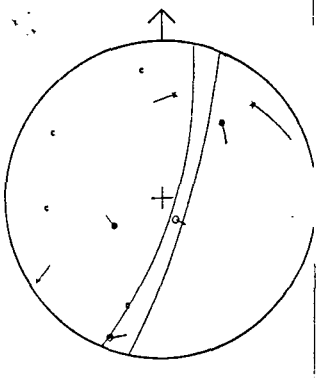

850830 1553

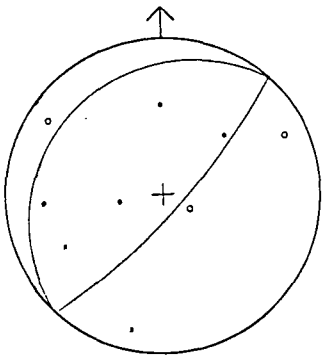

850830 1553

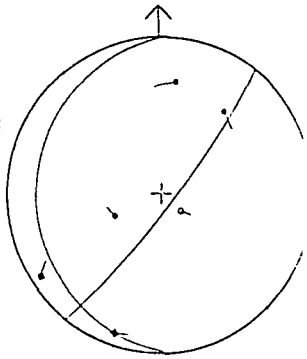

850819 0559

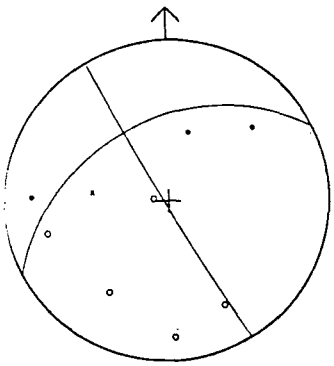

850819 0559

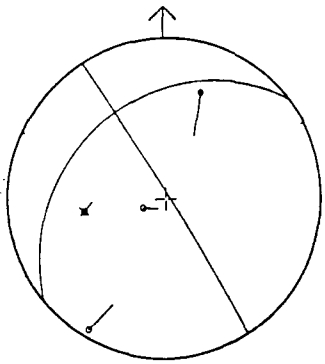

850902 0604

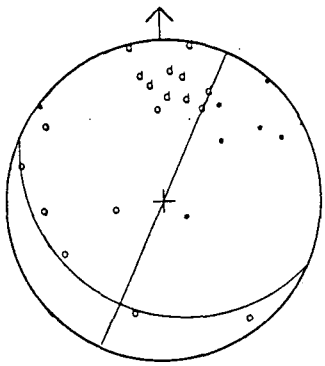

850902 0604

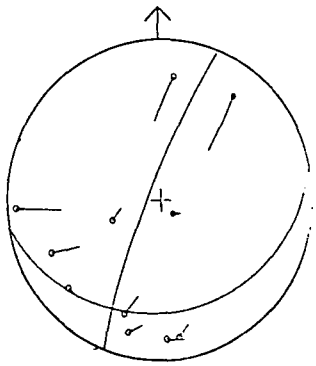

850824 1525

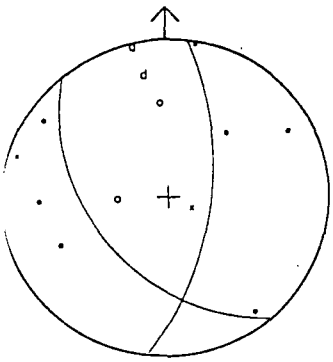

850824 1525

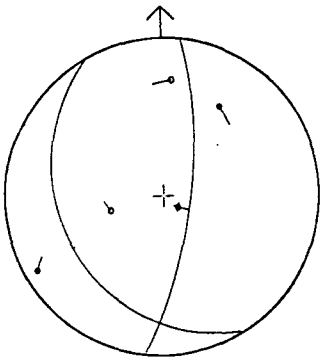

850903 0404

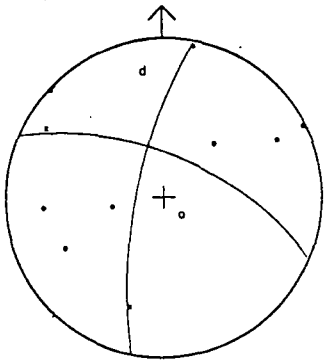

850903 0404

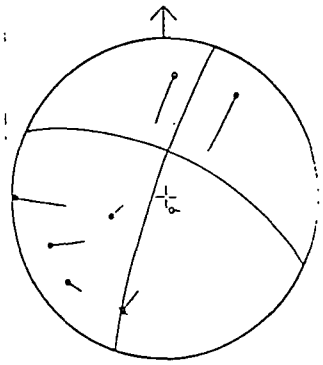

850903 1012

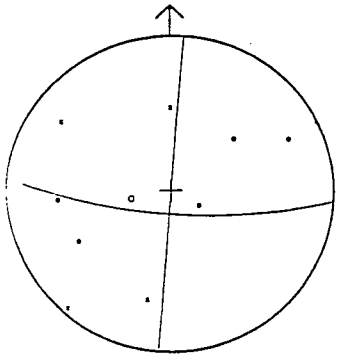

850903 1012

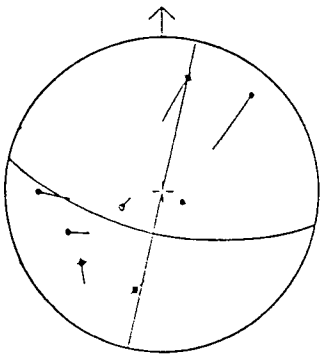

850911 2301

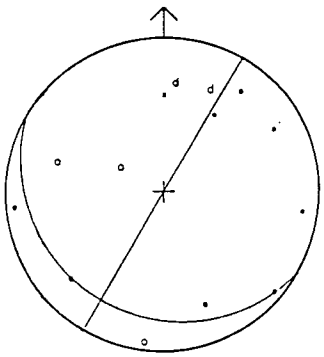

850911 2301

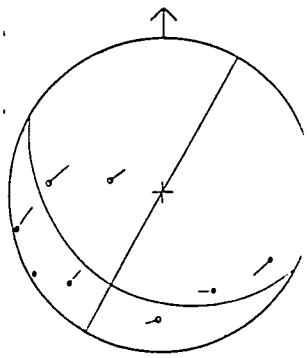

850904 0716

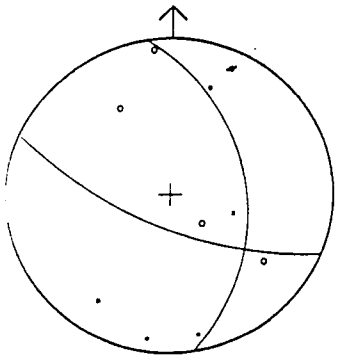

850904 0716

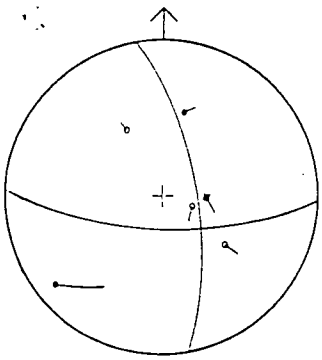

850913 2117

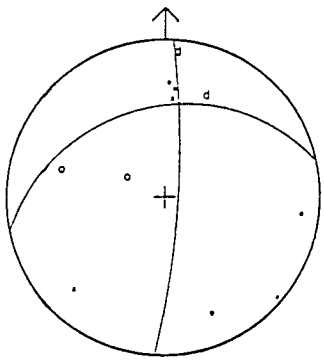

850913 2117

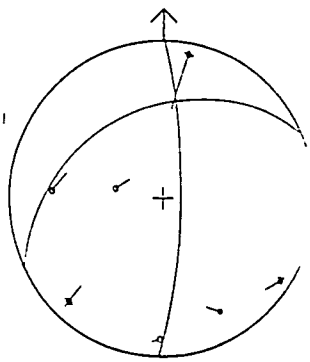

850904 0724

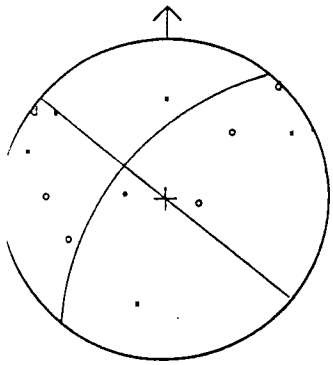

850904 0724

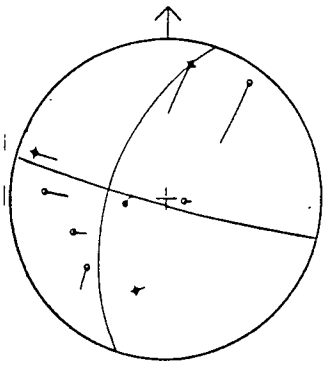

850921 1853

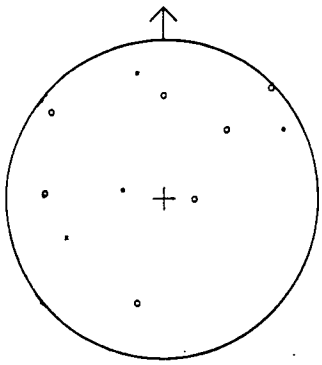

850921 1853

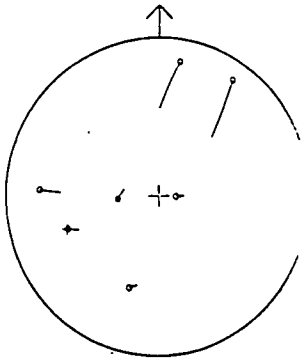

850907 0050

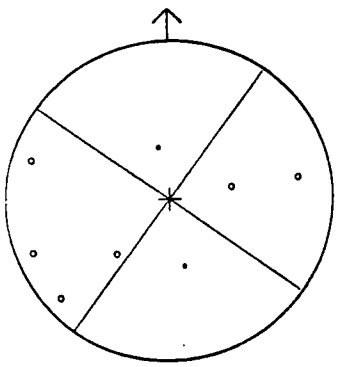

850907 0050

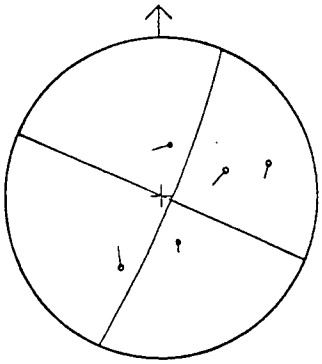

850921 2113

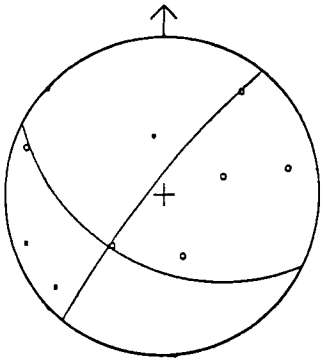

850921 2113

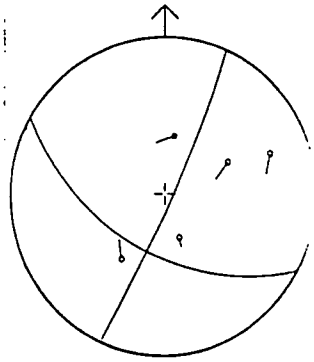

850923 1204

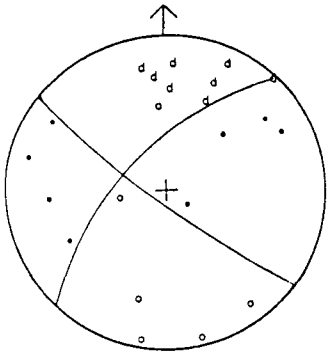

850923 1204